

HZDR-024

PRECISE NUCLEAR PHYSICS FOR THE SUN

Daniel Bemmerer

Wissenschaftlich-Technische Berichte
HZDR-024 · ISSN 2191-8708

WISSENSCHAFTLICH-
TECHNISCHE BERICHTE

hzdr
 HELMHOLTZ
ZENTRUM DRESDEN
ROSSENDORF

Wissenschaftlich-Technische Berichte
HZDR-024

Daniel Bemmerer

PRECISE NUCLEAR PHYSICS FOR THE SUN

HZDR

 **HELMHOLTZ**
| ZENTRUM DRESDEN
| ROSSENDORF

Precise nuclear physics for the Sun

Kumulative Habilitationsschrift

vorgelegt

der Fakultät Mathematik und Naturwissenschaften
der Technischen Universität Dresden

von

Dr. rer. nat. Daniel Bemmerer
geboren am 29.08.1972 in Berlin

Eingereicht am: 25.08.2011

Die Habilitationsschrift wurde in der Zeit von Oktober 2004 bis August 2011 an der Technischen Universität Dresden, Institut für Kern- und Teilchenphysik, und im Helmholtz-Zentrum Dresden-Rossendorf, Institut für Strahlenphysik, angefertigt.

0 List of publications at the base of this habilitation request

Study of the ${}^3\text{He}(\alpha,\gamma){}^7\text{Be}$ reaction at LUNA

- H1 **D. Bemmerer**, F. Confortola, H. Costantini, A. Formicola, Gy. Gyürky, R. Bonetti, C. Brogгинi, P. Corvisiero, Z. Elekes, Zs. Fülöp, G. Gervino, A. Guglielmetti, C. Gustavino, G. Imbriani, M. Junker, M. Laubenstein, A. Lemut, B. Limata, V. Lozza, M. Marta, R. Menegazzo, P. Prati, V. Roca, C. Rolfs, C. Rossi Alvarez, E. Somorjai, O. Straniero, F. Strieder, F. Terrasi and H.P. Trautvetter:
Activation measurement of the ${}^3\text{He}(\alpha,\gamma){}^7\text{Be}$ cross section at low energy.
Phys. Rev. Lett. 97, 122502 (2006).
- H2 Gy. Gyürky, F. Confortola, H. Costantini, A. Formicola, **D. Bemmerer**, R. Bonetti, C. Brogгинi, P. Corvisiero, Z. Elekes, Zs. Fülöp, G. Gervino, A. Guglielmetti, C. Gustavino, G. Imbriani, M. Junker, M. Laubenstein, A. Lemut, B. Limata, V. Lozza, M. Marta, R. Menegazzo, P. Prati, V. Roca, C. Rolfs, C. Rossi Alvarez, E. Somorjai, O. Straniero, F. Strieder, F. Terrasi and H.P. Trautvetter:
 ${}^3\text{He}(\alpha,\gamma){}^7\text{Be}$ cross section at low energies.
Phys. Rev. C 75, 035805 (2007).
- H3 F. Confortola, **D. Bemmerer**, H. Costantini, A. Formicola, Gy. Gyürky, P. Bezzon, R. Bonetti, C. Brogгинi, P. Corvisiero, Z. Elekes, Zs. Fülöp, G. Gervino, A. Guglielmetti, C. Gustavino, G. Imbriani, M. Junker, M. Laubenstein, A. Lemut, B. Limata, V. Lozza, M. Marta, R. Menegazzo, P. Prati, V. Roca, C. Rolfs, C. Rossi Alvarez, E. Somorjai, O. Straniero, F. Strieder, F. Terrasi, and H.P. Trautvetter:
Astrophysical S factor of the ${}^3\text{He}(\alpha,\gamma){}^7\text{Be}$ reaction measured at low energy via detection of prompt and delayed γ rays.
Phys. Rev. C 75, 065803 (2007).

Study of the ${}^{14}\text{N}(p,\gamma){}^{15}\text{O}$ reaction at LUNA

- H4 M. Marta, A. Formicola, Gy. Gyürky, **D. Bemmerer**, C. Brogгинi, A. Caciolli, P. Corvisiero, H. Costantini, Z. Elekes, Zs. Fülöp, G. Gervino, A. Guglielmetti, C. Gustavino, G. Imbriani, M. Junker, R. Kunz, A. Lemut, B. Limata, C. Mazzocchi, R. Menegazzo, P. Prati, V. Roca, C. Rolfs, M. Romano, C. Rossi Alvarez, E. Somorjai, O. Straniero, F. Strieder, F. Terrasi, H.P. Trautvetter, and A. Vomiero:
Precision study of ground state capture in the ${}^{14}\text{N}(p,\gamma){}^{15}\text{O}$ reaction.
Phys. Rev. C 78, 022802(R) (2008).
- H5 M. Marta, A. Formicola, **D. Bemmerer**, C. Brogгинi, A. Caciolli, P. Corvisiero, H. Costantini, Z. Elekes, Zs. Fülöp, G. Gervino, A. Guglielmetti, C. Gustavino, Gy. Gyürky, G. Imbriani, M. Junker, A. Lemut, B. Limata, C. Mazzocchi, R. Menegazzo, P. Prati, V. Roca, C. Rolfs, C. Rossi Alvarez, E. Somorjai, O. Straniero, F. Strieder, F. Terrasi, H.P. Trautvetter, and A. Vomiero:
The ${}^{14}\text{N}(p,\gamma){}^{15}\text{O}$ reaction studied with a composite germanium detector.
Phys. Rev. C 83, 045804 (2011)

Study of the $^{14}\text{N}(p,\gamma)^{15}\text{O}$ reaction at the HZDR Tandetron

- H6 M. Marta, E. Trompler, **D. Bemmerer**, R. Beyer, C. Broggini, A. Caciolli, M. Erhard, Zs. Fülöp, E. Grosse, Gy. Gyürky, R. Hannaske, A.R. Junghans, R. Menegazzo, C. Nair, R. Schwengner, T. Szücs, S. Vezzú, A. Wagner, and D. Yakorev:
Resonance strengths in the $^{14}\text{N}(p,\gamma)^{15}\text{O}$ and $^{15}\text{N}(p,\alpha\gamma)^{12}\text{C}$ reactions.
Phys. Rev. C 81, 055807 (2010).

Study of the $^{15}\text{N}(p,\gamma)^{16}\text{O}$ reaction at LUNA

- H7 **D. Bemmerer**, A. Caciolli, R. Bonetti, C. Broggini, F. Confortola, P. Corvisiero, H. Costantini, Z. Elekes, A. Formicola, Zs. Fülöp, G. Gervino, A. Guglielmetti, C. Gustavino, Gy. Gyürky, M. Junker, B. Limata, M. Marta, R. Menegazzo, P. Prati, V. Roca, C. Rolfs, C. Rossi Alvarez, E. Somorjai, and O. Straniero:
Direct measurement of the $^{15}\text{N}(p,\gamma)^{16}\text{O}$ total cross section at novae energies.
J. Phys. G 36, 045202 (2009).
- H8 A. Caciolli, C. Mazzocchi, V. Capogrosso, **D. Bemmerer**, C. Broggini, P. Corvisiero, H. Costantini, Z. Elekes, A. Formicola, Zs. Fülöp, G. Gervino, A. Guglielmetti, C. Gustavino, Gy. Gyürky, G. Imbriani, M. Junker, A. Lemut, M. Marta, R. Menegazzo, S. Palmerini, P. Prati, V. Roca, C. Rolfs, C. Rossi Alvarez, E. Somorjai, O. Straniero, F. Strieder, F. Terrasi, H.P. Trautvetter, and A. Vomiero:
Revision of the $^{15}\text{N}(p,\gamma)^{16}\text{O}$ reaction rate and oxygen abundance in H-burning zones.
Astronomy & Astrophysics 533, A66 (2011).

Background and feasibility of experiments in underground facilities

- H9 A. Caciolli, L. Agostino, **D. Bemmerer**, R. Bonetti, C. Broggini, F. Confortola, P. Corvisiero, H. Costantini, Z. Elekes, A. Formicola, Zs. Fülöp, G. Gervino, A. Guglielmetti, C. Gustavino, Gy. Gyürky, G. Imbriani, M. Junker, M. Laubenstein, A. Lemut, B. Limata, M. Marta, R. Menegazzo, P. Prati, V. Roca, C. Rolfs, C. Rossi Alvarez, E. Somorjai, O. Straniero, F. Strieder, F. Terrasi, and H.P. Trautvetter:
Ultra-sensitive in-beam γ -ray spectroscopy for nuclear astrophysics at LUNA.
Eur. Phys. J. A 39, 179-186 (2009).
- H10 T. Szücs, **D. Bemmerer**, C. Broggini, A. Caciolli, F. Confortola, P. Corvisiero, Z. Elekes, A. Formicola, Zs. Fülöp, G. Gervino, A. Guglielmetti, C. Gustavino, Gy. Gyürky, G. Imbriani, M. Junker, A. Lemut, M. Marta, C. Mazzocchi, R. Menegazzo, P. Prati, V. Roca, C. Rolfs, C. Rossi Alvarez, E. Somorjai, O. Straniero, F. Strieder, F. Terrasi, and H.P. Trautvetter:
An actively vetoed Clover γ -detector for nuclear astrophysics at LUNA
Eur. Phys. J. A 44, 513-519 (2010).
- H11 T. Szücs, **D. Bemmerer**, T. Cowan, D. Degering, Z. Elekes, Zs. Fülöp, Gy. Gyürky, A. Junghans, M. Köhler, M. Marta, R. Schwengner, A. Wagner, and K. Zuber:
Shallow-underground accelerator sites for nuclear astrophysics: Is the background low enough?
Eur. Phys. J. A 48, 8 (2012).

Reviews

- H12 Carlo Broggini, **Daniel Bemmerer**, Alessandra Guglielmetti, and Roberto Menegazzo: LUNA: Nuclear Astrophysics Deep Underground. **Annu. Rev. Nucl. Part. Science** 60, 53-73 (2010).
- H13 E. G. Adelberger, A. B. Balantekin, **D. Bemmerer**, C. A. Bertulani, J.-W. Chen, H. Costantini, M. Couder, R. Cyburt, B. Davids, S. J. Freedman, M. Gai, A. Garcia, D. Gazit, L. Gialanella, U. Greife, M. Hass, K. Heeger, W. C. Haxton, G. Imbriani, T. Itahashi, A. Junghans, K. Kubodera, K. Langanke, D. Leitner, M. Leitner, L. E. Marcucci, T. Motobayashi, A. Mukhamedzhanov, K. M. Nollett, F. M. Nunes, T.-S. Park, P. D. Parker, P. Prati, M. J. Ramsey-Musolf, R. G. Hamish Robertson, R. Schiavilla, E. C. Simpson, K. A. Snover, C. Spitaleri, F. Strieder, K. Suemmerer, H.-P. Trautvetter, R. E. Tribble, S. Typel, E. Uberseder, P. Vetter, M. Wiescher, and L. Winslow: Solar fusion cross sections II. **Rev. Mod. Phys.** 83, 195-246 (2011).

My contribution to the above publications

Publications H1-H3 result from my postdoc project at INFN Padua. Together with György Gyürky (ATOMKI Debrecen/Hungary), I was responsible for the activation analysis of the LUNA ${}^3\text{He}(\alpha,\gamma){}^7\text{Be}$ experiment. The activation data are the sole basis of papers H1-H2 and contribute half the data of paper H3. Papers H1-H2 were mainly written by me.

Publications H4-H5 concern the LUNA re-measurement of the ${}^{14}\text{N}(p,\gamma){}^{15}\text{O}$ cross section with a Clover detector. They result from the PhD thesis of Michele Marta, a TU Dresden PhD student advised by me at HZDR. I worked closely with Michele on all aspects of this analysis and wrote part of the analysis software. Papers H4-H5 were mainly written by me.

Publication H6 was written by me and results from an experiment at the HZDR 3.3 MV Tandem-tron proposed and led by me. The data are included in the theses of two TU Dresden students advised by me at HZDR: PhD student Michele Marta and Master's student Erik Trompler.

Publication H7 was written by me and results from a re-analysis of the spectra from my PhD thesis, where I had measured the ${}^{14}\text{N}(p,\gamma){}^{15}\text{O}$ cross section with natural nitrogen gas (99.6% ${}^{14}\text{N}$, 0.4% ${}^{15}\text{N}$). In publication H7, I developed a method to extract ${}^{15}\text{N}(p,\gamma){}^{16}\text{O}$ cross sections from the old data. Much of the spectrum integration was done by the Padua PhD student Antonio Caciolli while visiting HZDR. Publication H8 deals with a follow-up experiment by Antonio using solid enriched Ti^{15}N targets, where I led the target analysis and γ -efficiency determination and helped Antonio develop the analysis procedures.

Publications H9-H11 were written by me, and I developed the analysis procedures. The actual spectrum analysis and calculations were performed by the respective first authors, two PhD students (Antonio Caciolli from Padua and Tamás Szűcs from Debrecen).

For publication H12, I contributed text mainly to sections 3, 6, and 7. In addition, I was responsible for the figures, tables, and references. H12 is a review and uses material from publications H1-H4, H7, and H9-H10.

For publication H13, I participated in the working groups on the ${}^3\text{He}(\alpha,\gamma){}^7\text{Be}$, ${}^{14}\text{N}(p,\gamma){}^{15}\text{O}$, and "other CNO" reactions. H13 is a review and uses material from publications H1-H4, and H7.

Contents

0	List of publications at the base of this habilitation request	2
1	Introduction	6
2	State of the art: Astrophysical description of the Sun	7
3	The proton-proton chain of hydrogen burning (papers H1-H3)	9
3.1	Neutrino emissions from the proton-proton chain	9
3.2	Experiment on the ${}^3\text{He}(\alpha,\gamma){}^7\text{Be}$ reaction at LUNA (papers H1-H3)	10
3.3	Outlook	15
4	The carbon-nitrogen-oxygen cycles of hydrogen burning (papers H4-H8)	17
4.1	The ${}^{14}\text{N}(\text{p},\gamma){}^{15}\text{O}$ reaction and the rate of the first cycle (papers H4-H6)	18
4.2	The ${}^{15}\text{N}(\text{p},\gamma){}^{16}\text{O}$ reaction and the onset of the second cycle (papers H7-H8)	22
5	Future accelerator-based science underground (papers H9-H12)	26
5.1	Future science at the present LUNA 0.4 MV facility (paper H12)	26
5.2	Science at a possible higher-energy underground accelerator (papers H11-H12)	28
5.3	Background study in underground laboratories (papers H9-H11)	31
5.4	Possible scientific program at the Felsenkeller facility, Dresden (paper H11)	34
	Acknowledgments	37
	References	38
	Erklärung	49
	Reprints of publications at the base of this habilitation request	50

1 Introduction

For many centuries, the study of the Sun has been an important testbed for understanding stars that are further away. One of the first astronomical observations Galileo Galilei made in 1612 with the newly invented telescope concerned the sunspots, and in 1814, Joseph von Fraunhofer employed his new spectroscope to discover the absorption lines in the solar spectrum that are now named after him.

Even though more refined and new modes of observation are now available than in the days of Galileo and Fraunhofer, the study of the Sun is still high on the agenda of contemporary science, due to three guiding interests.

The first is connected to the ages-old human striving to understand the structure of the larger world surrounding us. Modern telescopes, some of them even based outside the Earth's atmosphere in space, have succeeded in observing astronomical objects that are billions of light-years away. However, for practical reasons precision data that are important for understanding stars can still only be gained from the Sun. In a sense, the observations of far-away astronomical objects thus call for a more precise study of the closeby, of the Sun, for their interpretation.

The second interest stems from the human desire to understand the essence of the world, in particular the elementary particles of which it consists. Large accelerators have been constructed to produce and collide these particles. However, man-made machines can never be as luminous as the Sun when it comes to producing particles. Solar neutrinos have thus served not only as an astronomical tool to understand the Sun's inner workings, but their behavior on the way from the Sun to the Earth is also being studied with the aim to understand their nature and interactions.

The third interest is strictly connected to life on Earth. A multitude of research has shown that even relatively slight changes in the Earth's climate may strongly affect the living conditions in a number of densely populated areas, mainly near the ocean shore and in arid regions. Thus, great effort is expended on the study of greenhouse gases in the Earth's atmosphere. Also the Sun, via the solar irradiance and via the effects of the so-called solar wind of magnetic particles on the Earth's atmosphere, may affect the climate. There is no proof linking solar effects to short-term changes in the Earth's climate. However, such effects cannot be excluded, either, making it necessary to study the Sun.

The experiments summarized in the present work contribute to the present-day study of our Sun by repeating, in the laboratory, some of the nuclear processes that take place in the core of the Sun. They aim to improve the precision of the nuclear cross section data that lay the foundation of the model of the nuclear reactions generating energy and producing neutrinos in the Sun.

In order to reach this goal, low-energy nuclear physics experiments are performed. Wherever possible, the data are taken in a low-background, underground environment. There is only one underground accelerator facility in the world, the Laboratory Underground for Nuclear Astrophysics (LUNA) 0.4 MV accelerator in the Gran Sasso laboratory in Italy. Much of the research described here is based on experiments at LUNA. Background and feasibility studies shown here lay the base for future, higher-energy underground accelerators. Finally, it is shown that such a device can even be placed in a shallow-underground facility such as the Dresden Felsenkeller without great loss of sensitivity.

2 State of the art: Astrophysical description of the Sun

A commonly used model of the inner workings of the Sun has been developed by John Bahcall over several decades [1] and has come to be called the standard solar model (SSM). Taking as its input the elemental composition and core temperature of the Sun, the SSM makes predictions for many observables. They include the total energy output, the inner structure of the Sun, as observed via the sound speed and density profiles, and the spectrum of emitted neutrinos (fig. 1). This latter observable proved to offer particularly rich insight, so it is discussed in some detail here.

Soon after the discovery of the neutrino [2], Ray Davis Jr. started observing the neutrinos emitted in the Sun, using the radiochemical detection of ^{37}Ar produced by the $^{37}\text{Cl}(\nu_e, e^-)^{37}\text{Ar}$ reaction [3]. The ^{37}Cl target was included in a large-scale underground detector in the Homestake former gold mine in South Dakota. The data were consistently a factor of two to three lower than what was predicted from the standard solar model. This discrepancy came to be called the solar neutrino problem.

After the Davis results were confirmed by a number of other radiochemical neutrino detectors [4, and references therein], attention turned to nuclear physics uncertainties as the possible solution to the problem. The relatively high-energy neutrinos emitted by the decays of ^7Be and ^8B , with their comparatively high probability of generating a signal in the detector, dominate the detected signal. One possible nuclear physics solution of the solar neutrino problem was a much higher rate of the $^3\text{He}(^3\text{He}, 2p)^4\text{He}$ reaction, due to a suggested narrow resonance near solar energies. This would have led to a reduction in importance of the pp-II and pp-III branches producing the ^7Be and ^8B neutrinos (sec. 3). However, a measurement of the $^3\text{He}(^3\text{He}, 2p)^4\text{He}$ cross section directly at the relevant energies failed to find such a resonance [5]. A strong reduction in the $^3\text{He}(\alpha, \gamma)^7\text{Be}$ cross section would have had the same result, but was also ruled out by experiment [H1].

Instead, the solar neutrino problem was finally solved by the discovery that neutrinos change flavor. Some of neutrinos of electron flavor emitted in the Sun are eventually detected as μ or τ flavor neutrinos on Earth [7]. Consequently, the predicted neutrino flux from the standard solar model and the observed neutrino flux were for the first time in mutual agreement.

However, soon thereafter a new problem emerged, called the solar abundance problem. Upgraded, three-dimensional models of the processes leading to the solar Fraunhofer absorption lines resulted in a downward revision of the deduced abundances of many elements that are heavier than helium, including carbon, nitrogen, and oxygen [8]. When using the standard assumption of a homogeneous elemental abundance over the entire Sun, these lower abundances for the "heavy" elements lead to a sound speed profile that is inconsistent with helioseismological measurements.

This as-yet unsolved problem [9] may be addressed by solar neutrino detectors [10]. The running Borexino [11] and the planned SNO+ [12] detectors expect to be sensitive not only to the monoenergetic neutrinos from the electron capture decay of ^7Be , but also to the neutrino fluxes from the β^+ decays of ^{13}N and ^{15}O . These neutrinos are emitted in the Bethe-Weizsäcker cycle of hydrogen burning (sec. 4). As this cycle contributes just 0.8% to the energy production of the Sun [6], it can be argued [10] that in good approximation the energy production, and the central temperature, are determined only by the pp-chain, as probed by the ^7Be and ^8B neutrinos. Those neutrino fluxes can therefore serve as thermometers for the solar core. In order to calibrate them, sufficiently precise nuclear physics data are needed, e.g. on the $^3\text{He}(\alpha, \gamma)^7\text{Be}$

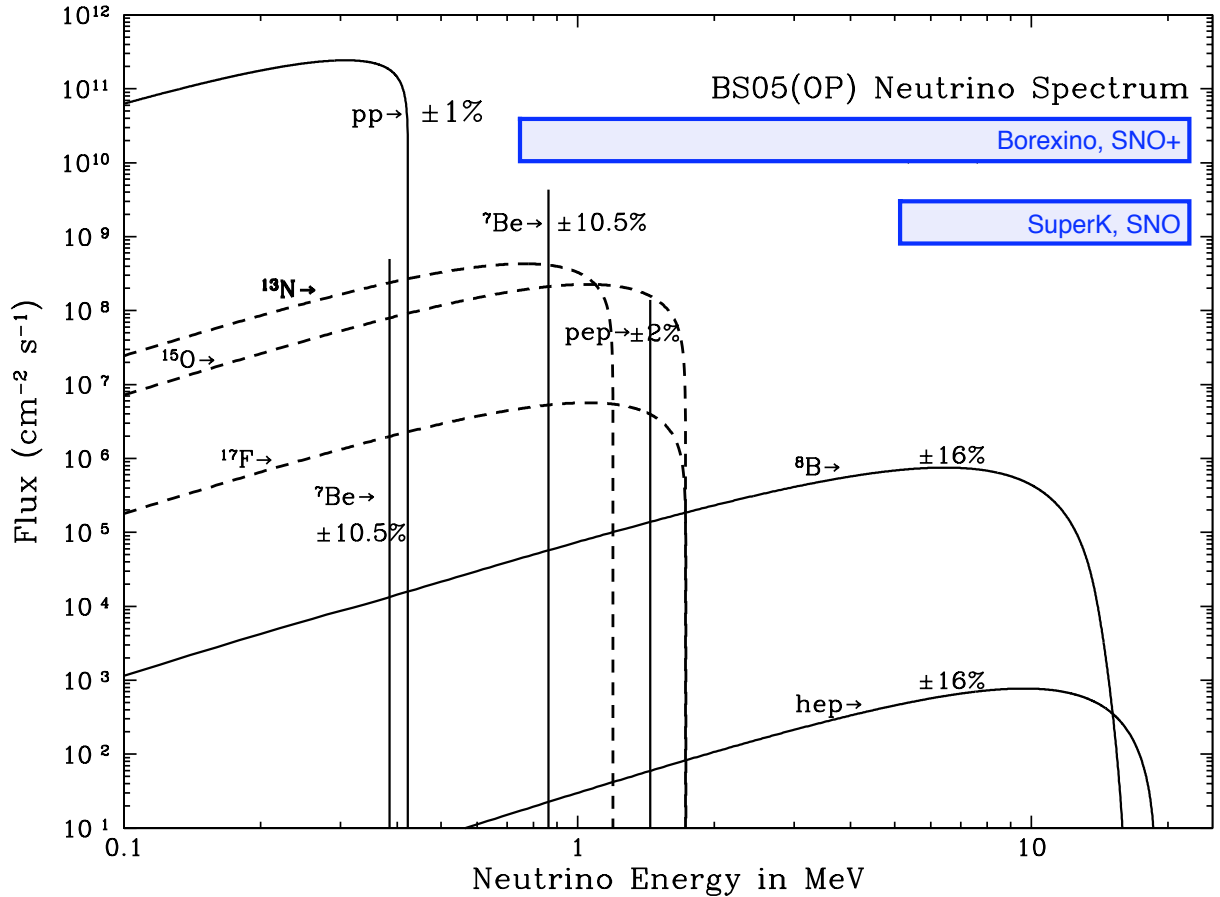


Figure 1: Predicted energy spectrum of solar neutrinos, according to the BS05 [6] update of the standard solar model. Figure taken from [6], adding the approximate sensitivity ranges for four Cherenkov-effect based neutrino detectors.

reaction (sec. 3.2).

Once the central temperature of the Sun has been determined, the flux of the ^{13}N and ^{15}O neutrinos can then be used to derive the amount of carbon and nitrogen in the solar core, independently from the elemental abundance measurements in the solar atmosphere. Also for this determination of the ^{12}C and ^{14}N abundances, precise nuclear physics data are needed, mainly on the $^{12}\text{C}(p,\gamma)^{13}\text{N}$ (sec. 5.1) and $^{14}\text{N}(p,\gamma)^{15}\text{O}$ (sec. 4.1) reactions.

The present work addresses the need for precise nuclear physics input data for the Sun, by providing improved nuclear reaction cross section data for the $^3\text{He}(\alpha,\gamma)^7\text{Be}$ and $^{14}\text{N}(p,\gamma)^{15}\text{O}$ reactions.

3 The proton-proton chain of hydrogen burning (papers H1-H3)

3.1 Neutrino emissions from the proton-proton chain

The proton-proton-chain (pp-chain) of hydrogen burning contributes 99.2% to the solar luminosity [6] and is therefore quasi solely responsible for energy generation in the Sun. Its rate is determined by the ${}^1\text{H}(p, e^+ \nu_e) {}^2\text{H}$ cross section, the so-called pp-reaction. Due to its very low value, this cross section cannot be studied in the laboratory with present techniques. However, theoretical calibrations have recently become rather precise, and an uncertainty of 0.9% has been recommended for its S-factor [H13]. The competing so-called pep-reaction ${}^1\text{H}(p, e^-, \nu_e) {}^2\text{H}$ plays only a minor role (fig. 2).

After the combustion of ${}^2\text{H}$ to ${}^3\text{He}$ via the ${}^2\text{H}(p, \gamma) {}^3\text{He}$ reaction [13], the pp-chain splits into three major branches, called pp-I, pp-II, and pp-III, respectively. The so-called hep branch given by the ${}^3\text{He}(p, e^+ \nu_e) {}^4\text{He}$ reaction has the highest neutrino endpoint energy of all pp-chain reactions (fig. 1), but plays no practical role due to its very low rate.

The pp-I branch directly converts ${}^3\text{He}$ to ${}^4\text{He}$ via the ${}^3\text{He}({}^3\text{He}, 2p) {}^4\text{He}$ reaction and dominates all other branches, burning 85% of the ${}^3\text{He}$. It leads to no further neutrino emission beyond the so-called pp-neutrinos from the ${}^1\text{H}(p, e^+ \nu_e) {}^2\text{H}$ reaction.

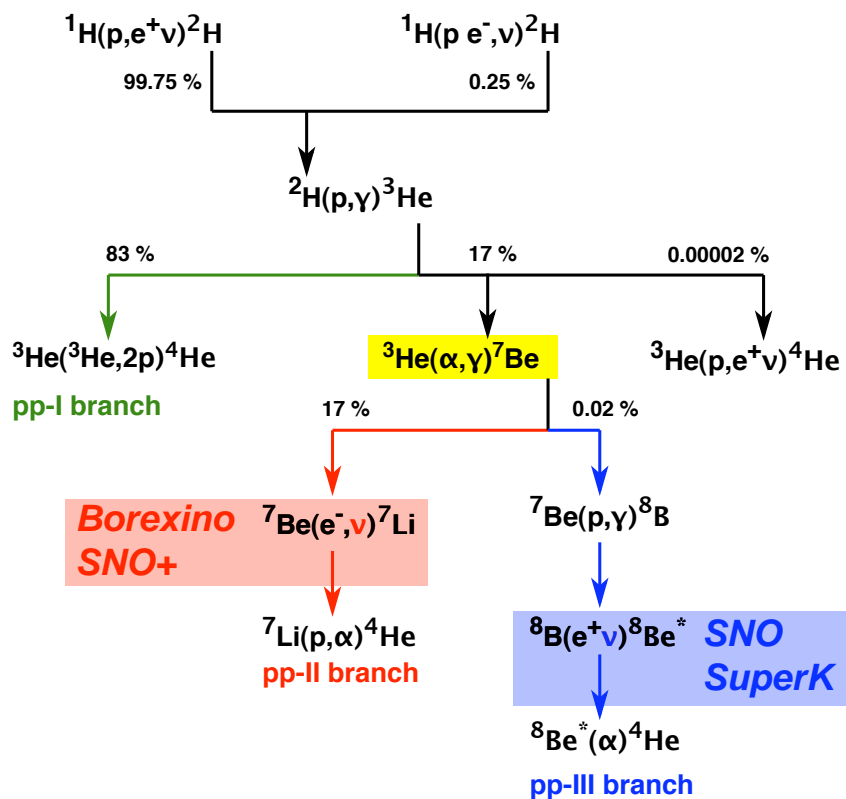


Figure 2: Nuclear reactions of the proton-proton chain (pp chain) of hydrogen burning. The three main branches pp-I (green), pp-II (red), and pp-III (blue) are given. The neutrinos detectable in modern Cherenkov-effect based detectors result from branches pp-II and pp-III and are indicated.

The pp-II and pp-III branches are both initiated by the ${}^3\text{He}(\alpha,\gamma){}^7\text{Be}$ reaction, and their rate scales almost linearly with its rate [14]. Together, these branches contribute about 17% to the Sun's luminosity. The ${}^7\text{Be}$ and ${}^8\text{B}$ neutrinos already detected in modern-day Cherenkov-effect based neutrino detectors (SNO, SuperK, Borexino, and SNO+) are due to the pp-II and pp-III chains.

Most prominent are the neutrinos from the β^+ decay of ${}^8\text{B}$ in the pp-III branch, which reach up to high energies in the spectrum due to the β -decay Q -value of 17.980 MeV and are therefore detected with relative ease. Recently, the neutrinos from the electron capture (EC) decay of ${}^7\text{Be}$ (Q -value 0.862 MeV) have been detected in the Borexino detector [11]. The same is expected for SNO+. The ${}^7\text{Be}$ EC neutrinos show two sharp lines at 0.384 and 0.862 MeV, the latter of which has already been detected. The signal of these lines can be separated from the background more easily than the neutrino continuum from β decay.

For the ${}^7\text{Be}$ and ${}^8\text{B}$ neutrino fluxes, highly precise data are now available. More than 10,000 ${}^8\text{B}$ neutrino events have been detected in the SuperK detector alone [15, 16]. When combining with the SNO data, the total uncertainty on this neutrino flux is ${}^{+2.4\%}_{-3.0\%}$ [17]. This number presupposes the Mikheyev-Smirnov-Wolkenstein (MSW) neutrino oscillation mechanism with a large mixing angle, which is favored by the SNO data [17]. For the ${}^7\text{Be}$ neutrino flux, the uncertainty quoted by the Borexino detector is currently 10%, a number that is expected to improve further as more statistics and a better understanding of systematic effects become available [11].

The precision of the neutrino flux data should be compared with the lesser precision of the nuclear physics input. For the ${}^3\text{He}(\alpha,\gamma){}^7\text{Be}$ cross section affecting both ${}^8\text{B}$ and ${}^7\text{Be}$ neutrino fluxes, the generally accepted uncertainty, before the present work started, was 9% [18]¹. The ${}^3\text{He}(\alpha,\gamma){}^7\text{Be}$ rate affects these two neutrino fluxes with a logarithmic derivative of 0.878 (${}^7\text{Be}$) and 0.846 (${}^8\text{B}$), respectively [14]. Therefore, just this one reaction already contributed $0.878 \times 9\% = 7.9\%$ ($0.846 \times 9\% = 7.6\%$) uncertainty to the ${}^7\text{Be}$ (${}^8\text{B}$) fluxes. This is the major nuclear physics contribution to the uncertainty, so further experimental study is clearly warranted.

Before describing the LUNA ${}^3\text{He}(\alpha,\gamma){}^7\text{Be}$ experiment, the other major nuclear physics uncertainty affecting the ${}^8\text{B}$ neutrino rate (but not the ${}^7\text{Be}$ neutrino rate) should be mentioned: The ${}^7\text{Be}(p,\gamma){}^8\text{B}$ reaction. Helped by a recent experiment [21, 22], the presently accepted uncertainty for this reaction rate is 7.5% [H13]. The logarithmic derivative for the ${}^8\text{B}$ neutrino flux is 1.0 [14], so it contributes 7.5% to the uncertainty of the predicted ${}^8\text{B}$ flux.

3.2 Experiment on the ${}^3\text{He}(\alpha,\gamma){}^7\text{Be}$ reaction at LUNA (papers H1-H3)

The ${}^3\text{He}(\alpha,\gamma){}^7\text{Be}$ reaction was studied at LUNA using both of the previously accepted techniques: First, the cross section was determined based on the offline determination of the ${}^7\text{Be}$ activity created in the experiment. In a second step, also the promptly emitted γ -rays from the reaction were detected and analyzed. For three runs at different beam energies, both methods were used in parallel, allowing to check for possible systematic discrepancies between them. Just such a systematic discrepancy between activation and in-beam γ method had previously been suggested, giving rise to some uncertainty [18].

The setup (fig. 3) consisted of a windowless ${}^3\text{He}$ gas target, with the pressure gradient maintained by differential pumping in three pumping stages. The ${}^3\text{He}$ gas from the exhaust of the pumps was collected, purified in a chemical getter and recirculated into the target. The buildup

¹Somewhat different uncertainties had been estimated by NACRE [19, 17%] and by Descouvemont [20, 8%]. However, the 9% recommended by the "Solar Fusion Cross Sections I" expert forum [18] was more widely accepted.

of impurities passing the getter, which mainly consisted of surviving nitrogen, was monitored using the particle spectra from double elastic scattering of the $^4\text{He}^+$ beam, firstly on the target gas (^3He and impurities), secondly on a carbon scattering foil to limit the scattered particle flux.

The aimed at systematic uncertainty for the cross section determination was 3%, very ambitious for a nuclear astrophysics experiment but necessary in order to match the precision given by the neutrino flux data. Therefore, the properties of beam, target, and detection system each had to be known to better than 3%.

The beam intensity was determined with a beam calorimeter with constant temperature gradient [23] going from 70°C at the hot side to 0°C at the cold side. It was electrically calibrated to 1.5% precision. The target pressure and temperature without beam were determined using a mockup chamber, containing ports to insert pressure and temperature gauges, prior to the experiment to better than 1% precision. With beam, the effective target density is reduced due to the beam heating effect [24], leading to an effective thinning of the gas due to the heat deposited by the beam. This effect was studied with the elastic scattering device of the present setup, giving the effective target density with 1.5% uncertainty [25].

For the activation method, the detection efficiency is given by the product of the efficiency to catch created ^7Be nuclei and the efficiency of the offline counting. For ^7Be created in the main gas target chamber, the geometric detection efficiency of the primary ^7Be catcher (spectrum in fig. 4, left panel), consisting of a copper cap mounted on the calorimeter hot side, is 100% due to the kinematic forward focusing of the reaction products. However, some ^7Be nuclei are elastically backscattered from the copper surface of the catcher. This effect was studied in a GEANT4 [26] simulation and by experiment. Experimentally, aluminium foil was mounted on the sides of the target chamber, forming a secondary catcher for backscattered ^7Be . Indeed,

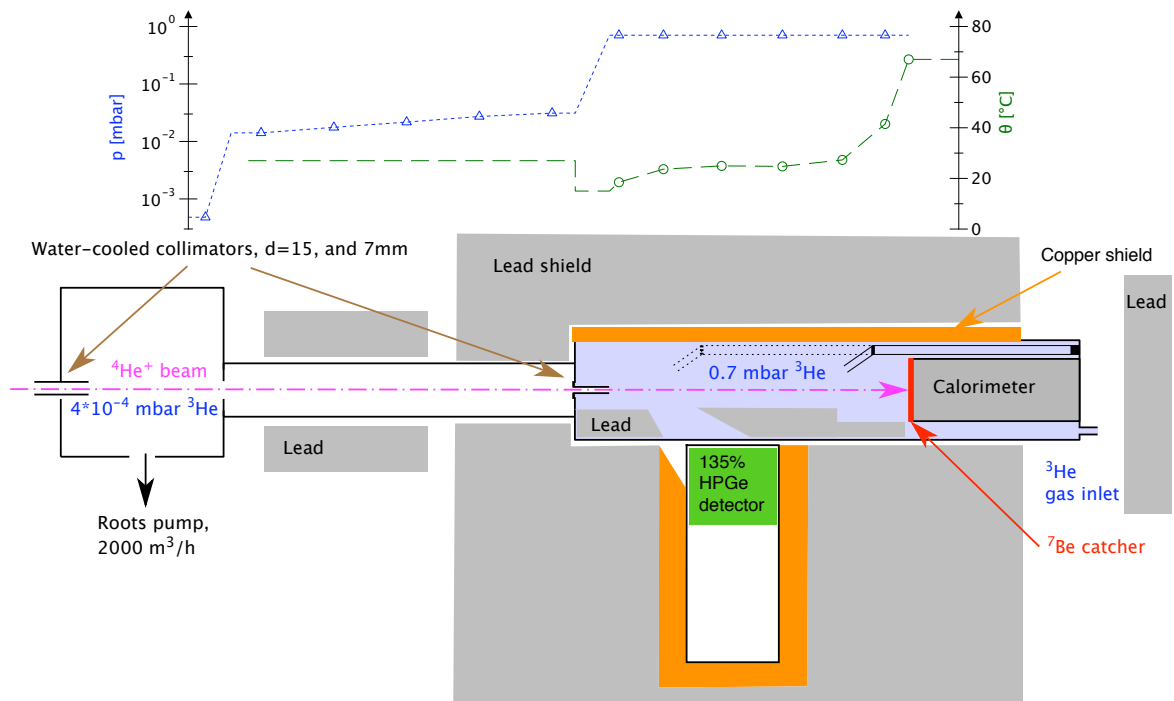


Figure 3: Setup for the study of the $^3\text{He}(\alpha,\gamma)^7\text{Be}$ reaction at LUNA. Above the drawing, the measured pressure (blue) and temperature (green) profiles are shown, for the positions along the beam axis shown in the drawing.

as predicted by the simulations, a tiny ${}^7\text{Be}$ activity of 0.8 mBq was found on the aluminium foil, detectable only in the very low background setting of the Gran Sasso deep underground γ -counting facility (fig. 4, upper right panel).

Further collection losses may occur if ${}^7\text{Be}$ is created not inside the main target chamber, but already in the low-pressure gas tube leading up to it or inside the narrow, 40 mm long collimator separating tube and main target chamber. Again, this effect was simulated and a specially prepared collimator catcher was mounted, showing a correction of 6.8 mBq (fig. 4, lower right panel) for an experiment with 316 mBq activity detected on the main catcher. The precise knowledge of these two corrections was crucial for the final precision attained.

Due to the low ${}^7\text{Be}$ activities of always less than 1 Bq, the activated catchers had to be counted in very close geometry, just a few mm above the endcap of the ultra low background high-purity germanium (HPGe) detector. In this geometry, it is very difficult to precisely calibrate the detection efficiency. Therefore, dedicated ${}^7\text{Be}$ calibration sources in the 100 Bq activity range were created, their activity was determined in far geometry based on ${}^{137}\text{Cs}$, ${}^{60}\text{Co}$, and ${}^{22}\text{Na}$ sources, and then they were used to calibrate the detector in close geometry. With this method, simulation based corrections could be minimized, and the counting efficiency was determined to $\pm 1.8\%$. The branching ratio for the emission of the 478 keV γ -ray in ${}^7\text{Be}$ decay is very precisely known, $(10.44 \pm 0.04)\%$ [27].

Based on these considerations, the final systematic uncertainty in the cross section determined by the activation method was 3.0% [H1-H3]. The in-beam γ -spectrometry data had a slightly higher systematic uncertainty of 3.6% due to the unknown γ -ray angular distribution [H3].

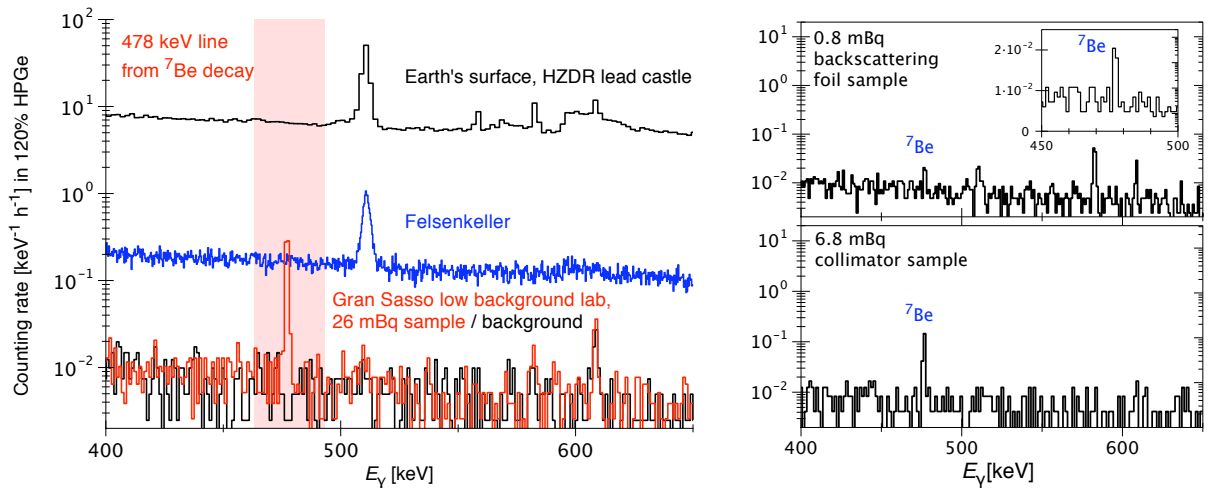


Figure 4: ${}^7\text{Be}$ spectra from the activation study of the ${}^3\text{He}(\alpha,\gamma){}^7\text{Be}$ reaction at LUNA. Left panel: weakest main ${}^7\text{Be}$ catcher studied (red), compared to the laboratory background in the Gran Sasso low background laboratory detector used for the study (black). The background is compared with that observed in the Felsenkeller shallow-underground facility [28] and in a state of the art lead shield at the Earth's surface [29]. – Right panel: The two weakest samples, showing the secondary catcher for backscattered ${}^7\text{Be}$ (top right), and the collimator catcher for ${}^7\text{Be}$ produced before the beam enters the main target chamber (bottom right).

The data points are then expressed as the astrophysical S-factor $S(E)$ [30, 31]

$$S(E) = \sigma(E) \cdot E \cdot \exp\left(2\pi\alpha Z_p Z_t \sqrt{\frac{\mu c^2}{2E}}\right) \quad (1)$$

with E the center-of-mass energy, $\sigma(E)$ the cross section, α the fine-structure constant, Z_p and Z_t the nuclear charges of target and projectile, $\mu = m_p m_t / (m_p + m_t)$ the reduced mass formed from projectile mass m_p and target mass m_t , and c the speed of light. This form removes the energy dependence of the cross section due to the Coulomb barrier penetrability and to kinematics.

The new LUNA data (fig.5, [H1-H3]) are lower in energy than ever before, so that now the entire Gamow peak for Big Bang nucleosynthesis is covered with experimental data.

A direct comparison of the LUNA data with other works is difficult, because they do not overlap in energy. Any comparison needs to assume some energy dependence, for example that of the Descouvemont R-matrix fit [20]. When rescaling this fit up to match the LUNA data, it is found to be in very good agreement with previous data from a higher-energy activation experiment by Nara Singh *et al.* at the Weizmann Institute [32]. However, after publication of the LUNA data, new data by Brown *et al.* from Seattle, using both activation and in-beam γ -spectrometry [33], at the same energy range as Nara Singh, suggest the S-factor may be even higher. Even

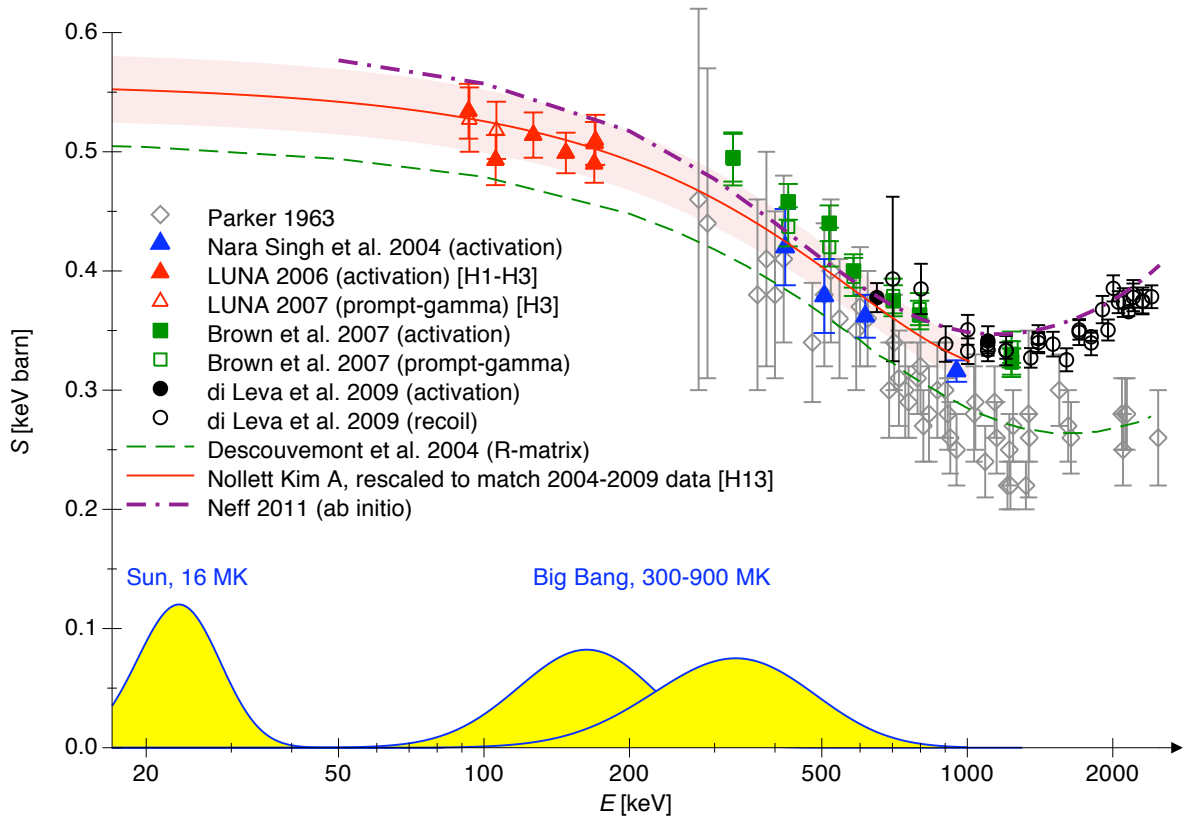


Figure 5: Astrophysical S-factor of the ${}^3\text{He}(\alpha, \gamma){}^7\text{Be}$ reaction from modern experiments [32–34] and [H1-H3], a previous R-matrix fit [20], a theoretical curve rescaled to match the modern data [H13], and ab-initio theory [35]. The historical Parker and Kavanagh data [36] are shown for comparison. The Gamow peaks for the Sun and for Big Bang nucleosynthesis have been added.

more recent data by di Leva *et al.* at Bochum using the ERNA recoil separator in addition to the activation and in-beam γ -spectroscopy methods at high energies [34] also lie higher than the rescaled Descouvemont curve.

Without considering whether or not data are directly at astrophysical energies, the following conclusion can be drawn: Of the four different modern experiments, two are consistent with Descouvemont $\times 1.08$ (Nara Singh *et al.* [32], LUNA [H1-H3]), two others with Descouvemont $\times 1.18$ (Brown *et al.* [33], di Leva *et al.* [34]). On a 2σ confidence level, all four experiments are consistent.

Therefore, a combined fit of these four data sets has been performed [H13]. This fit took also the distance between the experimental energies and the solar Gamow peak into account, by including a theoretical uncertainty for the extrapolation. The fit has been limited to data with $E < 1$ MeV, an energy range where there is less disagreement between the different theoretical curves [37–41, e.g.] than when including also higher energies. Because the data from the four modern works are comparatively better-documented, previous experiments [36, 42–49] were left out of the fit [H13]. Adopting the Nollett [41] implementation of Kim's [37] potential "A" and rescaling it to match the data from the four modern experiments, an average curve and uncertainty have been derived (fig. 5, red curve and shaded red area). This procedure results in a recommended S-factor of $S_{34}(0) = 0.56 \pm 0.02_{\text{exp}} \pm 0.02_{\text{theo}}$, i.e. with 3.6% experimental uncertainty [H13].

The experimental and theoretical situation in the ${}^3\text{He}(\alpha, \gamma){}^7\text{Be}$ reaction at $E > 1$ MeV has recently attracted much attention. This is so because at $E \approx 2$ MeV the recent di Leva data [34] are about 40% higher than the data by Parker and Kavanagh [36]. Those 50-year old data [36] follow the trend of the modern data very well for $E < 1$ MeV, with a normalization that is the recommended curve [H13] times a factor of 0.92. Also, the upwards turn taken by the di Leva data at $E > 1$ MeV is not in agreement with the energy dependence of the frequently used theoretical curves by Kajino [38] and Nollett [41].

In this framework, it is intriguing that the very recent ab-initio calculation by Neff using the fermionic molecular dynamics approach [35] reproduces the upturn of the di Leva data. Also at lower energies, the energy dependence and the absolute scale of the S-factor are very well reproduced by Neff. However, when closely inspecting the low-energy region, one sees that Neff overpredicts the LUNA data by 7%, more than their systematic uncertainty of just 3% [H1-H3]. Even still, it remains impressive and highly encouraging for the future that an essentially parameter-free theory manages to reproduce the experimental data so well over such a large energy range.

Taking the recommended [H13] $S_{34}(0) = 0.56 \pm 0.02_{\text{exp}} \pm 0.02_{\text{theo}}$ keV barn and combining experimental and theoretical uncertainties in quadrature, as they are uncorrelated, one arrives at 5% precision for the reaction rate, half the previous value of 9% [18].

Using again the logarithmic derivatives of 0.878 (${}^7\text{Be}$) and 0.846 (${}^8\text{B}$), respectively [14], the ${}^3\text{He}(\alpha, \gamma){}^7\text{Be}$ reaction rate alone now contributes 4.4% uncertainty to the solar ${}^7\text{Be}$ neutrino flux and 4.2% uncertainty to the solar ${}^8\text{B}$ neutrino flux, much less than before. Recalling that there is just 3.0% uncertainty for the measured ${}^8\text{B}$ solar neutrino flux [17], it is clear that significant progress has been achieved, but some future work is still necessary before the predicted ${}^8\text{B}$ neutrino flux has the same precision as the measured one.

3.3 Outlook

Regarding the ${}^3\text{He}(\alpha,\gamma){}^7\text{Be}$ reaction, it is clear from fig. 5 that the recommended curve [H13], while closely following the low-energy LUNA data [H1-H3], is a compromise between only marginally consistent experimental data at higher energy [32–34]. To address this problem, one new experiment should connect the low-energy LUNA data with the range up to 2 MeV, serving several purposes at the same time.

First, such an experiment should obtain at least one data point inside the solar Gamow peak, at least partially removing the need for extrapolations for the Sun. Second, it should resolve the tension between the different experiments around 1 MeV, decisively improving the uncertainty of any extrapolation. Third, it should address the energy region near 2 MeV where the Neff [35] theory curve nicely reproduces one of the two existing data sets, the di Leva one [34], whereas the previous data set [36] is much lower.

Using the given setup for the LUNA ${}^3\text{He}(\alpha,\gamma){}^7\text{Be}$ experiment [H1-H3] and the activation technique, at LUNA-0.4 MV the luminosity is sufficient to obtain a data point at $E = 35$ keV, at the upper edge of the solar Gamow peak, with an irradiation time of several months. At this energy, both screening and sputtering corrections would still be below 10%, so that they would not limit the uncertainty. The same setup could then be transported to a higher-energy accelerator, either one placed underground or with access to an underground activity-counting facility, for taking data up to 2 MeV.

A complementary approach to improve the knowledge on the ${}^3\text{He}(\alpha,\gamma){}^7\text{Be}$ reaction is to study

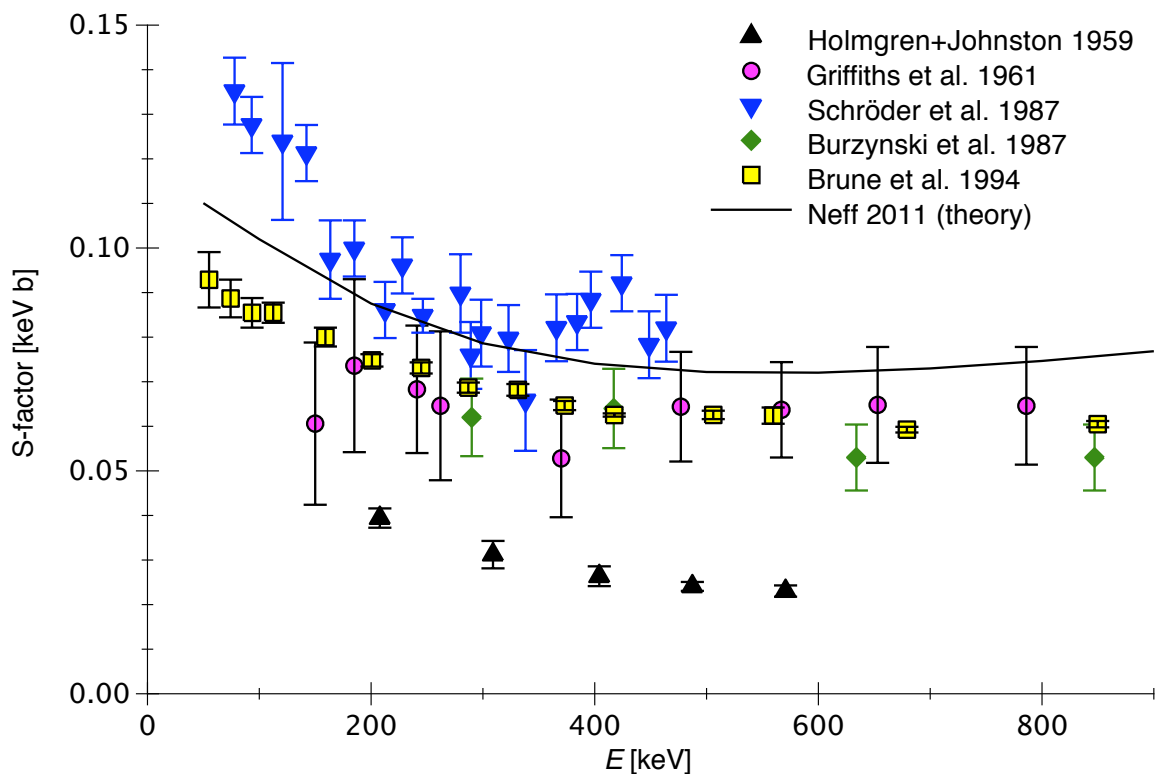


Figure 6: Astrophysical S-factor of the ${}^3\text{H}(\alpha,\gamma){}^7\text{Li}$ reaction from different experimental works [42, 50–53] and from theory [35].

its isospin mirror, the ${}^3\text{H}(\alpha,\gamma){}^7\text{Li}$ reaction. Also for this reaction, the ab initio work by Neff [35] presents an excitation function. Again, the energy dependence is very well reproduced, but in this case the generally adopted dataset by Brune *et al.* [53] is overpredicted by 15%, more than its systematic uncertainty of 6% (fig. 6).

Such an experiment would in principle be possible at the TU Dresden deuterium-tritium neutron generator in Rossendorf. The ion source normally supplying the deuterium beam would have to be run with helium gas instead, which involves little more than switching the gas supply and operating at different source parameters. In addition, a special, well-characterized tritium target would be necessary, supplanting the high-power resistant but less well-characterized D-T tritium target.

If an uncertainty below 10% is reached, such an experiment would be able to decide whether the Brune dataset [53] or the Neff calculation [35] are correct. By either strengthening or weakening the case for the correctness of the absolute scale of the Neff ab initio calculation, such an experiment would also have an impact on the understanding of the isospin mirror reaction, ${}^3\text{He}(\alpha,\gamma){}^7\text{Be}$.

4 The carbon-nitrogen-oxygen cycles of hydrogen burning (papers H4-H8)

The existence of the catalytic carbon-nitrogen-oxygen cycle of hydrogen burning was first postulated in 1938, by Hans Bethe [54] and Carl-Friedrich von Weizsäcker [55]. At the time, there was some debate on who of the two eminent scientists should be credited with the original discovery, and nowadays the CNO cycle is also called Bethe-Weizsäcker cycle to honor them both. Originally, it had been believed that this cycle dominates nuclear fusion in the Sun. According to the most recent solar model it contributes just 0.8% to the total solar luminosity [9]. The operation of the cycle presupposes the existence of ^{12}C as catalyst, which is almost completely transformed to ^{14}N over several millions of years. When the cycle has reached its equilibrium, a series of (p,γ) and (p,α) reactions and β^+ decays transforms four protons into one helium nucleus (fig. 7). There are three major sub-cycles:

1. The first cycle (also called CN cycle) starts with the $^{12}\text{C}(p,\gamma)^{13}\text{N}$ reaction, and its loop is closed by the $^{15}\text{N}(p,\alpha)^{12}\text{C}$ reaction (blue arrows in fig. 7).
2. The second cycle (also called NO cycle) starts with the $^{15}\text{N}(p,\gamma)^{16}\text{O}$ reaction, and its loop is closed by the $^{17}\text{O}(p,\alpha)^{14}\text{N}$ reaction (green arrows in fig. 7). The (p,γ) reaction on ^{15}N has a much lower rate than the (p,α) reaction, so this second cycle is strongly suppressed compared to the first cycle.
3. The third cycle starts with the $^{17}\text{O}(p,\gamma)^{18}\text{F}$ reaction, and its loop is closed by the $^{18}\text{O}(p,\alpha)^{15}\text{N}$ reaction (brown arrows in fig. 7). The (p,γ) reaction on ^{17}O is slower than the (p,α) reaction, so this cycle is again suppressed with respect to the second cycle.

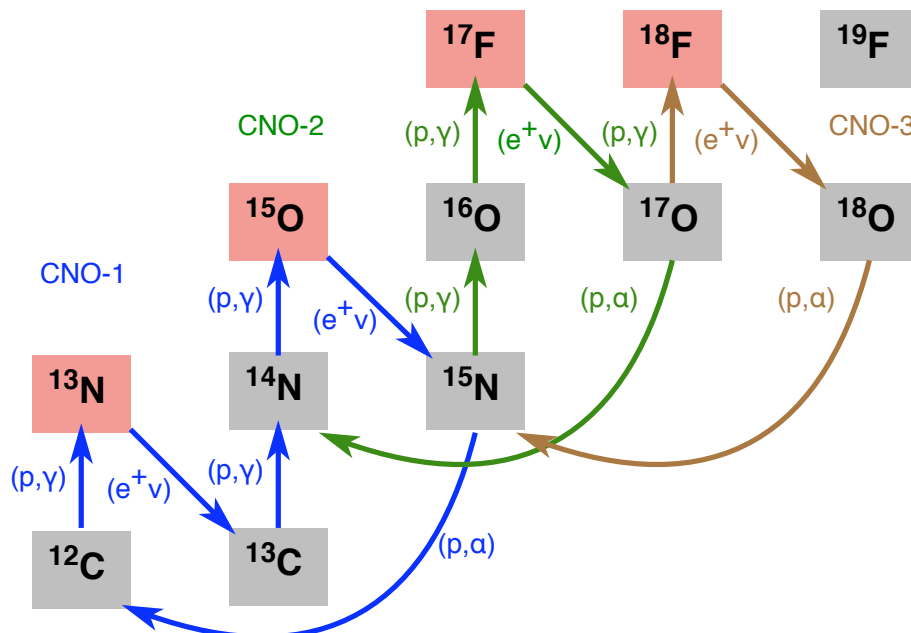


Figure 7: Nuclear reactions of the three carbon-nitrogen-oxygen (CNO) cycles of hydrogen burning. Stable nuclides are shaded gray, β^+ -unstable nuclides shaded red.

A fourth CNO cycle starts with the $^{18}\text{O}(p,\gamma)^{19}\text{F}$ reaction [56] and leads up to neon and sodium isotopes, where the neon-sodium and magnesium-aluminium cycles operate. However, these higher cycles are only relevant for scenarios with higher temperatures than in the center of the Sun, such as hydrogen shell burning in a red giant star or explosive hydrogen burning in a nova. Also the so-called hot CNO cycles [56] are activated at high temperature and density, when the rate of proton capture on the unstable isotopes ^{13}N ($t_{1/2} = 10$ min) and ^{15}O ($t_{1/2} = 2$ min) becomes higher than their β decay rate.

The bottleneck of the first CNO cycle is the $^{14}\text{N}(p,\gamma)^{15}\text{O}$ reaction. For solar conditions, it is 400 times slower than the next slowest process, the $^{12}\text{C}(p,\gamma)^{13}\text{N}$ reaction. Therefore, it entirely determines the rate once the cycle has reached its equilibrium.

4.1 The $^{14}\text{N}(p,\gamma)^{15}\text{O}$ reaction and the rate of the first cycle (papers H4-H6)

The $^{14}\text{N}(p,\gamma)^{15}\text{O}$ reaction (Q -value 7297 keV) proceeds through capture to the ground state and several excited states in ^{15}O . The states in the compound nucleus ^{15}O (fig. 8, left panel) have a double role. First, capture to each of these states has to be treated separately from capture to the other states, as the capture mechanism and therefore the size and energy dependence of the cross section may differ. Second, for capture to any one given state, neighboring states may act as resonances, above or below threshold, whose tails may contribute to the cross section. This latter point becomes important when fits in the R-matrix framework [57, 58] are attempted. This is illustrated in the right panel of fig. 8. There, as a function of the center-of-mass energy, the cross section for capture to several levels in ^{15}O is plotted, expressed as the astrophysical S-factor via eq. (1).

In addition to the direct capture process, there are three levels in ^{15}O that play a major role: The ones at 7556 and 8284 keV are well visible resonances at 259 and 987 keV center-of-mass energy in the $^{14}\text{N} + p$ excitation function. They dominate the cross section and its energy dependence over much of the region where experimental data are available, $E \geq 70$ keV. Their parameters must therefore be known with precision if one wants to describe the available experimental data at relatively high energy. However, the influence of these two levels does not seem to extend to the energy range relevant for the Sun, $E = 20$ -40 keV.

For the third important level at $E_x = 6792$ keV, the situation is much different. It lies 505 keV below the $^{14}\text{N} + p$ threshold and plays no role at the energies where experimental data are available. However, in its function as subthreshold resonance it is believed to cause a strong enhancement of capture to the ground state at very low energies, important for the Sun.

Capture to the ground state in ^{15}O had been the reason for a fascinating revision in the overall rate of the CNO cycle, downward by a factor of two. This revision was widely accepted before the present work began, laying the groundwork for the experiments described here. Therefore, it is summarized in the following two paragraphs.

For more than a decade, the accepted excitation function for the $^{14}\text{N}(p,\gamma)^{15}\text{O}$ reaction had been based on a seminal work published in 1987 by the group of Claus Rolfs [60]. In this work, the $^{14}\text{N}(p,\gamma)^{15}\text{O}$ reaction was studied over a wide energy range with germanium detectors. It concluded that at the energies relevant for the Sun, due to the above mentioned subthreshold resonance ground state capture contributed as much to the cross section as the strongest contribution, capture to the 6792 keV state, leading to an extrapolated total S-factor at zero energy of $S(0) = 3.2$ keV barn [60]. This result was adopted with minor modifications in the three widely used compilations by Caughlan and Fowler [61], by the NACRE collaboration [19],

and by the "Solar Fusion Cross Sections I" team [18].

However, after the year 2000 Doppler shift attenuation work [62], R-matrix fits [63, 64], and Coulomb dissociation studies [65] indicated that the subthreshold resonance had a lower γ -strength than indicated by Ref. [60]. The final straw came in 2004 by a cross section measurement that the LUNA collaboration carried out at its 0.4 MV deep underground accelerator, again under the leadership of Claus Rolfs [66]. These low-energy cross section data still reported an enhancement of ground state capture due to the subthreshold resonance, but much less than previously believed, and the total S-factor at zero energy was found to be $S(0) = 1.7$ keV barn, half the pre-2000 value.

This strong revision for a reaction with such a long history drew much attention to the need for precise and modern nuclear data for the Sun, the motivation for the present work.

However, the low-energy data by LUNA [66] ($E = 120$ -380 keV) and by a subsequent surface-based experiment at TUNL [67] ($E = 190$ -480 keV) had come with a price: Both experiments had used a very large HPGe detector in very close geometry. This led to large corrections, by up to a factor of 8, for the so-called true coincidence summing-in effect. This effect is due to the fact that the ground state contribution has a very small cross section in the 100-500 keV range where data are available (fig. 8), much smaller than the competing capture to the 6792 keV state. This latter capture leads to the emission of two γ -rays, the so-called primary of energy $E_{\gamma}^{\text{prim}} = Q + E - 6792$ keV, and the so-called secondary of energy $E_{\gamma}^{\text{sec}} = 6792$ keV. Analogous considerations apply for the 6172 and 5181 keV states. In close geometry, the absolute full energy peak detection efficiency for the primary γ -ray to the most important excited state can be larger than the branching ratio for ground state capture. This will lead to a summing-in peak that is larger than the true ground state capture peak and that is found at exactly the same energy in the γ -ray spectrum.

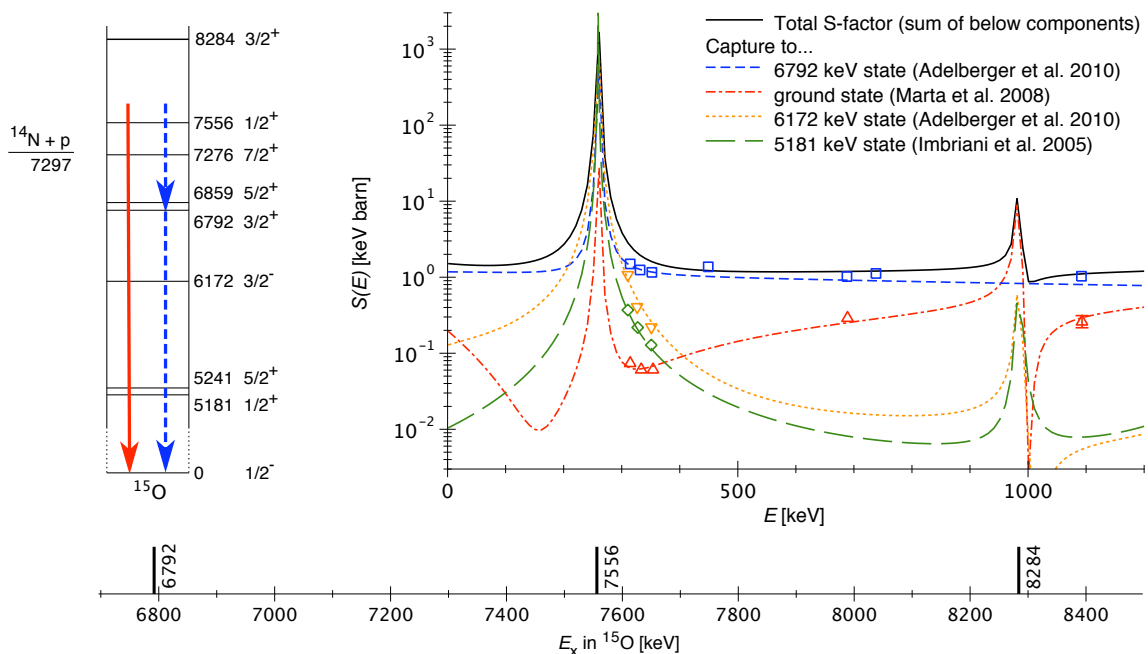


Figure 8: Level scheme of ^{15}O and astrophysical S-factor of the $^{14}\text{N}(p,\gamma)^{15}\text{O}$ reaction. In the right panel, both R-matrix fits [59, H4,H13] and the present experimental data [H4-H6] are shown.

The summing problem was one starting point for the present work. The second was a discrepancy between the two extrapolations by LUNA of $S_{\text{GS}}(0) = 0.25 \pm 0.06$ keV barn [66] and by TUNL of $S_{\text{GS}}(0) = 0.49 \pm 0.08$ keV barn [67]. Both numbers are consistent with the new, low total S-factor formed by the sum of the components from capture to the different levels in ^{15}O . However, the difference between the LUNA and TUNL $S_{\text{GS}}(0)$ values amounts to 15% of the total S-factor, limiting the precision of the astrophysical reaction rate. A third motivation for the present work was the need to provide a second independent set of data covering a wide energy range, updating Ref. [60] after almost a quarter century has passed.

In the present work, a new experiment was performed at the LUNA 0.4 MV underground accelerator. The ultra-low background prevalent in this facility is described in sec. 5. Solid titanium nitride (TiN) targets produced by the reactive sputtering technique and a large HPGe detector were used. However, this time the HPGe was a composite detector of the Clover type, consisting of four separate parts with a common high voltage and cryostat. This detector could be used in two modes: The add-back mode where the sum of the four parts was taken event by event, thereby forming a virtual large detector. For the singles mode, the data from each part were histogrammed separately, and the histograms were summed up at the end of the experiment.

Owing to the much smaller detection efficiency for one part of the detector in singles mode, on the one hand, and a somewhat larger distance between detector and target, on the other hand, the summing-in correction was reduced by a factor 30. This strongly reduced the concomitant systematic uncertainty. Three very precise data points could be deduced at $E \approx 300$ keV for ground state capture, in a sensitive minimum of the previous R-matrix fits (fig. 8). These data points were derived relative to the stronger transition to the 6792 keV state [H4].

This relative approach enabled low systematic uncertainties, and it allows to add these new data points to any other, absolute data set, giving three data points that are almost free from the summing effect. This was done first for the previous LUNA [59, 66] dataset, and the previous LUNA R-matrix fit was then repeated, leaving all other parameters unchanged. Then, the same procedure was repeated for the TUNL [67] dataset and TUNL R-matrix fit. In both cases, $S_{\text{GS}}(0) = 0.2$ keV barn was found, consistent with the previous LUNA extrapolation [66] but not with TUNL [67]. The fact that the TUNL R-matrix fit, just by adding three highly precise relative data points, converged on a much lower value than before shows the importance of precise data for a reliable extrapolation to lower energy, i.e. the energies directly relevant for the Sun. Finally, a new recommended R-matrix fit was developed. To this end, the Ref. [60] data were corrected for their summing-in effect, up to 50%, and the new LUNA-Clover relative data were transformed into absolute data using a weighted average of all previous data for capture to the 6792 keV states. The other LUNA and TUNL data [66, 67] were excluded, due to concerns about their quoted error bars given the very large summing corrections. The newly computed value is $S_{\text{GS}}(0) = 0.20 \pm 0.05$ keV barn [H4]. If one puts the concerns about the summing-in uncertainty aside and includes also Refs. [66, 67] in the fit, $S_{\text{GS}}(0) = 0.27 \pm 0.05$ keV barn is found [H13]

The spectra from the same experiment were then analyzed also in an absolute manner, giving cross sections for all four major transitions [H5]. These data have somewhat higher uncertainty than the relative ones, but they can still serve as independent cross-check of the accepted excitation function.

As a next step in the present work, a dedicated experiment was performed at the HZDR 3.3 MV Tandatron facility. This accelerator provides a proton beam of up to $15 \mu\text{A}$ intensity on target, much less than the $300 \mu\text{A}$ available at the LUNA 0.4 MV machine. Four large HPGe detectors

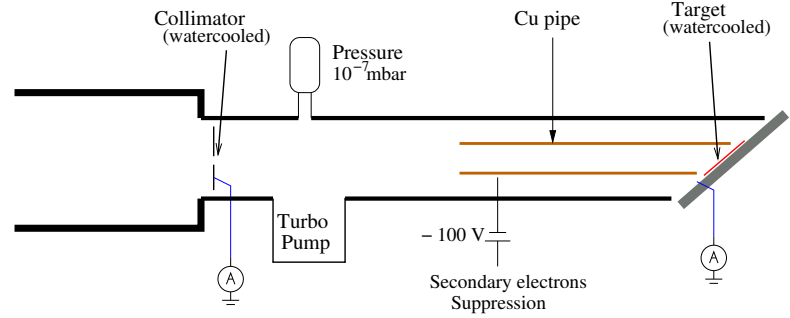
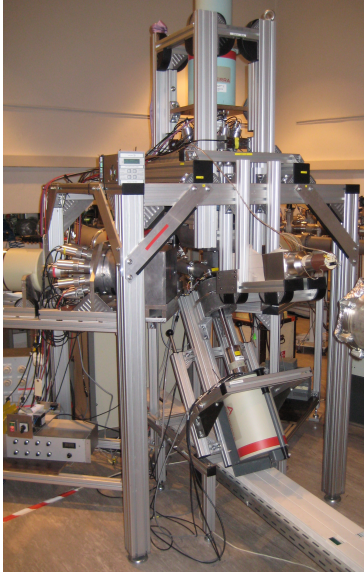


Figure 9: Experimental setup for the study of the $^{14}\text{N}(p,\gamma)^{15}\text{O}$ and $^{15}\text{N}(p,\alpha\gamma)^{12}\text{C}$ reactions at HZDR. Left panel: Photo of the setup with the beam coming from the back left corner. Right panel: schematic drawing of the target chamber, taken from M. Marta's PhD thesis.

Table 1: Relative and absolute resonance strength values $\omega\gamma$ for the $^{14}\text{N}(p,\gamma)^{15}\text{O}$ and $^{15}\text{N}(p,\alpha\gamma)^{12}\text{C}$ reactions from the present work [H6].

Reaction	Literature [68, 69]		Present		Literature $\omega\gamma$ [eV]	New recommended $\omega\gamma$ [eV]
	E_p [keV]	Γ_{lab} [keV]	$\omega\gamma_n/\omega\gamma_{278}$	$\omega\gamma$ [eV]		
$^{14}\text{N}(p,\gamma)^{15}\text{O}$	278	1.12 [70]	$\stackrel{\text{Def}}{1}$	—	0.0131 ± 0.0006 [H13]	—
$^{14}\text{N}(p,\gamma)^{15}\text{O}$	1058	3.8 [§]	27.8 ± 0.9	0.364 ± 0.020	0.31 ± 0.04 [60]	0.353 ± 0.018
$^{15}\text{N}(p,\alpha\gamma)^{12}\text{C}$	430	0.1	$(1.73 \pm 0.07) \cdot 10^3$	22.7 ± 1.4	21.1 ± 1.4 [71]	21.9 ± 1.0
$^{15}\text{N}(p,\alpha\gamma)^{12}\text{C}$	897	1.57	$(2.77 \pm 0.08) \cdot 10^4$	362 ± 20	293 ± 38 [72]	362 ± 20

[§] Literature: 3.9 ± 0.7 keV [68]. Present work: 3.8 ± 0.5 keV.

were placed at $\pm 127^\circ$, 90° , and 55° with respect to the proton beam direction. The three detectors at $\pm 127^\circ$ and 90° were equipped with a bismuth germanate (BGO) escape-suppression shield. As in the LUNA experiment [H4,H5], TiN targets were used, and the reaction was studied in the energy range $E = 0.5\text{-}2.0$ MeV (fig. 9).

A first and important step was the study of the two $^{14}\text{N}(p,\gamma)^{15}\text{N}$ resonances seen in fig. 8 and of two resonances in the $^{15}\text{N}(p,\alpha\gamma)^{12}\text{C}$ reaction at $E_p = 430$ and 897 keV. The yield is strongly enhanced in these resonances, so they can serve as important stepping stones for measurements of the much weaker yield far away from the resonances. The study of the ^{15}N resonances is enabled by the fact that the nitrogen isotopic ratio does not vary much. In atmospheric air, the ratio $^{14}\text{N}/^{15}\text{N}$ is constant to better than 1% over the entire Earth [73]. As a result, it is actually recommended as the standard for measurements of the nitrogen isotopic composition [74]. Therefore, the nitrogen isotopic composition of the TiN targets can be assumed to be equal to the recommended standard value [74].

Based on these considerations, the strengths of the resonances at $E_p = 1058$ keV in the $^{14}\text{N}(p,\gamma)^{15}\text{N}$ reaction and at $E_p = 430$ and 897 keV in the $^{15}\text{N}(p,\alpha\gamma)^{12}\text{C}$ reaction have been measured [H6], relative to the strength of the $E_p = 278$ keV resonance in $^{14}\text{N}(p,\gamma)^{15}\text{N}$ (table 1). This latter resonance strength had been measured several times in recent years, and a weighted

average for its strength has recently been adopted [H13]. This fact, and the recommendation [H13] to further improve its precision in future work, made this resonance an ideal reference point. In this way, the newly measured strengths of the three other resonances will also get more precise with future improvements in the 278 keV precision.

In a further step, also off-resonant data for the $^{14}\text{N}(p,\gamma)^{15}\text{N}$ reaction were taken at HZDR. However, due to the limited beam intensity and some initial problems with ion beam induced background, there are not enough data points to repeat the seminal work of Ref. [60]. However, the preliminary HZDR off-resonance cross section data in the energy range $E = 450\text{--}1150$ keV seem to suggest a somewhat higher normalization of the cross section for capture to the 6792 keV state with respect to the literature (fig. 8).

4.2 The $^{15}\text{N}(p,\gamma)^{16}\text{O}$ reaction and the onset of the second cycle (papers H7-H8)

The ratio of the reaction rates of the $^{15}\text{N}(p,\alpha)^{12}\text{C}$ and $^{15}\text{N}(p,\gamma)^{16}\text{O}$ reactions gives the number of times the first CNO cycle has to revolve for each time the second CNO cycle is activated (fig. 7).

The $^{15}\text{N}(p,\alpha)^{12}\text{C}$ reaction has recently been the object of a re-study in the Trojan Horse framework [75]. It mainly proceeds directly to the ground state of ^{12}C , bypassing the first excited state at 4439 keV in ^{12}C . Resonant capture to this latter state is also called the $^{15}\text{N}(p,\alpha\gamma)^{12}\text{C}$ reaction and is strongly enhanced at the $E_p = 430$ and 897 keV resonances (sec. 4.1). Even still, due to the overall dominance of $^{15}\text{N}(p,\alpha)^{12}\text{C}$ ground state capture the role of these resonances is confined to applied physics, namely hydrogen depth profiling. The recent Trojan Horse data [75] therefore represent the present best estimate of the $^{15}\text{N}(p,\alpha)^{12}\text{C}$ excitation function.

The $^{15}\text{N}(p,\gamma)^{16}\text{O}$ reaction is about 2000 times slower than $^{15}\text{N}(p,\alpha)^{12}\text{C}$. Its rate directly affects the nucleosynthetic output of the three stable oxygen isotopes $^{16,17,18}\text{O}$ (fig. 7). In principle, the dependence is linear, but in most realistic astrophysical scenarios it is diluted due to pre-existing ^{16}O that has been created via the $^{12}\text{C}(\alpha,\gamma)^{16}\text{O}$ reaction in a preceding helium burning phase. The $^{15}\text{N}(p,\gamma)^{16}\text{O}$ cross section had been measured by Hebbard in 1960 [76] and by Rolfs and Rodney in 1974 [77]. The latter data and its extrapolated $S_{1,15}(0) = 64 \pm 6$ keV barn were adopted in the reaction rate compilations [18, 19, 61].

The stable isotope ^{15}N , with its natural isotopic abundance of 0.4% [74], was included in the target gas of the LUNA experiment on the $^{14}\text{N}(p,\gamma)^{15}\text{O}$ reaction that was analyzed in the framework of my PhD thesis [78–80]. This fact enabled a later parasitic analysis of the spectra from the completed $^{14}\text{N}(p,\gamma)^{15}\text{O}$ experiment, concentrating on the γ -lines from the $^{15}\text{N}(p,\gamma)^{16}\text{O}$ reaction at $E_\gamma \approx 12$ MeV. In this γ -ray energy region, the laboratory background at the LUNA underground site is negligible, so even rather low counting rates can be detected. However, the $E_\gamma \approx 12$ MeV peak is contaminated by a contribution due to the $^{11}\text{B}(p,\gamma)^{12}\text{C}$ beam induced background reaction. This problem was solved by deriving a subtraction procedure where the $E_\gamma \approx 16$ MeV summing peak of $^{11}\text{B}(p,\gamma)^{12}\text{C}$ (Q -value 15.957 MeV) was used as a monitor to subtract the background stemming from the same reaction at $E_\gamma \approx 12$ MeV. The $^{15}\text{N}(p,\gamma)^{16}\text{O}$ reaction (Q -value 12.127 MeV) can only give rise to counts at $E_\gamma \approx 12$ MeV. A very conservative error estimate was adopted for this subtraction procedure, but still the resulting data were at the time of publication the most precise ones available [H7]. The fact that useful data can be extracted from a 0.4% contribution in the actual target shows the power of the technique of going deep underground.

Just previous to this publication [H7], an asymptotic normalization coefficient (ANC) measure-

ment and R-matrix fit by Mukhamedzhanov *et al.* [81] had predicted an S-factor at 100-200 keV, energies relevant for hydrogen burning in a nova, that was much lower than reported by Rolfs and Rodney [77]. This claim was based on the fact that the measured ANC [81], controlling direct capture, could not be brought into agreement with the previously published spectroscopic factor [77]. The new LUNA data [H7] showed this predicted reduction by direct cross section data (fig. 11).

Subsequently, two dedicated experiments with solid TiN targets, enriched in ^{15}N , have been performed at LUNA [82, H8]. In the first campaign [82], enriched solid Ti^{15}N targets and a HPGe detector were used to study the excitation function over a wide energy range, connecting low-energy LUNA data with higher-energy data taken at the Earth's surface at Notre Dame University, up to 1.8 MeV. These data [82] are consistent with the present [H7] except for some data points at $E \approx 200$ keV, i.e. on the rising slope of the wide $E = 312$ keV resonance (fig. 11). This extensive data set was then used to produce a new R-matrix fit [82] that closely resembles the previous one at low energy [81] but is lower on the wide $E = 312$ keV resonance, where Ref. [81] had still relied on the Rolfs and Rodney [77] data.

In the second LUNA experiment dedicated to the $^{15}\text{N}(p,\gamma)^{16}\text{O}$ reaction [H8], again enriched solid Ti^{15}N targets were used, but now the detector was again the borehole BGO summing detector of the previous, parasitic study [H7], greatly enhancing luminosity. This experiment covered the 312 keV resonance and extended the data down to 70 keV, lower than ever before.

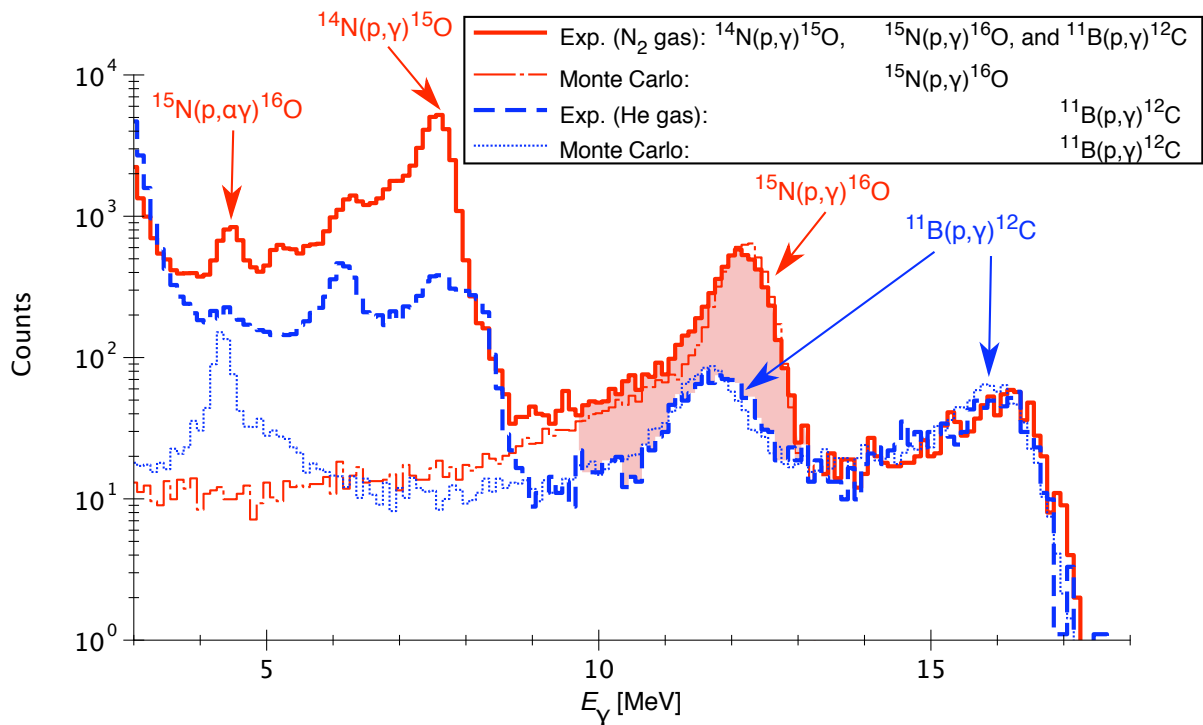


Figure 10: Experimental and simulated spectra for the $^{15}\text{N}(p,\gamma)^{16}\text{O}$ study with natural nitrogen gas [H7]. The experimental spectrum with $^{14}\text{N}+^{15}\text{N}$ target gas contains peaks from the $^{14}\text{N}(p,\gamma)^{15}\text{O}$ and $^{15}\text{N}(p,\gamma)^{16}\text{O}$ reactions and the $^{11}\text{B}(p,\gamma)^{12}\text{C}$ beam-induced background reaction. The experimental spectrum with helium gas contains just the beam induced background reactions. Spectra generated by the GEANT4 Monte Carlo code are shown to separate out the $^{15}\text{N}(p,\gamma)^{16}\text{O}$ and $^{11}\text{B}(p,\gamma)^{12}\text{C}$ contributions.

Great care was taken to precisely understand the targets, in order to limit the systematic uncertainty. The nitrogen isotopic composition and the Ti:N stoichiometry were measured with the heavy-ion elastic recoil detection (HI-ERD) [83] technique at the Munich tandem. The target stoichiometry as a function of depth and its change after irradiation by the intensive LUNA beam were studied using the $^{15}\text{N}(p,\alpha\gamma)^{12}\text{C}$ reaction at the HZDR 3.3 MV Tandatron. In addition, the target thickness was also measured by the secondary neutral mass spectrometry (SNMS) technique.

The large solid angle covered by the BGO detector and the large absolute detection efficiency limited the uncertainty due to possible angular distribution and branching ratio effects, and in the end a systematic uncertainty of 10% was achieved [H8]. This is higher than the very low 3.0% of the $^3\text{He}(\alpha,\gamma)^7\text{Be}$ case, mainly due to the higher uncertainties connected to using a solid target instead of a gas target.

The latest LUNA data [H8] are in good agreement with the two previous LUNA campaigns [82, H7]. On top of the 312 keV resonance, the [H8] normalization is slightly lower than Ref. [82], but still in agreement given the systematic uncertainties of each work. At $E \approx 200$ keV, the [H8] data lie between [H7] and Ref. [82]. None of the newer data [82, H7, H8] are in agreement with the previously accepted work [77], which is still at the basis of the widely used NACRE and CF88 reaction rate compilations [19, 61].

With the new data, now the complete Gamow peak for explosive hydrogen burning in an astrophysical nova is covered by precise experimental data, and a major part of the Gamow peak for hydrogen shell burning in red giant stars is also covered by data. Possible astrophysical implications include a 30% reduction in ^{16}O abundance in nova burning [84] and lower self-enrichment

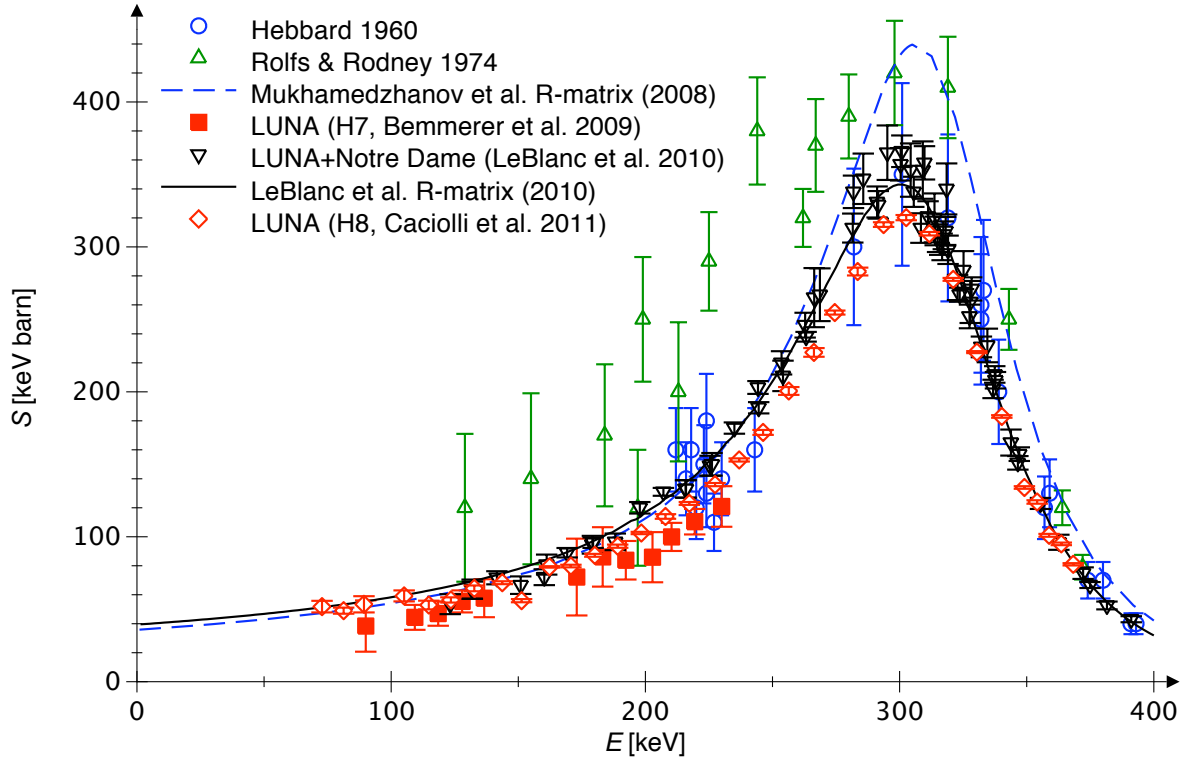


Figure 11: Astrophysical S-factor of the $^{15}\text{N}(p,\gamma)^{16}\text{O}$ reaction. Data points from this work [H7,H8] and from Refs. [76, 77, 82]. R-matrix curves from Refs. [81, 82].

during the so-called hot-bottom burning [85] process [H8].

When using the Ref. [82] dataset for an R-matrix fit, instead of $S_{1,15}(0) = 64 \pm 4$ keV barn [77] now $S_{1,15}(0) = 39.6 \pm 2.6$ keV barn is found [82]. This value has been obtained leaving the ANC controlling direct capture as a free parameter [82]. If, instead, the ANC is fixed to its measured value [81], the overall curve changes only slightly, and $S_{1,15}(0) = 33.1$ - 40.1 keV barn is found [86]. These values are consistent with the value of 36 ± 6 keV barn [81] which had been adopted as an interim recommendation before the two dedicated LUNA experiments were completed [H13].

None of the recent R-matrix fits [81, 82, 86] includes the very recent LUNA data [H8]. However, all the data and R-matrix fits give a very consistent overall picture, so it is justified to adopt the R-matrix numbers [82, 86] for the low-energy extrapolation.

5 Future accelerator-based science underground (papers H9-H12)

Most of the experimental data described in the previous sections have been obtained in the LUNA deep-underground laboratory. This is so because the nuclear reactions that are relevant in our Sun have a very low cross section at the relevant energy. In order to study them, one must use an ultra-low background environment, as is the case at LUNA, and a setup of very high "luminosity" L , for the present purposes defined as

$$L \stackrel{\text{Def}}{=} \Phi_{\text{Beam}} d_{\text{Target}} \eta_{\text{Detector}} \quad (2)$$

where Φ_{Beam} is the beam intensity, d_{Target} the effective thickness of the target, and η_{Detector} the detection efficiency. The existing 0.4 MV LUNA accelerator at Gran Sasso is close to the optimum for the beam intensity Φ_{Beam} , with an intensity of up to 0.5 mA for H^+ ions. A more intensive beam would lead to instability in solid targets and high beam-heating corrections in static gas targets. Only jet gas targets can withstand much more intensive beams, but in the past it has proven difficult to determine their absolute thickness [45, 49, e.g.].

Also for the target thickness d_{Target} , typical LUNA values of $10^{16} \dots 10^{18}$ atoms/cm² are close to the optimum. This is so because with the stopping power on the order of a few tens of eV per 10^{15} atoms/cm², the beam loses typically a few keV of energy in a 10^{17} atoms/cm² target. Far below the Coulomb barrier, an even higher energy loss leads to such a strong decrease in the cross section that only the first 10^{18} atoms/cm² or so of the target make a non-negligible contribution to the experimental yield.

Finally, also the detection efficiency η_{Detector} for the emitted radiation has been optimized in several cases at the present LUNA facility, using a borehole BGO detector with 70% detection efficiency for high-energy γ -rays [H7]. In the LUNA experiments with germanium detectors, typically about 20% of the solid angle available for detectors has been used, so also in that case there is only limited room for improvement.

In summary, the basic preconditions for highly sensitive experiments are all given at the present LUNA 0.4 MV facility. Therefore, besides limited upgrades in the experimental setups, the main task is to develop and carry out a scientific program that uses this potential to the fullest.

One major limitation of the present LUNA facility, however, cannot be overcome: the energy range given by the 0.4 MV accelerator. For this reason, there is a call in the community for new, higher-energy underground accelerators, [87–89, H13].

In the following sections, selected building blocks of a scientific program at the present LUNA 0.4 MV facility and at a higher-energy underground accelerator are outlined (secs. 5.1, 5.2). Subsequently, a study of background in underground γ -ray detectors is presented (sec. 5.3), and finally the implications for a possible low-background accelerator laboratory in the Felsenkeller facility in Dresden are discussed (sec. 5.4)

5.1 Future science at the present LUNA 0.4 MV facility (paper H12)

The scientific program for the upcoming years at the present LUNA 0.4 MV facility has been described in the collaboration's proposal for the years 2008-2012 (unpublished). Here, in the interest of brevity just two nuclear reactions will be reviewed, namely $^{22}\text{Ne}(p,\gamma)^{23}\text{Na}$, which is included in this proposal, and $^{12}\text{C}(p,\gamma)^{13}\text{N}$, which is not included but might be part of the science program beyond 2012.

The $^{22}\text{Ne}(p,\gamma)^{23}\text{Na}$ reaction takes part in hydrogen burning, in the neon-sodium cycle that is important in astrophysical novae. At novae temperatures, the reaction rate is dominated by a number of low-energy resonances [90]. However, for the resonances below $E_p = 0.4$ MeV, only upper limits exist in the literature [91]. The rate adopted in the most recent reaction rate compilation [90] uses indirect data [92] to quantify the strength of several of these resonances, adopting upper limits in several cases. The lowest-lying resonance with a directly measured strength is the one at $E_p = 479$ keV [93].

This lack of information makes the deduced reaction rate prone to error. There is a significant discrepancy (fig. 12) between the reaction rate shown in the NACRE compilation [19] and the rate given in the compilations by Iliadis and co-workers [94, 95]. This is mainly due to the inclusion of some low-energy resonances in the NACRE, but not in the Iliadis compilations. Therefore, both the rates and the quoted uncertainties should be taken with a grain of salt, until more experimental information is available.

A sensitivity study taking this discrepancy as an uncertainty found a significant impact on the nucleosynthetic output. For models of so-called CO novae, i.e. nova explosions taking place on a white dwarf consisting mainly of carbon and oxygen, the yields of the following nuclides were significantly affected by variations in the $^{22}\text{Ne}(p,\gamma)^{23}\text{Na}$ rate: ^{22}Ne (factor of 100), ^{23}Na (factor of 7), ^{24}Mg (factor of 70), ^{25}Mg (factor of 5), and even ^{26}Al (factor of 20).

It has been suggested that a number of presolar grains that have been isolated in meteorites show the imprints of nucleosynthesis in an astrophysical nova [96]. These grains contain signif-

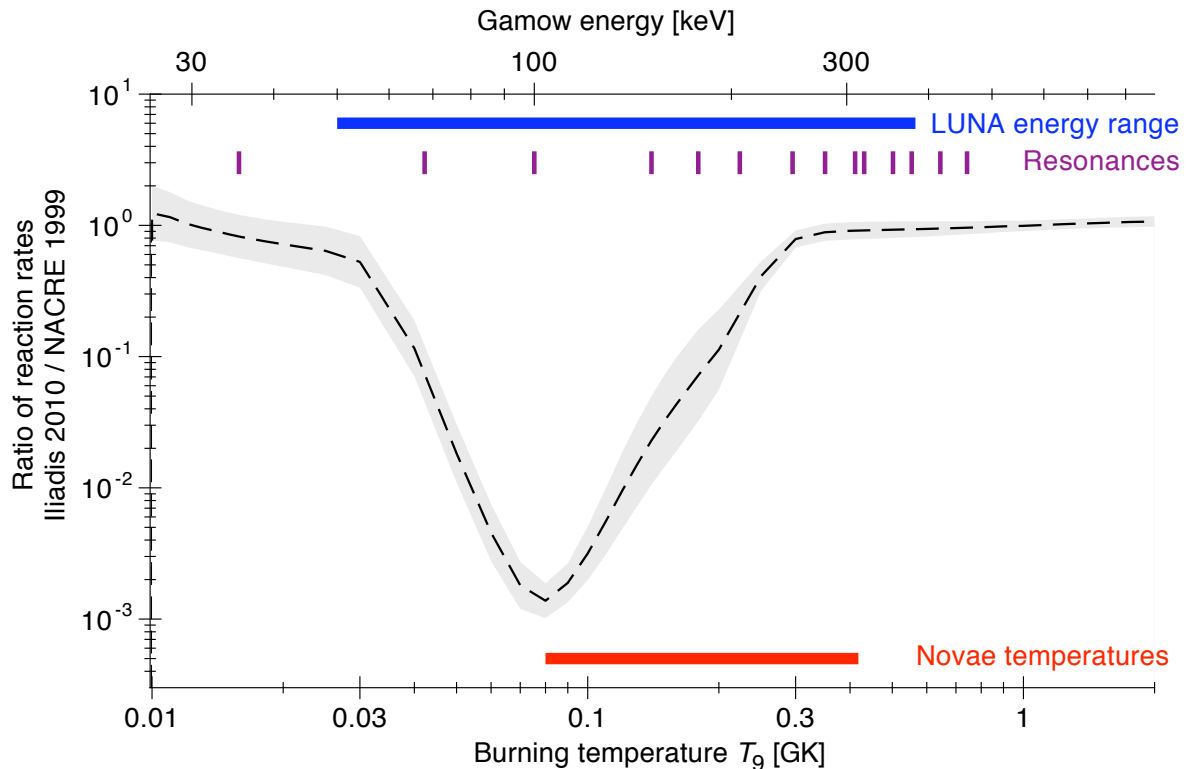


Figure 12: Astrophysical reaction rate of the $^{22}\text{Ne}(p,\gamma)^{23}\text{Na}$ reaction. The ratio of the Iliadis [94] and the previous NACRE [19] rates is plotted. The shaded area covers the nominal uncertainty range given by Iliadis.

ificant amounts of ^{22}Ne , most of it probably resulting from the in situ decay of radioactive ^{22}Na . However, some implantation of directly produced ^{22}Ne cannot be excluded [97]. A recent study found five presolar grains with significant ^{22}Ne content in the Murchison meteorite, but for most of the grains no clear assignment to a nucleosynthetic site could be made [98]. Very recent studies of nucleosynthesis in supernovae of type Ia indicate a strong dependence of the nucleosynthetic output on the ^{22}Ne abundance in the precursor [99, 100], even though in these cases the ^{22}Ne is believed to be predominantly produced by helium burning, not hydrogen burning.

Given the lack of experimental information on the hydrogen burning of the astrophysically important nucleus ^{22}Ne , a new study seems highly desirable. The previous upper limits for the low-energy resonance strengths in the $^{22}\text{Ne}(p,\gamma)^{23}\text{Na}$ reaction are in the μeV range [91, 92, 94], much higher than the typical sensitivity of LUNA experiments, which lies in the neV range. Consequently, a new study of this reaction at LUNA will start in early 2012, with me as working group leader.

The $^{12}\text{C}(p,\gamma)^{13}\text{N}$ reaction controls the onset of the CNO cycle of hydrogen burning. As the subsequent β^+ decay of ^{13}N and the $^{13}\text{C}(p,\gamma)^{14}\text{N}$ reaction proceed much faster, the $^{12}\text{C}(p,\gamma)^{13}\text{N}$ rate determines the speed with which ^{12}C in the solar core (for radii $R/R_{\text{Sun}} \leq 0.10$) is transmuted to ^{14}N . This conversion takes just a few million years and is thought to be so rapid to give rise to convection [10]. When the $^{12}\text{C} \rightarrow ^{14}\text{N}$ conversion is complete, the even slower $^{14}\text{N}(p,\gamma)^{15}\text{O}$ reaction takes over the control of the CNO rate.

However, a non-negligible part of the solar ^{13}N neutrino flux is believed to originate from regions outside the solar core, $R/R_{\text{Sun}} \approx 0.15$, where the temperature is still high enough for the $^{12}\text{C}(p,\gamma)^{13}\text{N}$ reaction to occur, but too low for a significant rate of the $^{14}\text{N}(p,\gamma)^{15}\text{O}$ reaction. This leads to a double-peaked structure in the locus of emission of solar ^{13}N neutrinos [101]. In order to correctly predict this part of the solar ^{13}N neutrino rate, it is necessary to precisely know the rate of the underlying $^{12}\text{C}(p,\gamma)^{13}\text{N}$ reaction.

This reaction has been studied directly for the last time almost 40 years ago by Rolfs and Azuma [102], down to energies of 150 keV. Even lower energies, down to 70 keV, had been reached in the 1950's by Lamb and Hester [103] in a study using the high-current injector at Livermore, with a very high beam intensity of 100 mA. However, an experiment at this accelerator by the same group on the $^{14}\text{N}(p,\gamma)^{15}\text{O}$ reaction [104] reported data that overestimated the cross section by more than 50% with respect to the presently accepted value [H13]. Newer studies either use indirect methods [105, 106] or present only a relative cross section [107]. Therefore, a new and precise direct cross section measurement seems highly desirable.

The $^{12}\text{C}(p,\gamma)^{13}\text{N}$ reaction now seems to be within reach of ab initio calculations using effective field theories in nuclear lattice models. These methods have recently been used with great success to calculate the $^3\text{He}(\alpha,\gamma)^7\text{Be}$ reaction [35, see also sec. 3.2], so an extension to slightly larger nuclei holds promise. However, precise calculated cross sections should be compared to similarly precise data, reaffirming the need for new low-energy $^{12}\text{C}(p,\gamma)^{13}\text{N}$ data.

5.2 Science at a possible higher-energy underground accelerator (papers H11-H12)

The idea for a new, higher-energy underground accelerator is based on the success of the existing 0.4 MV LUNA machine [89, H11], so it is logical that an important part of the science program at a new accelerator is actually the continuation of work started at the low LUNA energies to higher energy.

For two nuclear reactions currently limiting the precision of the solar model, ${}^3\text{He}(\alpha,\gamma){}^7\text{Be}$ and ${}^{14}\text{N}(\text{p},\gamma){}^{15}\text{O}$, the low-energy LUNA work has pioneered precision cross section measurements.

For the ${}^3\text{He}(\alpha,\gamma){}^7\text{Be}$ reaction, it is clear that a future improvement of the precision could be achieved most easily by extending the precise LUNA data with the same technique and setup both to lower and to higher energies, clarifying discrepancies and providing one data point in the solar Gamow peak (sec. 3.2).

The situation is different for ${}^{14}\text{N}(\text{p},\gamma){}^{15}\text{O}$. Whereas in the ${}^3\text{He}(\alpha,\gamma){}^7\text{Be}$ case there are several independent experiments providing high-energy data and one consistent data set over a wide energy range is called for, for ${}^{14}\text{N}(\text{p},\gamma){}^{15}\text{O}$ there is only one comprehensive dataset covering a wide energy region [60], so no discrepancies are possible. However, this experiment is now almost a quarter century old, and in the meantime the data [60] had to be corrected [66] for an erroneously neglected summing-in effect of up to 50%. The presently recommended extrapolated S-factor values at zero energy [H13] are significantly different from what was suggested by Ref. [60].

Therefore and in view of the increased need for precision, it seems necessary to repeat this study [60] and re-measure the ${}^{14}\text{N}(\text{p},\gamma){}^{15}\text{O}$ cross section over a wide energy range. This has in part already been done in the present study in an experiment at the surface of the Earth (sec. 4.1). However, due to the limited beam intensity at the HZDR 3.3 MV Tandatron of just $15\ \mu\text{A}\ \text{H}^+$ and to the limited availability of beamtime, only a few data points could be obtained for the two strongest transitions, and it was not possible to take data in an energy range overlapping with the LUNA range (fig. 8).

A high-intensity accelerator in a low-background, underground setting would be the ideal tool to provide the necessary new data linking high and low energy regions for both the ${}^3\text{He}(\alpha,\gamma){}^7\text{Be}$ and the ${}^{14}\text{N}(\text{p},\gamma){}^{15}\text{O}$ reactions.

Another case in point is the ${}^2\text{H}(\alpha,\gamma){}^6\text{Li}$ reaction, which is currently under study at the LUNA 0.4 MV accelerator. It is important for the production of the isotope ${}^6\text{Li}$ in the Big Bang. This isotope has been detected in some metal-poor halo stars [108, 109]. These same stars are used to establish the amount of ${}^7\text{Li}$ produced in the Big Bang, so the question is whether the detected amount of ${}^6\text{Li}$ is, in fact, primordial. This would be highly unexpected, as standard Big Bang nucleosynthesis predicts a ${}^6\text{Li}$ production that is four orders of magnitude below ${}^7\text{Li}$ [110] and would not be detectable in those stars.

The only possible solution for the ${}^6\text{Li}$ problem would then be new physics [111, 112], making this isotope a sensitive probe for some extensions the standard model. It should be noted that the ${}^6\text{Li}$ detections of Ref. [109] have recently been criticized, however even the critics conclude that some metal-poor stars remain with detected ${}^6\text{Li}$ at the 2σ level [113, 114]. In this framework, it seems important to remove the nuclear physics uncertainties associated with standard Big Bang production of ${}^6\text{Li}$, which proceeds mainly by the highly uncertain ${}^2\text{H}(\alpha,\gamma){}^6\text{Li}$ reaction [110]. Consequently, this reaction has recently been studied by Coulomb dissociation at GSI [115], but due to dominating nuclear breakup no experimental cross sections could be extracted.

The LUNA spectra of the ${}^2\text{H}(\alpha,\gamma){}^6\text{Li}$ reaction show significant ion beam induced background, which is highly unusual for LUNA experiments. Energetic deuterons created by elastic scattering of the incident α -beam give rise to the ${}^2\text{H}(\text{d},\text{n}){}^3\text{He}$ reaction producing up to 10 neutrons per second. The neutrons, in turn, cause background by capture and inelastic scattering in the germanium detector material (with $A \in \{70, 72, 73, 74, 76\}$):



This background is only significant in an underground facility, as it is still well below the no-beam counting rate above ground (fig. 13). However, it presents a formidable obstacle to a cross section measurement, because the expected signal is ten times lower. In order to derive a cross section from the LUNA 0.4 MV data, the neutron-induced background has to be subtracted out. Whether or not this is possible is currently under study.

An alternative path would be to use a higher-energy underground accelerator. Using 1.3 MeV α -beam energy instead of the 0.4 MeV which are the maximum available at the present facility, it is expected that the background would be reduced by a factor of three due to the lower Rutherford scattering cross section, combined with an only slightly higher cross section for the ${}^2\text{H}(d,n){}^3\text{He}$ reaction. At the same time, the expected signal would be five times greater, greatly aiding detectability.

Looking beyond the nuclear reactions that have been studied at the LUNA 0.4 MV facility, two major areas have recently attracted great interest in the astrophysical community. These are the reactions of stellar helium burning and the reactions providing the neutrons for the astrophysical s-process (slow neutron capture process).

Helium burning ensues in red giant stars after the pure hydrogen burning phase has been completed. The relevant reactions are still not understood on a sufficient level of precision [116]. This concerns e.g. the ${}^{12}\text{C}(\alpha,\gamma){}^{16}\text{O}$, ${}^{16}\text{O}(\alpha,\gamma){}^{20}\text{Ne}$, and ${}^{18}\text{O}(\alpha,\gamma){}^{22}\text{Ne}$ reactions. The ${}^{12}\text{C}(\alpha,\gamma){}^{16}\text{O}$ reaction has been called the "holy grail of nuclear astrophysics" already by 1983 Nobel Laureate William A. Fowler, both because of its importance and of the great difficulty

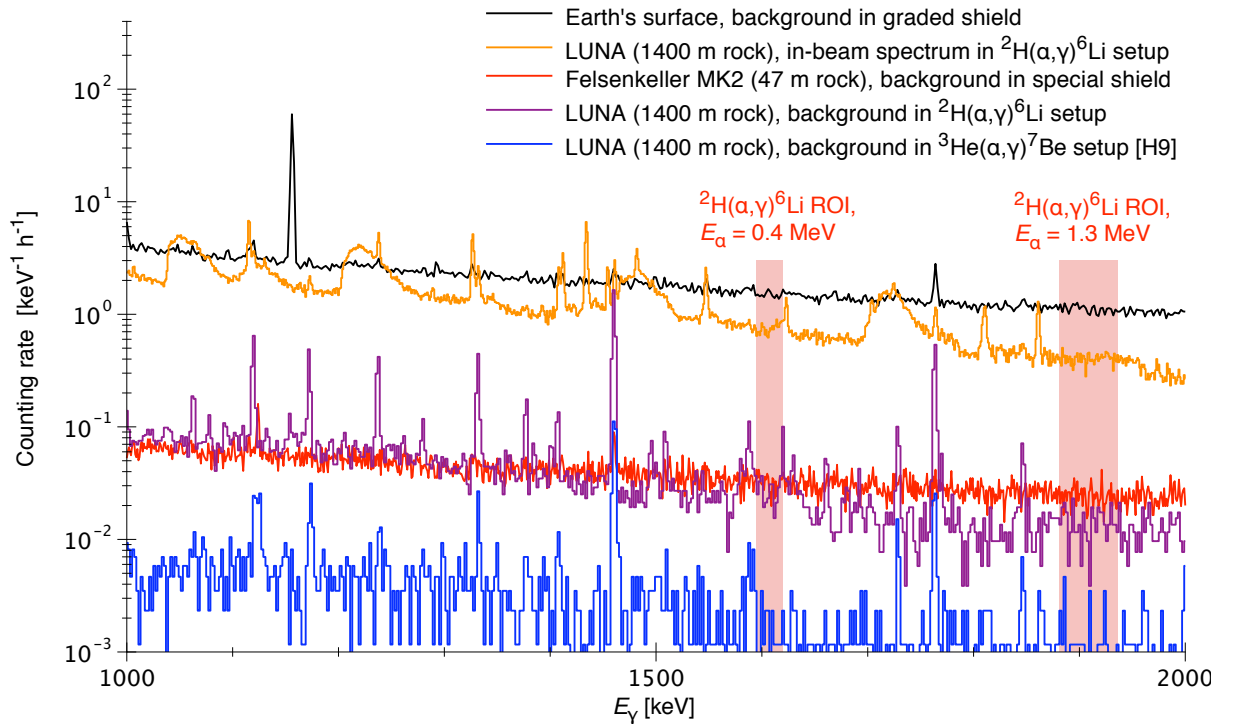


Figure 13: In-beam spectrum from the ${}^2\text{H}(\alpha,\gamma){}^6\text{Li}$ experiment at the LUNA 0.4 MV accelerator, at $E_\alpha = 400 \text{ keV}$ (orange curve). For comparison, the no-beam background is also shown for the following sites: At the surface of the Earth (black curve), in Felsenkeller MK2 (red curve), in the LUNA ${}^2\text{H}(\alpha,\gamma){}^6\text{Li}$ setup (purple curve), and in the previous LUNA ${}^3\text{He}(\alpha,\gamma){}^7\text{Be}$ setup (blue curve, [H9]).

in obtaining a precise estimate of its rate. Indeed, the $^{12}\text{C}(\alpha,\gamma)^{16}\text{O}$ rate strongly affects the nucleosynthetic output of supernova explosions. Therefore, supernova modelers call for 10% precision in its rate [117], while the state of the art is 30% uncertainty [116].

The composition of the ashes of helium burning in red giant stars is important, because some red giant stars that are part of a binary system may give rise to a supernova explosion of type Ia. Recently, it has even been suggested that type Ia supernovae may be the astrophysical sites for the little-understood p-process of nucleosynthesis, if they are provided with the correct fuel [99, 100].

The so-called slow neutron capture process or astrophysical s-process is believed to take place in red giant stars, as well. The main s-process is believed to be understood [85, 118], owing in part to extensive nuclear reaction cross section measurements [119, 120]. However, this statement is not true for the so-called weak s-process. Many of its nodes have been inaccessible because they require the use of radioactive or strongly enriched targets. These cases will be addressed at the upcoming FRANZ facility at Frankfurt University [121].

The two nuclear reactions providing the neutrons in the first place are not well-studied, either: The $^{13}\text{C}(\alpha,n)^{16}\text{O}$ reaction has recently been re-studied [122], however the data did not reach the astrophysically relevant low energies, leading to some uncertainty in the extrapolation. Also for the second neutron source reaction, $^{22}\text{Ne}(\alpha,n)^{25}\text{Mg}$, the experimental data did not reach the required low energies [123]. In both cases, repeating the experiment in an environment with a much lower neutron background such as an underground laboratory would allow to reach lower energies and put the assumed reaction rate on firm ground.

Finally, three other astrophysical scenarios should be mentioned that would also benefit from new and precise cross section data for their modeling: Big Bang nucleosynthesis [124], hydrogen burning beyond the CNO cycles [56], and stellar carbon burning [125].

5.3 Background study in underground laboratories (papers H9-H11)

The reason for placing an accelerator underground is the strongly reduced background, above all in γ -detectors. The first paper showing in detail background data of γ -detectors at the LUNA facility in the energy region above 2.615 MeV was written as a product of my PhD thesis [126]. However, that study just considered unshielded detectors placed deep underground.

The effects of additional active or passive shielding in underground laboratories were discussed in detail in two further papers [H9, H10]. First, the effects of passive shielding were studied, concentrating on the setup developed for the LUNA $^3\text{He}(\alpha,\gamma)^7\text{Be}$ experiment and on γ -energies below 2.615 MeV [H9]. The fact that the effectiveness of passive shields is greatly enhanced by moving the setup deep underground [127] was now confirmed, for the first time, also for typical in-beam setups [H9], as opposed to activity-counting setups which do not require apertures for entry and exit of the ion beam. It is clear that by going deep underground, the counting rate is reduced by more than two orders of magnitude, even when comparing with a well-shielded low-background setup at the surface of the Earth (fig. 14).

In addition, detailed numbers on the observed background at LUNA were published, establishing a benchmark for possible other underground accelerator laboratories. Using typical parameters for beam intensity and target thickness, the background numbers were converted to the cross section at which the signal would be equal to the remaining background, a figure of merit for the low-background environment [H9].

As a next step, the effect of active shielding on the no-beam counting rate was studied. This addresses a frequent critique of underground accelerator experiments, claiming that a similar background suppression can also be reached by active veto detectors. This is not true, due to the fact that muons may create neutrons in material adjacent to the detector, which, in turn, give rise to background – a background that is difficult to veto.

Indeed, the data show that one and the same detector, a Clover-type HPGe with a specially fitted BGO anticompton shield, shows much lower background deep underground, even when the actively vetoed spectra are compared (fig. 15, [H10]). In addition to this background study, the special features of the composite, Clover-type detector used have been employed to extract improved branching ratios for weak branches in the decay of the $E_p = 223$ keV resonance in the $^{24}\text{Mg}(p,\gamma)^{25}\text{Al}$ reaction [H10].

Subsequently, the detailed background data gained for the LUNA deep-underground site have been compared with a less deep site, the Dresden Felsenkeller, shielded by just 47 m of rock [H11]. When using no active shielding, it turns out that Felsenkeller is an intermediate solution, on a logarithmic scale, between the surface of the Earth and a deep-underground setting: By moving from the surface of the Earth to Felsenkeller, the background is reduced by about a factor of 30. Another factor of 30 is gained by moving deep underground to LUNA (fig. 14). This means that without active shield, Felsenkeller holds a decisive advantage over setups at the surface of the Earth, but cannot compete with a deep-underground setting such as LUNA.

This picture changes when considering actively shielded setups (fig. 15). While the non-vetoed

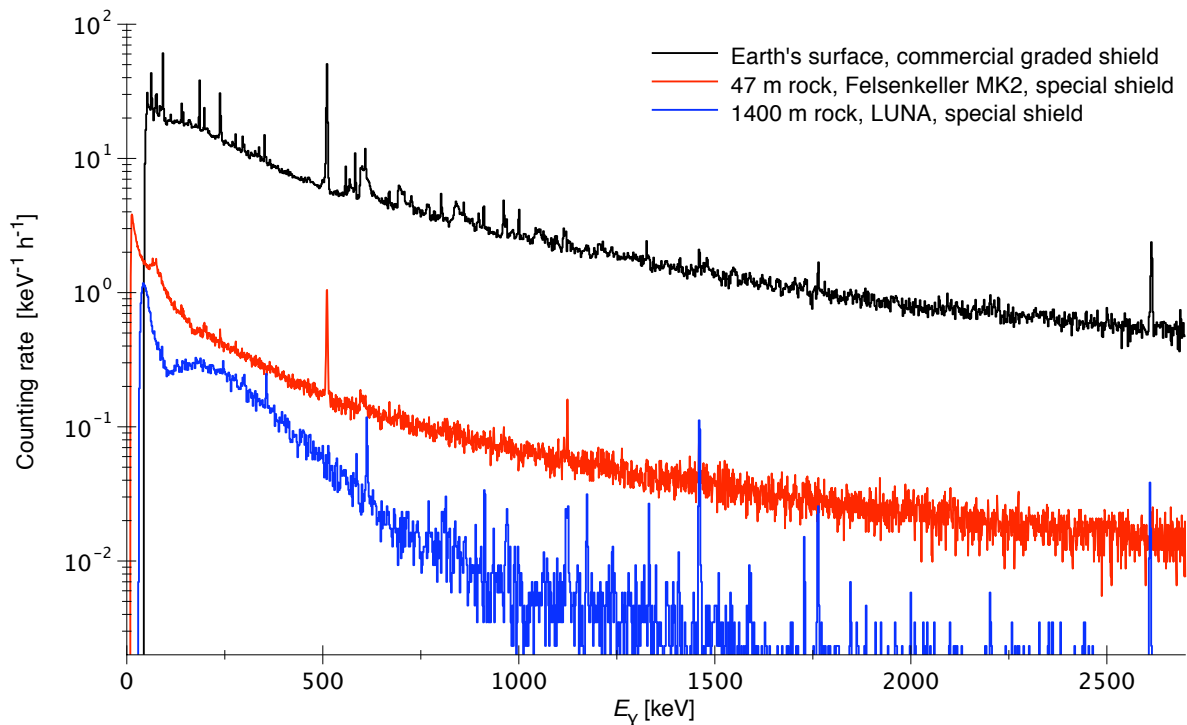


Figure 14: Laboratory background spectra in passively shielded high-purity germanium γ -detectors at several sites: At the surface of the Earth in a commercial graded shield [29], in the shallow-underground Felsenkeller laboratory below 47 m of rock in a special shield [28], and below 1400 m of rock in the LUNA deep-underground facility [H9]. The counting rates have been rescaled to match 137% relative efficiency [H9].

spectra show the same behavior as before, in the crucial 6-8 MeV region of interest that is relevant for the $^{14}\text{N}(p,\gamma)^{15}\text{O}$ and $^{12}\text{C}(\alpha,\gamma)^{16}\text{O}$ reactions, the vetoed background in Felsenkeller is now only a factor 3 higher than the vetoed background in one and the same detector at LUNA. This can be explained by the fact that the laboratory background at the LUNA site is actually not dominated by cosmic-ray induced muons any more, as they have been suppressed by six orders of magnitude due to the 1400 m thick rock overburden. Instead, at LUNA the neutron flux dominates the background counting rate. It is mainly given by depth-independent effects, most importantly (α,n) reactions in the rock surrounding the laboratories [128].

In principle, it is possible to protect an experimental setup against these high-energy neutrons from the laboratory walls by passive shielding, such as a sufficiently thick polyethylene layer. This is in fact done for the highly sensitive setups used for rare event searches, in particular for dark matter and neutrinoless double beta decay related work [129] where ideally no event is detected over several years. However, the requirements of low-background nuclear astrophysics studies, with one event per day or more, are less stringent. Therefore, no neutron shield is necessary at the LUNA site, and none is used.

For a shallow-underground laboratory such as Felsenkeller this means that with active shielding, the background level is not far from the ideal, deep-underground setting of LUNA. Consequently, for a number of important astrophysical scenarios, low-energy data can be taken with no or little limitation also in a shallow-underground facility such as Felsenkeller. A detailed list of possible reactions and counting rates has been computed [H11].

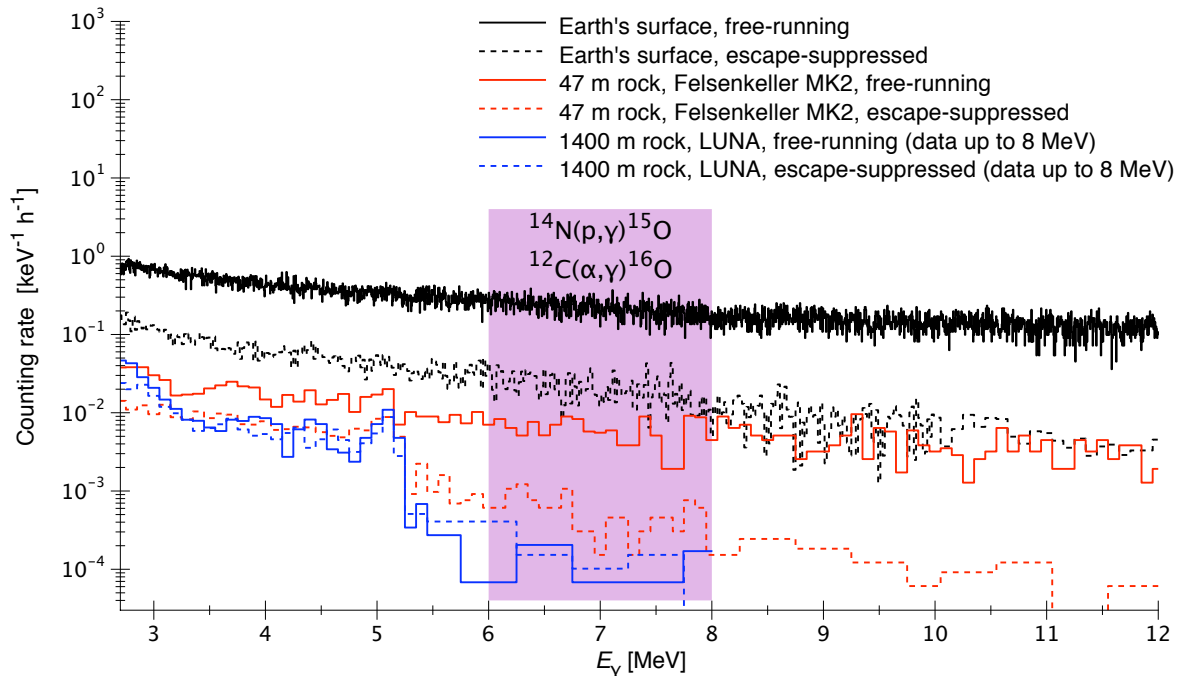


Figure 15: Laboratory background spectra in one and the same actively shielded γ -detector at several sites: At the Earth's surface [H10], at the Felsenkeller laboratory below 47 m of rock, and deep underground at LUNA below 1400 m of rock [H10]. The 6-8 MeV region of interest relevant for the $^{14}\text{N}(p,\gamma)^{15}\text{O}$ and $^{12}\text{C}(\alpha,\gamma)^{16}\text{O}$ reactions is shaded.

5.4 Possible scientific program at the Felsenkeller facility, Dresden (paper H11)

Given the obvious scientific interest of a higher-energy underground accelerator (sec. 5.2), on the one hand, and the clear feasibility of installing such a device in the Felsenkeller shallow-underground facility in Dresden (sec. 5.3), on the other hand, the case can be made to install a high-intensity accelerator of 2-5 MV acceleration potential there, with an ion source capable of supplying intensive beams of hydrogen and helium, possibly also carbon and nitrogen ions.

The Felsenkeller tunnels have been dug in the 1850's and hosted the ice cellar of the nearby brewery. Currently, one tunnel is used for the low-background γ -counting and tritium measurement facility of Verein für Kernverfahrenstechnik und Analytik Rossendorf (VKTA). This facility has been established in 1982 and is a founding member of the collaboration of European underground laboratories. Some of the other tunnels are used for storage, some not at all. Clearly, there would be enough space to place an ion accelerator inside, even assuming the most space-consuming option, a 5 MV tandem device (fig. 16).

The science driving research at such a facility could encompass:

1. The nuclear reactions of stellar hydrogen burning, in the Sun and in other stars, complementing the low-energy data by the LUNA 0.4 MV machine.
2. The nuclear reactions of Big Bang nucleosynthesis, again complementing the low-energy data by the LUNA 0.4 MV machine.
3. The nuclear reactions of stellar helium burning, including the so-called "holy grail of nuclear astrophysics", the $^{12}\text{C}(\alpha,\gamma)^{16}\text{O}$ reaction.
4. The nuclear reactions providing the neutrons for the astrophysical s-process: $^{13}\text{C}(\alpha,n)^{16}\text{O}$ and $^{22}\text{Ne}(\alpha,n)^{25}\text{Mg}$.

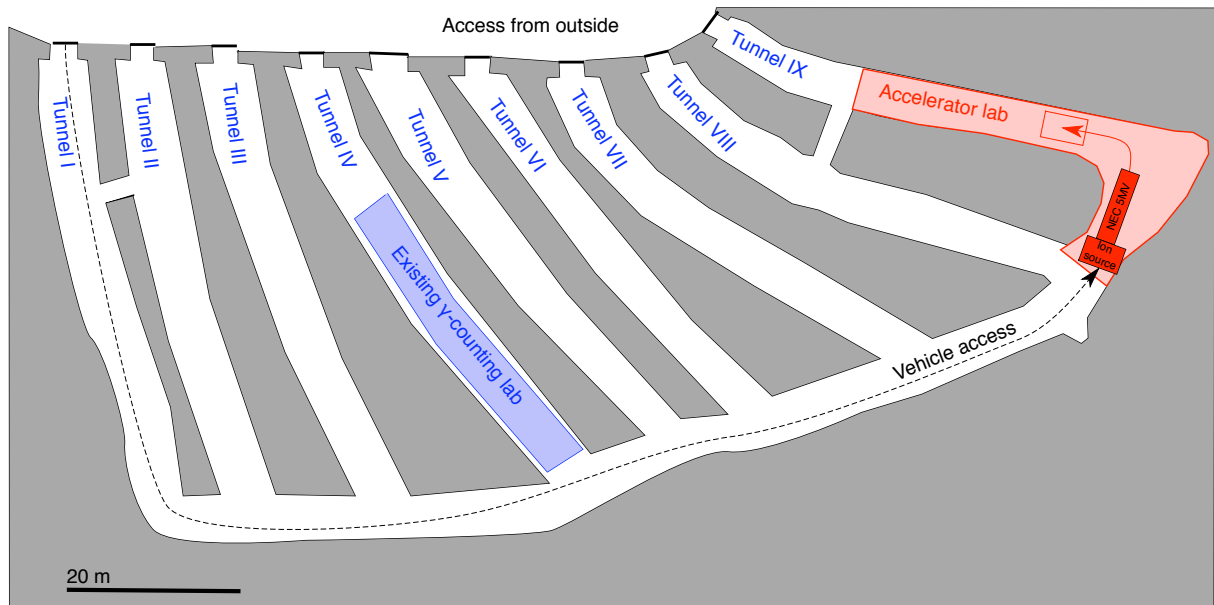


Figure 16: Schematic layout of the underground tunnel system at the Felsenkeller site. The existing VKTA γ -counting facility is marked in blue, and a possible accelerator laboratory is marked in red.

5. Nuclear reactions relevant for radioactive nuclides whose decay can be observed in astronomical objects, such as ^{26}Al , ^{44}Ti , and ^{60}Fe .
6. Low-background uses of applied nuclear physics, e.g. for high-sensitivity impurity analyses and depth profiles.

The science case for points 1-4 has been summarized in sec. 5.2. Regarding point 5, there is a very recent textbook devoted to astronomy with radioactivities that nicely summarizes this topic [130]. Some remarks on point 6 will be made near the end of the present section.

The astrophysically motivated points 1-5 intersect with the science addressed at several other facilities, two of which deserve special mention here: The LUNA 0.4 MV accelerator and the future Facility for Antiproton and Ion Research (FAIR) in Darmstadt/Germany. The synergies between Felsenkeller, LUNA-0.4 MV and the NuSTAR (Nuclear Structure, Astrophysics, and Reactions) branch of FAIR are shown graphically in fig. 17.

Another synergy is between the planned study of the two neutron source reactions for the astrophysical s-process, and the future "Frankfurter Neutronenquelle am Stern-Gerlach-Zentrum" (FRANZ) [121] facility at Frankfurt University where the neutron capture reactions of the s-process, in particular the so-called weak s-process, will be studied.

Looking beyond astrophysics, it is obvious that analytical techniques must become ever more sensitive, in order to keep up with the demands of geophysics, nanoscience, and the semiconductor industry. Placing an accelerator in a low-background setting underground will benefit those analytical techniques that use a low-energy ion beam as a probe and detect emitted γ -rays. It is conceivable that two such techniques would benefit most from the underground setting:

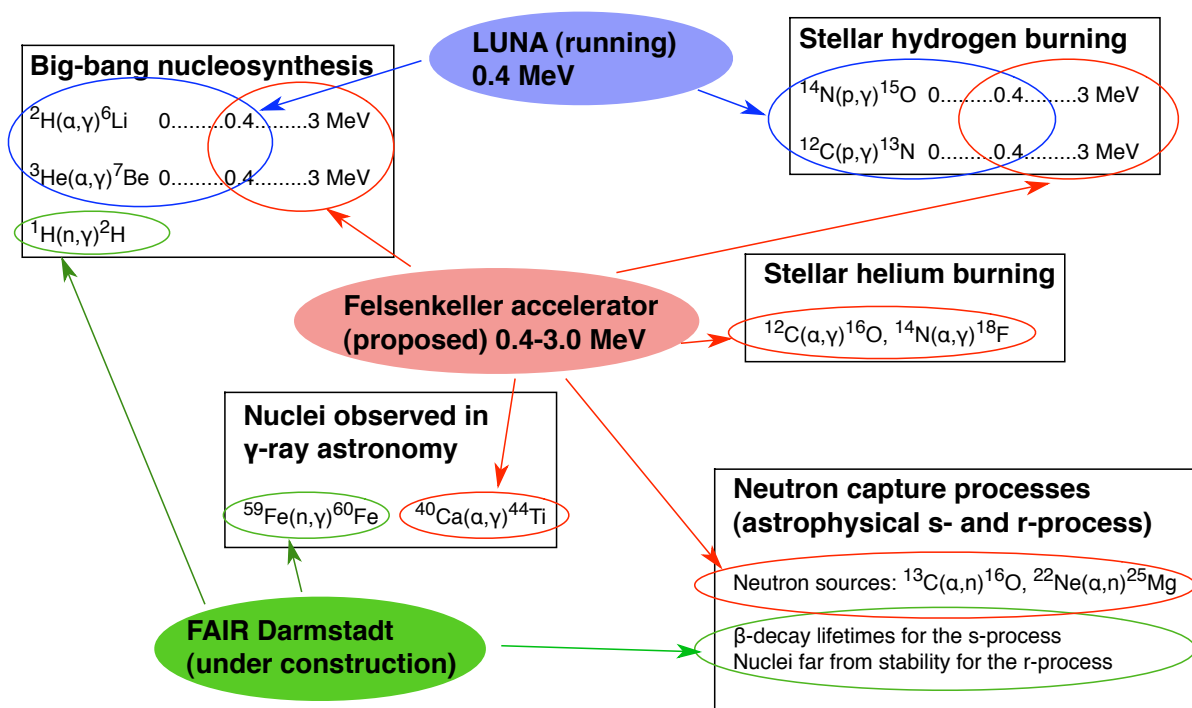


Figure 17: Intersection of the science case of a possible Felsenkeller accelerator with the present LUNA 0.4 MV accelerator and the future FAIR facility in Darmstadt/Germany.

First, the technique of proton induced gamma-ray emission (PIGE) is usually limited in sensitivity by beam-induced background from the sample. However, for very clean samples, cosmic-ray induced background starts to play a role. Following an international call to action [131], there are recent efforts to improve the cross section database for typical PIGE nuclides [132, e.g.]. The additional use of an underground facility could make PIGE into a highly sensitive tool.

Second, hydrogen depth profiling is often done by the $^{15}\text{N}(p,\alpha\gamma)^{12}\text{C}$ reaction in inverse kinematics, using a ^{15}N beam. For samples with small hydrogen concentrations, one is forced to use high ^{15}N beam intensities to overcome the background, which may result in modifications to the sample under study. An alternative approach would be to use low beam intensities and a low-background underground facility.

Concluding this section about possible science at a Felsenkeller accelerator, one example from a running project is shown here, in which the existing VKTA Felsenkeller γ -counting facility is used to count very low activity samples. The experiment is designed to measure resonance strengths in the $^{40}\text{Ca}(\alpha,\gamma)^{44}\text{Ti}$ reaction. This reaction is responsible for the production of ^{44}Ti in the α -rich freezeout phase of a supernova [133]. ^{44}Ti is one of the radionuclides observable in space [130], and the importance of the $^{40}\text{Ca}(\alpha,\gamma)^{44}\text{Ti}$ reaction has recently been underlined [134].

The ^{44}Ti sample shown here has been produced via activation at the surface-based 3.3 MV HZDR Tandatron in Rossendorf, using $1\ \mu\text{A}$ $^4\text{He}^+$ beam intensity over several days. Owing to the very low background at Felsenkeller, its very weak ^{44}Ti activity of 3 mBq could be detected directly and through its daughter ^{44}Sc , both of which would have been impossible in a low-background setup at the surface of the Earth. This study is still ongoing, but it is hoped that it will significantly improve the understanding of the nuclear physics of ^{44}Ti production.

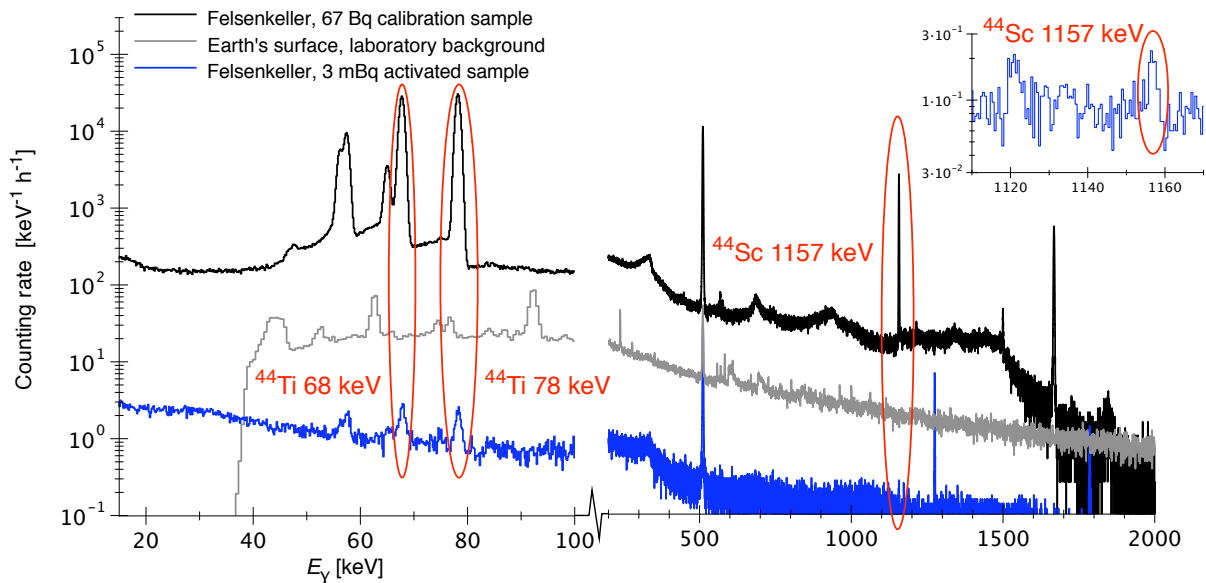


Figure 18: $^{40}\text{Ca}(\alpha,\gamma)^{44}\text{Ti}$ activation spectrum recorded in the VKTA Felsenkeller facility.

Acknowledgments

It is a pleasure to acknowledge the directors of the Institute of Radiation Physics of Helmholtz-Zentrum Dresden-Rossendorf, Prof. Dr. Eckart Grosse (up to 2007) and Prof. Dr. Thomas Cowan (from 2008 on) for enabling me to pursue my research, for their guidance and encouragement. The collaboration with Prof. Dr. Kai Zuber, Institute for Nuclear and Particle Physics, Technical University of Dresden, has been particularly fruitful and inspiring.

The study of the ${}^3\text{He}(\alpha,\gamma){}^7\text{Be}$ reaction has been carried out during my time as postdoc in the group of Dr. Carlo Broggini at Istituto Nazionale di Fisica Nucleare in Padua/Italy. I want to particularly thank Carlo for this great opportunity and a highly motivating environment.

I am indebted to many colleagues who have helped me at various stages of the research described here. To name just a few, Dr. Chavkat Akhmadaliev, Dr. Carlos Rossi Alvarez, Dr. Andreas Bergmaier, Dr. Detlev Degering, Dr. Alba Formicola, Dr. Zsolt Fülöp, Dr. Carlo Gustavo, Dr. György Gyürky, Dr. Arnd Junghans, Dr. Matthias Junker, Prof. Dr. Burkhard Kämpfer, Dr. Matthias Laubenstein, Dr. Roberto Menegazzo, Dr. Ronald Schwengner, and Dr. Andreas Wagner have all been highly helpful. I am deeply grateful to all my colleagues in the LUNA collaboration.

Several students have, in some sense or other, worked together with me on this topic, and I am very grateful to them: Michael Anders, Dr. Antonio Cacioli, Dr. Valentina Lozza, Michele Marta, Konrad Schmidt, Tamás Szücs, and Erik Trompler. Marko Röder and Dmitry Yakorev address new challenges that lie beyond the scope of the present work, namely detector development and the astrophysical r-process.

This work has been supported by Deutsche Forschungsgemeinschaft (BE 4100-2/1), the European Union (FP6-ILIAS, FP6-AIM, FP7-SPIRIT), INFN (Fondo Affari Internazionali), and EuroGENESIS.

References

- [1] J. N. Bahcall. *Neutrino astrophysics*. Cambridge and New York, Cambridge University Press, 1989.
- [2] Frederick Reines and Clyde Cowan. The Neutrino. *Nature*, 178:446–449, 1956.
- [3] R. Davis. Nobel Lecture: A half-century with solar neutrinos. *Rev. Mod. Phys.*, 75:985–994, 2003.
- [4] GNO Collaboration, M. Altmann, M. Balata, P. Belli, E. Bellotti, R. Bernabei, E. Burkert, C. Cattadori, R. Cerulli, M. Chiarini, M. Cribier, S. D’Angelo, G. Del Re, K. H. Ebert, F. von Feilitzsch, N. Ferrari, W. Hampel, F. X. Hartmann, E. Henrich, G. Heusser, F. Kaether, J. Kiko, T. Kirsten, T. Lachenmaier, J. Lanfranchi, M. Laubenstein, K. Lützenkirchen, K. Mayer, P. Moegel, D. Motta, S. Nisi, J. Oehm, L. Pandola, F. Petricca, W. Potzel, H. Richter, S. Schoenert, M. Wallenius, M. Wojcik, and L. Zanutti. Complete results for five years of GNO solar neutrino observations. *Phys. Lett. B*, 616:174–190, 2005.
- [5] R. Bonetti, C. Brogгинi, L. Campajola, P. Corvisiero, A. D’Alessandro, M. Dessalvi, A. D’Onofrio, A. Fubini, G. Gervino, L. Gialanella, U. Greife, A. Guglielmetti, C. Gustavino, G. Imbriani, M. Junker, P. Prati, V. Roca, C. Rolfs, M. Romano, F. Schuemann, F. Strieder, F. Terrasi, H. P. Trautvetter, and S. Zavatarelli. First Measurement of the ${}^3\text{He}({}^3\text{He},2p){}^4\text{He}$ Cross Section down to the Lower Edge of the Solar Gamow Peak. *Phys. Rev. Lett.*, 82:5205–5208, 1999.
- [6] J. N. Bahcall, A. M. Serenelli, and S. Basu. New Solar Opacities, Abundances, Helioseismology, and Neutrino Fluxes. *Astrophys. J.*, 621:L85–L88, 2005.
- [7] Q. R. Ahmad et al. Direct Evidence for Neutrino Flavor Transformation from Neutral-Current Interactions in the Sudbury Neutrino Observatory. *Phys. Rev. Lett.*, 89:011301, 2002.
- [8] M. Asplund, N. Grevesse, A. J. Sauval, and P. Scott. The Chemical Composition of the Sun. *Annu. Rev. Astron. Astroph.*, 47:481–522, 2009.
- [9] A. M. Serenelli, S. Basu, J. W. Ferguson, and M. Asplund. New Solar Composition: The Problem with Solar Models Revisited. *Astrophys. J. Lett.*, 705:L123–L127, 2009.
- [10] W. C. Haxton and A. M. Serenelli. CN-Cycle Solar Neutrinos and Sun’s Primordial Core Metallicity. *Astrophys. J.*, 687:678–691, 2008.
- [11] C. Arpesella, H. O. Back, M. Balata, G. Bellini, J. Benziger, S. Bonetti, A. Brigatti, B. Caccianiga, L. Cadonati, F. Calaprice, C. Carraro, G. Cecchet, A. Chavarria, M. Chen, F. Dalnoki-Veress, D. D’Angelo, A. de Bari, A. de Bellefon, H. de Kerret, A. Derbin, M. Deutsch, A. di Credico, G. di Pietro, R. Eisenstein, F. Elisei, A. Etenko, R. Fernholz, K. Fomenko, R. Ford, D. Franco, B. Freudiger, C. Galbiati, F. Gatti, S. Gazdara, M. Giammarchi, D. Giugni, M. Goeger-Neff, T. Goldbrunner, A. Goretti, C. Grieb, C. Hagner, W. Hampel, E. Harding, S. Hardy, F. X. Hartman, T. Hertrich, G. Heusser, A. Ianni, A. Ianni, M. Joyce, J. Kiko, T. Kirsten, V. Kobychiev, G. Korga, G. Korschinek, D. Kryn, V. Lagomarsino, P. Lamarche, M. Laubenstein, C. Lendvai, M. Leung, T. Lewke, E. Litvinovich, B. Loer, P. Lombardi, L. Ludhova, I. Machulin, S. Malvezzi, S. Manecki, J. Maneira, W. Maneschg, I. Manno, D. Manuzio, G. Manuzio, A. Martemianov, F. Masetti,

- U. Mazzucato, K. McCarty, D. McKinsey, Q. Meindl, E. Meroni, L. Miramonti, M. Misi-
aszek, D. Montanari, M. E. Monzani, V. Muratova, P. Musico, H. Neder, A. Nelson,
L. Niedermeier, L. Oberauer, M. Obolensky, M. Orsini, F. Ortica, M. Pallavicini, L. Papp,
S. Parmeggiano, L. Perasso, A. Pocar, R. S. Raghavan, G. Ranucci, W. Rau, A. Razeto,
E. Resconi, P. Risso, A. Romani, D. Rountree, A. Sabelnikov, R. Saldanha, C. Salvo,
D. Schimizzi, S. Schönert, T. Shutt, H. Simgen, M. Skorokhvatov, O. Smirnov, A. Son-
nenschein, A. Sotnikov, S. Sukhotin, Y. Suvorov, R. Tartaglia, G. Testera, D. Vignaud,
S. Vitale, R. B. Vogelaar, F. von Feilitzsch, R. von Hentig, T. von Hentig, M. Wojcik,
M. Wurm, O. Zaimidoroga, S. Zavatarelli, and G. Zuzel. Direct measurement of the ${}^7\text{Be}$
solar neutrino flux with 192 days of Borexino data. *Phys. Rev. Lett.*, 101:091302, 2008.
- [12] M. C. Chen. The SNO Liquid Scintillator Project. *Nucl. Phys. B (Proc. Suppl.)*, 145:65–68,
2005.
- [13] C. Casella, H. Costantini, A. Lemut, B. Limata, R. Bonetti, C. Brogгинi, L. Campajola,
P. Corvisiero, J. Cruz, A. D’Onofrio, A. Formicola, Z. Fülöp, G. Gervino, L. Gialanella,
A. Guglielmetti, C. Gustavino, G. Gyurky, G. Imbriani, A. P. Jesus, M. Junker, A. Ordine,
J. V. Pinto, P. Prati, J. P. Ribeiro, V. Roca, D. Rogalla, C. Rolfs, M. Romano, C. Rossi-
Alvarez, F. Schuemann, E. Somorjai, O. Straniero, F. Strieder, F. Terrasi, H. P. Trautvetter,
and S. Zavatarelli. First measurement of the $d(p,\gamma){}^3\text{He}$ cross section down to the solar
Gamow peak. *Nucl. Phys. A*, 706:203–216, 2002.
- [14] C. Peña-Garay and A. Serenelli. Solar neutrinos and the solar composition problem.
ArXiv e-prints, 0811.2424, 2008.
- [15] J. Hosaka et al. Solar neutrino measurements in Super-Kamiokande-I. *Phys. Rev. D*,
73:112001, 2006.
- [16] J. P. Cravens et al. Solar neutrino measurements in Super-Kamiokande-II. *Phys. Rev. D*,
78:032002, 2008.
- [17] B. Aharmim, S. N. Ahmed, A. E. Anthony, N. Barros, E. W. Beier, A. Bellerive, B. Bel-
tran, M. Bergevin, S. D. Biller, K. Boudjemline, M. G. Boulay, T. H. Burritt, B. Cai, Y. D.
Chan, D. Chauhan, M. Chen, B. T. Cleveland, G. A. Cox, X. Dai, H. Deng, J. Detwiler,
M. Dimarco, P. J. Doe, G. Doucas, P.-L. Drouin, C. A. Duba, F. A. Duncan, M. Dunford,
E. D. Earle, S. R. Elliott, H. C. Evans, G. T. Ewan, J. Farine, H. Fergani, F. Fleurot, R. J.
Ford, J. A. Formaggio, N. Gagnon, J. T. Goon, K. Graham, E. Guillian, S. Habib, R. L.
Hahn, A. L. Hallin, E. D. Hallman, P. J. Harvey, R. Hazama, W. J. Heintzelman, J. Heise,
R. L. Helmer, A. Hime, C. Howard, M. A. Howe, M. Huang, B. Jamieson, N. A. Jelley, K. J.
Keeter, J. R. Klein, L. L. Kormos, M. Kos, C. Kraus, C. B. Krauss, T. Kutter, C. C. M. Kyba,
J. Law, I. T. Lawson, K. T. Lesko, J. R. Leslie, I. Levine, J. C. Loach, R. MacLellan, S. Ma-
jerus, H. B. Mak, J. Maneira, R. Martin, N. McCauley, A. B. McDonald, S. McGee, M. L.
Miller, B. Monreal, J. Monroe, B. Morissette, B. G. Nickel, A. J. Noble, H. M. O’Keeffe,
N. S. Oblath, G. D. Orebi Gann, S. M. Oser, R. A. Ott, S. J. M. Peeters, A. W. P. Poon,
G. Prior, S. D. Reitzner, K. Rielage, B. C. Robertson, R. G. H. Robertson, M. H. Schwen-
dener, J. A. Secrest, S. R. Seibert, O. Simard, D. Sinclair, P. Skensved, T. J. Sonley, L. C.
Stonehill, G. Tešić, N. Tolich, T. Tsui, C. D. Tunnell, R. van Berg, B. A. Vandevender, C. J.
Virtue, B. L. Wall, D. Waller, H. Wan Chan Tseung, D. L. Wark, N. West, J. F. Wilkerson,
J. R. Wilson, J. M. Wouters, A. Wright, M. Yeh, F. Zhang, K. Zuber, and SNO Collabora-
tion. Low-energy-threshold analysis of the Phase I and Phase II data sets of the Sudbury
Neutrino Observatory. *Phys. Rev. C*, 81:055504, 2010.

- [18] E.G. Adelberger, S. M. Austin, J. N. Bahcall, A. B. Balantekin, G. Bogaert, L. S. Brown, L. Buchmann, F. E. Cecil, A. E. Champagne, L. de Braekeleer, C. A. Duba, S. R. Elliott, S. J. Freedman, M. Gai, G. Goldring, C. R. Gould, A. Gruzinov, W. C. Haxton, K. M. Heeger, E. Henley, C. W. Johnson, M. Kamionkowski, R. W. Kavanagh, S. E. Koonin, K. Kubodera, K. Langanke, T. Motobayashi, V. Pandharipande, P. Parker, R. G. Robertson, C. Rolfs, R. F. Sawyer, N. Shaviv, T. D. Shoppa, K. A. Snover, E. Swanson, R. E. Tribble, S. Turck-Chièze, and J. F. Wilkerson. Solar fusion cross sections. *Rev. Mod. Phys.*, 70:1265–1291, 1998.
- [19] Carmen Angulo, M. Arnould, M. Rayet, P. Descouvemont, D. Baye, C. Leclercq-Willain, A. Coc, S. Barhoumi, P. Aguer, C. Rolfs, R. Kunz, J. W. Hammer, A. Mayer, T. Paradelis, S. Kossionides, C. Chronidou, K. Spyrou, S. degl’Innocenti, G. Fiorentini, B. Ricci, S. Zavatarelli, C. Providencia, H. Wolters, J. Soares, C. Grama, J. Rahighi, A. Shotter, and M. Laméhi Rachti. A compilation of charged-particle induced thermonuclear reaction rates. *Nucl. Phys. A*, 656:3–187, 1999.
- [20] Pierre Descouvemont, Abderrahim Adahchour, Carmen Angulo, Alain Coc, and Elisabeth Vangioni-Flam. Compilation and R-matrix analysis of Big Bang nuclear reaction rates. *At. Data Nucl. Data Tables*, 88:203–236, 2004.
- [21] A. R. Junghans, E. C. Mohrmann, K. A. Snover, T. D. Steiger, E. G. Adelberger, J. M. Casandjian, H. E. Swanson, L. Buchmann, S. H. Park, and A. Zyuzin. ${}^7\text{Be}(p,\gamma){}^8\text{B}$ Astrophysical S Factor from Precision Cross Section Measurements. *Phys. Rev. Lett.*, 88:041101, 2002.
- [22] A. R. Junghans, K. A. Snover, E. C. Mohrmann, E. G. Adelberger, and L. Buchmann. Updated S factors for the ${}^7\text{Be}(p,\gamma){}^8\text{B}$ reaction. *Phys. Rev. C*, 81:012801(R), 2010.
- [23] C. Casella, H. Costantini, A. Lemut, B. Limata, D. Bemmerer, R. Bonetti, C. Broggini, L. Campajola, P. Cocconi, P. Corvisiero, J. Cruz, A. D’Onofrio, A. Formicola, Z. Fülöp, G. Gervino, L. Gialanella, A. Guglielmetti, C. Gustavino, G. Gyurky, A. Loiano, G. Imbriani, A. P. Jesus, M. Junker, P. Musico, A. Ordine, F. Parodi, M. Parolin, J. V. Pinto, P. Prati, J. P. Ribeiro, V. Roca, D. Rogalla, C. Rolfs, M. Romano, C. Rossi-Alvarez, A. Rottura, F. Schuemann, E. Somorjai, F. Strieder, F. Terrasi, H. P. Trautvetter, A. Vomiero, and S. Zavatarelli. A new setup for the underground study of capture reactions. *Nucl. Inst. Meth. A*, 489:160–169, 2002.
- [24] J. Görres, K. Kettner, H. Kräwinkel, and C. Rolfs. The influence of intense ion beams on gas target densities. *Nucl. Inst. Meth.*, 177:295–303, 1980.
- [25] M. Marta, F. Confortola, D. Bemmerer, C. Boiano, R. Bonetti, C. Broggini, M. Casanova, P. Corvisiero, H. Costantini, Z. Elekes, A. Formicola, Z. Fülöp, G. Gervino, A. Guglielmetti, C. Gustavino, G. Gyürky, G. Imbriani, M. Junker, A. Lemut, B. Limata, R. Menegazzo, P. Prati, V. Roca, C. Rolfs, M. Romano, C. Rossi Alvarez, E. Somorjai, F. Strieder, F. Terrasi, and H. P. Trautvetter. Study of beam heating effect in a gas target through Rutherford scattering. *Nucl. Inst. Meth. A*, 569:727–731, 2006.
- [26] S. Agostinelli et al. GEANT 4 - a simulation toolkit. *Nucl. Inst. Meth. A*, 506:250–303, 2003.
- [27] D.R. Tilley, C.M. Cheves, J.L. Godwin, G.M. Hale, H.M. Hofmann, J.H. Kelley, C.G. Sheu, and H.R. Weller. Energy levels of light nuclei $A = 5, 6, 7$. *Nucl. Phys. A*, 708:3–163, 2002.

- [28] M. Köhler, D. Degering, M. Laubenstein, P. Quirin, M.-O. Lampert, M. Hult, D. Arnold, S. Neumaier, and J.-L. Reyss. A new low-level γ -ray spectrometry system for environmental radioactivity at the underground laboratory Felsenkeller. *Appl. Radiat. Isot.*, 67:736–740, 2009.
- [29] Martin Erhard. *Photoaktivierung des p -Kerns ^{92}Mo am Bremsstrahlungsmessplatz von ELBE*. PhD thesis, TU Dresden, 2009.
- [30] Claus Rolfs and William Rodney. *Cauldrons in the Cosmos*. University of Chicago Press, Chicago, 1988.
- [31] Christian Iliadis. *Nuclear Physics of Stars*. Wiley-VCH, Weinheim, 2007.
- [32] B.S. Nara Singh, M. Hass, Y. Nir-El, and G. Haquin. New Precision Measurement of the $^3\text{He}(^4\text{He},\gamma)^7\text{Be}$ Cross Section. *Phys. Rev. Lett.*, 93:262503, 2004.
- [33] T. A. D. Brown, C. Bordeanu, K. A. Snover, D. W. Storm, D. Melconian, A. L. Sallaska, S. K. L. Sjue, and S. Triambak. $^3\text{He}+^4\text{He} \rightarrow ^7\text{Be}$ astrophysical S factor. *Phys. Rev. C*, 76:055801, 2007.
- [34] A. di Leva, L. Gialanella, R. Kunz, D. Rogalla, D. Schürmann, F. Strieder, M. de Cesare, N. de Cesare, A. D’Onofrio, Z. Fülöp, G. Gyürky, G. Imbriani, G. Mangano, A. Ordine, V. Roca, C. Rolfs, M. Romano, E. Somorjai, and F. Terrasi. Stellar and Primordial Nucleosynthesis of ^7Be : Measurement of $^3\text{He}(\alpha,\gamma)^7\text{Be}$. *Phys. Rev. Lett.*, 102:232502, 2009.
- [35] T. Neff. Microscopic Calculation of the $^3\text{He}(\alpha,\gamma)^7\text{Be}$ and $^3\text{H}(\alpha,\gamma)^7\text{Li}$ Capture Cross Sections Using Realistic Interactions. *Phys. Rev. Lett.*, 106:042502, 2011.
- [36] P.D. Parker and R.W. Kavanagh. $\text{He}^3(\alpha,\gamma)\text{Be}^7$ Reaction. *Phys. Rev.*, 131:2578–2582, 1963.
- [37] B.T. Kim, T. Izumoto, and K. Nagatani. Radiative capture reaction $^3\text{He}(\alpha,\gamma)^7\text{Be}$ at low energies. *Phys. Rev. C*, 23:33, 1981.
- [38] Toshitaka Kajino. The $^3\text{He}(\alpha,\gamma)^7\text{Be}$ and $^3\text{H}(\alpha,\gamma)^7\text{Li}$ reactions at astrophysical energies. *Nucl. Phys. A*, 460:559–580, 1986.
- [39] T. Mertelmeier and H.M. Hoffmann. Consistent cluster model description of the electromagnetic properties of lithium and beryllium nuclei. *Nucl. Phys. A*, 459:387–416, 1986.
- [40] A. Csóto and Karlheinz Langanke. Study of the $^3\text{He}(^4\text{He},\gamma)^7\text{Be}$ and $^3\text{H}(^4\text{He},\gamma)^7\text{Li}$ Reactions in an Extended Two-Cluster Model. *Few-Body Systems*, 29:121–130, 2000.
- [41] K. M. Nollett. Radiative α -capture cross sections from realistic nucleon-nucleon interactions and variational Monte Carlo wave functions. *Phys. Rev. C*, 63:054002, 2001.
- [42] H. D. Holmgren and R. L. Johnston. $\text{H}^3(\alpha,\gamma)\text{Li}^7$ and $\text{He}^3(\alpha,\gamma)\text{Be}^7$ Reactions. *Phys. Rev.*, 113:1556–1559, 1959.
- [43] K. Nagatani, M.R. Dwarakanath, and D. Ashery. The $^3\text{He}(\alpha,\gamma)^7\text{Be}$ reaction at very low energy. *Nucl. Phys. A*, 128:325–332, 1969.
- [44] J. L. Osborne, C. A. Barnes, R. W. Kavanagh, R. M. Kremer, G. J. Mathews, J. L. Zyskind, P. D. Parker, and A. J. Howard. Low-Energy $^3\text{He}(\alpha,\gamma)^7\text{Be}$ Cross-Section Measurements. *Phys. Rev. Lett.*, 48:1664–1666, 1982.

- [45] H. Kräwinkel, Hans Werner Becker, Lothar Buchmann, Joachim Görres, K.U. Kettner, W.E. Kieser, R. Santo, P. Schmalbrock, Hanns-Peter Trautvetter, A. Vlieks, Claus Rolfs, J.W. Hammer, R.E. Azuma, and W.S. Rodney. The ${}^3\text{He}(\alpha,\gamma){}^7\text{Be}$ Reaction and the Solar Neutrino Problem. *Z. Phys. A*, 304:307–332, 1982.
- [46] R. G. H. Robertson, P. Dyer, T. J. Bowles, R. E. Brown, N. Jarmie, C. J. Maggiore, and S. M. Austin. Cross section of the capture reaction ${}^3\text{He}(\alpha,\gamma){}^7\text{Be}$. *Phys. Rev. C*, 27:11–17, 1983.
- [47] H. Volk, H. Kräwinkel, R. Santo, and L. Wallek. Activation Measurement of the ${}^3\text{He}({}^4\text{He},\gamma){}^7\text{Be}$ Reaction. *Z. Phys. A*, 310:91–94, 1983.
- [48] T.K. Alexander, G.C. Ball, W.N. Lennard, and H. Geissel. Measurement of the absolute cross section of the ${}^3\text{He}({}^4\text{He},\gamma){}^7\text{Be}$ reaction at $E_{c.m.} = 525$ keV. *Nucl. Phys. A*, 427:526–544, 1984.
- [49] M. Hilgemeier, H. W. Becker, C. Rolfs, H. P. Trautvetter, and J. W. Hammer. Absolute Cross Section of the ${}^3\text{He}(\alpha,\gamma){}^7\text{Be}$ Reaction. *Z. Phys. A*, 329:243–254, 1988.
- [50] G. M. Griffiths, R. A. Morrow, P. J. Riley, and J. B. Warren. The $\text{T}(\alpha,\gamma)\text{Li}$ reaction. *Can. J. Phys.*, 39:1397, 1961.
- [51] U. Schröder, A. Redder, C. Rolfs, R. E. Azuma, L. Buchmann, C. Campbell, J. D. King, and T. R. Donoghue. Astrophysical S factor of ${}^3\text{H}(\alpha,\gamma){}^7\text{Li}$. *Phys. Lett. B*, 192:55–58, 1987.
- [52] S. Burzyński, K. Czerski, A. Marcinkowski, and P. Zupranski. The ${}^3\text{H}(\alpha,\gamma){}^7\text{Li}$ reaction in the energy range from 0.7 to 2.0 MeV. *Nucl. Phys. A*, 473:179–188, 1987.
- [53] C. R. Brune, R. W. Kavanagh, and C. Rolfs. ${}^3\text{H}(\alpha,\gamma){}^7\text{Li}$ reaction at low energies. *Phys. Rev. C*, 50:2205–2218, 1994.
- [54] Hans Bethe. Energy production in stars. *Phys. Rev.*, 55:103, 1939.
- [55] Carl-Friedrich von Weizsäcker. Über Elementumwandlungen im Innern der Sterne. II. *Phys. Z.*, 39:633–646, 1938.
- [56] Michael Wiescher, Joachim Görres, Ethan Überseder, Gianluca Imbriani, and Marco Pig-natari. The Cold and Hot CNO Cycles. *Annu. Rev. Nucl. Part. Sci.*, 60:381–410, 2010.
- [57] Pierre Descouvemont and Daniel Baye. The R-matrix theory. *Rep. Prog. Phys.*, 73:036301, 2010.
- [58] Richard Azuma, E. Überseder, E. C. Simpson, C. R. Brune, H. Costantini, R. J. de Boer, J. Görres, M. Heil, P. J. Leblanc, C. Ugalde, and M. Wiescher. AZURE: An R-matrix code for nuclear astrophysics. *Phys. Rev. C*, 81:045805, 2010.
- [59] Gianluca Imbriani, H. Costantini, A. Formicola, A. Vomiero, C. Angulo, D. Bemmerer, R. Bonetti, C. Broggini, F. Confortola, P. Corvisiero, J. Cruz, P. Descouvemont, Z. Fülöp, G. Gervino, A. Guglielmetti, C. Gustavino, G. Gyürky, A. P. Jesus, M. Junker, J. N. Klug, A. Lemut, R. Menegazzo, P. Prati, V. Roca, C. Rolfs, M. Romano, C. Rossi-Alvarez, F. Schümann, D. Schürmann, E. Somorjai, O. Straniero, F. Strieder, F. Terrasi, and H. P. Trautvetter. S-factor of ${}^{14}\text{N}(p,\gamma){}^{15}\text{O}$ at astrophysical energies. *Eur. Phys. J. A*, 25:455–466, 2005.

- [60] Uwe Schröder, H. W. Becker, G. Bogaert, J. Görres, C. Rolfs, H. P. Trautvetter, R. E. Azuma, C. Campbell, J. D. King, and J. Vise. Stellar reaction rate of $^{14}\text{N}(p,\gamma)^{15}\text{O}$ and hydrogen burning in massive stars. *Nucl. Phys. A*, 467:240–260, 1987.
- [61] G.R. Caughlan and W.A. Fowler. Thermonuclear Reaction Rates V. *At. Data Nucl. Data Tables*, 40:283–334, 1988.
- [62] P.F. Bertone, A. E. Champagne, D. C. Powell, C. Iliadis, S. E. Hale, and V. Y. Hansper. Lifetime of the 6793-keV state in ^{15}O . *Phys. Rev. Lett.*, 87:152501, 2001.
- [63] Carmen Angulo and Pierre Descouvemont. The $^{14}\text{N}(p,\gamma)^{15}\text{O}$ low-energy S -factor. *Nucl. Phys. A*, 690:755–768, 2001.
- [64] A.M. Mukhamedzhanov, P. Bém, B. A. Brown, V. Burjan, C. A. Gagliardi, V. Kroha, J. Novák, F. M. Nunes, Š. Iskoř, F. Pirlpesov, E. Šimečková, R. E. Tribble, and J. Vincour. Asymptotic normalization coefficients for $^{14}\text{N} + p \rightarrow ^{15}\text{O}$ and the astrophysical S factor for $^{14}\text{N}(p,\gamma)^{15}\text{O}$. *Phys. Rev. C*, 67:065804, 2003.
- [65] K. Yamada, T. Motobayashi, H. Akiyoshi, N. Aoi, Z. Fülöp, T. Gomi, Y. Higurashi, N. Imai, N. Iwasa, H. Iwasaki, Y. Iwata, H. Kobayashi, M. Kurokawa, Z. Liu, T. Minemura, S. Ozawa, H. Sakurai, M. Serata, S. Shimoura, S. Takeuchi, T. Teranishi, Y. Yanagisawa, K. Yoshida, and M. Ishihara. E1 strength of the subthreshold $3/2^+$ state in ^{15}O studied by Coulomb excitation. *Phys. Lett. B*, 579:265–270, 2004.
- [66] A. Formicola, G. Imbriani, H. Costantini, C. Angulo, D. Bemmerer, R. Bonetti, C. Brogini, P. Corvisiero, J. Cruz, P. Descouvemont, Z. Fülöp, G. Gervino, A. Guglielmetti, C. Gustavino, G. Gyürky, A. P. Jesus, M. Junker, A. Lemut, R. Menegazzo, P. Prati, V. Roca, C. Rolfs, M. Romano, C. Rossi Alvarez, F. Schümann, E. Somorjai, O. Straniero, F. Strieder, F. Terrasi, H. P. Trautvetter, A. Vomiero, and S. Zavatarelli. Astrophysical S -factor of $^{14}\text{N}(p,\gamma)^{15}\text{O}$. *Phys. Lett. B*, 591:61–68, 2004.
- [67] R. C. Runkle, A. E. Champagne, C. Angulo, C. Fox, C. Iliadis, R. Longland, and J. Pollanen. Direct Measurement of the $^{14}\text{N}(p,\gamma)^{15}\text{O}$ S Factor. *Phys. Rev. Lett.*, 94:082503, 2005.
- [68] Fay Ajzenberg-Selove. Energy levels of light nuclei $A = 13-15$. *Nucl. Phys. A*, 523:1–196, 1991.
- [69] D.R. Tilley, H.R. Weller, and C.M. Cheves. Energy levels of light nuclei $A = 16-17$. *Nucl. Phys. A*, 564:1–183, 1993.
- [70] M. Borowski, K. P. Lieb, M. Uhrmacher, and W. Bolse. Precision Measurements of the 278 keV $^{14}\text{N}(p,\gamma)$ and the 151 keV $^{18}\text{O}(p,\alpha)$ Resonance Parameters. In *AIP Conf. Proc. 1090: Capture Gamma-Ray Spectroscopy and Related Topics*, page 450, 2009.
- [71] H.W. Becker, M. Bahr, M. Berheide, L. Borucki, M. Buschmann, C. Rolfs, G. Roters, S. Schmidt, W.H. Schulte, G.E. Mitchell, and J.S. Schweitzer. Hydrogen depth profiling using ^{18}O ions. *Z. Phys. A*, 351:453–465, 1995.
- [72] F. Zijderhand and C. van der Leun. Strong M2 transitions. *Nucl. Phys. A*, 460:181–200, 1986.
- [73] André Mariotti. Atmospheric nitrogen is a reliable standard for natural ^{15}N abundance measurements. *Nature*, 303:685–687, 1983.

- [74] T. B. Coplen, J. K. Böhlke, P. de Bièvre, T. Ding, N. E. Holden, J. A. Hopple, H. R. Krouse, A. Lamberty, H. S. Peiser, K. Révész, S.E. Rieder, K. J. R. Rosman, E. Roth, P.D.P. Taylor, R. D. Vocke, Jr., and Y. K. Xiao. Isotope-abundance variations of selected elements (IUPAC Technical Report). *Pure Appl. Chem.*, 74:1987–2017, 2002.
- [75] M. La Cognata, V. Z. Goldberg, A. M. Mukhamedzhanov, C. Spitaleri, and R. E. Tribble. Improved determination of the astrophysical S(0) factor of the $^{15}\text{N}(p,\alpha)^{12}\text{C}$ reaction. *Phys. Rev. C*, 80:012801, 2009.
- [76] D. F. Hebbard. Proton capture by N^{15} . *Nucl. Phys.*, 15:289–315, 1960.
- [77] Claus Rolfs and W.S. Rodney. Proton capture by ^{15}N at stellar energies. *Nucl. Phys. A*, 235:450–459, 1974.
- [78] Daniel Bemmerer. *Experimental study of the $^{14}\text{N}(p,\gamma)^{15}\text{O}$ reaction at energies far below the Coulomb barrier*. PhD thesis, Technische Universität Berlin, 2004. http://edocs.tu-berlin.de/diss/2004/bemmerer_daniel.htm.
- [79] A. Lemut, D. Bemmerer, F. Confortola, R. Bonetti, C. Broggini, P. Corvisiero, H. Costantini, J. Cruz, A. Formicola, Z. Fülöp, G. Gervino, A. Guglielmetti, C. Gustavino, G. Gyürky, G. Imbriani, A. P. Jesus, M. Junker, B. Limata, R. Menegazzo, P. Prati, V. Roca, D. Rogalla, C. Rolfs, M. Romano, C. Rossi Alvarez, F. Schümann, E. Somorjai, O. Straniero, F. Strieder, F. Terrasi, and H. P. Trautvetter. First measurement of the $^{14}\text{N}(p,\gamma)^{15}\text{O}$ cross section down to 70 keV. *Phys. Lett. B*, 634:483, 2006.
- [80] Daniel Bemmerer, F. Confortola, A. Lemut, R. Bonetti, C. Broggini, P. Corvisiero, H. Costantini, J. Cruz, A. Formicola, Z. Fülöp, G. Gervino, A. Guglielmetti, C. Gustavino, G. Gyürky, G. Imbriani, A. Jesus, M. Junker, B. Limata, R. Menegazzo, P. Prati, V. Roca, C. Rolfs, D. Rogalla, M. Romano, C. Rossi-Alvarez, F. Schümann, E. Somorjai, O. Straniero, F. Strieder, F. Terrasi, and H. P. Trautvetter. Low energy measurement of the $^{14}\text{N}(p,\gamma)^{15}\text{O}$ total cross section at the LUNA underground facility. *Nucl. Phys. A*, 779:297–317, 2006.
- [81] A. M. Mukhamedzhanov, P. Bém, V. Burjan, C. A. Gagliardi, V. Z. Goldberg, Z. Hons, M. La Cognata, V. Kroha, J. Mrázek, J. Novák, Š. Piskoř, R. G. Pizzone, A. Plunkett, S. Romano, E. Šimečková, C. Spitaleri, L. Trache, R. E. Tribble, F. Veselý, and J. Vincour. New astrophysical S factor for the $^{15}\text{N}(p,\gamma)^{16}\text{O}$ reaction via the asymptotic normalization coefficient (ANC) method. *Phys. Rev. C*, 78:015804, 2008.
- [82] P. J. LeBlanc, G. Imbriani, J. Görres, M. Junker, R. Azuma, M. Beard, D. Bemmerer, A. Best, C. Broggini, A. Caciolli, P. Corvisiero, H. Costantini, M. Couder, R. Deboer, Z. Elekes, S. Falahat, A. Formicola, Z. Fülöp, G. Gervino, A. Guglielmetti, C. Gustavino, G. Gyürky, F. Käppeler, A. Kontos, R. Kuntz, H. Leiste, A. Lemut, Q. Li, B. Limata, M. Marta, C. Mazzocchi, R. Menegazzo, S. O'Brien, A. Palumbo, P. Prati, V. Roca, C. Rolfs, C. Rossi Alvarez, E. Somorjai, E. Stech, O. Straniero, F. Strieder, W. Tan, F. Terrasi, H. P. Trautvetter, E. Uberseder, and M. Wiescher. Constraining the S factor of $^{15}\text{N}(p,\gamma)^{16}\text{O}$ at astrophysical energies. *Phys. Rev. C*, 82:055804, 2010.
- [83] R. Grötzschel, E. Hentschel, R. Klages, U. Kreissig, C. Neelmeijer, W. Assmann, and R. Behrisch. Elemental analysis of thin layers by elastic heavy ion scattering. *Nucl. Inst. Meth. B*, 63:77–82, 1992.

- [84] Christian Iliadis, Art Champagne, Jordi José, Sumner Starrfield, and Paul Tupper. The effects of thermonuclear reaction-rate variations on nova nucleosynthesis: A sensitivity study. *Astrophys. J. Suppl. Ser.*, 142:105–137, 2002.
- [85] F. Herwig. Evolution of Asymptotic Giant Branch Stars. *Annu. Rev. Astron. Astroph.*, 43:435–479, 2005.
- [86] A. M. Mukhamedzhanov, Marco La Cognata, and V. Kroha. Astrophysical S factor for the $^{15}\text{N}(p,\gamma)^{16}\text{O}$ reaction. *Phys. Rev. C*, 83:044604, 2011.
- [87] *The Frontiers of Nuclear Science, A Long Range Plan*. DOE/NSF Nuclear Science Advisory Committee, 2008.
- [88] Workshop on underground nuclear-reaction experiments for astrophysics and applications. Dresden/Germany, 28.-30.04.2010. <http://www.hzdr.de/felsenkeller>, 2010.
- [89] Nuclear Physics European Collaboration Committee. *Long Range Plan: Perspectives of Nuclear Physics in Europe*. NuPECC, 2010.
- [90] C. Iliadis, R. Longland, A. E. Champagne, and A. Coc. Charged-particle thermonuclear reaction rates: III. Nuclear physics input. *Nucl. Phys. A*, 841:251–322, 2010. <http://www.sciencedirect.com/science/article/pii/S0375947410004203>.
- [91] J. Görres, C. Rolfs, P. Schmalbrock, H. P. Trautvetter, and J. Keinonen. Search for low-energy resonances in $^{21}\text{Ne}(p,\gamma)^{22}\text{Na}$ and $^{22}\text{Ne}(p,\gamma)^{23}\text{Na}$. *Nucl. Phys. A*, 385:57–75, 1982.
- [92] S. E. Hale, A. E. Champagne, C. Iliadis, V. Y. Hansper, D. C. Powell, and J. C. Blackmon. Investigation of the $^{22}\text{Ne}(p,\gamma)^{23}\text{Na}$ reaction via ($^3\text{He},d$) spectroscopy. *Phys. Rev. C*, 65:015801, 2002.
- [93] R. Longland, C. Iliadis, J. M. Cesaratto, A. E. Champagne, S. Daigle, J. R. Newton, and R. Fitzgerald. Resonance strength in $^{22}\text{Ne}(p,\gamma)^{23}\text{Na}$ from depth profiling in aluminum. *Phys. Rev. C*, 81:055804, 2010.
- [94] C. Iliadis, R. Longland, A. E. Champagne, A. Coc, and R. Fitzgerald. Charged-particle thermonuclear reaction rates: II. Tables and graphs of reaction rates and probability density functions. *Nucl. Phys. A*, 841:31–250, 2010.
- [95] C. Iliadis, J. M. D’Auria, S. Starrfield, W. J. Thompson, and M. Wiescher. Proton-induced Thermonuclear Reaction Rates for $A=20-40$ Nuclei. *Astrophys. J. Suppl. Ser.*, 134:151–171, 2001.
- [96] Sachiko Amari, Xia Gao, Larry R. Nittler, Ernst Zinner, Jordi José, Margarita Hernanz, and Roy S. Lewis. Presolar grains from novae. *Astrophys. J.*, 551:1065–1072, 2001.
- [97] Jordi José, Margarita Hernanz, Sachiko Amari, Katharina Lodders, and Ernst Zinner. The imprint of nova nucleosynthesis in presolar grains. *Astrophys. J.*, 612:414–428, 2004.
- [98] P. R. Heck, S. Amari, P. Hoppe, H. Baur, R. S. Lewis, and R. Wieler. Ne Isotopes in Individual Presolar Graphite Grains from the Murchison Meteorite Together with He, C, O, Mg-Al Isotopic Analyses as Tracers of Their Origins. *Astrophys. J.*, 701:1415–1425, 2009.
- [99] M. Kusakabe, N. Iwamoto, and K. Nomoto. Production of the p-process Nuclei in the Carbon-deflagration Model for Type Ia Supernovae. *Astrophys. J.*, 726:25, 2011.

- [100] Claudia Travaglio, Fritz Röpke, Roberto Gallino, and Wolfgang Hillebrandt. Type Ia supernovae as sites of p-process: two-dimensional models coupled to nucleosynthesis. *Astrophys. J.*, 739:93, 2011.
- [101] J. N. Bahcall, A. M. Serenelli, and S. Basu. 10,000 Standard Solar Models: A Monte Carlo Simulation. *Astrophys. J. Suppl. Ser.*, 165:400–431, 2006.
- [102] Claus Rolfs and Richard Azuma. Interference effects in $^{12}\text{C}(p,\gamma)^{13}\text{N}$ and direct capture to unbound states. *Nucl. Phys. A*, 227:291–308, 1974.
- [103] W. A. Lamb and R. E. Hester. Radiative Capture of Protons in Carbon from 80 to 126 keV. *Phys. Rev.*, 107:550–553, 1957.
- [104] W.S. Lamb and R.E. Hester. Transmutation of nitrogen by protons from 100 keV to 135 keV. *Phys. Rev.*, 108:1304–1307, 1957.
- [105] N. Burtebaev, S. B. Igamov, R. J. Peterson, R. Yarmukhamedov, and D. M. Zazulin. New measurements of the astrophysical S factor for $^{12}\text{C}(p,\gamma)^{13}\text{N}$ reaction at low energies and the asymptotic normalization coefficient (nuclear vertex constant) for the $p+^{12}\text{C}\rightarrow^{13}\text{N}$ reaction. *Phys. Rev. C*, 78:035802, 2008.
- [106] Z. Li, J. Su, B. Guo, Z. Li, X. Bai, J. Liu, Y. Li, S. Yan, B. Wang, Y. Wang, G. Lian, S. Zeng, E. Li, Y. Chen, N. Shu, Q. Fan, and W. Liu. Determination of the $^{12}\text{C}(p,\gamma)^{13}\text{N}$ reaction rates from the $^{12}\text{C}(^7\text{Li},^6\text{He})^{13}\text{N}$ reaction. *Science in China G: Physics and Astronomy*, 53:658–663, 2010.
- [107] C. D. Nesaraja, C. R. Brune, B. T. Crowley, J. H. Kelley, S. O. Nelson, R. M. Prior, K. Sabourov, D. R. Tilley, A. Tonchev, and H. R. Weller. Ratio of S factors for (p, γ) reactions on ^{12}C and ^{13}C at astrophysically relevant energies. *Phys. Rev. C*, 64:065804, 2001.
- [108] V. V. Smith, D. L. Lambert, and P. E. Nissen. The $^6\text{Li}/^7\text{Li}$ ratio in the metal-poor halo dwarfs HD 19445 and HD 84937. *Astrophys. J.*, 408:262–276, 1993.
- [109] M. Asplund, D. L. Lambert, P. E. Nissen, F. Primas, and V. V. Smith. Lithium Isotopic Abundances in Metal-poor Halo Stars. *Astrophys. J.*, 644:229–259, 2006.
- [110] P. D. Serpico, S. Esposito, F. Iocco, G. Mangano, G. Miele, and O. Pisanti. Nuclear reaction network for primordial nucleosynthesis: a detailed analysis of rates, uncertainties and light nuclei yields. *J. Cosmol. Astropart. Phys.*, 2004:010, 2004.
- [111] M. Kusakabe, T. Kajino, and G. J. Mathews. ^6Li production by the radiative decay of long-lived particles. *Phys. Rev. D*, 74:023526, 2006.
- [112] K. Jedamzik and M. Pospelov. Big Bang nucleosynthesis and particle dark matter. *New Journal of Physics*, 11:105028, 2009.
- [113] M. Steffen, R. Cayrel, P. Bonifacio, H.-G. Ludwig, and E. Caffau. Convection and ^6Li in the atmospheres of metal-poor halo stars. In C. Charbonnel, M. Tosi, F. Primas, & C. Chiappini, editor, *IAU Symposium*, volume 268 of *IAU Symposium*, pages 215–220, 2010.
- [114] M. Spite and F. Spite. Li isotopes in metal-poor halo dwarfs: a more and more complicated story. In C. Charbonnel, M. Tosi, F. Primas, & C. Chiappini, editor, *IAU Symposium*, volume 268 of *IAU Symposium*, pages 201–210, 2010.

- [115] F. Hammache, M. Heil, S. Typel, D. Galaviz, K. Sümmerer, A. Coc, F. Uhlig, F. Attallah, M. Caamano, D. Cortina, H. Geissel, M. Hellström, N. Iwasa, J. Kiener, P. Koczon, B. Kohlmeyer, P. Mohr, E. Schwab, K. Schwarz, F. Schümann, P. Senger, O. Sorlin, V. Tatischeff, J. P. Thibaud, E. Vangioni, A. Wagner, and W. Walus. High-energy breakup of ${}^6\text{Li}$ as a tool to study the Big Bang nucleosynthesis reaction ${}^2\text{H}(\alpha,\gamma){}^6\text{Li}$. *Phys. Rev. C*, 82:065803, 2010.
- [116] Lothar Buchmann and C Barnes. Nuclear reactions in stellar helium burning and later hydrostatic burning stages. *Nucl. Phys. A*, 777:254, 2006.
- [117] S. E. Woosley and A. Heger. Nucleosynthesis and remnants in massive stars of solar metallicity. *Phys. Rep.*, 442:269–283, 2007.
- [118] C. Sneden, J. J. Cowan, and R. Gallino. Neutron-Capture Elements in the Early Galaxy. *Annu. Rev. Astron. Astroph.*, 46:241–288, 2008.
- [119] Z. Y. Bao, H. Beer, F. Käppeler, F. Voss, K. Wisshak, and T. Rauscher. Neutron Cross Sections for Nucleosynthesis Studies. *At. Data Nucl. Data Tables*, 76:70–154, 2000.
- [120] F. Käppeler, R. Gallino, S. Bisterzo, and W. Aoki. The s process: Nuclear physics, stellar models, and observations. *Rev. Mod. Phys.*, 83:157–194, 2011.
- [121] R. Reifarth, L. P. Chau, M. Heil, F. Käppeler, O. Meusel, R. Plag, U. Ratzinger, A. Schempp, and K. Volk. Opportunities for Nuclear Astrophysics at FRANZ. *Publ. Astron. Soc. Australia*, 26:255–258, 2009.
- [122] Michael Heil, R. Detwiler, R. E. Azuma, A. Couture, J. Daly, J. Görres, F. Käppeler, R. Reifarth, P. Tischhauser, C. Ugalde, and M. Wiescher. The ${}^{13}\text{C}(\alpha,n)$ reaction and its role as a neutron source for the s process. *Phys. Rev. C*, 78:025803, 2008.
- [123] M. Jaeger, R. Kunz, A. Mayer, J. W. Hammer, G. Staudt, K. L. Kratz, and B. Pfeiffer. ${}^{22}\text{Ne}(\alpha,n){}^{25}\text{Mg}$: The Key Neutron Source in Massive Stars. *Phys. Rev. Lett.*, 87:202501, 2001.
- [124] F. Iocco, G. Mangano, G. Miele, O. Pisanti, and P. D. Serpico. Primordial nucleosynthesis: From precision cosmology to fundamental physics. *Phys. Rep.*, 472:1–76, 2009.
- [125] L.R. Gasques, E.F. Brown, Alessandro Chieffi, C.L. Jiang, Marco Limongi, Claus Rolfs, Michael Wiescher, and D.G. Yakovlev. Implications of low-energy fusion hindrance on stellar burning and nucleosynthesis. *Phys. Rev. C*, 76:035802, 2007.
- [126] Daniel Bemmerer, F. Confortola, A. Lemut, R. Bonetti, C. Broggini, P. Corvisiero, H. Costantini, J. Cruz, A. Formicola, Z. Fülöp, G. Gervino, A. Guglielmetti, C. Gustavino, G. Gyürky, G. Imbriani, A. P. Jesus, M. Junker, B. Limata, R. Menegazzo, P. Prati, V. Roca, D. Rogalla, C. Rolfs, M. Romano, C. Rossi Alvarez, F. Schümann, E. Somorjai, O. Straniero, F. Strieder, F. Terrasi, H. P. Trautvetter, and A. Vomiero. Feasibility of low-energy radiative-capture experiments at the LUNA underground accelerator facility. *Eur. Phys. J. A*, 24:313–319, 2005.
- [127] Gerd Heusser. Low-radioactivity background techniques. *Annu. Rev. Nucl. Part. Sci.*, 45:543–590, 1995.
- [128] H. Wulandari, J. Jochum, W. Rau, and F. von Feilitzsch. Neutron flux at the Gran Sasso underground laboratory revisited. *Astropart. Phys.*, 22:313–322, 2004.

- [129] Joseph A. Formaggio and C.J. Martoff. Backgrounds to sensitive experiments underground. *Annu. Rev. Nucl. Part. Sci.*, 54:361–412, 2004.
- [130] Roland Diehl, Dieter Hartmann, and Nikos Prantzos, editors. *Astronomy with Radioactivities*, volume 812 of *Lecture Notes in Physics*. Springer, 2011.
- [131] Daniel Abriola and Adelaide Pedro de Jesus. Assessment of Nuclear Data Needs for Particle Induced Gamma Ray Emission (PIGE). Technical Report INDC(NDS)-0568, International Atomic Energy Agency, Nuclear Data Section, 2010.
- [132] Maria Micaela Leal da Fonseca. *Análise de elementos leves por reacções nucleares com produção de radiação gama*. PhD thesis, Universidade Nova de Lisboa, Faculdade de Ciências e Tecnologia, 2011.
- [133] L.-S. The, D. D. Clayton, R. Diehl, D. H. Hartmann, A. F. Iyudin, M. D. Leising, B. S. Meyer, Y. Motizuki, and V. Schönfelder. Are ^{44}Ti -producing supernovae exceptional? *Astron. Astrophys.*, 450:1037–1050, 2006.
- [134] R. Hoffman, S. A. Sheets, J. T. Burke, N. D. Scielzo, T. Rauscher, E. B. Norman, S. Tumey, T. A. Brown, P. G. Grant, A. M. Hurst, L. Phair, M. A. Stoyer, T. Wooddy, J. L. Fisker, , and D. Bleuel. Reaction rate sensitivity of ^{44}Ti production in massive stars and implications of a thick target yield measurement of $^{40}\text{Ca}(\alpha,\gamma)^{44}\text{Ti}$. *Astrophys. J.*, 715:1383–1399, 2010.

Erklärung

Hiermit erkläre ich, dass ich die Habilitationsschrift selbst und ohne andere als die darin angegebenen Hilfsmittel angefertigt habe, sowie dass die wörtlich oder inhaltlich übernommenen Stellen als solche gekennzeichnet wurden. Mein eigener Beitrag zu den in Abschnitt 0 aufgelisteten Publikationen ist ebenfalls in Abschnitt 0 zusammengefasst.

Dresden, den 25.08.2011

(Daniel Bemmerer)

Reprints of publications at the base of this habilitation request

The publications listed in sec. 0 are reproduced on the subsequent pages.

	Journal reference, and link	Link to the reproduced publication
H1	Phys. Rev. Lett. 97, 122501 (2006)	nucl-ex/0609013
H2	Phys. Rev. C 75, 035805 (2007).	nucl-ex/0702003
H3	Phys. Rev. C 75, 065803 (2007).	0705_2151
H4	Phys. Rev. C 78, 022802(R) (2008).	0807_4919
H5	Phys. Rev. C 83, 045804 (2011)	1103_5393
H6	Phys. Rev. C 81, 055807 (2010).	1005_1873
H7	J. Phys. G 36, 045202 (2009).	0902_0783
H8	Astronomy & Astrophysics 533, A66 (2011).	1107_4514
H9	Eur. Phys. J. A 39, 179-186 (2009).	0812_3223
H10	Eur. Phys. J. A 44, 513-519 (2010).	1003_6072
H11	Eur. Phys. J. A 48, 8 (2012).	Eur. Phys. J. A 48, 8 (2012).
H12	Annu. Rev. Nucl. Part. Science 60, 53-73 (2010).	1010_4165
H13	Rev. Mod. Phys. 83, 195-246 (2011).	1004_2318v3

Activation measurement of the ${}^3\text{He}(\alpha, \gamma){}^7\text{Be}$ cross section at low energy

D. Bemmerer,¹ F. Confortola,² H. Costantini,² A. Formicola,³ Gy. Gyürky,⁴ R. Bonetti,⁵ C. Broggini,^{1,*} P. Corvisiero,² Z. Elekes,⁴ Zs. Fülöp,⁴ G. Gervino,⁶ A. Guglielmetti,⁵ C. Gustavino,³ G. Imbriani,⁷ M. Junker,³ M. Laubenstein,³ A. Lemut,² B. Limata,⁷ V. Lozza,¹ M. Marta,⁵ R. Menegazzo,¹ P. Prati,² V. Roca,⁷ C. Rolfs,⁸ C. Rossi Alvarez,¹ E. Somorjai,⁴ O. Straniero,⁹ F. Strieder,⁸ F. Terrasi,¹⁰ and H.P. Trautvetter⁸

(The LUNA Collaboration)

¹*Istituto Nazionale di Fisica Nucleare (INFN), Sezione di Padova, via Marzolo 8, 35131 Padova, Italy*

²*Università di Genova and INFN Sezione di Genova, Genova, Italy*

³*INFN, Laboratori Nazionali del Gran Sasso (LNGS), Assergi (AQ), Italy*

⁴*Institute of Nuclear Research (ATOMKI), Debrecen, Hungary*

⁵*Istituto di Fisica Generale Applicata, Università di Milano and INFN Sezione di Milano, Italy*

⁶*Dipartimento di Fisica Sperimentale, Università di Torino and INFN Sezione di Torino, Torino, Italy*

⁷*Dipartimento di Scienze Fisiche, Università di Napoli "Federico II", and INFN Sezione di Napoli, Napoli, Italy*

⁸*Institut für Experimentalphysik III, Ruhr-Universität Bochum, Bochum, Germany*

⁹*Osservatorio Astronomico di Collurania, Teramo, and INFN Sezione di Napoli, Napoli, Italy*

¹⁰*Seconda Università di Napoli, Caserta, and INFN Sezione di Napoli, Napoli, Italy*

(Dated: July 5, 2006)

The nuclear physics input from the ${}^3\text{He}(\alpha, \gamma){}^7\text{Be}$ cross section is a major uncertainty in the fluxes of ${}^7\text{Be}$ and ${}^8\text{B}$ neutrinos from the Sun predicted by solar models and in the ${}^7\text{Li}$ abundance obtained in big-bang nucleosynthesis calculations. The present work reports on a new precision experiment using the activation technique at energies directly relevant to big-bang nucleosynthesis. Previously such low energies had been reached experimentally only by the prompt- γ technique and with inferior precision. Using a windowless gas target, high beam intensity and low background γ -counting facilities, the ${}^3\text{He}(\alpha, \gamma){}^7\text{Be}$ cross section has been determined at 127, 148 and 169 keV center-of-mass energy with a total uncertainty of 4%. The sources of systematic uncertainty are discussed in detail. The present data can be used in big-bang nucleosynthesis calculations and to constrain the extrapolation of the ${}^3\text{He}(\alpha, \gamma){}^7\text{Be}$ astrophysical S-factor to solar energies.

PACS numbers: 25.55.-e, 26.20.+f, 26.35.+c, 26.65.+t

The ${}^3\text{He}(\alpha, \gamma){}^7\text{Be}$ reaction is a critical link in the ${}^7\text{Be}$ and ${}^8\text{B}$ branches of the proton-proton (p-p) chain of solar hydrogen burning [1]. At low energies its cross section $\sigma(E)$ (E denotes the center of mass energy, E_α the ${}^4\text{He}$ beam energy in the laboratory system) can be parameterized by the astrophysical S-factor $S(E)$ defined as

$$S(E) = \sigma(E) \cdot E \exp(2\pi\eta(E))$$

with $\eta(E) \propto E^{-0.5}$ [2]. The 9.4% uncertainty [3] in the S-factor extrapolation to the solar Gamow energy (23 keV) contributes 8% to the uncertainty in the predicted fluxes of solar neutrinos from the decays of ${}^7\text{Be}$ and ${}^8\text{B}$ [4]. The interior of the Sun, in turn, can be studied [4, 5] by comparing this prediction with the data from neutrino detectors [6, 7], which determine the ${}^8\text{B}$ neutrino flux with a total uncertainty as low as 3.5% [7].

Furthermore, the production of ${}^7\text{Li}$ in big-bang nucleosynthesis (BBN) is highly sensitive to the ${}^3\text{He}(\alpha, \gamma){}^7\text{Be}$ cross section in the energy range $E \approx 160\text{--}380\text{ keV}$ [8], with an adopted uncertainty of 8% [9]. Based on the baryon-to-photon ratio from observed anisotropies in the cosmic microwave background [10], network calculations predict primordial ${}^7\text{Li}$ abundances [11] that are significantly higher than observations [12, 13]. A lower ${}^3\text{He}(\alpha, \gamma){}^7\text{Be}$ cross section at relevant energies may explain part of this discrepancy.

The ${}^3\text{He}(\alpha, \gamma){}^7\text{Be}$ (Q -value: 1.586 MeV) reaction leads to the emission of prompt γ -rays, and the final ${}^7\text{Be}$ nucleus decays with a half-life of 53.22 ± 0.06 days, emitting a 478 keV γ -ray in $10.44 \pm 0.04\%$ of the cases [14]. The cross section can be measured by detecting either the induced ${}^7\text{Be}$ activity (activation method) or the prompt γ -rays from the reaction (prompt- γ method). Previous activation studies [15, 16, 17, 18] cover the energy range $E = 420\text{--}2000\text{ keV}$. Prompt γ -ray measurements [15, 19, 20, 21, 22, 23, 24] cover $E = 107\text{--}2500\text{ keV}$, although with limited precision at low energies.

The global shape of the S-factor curve is well reproduced by theoretical calculations [25, 26]. However, the slope has been questioned [26] for $E \leq 300\text{ keV}$, where there are no high-precision data. Furthermore, a global analysis [3] indicates that S-factor data obtained with the activation method are systematically higher than the prompt- γ results. A recent activation study [18] reduces this discrepancy to 9% for the extrapolated $S(0)$ [3], still not at the precision level of the ${}^8\text{B}$ neutrino data [7]. Precise ${}^3\text{He}(\alpha, \gamma){}^7\text{Be}$ measurements at low energies have been recommended to study the solar interior [4, 5, 27], to sharpen big-bang ${}^7\text{Li}$ abundance predictions [8, 28], and to investigate the low-energy slope of the S-factor curve [26]. The aim of the present work is to provide high precision activation data at energies directly relevant to

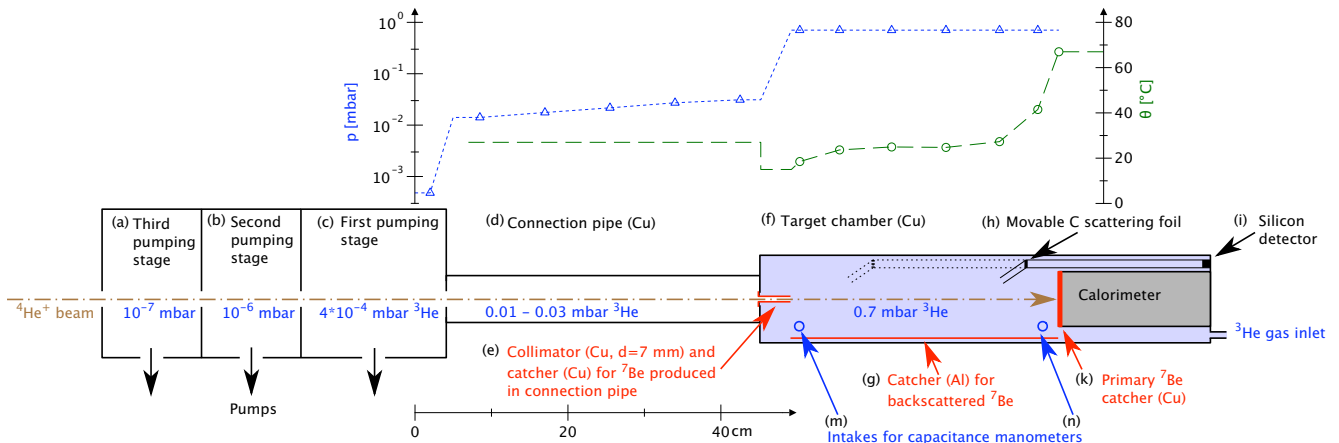


FIG. 1: Schematic view of the target chamber used for the irradiations. Above: pressure (p , triangles) and temperature (θ , circles) values measured without ion beam and interpolated profile between the data points (lines). See text for details.

big-bang nucleosynthesis and low enough to effectively constrain the extrapolation to solar energies.

The Laboratory for Underground Nuclear Astrophysics (LUNA) [29] in Italy's Gran Sasso underground laboratory (LNGS) has been designed for measuring low nuclear cross sections for astrophysical purposes [30, 31, 32, 33, 34, 35]. The irradiations have been carried out at the 400 kV LUNA2 accelerator [36] at energies $E_\alpha = 300, 350$ and 400 keV, with a typical current of $200 \mu\text{A}$ $^4\text{He}^+$. The beam energy is obtained from a precision resistor chain and has 5 eV/h long-term stability [36]. The $^3\text{He}(\alpha, \gamma)^7\text{Be}$ reaction takes place in a differentially pumped windowless gas target (Fig. 1, similar to the one described previously [37]) filled with enriched ^3He gas (isotopic purity $>99.95\%$, pressure 0.7 mbar, target thickness $9\text{--}10$ keV). The exhaust from the first and second pumping stages is cleaned in a getter-based gas purifier and recirculated into the target. The ion beam from the accelerator passes three pumping stages (Fig. 1 a-c), a connection pipe (d), enters the target chamber (f) through an aperture of 7 mm diameter (e) and is finally stopped on a detachable oxygen free high conductivity (OFHC) copper disk (k) of 70 mm diameter that serves as the primary catcher for the produced ^7Be and as the hot side of a calorimeter with constant temperature gradient [37]. A precision of 1.5% for the beam intensity is obtained from the difference between the calorimeter power values with and without incident ion beam, taking into account the calculated energy loss in the target gas [38] and using a calibration curve determined by measuring the electrical charge in the same setup without gas, applying a proper secondary electron suppression voltage. The effective target thickness depends on the pressure (monitored during the irradiations with two capacitance manometers, Fig. 1 m-n), the pressure and temperature profile (measured without ion beam, resulting density uncertainty 0.6%), the thinning of the target

gas through the beam heating effect [39] and the fraction of gases other than ^3He . In order to study the latter two effects, a $100 \mu\text{m}$ thick silicon detector (Fig. 1i) detects projectiles that have been elastically scattered first in the target gas and subsequently in a movable $15 \mu\text{g}/\text{cm}^2$ carbon foil (h). The beam heating effect has been investigated in a wide beam energy and intensity range, and a correction of $4.9 \pm 1.3\%$, $5.4 \pm 1.3\%$ and $5.7 \pm 1.3\%$ was found for the irradiations at $E_\alpha = 300, 350$ and 400 keV, respectively. The amount of contaminant gases (mainly nitrogen) is monitored with the silicon detector during the irradiations, kept below $1.0 \pm 0.1\%$ and corrected for in the analysis. Further details of the elastic scattering measurements are described elsewhere [40].

The catchers are irradiated with charges of $60\text{--}220$ C, accumulating ^7Be activities of $0.2\text{--}0.5$ Bq. The effective center of mass energy E^{eff} is calculated assuming a constant S-factor over the target length [2]. The uncertainties of 0.3 keV in E_α [36] and of 4.4% in the energy loss [38] result in an S-factor uncertainty of $0.5\text{--}0.8\%$. Calculations for the straggling of the ^4He beam and of the produced ^7Be nuclei in the ^3He gas and for the emission cone of ^7Be (opening angle $1.8\text{--}2.1^\circ$) show that 99.8% of the ^7Be produced inside the target chamber, including the 7 mm collimator, reaches the primary catcher.

After the irradiation, the catcher is dismantled and counted in close geometry subsequently with two 120% relative efficiency HPGe detectors called LNGS1 (Fig. 2) and LNGS2, both properly shielded with copper and lead, in the LNGS underground counting facility [41]. Detector LNGS1 is additionally equipped with an anti-radon box, and its laboratory background is two orders of magnitude lower than with equivalent shielding overground [41]. In order to obtain the photopeak counting efficiencies, three homogeneous ^7Be sources of $200\text{--}800$ Bq activity and 8 mm active diameter were prepared with the $^7\text{Li}(p, n)^7\text{Be}$ reaction at ATOMKI. Their activity

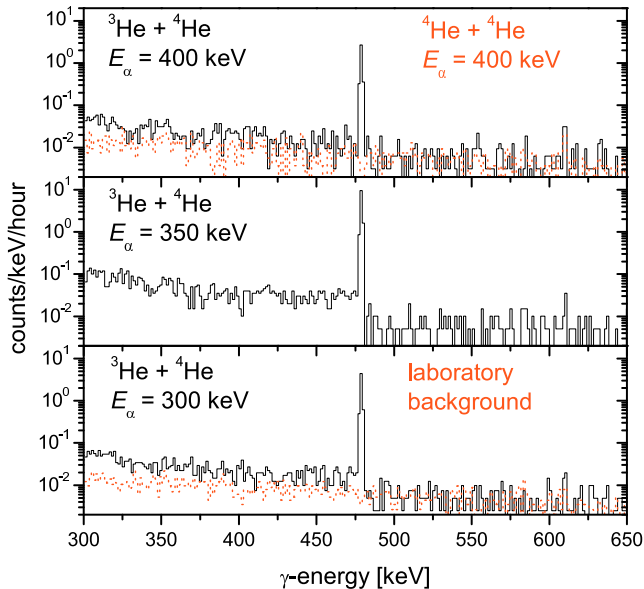


FIG. 2: Offline γ -counting spectra, detector LNGS1. Solid black line: ${}^3\text{He}$ gas bombarded at $E_\alpha = 400, 350, 300$ keV (top to down), respectively. Dotted red line, top panel: ${}^4\text{He}$ gas bombarded at $E_\alpha = 400$ keV. Dotted red line, bottom panel: laboratory background.

TABLE I: Systematic uncertainties in the ${}^3\text{He}(\alpha, \gamma){}^7\text{Be}$ astrophysical S-factor, neglecting contributions below 0.2%.

Source	Uncertainty
${}^7\text{Be}$ counting efficiency	1.8%
Beam intensity	1.5%
Beam heating effect	1.3%
Target pressure and temperature without beam	0.6%
${}^7\text{Be}$ backscattering	0.5%
Incomplete ${}^7\text{Be}$ collection	0.4%
${}^7\text{Be}$ distribution in catcher	0.4%
478 keV γ -ray branching [14]	0.4%
Effective energy	0.5–0.8%
Total:	2.9–3.0%

was determined with two HPGe detectors (each efficiency based on an independent set of commercial γ -ray sources) at ATOMKI and with one HPGe detector, called LNGS3 (efficiency based on a third set of commercial sources), at LNGS, giving consistent results and a final activity uncertainty of 1.8%. The three ${}^7\text{Be}$ sources were then used to calibrate detectors LNGS1 and LNGS2 in the same geometry as the activated samples. The ${}^7\text{Be}$ distribution in the catchers has been calculated from the ${}^7\text{Be}$ emission angle and straggling, and GEANT4 [42] simulations gave $0.8 \pm 0.4\%$ to $1.0 \pm 0.4\%$ correction for the γ -ray efficiency because of the tail of the distribution at high radii.

In order to investigate parasitic production of ${}^7\text{Be}$

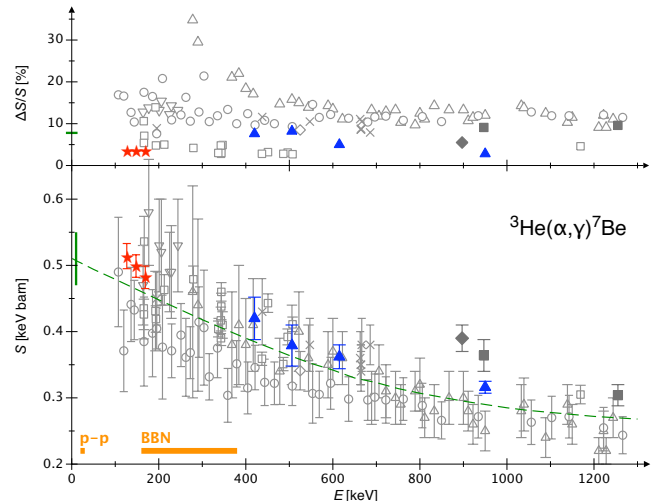


FIG. 3: Lower panel: astrophysical S-factor for ${}^3\text{He}(\alpha, \gamma){}^7\text{Be}$. Activation data: filled squares [15], filled diamonds [16], filled triangles [18], stars (present work). Prompt- γ data: triangles [20], inverted triangles [21], circles [22] (renormalized by a factor 1.4 [24]), squares [15], diamonds [23], crosses [24]. Dashed line: previously adopted R-matrix fit [9]. Horizontal bars: energies relevant for p-p chain and for BBN. — Upper panel: uncertainties (systematic and statistical combined in quadrature) of the data and of the R-matrix $S(0)$ [9].

through, e.g., the ${}^6\text{Li}(d, n){}^7\text{Be}$ and ${}^{10}\text{B}(p, \alpha){}^7\text{Be}$ reactions induced by possible traces of ${}^2\text{DH}_2^+$ in the ${}^4\text{He}^+$ beam, the enriched ${}^3\text{He}$ target gas was replaced with 0.7 mbar ${}^4\text{He}$, and a catcher was bombarded at the highest available energy of $E_\alpha = 400$ keV. Despite the high applied dose of 104 C, in 16 days counting time no ${}^7\text{Be}$ has been detected (Fig. 2, top panel), establishing a 2σ upper limit of 0.1% for parasitic ${}^7\text{Be}$.

Furthermore, ${}^7\text{Be}$ losses by backscattering from the primary catcher and by incomplete collection were studied experimentally at $E_\alpha = 400$ keV and with Monte Carlo simulations at 300, 350 and 400 keV. For the backscattering study, parts of the inner surface of the chamber were covered by aluminum foil functioning as secondary catcher (Fig. 1g). It was found that $1.3 \pm 0.5\%$ of the created ${}^7\text{Be}$ is lost due to backscattering, consistent with 1.5% obtained in a GEANT4 [42] simulation using a SRIM-like multiple scattering process [43]. At lower energies, the simulation result was used as backscattering correction (up to 2.2%, adopted uncertainty 0.5%).

Incomplete ${}^7\text{Be}$ collection occurs since 3.5% of the total ${}^3\text{He}$ target thickness are in the connecting pipe, and a part of the ${}^7\text{Be}$ created there does not reach the primary catcher but is instead implanted into the 7 mm collimator (Fig. 1e). At $E_\alpha = 400$ keV, a modified collimator functioning as secondary catcher was used, and a $2.6 \pm 0.4\%$ effect was observed, consistent with a simulation ($2.1 \pm 0.4\%$). For $E_\alpha = 300$ and 350 keV, incomplete

TABLE II: Cross section and S-factor results, relative uncertainties, and electron screening [44] enhancement factors f .

E^{eff} [keV]	$\sigma(E^{\text{eff}})$ [10^{-9} barn]	$S(E^{\text{eff}})$ [keV barn]	$\Delta S/S$		f
			stat.	syst.	
126.5	1.87	0.514	2.0 %	3.0 %	1.012
147.7	4.61	0.499	1.7 %	2.9 %	1.009
168.9	9.35	0.482	2.0 %	2.9 %	1.008

${}^7\text{Be}$ collection was corrected for based on the simulation (up to 2.3 % correction, adopted uncertainty 0.4 %).

Sputtering losses of ${}^7\text{Be}$ by the ${}^4\text{He}$ beam were simulated [38], showing that for the present beam energies sputtering is 10^4 times less likely than transporting the ${}^7\text{Be}$ even deeper into the catcher, so it has been neglected.

The systematic uncertainties are summarized in Table I, giving a total value of 3%. For the present low energies an electron screening enhancement factor f [44] of up to 1.012 has been calculated in the adiabatic limit, but not corrected for (Table II).

The present data (Table II, lower panel of Fig. 3) are the first activation results at energies directly relevant to big-bang ${}^7\text{Li}$ production. Their uncertainty of 4% (systematic and statistical combined in quadrature) is comparable to or lower than previous activation studies at high energy and lower than prompt- γ studies at comparable energy (upper panel of Fig. 3).

To give an estimate for the low-energy implications, rescaling the most recent R-matrix fit [9] to the present data results in $S(0) = 0.547 \pm 0.017$ keV barn, consistent with, but more precise than, Ref. [18]. All activation data combined (Refs. [15, 16, 17, 18] and the present work) give $S(0) = 0.550 \pm 0.012$ keV barn, higher than the weighted average of all previous prompt- γ studies, $S(0) = 0.507 \pm 0.016$ keV barn [3]. Prompt- γ experiments with precision comparable to the 4% reached in the present activation work are now called for in order to verify the normalization of the prompt- γ data.

This work was supported by INFN and in part by: TARI RII-CT-2004-506222, OTKA T42733 and T49245, and BMBF (05CL1PC1-1).

- [1] J. N. Bahcall et al., *Astrophys. J.* **621**, L85 (2005).
- [2] C. Rolfs and W. Rodney, *Cauldrons in the Cosmos* (University of Chicago Press, Chicago, 1988).
- [3] E. Adelberger et al., *Rev. Mod. Phys.* **70**, 1265 (1998).
- [4] J. N. Bahcall and M. H. Pinsonneault, *Phys. Rev. Lett.* **92**, 121301 (2004).
- [5] G. Fiorentini and B. Ricci, astro-ph/0310753.
- [6] S. Ahmed et al., *Phys. Rev. Lett.* **92**, 181301 (2004).
- [7] J. Hosaka et al., *Phys. Rev. D* **73**, 112001 (2006).
- [8] S. Burles et al., *Phys. Rev. Lett.* **82**, 4176 (1999).
- [9] P. Descouvemont et al., *At. Data Nucl. Data Tables* **88**, 203 (2004).
- [10] D. Spergel et al., *Astrophys. J. Suppl.* **148**, 175 (2003).
- [11] A. Coc et al., *Astrophys. J.* **600**, 544 (2004).
- [12] S. Ryan et al., *Astrophys. J. Lett.* **530**, L57 (2000).
- [13] P. Bonifacio et al., *Astron. Astrophys.* **390**, 91 (2002).
- [14] D. Tilley et al., *Nucl. Phys. A* **708**, 3 (2002).
- [15] J. Osborne et al., *Phys. Rev. Lett.* **48**, 1664 (1982), *Nucl. Phys. A* **419**, 115 (1984).
- [16] R. Robertson et al., *Phys. Rev. C* **27**, 11 (1983).
- [17] H. Volk et al., *Z. Phys. A* **310**, 91 (1983).
- [18] B. N. Singh et al., *Phys. Rev. Lett.* **93**, 262503 (2004).
- [19] H. Holmgren and R. Johnston, *Phys. Rev.* **113**, 1556 (1959).
- [20] P. Parker and R. Kavanagh, *Phys. Rev.* **131**, 2578 (1963).
- [21] K. Nagatani et al., *Nucl. Phys. A* **128**, 325 (1969).
- [22] H. Kräwinkel et al., *Z. Phys. A* **304**, 307 (1982).
- [23] T. Alexander et al., *Nucl. Phys. A* **427**, 526 (1984).
- [24] M. Hilgemeier et al., *Z. Phys. A* **329**, 243 (1988).
- [25] T. Kajino, *Nucl. Phys. A* **460**, 559 (1986).
- [26] A. Csötó and K. Langanke, *Few-Body Systems* **29**, 121 (2000).
- [27] J. N. Bahcall et al., astro-ph/0511337.
- [28] P. Serpico et al., *J. Cosmol. Astropart. Ph.* **12**, 010 (2004).
- [29] U. Greife et al., *Nucl. Inst. Meth. A* **350**, 327 (1994).
- [30] R. Bonetti et al., *Phys. Rev. Lett.* **82**, 5205 (1999).
- [31] C. Casella et al., *Nucl. Phys. A* **706**, 203 (2002).
- [32] A. Formicola et al., *Phys. Lett. B* **591**, 61 (2004).
- [33] D. Bemmerer et al., *Eur. Phys. J. A* **24**, 313 (2005).
- [34] G. Imbriani et al., *Eur. Phys. J. A* **25**, 455 (2005).
- [35] A. Lemut et al., *Phys. Lett. B* **634**, 483 (2006).
- [36] A. Formicola et al., *Nucl. Inst. Meth. A* **507**, 609 (2003).
- [37] C. Casella et al., *Nucl. Inst. Meth. A* **489**, 160 (2002).
- [38] J. Ziegler, SRIM 2003.26, <http://www.srim.org>.
- [39] J. Görres et al., *Nucl. Inst. Meth.* **177**, 295 (1980).
- [40] M. Marta, Master's thesis, Politecnico di Milano (2005), and to be submitted to *Nucl. Inst. Meth. A*.
- [41] C. Arpesella, *Appl. Radiat. Isot.* **47**, 991 (1996).
- [42] S. Agostinelli et al., *Nucl. Inst. Meth. A* **506**, 250 (2003).
- [43] M. H. Mendenhall and R. A. Weller, *Nucl. Inst. Meth. B* **227**, 420 (2005).
- [44] H. Assenbaum et al., *Z. Phys. A* **327**, 461 (1987).

* Corresponding author, broggin@pd.infn.it.

${}^3\text{He}(\alpha, \gamma){}^7\text{Be}$ cross section at low energies

Gy. Gyürky,¹ F. Confortola,² H. Costantini,² A. Formicola,³ D. Bemmerer,^{4,5} R. Bonetti,⁶ C. Broggini,⁴ P. Corvisiero,² Z. Elekes,¹ Zs. Fülöp,¹ G. Gervino,⁷ A. Guglielmetti,⁶ C. Gustavino,³ G. Imbriani,⁸ M. Junker,³ M. Laubenstein,³ A. Lemut,² B. Limata,⁸ V. Lozza,⁴ M. Marta,⁶ R. Menegazzo,⁴ P. Prati,² V. Roca,⁸ C. Rolfs,⁹ C. Rossi Alvarez,⁴ E. Somorjai,¹ O. Straniero,¹⁰ F. Strieder,⁹ F. Terrasi,¹¹ and H.P. Trautvetter⁹

(The LUNA Collaboration)

¹*Institute of Nuclear Research (ATOMKI), Debrecen, Hungary*

²*Università di Genova and INFN Sezione di Genova, Genova, Italy*

³*INFN, Laboratori Nazionali del Gran Sasso (LNGS), Assergi (AQ), Italy*

⁴*Istituto Nazionale di Fisica Nucleare (INFN), Sezione di Padova, via Marzolo 8, 35131 Padova, Italy*

⁵*Forschungszentrum Dresden-Rossendorf, Postfach 510119, 01314 Dresden, Germany*

⁶*Istituto di Fisica Generale Applicata, Università di Milano and INFN Sezione di Milano, Italy*

⁷*Dipartimento di Fisica Sperimentale, Università di Torino and INFN Sezione di Torino, Torino, Italy*

⁸*Dipartimento di Scienze Fisiche, Università di Napoli "Federico II", and INFN Sezione di Napoli, Napoli, Italy*

⁹*Institut für Experimentalphysik III, Ruhr-Universität Bochum, Bochum, Germany*

¹⁰*Osservatorio Astronomico di Collurania, Teramo, and INFN Sezione di Napoli, Napoli, Italy*

¹¹*Seconda Università di Napoli, Caserta, and INFN Sezione di Napoli, Napoli, Italy*

The flux of ${}^7\text{Be}$ and ${}^8\text{B}$ neutrinos from the Sun and the production of ${}^7\text{Li}$ via primordial nucleosynthesis depend on the rate of the ${}^3\text{He}(\alpha, \gamma){}^7\text{Be}$ reaction. In extension of a previous study showing cross section data at 127 - 167 keV center of mass energy, the present work reports on a measurement of the ${}^3\text{He}(\alpha, \gamma){}^7\text{Be}$ cross section at 106 keV performed at Italy's Gran Sasso underground laboratory by the activation method. This energy is closer to the solar Gamow energy than ever reached before. The result is $\sigma = 0.567 \pm 0.029_{\text{stat}} \pm 0.016_{\text{syst}}$ nbarn. The data are compared with previous activation studies at high energy, and a recommended $S(0)$ value for all ${}^3\text{He}(\alpha, \gamma){}^7\text{Be}$ activation studies, including the present work, is given.

PACS numbers: 25.55.-e, 26.20.+f, 26.35.+c, 26.65.+t

I. INTRODUCTION

The ${}^3\text{He}(\alpha, \gamma){}^7\text{Be}$ and ${}^3\text{He}({}^3\text{He}, 2\text{p}){}^4\text{He}$ reactions compete in the proton-proton (p-p) chain of solar hydrogen burning. The ratio of their rates at the temperature of the solar center determines how much the ${}^7\text{Be}$ and ${}^8\text{B}$ branches of the p-p chain contribute to solar hydrogen burning. The ${}^3\text{He}({}^3\text{He}, 2\text{p}){}^4\text{He}$ cross section being comparatively well known [1], the predicted flux of solar neutrinos from ${}^7\text{Be}$ and ${}^8\text{B}$ decay [2] depends on the ${}^3\text{He}(\alpha, \gamma){}^7\text{Be}$ cross section: The 9% uncertainty in its extrapolation to the solar Gamow energy (23 keV) obtained in a global analysis [3] contributes 8% [4] to the uncertainty in the predicted fluxes for solar ${}^7\text{Be}$ and ${}^8\text{B}$ neutrinos, in both cases the major nuclear contribution to the total uncertainty. The flux of solar ${}^8\text{B}$ neutrinos has been measured in the SNO and SuperKamiokande neutrino detectors [5, 6], with a total uncertainty as low as 3.5% [6]. The solar ${}^7\text{Be}$ neutrino flux is planned to be measured in the Borexino and KamLAND neutrino detectors.

The production of ${}^7\text{Li}$ in big-bang nucleosynthesis (BBN) is also highly sensitive to the ${}^3\text{He}(\alpha, \gamma){}^7\text{Be}$ cross section in the energy range $E \approx 160\text{--}380$ keV [7]. A recent compilation for the purpose of BBN adopts 8% uncertainty [8] for the cross section. Based on the baryon to photon ratio from observed anisotropies in the cosmic microwave background [9], nucleosynthesis network calculations predict primordial ${}^7\text{Li}$ abundances [10] that

are significantly higher than observations of old stars [11, 12]. Either a completely new interpretation of the stellar abundance data [13, e.g.] or a dramatically lower ${}^3\text{He}(\alpha, \gamma){}^7\text{Be}$ cross section at relevant energies may explain this discrepancy.

Since the cross section of ${}^3\text{He}(\alpha, \gamma){}^7\text{Be}$ reaction is of the order of attobarn at $E = 23$ keV, the cross section data from experiments carried out at higher energies are parameterized by the astrophysical S factor $S(E)$ defined as

$$S(E) = \sigma(E) \cdot E \exp(2\pi\eta(E))$$

where $2\pi\eta(E) = 164.12 \cdot E^{-0.5}$ is the Sommerfeld parameter [14], and E the center of mass energy in keV. The S factor is then used to extrapolate the data to the low energies of astrophysical interest, and often its extrapolation to zero energy, $S(0)$, is quoted.

The ${}^3\text{He}(\alpha, \gamma){}^7\text{Be}$ reaction has a Q value of 1.586 MeV [15], and at low energy it proceeds via radiative capture into the ground state and the first excited state of ${}^7\text{Be}$ (Fig. 1). The final ${}^7\text{Be}$ nucleus decays with a half-life of 53.22 ± 0.06 days to ${}^7\text{Li}$, emitting a 478 keV γ -ray in $10.44 \pm 0.04\%$ of the cases [16]. The cross section can be measured by detecting either the induced ${}^7\text{Be}$ activity (activation method) or the prompt γ -rays from the

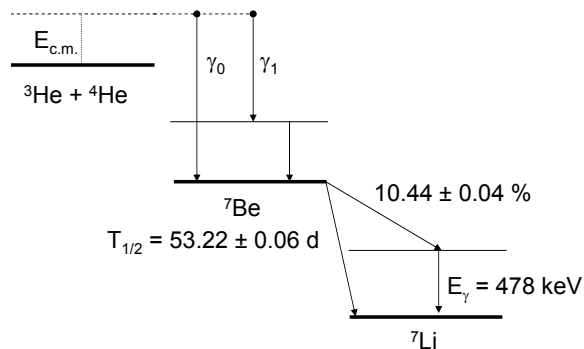


FIG. 1: Level diagram of the ${}^3\text{He}(\alpha,\gamma){}^7\text{Be}$ reaction ($Q = 1.586$ MeV) and the decay of ${}^7\text{Be}$.

reaction (prompt- γ method)¹.

Previous studies of the ${}^3\text{He}(\alpha,\gamma){}^7\text{Be}$ reaction [18, 19, 20, 21] that used the activation technique cover the energy range $E = 420$ – 2000 keV and are briefly recalled here.

Osborne *et al.* [18] have measured the cross section by the activation technique at two energies, $E = 945$ and 1250 keV. A ${}^3\text{He}$ gas cell closed by a Ni+Cu window has been bombarded by an α -beam, and the activity of ${}^7\text{Be}$ implanted into a Ta catcher foil has been measured with a Ge(Li) detector.

A similar experimental technique (gas cell with Ni window, Au catcher foil, Ge(Li) detector) has been used by Robertson *et al.* [19]. The beam intensity was measured by current integration as well as by Rutherford Backscattering (RBS) from a gold foil. An attempt was made to study the loss of ${}^7\text{Be}$ from the catcher, giving a 20% upper limit. The cross section was determined at $E = 987$ keV, with both direct (${}^3\text{He}$ gas cell and α -beam) and inverse (${}^4\text{He}$ gas cell and ${}^3\text{He}$ -beam) kinematics yielding consistent results.

Volk *et al.* [20] measured the energy integrated cross section using a 0.8 bar ${}^3\text{He}$ gas cell in which the α -beam stopped. The created ${}^7\text{Be}$ was collected onto an Al foil. The energy dependence of the cross section from a previous prompt- γ study was adopted in order to derive an $S(0)$ value.

Recently, Nara Singh *et al.* [21] carried out a precise activation experiment at $E = 420$ – 950 keV. A ${}^3\text{He}$ gas cell closed with a Ni window has been bombarded with α -beam. The beam intensity was measured by both current integration and RBS. The produced ${}^7\text{Be}$ was collected on a Cu catcher and the activity was measured by a HPGe detector.

Cross section measurements by the prompt γ -ray method [18, 22, 23, 24, 25, 26, 27] cover the energy range

$E = 107$ – 2500 keV, although with limited precision at low energies. A global analysis of all available experimental data [3] indicates that S factor data obtained with the activation method are systematically 13% higher than the prompt- γ results.

Theoretical calculations reproduce the global shape of the S factor curve rather well [28, 29, 30, e.g.]. However, the slope of this curve has been questioned [29] for $E \leq 300$ keV, where there are no high-precision data.

The aim of the present activation study is to provide high precision data at energies that are low enough to effectively constrain the extrapolation to solar energies and high enough to be relevant for big-bang nucleosynthesis. In order to study the solar interior [4, 31, 32], to investigate the low-energy slope of the S factor curve [29] and to sharpen big bang ${}^7\text{Li}$ abundance predictions [7, 33], such precision ${}^3\text{He}(\alpha,\gamma){}^7\text{Be}$ measurements have been recommended. In the present work, a new experimental cross section number is reported at $E = 106$ keV, lower than ever before reached by direct experiment. In addition, cross section data at $E = 127$ – 169 keV that have been published previously in abbreviated form [34] are presented with full detail here. The impact of the present result for big-bang nucleosynthesis is analyzed, and a new $S(0)$ for the activation method based on all available experimental data is recommended.

II. EXPERIMENT

A. The accelerator

The Laboratory for Underground Nuclear Astrophysics (LUNA) [35] in Italy's Gran Sasso underground laboratory (LNGS) has been designed for measuring low nuclear cross sections for astrophysical purposes. Its low laboratory background [36] has made it possible to study several reactions of astrophysical relevance [1, 37, 38, 39, 40].

The irradiations for the present study have been carried out at the 400 kV LUNA2 accelerator [41] at energies $E_\alpha = 250, 300, 350$ and 400 keV, with a typical current of $200 \mu\text{A } {}^4\text{He}^+$. The beam energy is obtained with an uncertainty as low as 300 eV from a precision resistor chain calibrated through radiative-capture reactions, and it exhibits an energy spread of less than 100 eV [41].

The beam intensity is measured using a beam calorimeter with constant temperature gradient similar to the one described previously [42], and a precision of 1.5% is obtained from the difference between the calorimeter power values with and without incident ion beam, taking into account the calculated energy loss in the target gas [43]. The calorimeter has been calibrated at various beam energy and intensity values using the evacuated gas target chamber as a Faraday cup, with a proper secondary electron suppression voltage applied.

¹ An experiment based on a third method to measure the cross section, namely the detection of ${}^7\text{Be}$ nuclei in a recoil mass separator, is in progress at the ERNA facility [17].

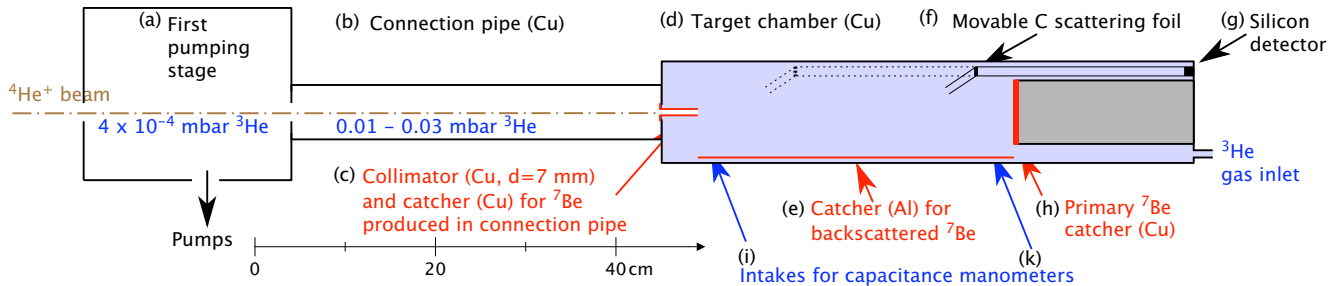


FIG. 2: (Color online) Schematic view of the target chamber used for the irradiations. See text for details.

B. The gas target setup

The ${}^3\text{He}(\alpha, \gamma){}^7\text{Be}$ reaction takes place in a differentially pumped windowless gas target (Fig. 2) filled with enriched ${}^3\text{He}$ gas (isotopic purity $>99.95\%$, pressure 0.7 mbar , corresponding target thickness $8\text{--}10\text{ keV}$). The exhaust from the first pumping stage ($2050\frac{\text{m}^3}{\text{h}}$ Roots pump) and the second pumping stage (three $1000\frac{1}{\text{s}}$ turbomolecular pumps) is compressed by a $500\frac{\text{m}^3}{\text{h}}$ Roots blower and an oil-free forepump, cleaned in a getter-based gas purifier and recirculated into the target. After passing the three pumping stages (the one closest to the target is shown in Fig. 2 a) and a connection pipe (b), the ion beam from the accelerator enters the target chamber (d) through an aperture of 7 mm diameter (c) and is finally stopped on a disk (h) of 70 mm diameter that serves as the primary catcher for the produced ${}^7\text{Be}$ and as the hot side of the beam calorimeter described above.

The pressure in the gas target chamber has been monitored continuously during the irradiations at two positions with capacitance manometers, (Fig. 2 i-k). The pressure and temperature profiles (Fig. 3) have been measured without ion beam in a chamber of the same dimen-

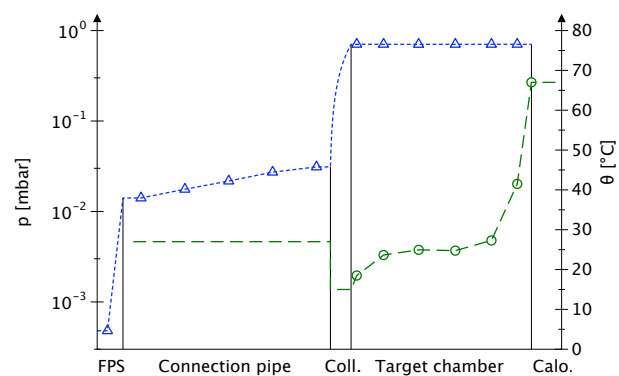


FIG. 3: (Color online) Measured pressure (p , blue triangles) and temperature (θ , green circles) profile inside the target chamber and adjacent regions: First pumping stage (FPS), connection pipe, collimator (Coll.), target chamber, calorimeter (Calo.). The dashed lines indicate the interpolated profile adopted where there are no data.

sions as the actual gas target chamber but with several ports along the beam path for pressure and temperature sensors. The pressure has been found to be equal to better than 0.25% at the different positions. The temperature profile has been observed to vary monotonously between the watercooled collimator (15°C) and the hot side of the calorimeter (67°C). Linear interpolations have been used to calculate pressure and temperature between the measured positions. In order to reflect the uncertainty from the linear interpolation, a relative uncertainty of 13% has been assigned to the part of the target thickness contained in the 7 mm collimator (which comprises 5% of the total target thickness and where the pressure drop is significant), resulting in 0.7% uncertainty for the total target thickness. Combining this uncertainty with the 0.25% manometer precision and with the 0.3% uncertainty from the temperature measurement, a precision of 0.8% for the target thickness without ion beam is obtained.

The thinning of the target gas through the beam heating effect [44] and the fraction of gases other than ${}^3\text{He}$ have been measured in order to obtain the effective target thickness. For this purpose, a $100\mu\text{m}$ thick silicon detector (Fig. 2 g) detects projectiles that have been elastically scattered first in the target gas and subsequently

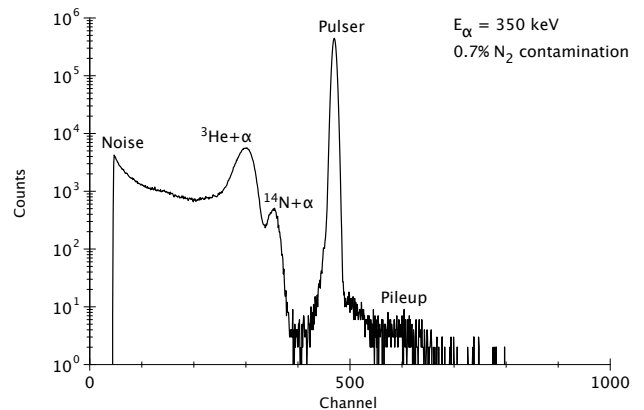


FIG. 4: Elastic scattering spectrum taken with the silicon detector at $E_\alpha = 350\text{ keV}$, showing a contamination of 0.7% N_2 in the ${}^3\text{He}$ gas.

in a movable $15 \mu\text{g}/\text{cm}^2$ carbon foil (f). The beam heating effect has thus been investigated at several positions along the chamber in a wide beam energy and intensity range, and the average corrections shown in Table III were found. The amount of contaminant gases (mainly nitrogen) is monitored with the silicon detector during the irradiations (Fig. 4), kept below $1.0 \pm 0.1\%$ and corrected for in the analysis. Further details of the elastic scattering measurements are described elsewhere [45, 46].

C. Sample irradiation

The catchers are irradiated with charges of 60–200 C, accumulating ^7Be activities of 0.03–0.6 Bq. Table I shows details of the irradiations.

Calculations for the straggling of the ^4He beam and of the produced ^7Be nuclei in the ^3He gas and for the emission cone of ^7Be (opening angle 1.8 – 2.1°) have been carried out and show that 99.8% of the ^7Be produced inside the target chamber, including the 7 mm collimator, reaches the primary catcher.

D. Offline ^7Be counting

After the irradiation, the catcher is dismantled and counted subsequently with two 120% relative efficiency HPGe detectors called LNGS1 (Fig. 5) and LNGS2 (Fig. 6), both properly shielded with copper and lead, in the LNGS underground counting facility [47]. Detector LNGS1 is additionally equipped with an anti-radon box, and its laboratory background is two orders of magnitude lower than with equivalent shielding overground [47].

The samples have been counted in close geometry, e.g. in the case of detector LNGS1 the distance between sample and detector endcap was 5 mm. In order to obtain a precise efficiency calibration at this close distance, three homogeneous ^7Be sources of 200–800 Bq activity and 8 mm active diameter were prepared with the $^7\text{Li}(p,n)^7\text{Be}$ reaction. Thin layers of LiF ($\approx 20 \mu\text{g}/\text{cm}^2$) evaporated onto Ta backings and protected by evaporated gold layers ($\approx 5 \mu\text{g}/\text{cm}^2$) have been irradiated by

TABLE I: Details of the irradiations. In all cases the target pressure was 0.7 mbar.

Sample	E_α [keV]	Target gas	Irradiation [days]	Charge [Coulombs]	Average current [μA]
D	249.8	^3He	6.5	83	149
B	298.8	^3He	10.5	215	237
A	348.4	^3He	9.5	203	248
F	398.2	^3He	2.9	63	250
E	400.2	^4He	6.5	104	187

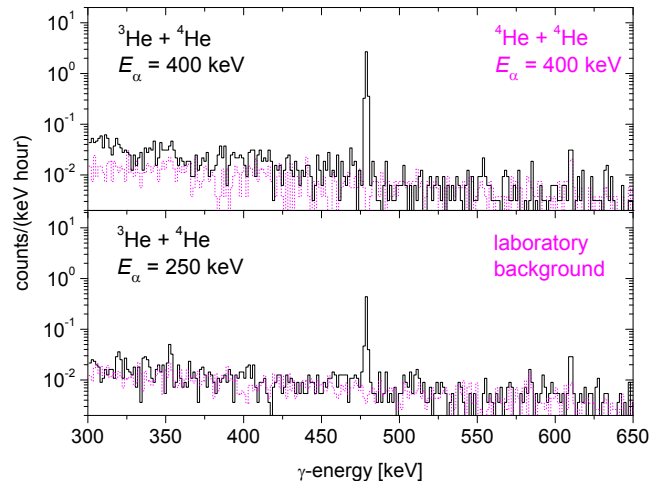


FIG. 5: (Color online) Offline γ -counting spectra, detector LNGS1. Solid black line: ^3He gas bombarded at $E_\alpha = 400$ keV (top panel, sample F) and 250 keV (bottom panel, sample D), respectively. Dotted red line, top panel: ^4He gas bombarded at $E_\alpha = 400$ keV (sample E). Dotted red line, bottom panel: laboratory background.

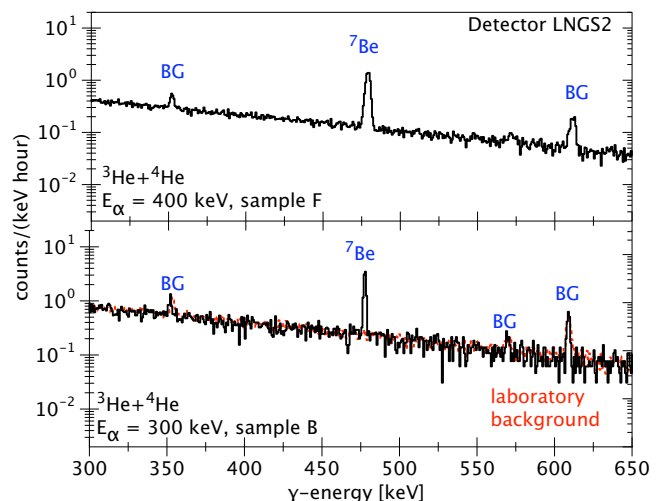


FIG. 6: (Color online) Offline γ -counting spectra, detector LNGS2. Solid black line: ^3He gas bombarded at $E_\alpha = 400$ keV (sample F) and 300 keV (sample B), respectively. Dotted red line, bottom panel: laboratory background.

2.5 MeV protons from the ATOMKI Van de Graaff accelerator. The absolute activity of the calibration sources was subsequently determined in far geometry with two HPGe detectors at ATOMKI and with one HPGe detector, called LNGS3, at LNGS. The absolute efficiency of each of these three detectors has been determined using a set of commercial γ -ray calibration sources. The three source kits used for calibrating the detectors were mutually independent. All three measurements gave consistent results, and the activities of the ^7Be calibration sources have been determined with a final uncertainty of 1.8%.

The three ^7Be calibration sources were then used to calibrate detectors LNGS1 and LNGS2 at close geometry. Owing to the relatively low activities of the calibration sources, random coincidence summing effect and deadtime correction were negligible. In the case of detector LNGS2 which has a horizontal geometry, calibration sources and samples were placed horizontally in front of the detector, and not vertically in top of it as in the case of detector LNGS1. The impact of statistical sub-millimeter variations in the distance between source/sample and detector endcap resulting from the horizontal geometry of detector LNGS2 has been evaluated by moving the calibrated sources. An additional uncertainty of 1.2% resulting from this effect is included in the final statistical uncertainties given for detector LNGS2.

The ^7Be distribution in the catchers has been calculated from the ^7Be emission angle and straggling, and GEANT4 [48] simulations give $0.8\pm 0.4\%$ to $1.5\pm 0.4\%$ correction for the γ -ray efficiency because of the tail of the distribution at high radii.

Without aiming for high precision, the half life of ^7Be in the Cu host material has been determined from the decay curve measured on the present, weak activated samples (Fig. 7). The weighted average of all measured samples gives a half life of 52.2 ± 1.5 days, compatible with 53.22 ± 0.06 days from a recent compilation [16]. The value from Ref. [16] has been used for the data analysis.

The activity values referring to the end of the irradiations measured with the two HPGe detectors are in all cases in good agreement (Table II). For each sample, the weighted average of the activity values has been used for the data analysis.

E. Parasitic ^7Be production in the primary catcher

Oxygen free high conductivity (OFHC) copper has been studied as a possible material for the primary catcher. This material has good heat conductivity (required for the beam calorimeter described above), sus-

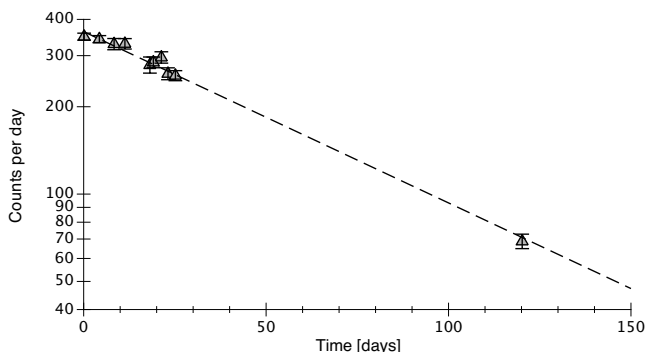


FIG. 7: Counting rate of sample A on detector LNGS2 as a function of time. The dashed line is an exponential fit to the data.

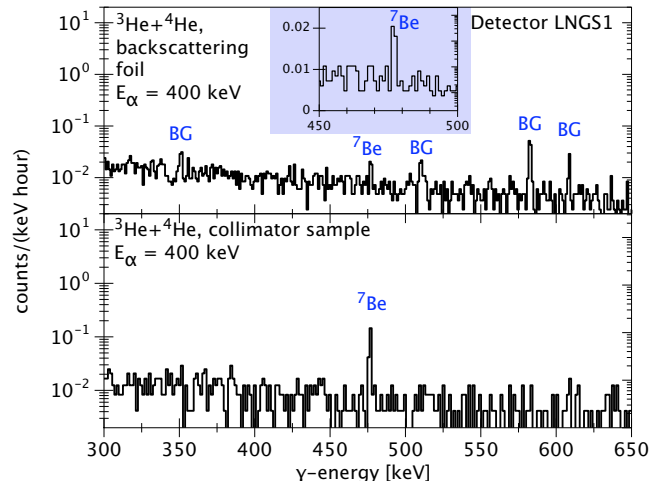


FIG. 8: (Color online) Offline γ -counting spectra, detector LNGS1. Collimator and backscattering foil counted in order to study ^7Be losses. The peaks marked with BG in the upper panel are background lines from impurities in the Al foil. The inset in the upper panel has a linear ordinate.

tains high α -doses without blistering, and has a relatively low charge number in order to limit backscattering of ^7Be nuclei. Since possible ^6Li or ^{10}B impurities in the catcher material can give rise to unwanted ^7Be production through the $^6\text{Li}(d,p)^7\text{Be}$ and $^{10}\text{B}(p,\alpha)^7\text{Be}$ reactions induced by traces of $^2\text{D}_2^+$ or even $^2\text{D}_2^+$ in the $^4\text{He}^+$ beam, this material was studied in detail prior to adopting it for the main experiment.

Samples from the material to be used for the catcher was irradiated with 700 keV protons and deuterons at the ATOMKI Van de Graaff accelerator. After the irradiations, the γ -activity of the samples has been observed, showing no γ -peak from ^7Be decay. Based on the known cross section of the $^6\text{Li}(d,p)^7\text{Be}$ [49, 50, 51] and $^{10}\text{B}(p,\alpha)^7\text{Be}$ [52, 53] reactions, an upper limit of 3 ppm has been determined for the concentration of both ^6Li and ^{10}B . By varying the settings of the LUNA2 analyzing magnet and taking the isotopic abundance of deuterium

TABLE II: Counting times τ and activities measured for the different catchers with the two HPGe detectors. Uncertainties are purely statistical, in the case of detector LNGS2 also including the 1.2% repositioning uncertainty discussed in the text.

Sample	LNGS1		LNGS2		Adopted Activity [mBq]
	τ [days]	Activity [mBq]	τ [days]	Activity [mBq]	
D	16	25.3 ± 1.3	-	-	25.3 ± 1.3
B	12	208 ± 6	21	203 ± 6	205 ± 4
A	6	472 ± 14	22	495 ± 11	486 ± 9
F	10	319 ± 11	11	310 ± 8	313 ± 6
E	16	$<0.21 (2\sigma)$	-	-	$<0.21 (2\sigma)$

into account, an order-of-magnitude upper limit of 10^{-7} d/α has been obtained. Combining this fraction with the above mentioned upper limits for ${}^6\text{Li}$ and ${}^{10}\text{B}$ contaminations and the ${}^6\text{Li}(d,p){}^7\text{Be}$ and ${}^{10}\text{B}(p,\alpha){}^7\text{Be}$ cross sections at lower energy, the induced ${}^7\text{Be}$ activity from parasitic reactions is shown to be six orders of magnitude less than the activity from the ${}^3\text{He}(\alpha,\gamma){}^7\text{Be}$ reaction expected using the ${}^3\text{He}(\alpha,\gamma){}^7\text{Be}$ cross section from Ref. [28].

The only excess activity detected on the samples irradiated at ATOMKI was ${}^{24}\text{Na}$ produced by the ${}^{23}\text{Na}(d,p){}^{24}\text{Na}$ reaction. However, the half life of ${}^{24}\text{Na}$ (15 h) is short compared with that of ${}^7\text{Be}$, so in the main experiment the offline γ -counting spectra taken immediately after the irradiation was concluded were compared with spectra taken several days later, when any possible ${}^{24}\text{Na}$ traces have decayed out. Thus, Compton background from the 2.754 MeV γ -ray following the decay of ${}^{24}\text{Na}$ has been ruled out as a significant contributor of background in the offline γ -counting.

Based on these considerations, OFHC copper was finally selected as material for the primary catcher. In order to rule out not only ${}^6\text{Li}(d,p){}^7\text{Be}$, ${}^{10}\text{B}(p,\alpha){}^7\text{Be}$, and ${}^{23}\text{Na}(d,p){}^{24}\text{Na}$, but any possible source of parasitic ${}^7\text{Be}$, during the main experiment for one catcher the enriched ${}^3\text{He}$ target gas was replaced with 0.7 mbar ${}^4\text{He}$. This catcher was then bombarded at the highest available energy of $E_\alpha = 400$ keV. Despite the high applied dose of 104 C, in 16 days counting time no ${}^7\text{Be}$ has been detected (Fig. 5, top panel, and Table II), establishing a 2σ upper limit of 0.1% for parasitic ${}^7\text{Be}$.

F. ${}^7\text{Be}$ losses

${}^7\text{Be}$ losses by backscattering from the primary catcher and by incomplete collection were studied experimentally at $E_\alpha = 400$ keV and with Monte Carlo simulations at 250, 300, 350 and 400 keV. For the backscattering study, parts of the inner surface of the chamber were covered by aluminum foil functioning as secondary catcher (Fig. 2e), and the foil sample was subsequently counted on detector LNGS1 (Fig. 8, upper panel). It was found that $1.3 \pm 0.5\%$ of the created ${}^7\text{Be}$ is lost due to backscattering, consistent with 1.5% obtained in a GEANT4 [48] simulation using a SRIM-like multiple scattering process [54]. At lower energies, the simulation result of up to 2.9% was used as backscattering correction (Table III, column 7), with an adopted uncertainty of 0.5%.

Incomplete ${}^7\text{Be}$ collection occurs since 3.5% of the total ${}^3\text{He}$ target thickness are in the connecting pipe, and a part of the ${}^7\text{Be}$ created there does not reach the primary catcher but is instead implanted into the 7 mm collimator (Fig. 2c). At $E_\alpha = 400$ keV, a modified collimator functioning as secondary catcher was used and counted on detector LNGS1 (Fig. 8, lower panel). A $2.6 \pm 0.4\%$ effect was observed, consistent with a simulation ($2.1 \pm 0.4\%$). For $E_\alpha = 250$ –350 keV, incomplete ${}^7\text{Be}$ collection was corrected for based on the simulation (up to 2.4% cor-

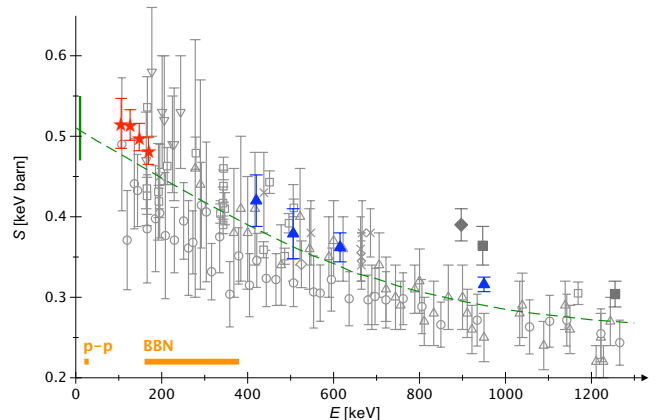


FIG. 9: (Color online) Astrophysical S factor for ${}^3\text{He}(\alpha,\gamma){}^7\text{Be}$. Activation data: filled squares [18], filled diamonds [19], filled triangles [21], stars (present work). Prompt- γ data: triangles [23], inverted triangles [24], circles [25] (renormalized by a factor 1.4 [27]), squares [18], diamonds [26], crosses [27]. Dashed line: previously adopted R-matrix fit [8]. Horizontal bars: energies relevant for solar p-p hydrogen burning and for big bang nucleosynthesis.

rection, adopted uncertainty 0.5%).

Sputtering losses of ${}^7\text{Be}$ by the ${}^4\text{He}$ beam were simulated [43], showing that for the present beam energies sputtering is 10^4 times less likely than transporting the ${}^7\text{Be}$ even deeper into the catcher, so it has been neglected.

All Monte Carlo calculations mentioned in sections II.D–II.F have been carried on until a statistical uncertainty of 0.2% or better was reached, negligible compared to the systematic uncertainties discussed in the appropriate section.

III. RESULTS

The effective center of mass energy E^{eff} has been calculated assuming a constant S factor over the target length [14]. The uncertainties of 0.3 keV in E_α [41] and of 4.4% in the energy loss [43] lead to 0.16 keV uncertainty in E^{eff} and thus contribute 0.5% (at $E^{\text{eff}} = 169$ keV) to 1.1% (at $E^{\text{eff}} = 106$ keV) to the S factor uncertainty.

The effective energy and cross section results for each sample are shown in the last two columns of Table III. The systematic uncertainties are summarized in Table IV, giving a total value of 3%. For the present low energies an electron screening enhancement factor f [55] of up to 1.016 has been calculated in the adiabatic limit, but not corrected for (Table V).

The present data (Table V and Fig. 9) touch the energy range relevant to big-bang ${}^7\text{Li}$ production. Their uncertainty of at most 6% (systematic and statistical combined in quadrature) is comparable to or lower than previous activation studies at high energy and lower than prompt- γ studies at comparable energy.

TABLE III: Experimental (exp) and calculated (calc) corrections for irradiation and collection for each run. Effective energy and cross section are given in the final two columns. Only the statistical uncertainty is given. See Table V for the adopted systematic uncertainty.

Run	E_α [keV]	Target gas	Corrections				E^{eff} [keV]	$\sigma(E^{\text{eff}})$ [10^{-9} barn]
			Beam heating	Contaminant gases	Backscattering	Collection losses		
D	249.8	^3He	2.9 %	0.5 % _{exp}	2.9 % _{calc}	2.4 % _{calc}	105.6	0.567±0.029
B	298.8	^3He	4.9 %	0.3 % _{exp}	2.2 % _{calc}	2.3 % _{calc}	126.5	1.87±0.04
A	348.4	^3He	5.4 %	0.3 % _{exp}	1.8 % _{calc}	2.2 % _{calc}	147.7	4.61±0.07
F	398.2	^3He	5.7 %	1.0 % _{calc}	1.3 % _{exp}	2.6 % _{exp}	168.9	9.35±0.19

TABLE IV: Systematic uncertainties in the $^3\text{He}(\alpha, \gamma)^7\text{Be}$ astrophysical S factor. The uncertainty resulting from the effective energy affects only the S factor result, not the cross section.

Source	Uncertainty
^7Be counting efficiency	1.8 %
Beam intensity	1.5 %
Beam heating effect	1.3 %
Effective energy	0.5–1.1 %
Target pressure and temperature without beam	0.8 %
Incomplete ^7Be collection	0.5 %
^7Be backscattering	0.5 %
^7Be distribution in catcher	0.4 %
478 keV γ -ray branching [16]	0.4 %
^7Be half-life [16]	0.1 %
N_2 contamination in target gas	0.1 %
Parasitic ^7Be production	0.1 %
Total:	3.0–3.1 %

TABLE V: Cross section and S factor results, relative uncertainties, and electron screening [55] enhancement factors f .

E^{eff} [keV]	$\sigma(E^{\text{eff}})$ [10^{-9} barn]	$S(E^{\text{eff}})$ [keV barn]	$\Delta S/S$		f
			stat.	syst.	
105.6	0.567	0.516	5.2 %	3.1 %	1.016
126.5	1.87 ^a	0.514	2.0 %	3.0 %	1.012
147.7	4.61 ^a	0.499	1.7 %	3.0 % ^b	1.009
168.9	9.35 ^a	0.482	2.0 %	3.0 % ^b	1.008

^aCross section previously published in abbreviated form [34].

^bSystematic uncertainty 0.1 % higher than the one given in Ref. [34]. The conclusions of Ref. [34] are unaffected.

IV. CONCLUSION

In order to obtain a recommended $S(0)$ value for the activation method, following Ref. [3] it is instructive to

list the extrapolated $S(0)$ values for the different ac-

TABLE VI: Extrapolated S factor $S(0)$ from activation studies of $^3\text{He}(\alpha, \gamma)^7\text{Be}$.

	Ref.	$S(0)$ [keV barn]
Osborne <i>et al.</i>	[18]	0.535±0.040
Robertson <i>et al.</i>	[19]	0.63±0.04
Volk <i>et al.</i>	[20]	0.56±0.03
Nara Singh <i>et al.</i>	[21]	0.53±0.02
present work		0.547±0.017
Weighted average, all activation studies		0.553±0.012
Weighted average, all prompt- γ studies [3]		0.507±0.016

tivation studies together with their quoted uncertainty (table VI). For the present data, adopting the curve shape from Ref. [8] an extrapolated $S(0) = 0.547\pm 0.017$ keV barn is obtained. The weighted average of all activation studies, including the present work, is found to be 0.553 ± 0.012 keV barn, significantly higher than the weighted average of all prompt- γ studies, 0.507 ± 0.016 keV barn [3].

With the addition of the new data, the systematic difference in normalization between prompt- γ and activation studies of $^3\text{He}(\alpha, \gamma)^7\text{Be}$ is now smaller than in Ref. [3]. However, it is still significant and much larger than the uncertainty required to match, e.g., the 3.5 % precision of the solar ^8B neutrino data [6].

In conclusion, prompt- γ experiments with precision comparable to the present activation data are called for in order to verify the normalization of the prompt- γ data.

Acknowledgments

This work was supported by INFN and in part by the European Union (TARI RII-CT-2004-506222), the Hungarian Scientific Research Fund (T42733 and T49245), and the German Federal Ministry of Education and Research (05CL1PC1-1).

-
- [1] R. Bonetti et al., Phys. Rev. Lett. **82**, 5205 (1999).
- [2] J. N. Bahcall, A. M. Serenelli, and S. Basu, Astrophys. J. **621**, L85 (2005).
- [3] E. Adelberger et al., Rev. Mod. Phys. **70**, 1265 (1998).
- [4] J. N. Bahcall and M. H. Pinsonneault, Phys. Rev. Lett. **92**, 121301 (2004).
- [5] B. Aharmim et al., Phys. Rev. C **72**, 055502 (2005).
- [6] J. Hosaka et al., Phys. Rev. D **73**, 112001 (2006).
- [7] S. Burles, K. M. Nollett, J. W. Truran, and M. S. Turner, Phys. Rev. Lett. **82**, 4176 (1999).
- [8] P. Descouvemont, A. Adahchour, C. Angulo, A. Coc, and E. Vangioni-Flam, At. Data Nucl. Data Tables **88**, 203 (2004).
- [9] D. Spergel et al., Astrophys. J. Suppl. **148**, 175 (2003).
- [10] A. Coc, E. Vangioni-Flam, P. Descouvemont, A. Adahchour, and C. Angulo, Astrophys. J. **600**, 544 (2004).
- [11] S. Ryan, T. Beers, K. Olive, B. Fields, and J. Norris, Astrophys. J. Lett. **530**, L57 (2000).
- [12] P. Bonifacio et al., Astron. Astrophys. **390**, 91 (2002).
- [13] A. Korn et al., Nature **442**, 657 (2006).
- [14] C. Rolfs and W. Rodney, *Cauldrons in the Cosmos* (University of Chicago Press, Chicago, 1988).
- [15] G. Audi, A. Wapstra, and C. Thibault, Nucl. Phys. A **729**, 337 (2003).
- [16] D. Tilley, C. M. Cheves, J. L. Godwin, G. M. Hale, H. M. Hofmann, J. H. Kelley, C. G. Sheu, and H. R. Weller, Nucl. Phys. A **708**, 3 (2002).
- [17] A. di Leva et al., AIP Conf. Proc. **831**, 378 (2006).
- [18] J. Osborne, C. A. Barnes, R. W. Kavanagh, R. M. Kremer, G. J. Matthews, J. L. Zyskind, P. D. Parker, and A. J. Howard, Phys. Rev. Lett. **48**, 1664 (1982), Nucl. Phys. A **419**, 115 (1984).
- [19] R. Robertson, P. Dyer, T. J. Bowles, R. E. Brown, N. Jarmie, C. J. Maggiore, and S. M. Austin, Phys. Rev. C **27**, 11 (1983).
- [20] H. Volk, H. Kräwinkel, R. Santo, and L. Wallek, Z. Phys. A **310**, 91 (1983).
- [21] B. N. Singh, M. Hass, Y. Nir-El, and G. Haquin, Phys. Rev. Lett. **93**, 262503 (2004).
- [22] H. Holmgren and R. Johnston, Phys. Rev. **113**, 1556 (1959).
- [23] P. Parker and R. Kavanagh, Phys. Rev. **131**, 2578 (1963).
- [24] K. Nagatani, M. R. Dwarakanath, and D. Ashery, Nucl. Phys. A **128**, 325 (1969).
- [25] H. Kräwinkel et al., Z. Phys. A **304**, 307 (1982).
- [26] T. Alexander, G. C. Ball, W. N. Lennard, H. Geissel, and H.-B. Mak, Nucl. Phys. A **427**, 526 (1984).
- [27] M. Hilgemeier, H. W. Becker, C. Rolfs, H. P. Trautvetter, and J. W. Hammer, Z. Phys. A **329**, 243 (1988).
- [28] T. Kajino, Nucl. Phys. A **460**, 559 (1986).
- [29] A. Csótó and K. Langanke, Few-Body Systems **29**, 121 (2000).
- [30] L. Marcucci, K. M. Nollett, R. Schiavilla, and R. Wiringa, Nucl. Phys. A **777**, 111 (2006).
- [31] G. Fiorentini and B. Ricci (2003), astro-ph/0310753.
- [32] J. N. Bahcall, A. M. Serenelli, and S. Basu, astro-ph/0511337.
- [33] P. Serpico, S. Esposito, F. Iocco, G. Mangano, G. Miele, and O. Pisanti, J. Cosmol. Astropart. Ph. **12**, 10 (2004).
- [34] D. Bemmerer et al., Phys. Rev. Lett. **97**, 122502 (2006).
- [35] U. Greife et al., Nucl. Inst. Meth. A **350**, 327 (1994).
- [36] D. Bemmerer et al., Eur. Phys. J. A **24**, 313 (2005).
- [37] C. Casella et al., Nucl. Phys. A **706**, 203 (2002).
- [38] A. Formicola et al., Phys. Lett. B **591**, 61 (2004).
- [39] G. Imbriani et al., Eur. Phys. J. A **25**, 455 (2005).
- [40] A. Lemut et al., Phys. Lett. B **634**, 483 (2006).
- [41] A. Formicola et al., Nucl. Inst. Meth. A **507**, 609 (2003).
- [42] C. Casella et al., Nucl. Inst. Meth. A **489**, 160 (2002).
- [43] J. Ziegler, SRIM 2003.26, <http://www.srim.org>.
- [44] J. Görres, K. U. Kettner, H. Kräwinkel, and C. Rolfs, Nucl. Inst. Meth. **177**, 295 (1980).
- [45] M. Marta, Master's thesis, Politecnico di Milano (2005).
- [46] M. Marta et al., Nucl. Inst. Meth. A **569**, 727 (2006).
- [47] C. Arpesella, Appl. Radiat. Isot. **47**, 991 (1996).
- [48] S. Agostinelli et al., Nucl. Inst. Meth. A **506**, 250 (2003).
- [49] J. Szabó, Z. T. Bödy, S. Szegedi, and M. Várnagy, Nucl. Phys. A **289**, 526 (1977).
- [50] F. Hirst et al., Phil. Mag. **45**, 726 (1954).
- [51] L. Ruby et al., Nucl. Sci. Eng. **71**, 280 (1979).
- [52] J. Szabo et al., in *Proceedings of Conference on Nuclear Data for Science and Technology* (1982), p. 956.
- [53] W.E.Burcham and J.M.Freeman, Phil. Mag. **41**, 337 (1950).
- [54] M. H. Mendenhall and R. A. Weller, Nucl. Inst. Meth. B **227**, 420 (2005).
- [55] H. Assenbaum, K. Langanke, and C. Rolfs, Z. Phys. A **327**, 461 (1987).

Astrophysical S-factor of the ${}^3\text{He}(\alpha,\gamma){}^7\text{Be}$ reaction measured at low energy via prompt and delayed γ detection

F. Confortola,¹ D. Bemmerer,^{2,*} H. Costantini,¹ A. Formicola,³ Gy. Gyürky,⁴ P. Bezzon,⁵ R. Bonetti,⁶ C. Brogini,^{2,†} P. Corvisiero,¹ Z. Elekes,⁴ Zs. Fülöp,⁴ G. Gervino,⁷ A. Guglielmetti,⁶ C. Gustavino,³ G. Imbriani,⁸ M. Junker,³ M. Laubenstein,³ A. Lemut,¹ B. Limata,⁹ V. Lozza,² M. Marta,⁶ R. Menegazzo,² P. Prati,¹ V. Roca,⁹ C. Rolfs,¹⁰ C. Rossi Alvarez,² E. Somorjai,⁴ O. Straniero,⁸ F. Strieder,¹⁰ F. Terrasi,¹¹ and H.P. Trautvetter¹⁰

(The LUNA Collaboration)

¹Università degli Studi Genova & INFN Genova, Via Dodecaneso 33, 16146 Genova, Italy

²INFN Sezione di Padova, Via Marzolo 8, 35131 Padova, Italy

³INFN, Laboratori Nazionali del Gran Sasso, S.S. 17bis km 18.890, Assergi, L'Aquila, Italy

⁴ATOMKI, Debrecen, Hungary

⁵INFN, Laboratori Nazionali di Legnaro, Padova, Italy

⁶Istituto di Fisica Generale Applicata, Università di Milano & INFN Milano, Milano, Italy

⁷Dipartimento di Fisica Sperimentale, Università di Torino & INFN Torino, Torino, Italy

⁸INAF, Osservatorio Astronomico di Collurania, Teramo, Italy

⁹Dipartimento di Scienze Fisiche, Università "Federico II" & INFN Napoli, Napoli, Italy

¹⁰Institut für Experimentalphysik III, Ruhr-Universität Bochum, Bochum, Germany

¹¹Dipartimento di Scienze Ambientali, Seconda Università di Napoli, Caserta & INFN Napoli, Napoli, Italy

(Dated: May 15, 2007)

Solar neutrino fluxes depend both on astrophysical and on nuclear physics inputs, namely on the cross sections of the reactions responsible for neutrino production inside the Solar core. While the flux of solar ${}^8\text{B}$ neutrinos has been recently measured at Superkamiokande with a 3.5% uncertainty and a precise measurement of ${}^7\text{Be}$ neutrino flux is foreseen in the next future, the predicted fluxes are still affected by larger errors. The largest nuclear physics uncertainty to determine the fluxes of ${}^8\text{B}$ and ${}^7\text{Be}$ neutrinos comes from the ${}^3\text{He}(\alpha,\gamma){}^7\text{Be}$ reaction. The uncertainty on its S-factor is due to an average discrepancy in results obtained using two different experimental approaches: the detection of the delayed γ rays from ${}^7\text{Be}$ decay and the measurement of the prompt γ emission. Here we report on a new high precision experiment performed with both techniques at the same time. Thanks to the low background conditions of the Gran Sasso LUNA accelerator facility, the cross section has been measured at $E_{cm} = 170, 106$ and 93 keV, the latter being the lowest interaction energy ever reached. The S-factors from the two methods do not show any discrepancy within the experimental errors. An extrapolated $S(0) = 0.560 \pm 0.017$ keV barn is obtained. Moreover, branching ratios between the two prompt γ -transitions have been measured with 5-8% accuracy.

PACS numbers: 25.55.-e, 26.20.+f, 26.65.+t

Keywords: ${}^3\text{He}(\alpha,\gamma){}^7\text{Be}$, p-p chain, direct measurement, underground accelerator

Forty years ago, John Bahcall and Raymond Davis started to explore the solar interior by studying the neutrinos emitted by the Sun [1]. The results of the first neutrino detection experiment [2] originated the so called solar neutrino puzzle, consisting in a deficit of measured neutrinos with respect to the theoretical predictions of the Standard Solar Model (SSM). After thirty years of experiments, SNO and Kamland [3, 4] observed neutrino oscillations and proved that the missing solar electron neutrinos actually change their flavour during the travel to the Earth. This closed the neutrino puzzle. Therefore, the high precision measurement of ${}^8\text{B}$ neutrino flux [5], together with the foreseen measurement of ${}^7\text{Be}$ neutrinos [6], can now be used to understand physical and chemical properties of the Sun, provided that nuclear re-

action cross sections are known with similar accuracy [7]. The ${}^3\text{He}(\alpha,\gamma){}^7\text{Be}$ reaction is the onset of the ${}^7\text{Be}$ and ${}^8\text{B}$ branches of the proton-proton (p-p) chain of hydrogen burning. The 9% error [8] on its cross section is presently the main nuclear physics uncertainty on the prediction of ${}^7\text{Be}$ and ${}^8\text{B}$ neutrino fluxes [9].

At stellar energies the ${}^3\text{He}(\alpha,\gamma){}^7\text{Be}$ cross section $\sigma(E)$ drops exponentially with the energy and can be parametrized as:

$$\sigma(E) = \frac{S(E)}{E} e^{-2\pi\eta(E)} \quad (1)$$

where $S(E)$ is the astrophysical factor, η is the Sommerfeld parameter [10], and E is the center of mass energy.

${}^3\text{He}(\alpha,\gamma){}^7\text{Be}$ is a radiative capture reaction (Q-value: 1.586 MeV) into the first excited state ($E_x=429$ keV) and the ground state of ${}^7\text{Be}$ that subsequently decays by electron capture into ${}^7\text{Li}$ with a terrestrial half life of 53.22 ± 0.06 days [11].

In the last forty years the ${}^3\text{He}(\alpha,\gamma){}^7\text{Be}$ reaction has been measured using two techniques. In the first ap-

*Present address: Forschungszentrum Dresden-Rossendorf, Dresden, Germany

†Corresponding author: *E-mail address:* brogini@pd.infn.it

proach direct α -capture γ -rays were detected (prompt γ method) [12, 13, 14, 15, 16, 17, 18], while, in the second, the delayed ${}^7\text{Be}$ -decay γ rays were counted (activation method) [12, 19, 20, 21]. Previous activation results are, on the average, 13% higher than prompt γ data and this is the origin of the large uncertainty quoted on the reaction cross section [8]. Up to now, no explanation has been obtained for this discrepancy that could be due either to systematic experimental errors (angular distribution, branching ratio effects, parasitic reactions producing ${}^7\text{Be}$) or to the existence of a non radiative capture (E0 monopole) [22]. Recently, the discrepancy on the extrapolated $S(0)$ has been reduced by an activation study at $420 < E < 950$ keV [21] to 9%. High accuracy (4%) activation data were obtained also at LUNA, at center of mass energies down to 106 keV [23, 24]. Nevertheless, high accuracy prompt gamma data are also needed to verify the claimed discrepancy.

We have performed a new high accuracy measurement using simultaneously prompt and activation methods with the same experimental setup. The experiment has been carried out using the underground LUNA 400 kV accelerator [25] at the Gran Sasso National Laboratory (LNGS).

Three couples of cross section values have been measured (prompt γ and activation) at $E_\alpha = 220, 250$ and 400 keV. A sketch of the interaction chamber is given in Fig. 1. The α beam enters the ${}^3\text{He}$ extended windowless gas target [24] through a 7 mm diameter collimator and is stopped on a detachable copper disk that serves as the primary catcher for the produced ${}^7\text{Be}$ and as the hot side of a calorimeter [26]. The latter measures the beam intensity (about 250 μA) with an accuracy of 1.5%. The high beam current decreases the ${}^3\text{He}$ density along the beam path [27]: this effect has been monitored with a silicon detector by double Rutherford scattering providing an accuracy of 1.3% on the gas density determination [28]. The same detector is also used to measure the gas contamination (mainly N_2) that has remained below $(2.7 \pm 0.3)\%$.

Prompt γ rays are counted with a 135% ultra low-background HPGe detector shielded with 5 cm of OFHC copper and 25 cm of lead. The detector and the shield are enclosed in a sealed plastic box flushed with dry N_2 to reduce ${}^{222}\text{Rn}$ background. Thanks to the underground environment where cosmic muons are strongly reduced [29], the shielding suppression factor is of five orders of magnitude for γ rays below 2 MeV. A lead collimator is positioned inside the target chamber to collect mostly γ rays emitted at 55° . At this angle the contribution of the second Legendre polynomial in the angular distribution expression, vanishes. Therefore the inner collimator reduces the systematic error due to prompt γ angular distribution uncertainties and also shields the detector from possible beam-induced radiation coming from the entrance collimator and the calorimeter cap. The effective target length seen by the HPGe detector is approximately 12 cm, corresponding to an energy loss $\Delta E = 3$

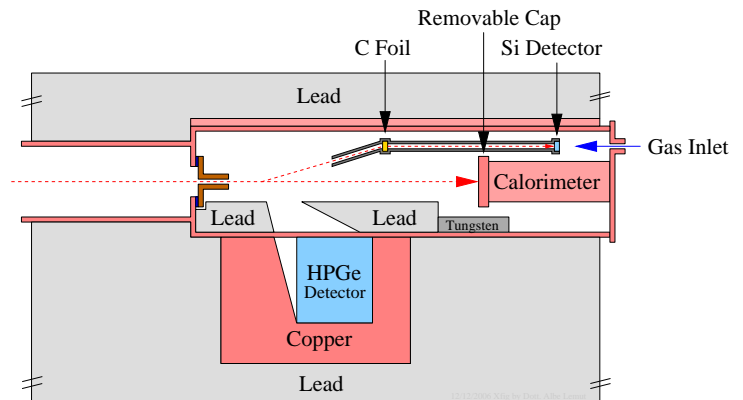


FIG. 1: Schematic view of the interaction chamber with the position of the HPGe detector and of the 100 μm silicon detector used for ${}^3\text{He}$ density monitoring. The distance between the entrance collimator and the calorimeter is 35 cm. The thickness of the internal collimator is 3 cm for the Lead part and 1.6 cm for the Tungsten part.

keV at $P_{\text{target}} = 0.7$ mbar (value used in all the runs) and $E_\alpha = 400$ keV.

The photopeak detection efficiency is determined by a Monte Carlo code [30] calibrated with ${}^{60}\text{Co}$ and ${}^{137}\text{Cs}$ radioactive point-like sources moved along the beam path. The Monte Carlo reproduces the experimental efficiency within the source activity uncertainties (1.5%). The spectra collected at $E_\alpha = 220, 250$ and 400 keV, with a total charge of 637, 407 and 113 C respectively, are shown in Fig. 2 together with laboratory background. Beam induced gamma-ray background has been measured with ${}^4\text{He}$ gas in the target at $E_\alpha = 400$ keV: no difference with laboratory background has been observed. In the data analysis only the two primary transitions at $E_\gamma = Q + E_{cm}$ and $E_\gamma = Q + E_{cm} - 429$ keV, have been considered. Theoretical angular distribution functions are calculated by [31] down to 210 keV interaction energy. A linear extrapolation of the curves of [31] has been done and the coefficients of the Legendre polynomials adopted in the detection efficiency calculation are: $a_1 = -0.05$ and $a_1 = 0$ for the transition to the ground and to the first excited state, respectively and $a_2 = -0.1$ for both transitions. These values are in agreement with recent theoretical predictions [32]. With the Monte Carlo code, we have conservatively varied 100% both a_1 and a_2 coefficients obtaining a global 2.5% variation of the detection efficiency. This value has been assumed as a systematic uncertainty and turns out to be the major contribution to the error budget of the prompt γ method. The in-beam runs provide accurate branching ratios between the two transitions $\sigma(\text{DC} \rightarrow 429)/\sigma(\text{DC} \rightarrow 0)$: 0.417 ± 0.020 , 0.415 ± 0.029 and 0.38 ± 0.03 at $E_\alpha = 400, 250$ and 220 keV, respectively. Our values are consistent with, but more precise than, latest branching ratio measurements [12, 16] and are in agreement with theoretical calculations [33].

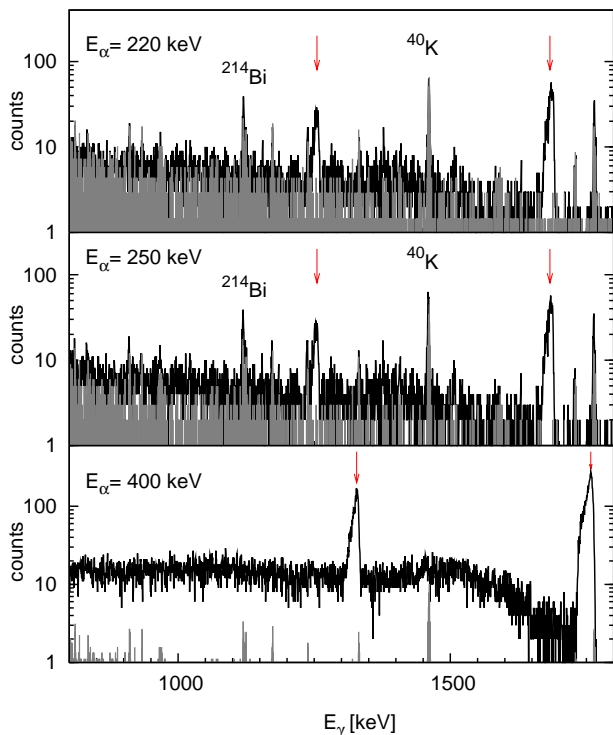


FIG. 2: γ -ray spectrum at $E_\alpha = 220, 250$ and 400 keV compared with natural laboratory background (in grey) normalized to beam-measurement live times (respectively: 31.2 days, 21.3 days and 4.8 days). Arrows indicate the primary transition peaks to the first excited state and to the ground state.

During the runs in which prompt γ -rays are detected, the ${}^7\text{Be}$ nuclei produced inside the gas target get implanted into the removable calorimeter cap. After each run, the cap is dismantled and moved to LNGS underground low-activity counting facility [29]. Details and accuracy of the activation method at LUNA are discussed elsewhere [23, 24]. Since we have simultaneously used the same beam and target for both methods, some systematic uncertainties (beam intensity, target density and purity) cancel out in the comparison between the two techniques.

Results are reported in Table I and shown in Fig. 3 together with all previous literature data. For each couple of data (prompt γ and activation) obtained at the same E_α , the effective energy (E_{eff}), calculated as described in [23], is slightly different. Indeed the target of the prompt γ experiment, defined by the inner collimator (Fig. 1), is a fraction of the whole target contributing to ${}^7\text{Be}$ production. The E_{eff} difference corresponds to an S-factor change smaller than 0.1% according to the

energy dependence given in [34]. In the comparison between prompt and activation S-factors, we have therefore neglected the E_{eff} differences and considered a total uncertainty given by the statistical and reduced systematic errors summed in quadrature (Table I). The mean percentage difference between the S-factor values in Table I ($\Delta S = (S_a - S_p) / ((S_a + S_p) / 2)$) is $\Delta S_m = -0.014 \pm 0.042$. This result limits to +2.8% (maximum ΔS_m value at 1σ level) possible non-radiative contributions to the reaction cross section. S-factor activation values at $E_\alpha = 400$ and 250 keV are compatible with those previously obtained at LUNA with the same setup [23, 24]. Considering the average of the new and old activation values at the same beam energy, ΔS_m does not change. A simultaneous measurement with both activation and prompt γ technique at energies around $E_{cm} = 1$ MeV, where the oldest activation experiments [12, 19] were performed, would be useful to look for non-radiative contributions in a higher energy region than the one explored in the present experiment. To deduce the extrapolated $S(0)$, the fit of [34] has been rescaled using the present activation and prompt γ data separately. The weighted average between the two $S(0)$ values has been calculated adopting as weights the statistical error obtained from the fit and the reduced systematic error. We get $S(0) = 0.560 \pm 0.017$ keV barn where the final uncertainty also includes the systematic error common to the two methods. Performing the same calculation considering also the most recent and very accurate results from [21, 23, 24] or using the theoretical function [35] adopted in the NACRE compilation [36], instead of the R-matrix fit by [34], the extrapolated $S(0)$ changes less than 1%. Low energy accurate data in fact minimize the uncertainty upon extrapolation. However, a refined measurement of the slope of the S-factor in a wide energy range would be useful to confirm theoretical calculations reducing the uncertainty on the extrapolated $S(0)$. The uncertainty on the predicted ${}^8\text{B}$ neutrino flux due to S_{34} is now reduced from 7.5% to 2.4% and the total uncertainty, including astrophysical parameters, goes from 12% to 10% [37]. Similarly, the uncertainty on ${}^7\text{Be}$ predicted flux goes from 9.4% to 5.5%, being the contribution of S_{34} error reduced from 8% to 2.5% [37].

Acknowledgments

A particular thank goes to Carlos Peña Garay for fruitful and enlightening discussions. The authors are indebted to the INFN technical staff at Gran Sasso, Genova, Padova and Legnaro for their support during the experiment. This work was supported by INFN and in part by: TARI RII-CT-2004-506222, OTKA T42733 and T49245, and BMBF (05C11PC1-1)

[1] J. N. Bahcall, Phys. Rev. Lett. **12**, 300 (1964).

[2] R. Davis, Phys. Rev. Lett. **12**, 303 (1964).

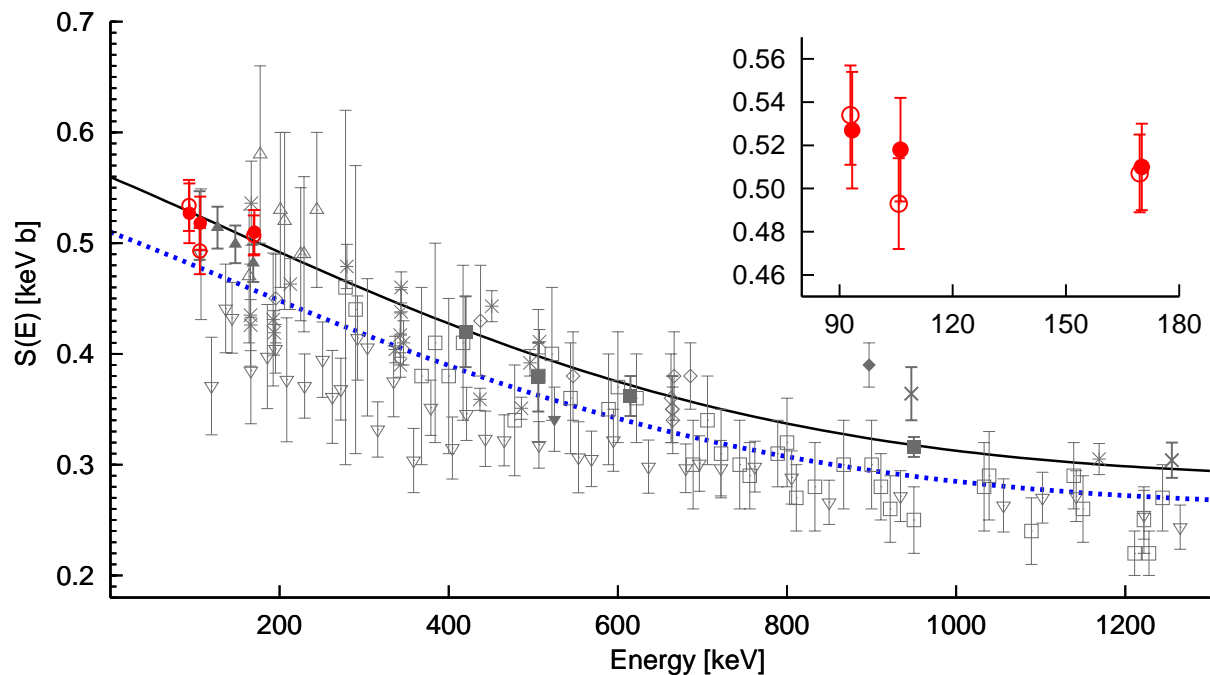


FIG. 3: Overview of all available S-factor values for the ${}^3\text{He}(\alpha,\gamma){}^7\text{Be}$ reaction. Filled and open circles: present work. Prompt- γ data: open squares [14], open triangles [15], stars [12], open inverse triangles [16], filled inverse triangles [17], open diamonds [18]. Activation data: filled diamonds [19], crosses [12], filled squares [21], filled triangles [23, 24]. Dashed line: most recent R-matrix fit [34], solid line: fit [34] normalized to present data. In the inset a zoom of prompt γ (filled circles) and activation (open circles) data obtained in this work.

- [3] Q. R. Ahmad *et al.*, Phys. Rev. Lett. **87**, 71301 (2001).
 [4] K. Eguchi *et al.*, Phys. Rev. Lett. **90**, 21802 (2003).
 [5] J. Hosaka *et al.*, Phys. Rev. D **73**, 112001 (2003).
 [6] G. Alimonti *et al.*, Astropart. Ph. **16**, 205 (2002).
 [7] G. Fiorentini and B. Ricci, astro-ph/0310753 (2003).
 [8] E. Adelberger *et al.*, Rev. Mod. Phys. **70**, 1265 (1998).
 [9] J. N. Bahcall and M. H. Pinsonneault, Phys. Rev. Lett. **92**, 121301 (2004).
 [10] C. Rolfs and W. S. Rodney, *Cauldrons in the Cosmos* (University of Chicago Press, 1988).
 [11] D. Tilley *et al.*, Nuc. Phys. A **708**, 3 (2002).
 [12] J. Osborne *et al.*, Phys. Rev. Lett. **48**, 1664 (1982).
 [13] H. Holmgren and R. Johnston, Phys. Rev. **113**, 1556 (1959).
 [14] P. Parker and R. Kavanagh, Phys. Rev. **131**, 2578 (1963).
 [15] K. Nagatani, M. R. Dwarakanath, and D. Ashery, Nucl. Phys. A **128**, 325 (1969).
 [16] H. Kr awinkel *et al.*, Z. Phys. A **304**, 307 (1982).
 [17] T. Alexander *et al.*, Nucl. Phys. A **427**, 526 (1984).
 [18] M. Hilgemeier *et al.*, Z. Phys. A **329**, 243 (1988).
 [19] R. Robertson *et al.*, Phys. Rev. C **27**, 11 (1983).
 [20] H. Volk *et al.*, Z. Phys. A **310**, 91 (1988).
 [21] B. N. Singh *et al.*, Phys. Rev. Lett. **93**, 262503 (2004).
 [22] M. Nessin, T. H. Kruse, and K. E. Eklund, Phys. Rev. **125**, 639 (1962).
 [23] D. Bemmerer *et al.*, Phys. Rev. Lett. **97**, 122502 (2006).
 [24] G. Gy urky *et al.*, Phys. Rev. C **75**, 35805 (2007).
 [25] A. Formicola *et al.*, Nucl. Instr. Meth. Phys. Res. A **507**, 609 (2003).
 [26] C. Casella *et al.*, Nucl. Instr. Meth. Phys. Res. A **489**, 160 (2002).
 [27] J. G orres *et al.*, Nucl. Instr. Meth. Phys. Res. **177**, 295 (1980).
 [28] M. Marta *et al.*, Nucl. Instr. Meth. Phys. Res. A **569**, 727 (2006).
 [29] C. Arpesella *et al.*, Appl. Radiat. Isot. **47**, 991 (1996).
 [30] C. Arpesella *et al.*, Nucl. Instr. Meth. Phys. Res. A **360**, 607 (1995).
 [31] T. A. Tombrello and P. D. Parker, Phys. Rev. **131**, 2582 (1963).
 [32] B. T. Kim, T. Izumoto, and K. Nagatani, Phys. Rev. C **23**, 33 (1981).
 [33] T. Kajino, Nucl. Phys. A **460**, 559 (1986).
 [34] P. Descouvemont *et al.*, At. Data and Nuc. Data. Tab. A **88**, 203 (2004).
 [35] T. Kajino H. Toki and S. M. Austin, Astrophys. J. **319**, 531 (1987).
 [36] C. Angulo *et al.*, Nucl. Phys. A **656**, 3 (1999).
 [37] C. Pe na Garay, private communication (2006).

$E\alpha$ (keV)	Method	E_{eff} (keV)	$\sigma(E_{eff})$ (nbarn)	$S(E_{eff})$ (keV barn)	ΔS stat. (keV barn)	ΔS syst. (keV barn)	ΔS red. syst. (keV barn)
400	p	170.1	10.25	0.510	0.008	0.019	0.015
400	a	169.5	10.00	0.507	0.010	0.015	0.010
250	p	106.1	0.588	0.518	0.014	0.019	0.016
250	a	105.7	0.546	0.493	0.015	0.015	0.011
220	p	93.3	0.235	0.527	0.018	0.020	0.016
220	a	92.9	0.232	0.534	0.016	0.017	0.013

TABLE I: Cross section and S-factor results with corresponding uncertainties for the prompt (p) and activation (a) methods. In the last column the reduced systematic uncertainty is reported where contributions common to the two methods have been subtracted.

Precision study of ground state capture in the $^{14}\text{N}(p,\gamma)^{15}\text{O}$ reaction

M. Marta,¹ A. Formicola,² Gy. Gyürky,³ D. Bemmerer,¹ C. Broggini,⁴ A. Cacioli,^{4,5} P. Corvisiero,⁶ H. Costantini,⁶ Z. Elekes,³ Zs. Fülöp,³ G. Gervino,⁷ A. Guglielmetti,⁸ C. Gustavino,² G. Imbriani,⁹ M. Junker,² R. Kunz,¹⁰ A. Lemut,⁶ B. Limata,⁹ C. Mazzocchi,⁸ R. Menegazzo,⁴ P. Prati,⁶ V. Roca,⁹ C. Rolfs,¹⁰ M. Romano,⁹ C. Rossi Alvarez,⁴ E. Somorjai,³ O. Straniero,¹¹ F. Strieder,¹⁰ F. Terrasi,¹² H.P. Trautvetter,¹⁰ and A. Vomiero¹³

(The LUNA Collaboration)

¹*Forschungszentrum Dresden-Rossendorf, Bautzner Landstr. 128, 01328 Dresden, Germany*

²*INFN, Laboratori Nazionali del Gran Sasso (LNGS), Assergi (AQ), Italy*

³*Institute of Nuclear Research (ATOMKI), Debrecen, Hungary*

⁴*Istituto Nazionale di Fisica Nucleare (INFN), Sezione di Padova, via Marzolo 8, 35131 Padova, Italy*

⁵*Dipartimento di Fisica, Università di Padova, Italy*

⁶*Università di Genova and INFN Sezione di Genova, Genova, Italy*

⁷*Dipartimento di Fisica Sperimentale, Università di Torino and INFN Sezione di Torino, Torino, Italy*

⁸*Istituto di Fisica Generale Applicata, Università di Milano and INFN Sezione di Milano, Italy*

⁹*Dipartimento di Scienze Fisiche, Università di Napoli "Federico II", and INFN Sezione di Napoli, Napoli, Italy*

¹⁰*Institut für Experimentalphysik III, Ruhr-Universität Bochum, Bochum, Germany*

¹¹*Osservatorio Astronomico di Collurania, Teramo, and INFN Sezione di Napoli, Napoli, Italy*

¹²*Seconda Università di Napoli, Caserta, and INFN Sezione di Napoli, Napoli, Italy*

¹³*INFN, Laboratori Nazionali di Legnaro, Legnaro, Italy*

(Dated: July 30, 2008)

The rate of the hydrogen-burning carbon-nitrogen-oxygen (CNO) cycle is controlled by the slowest process, $^{14}\text{N}(p,\gamma)^{15}\text{O}$, which proceeds by capture to the ground and several excited states in ^{15}O . Previous extrapolations for the ground state contribution disagreed by a factor 2, corresponding to 15% uncertainty in the total astrophysical S-factor. At the Laboratory for Underground Nuclear Astrophysics (LUNA) 400 kV accelerator placed deep underground in the Gran Sasso facility in Italy, a new experiment on ground state capture has been carried out at 317.8, 334.4, and 353.3 keV center-of-mass energy. Systematic corrections have been reduced considerably with respect to previous studies by using a Clover detector and by adopting a relative analysis. The previous discrepancy has been resolved, and ground state capture no longer dominates the uncertainty of the total S-factor.

PACS numbers: 25.40.Ep, 25.40.Lw, 26.20.Cd, 26.65.+t

Recent data on the abundance of the elements carbon, nitrogen, and oxygen (CNO) in the solar atmosphere [1] lead to a contradiction between solar model predictions and measurements for several helioseismological quantities [2]. In the present precision era, this puzzle represents the foremost problem of the standard solar model [2] since the resolution of the solar neutrino puzzle [3]. In order to address this point, it has been suggested to determine the CNO abundances in the solar center from neutrino data [4]. Neutrinos emitted in solar CNO cycle burning are expected to lead to about 1000 events/year both in the Borexino detector [5] and in the proposed SNO+ detector [6]. A correct interpretation of this expected data, based on the known solar core temperature and known neutrino properties [4], requires the rate of the CNO cycle to be known with systematical uncertainty matching these statistics.

terized¹ as the astrophysical S-factor

$$S(E) = \sigma E \exp \left[212.4/\sqrt{E} \right], \quad (1)$$

has been extensively studied in the past [8, and references therein]. Recently, it has been shown that capture to the ground state in ^{15}O (fig. 1), previously [8] believed to account for half of the S-factor² extrapolated to zero energy $S_{\text{tot}}(0)$, is strongly suppressed [9, 10, 11, 12, 13, 14, 15]. This finding is independently supported by a reduction in the γ -width of the subthreshold state at 6792 keV in ^{15}O seen in Doppler shift attenuation [9] and Coulomb excitation [12] works, and by fits [10, 11, 13, 14, 15] in the R-matrix framework (table I). The resulting 50% reduction in the total cross section has subsequently been directly observed at an energy as low as $E \approx 70$ keV [16].

The rate of the CNO cycle is controlled [7] by the $^{14}\text{N}(p,\gamma)^{15}\text{O}$ reaction. Its cross section $\sigma(E)$, param-

¹ E_p denotes the beam energy in the laboratory system, and E the effective energy in the center of mass system in keV.

² $S_i(0)$ denotes the S-factor, extrapolated to zero energy, for capture to the state at i keV in ^{15}O . $S_{\text{GS}}(0)$ and $S_{\text{tot}}(0)$ refer to ground state capture and to the total S-factor, respectively.

TABLE I: Measured quantities used to obtain an extrapolated $S_{\text{GS}}(0)$ [keV barn] in recent studies.

Group	Quantity used [taken from]	$S_{\text{GS}}(0)$
TUNL [9]	γ -width [9]	0.12–0.45
Brussels [10]	Cross section [8]	$0.08^{+0.13}_{-0.06}$
Texas A&M [11]	ANC [11], cross section [8]	0.15 ± 0.07
LUNA [13]	Cross section [8, 13] ^a	0.25 ± 0.06
TUNL [14]	Cross section [14]	0.49 ± 0.08

^aRef. [8] data have been corrected [13] for summing-in.

For the Gamow peak of the Sun ($E \approx 27$ keV), however, extrapolations remain indispensable. For the dominant contribution to $S_{\text{tot}}(0)$, i.e. capture to the state at 6792 keV, recent experimental data and R-matrix fits are consistent [14, 15]. For capture to the ground state, recent experimental data ($E \approx 120$ –480 keV) from LUNA [13, 15] and TUNL [14] are consistent with each other, and they both rule out a previous R-matrix fit [11]. However, the extrapolated $S_{\text{GS}}(0)$ values [13, 14] disagree significantly (table I). This discrepancy has 15% impact on $S_{\text{tot}}(0)$, limiting its precision. In addition to differently treating previous data [8] in the fit, Refs. [13, 14] had employed large germanium detectors in close geometry, enhancing the detection efficiency but incurring true coincidence summing-in corrections of 100–250% for the ground state data, which, in turn, lead to considerable systematic uncertainty.

The aim of the present work is to address the conflicting extrapolations [13, 14] with a precision cross section measurement. In order to minimize the uncertainties, the analysis is limited to the ratio of the cross sections for capture to the ground state and to the 6792 keV state. An energy range above the 259 keV resonance, where the fits for ground state capture pass through a sensitive minimum [10], has been selected [17]. A second sensitive energy region lies below the 259 keV resonance. Since the cross section is a factor 100 lower there, the latter energies were not probed in the present work. The experiment was performed at the Laboratory for Underground Nuclear Astrophysics (LUNA) at the Gran Sasso National Laboratory (Italy), which has ultra-low γ -ray laboratory background [18]. A Clover detector was used, reducing the summing-in correction by a factor 30 (table II).

The H^+ beam of $E_p = 359, 380, \text{ and } 399$ keV and 0.25–0.45 mA intensity from the LUNA2 400 kV accelerator [19] impinged on a sputtered TiN target, with 55 keV thickness measured on the $E = 259$ keV resonance. The γ -rays from the reaction to be studied were detected in a Eurisys Clover-BGO detection system [20]. The front end of the Clover crystals was positioned at 9.5 cm distance from the target, at an angle of 55° with respect to the beam axis. The output signal from each of the four Clover segments was split into two branches; of these

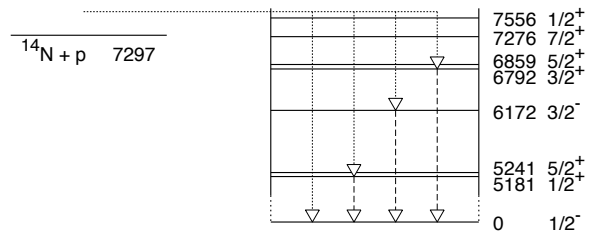


FIG. 1: Energy levels of ^{15}O , in keV [15, 21].

branches, one branch was recorded separately, and the four spectra were summed in the offline analysis (singles mode). The second branches of the four signals were added online in an analog summing unit (adback mode). For experiments off the 259 keV resonance, the adback mode data were recorded in anticoincidence with the BGO anti-Compton shield.

The γ -ray detection efficiency was obtained using ^{137}Cs and ^{60}Co radioactive sources calibrated to 1.5% and 0.75%, respectively. The efficiency curve was extended to high energy based on spectra recorded at the 259 keV resonance, using the known 1:1 γ -ray cascades for the excited states at 6172 and 6792 keV. The γ -rays from the decay of this $1/2^+$ resonance are isotropic, and their angular correlations are well known [22]. The calculated summing-out correction in adback mode is 2.9%, with an assumed relative uncertainty of 20%, consistent with a GEANT4 [26] simulation showing $(4.5 \pm 1.8)\%$ correction. As a check on the quality of the efficiency curve, the experimental cascade ratio for the 5181 keV excited state (not used in the fit) was found to be reproduced within 1% statistics.

The branching ratio for decay of the 259 keV resonance to the ground state was found to be $(1.56 \pm 0.08)\%$ in adback mode and $(1.53 \pm 0.06)\%$ in singles mode, taking into account $(42 \pm 2)\%$ and $(7.4 \pm 0.3)\%$ summing-in correction, respectively. This confirms that the summing-in correction for the adback mode is accurate. Furthermore, the GEANT4 simulation showed $(40.2 \pm 1.4)\%$ and $(7.8 \pm 0.9)\%$ summing-in correction for adback and singles, respectively, in good agreement with the above data. The branching ratio is in good agreement with the previous LUNA value [15] and in fair agreement with TUNL [14].

Off resonance, the spectra (fig. 2, rows 1–3) show some on-resonance contribution due to the tail of the target profile. The secondary γ -ray from the decay of the 6792 keV level (fig. 2, middle column) therefore contains 13–55% on-resonance capture, and it was rescaled with the on/off-resonance ratio obtained from the primary γ -rays (fig. 2, left column). Subsequently, the cross section ratio

$$R_{\text{GS}/6792}(E) = \frac{\sigma_{\text{GS}}(E)}{\sigma_{6792}(E)} \quad (2)$$

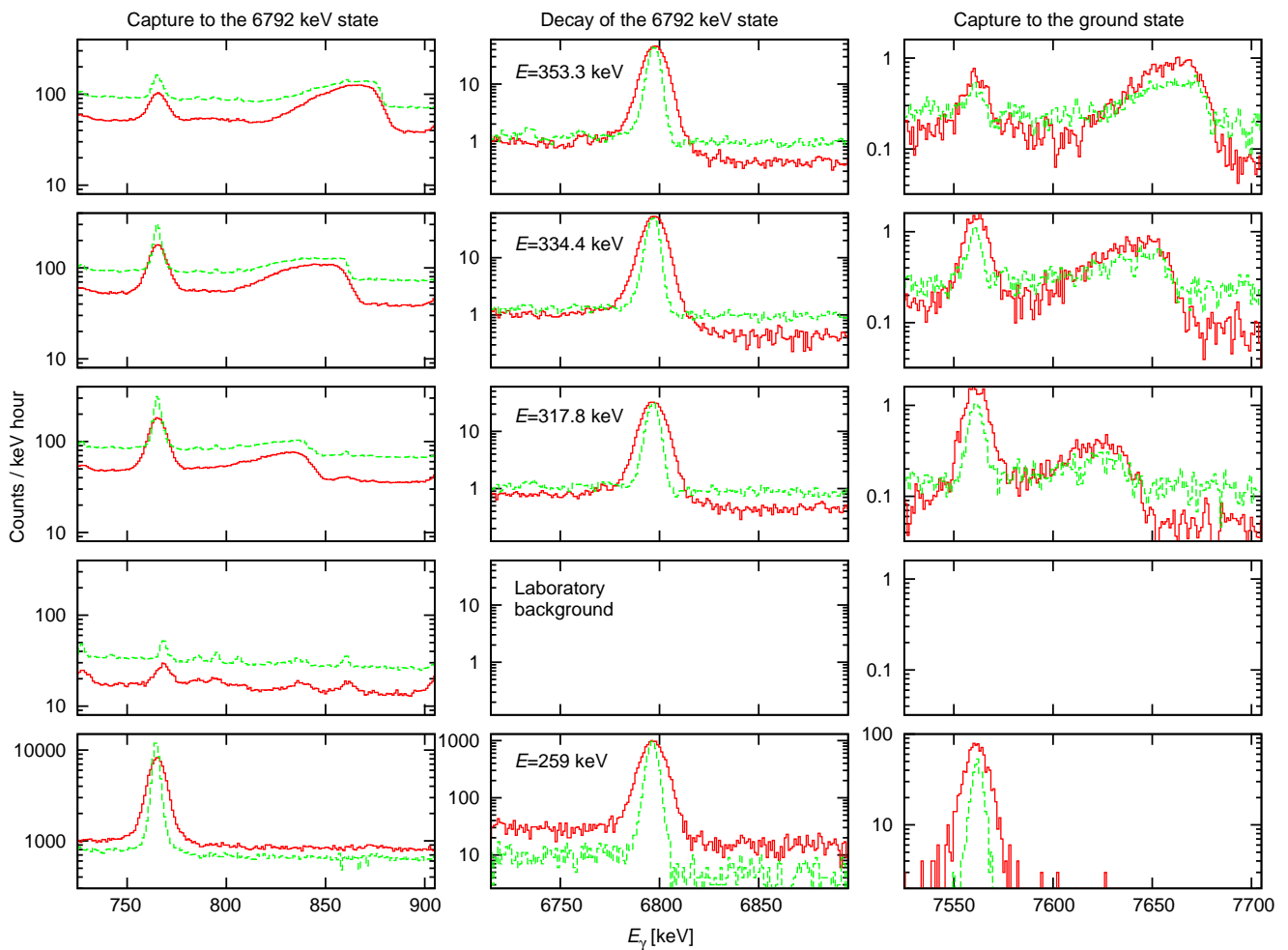


FIG. 2: (color online) Solid red (dashed green) line: γ -ray spectra for addback (singles) mode. First three rows: off-resonance data. Fourth row: laboratory background, negligible at high γ -energy. Fifth row: data at the $E = 259$ keV resonance.

with $\sigma_{\text{GS}}(E)$ and $\sigma_{6792}(E)$ the cross sections for capture to the ground state and to the 6792 keV state in ^{15}O , respectively, was calculated for each bombarding energy (table II). The addback and singles mode data for $R_{\text{GS}/6792}$ were found to be in agreement. Because of their lower statistical uncertainty, the addback data were adopted for the further analysis.

The systematic uncertainty for $R_{\text{GS}/6792}$ (table II) depends on (1) the summing-in correction for the ground state γ -ray (up to 4.6% and 0.9% effect on $R_{\text{GS}/6792}$ for the addback and singles mode, respectively, taking into account the calculated [7] angular correlation), and (2) the slope of the detection efficiency curve over the energy range $E_\gamma = 6792\text{--}7650$ keV (known to 0.8%). For the cascade 6792 keV γ -ray, (3) the anticoincidence efficiency (1.2% effect), and (4) the summing-out correction (0.6% effect) contribute to the systematic uncertainty for $R_{\text{GS}/6792}$. The effects of e.g. target composition and profile, stopping power, beam intensity, and absolute γ -ray

TABLE II: Cross section ratio $R_{\text{GS}/6792}(E)$ and relative uncertainty. The size of the summing-in correction is also given.

E [keV]	mode	$R_{\text{GS}/6792}(E)$ [10^{-2}]	stat. uncertainty	syst. uncertainty	Summing-in correction
317.8 ± 1.5	addback	4.71	5.9%	5.4%	30%
	singles	4.67	14%	2.7%	4.3%
334.4 ± 1.5	addback	5.00	5.1%	3.9%	21%
	singles	5.07	13%	2.5%	3.4%
353.3 ± 1.5	addback	5.30	3.6%	3.5%	19%
	singles	5.15	10%	2.3%	3.2%

detection efficiency cancel out in the relative experiment. The effective energy E was determined from the centroids of the γ -lines for capture to the ground state and to the 6792 keV state and leads to 2.4% uncertainty.

The absolute cross section for the ground state transition obtained from the present data was determined by the ratios given in table II normalized with the weighted

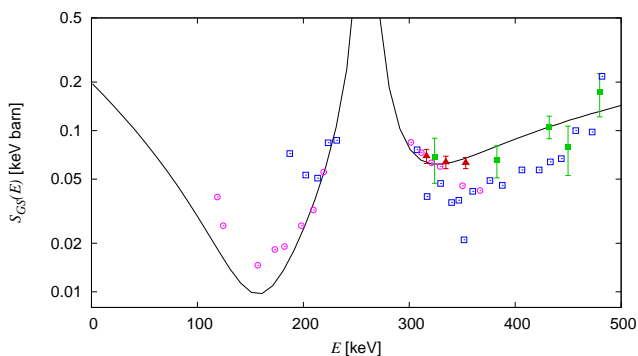


FIG. 3: S-factor for capture to the ground state. Full triangles: present data. Full squares: Ref. [8]. Line: Present best R-matrix fit. Data from [13, 15] (empty circles) and [14] (empty squares) are shown for comparison but were not used in the fit; their error bars have been omitted for clarity.

average (uncertainty 7.5%) of the S-factor results for the 6792 keV transition given in Refs. [8, 14, 15]. From such a combined fit an ANC of $4.8 \text{ fm}^{-1/2}$ was obtained for the 6792 keV state, in good agreement with Refs. [11, 23] and resulting in $\gamma^2 = 0.4 \text{ MeV}$ for the reduced width of the subthreshold state. For the strength of the 259 keV resonance, 13.1 meV (weighted average of [14, 15, 16, 21]) was adopted, for its proton width 0.99 keV [13], and for the ground state branching, 1.63% (weighted average of [14, 15] and the present work) was used. For all other parameters, the previous values were taken without any change [13]: ANC for ground state capture: $7.3 \text{ fm}^{-1/2}$. $E = 0.987 \text{ MeV}$ resonance: $\Gamma_\gamma = 26 \text{ meV}$, $\Gamma_p = 3 \text{ keV}$. $E = 2.187 \text{ MeV}$ resonance: $\Gamma_\gamma = 4.4 \text{ eV}$, $\Gamma_p = 0.27 \text{ MeV}$. Background pole at $E = 6 \text{ MeV}$, $\Gamma_p = 8 \text{ MeV}$. In order to limit the systematic uncertainty due to summing-in to less than the statistical error, only data with less than 50% summing-in correction were used for the R-matrix analysis: i.e. [8] (corrected [13] for summing-in) and the present data. The interference pattern around the 259 keV resonance is fixed by the results of [13, 14, 15], and the interaction radius was set to 5.5 fm [13]. The best fit (fig. 3) varying only the γ -widths of the subthreshold state and of the background pole results in $S_{\text{GS}}(0) = 0.20 \text{ keV barn}$ with a γ -width $\Gamma_\gamma = 0.9 \pm 0.2 \text{ eV}$ for the subthreshold state, in agreement with Coulomb excitation work [12] and with lifetime measurements [9, 24]. A full R-matrix analysis including a detailed error determination for all parameters is beyond the scope of the present work. Therefore, the previous relative uncertainty of 24% in $S_{\text{GS}}(0)$ [13] is adopted here, giving $S_{\text{GS}}(0) = 0.20 \pm 0.05 \text{ keV barn}$.

In summary, owing to the present high precision data, ground state capture now contributes less than 4% uncertainty to the total $S_{\text{tot}}(0)$, instead of the previous 15%, based on a data set which is nearly free from summing problems. On the basis of the present result, $S_{\text{tot}}(0) = 1.57 \pm 0.13 \text{ keV barn}$ is recommended, with the uncertainty including also systematic effects. For this sum, $S_{6172}(0) = 0.09 \pm 0.07 \text{ keV barn}$ [11, 14, 15, 25] has been adopted. Further improvements in $S_{\text{tot}}(0)$ precision would require a fresh study of this contribution. In the meantime, the present ground state data pave the way for a measurement of the solar central metallicity [4].

The use of the R-matrix code [10] written by P. Descouvemont (ULB Brussels) is gratefully acknowledged. One of us (H.P.T.) thanks R.E. Azuma, E. Simpson, and A. Champagne for fruitful discussions. — The present work has been supported by INFN and in part by the EU (ILIAS-TA RII3-CT-2004-506222), OTKA (T49245 and K68801), and DFG (Ro 429/41).

-
- [1] M. Asplund, N. Grevesse, and A. Jacques Sauval, *Nucl. Phys. A* **777**, 1 (2006).
 - [2] J. N. Bahcall, A. M. Serenelli, and S. Basu, *Astrophys. J. Suppl. Ser.* **165**, 400 (2006).
 - [3] Q. R. Ahmad et al., *Phys. Rev. Lett.* **89**, 011301 (2002).
 - [4] W. Haxton, arXiv:0710.2295 (2007).
 - [5] C. Arpesella et al., *Phys. Lett. B* **658**, 101 (2008).
 - [6] M. C. Chen, *Nucl. Phys. B (Proc. Suppl.)* **145**, 65 (2005).
 - [7] C. Iliadis, *Nuclear Physics of Stars* (Wiley-VCH, 2007).
 - [8] U. Schröder et al., *Nucl. Phys. A* **467**, 240 (1987).
 - [9] P. Bertone et al., *Phys. Rev. Lett.* **87**, 152501 (2001).
 - [10] C. Angulo and P. Descouvemont, *Nucl. Phys. A* **690**, 755 (2001).
 - [11] A. Mukhamedzhanov et al., *Phys. Rev. C* **67**, 065804 (2003).
 - [12] K. Yamada et al., *Phys. Lett. B* **579**, 265 (2004).
 - [13] A. Formicola et al., *Phys. Lett. B* **591**, 61 (2004).
 - [14] R. C. Runkle et al., *Phys. Rev. Lett.* **94**, 082503 (2005).
 - [15] G. Imbriani et al., *Eur. Phys. J. A* **25**, 455 (2005).
 - [16] A. Lemut et al., *Phys. Lett. B* **634**, 483 (2006).
 - [17] H.-P. Trautvetter et al., *J. Phys. G* **35**, 014019 (2008).
 - [18] D. Bemmerer et al., *Eur. Phys. J. A* **24**, 313 (2005).
 - [19] A. Formicola et al., *Nucl. Inst. Meth. A* **507**, 609 (2003).
 - [20] Z. Elekes et al., *Nucl. Inst. Meth. A* **503**, 580 (2003).
 - [21] F. Ajzenberg-Selove, *Nucl. Phys. A* **523**, 1 (1991).
 - [22] B. Povh and D. F. Hebbard, *Phys. Rev.* **115**, 608 (1959).
 - [23] P. F. Bertone et al., *Phys. Rev. C* **66**, 055804 (2002).
 - [24] D. Schürmann et al., *Phys. Rev. C* **77**, 055803 (2008).
 - [25] S. O. Nelson et al., *Phys. Rev. C* **68**, 065804 (2003).
 - [26] S. Agostinelli et al., *Nucl. Inst. Meth. A* **506**, 250 (2003).

The $^{14}\text{N}(\text{p},\gamma)^{15}\text{O}$ reaction studied with a composite germanium detector

M. Marta,^{1,*} A. Formicola,² D. Bemmerer,¹ C. Broggini,³ A. Cacioli,^{3,4} P. Corvisiero,⁵ H. Costantini,⁵
 Z. Elekes,⁶ Zs. Fülöp,⁶ G. Gervino,⁷ A. Guglielmetti,⁸ C. Gustavino,² Gy. Gyürky,⁶ G. Imbriani,⁹
 M. Junker,² A. Lemut,⁵ B. Limata,⁹ C. Mazzocchi,⁸ R. Menegazzo,³ P. Prati,⁵ V. Roca,⁹ C. Rolfs,¹⁰
 C. Rossi Alvarez,³ E. Somorjai,⁶ O. Straniero,¹¹ F. Strieder,¹⁰ F. Terrasi,¹² H.P. Trautvetter,¹⁰ and A. Vomiero¹³

(The LUNA Collaboration)

¹*Helmholtz-Zentrum Dresden-Rossendorf, Bautzner Landstr. 400, 01328 Dresden, Germany*[†]

²*INFN, Laboratori Nazionali del Gran Sasso (LNGS), Assergi (AQ), Italy*

³*Istituto Nazionale di Fisica Nucleare (INFN), Sezione di Padova, via Marzolo 8, 35131 Padova, Italy*

⁴*Dipartimento di Fisica, Università degli studi di Siena, Italy*

⁵*Università di Genova and INFN Sezione di Genova, Genova, Italy*

⁶*Institute of Nuclear Research (ATOMKI), Debrecen, Hungary*

⁷*Dipartimento di Fisica Sperimentale, Università di Torino and INFN Sezione di Torino, Torino, Italy*

⁸*Università degli Studi di Milano and INFN, Sezione di Milano, Italy*

⁹*Dipartimento di Scienze Fisiche, Università di Napoli "Federico II", and INFN Sezione di Napoli, Napoli, Italy*

¹⁰*Institut für Experimentalphysik III, Ruhr-Universität Bochum, Bochum, Germany*

¹¹*Osservatorio Astronomico di Collurania, Teramo, and INFN Sezione di Napoli, Napoli, Italy*

¹²*Seconda Università di Napoli, Caserta, and INFN Sezione di Napoli, Napoli, Italy*

¹³*Consiglio nazionale delle ricerche, CNR-IDASC Sensor Lab, Brescia, Italy*

The rate of the carbon-nitrogen-oxygen (CNO) cycle of hydrogen burning is controlled by the $^{14}\text{N}(\text{p},\gamma)^{15}\text{O}$ reaction. The reaction proceeds by capture to the ground states and several excited states in ^{15}O . In order to obtain a reliable extrapolation of the excitation curve to astrophysical energy, fits in the R-matrix framework are needed. In an energy range that sensitively tests such fits, new cross section data are reported here for the four major transitions in the $^{14}\text{N}(\text{p},\gamma)^{15}\text{O}$ reaction. The experiment has been performed at the Laboratory for Underground Nuclear Astrophysics (LUNA) 400 kV accelerator placed deep underground in the Gran Sasso facility in Italy. Using a composite germanium detector, summing corrections have been considerably reduced with respect to previous studies. The cross sections for capture to the ground state and to the 5181, 6172, and 6792 keV excited states in ^{15}O have been determined at 359, 380, and 399 keV beam energy. In addition, the branching ratios for the decay of the 278 keV resonance have been remeasured.

PACS numbers: 25.40.Ep, 25.40.Lw, 26.20.Cd, 26.65.+t

I. INTRODUCTION

The stellar rate of the carbon-nitrogen-oxygen (CNO) cycle of hydrogen burning [1, 2] is controlled by the slowest process, the $^{14}\text{N}(\text{p},\gamma)^{15}\text{O}$ reaction [3]. In the Sun, hydrogen burning proceeds mainly by the competing proton-proton chain, and the CNO cycle contributes only 0.8% to the energy production [4]. However, solar CNO hydrogen burning gives rise to neutrino emission lines from the β^+ decay of ^{13}N and ^{15}O [4]. It has recently been suggested [5] to use the expected CNO neutrino flux data from the Borexino detector [6] and the planned SNO+ [7] detector to measure the abundance of carbon and nitrogen in the solar core. This would address the so-called solar metallicity problem [8, 9], which is given by the fact that the new solar metallicities [10] lead to inconsistencies in the standard solar model. The

correct interpretation of the expected CNO neutrino data requires, however, that the nuclear reaction rate of the CNO cycle, which is determined by the $^{14}\text{N}(\text{p},\gamma)^{15}\text{O}$ cross section, be known with sufficient precision.

The $^{14}\text{N}(\text{p},\gamma)^{15}\text{O}$ cross section $\sigma(E)$ can be parameterized using the astrophysical S-factor

$$S(E) = \sigma E \exp \left[212.4/\sqrt{E} \right], \quad (1)$$

with E denoting the energy in the center of mass system in keV.

The excitation function has been studied previously [11–13, e.g.], and these data determine the recommended value in the current nuclear reaction rate compilations for astrophysics [14–16]. Subsequently, a number of new experimental and theoretical results on this reaction have been reported [17–26], showing that the recommended value of the reaction rate [14–16] has to be revised downward by a factor of two. In particular, capture to the ground state in ^{15}O (fig. 1) was shown to be strongly suppressed [17–23]. This reduction is now adopted in a very recent compilation [27]. However, some open questions remain.

In particular, two groups have in recent years presented cross section data and performed R-matrix fits

*Present address: GSI Helmholtzzentrum für Schwerionenforschung, Darmstadt, Germany

[†]As of 1 January 2011, Forschungszentrum Dresden-Rossendorf (FZD) has been renamed to Helmholtz-Zentrum Dresden-Rossendorf (HZDR).

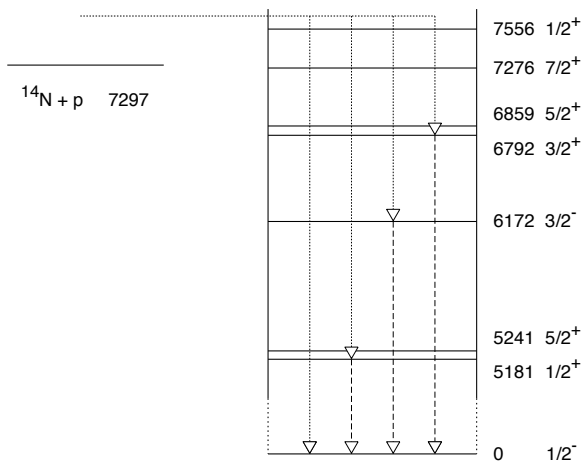


FIG. 1: Level scheme of ^{15}O , in keV [23, 28]. The most important γ -transitions are denoted by arrows.

based on their new data: LUNA [21, 23] and TUNL [22]. These two works show excellent agreement when it comes to the most important contribution to the total S-factor, namely capture to the state at 6792 keV: 1.20 ± 0.05 keV barn [23] and 1.15 ± 0.05 keV barn [22], respectively. However, their results differ by much more than the quoted uncertainties when it comes to the second most important contribution, capture to the ground state: Whereas LUNA reported¹ $S_{\text{GS}}(0) = 0.25 \pm 0.06$ keV barn [21], the TUNL value is double that, 0.49 ± 0.08 keV barn [22]. This discrepancy amounts to about 15% of the total extrapolated $S_{\text{tot}}(0)$, dominating the uncertainty.

The only significant methodical difference between the two fits from LUNA [21, 23] and TUNL [22] is the treatment of high-energy data. The LUNA fit is a global fit, based on the LUNA data presented in the same paper, and on the Schröder *et al.* data [13] which had been corrected for the summing-in effect. The TUNL fit, on the other hand, is a partial fit based solely on the TUNL data presented in the same paper, with the higher-energy R-matrix poles kept fixed based on a previous fit of the Schröder *et al.* data [13]. The starting values and general procedure for both fits are otherwise the same [18].

The experimental data points by LUNA [21, 23] and TUNL [22] are generally in agreement with each other, but they show some systematic uncertainty due to the fact that both groups had employed large germanium detectors in close geometry. This arrangement had been chosen in order to obtain a high enough detection efficiency for the weak ground state capture line. However,

in this way both groups also incurred true coincidence summing-in corrections of more than 100% for the ground state data. Such a large correction entails considerable systematic uncertainty.

The aim of the present work is to address the conflicting extrapolations [21, 22] in two ways. The experimental problem of the previous high summing-in correction is solved by using a Clover detector. The problem of the selection of the database is solved by providing the ground state cross section relative to that for the well-known capture to the state at 6792 keV. The present relative data can then be added to one particular data set without introducing additional scaling uncertainty. Alternatively, they can be rescaled to absolute data using an overall fit of 6792 keV capture based on several independent works, strongly reducing the scaling uncertainty.

For the present experiment, the energy range of $E = 317\text{--}353$ keV has been selected, far enough above the 259 keV resonance to limit resonant contributions, and at the same time a region where a sensitive minimum [18] of R-matrix fits is observed. In principle, such a measurement would also have been possible at $E \approx 170$ keV, in a second sensitive minimum. However, the yield is a factor 100 lower there, so that the present energy range was chosen for practical purposes.

The present relative cross section data have been published previously in abbreviated form [25]. The present work provides full details of that experiment and analysis. In addition, new branching ratios for the decay of the 259 keV resonance obtained in even farther geometry are presented here. The absolute off-resonance $^{14}\text{N}(p,\gamma)^{15}\text{O}$ cross section for capture to the ground state and the 5181, 6172, and 6792 keV excited states is derived at $E_p = 359, 380, \text{ and } 399$ keV. In order to improve the reliability, this latter analysis is performed in two independent ways, namely by the γ -line shape method [29] and by the classical peak integral approach.

II. EXPERIMENT

The experiment was performed in the Laboratory for Underground Nuclear Astrophysics (LUNA) at the Gran Sasso National Laboratory (Italy) [30, 31]. At the LUNA site, the γ -ray laboratory background for $E_\gamma > 3$ MeV is strongly reduced due to the rock overburden equivalent to 3800 meters water [32, 33]. Also for $E_\gamma \leq 3$ MeV with proper shielding the γ -ray background has been found to be much lower than in comparable laboratories at the surface of the Earth [34]. The unique location of LUNA has enabled the study of several nuclear reactions of astrophysical importance [21, 35–40].

A. Setup

The LUNA2 400 kV accelerator [29] provided a H^+ beam of $E_p = 359, 380, \text{ and } 399$ keV, with 0.25–0.45 mA

¹ $S_i(0)$ denotes the S-factor, extrapolated to zero energy, for capture to the state at i keV in ^{15}O . $S_{\text{GS}}(0)$ and $S_{\text{tot}}(0)$ refer to ground state capture and to the total S-factor, respectively.

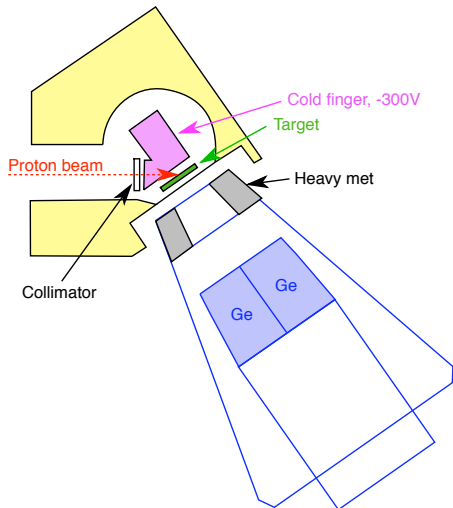


FIG. 2: (Color online) Schematic view of the experimental setup.

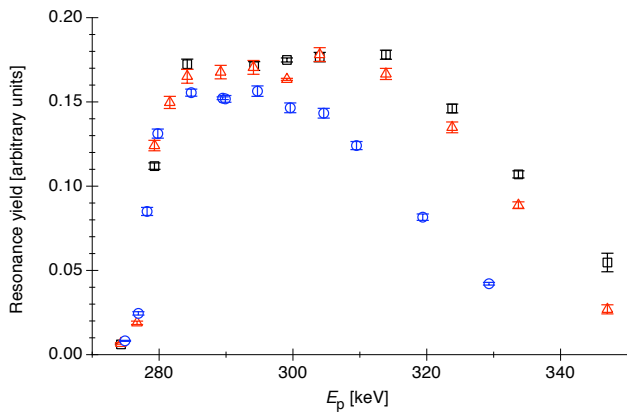


FIG. 3: (Color online) Scans of the $E_p = 278$ keV resonance at the beginning of the experiment (black squares), one day with 29 C dose later (red triangles), and at the end of the experiment after a total accumulated dose of 267 C (blue circles).

intensity. The ion beam passed a collimator of 5 mm diameter, which absorbed a few percent of the full beam intensity, and a cold trap cooled by liquid nitrogen (fig. 2), before hitting the target. Secondary electrons emitted from the target surface were suppressed by applying -300 V suppression voltage to the cold trap. The reproducibility of the current from run to run is estimated to be 2%.

B. Target

A titanium nitride target produced by reactive sputtering at Laboratori Nazionali di Legnaro was used for the experiments. The target had 60 keV energetic width at the $E_p = 278$ keV resonance (fig. 3), when irradiated

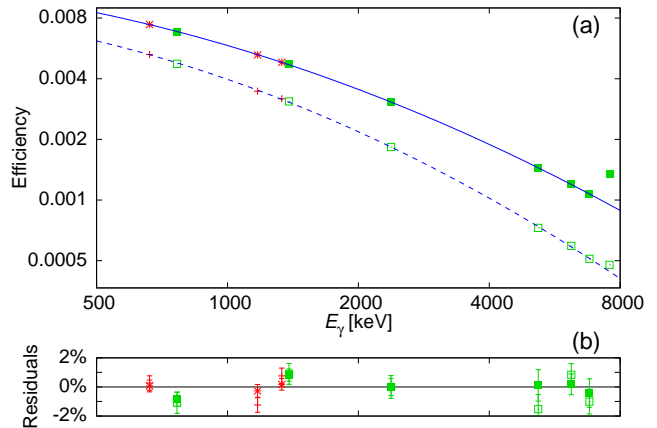


FIG. 4: (Color online) (a) γ -ray detection efficiency for the detector at 9.5 cm distance from the target, as determined with radioactive sources and the two-line method at the 259 keV resonance. Solid (dashed) curve, efficiency for addback (singles) mode. (b) Residuals. The data point at 7556 keV is not yet corrected for summing-in. It was excluded from the fit, and is shown here for illustration only. The pair of γ -rays at 5181 and 2375 keV was also not included in the fit but is plotted here as a check on the reliability of the curve.

under 55° angle. In order to obtain its stoichiometry, the stopping power at the resonance energy, the beam current and the strength of the monitor resonance must be known. For the stopping of protons in titanium and nitrogen, the values from the SRIM software [41] have been used. For the strength of the resonance, $\omega\gamma = 13.1 \pm 0.6$ meV was adopted, the recommended value from Ref. [27]. Based on this number, a stoichiometric ratio Ti:N of 1:0.93 has been determined. The target stoichiometry gives rise to 6% systematic uncertainty in the absolute cross section results, mainly from the reference $\omega\gamma$ value.

In order to properly correct for the change of the target under intense proton bombardment, during the experiment the target profile was monitored every day by scanning the $E_p = 278$ keV resonance (fig. 3). The sharp low-energy edge of the profile is given by the convolution of the 0.1 keV energy spread of the beam [29] and the 1.06 keV natural width of the resonance [42]. On the ensuing constant plateau, the step height is proportional to the inverse of the effective stopping power per ^{14}N nucleus in the compound.

A reduction of up to 7% in the integral of the target profile was observed from day to day, with a typical proton dose of 24 C ($1.5 \cdot 10^{20}$ H^+ ions) deposited on the target per day. It is estimated that the target composition is known with 5% precision for any given time during the experiment.

C. Detection of emitted γ -rays

The γ -rays emitted from the target were detected in a Eurisys Clover-BGO detection system [43] placed at an angle of 55° with respect to the beam axis. The front end of the Clover detectors was at 9.5 cm distance from the target. For the branching-ratio measurement (sec. III D), the front end was placed at 19.5 cm distance from the target instead.

The output signal from each of the four Clover crystals was split into two branches called branch 'S' and branch 'A'. For branch 'S', each of the four signals was amplified and digitized separately, and the four spectra were gain-matched and summed in the offline analysis, giving the so-called singles mode.

For branch 'A', the preamplifier output signals were gain-matched and added in a homemade analog summing unit. The added signal was then amplified and digitized, giving the so-called addback mode spectra. Typical resolutions for addback (singles) mode were 9 keV (3.3 keV) at 1.3 MeV and 12 keV (6 keV) at 6.8 MeV. For experiments off the 259 keV resonance, the addback mode data were recorded in anticoincidence with the BGO escape-suppression shield to reduce the Compton background.

The γ -ray detection efficiency was measured using ^{137}Cs and ^{60}Co radioactive sources calibrated to 1.5% and 0.75% (1σ confidence range), respectively. The efficiency curve (fig. 4, upper panel) was then extended to high energy based on spectra recorded at the 259 keV $1/2^+$ resonance, using the known 1:1 γ -ray cascades for the excited states at 6172 and 6792 keV [42]. The γ -rays from the decay of this $1/2^+$ resonance are isotropic [42]. The angular correlations of 8-10% between primary and secondary γ -ray are experimentally well known [44]. They result in up to 0.4% correction on the efficiency curve, because they affect the summing-out correction. For the worst case, the 6792 keV γ -ray, the calculated summing-out correction is 3.6% in addback mode (1.1% in singles mode), with an assumed relative uncertainty of 20%. This result is consistent with a GEANT4 [45] simulation showing $(4.5 \pm 1.8)\%$ correction.

As a check on the quality of the efficiency curve, the experimental cascade ratio for the 5181 keV excited state (not used in the fit) was found to be reproduced within 1% statistics (fig. 4, lower panel), again assuming 1:1 γ -ray cascade ratio [42].

III. DATA ANALYSIS AND RESULTS

The first part of the analysis concentrated on the ratio of the cross sections for radiative proton capture to the ground state and the fourth excited state at 6792 keV in ^{15}O , determined with the detector at 9.5 cm distance from the target. These relative data have been reported previously in abbreviated form [25] and are discussed in details in sec. III A. Subsequently, also absolute cross section data for the four most important γ -transitions

are derived from the spectra. This analysis is performed both by classical peak integrals for the addback mode data (sec. III B), and by γ -line shape analysis for the singles mode data (sec. III C). Finally, by moving the detector to 19.5 cm distance from the target, more precise branching ratios for the decay of the 259 keV resonance are presented (sec. III D).

A. Ratio of the cross sections for capture to the ground state and the 6792 keV excited state in ^{15}O

For the relative analysis, the number of counts in the ground state capture peak at $E_\gamma \approx 7600$ keV is compared with the number of counts in the secondary γ -ray at 6792 keV (fig. 5). In such an analysis, only the relative uncertainty when extending the efficiency curve over this limited energy range contributes to the uncertainty of the ratio (0.8% effect).

The 6792 keV counting rate contains some on-resonant contribution. This is due to the 60 keV (full width at half maximum) thick target. When the beam slows down to the strong resonance at $E_p = 278$ keV, it still finds some TiN in the tail of the target. In order to correct for this effect, the primary γ -rays for capture to this level are analyzed, as well, and the 6792 keV counting rate is rescaled with the resonant/off-resonant ratio as obtained from the low-energy primaries (fig. 6). The reduction in 6792 keV counting rate by the escape-suppression shield contributes 1.2% to the final uncertainty, and the summing-out correction for this peak contributes 0.6%.

Based on these data, the ratio

$$R_{\text{GS}/6792}(E) = \frac{\sigma_{\text{GS}}(E)}{\sigma_{6792}(E)} \quad (2)$$

has been calculated (table I). The present data supersede the data published previously in abbreviated form [25], due to an upgraded background determination (fig. 6, blue dashed lines), described in section III B. The ratio depends only on the counting rates for the $E_\gamma \approx 7600$ keV ground state capture γ -ray, for the $E_\gamma = 6792$ keV γ -ray (corrected for resonant capture as described above), and on the ratio of the γ -detection efficiencies at $E_\gamma \approx 7600$ and 6792 keV. For the ground state capture γ -ray, a summing-in correction of up to 30% (4.3%) for addback (singles) mode was taken into account (table I, last column).

When computing $R_{\text{GS}/6792}(E)$, the current measurement and the target stoichiometry and profile cancel out, eliminating the major sources of uncertainty. Therefore, the relative analysis method allows to derive data with much better precision than for absolute data. The present relative data can then be rescaled with averaged data for the well-studied cross section for capture to the 6792 keV state, and uniquely precise data for capture to the ground state can be obtained.

The effective interaction energies have been determined for each γ -line with two methods: First, the cen-

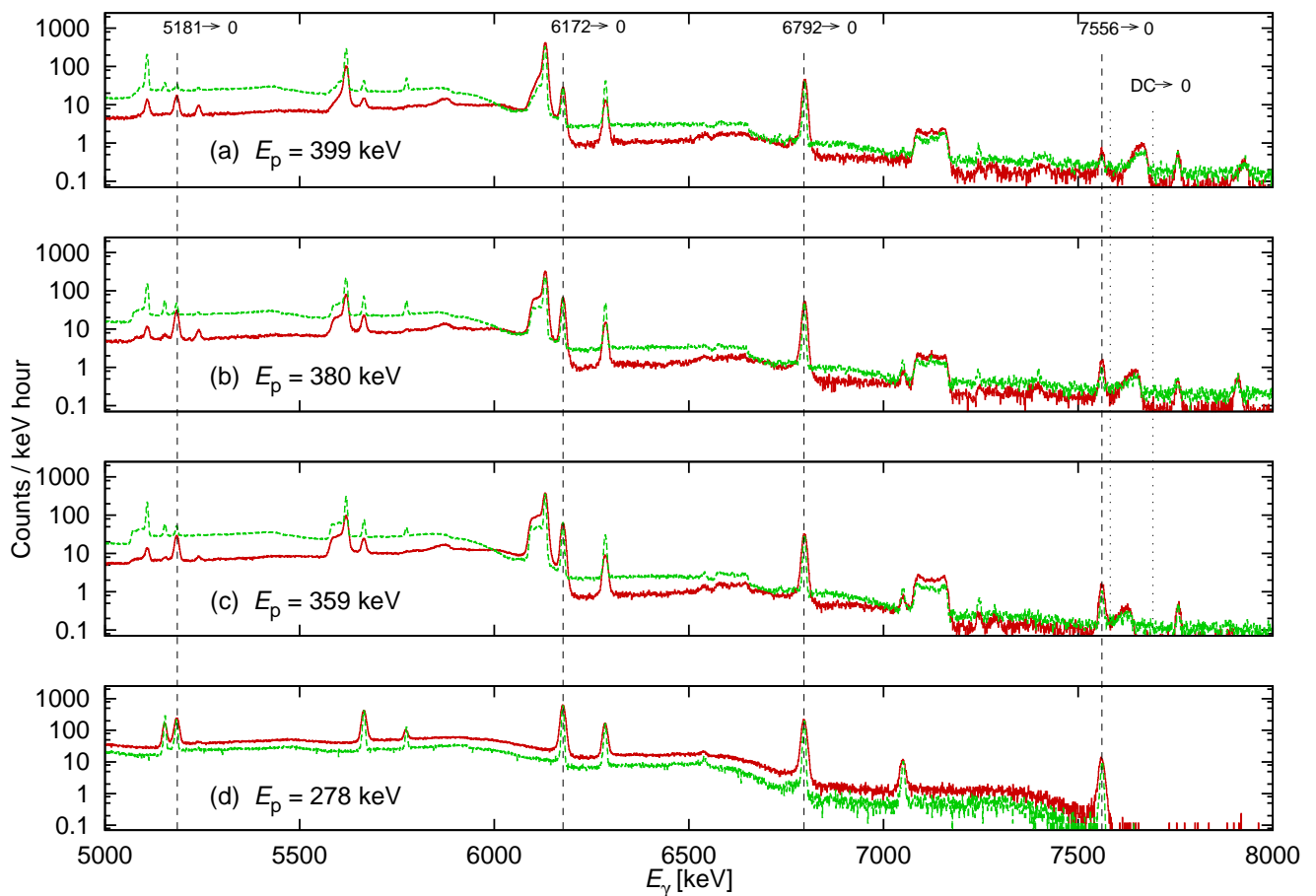


FIG. 5: (Color online) High-energy part of the γ -ray spectra for addback mode (red full line) and singles mode (green dashed line). (a)-(c): Off-resonant spectra at $E_p = 399, 380,$ and 359 keV, respectively, with the detector at 9.5 cm distance from the target. (d): On-resonance spectrum on the $E_p = 278$ keV resonance, with the detector at 19.5 cm distance from the target. The resonant contribution by the tail of the target is well visible also in the off-resonant spectra. The contaminant peaks stem from the $^{19}\text{F}(p,\alpha\gamma)^{16}\text{O}$ reaction.

TABLE I: Cross section ratio $R_{\text{GS}/6792}(E)$ and relative uncertainty. The size of the summing-in correction is also given. The present data supersede Ref. [25], due to an improved background determination.

E [keV]	mode	$R_{\text{GS}/6792}(E)$ [10^{-2}]	stat. uncertainty	syst. uncertainty	Summing-in correction
315.3 ± 1.3	addback	5.24	11%	5.4%	30%
	singles	5.22	15%	2.7%	4.3%
333.1 ± 1.0	addback	5.33	4.8%	3.9%	21%
	singles	5.58	11%	2.5%	3.4%
353.3 ± 1.0	addback	5.20	3.5%	3.5%	19%
	singles	5.43	8.0%	2.3%	3.2%

triod of the off-resonant primary γ -line has been used, taking into account the reaction Q -value and γ -level energies. Second, the average energy, weighted with the predicted counts from the known target profile and the expected energy dependence of the cross section from the

R-matrix S-factor curve [23]. The two values were never more than 2.6 keV apart, and their average was adopted for each line. The results are slightly different for ground state capture and capture to the 6792 keV state, because the S-factor curve from previous R-matrix fits has a different slope for these two transitions. Therefore, the average of the two values is adopted as effective energy to be connected with the cross section ratio $R_{\text{GS}/6792}(E)$, with the assigned 1σ error bar covering both effective energy values.

For the relative data, the total systematic uncertainty is $3.5 - 5.4\%$ in addback mode (table II). For singles mode, due to the lower summing corrections, it is $2.3 - 2.7\%$.

For all three data points, the addback and singles mode data are in good agreement. Due to the higher γ -efficiency of the addback mode data (which, in turn, is due to the well-known addback factor of Clover-type detectors [46], which has been redetermined for the present

detector and geometry [33]) and due to the background reduction achieved by the escape-suppression shield for the adback mode data, the adback data have much better statistics than the singles mode. Therefore, the adback data are adopted for the further analysis despite their slightly higher systematic uncertainty.

B. Absolute cross sections based on the peak integrals of the adback mode data

As a second step, the absolute cross section for capture to the excited states at 5181, 6172, and 6792 keV and to the ground state of ^{15}O has been derived, accepting that the systematic uncertainty (table II) includes now also the contributions from current measurement, target stoichiometry and profile, and absolute detection efficiency. Only the adback mode data were considered.

In order to obtain the net counting rate, a straight-line background based on two flat regions to the left and right of the region of interest (ROI) has been subtracted from the integral over the ROI. This procedure was applied for every secondary except for the decay of the 6172 keV excited state, where a different method was applied. It was repeated for each transition of the run at 399 keV, both for the primary (resonant and non-resonant) and secondary γ -rays.

However, in many cases it was not possible to apply this method of background determination: At $E_p = 359$ and 380 keV, the off-resonant part of the primaries lie close to the resonant peak (fig. 6, second and third row). The secondary at $E_\gamma \approx 6172$ keV was problematic, as well, due to the $^{19}\text{F}(p,\alpha\gamma)^{16}\text{O}$ background peak at $E_\gamma \approx 6130$ keV (fig. 5). For these spectra, a different method was instead used to estimate the background: The ratio between the difference in average counts per channel observed to the left and right of the peak, and the net area of the peak itself, was calculated. The ratios observed on the resonance, where no additional resonant contribution exists and where beam-induced background is negligible, have then been used to calculate the background at the same γ -energy in the problematic spectra. For those problematic spectra, a minimum uncertainty of 5% has been assumed for the quantity subtracted from the raw integral of the ROI. Finally, it was ensured that the 1σ uncertainty of the counts includes also results with different choices of background regions.

The net counting rate was then determined from the secondary γ -ray, rescaled for its non-resonant/resonant contributions determined by the primary γ -rays. Based on the counting rate, the target stoichiometry and profile (sec. II B, fig. 3), the beam current measurement, and the γ -detection efficiency (fig. 4), the cross section was calculated for these transitions. The angular distribution was assumed to exhibit negligible contributions from all Legendre polynomials except for zero and second order. The second order Legendre polynomial cancels out at the present detection angle of 55° .

TABLE II: Systematic uncertainties affecting cross section ratios ("relative", sec. III A) and absolute cross sections ("absolute", secs. III B and III C) for adback mode.

Affecting data...	Description	Amount
Relative Absolute	Summing-in, ground state line	3-5%
Relative Absolute	Escape-suppression efficiency	1.2%
Relative Absolute	Slope of γ -efficiency curve	0.8%
Relative Absolute	Summing-out	0.6%
Absolute	Target, original stoichiometry	6%
Absolute	Target, profile change	5%
Absolute	Assumption on S-factor slope	1-9%
Absolute	Beam current reproducibility	2%
Absolute	Normalization of γ -efficiency	1.8%
Relative	Total, adback mode	3.5-5.4%
Absolute	Total, adback mode	9-12%

For the determination of the astrophysical S-factor from a single data point, it is necessary to make some assumption on the relative shape of the S-factor curve. For the present analysis, the S-factor was assumed to vary over the target thickness as given by the previous LUNA R-matrix curve [23]. In order to check the uncertainty introduced by this assumption, the present analysis was repeated assuming a flat S-factor, and the full difference (1-9%, depending on the transition and beam energy) was adopted as systematic uncertainty. The effective interaction energy [47] was calculated based on the known target profile and the assumed S-factor behaviour. The uncertainties are half of the difference obtained by using a flat S-factor instead of the LUNA's curve [23].

C. Absolute cross sections based on the γ -line shape analysis of the singles mode data

Subsequently, the absolute cross section for capture to the excited states at 5181, 6172, and 6792 keV and to the ground state of ^{15}O has also been calculated based on the γ -line shape analysis approach. To this end, only the singles mode data, which are essentially free from summing corrections, have been used. This approach is thus complementary to the one described in the previous section, which calculated peak integrals and used only the adback mode data.

The γ -line shape analysis method has been described previously in details [21, 23, 29], so it will only be outlined here. The analysis of the line shape of the primary γ -ray is possible because the observed line shape of a primary transition is determined by the cross section behavior $\sigma(E)$ in the proton energy interval spanned by the incident beam during the slowing-down process in the target. Each center-of-mass beam energy E (at which the reaction takes place) corresponds to a γ -ray energy

$$E_\gamma = E + Q - E_x + \Delta E_{\text{Doppler}} - \Delta E_{\text{Recoil}}, \quad (3)$$

with Q the reaction Q -value, E_x the energy of the excited state, and $\Delta E_{\text{Doppler}/\text{Recoil}}$ the appropriate Doppler and

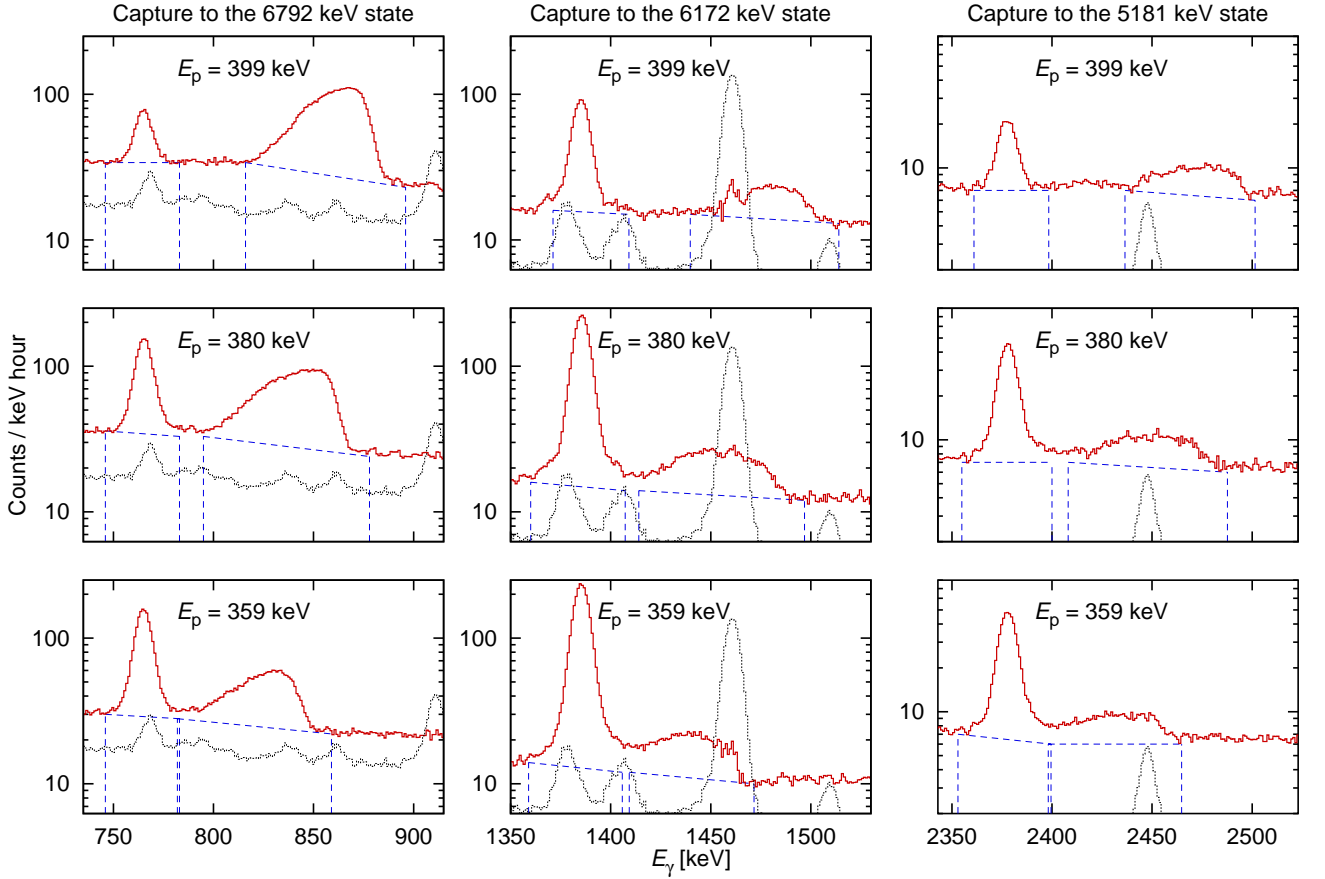


FIG. 6: (Color online) Low-energy part of the γ -ray spectra for addback mode (red full line), after subtraction of the laboratory background. For completeness, the laboratory background is also included (black dotted line). Rows from top to bottom: $E_p = 399, 380, 359$ keV. Columns from left to right: Primary γ -ray for capture to the excited state at 6792, 6172, 5181 keV. The peak from resonant capture (by the tail of the target) is clearly visible at the left of each panel. The non-resonant capture has a shape reflecting the profile of the target, convoluted with the energy-dependent cross section. The analysis of the 6172 primary (central column) is hampered by the strong ^{40}K laboratory background line; this is reflected in higher uncertainty for this transition. The regions of interest and the assumed background are shown by blue dashed lines.

recoil corrections. The γ -line shape is also influenced by the energy loss of the protons in the target, because the stopping power of the protons in titanium nitride is a function of proton energy [41].

The number of counts N_i in channel i of the γ -spectrum, corresponding to the energy bin $[E_{\gamma i}, E_{\gamma i} + \delta E_{\gamma}]$, where δE is the dispersion in units of keV per channel, is given by the expression

$$N_i = \frac{\sigma(E_i) \delta E_{\gamma} \eta_{fe}(E_{\gamma i}) b_k}{\varepsilon(E_i)} \quad (4)$$

for $E_i \leq E$. Here E_i is the center-of-mass proton energy corresponding to channel i , E is the incident proton energy in the center-of-mass, $\sigma(E_i)$ is the cross section under study, $\eta_{fe}(E_{\gamma, i})$ is the γ -ray detection efficiency, $\varepsilon(E_i)$ is the stopping power and b_k is the branching of the transition under study. The conversion from $E_{\gamma, i}$ to E_i includes the Doppler and recoil effects, as shown in eq. (3). The resulting count rate is folded with the known

energy resolution ΔE_{γ} of the γ -ray detector to obtain the experimental line-shape.

To facilitate the fit, the cross section $\sigma(E)$ entering into eq. (4) is then parameterized, in the limited energy window defined by the target thickness ΔE_{Target} , as the sum of a resonant term described by the Breit-Wigner formula, and a non-resonant term, for which a constant astrophysical S-factor S_{nr} is assumed:

$$\sigma(E_i) = \frac{\lambda^2 \omega \gamma}{\pi} \frac{\Gamma}{(E_i - E_R)^2 + (\Gamma/2)^2} + \frac{S_{\text{nr}} e^{-2\pi\eta}}{E_i} \quad (5)$$

Here, λ is the de Broglie wavelength, $\omega \gamma$ the strength value of the 259 keV resonance (here, 12.9 meV was used [23], very close to the recently recommended value of 13.1 meV [27]), E_R the energy of the resonance, Γ the energy-dependent total width of the resonance, and $e^{-2\pi\eta}$ is the Sommerfeld parameter. Since the branching ratios and the $\omega \gamma$ of the resonance are kept fixed, the free parameters in this procedure are the non-resonant

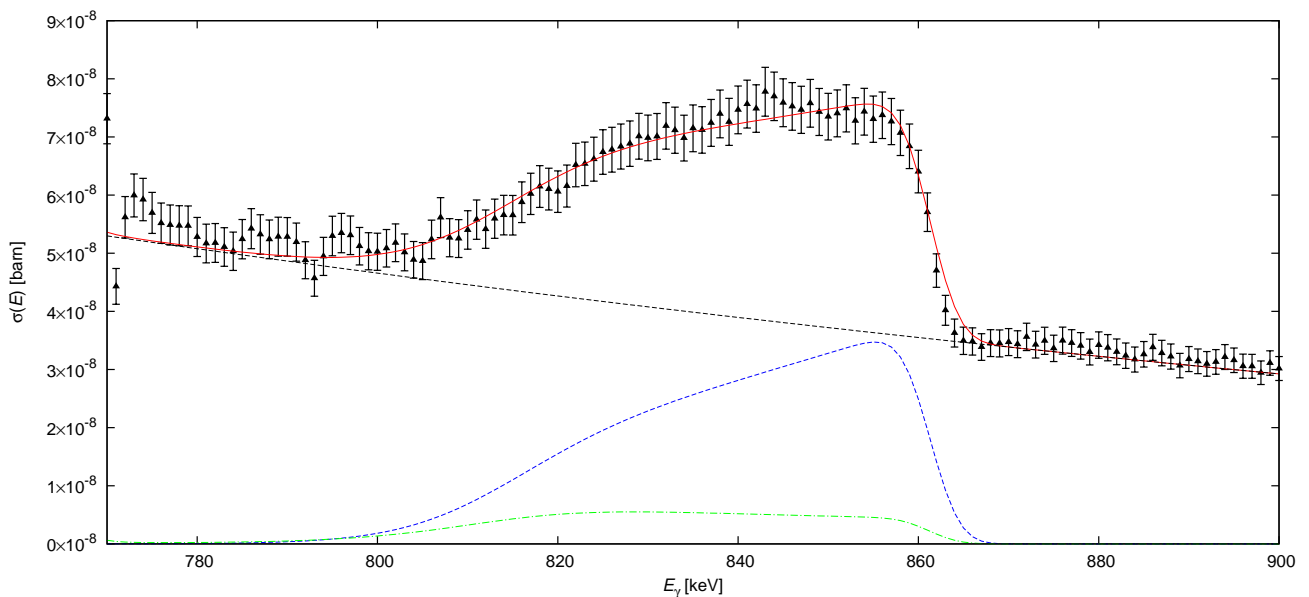


FIG. 7: (Color online) Typical γ -ray line shape obtained at $E_p = 380$ keV, in singles mode, for capture to the 6792 keV state. The dashed black line is the assumed background, fitted outside the peak area. The dash-dotted (green) line corresponds to the expected resonant contribution (first part of eq. (5)), and the dotted (blue) line to the fitted non resonant part (second part of eq. (5)). The solid (red) line is the sum of these two components and the background.

S-factor S_{nr} , the background parameters and the energy of the beam. They are fitted to best reflect the shape of the primary γ -line by reducing the χ^2 . After the fit has converged, the cross section σ under study here is given by the average of the $\sigma(E_i)$ values, weighted for their contribution to the total statistics.

Figure 7 shows a typical case for the primary γ -ray spectrum, together with the fit described above. The drop in the γ -ray yield towards lower energies reflects mainly the drop of the cross section due to the lower Coulomb barrier penetrability at lower energy. The energy of the high energy edge of the peak provides an independent cross-check on the assumed beam energy from the accelerator energy calibration [29]. Possible variations of the stoichiometry of the titanium nitride target during the beam bombardment have been monitored as described above (sec. II B and fig. 3).

The final astrophysical S-factor obtained from the line-shape analysis described in the present section was found to be in excellent agreement with the data from the peak-integral approach described in the previous section. It should be noted that while the present line-shape analysis is based on the singles mode spectra, the peak integral analysis is based on the addback mode data. The agreement between these two approaches confirms their reliability.

The final S-factor values from the present experiment are obtained by forming the simple average value of the two approaches (secs. III B and III C). The data are summarized in table III and plotted in fig. 8.

D. Branching ratios for the decay of the 259 keV resonance, obtained in far distance

In order to determine the branching ratios for the decay of the 259 keV $\frac{1}{2}^+$ resonance ($E_x = 7556$ keV in ^{15}O), the Clover detector was moved to a farther geometry, with its front face at 19.5 cm distance from the target position, again at an angle of 55° with respect to the beam direction. For the branching ratio analysis, both addback and singles mode data have been analyzed and were found to agree within their statistical uncertainty in all cases. In the following text, only the singles mode data will be discussed.

The detection efficiency was again established as described above (sec. II C), with an analogous quality of the efficiency curve as the one shown for the 9.5 cm geometry (fig. 4). It should be noted that the efficiency curve does not depend on the branching ratios, just on the assumption of 1:1 cascade ratios without feeding or intermediate decay corrections for the two transitions through the states at 6172 and 6792 keV, and on the assumption of isotropy [44].

For the determination of the decay branchings of the 259 keV resonance, only the secondary γ -rays at 5181, 5241, 6172, and 6792 keV and the ground state primary γ -ray at 7556 keV were used (fig. 5, bottom panel). Therefore only the relative γ -efficiency in the limited energy range 5181-7556 keV is needed. Owing to the good quality of the γ -efficiency curve, over this limited energy range the efficiencies relative to the 6172 keV normaliza-

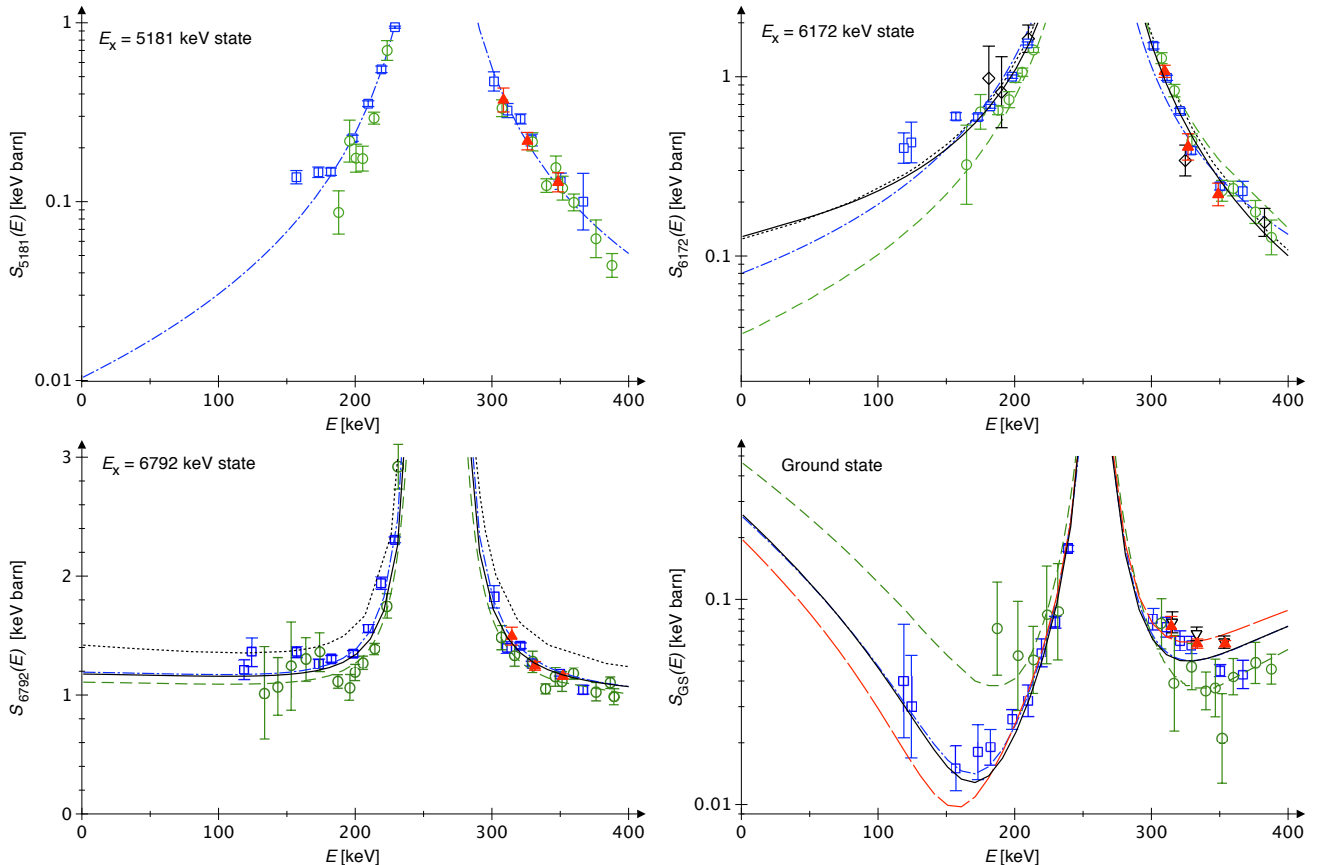


FIG. 8: (Color online) S-factor for capture to the excited states at 5181, 6172, and 6792 keV and to the ground state in ^{15}O . Data: Black diamonds [13], blue squares [21, 23], green circles [22], red full triangles (present work, average of secs. IIIB and IIIC). R-matrix fits: Black dotted curve [19], blue dash-dotted curve [21, 23], green dashed curve [22], black full curve [27], red long-dashed curve [25]. — For ground state capture, the black inverted triangles represent the present relative data (sec. III A), rescaled with the averaged S-factor for capture to the 6792 keV state as described in the text. For capture to the 5181 keV state, no R-matrix fits are given in Refs. [19, 22]. Error bars reflect the statistical uncertainty.

TABLE III: S-factor results for capture to the ground state and to the excited states at 5181, 6172, and 6792 keV. The effective energy E is given in keV, the S-factor S in keV barn, and the relative uncertainties for S in percent.

Capture to ground state				Capture to 5181 keV state				Capture to 6172 keV state				Capture to 6792 keV state			
E	S_{GS}	Δ_{stat}	Δ_{syst}	E	S_{5181}	Δ_{stat}	Δ_{syst}	E	S_{6172}	Δ_{stat}	Δ_{syst}	E	S_{6792}	Δ_{stat}	Δ_{syst}
314.6 ± 1.0	0.074	11%	12%	310.6 ± 2.2	0.370	16%	11%	310.5 ± 1.0	1.072	8%	12%	315.9 ± 1.3	1.495	5.0%	9%
333.6 ± 1.0	0.061	5%	11%	327.6 ± 1.6	0.218	12%	12%	326.6 ± 1.0	0.406	18%	12%	332.6 ± 1.0	1.245	3.0%	9%
353.9 ± 1.0	0.061	4%	10%	350.9 ± 2.5	0.128	13%	10%	351.1 ± 2.2	0.220	15%	10%	352.7 ± 1.0	1.157	1.7%	9%

tion point are known on the level of $\pm 0.5\%$, enabling a precise determination of the branching ratios.

For the major transitions through the excited states at 5181, 6172, and 6792 keV, the present branching ratios (tab. IV) are in excellent agreement with the modern literature [22, 23]. However, some minor discrepancies arise when it comes to the minor transitions.

The ground state transition has been the subject of discussion in recent years. It is now well-known that the previously accepted value of $(3.5 \pm 0.5)\%$ [12, 42, 48] was much too high, probably due to summing-in. The

two most recent previous branching ratio measurements [22, 23] were both performed at about 20 cm distance, where there is still more than 10% summing-in correction. The present value of $(1.49 \pm 0.04)\%$ has been obtained at 19.5 cm distance, with just 2.0% summing-in correction for the singles mode data, much less than in previous works. Note that the value $(1.53 \pm 0.06)\%$ from an abbreviated version of the present work [25] had been obtained in closer geometry, at 9.5 cm distance, with 7.4% summing-in correction. The present $(1.49 \pm 0.04)\%$ ground state branching supersedes all previous LUNA

TABLE IV: Branching ratios for the decay of the 259 keV resonance ($E_x = 7556$ keV in ^{15}O) obtained with the Clover detector in singles mode, at 19.5 cm distance from the target. The numbers are compared with previous data [22, 23, 42].

	Branching [%]			
	Ajzenberg-Selove [42]	TUNL [22]	LUNA [23]	LUNA, present work
7556 \rightarrow 0	3.5 \pm 0.5	1.70 \pm 0.07	1.6 \pm 0.1	1.49 \pm 0.04
\rightarrow 5181	15.8 \pm 0.6	17.3 \pm 0.2	17.1 \pm 0.2	17.3 \pm 0.2
\rightarrow 5241			0.6 \pm 0.3	0.15 \pm 0.03
\rightarrow 6172	57.5 \pm 0.4	58.3 \pm 0.5	57.8 \pm 0.3	58.3 \pm 0.4
\rightarrow 6792	23.2 \pm 0.6	22.7 \pm 0.3	22.9 \pm 0.3	22.6 \pm 0.3

branching ratio measurements of the 259 keV resonance, i.e. [23, 25].

For the transition to the 5241 keV state, the previous (0.6 \pm 0.3)% value [23] was possibly affected by feeding through higher-lying excited states. Based on the difference between 5241 \rightarrow 0 and 7556 \rightarrow 5241 γ -rays, this feeding contribution amounts to (0.20 \pm 0.10)% of the total decay branching. It is probably due to the 6859 keV state, which decays to 100% to the 5241 keV state [42]. However, such a weak feeding could possibly also arise through the 6172 or 6792 keV states, so in absence of conclusive evidence this (0.20 \pm 0.10)% is not assigned to any transition.

For the transition to the 5181 keV state, the present data confirms the slightly higher modern values [22, 23] with respect to the compilation [42].

IV. R-MATRIX ANALYSIS OF GROUND STATE CAPTURE

For the purpose of an R-matrix analysis, the present relative data (sec. III A, table I) have been renormalized using a weighted average S-factor for capture to the 6792 keV state. Based on these values and the corrected Schröder data [13, 21], a new R-matrix fit for ground state capture has already been presented in the abbreviated form of the present work [25]. The present updated relative data are close to the values published in abbreviated form [25], so this update does not warrant a revised fit.

Also the present absolute data (sec. III B) do not significantly deviate from the relative data, renormalized as stated above (fig. 8, bottom right panel). It should be noted that the present absolute data for capture to the 6792 keV state (fig. 8, bottom left panel) are in excellent agreement with previous data [22, 23] and R-matrix fits [22, 23], confirming that the renormalization procedure was adequate. By design the absolute data have higher uncertainty than the relative data (table II) that have already been included in the fit [25], so no new R-matrix fit is attempted here.

The previous fit [25] is instead shown again here (fig. 8, bottom right panel), leading to $S_{\text{GS}}(0) =$

0.20 \pm 0.05 keV barn. That value is lower than the recently recommended 0.27 \pm 0.05 keV barn [27], but still in agreement given the error bars. The difference is mainly due to the fact that in the present work, only the present and the Schröder [13] data (corrected for summing-in [21]) are included. The data from Refs. [22, 23] are excluded due to concerns about the summing corrections. In Ref. [27], instead, the data from Refs. [22, 23] have also been included in the fit.

V. SUMMARY AND OUTLOOK

The $^{14}\text{N}(p,\gamma)^{15}\text{O}$ reaction has been studied with a composite Clover-type detector at the LUNA underground facility at $E_p = 359, 380,$ and 399 keV, in an energy range important for future R-matrix fits of capture to the ground state in ^{15}O . Precise cross section ratios for ground state capture relative to capture to the 6792 keV state have been presented, updating and extending their previous abbreviated publication [25].

The present, precise relative cross section data (table I) helped resolve the discrepancy between the previous, conflicting extrapolations for ground state capture [21, 22], in favour of Ref. [21]. The present recommended value of $S_{\text{GS}}(0) = 0.20\pm 0.05$ keV barn is based on a dataset where the summing-in correction is not larger than 50% [13] for the high-energy data and not larger than 30% for the present, lower-energy data.

The present absolute cross sections for capture to the excited states at 5181, 6172, and 6792 keV (fig. 8, table III) have been obtained with two independent analysing methods (secs. III B and III C). They are generally in good agreement with previous works [22, 23] and in some cases more precise. They are in overall good agreement with the most recent R-matrix fit [27]. Because of their limited energy span, the present data alone cannot form the basis of new extrapolations. However, they may serve as useful reference points in an energy range that may be accessible not only at LUNA, but also at future underground accelerators.

The new branching ratios for the decay of the 259 keV resonance that are shown here improve the precision of the database for this resonance. Since this resonance is often used as normalization point for experimental work on the $^{14}\text{N}(p,\gamma)^{15}\text{O}$ reaction [21–23, 26, e.g.], this improved information again facilitates future precision studies of this reaction.

The present data are an important ingredient in updates of the standard solar model [5, 8, 9]. When experimental data for the flux of solar CNO neutrinos due to the β -decay of ^{13}N and ^{15}O become available from Borexino [6] or SNO+ [7], precise $^{14}\text{N}(p,\gamma)^{15}\text{O}$ cross sections may contribute to a direct measurement of the solar metallicity through a comparison of CNO and ^8B neutrino fluxes [5].

Possible next steps in improving the precision for the extrapolated S-factor of this reaction [27] are to re-study

the cross section at higher energies [26], in order to improve the extrapolation, and a remeasurement of the strength of the 259 keV resonance.

(K68801 and NN 83261), and DFG (BE4100/2-1 and RO439/41-1).

Acknowledgments

This work has been supported by INFN and in part by the EU (ILIAS-TA RII3-CT-2004-506222), OTKA

-
- [1] H. Bethe, Phys. Rev. **55**, 103 (1939).
 [2] C.-F. von Weizsäcker, Phys. Z. **39**, 633 (1938).
 [3] C. Iliadis, *Nuclear Physics of Stars* (Wiley-VCH, Weinheim, 2007).
 [4] J. N. Bahcall, A. M. Serenelli, and S. Basu, *Astrophys. J.* **621**, L85 (2005).
 [5] W. C. Haxton and A. M. Serenelli, *Astrophys. J.* **687**, 678 (2008).
 [6] C. Arpesella et al., Phys. Rev. Lett. **101**, 091302 (2008).
 [7] M. C. Chen, Nucl. Phys. B (Proc. Suppl.) **145**, 65 (2005).
 [8] C. Peña-Garay and A. Serenelli, ArXiv e-prints (2008), 0811.2424.
 [9] A. M. Serenelli, S. Basu, J. W. Ferguson, and M. Asplund, *Astrophys. J. Lett.* **705**, L123 (2009).
 [10] M. Asplund, N. Grevesse, A. J. Sauval, and P. Scott, *Ann. Rev. Astron. Astroph.* **47**, 481 (2009).
 [11] W. Lamb and R. Hester, Phys. Rev. **108**, 1304 (1957).
 [12] D. F. Hebbard and G. M. Bailey, Nucl. Phys. **49**, 666 (1963).
 [13] U. Schröder et al., Nucl. Phys. A **467**, 240 (1987).
 [14] G. Caughlan and W. Fowler, *At. Data Nucl. Data Tables* **40**, 283 (1988).
 [15] E. Adelberger et al., Rev. Mod. Phys. **70**, 1265 (1998).
 [16] C. Angulo et al., Nucl. Phys. A **656**, 3 (1999).
 [17] P. Bertone et al., Phys. Rev. Lett. **87**, 152501 (2001).
 [18] C. Angulo and P. Descouvemont, Nucl. Phys. A **690**, 755 (2001).
 [19] A. Mukhamedzhanov et al., Phys. Rev. C **67**, 065804 (2003).
 [20] K. Yamada et al., Phys. Lett. B **579**, 265 (2004).
 [21] A. Formicola et al., Phys. Lett. B **591**, 61 (2004).
 [22] R. C. Runkle et al., Phys. Rev. Lett. **94**, 082503 (2005).
 [23] G. Imbriani et al., Eur. Phys. J. A **25**, 455 (2005).
 [24] D. Schürmann, et al., Phys. Rev. C **77**, 055803 (2008).
 [25] M. Marta et al., Phys. Rev. C **78**, 022802(R) (2008).
 [26] M. Marta et al., Phys. Rev. C **81**, 055807 (2010).
 [27] E. Adelberger et al., Rev. Mod. Phys., in press (2010), 1004.2318.
 [28] F. Ajzenberg-Selove, Nucl. Phys. A **523**, 1 (1991).
 [29] A. Formicola et al., Nucl. Inst. Meth. A **507**, 609 (2003).
 [30] H. Costantini et al., Rep. Prog. Phys. **72**, 086301 (2009).
 [31] C. Broggini, D. Bemmerer, A. Guglielmetti, and R. Menegazzo, *Annu. Rev. Nucl. Part. Sci.* **60**, 53 (2010).
 [32] D. Bemmerer et al., Eur. Phys. J. A **24**, 313 (2005).
 [33] T. Szücs et al., Eur. Phys. J. A **44**, 513 (2010).
 [34] A. Cacioli et al., Eur. Phys. J. A **39**, 179 (2009).
 [35] R. Bonetti et al., Phys. Rev. Lett. **82**, 5205 (1999).
 [36] G. Imbriani et al., *Astron. Astrophys.* **420**, 625 (2004).
 [37] A. Lemut, D. Bemmerer, et al., Phys. Lett. B **634**, 483 (2006).
 [38] D. Bemmerer et al., Phys. Rev. Lett. **97**, 122502 (2006).
 [39] D. Bemmerer et al., J. Phys. G **36**, 045202 (2009).
 [40] B. Limata et al., Phys. Rev. C **82**, 015801 (2010).
 [41] J. Ziegler (2008), Software SRIM, URL <http://www.srim.org>.
 [42] F. Ajzenberg-Selove, Nucl. Phys. A **523**, 1 (1991).
 [43] Z. Elekes et al., Nucl. Inst. Meth. A **503**, 580 (2003).
 [44] B. Povh and D. F. Hebbard, Phys. Rev. **115**, 608 (1959).
 [45] S. Agostinelli et al., Nucl. Inst. Meth. A **506**, 250 (2003).
 [46] G. Duchêne et al., Nucl. Inst. Meth. A **432**, 90 (1999).
 [47] C. Rolfs and W. Rodney, *Cauldrons in the Cosmos* (University of Chicago Press, Chicago, 1988).
 [48] T. Tabata and K. Okano, J. Phys. Soc. Japan **15**, 1552 (1960).

Resonance strengths in the $^{14}\text{N}(p,\gamma)^{15}\text{O}$ and $^{15}\text{N}(p,\alpha\gamma)^{12}\text{C}$ reactions

Michele Marta,¹ Erik Trompler,¹ Daniel Bemmerer,¹ Roland Beyer,¹ Carlo Brogini,² Antonio Cacioli,² Martin Erhard,² Zsolt Fülöp,³ Eckart Grosse,¹ György Gyürky,³ Roland Hannaske,¹ Arnd R. Junghans,¹ Roberto Menegazzo,² Chithra Nair,¹ Ronald Schwengner,¹ Tamás Szücs,^{3,1} Simone Vezzú,⁴ Andreas Wagner,¹ and Dmitry Yakorev¹

¹*Forschungszentrum Dresden-Rossendorf (FZD), Dresden, Germany*

²*Istituto Nazionale di Fisica Nucleare (INFN), Sezione di Padova, Italy*

³*Institute of Nuclear Research (ATOMKI), Debrecen, Hungary*

⁴*Coordinamento Interuniversitario Veneto per le Nanotecnologie (CIVEN), Venice, Italy*

(Dated: As accepted by Phys.Rev. C, 28 May 2010)

The $^{14}\text{N}(p,\gamma)^{15}\text{O}$ reaction is the slowest reaction of the carbon-nitrogen-oxygen cycle of hydrogen burning in stars. As a consequence, it determines the rate of the cycle. The $^{15}\text{N}(p,\alpha\gamma)^{12}\text{C}$ reaction is frequently used in inverse kinematics for hydrogen depth profiling in materials. The $^{14}\text{N}(p,\gamma)^{15}\text{O}$ and $^{15}\text{N}(p,\alpha\gamma)^{12}\text{C}$ reactions have been studied simultaneously, using titanium nitride targets of natural isotopic composition and a proton beam. The strengths of the resonances at $E_p = 1058$ keV in $^{14}\text{N}(p,\gamma)^{15}\text{O}$ and at $E_p = 897$ and 430 keV in $^{15}\text{N}(p,\alpha\gamma)^{12}\text{C}$ have been determined with improved precision, relative to the well-known resonance at $E_p = 278$ keV in $^{14}\text{N}(p,\gamma)^{15}\text{O}$. The new recommended values are $\omega\gamma = 0.353 \pm 0.018$, 362 ± 20 , and 21.9 ± 1.0 eV for their respective strengths. In addition, the branching ratios for the decay of the $E_p = 1058$ keV resonance in $^{14}\text{N}(p,\gamma)^{15}\text{O}$ have been redetermined. The data reported here should facilitate future studies of off-resonant capture in the $^{14}\text{N}(p,\gamma)^{15}\text{O}$ reaction that are needed for an improved R-matrix extrapolation of the cross section. In addition, the data on the 430 keV resonance in $^{15}\text{N}(p,\alpha\gamma)^{12}\text{C}$ may be useful for hydrogen depth profiling.

PACS numbers: 25.40.Lw, 25.40.Ny, 26.20.Cd, 81.70.Jb

I. INTRODUCTION

The carbon-nitrogen-oxygen (CNO) cycle [1, 2] dominates stellar hydrogen burning for temperatures of 20–150 MK [3]. A quantitative understanding of its rate affects, for instance, the dredge-up of nucleosynthetic material to the surface of so-called carbon stars [4]. At lower temperatures, hydrogen burning is dominated by the proton-proton (pp) chain instead. In our Sun, the CNO cycle accounts for just 0.8% of energy production [5], but it provides an interesting neutrino signal.

The solar CNO neutrino flux is proportional to the abundance of carbon and nitrogen in the solar core [6]. This abundance is closely connected to the so-called solar composition problem: There are newly revised elemental abundance data for the solar atmosphere from an improved analysis of Fraunhofer absorption lines [7]. This new elemental composition, when fed into the accepted standard solar model, leads to predicted observables such as the sound speed and density profiles, the depth of the convective zone, and the abundance of helium on the surface [8–10], that are in disagreement with helioseismological data [11]. The solar composition problem might be solved if the elemental composition is different in the solar core than in the atmosphere.

Two key ingredients for a study of the carbon and nitrogen abundance in the solar core are already available: First, the experimental data on the flux of ^8B neutrinos from the Sun have reached a precision of 3% for the Super-Kamiokande I data [12], and the oscillation parameters for solar neutrinos have by now been well-

constrained, most notably by data from the SNO [13] and KamLAND [14] neutrino detectors. The flux of solar ^7Be neutrinos is under study in the Borexino detector and currently known with 10% precision [15], a number that is expected to improve in the near future. Second, the nuclear reaction cross sections involved in producing these neutrinos are rather well-known [16–20]. Therefore, the ^8B and ^7Be neutrinos can be used as a thermometer [6] to measure the temperature of the solar core (approximately 16 MK).

A third ingredient, the flux of CNO neutrinos from the β^+ decay of ^{13}N and ^{15}O , has not yet been measured online. However, it is believed that both Borexino and the planned SNO+ detector [21] can provide such data in the near future. A fourth ingredient are the nuclear reaction rates involved in the production of the CNO neutrinos. The rate of the reaction controlling the rate, $^{14}\text{N}(p,\gamma)^{15}\text{O}$, is currently known with only 8% precision [22], not enough to resolve the solar composition problem.

The $^{14}\text{N}(p,\gamma)^{15}\text{O}$ reaction proceeds through capture to a number of excited states and the ground state of ^{15}O (fig. 1, left panel). The last comprehensive study of this reaction covering a wide energy range goes back to the 1980's [25]. In more recent years, many of the results of Ref. [25] have come under renewed scrutiny. The γ -width of the subthreshold state at 6792 keV is now believed to be much lower than assumed in Ref. [25]. This conclusion was reached in Doppler shift attenuation experiments [26, 27], a Coulomb excitation study [28], and R-matrix fits [22, 29, 30]. The off-resonant capture

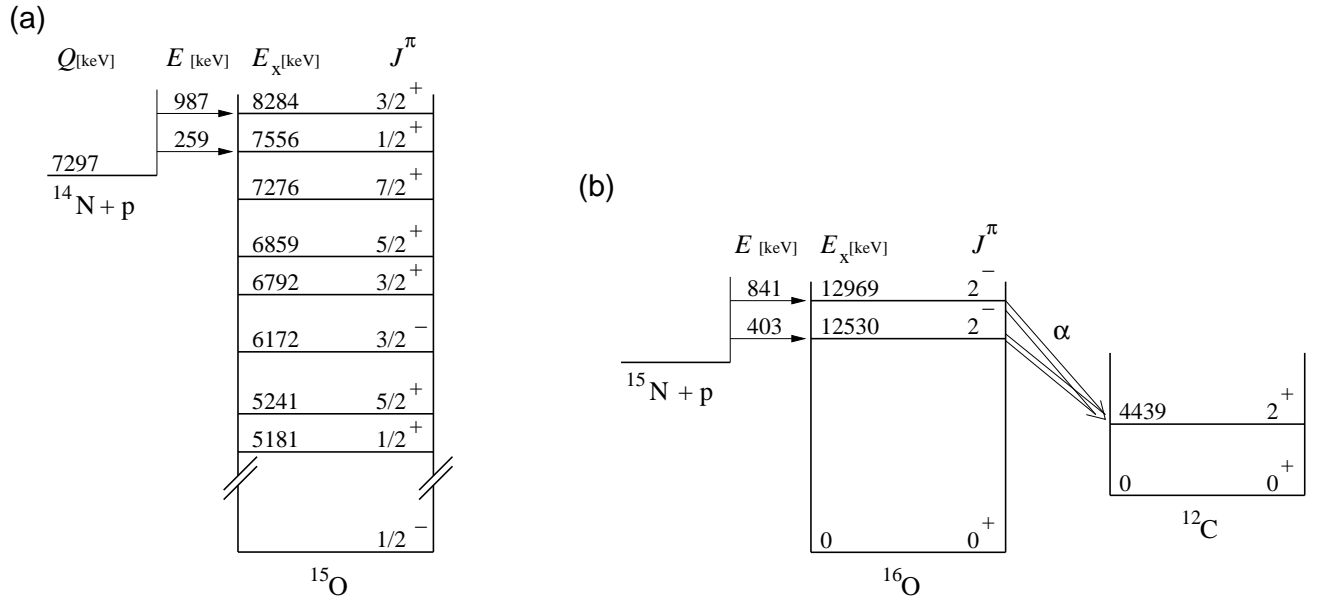


FIG. 1: (a) Level scheme of ^{15}O showing the first eight excited states (energies E_x and Q -value Q [23, 24] in keV) relevant to the $^{14}\text{N}(p,\gamma)^{15}\text{O}$ reaction. (b) Level scheme of the $^{15}\text{N}(p,\alpha\gamma)^{12}\text{C}$ reaction (Q -value 4965 keV).

cross-sections have also been re-investigated at energies¹ $70 \text{ keV} < E < 500 \text{ keV}$, in some cases significantly revising the Ref. [25] data [22, 24, 31–34]. An analyzing power study even questioned the transition mode for some decays of excited states [35]. In summary, the new recommended total cross section at astrophysical energies [22] is a factor two lower than previously believed [25], so the accepted reaction rate databases for astrophysical modeling [36–38] will have to be revised accordingly.

Despite all the efforts on the γ -width of the 6792 keV state and on low-energy cross sections, for higher energies $E \geq 500 \text{ keV}$ no experimental re-investigation of the $^{14}\text{N}(p,\gamma)^{15}\text{O}$ cross section has been performed since the 1980's. However, for this reaction also precise high-energy data play a role [29, 30] in extrapolating the cross section in the R-matrix framework to ultra-low astrophysical energies such as the solar Gamow peak at 28 keV.

The logical first step of a re-investigation of $^{14}\text{N}(p,\gamma)^{15}\text{O}$ at $E \geq 500 \text{ keV}$ is a renewed study of the sharp resonance at $E_p = 1058 \text{ keV}$. Due to the complicated R-matrix scheme with at least five poles and also direct capture contributions, its parameters cannot directly be transformed into formal R-matrix parameters. However, they can be used as outside constraints for an R-matrix fit, and as normalization points for off-resonant capture studies. The most precise available reference point for a study of this high-energy resonance is the low-energy $^{14}\text{N}(p,\gamma)^{15}\text{O}$ resonance at $E_p = 278 \text{ keV}$. Its

resonance strength

$$\omega\gamma = \frac{2J+1}{(2j_1+1)(2j_2+1)} \frac{\Gamma_1\Gamma_2}{\Gamma} \quad (1)$$

(with j_1, j_2, J the total angular momenta and Γ_i the widths) has been measured several times with consistent results [24, 32, 33, 39], and based on these works an averaged value of $\omega\gamma_{278} = 13.1 \pm 0.6 \text{ meV}$ has recently been recommended [40]. The resonance is very narrow [41], and the isotropy of its emitted γ -rays makes it also a convenient tool for a relative γ -efficiency calibration.

Two further reference points offer themselves, the resonances at $E_p = 430$ and 897 keV in the $^{15}\text{N}(p,\alpha\gamma)^{12}\text{C}$ reaction. For practical reasons, many ^{14}N targets contain also ^{15}N with its natural and exceptionally stable isotopic abundance of 0.3663%. The two $^{15}\text{N}(p,\alpha\gamma)^{12}\text{C}$ resonances are rather sharp and sufficiently strong to stand out despite the small isotopic abundance of ^{15}N . The resonance at $E_p = 430 \text{ keV}$ is frequently used for hydrogen depth profiling using 6.39 MeV ^{15}N ions [42, e.g.], with the 4.439 MeV γ -ray from the reaction being detected. Owing to this application, the total energetic width Γ of this resonance has been studied frequently [43–45]. However, its $\omega\gamma$ has so far been measured only once with precision better than 10% [46].

The aim of the present work is to provide precise values for the strengths of three resonances: The resonance at $E_p = 1058 \text{ keV}$ in $^{14}\text{N}(p,\gamma)^{15}\text{O}$ and the resonances at $E_p = 430$ and 897 keV in $^{15}\text{N}(p,\alpha\gamma)^{12}\text{C}$. In addition, the branching ratios of the decay of the $E_p = 1058 \text{ keV}$ resonance in $^{14}\text{N}(p,\gamma)^{15}\text{O}$ are re-studied. These three resonances may then serve as normalization points in a re-investigation of the $^{14}\text{N}(p,\gamma)^{15}\text{O}$ reaction for $E > 500 \text{ keV}$. In addition, improved absolute strength values

¹ In the following text, E_p denotes the proton energy in the laboratory system, E the center of mass energy.

for the $^{15}\text{N}(p,\alpha\gamma)^{12}\text{C}$ resonances will aid an absolute calibration of hydrogen depth profiling with ^{15}N beams.

II. EXPERIMENTAL SETUP

A. Ion beam, beam transport, and target chamber

The H^+ beam for the experiment was provided by the 3 MV Tandatron accelerator [47] at Forschungszentrum Dresden-Rossendorf (FZD). The beam reached the target chamber (fig. 2) after passing a switching magnet, an electrostatic quadrupole lens, electrostatic dipoles and a neutral particle trap. The neutral particle trap consisted of an electric dipole positioned 1 m upstream from the target, bending the beam by 7° . The neutral particles continued at 0° and were absorbed on the internal wall.

A copper collimator of 5 mm diameter was placed 45 cm upstream from the target. A 12 cm long copper pipe was inserted coaxial to the beam, at 5 mm distance from the target. The copper pipe was biased with -100 V to suppress secondary electrons from the target which might affect the electrical beam current reading. It is estimated that the electrical currents are accurate to $\pm 1.0\%$ in this Faraday cup. The vacuum measured at 40 cm distance from the target was typically $1 \cdot 10^{-7}$ mbar during the irradiations.

The beam intensity on the target ranged from 1-15 μA . The current on the collimator was always comparable in size to the target current, so no beam wobbling was necessary. The absolute proton beam energy E_p was calibrated based on the known energies of eight resonances in the $^{14}\text{N}(p,\gamma)^{15}\text{O}$, $^{15}\text{N}(p,\alpha\gamma)^{12}\text{C}$, and $^{27}\text{Al}(p,\gamma)^{28}\text{Si}$ reactions ranging in energy from $E_p = 278$ to 2047 keV. The observed beam energy spread was 1.1 keV (FWHM) at $E_p = 897$ keV.

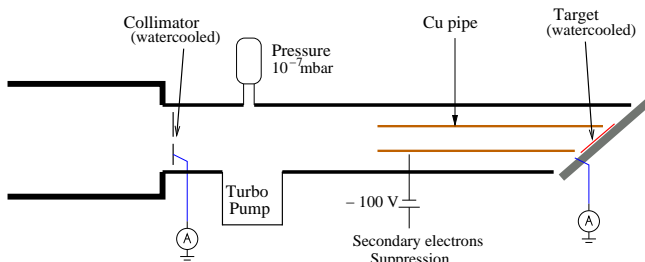


FIG. 2: (Color online) Schematic view of the target chamber (see text).

B. Targets

For the experiment, titanium nitride targets have been used. They were produced with the reactive sputtering technique at the CIVEN facility in Venice/Italy, using

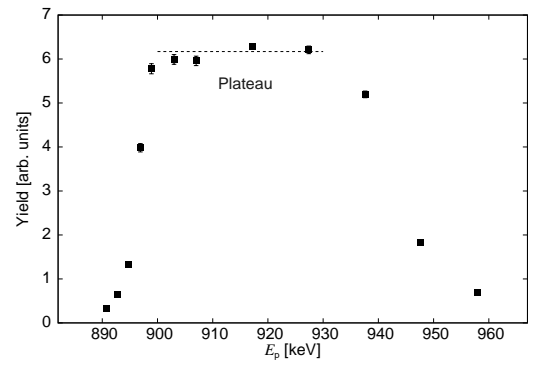


FIG. 3: Depth profile of nitrogen content in the target, obtained by scanning the $^{15}\text{N}(p,\alpha\gamma)^{12}\text{C}$ resonance at $E_p = 897$ keV for a virgin target. Plotted is the yield of the 4.44 MeV γ -ray versus proton energy (squares) and average yield in the plateau region (dashed line).

nitrogen gas of natural isotopic abundance. This technique usually leads to highly stable targets with stoichiometry close to Ti_1N_1 . The abundance of ^{15}N in the nitrogen contained in atmospheric air, $(0.3663 \pm 0.0004)\%$ [48], has been found to be exceedingly stable [49], so it is even defined as the abundance standard by the International Union of Pure and Applied Chemistry [48]. In a recent study using commercial nitrogen tank gas of natural abundance, the $^{15}\text{N}/^{14}\text{N}$ ratio was checked by mass spectrometry and found to be consistent with the natural abundance [50]. For the purpose of the present work, the standard isotopic abundance [48] is assumed to hold with 1.0% uncertainty [51]. Any effects of target degradation under the ion beam are expected to derive from atomic processes with negligible isotopic effects, so it is assumed here that the relevant behavior of the ^{15}N atoms tracks that of the ^{14}N atoms. Consequently, the same targets could be used for a parallel study of proton capture on ^{14}N and ^{15}N .

Four different samples have been used, all consisting of a $200 \mu\text{g}/\text{cm}^2$ thick layer of TiN on a 0.22 mm thick tantalum backing. The targets were placed tilted by 55° with respect to the beam axis and were directly water-cooled.

The nitrogen content of the targets and its distribution have been checked at regular intervals by scanning the $^{15}\text{N}(p,\alpha\gamma)^{12}\text{C}$ resonance at $E_p = 897$ keV (width $\Gamma_{\text{lab}} = 1.57$ keV [52], slightly larger than the observed beam energy spread), recording the yield of the 4.44 MeV γ -ray from the decay of the first excited state of ^{12}C . The targets showed a rectangular depth profile (fig. 3), with an energetic width of typically 50 keV at $E_p = 897$ keV and at 55° . The observed high-energy tail of the target is consistent with the expected 13 keV energy straggling at the target end. The plateau of this resonance scan was allowed to decrease by up to 15% under irradiation, then the target was replaced.

C. Detection of emitted photons

The γ -ray detection system consisted of four high-purity germanium (HPGe) detectors (fig. 4). Three 100% (relative efficiency) HPGe detectors with bismuth germanate (BGO) escape-suppression shield (surrounded by a 2 cm thick lead shield) and a 10 cm frontal lead shield with a cone-shaped opening of 3-5 cm diameter were used: Two were placed horizontally at 127° (left and right) relative to the beam direction, with front faces at 32 cm from the target (hereafter called *Det1* and *Det3*). The third was placed at 90° directly above the target, at 28 cm distance (*Det2*). These three detectors are also used in the nuclear resonance fluorescence (NRF) setup [53] at the ELBE accelerator. Care was taken so that their shielding and position with respect to the target reproduced the conditions in the NRF setup to ± 0.5 cm.

A fourth smaller HPGe detector (*Det4*, 60% rel. eff., no escape-suppression, surrounded by a 1 cm thick lead shield) was placed at 4 cm distance from the target, at downwards angle 55° . This particular setup allowed to observe the emitted photons at three different angles, 55° , 90° , and 127° , and to check the reproducibility for one angle, owing to the two detectors at $\pm 127^\circ$. The second order Legendre polynomial approximately vanishes for angles 55° and 127° , so that angular correlation effects are diluted at these angles.

The γ -detection efficiencies of the detectors have been measured at low energy (from 662 to 1836 keV) by means of calibrated radioactive sources (^{137}Cs , ^{60}Co , ^{88}Y from Physikalisch-Technische Bundesanstalt, quoted 2σ relative activity uncertainty 0.8-1.2%). The efficiency curve was then extended to higher energy (fig. 5) by means of resonant nuclear reaction γ -cascades of known ratios and angular distributions [54]. The resonances in $^{11}\text{B}(p,\gamma)^{12}\text{C}$ at $E_p = 675$ keV [55], $^{27}\text{Al}(p,\gamma)^{28}\text{Si}$ at $E_p = 992$ keV [56] and $^{14}\text{N}(p,\gamma)^{15}\text{O}$ at $E_p = 278$ keV [22] were used for this purpose. For the following analysis, ratios of yields of two high-energy γ -rays from the same detector have been used. Therefore only γ -efficiency ratios and not absolute efficiency values were needed.

III. EXPERIMENTAL PROCEDURE

A. 278 and 1058 keV resonances in $^{14}\text{N}(p,\gamma)^{15}\text{O}$

The $^{14}\text{N}(p,\gamma)^{15}\text{O}$ reaction proceeds through radiative capture into one of the states of ^{15}O (fig. 1, left panel). Non-radiative transitions are negligible. True coincidence summing effects amount to $\leq 3\%$ ($\leq 0.5\%$ uncertainty) in *Det4* and have been corrected for analytically; they are negligible in the other detectors. Two sharp resonances in the energy range relevant for R-matrix fits have been studied here, at $E_p = 278$ and 1058 keV (corresponding to $E = 259$ and 987 keV, fig. 1, left panel). The proper proton energy for the on-resonance run (fig. 6) has been chosen based on a scan of the resonance profile, in order

to be sure to completely cover its energetic width with the target thickness.

The angular distribution of the $1/2^+$ resonance at $E_p = 278$ keV is expected to be isotropic [23, 25]. This assumption was experimentally verified here (fig 7, left panel) for transitions through the 6172 keV state. The present precision is limited by statistics, because the beam intensity of the 3 MV Tandetron was only $1 \mu\text{A}$ at these low energies. Also the other transitions are found to be isotropic, but within somewhat higher statistical uncertainty. For the present purposes, all γ -rays from the decay of this resonance are assumed to exhibit isotropy. Combining the data from all four detectors and all transitions, 1.3% is reached for the statistical uncertainty of the yield of this reference resonance.

For the $E_p = 1058$ keV resonance, the width was determined here to be $\Gamma_{\text{lab}} = 3.8 \pm 0.5$ keV, in good agreement with the literature [23]. The proton beam energy chosen for the strength determination was 16 keV above the resonance energy. Off-resonance runs were performed well below and above the resonance, in order to determine and subtract the contribution given by non-resonant capture. The subtraction amounted to $\approx 100\%$ for the $6792 \rightarrow 0$ transition, which proceeds only through the non-resonant mechanism at these energies, and less than 6% for the $5241 \rightarrow 0$ and $8284 \rightarrow 0$ transitions. The angular distribution was checked for the two most intense transitions, i.e. the decay of the 5241 keV and of the 8284 keV excited state to the ground state. They were found to be compatible with isotropy within statistics (fig. 7, right panel). For the analysis, isotropy has been assumed and 3% has been adopted as the uncertainty for the angular distribution.

B. 430 and 897 keV resonances in $^{15}\text{N}(p,\alpha\gamma)^{12}\text{C}$

Resonant capture in $^{15}\text{N}(p,\alpha\gamma)^{12}\text{C}$ proceeds via (1) formation of the compound nucleus ^{16}O and (2) emission of an α particle and a $^{12}\text{C}^*(4439)$ excited nucleus, which then (3) decays to the ground state by emitting a photon (fig. 1, right panel). The $E_\gamma = 4439$ keV peak is affected by Doppler broadening, with an observed γ -peak width in *Det4* of 53 keV for the 430 keV resonance and 64 keV for the 897 keV resonance.

The angular distributions of the 4439 keV γ -rays at the two resonances in $^{15}\text{N}(p,\alpha\gamma)^{12}\text{C}$ are strongly anisotropic but well-known from experiment [57]. The pattern (fig. 8) is similar for both resonances due to the same spin and parity of the excited levels in ^{16}O and ^{12}C . The present data are in fair agreement with the literature (fig. 8). For the further analysis, the literature angular distribution has been assumed to be correct. In order to make the angular data comparable, for the close-distance *Det4* non-negligible attenuation coefficients $Q_{2,4}$ calculated based on the prescription given by Ref. [58] were taken into account (table I). These coefficients are consistent with unity for the far-distance detectors *Det1,2,3*.

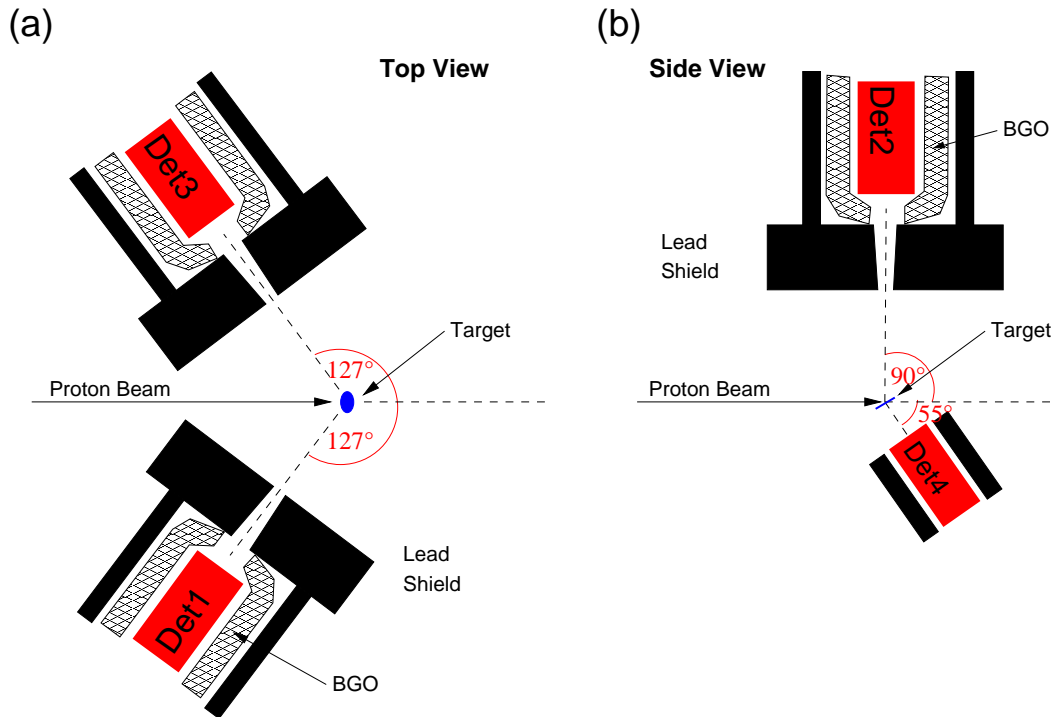


FIG. 4: (Color online) Scheme of the γ -ray detection setup. Panel (a) shows the two 100% HPGe detectors (*Det1* and *Det3*) at $\pm 127^\circ$ (left and right). Panel (b) shows one 100% HPGe detector (*Det2*) at 90° above the target and a 60% HPGe detector (*Det4*) at 55° below the target.

TABLE I: Experimental yield ratio 430/897 of the two $^{15}\text{N}(p,\alpha\gamma)^{12}\text{C}$ resonances at different angles: Uncorrected value (column 8), and value that was corrected for angular effects (column 9). The attenuation factors $Q_{2,4}$ calculated following Ref. [58] and the literature angular distribution coefficients $W_i(\theta)$ [57] are also given (columns 4-5 and 6-7, respectively).

Detector	θ	d [cm]	Calculated		Literature [57]		Uncorrected exp. yield ratio 430/897	Corrected
			Q_2	Q_4	$W_{430}(\theta)$	$W_{897}(\theta)$		
<i>Det1</i> [present]	-127°	32	$1.00^{+0.00}_{-0.01}$	$1.00^{+0.00}_{-0.01}$	0.69 ± 0.01	0.85 ± 0.01	0.071 ± 0.002	0.087 ± 0.004
<i>Det2</i> [present]	90°	28	$1.00^{+0.00}_{-0.01}$	$1.00^{+0.00}_{-0.01}$	1.11 ± 0.02	1.02 ± 0.02	0.100 ± 0.003	0.091 ± 0.004
<i>Det3</i> [present]	127°	32	$1.00^{+0.00}_{-0.01}$	$1.00^{+0.00}_{-0.01}$	0.69 ± 0.01	0.85 ± 0.01	0.070 ± 0.002	0.086 ± 0.004
<i>Det4</i> [present]	55°	4	0.70 ± 0.05	0.25 ± 0.09	0.92 ± 0.03	0.96 ± 0.01	0.076 ± 0.001	0.079 ± 0.003
<i>Det4'</i> [59]	0°	10	0.94 ± 0.02	0.80 ± 0.04	1.98 ± 0.05	1.57 ± 0.05	0.106 ± 0.001	0.084 ± 0.004

As a reliability check, the ratio 430/897 of the yields of the 4439 keV γ -peak for two consecutive runs on the two different resonances was calculated for all detectors (table I). The same ratio has also been calculated for a similar experiment [59] with targets enriched in ^{15}N and *Det4'* placed at 0° , where the anisotropy is very pronounced, and 10 cm distance (table I, last line). The yield ratio depends only on the effective detection angle of the device, hence the angular distribution and its attenuation. After correcting for these two effects, the values for the yield ratio are consistent (table I).

IV. DATA ANALYSIS AND RESULTS

A. Branching ratios for the decay of 1058 keV resonance in $^{14}\text{N}(p,\gamma)^{15}\text{O}$

The branching ratios for the decay of the $E_p = 1058$ keV resonance have been measured using the high-statistics spectra of *Det4* (table II), with the off-resonant contribution subtracted based on reference runs below and above the resonance. Since *Det4* is located at 55° where the second order Legendre polynomial vanishes, angular corrections have been neglected for all transitions. For the two strongest transitions, this assumption was verified experimentally (sec. III A). The branching ratios were determined also for some of the weaker transitions. The branching ratios in the standard compilation

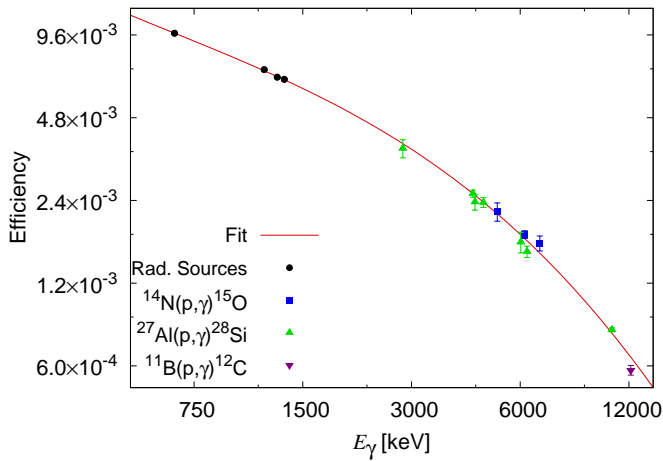


FIG. 5: (Color online) Data and parameterization of the full-energy peak γ -detection efficiency of *Det4*.

[23] are based on one work [60]. The only exception is the weak $8284 \rightarrow 5181$ branch reported by Ref. [25], which was adopted, leading to a recalculation of the other branches [23].

For the two strongest transitions, $8284 \rightarrow 0$ and $8284 \rightarrow 5241$, the present branchings are in agreement with Ref. [25], but not with Ref. [60]. The present data show the $8284 \rightarrow 5241$ transition to be stronger than reported in Ref. [60]. In that work [60], a sodium iodide scintillating detector had been used that was surrounded with a large Compton-suppressing guard detector. It is conceivable that the guard efficiency correction applied in Ref. [60] might have been different for the single $8284 \rightarrow 0$ γ -ray than for the γ -rays of the $8284 \rightarrow 5241 \rightarrow 0$ cascade, leading to some systematic uncertainty. The present values for the weaker transitions $8284 \rightarrow 6859$, $8284 \rightarrow 6172$, and $8284 \rightarrow 5181$ are in good agreement with the literature [25, 60] but show generally lesser precision.

Due to the significant differences observed in the strongest two branches, new recommended values are necessary for future calibration purposes. For $8284 \rightarrow 0$ and $8284 \rightarrow 5241$, the outlying values by Ref. [60] are omitted and a weighted average of Ref. [25] and the present data is formed. For the other three transitions, a weighted average of Refs. [25, 60] and the present data is adopted (table II).

B. Relative resonance strengths

The total width of the three resonances under study here is small compared to the energy loss in the present targets (table III). Therefore, the classical definition of the thick target yield [3] is applicable:

$$Y_{\infty}^i = \frac{\lambda^2}{2} \beta^i \frac{\omega\gamma}{\epsilon}; \quad Y_{\infty} = \frac{\sum_i Y_{\infty}^i}{\sum_i \beta^i} = \frac{\lambda^2}{2} \frac{\omega\gamma}{\epsilon} \quad (2)$$

where Y_{∞}^i is the experimental yield for branch i with branching ratio β^i corrected for γ -efficiency and angular distribution, and λ is the de Broglie wavelength at the resonance energy. ϵ is the effective stopping power [3], i.e. the stopping power per nucleus taking part in the reaction under study. If the target of interest is ^{14}N , ϵ is given by:

$$\epsilon^{14}(E_p) = \epsilon_{\text{N}}(E_p) \left(1 + \frac{n_{^{15}\text{N}}}{n_{^{14}\text{N}}}\right) + \epsilon_{\text{Ti}}(E_p) \frac{n_{\text{Ti}}}{n_{^{14}\text{N}}} \quad (3)$$

and analogously for ^{15}N as target:

$$\epsilon^{15}(E_p) = \epsilon_{\text{N}}(E_p) \left(1 + \frac{n_{^{14}\text{N}}}{n_{^{15}\text{N}}}\right) + \epsilon_{\text{Ti}}(E_p) \frac{n_{\text{Ti}}}{n_{^{15}\text{N}}} = \frac{n_{^{14}\text{N}}}{n_{^{15}\text{N}}} \epsilon^{14}(E_p). \quad (4)$$

The isotopic abundance $n_{^{15}\text{N}}/n_{^{14}\text{N}}$ is always taken to be the standard value, 0.3663 / 99.6337 [48], with an uncertainty of 1.0% [51]. The ratio of resonance strengths for two different resonances at $E_p = n$ keV ($n \in \{430; 897; 1058\}$) and at $E_p = 278$ keV, the reference strength, is then given by:

$$\frac{\omega\gamma_n}{\omega\gamma_{278}} = \frac{Y_{\infty,n}}{Y_{\infty,278}} \frac{\lambda_{278}^2}{\lambda_n^2} \frac{\epsilon^a(n)}{\epsilon^{14}(278)}; \quad a \in \{14; 15\}. \quad (5)$$

The ratio of yields $Y_{\infty,n}/Y_{\infty,278}$ was taken from the weighted average of the ratios obtained for each of the four detectors, after checking that they were consistent. The ratio of effective stopping powers at different energies $\epsilon^a(n)/\epsilon^{14}(278)$ is only slightly dependent on the target stoichiometry $n_{\text{Ti}}/n_{^{14}\text{N}}$. The main uncertainty associated with stopping powers is their absolute scale and not the energy dependence beyond the Bragg peak [61], and only the energy dependence is needed here. The stoichiometric ratio varied for the worst case from $\text{Ti}_1\text{N}_{0.93}$ (virgin target) to $\text{Ti}_1\text{N}_{0.80}$ (after a H^+ dose of 0.97 Coulomb). Using the stopping powers from SRIM [62], this change affected $\epsilon^{14}(1058)/\epsilon^{14}(278)$ by just 0.1%. In order to include also theoretical uncertainties, 1.0% uncertainty is assumed for $\epsilon^a(n)/\epsilon^{14}(278)$.

The target deterioration under beam bombardment has been corrected for based on the change observed in the yield of the $E_p = 897$ keV resonance in $^{15}\text{N}(p,\alpha\gamma)^{12}\text{C}$ that was used for the regular target scans (fig. 3), leading to 0.9% uncertainty.

For calculating the reference yield of the $E_p = 278$ keV resonance, the yields of the three peaks corresponding to the decay of the $E_x = 6792$, 6172, and 5182 keV excited states of ^{15}O and their precisely known branching ratios [24] have been used. The strength of the $E_p = 1058$ keV resonance has been obtained based on the yields from the two strongest transitions, $5241 \rightarrow 0$ and $8284 \rightarrow 0$, and the presently measured branching ratios (sec. IV A, tab. II).

For the two resonances in $^{15}\text{N}(p,\alpha\gamma)^{12}\text{C}$, the broad γ -peak at 4439 keV was used to calculate the yield. Their strength ratio was found to be $\omega\gamma_{430}/\omega\gamma_{897} = (6.25 \pm 0.17) \cdot 10^{-2}$, in fair agreement with the literature value of $(5.8 \pm 0.2) \cdot 10^{-2}$. That value had been obtained with two detectors placed at 55° [63], neglecting angular

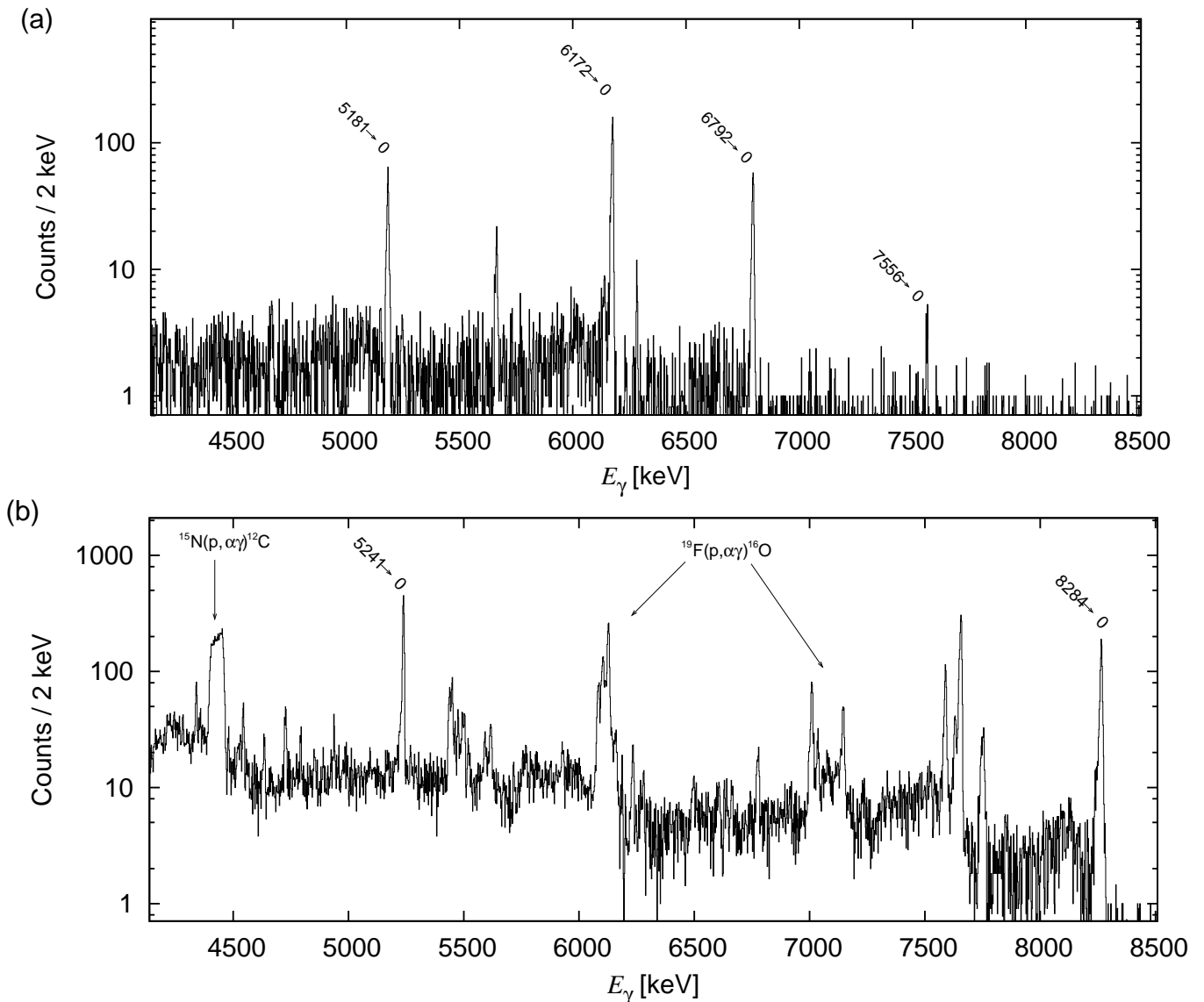


FIG. 6: γ -ray spectra of *Det1* acquired on the two resonances in the $^{14}\text{N}(p, \gamma)^{15}\text{O}$ reaction, at $E_p = 278$ keV (a) and $E_p = 1058$ keV (b). The transitions of interest for the reaction under study are marked with tilted tags. The most intense peaks of beam induced background from the $^{19}\text{F}(p, \alpha\gamma)^{16}\text{O}$ and $^{15}\text{N}(p, \alpha\gamma)^{12}\text{C}$ reaction are shown as well.

distribution effects and the resultant uncertainty. The present error bar includes these effects. Because of a target change, the ratio $\omega\gamma_{430}/\omega\gamma_{278}$ had to be calculated in two steps

$$\frac{\omega\gamma_{430}}{\omega\gamma_{278}} = \frac{\omega\gamma_{430}}{\omega\gamma_{897}} \frac{\omega\gamma_{897}}{\omega\gamma_{278}} \quad (6)$$

leading to slightly higher uncertainty. All the errors for the resonance strength ratios are summarized in table IV.

Using these strength ratios and the reference strength $\omega\gamma_{278} = 13.1 \pm 0.6$ meV [40], new absolute resonance strengths have been obtained for the three resonances under study (table III).

V. DISCUSSION

Near the 1058 keV resonance in $^{14}\text{N}(p, \gamma)^{15}\text{O}$, R-matrix fits for the strongest contribution, ground state capture, show a pronounced interference pattern [22, 29, 30]. Therefore, the shape of the excitation curve for this transition does not obey the ideal Breit-Wigner form. Since the present, rather thick target covers the entirety of the energy range directly affected by the resonance, the present strength value is unaffected by this fact. Still, it should be noted that due to the interference, the formal R-matrix parameters for this resonance are quite far from the experimental values. The present and more precise strength value can therefore not be used directly in an R-matrix code. However, in the future it can be compared

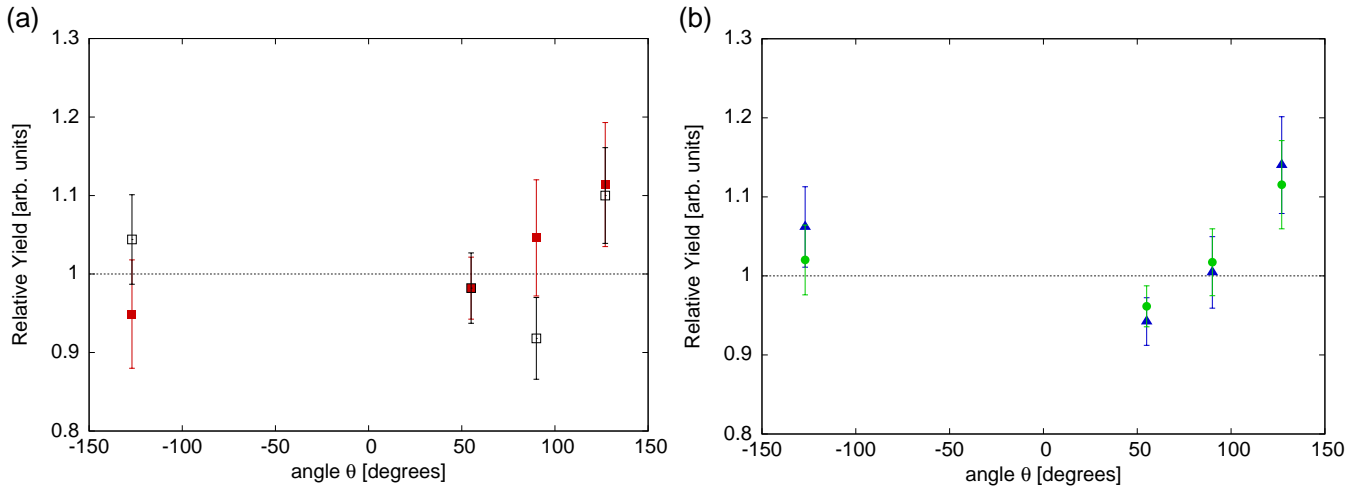


FIG. 7: (Color online) (a) Angular distribution of γ -rays of the $E_p = 278$ keV resonance in $^{14}\text{N}(p,\gamma)^{15}\text{O}$, obtained for $7556 \rightarrow 6172$ (red full squares) and $6172 \rightarrow 0$ (black empty squares) transitions. (b) The same for the $E_p = 1058$ keV resonance, $8284 \rightarrow 0$ (blue triangles) and $5241 \rightarrow 0$ (green circles) transitions.

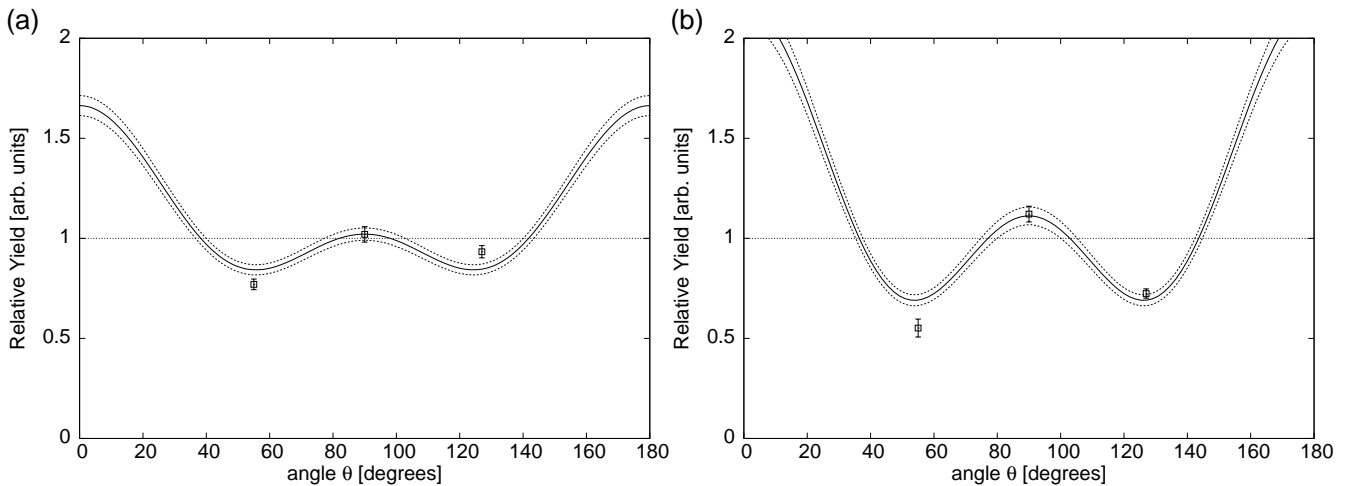


FIG. 8: Angular distribution of γ -rays emitted by $^{15}\text{N}(p,\alpha\gamma)^{12}\text{C}$ on the $E_p = 897$ keV (a) and 430 keV (b) resonances. The curves parameterize the literature experimental angular distribution [57], unfolded for attenuation. The data points are from the present experiment, again unfolded by the respective attenuation coefficients $Q_{2,4}$ (table I). The data of *Det1* (-127°) and *Det3* (127°) are consistent and have been averaged for this plot at 127° .

with the predicted strength from an updated R-matrix code with the proper resonance treatment [64, e.g.], as soon as such a code is publicly available.

For the other branches of the 1058 keV resonance and also for all the other resonances under study here, such an interference pattern either does not exist or is negligible when compared to the on-resonance capture.

The present strength value of the 1058 keV resonance in $^{14}\text{N}(p,\gamma)^{15}\text{O}$ is higher than the previous number [25], but still in agreement within the uncertainty. Therefore, a weighted average of the two numbers is formed and recommended for future use (table III).

Also for the 897 keV resonance in $^{15}\text{N}(p,\alpha\gamma)^{12}\text{C}$, the present value is higher than the literature [63]. That value [63] had been obtained just with two detectors

at 55° angle and neglecting angular distribution effects. However, the literature angular distribution [57] is lower than unity at 55° (fig. 8, also confirmed by the present data) so this assumption leads to a systematically low value. Consequently, the $\omega\gamma$ value from the present experiment is recommended for future use.

For the 430 keV resonance, the present strength, determined based on γ -spectroscopy, has the same precision as the literature value which had been obtained by α -spectroscopy instead [46]. That work [46] had used an α -detector at 30° and applied the α -particle angular distribution from a previous experiment and R-matrix fit [65]. Based on the two independent results from α -spectroscopy [46] and from γ -spectroscopy (present work), a weighted average for the strength is recom-

TABLE II: Branching ratios, in %, for the decay of the resonance at $E_p = 1058$ keV in $^{14}\text{N}(p,\gamma)^{15}\text{O}$ from the literature [25, 60], from the standard compilation [23] based on these papers, and from the present work. See text for a discussion of the new recommended values.

E_x [keV]	Ref. [60]	Ref. [25]	Compilation [23]	Present work	New recommended
6859	1.2 ± 0.3^a	1.2 ± 0.2	1.2 ± 0.3	1.2 ± 0.3	1.2 ± 0.2
6172	2.2 ± 0.6^a	2.6 ± 0.1	2.2 ± 0.6	1.7 ± 0.4	2.5 ± 0.1
5241	42.7 ± 0.5^a	46 ± 2	42.2 ± 0.5	45.4 ± 0.8	45.2 ± 0.7
5181		1.2 ± 0.1^a	1.2 ± 0.1	1.1 ± 0.6	1.2 ± 0.1
0	53.8 ± 0.25^a	49 ± 2	53.2 ± 0.25	50.5 ± 0.8	49.9 ± 0.7

^aAdopted in the compilation [23].

TABLE III: Relative and absolute resonance strength values $\omega\gamma$. The errors for the new absolute $\omega\gamma$ values include the uncertainty from the reference strength $\omega\gamma_{278}$. See the text for a discussion of the new recommended values.

Reaction	Literature [23, 52]		Present		Literature	New recommended
	E_p [keV]	Γ_{lab} [keV]	$\omega\gamma_n/\omega\gamma_{278}$	$\omega\gamma$ [eV]	$\omega\gamma$ [eV]	$\omega\gamma$ [eV]
$^{14}\text{N}(p,\gamma)^{15}\text{O}$	278	1.12^a	$\stackrel{\text{Def}}{=} 1$	—	0.0131 ± 0.0006^b	—
$^{14}\text{N}(p,\gamma)^{15}\text{O}$	1058	3.8^c	27.8 ± 0.9	0.364 ± 0.021	0.31 ± 0.04 [25]	0.353 ± 0.018
$^{15}\text{N}(p,\alpha\gamma)^{12}\text{C}$	430	0.1	$(1.73\pm 0.07)\cdot 10^3$	22.7 ± 1.4	21.1 ± 1.4 [46]	21.9 ± 1.0
$^{15}\text{N}(p,\alpha\gamma)^{12}\text{C}$	897	1.57	$(2.77\pm 0.09)\cdot 10^4$	362 ± 20	293 ± 38 [63]	362 ± 20

^aRef. [41].

^bWeighted average [40] of Refs. [24, 32, 33, 39].

^cLiterature: 3.9 ± 0.7 keV [23]. Present work: 3.8 ± 0.5 keV (sec. III A).

TABLE IV: Uncertainties affecting the resonance strength ratios $\omega\gamma_n/\omega\gamma_{\text{ref}}$. The 1058 and 897 keV resonances are referred to the 278 keV resonance, $\omega\gamma_{\text{ref}} = \omega\gamma_{278}$. The 429 keV resonance is referred to the 897 keV resonance, $\omega\gamma_{\text{ref}} = \omega\gamma_{897}$. Its uncertainty includes also the 1.0% from the isotopic abundance $n_{^{15}\text{N}}/n_{^{14}\text{N}}$.

	1058 keV	897 keV	430 keV
Counting statistics	1.7%	1.6%	1.0%
γ -efficiency (relative) [54]	0.7%	1.3%	
Decay branching ratio	1.2%	0.5%	
Angular distribution	1.8%	1.1%	1.9%
Stopping power ratio	1.0%	1.0%	1.0%
Isotopic abundance $n_{^{15}\text{N}}/n_{^{14}\text{N}}$		1.0%	
Target degradation $n_{^{14}\text{N}}/n_{\text{Tl}}$	0.9%	0.9%	0.8%
Beam intensity	1.0%	1.0%	1.0%
Final uncertainty of $\omega\gamma_n/\omega\gamma_{\text{ref}}$	3.3%	3.1%	2.7%
Reference strength $\omega\gamma_{\text{ref}}$	4.6%	4.6%	5.5%
Final uncertainty of $\omega\gamma_n$	5.7%	5.5%	6.1%

mended that has just 4% uncertainty (table III).

VI. SUMMARY AND OUTLOOK

The resonance strength $\omega\gamma$ has been measured for the 1058 keV resonance in $^{14}\text{N}(p,\gamma)^{15}\text{O}$ and the 430 and 897 keV resonances in $^{15}\text{N}(p,\alpha\gamma)^{12}\text{C}$, relative to the well-known strength of the 278 keV resonance in $^{14}\text{N}(p,\gamma)^{15}\text{O}$. A called-for improvement in the precision of this reference point [40] will therefore also lead to an improvement in

the understanding of the other three resonances.

For the major transitions, the angular distributions of the 278 and 1058 keV resonances in $^{14}\text{N}(p,\gamma)^{15}\text{O}$ have been verified experimentally to be consistent with the expected isotropy. The decay branching ratios of the 1058 keV resonance in $^{14}\text{N}(p,\gamma)^{15}\text{O}$ have been determined and updated values are recommended.

Three well-understood, sharp resonances are now available as natural normalization points for cross section measurements. The new, precise strength of the 430 keV resonance in $^{15}\text{N}(p,\alpha\gamma)^{12}\text{C}$ has the potential to serve as a highly precise standard value to make hydrogen depth profiling absolute. The road is paved for a re-measurement of the astrophysically important $^{14}\text{N}(p,\gamma)^{15}\text{O}$ off-resonance cross section at energies near 1 MeV.

Acknowledgments

The support by the staff and operators of the FZD ion beam center, technical support by Michael Fauth, Andreas Hartmann, and Manfred Sobiella (FZD), and target analyses performed by Alberto Vomiero (CNR Brescia, Italy) are gratefully acknowledged. This work was supported in part by the European Union, Research Infrastructures Transnational Access (RITA 025646) to the AIM facility, by DFG (BE4100/2-1), and by OTKA (T68801). T.S. acknowledges support from the Herbert Quandt Foundation.

-
- [1] C.-F. von Weizsäcker, *Phys. Z.* **39**, 633 (1938).
- [2] H. Bethe, *Phys. Rev.* **55**, 103 (1939).
- [3] C. Iliadis, *Nuclear Physics of Stars* (Wiley-VCH, 2007).
- [4] F. Herwig, S. M. Austin, and J. C. Lattanzio, *Phys. Rev. C* **73**, 025802 (2006).
- [5] J. N. Bahcall and M. H. Pinsonneault, *Phys. Rev. Lett.* **92**, 121301 (2004).
- [6] W. C. Haxton and A. M. Serenelli, *Astrophys. J.* **687**, 678 (2008).
- [7] M. Asplund, N. Grevesse, A. J. Sauval, and P. Scott, *Ann. Rev. Astron. Astroph.* **47**, 481 (2009), 0909.0948.
- [8] S. Turck-Chièze *et al.*, *Phys. Rev. Lett.* **93**, 211102 (2004), arXiv:astro-ph/0407176.
- [9] J. N. Bahcall, A. M. Serenelli, and S. Basu, *Astrophys. J. Suppl. Ser.* **165**, 400 (2006).
- [10] A. M. Serenelli, S. Basu, J. W. Ferguson, and M. Asplund, *Astrophys. J. Lett.* **705**, L123 (2009), 0909.2668.
- [11] S. Basu, W. J. Chaplin, Y. Elsworth, R. New, and A. M. Serenelli, *Astrophys. J.* **699**, 1403 (2009), 0905.0651.
- [12] J. Hosaka *et al.*, *Phys. Rev. D* **73**, 112001 (2006).
- [13] B. Aharmim *et al.*, *Phys. Rev. Lett.* **101**, 111301 (2008), 0806.0989.
- [14] S. Abe *et al.*, *Phys. Rev. Lett.* **100**, 221803 (2008), 0801.4589.
- [15] C. Arpesella *et al.*, *Phys. Rev. Lett.* **101**, 091302 (2008).
- [16] B.S. Nara Singh, M. Hass, Y. Nir-El, and G. Haquin, *Phys. Rev. Lett.* **93**, 262503 (2004).
- [17] D. Bemmerer *et al.*, *Phys. Rev. Lett.* **97**, 122502 (2006).
- [18] T. A. D. Brown *et al.*, *Phys. Rev. C* **76**, 055801 (2007), 0710.1279.
- [19] A. Di Leva *et al.*, *Phys. Rev. Lett.* **102**, 232502 (2009).
- [20] A. R. Junghans, K. A. Snover, E. C. Mohrmann, E. G. Adelberger, and L. Buchmann, *Phys. Rev. C* **81**, 012801(R) (2010).
- [21] M. C. Chen, *Nucl. Phys. B (Proc. Suppl.)* **145**, 65 (2005).
- [22] M. Marta *et al.*, *Phys. Rev. C* **78**, 022802(R) (2008).
- [23] F. Ajzenberg-Selove, *Nucl. Phys. A* **523**, 1 (1991).
- [24] G. Imbriani *et al.*, *Eur. Phys. J. A* **25**, 455 (2005).
- [25] U. Schröder *et al.*, *Nucl. Phys. A* **467**, 240 (1987).
- [26] P. Bertone *et al.*, *Phys. Rev. Lett.* **87**, 152501 (2001).
- [27] D. Schürmann *et al.*, *Phys. Rev. C* **77**, 055803 (2008).
- [28] K. Yamada *et al.*, *Phys. Lett. B* **579**, 265 (2004).
- [29] C. Angulo and P. Descouvemont, *Nucl. Phys. A* **690**, 755 (2001).
- [30] A. Mukhamedzhanov *et al.*, *Phys. Rev. C* **67**, 065804 (2003).
- [31] A. Formicola *et al.*, *Phys. Lett. B* **591**, 61 (2004).
- [32] R. C. Runkle *et al.*, *Phys. Rev. Lett.* **94**, 082503 (2005).
- [33] A. Lemut *et al.*, *Phys. Lett. B* **634**, 483 (2006).
- [34] D. Bemmerer *et al.*, *Nucl. Phys. A* **779**, 297 (2006).
- [35] S. O. Nelson *et al.*, *Phys. Rev. C* **68**, 065804 (2003).
- [36] G. Caughlan and W. Fowler, *At. Data Nucl. Data Tables* **40**, 283 (1988).
- [37] C. Angulo *et al.*, *Nucl. Phys. A* **656**, 3 (1999).
- [38] E. Adelberger *et al.*, *Rev. Mod. Phys.* **70**, 1265 (1998).
- [39] H. Becker, W. Kieser, C. Rolfs, H. Trautvetter, and M. Wiescher, *Z. Phys. A* **305**, 319 (1982).
- [40] E. Adelberger *et al.*, *Rev. Mod. Phys.*, submitted (2010), 1004.2318.
- [41] M. Borowski, K. P. Lieb, M. Uhrmacher, and W. Borse, Precision Measurements of the 278 keV $^{14}\text{N}(p,\gamma)$ and the 151 keV $^{18}\text{O}(p,\alpha)$ Resonance Parameters, in *AIP Conf. Proc. 1090: Capture Gamma-Ray Spectroscopy and Related Topics*, p. 450, 2009.
- [42] L. S. Wielunski *et al.*, *Nucl. Inst. Meth. B* **190**, 693 (2002).
- [43] B. Maurel and G. Amsel, *Nucl. Inst. Meth.* **218**, 159 (1983).
- [44] M. Zinke-Allmang, S. Kalbitzer, and M. Weiser, *Z. Phys. A* **320**, 697 (1985).
- [45] T. Osipowicz, K. P. Lieb, and S. Brüssermann, *Nucl. Inst. Meth. B* **18**, 232 (1987).
- [46] H. Becker *et al.*, *Z. Phys. A* **351**, 453 (1995).
- [47] M. Friedrich, W. Bürger, D. Henke, and S. Turuc, *Nucl. Inst. Meth. A* **382**, 357 (1996).
- [48] T. B. Coplen *et al.*, *Pure Appl. Chem.* **74**, 1987 (2002).
- [49] A. Mariotti, *Nature* **303**, 685 (1983).
- [50] D. Bemmerer *et al.*, *J. Phys. G* **36**, 045202 (2009).
- [51] G. Junk and H. Svec, *Geochim. Cosmochim. Acta* **14**, 234 (1958).
- [52] D. Tilley, H. Weller, and C. Cheves, *Nucl. Phys. A* **564**, 1 (1993).
- [53] R. Schwengner *et al.*, *Nucl. Inst. Meth. A* **555**, 211 (2005).
- [54] E. Trompler, Messung des Wirkungsquerschnitts astro-physikalisch relevanter Kernreaktionen, Master's thesis, Technische Universität Dresden, 2009, FZD Report FZD-523.
- [55] F. Zijderhand, F. P. Jansen, C. Alderliesten, and C. van der Leun, *Nucl. Inst. Meth. A* **286**, 490 (1990).
- [56] A. Anttila, J. Keinonen, M. Hautala, and I. Forsblom, *Nucl. Inst. Meth.* **147**, 501 (1977).
- [57] A. A. Kraus, A. P. French, W. A. Fowler, and C. C. Lauritsen, *Phys. Rev.* **89**, 299 (1953).
- [58] M. E. Rose, *Phys. Rev.* **91**, 610 (1953).
- [59] A. Cacioli, *Underground study of $^{15}\text{N}(p,\gamma)^{16}\text{O}$ at stellar energies*, PhD thesis, Università degli studi di Padova, 2010.
- [60] A. E. Evans, B. Brown, and J. B. Marion, *Phys. Rev.* **149**, 863 (1966).
- [61] J. F. Ziegler, J. P. Biersack, and M. D. Ziegler, *SRIM. The Stopping and Range of Ions in Matter* (SRIM Co., Chester, Maryland, 2008).
- [62] J. Ziegler, *SRIM version 2008.02*, <http://www.srim.org>, Software SRIM, 2008.
- [63] F. Zijderhand and C. van der Leun, *Nucl. Phys. A* **460**, 181 (1986).
- [64] R. Azuma *et al.*, *Phys. Rev. C* **81**, 045805 (2010).
- [65] R. A. Leavitt *et al.*, *Nucl. Phys. A* **410**, 93 (1983).

Direct measurement of the $^{15}\text{N}(p,\gamma)^{16}\text{O}$ total cross section at novae energies

D Bemmerer^{1‡}, A Cacioli^{2,3}, R Bonetti^{4§}, C Brogini²,
 F Confortola⁵, P Corvisiero⁵, H Costantini⁵, Z Elekes⁶,
 A Formicola⁷, Zs Fülöp⁶, G Gervino⁸, A Guglielmetti⁴,
 C Gustavino⁷, Gy Gyürky⁶, M Junker⁷, B Limata⁹, M Marta¹,
 R Menegazzo², P Prati⁵, V Roca⁹, C Rolfs¹⁰, C Rossi Alvarez²,
 E Somorjai⁶, and O Straniero¹¹
 (The LUNA collaboration)

¹ Forschungszentrum Dresden-Rossendorf, Dresden, Germany

² Istituto Nazionale di Fisica Nucleare (INFN), Sezione di Padova, Italy

³ Università di Padova, Padova, Italy

⁴ Istituto di Fisica Generale Applicata, Università di Milano and INFN Sezione di Milano, Italy

⁵ Università di Genova and INFN Sezione di Genova, Genova, Italy

⁶ Institute of Nuclear Research (ATOMKI), Debrecen, Hungary

⁷ INFN, Laboratori Nazionali del Gran Sasso (LNGS), Assergi (AQ), Italy

⁸ Dipartimento di Fisica Sperimentale, Università di Torino and INFN Sezione di Torino, Torino, Italy

⁹ Dipartimento di Scienze Fisiche, Università di Napoli "Federico II" and INFN Sezione di Napoli, Napoli, Italy

¹⁰ Institut für Experimentalphysik III, Ruhr-Universität Bochum, Germany

¹¹ Osservatorio Astronomico di Collurania, Teramo, and INFN Sezione di Napoli, Napoli, Italy

Abstract. The $^{15}\text{N}(p,\gamma)^{16}\text{O}$ reaction controls the passage of nucleosynthetic material from the first to the second carbon-nitrogen-oxygen (CNO) cycle. A direct measurement of the total $^{15}\text{N}(p,\gamma)^{16}\text{O}$ cross section at energies corresponding to hydrogen burning in novae is presented here. Data have been taken at 90 – 230 keV center-of-mass energy using a windowless gas target filled with nitrogen of natural isotopic composition and a bismuth germanate summing detector. The cross section is found to be a factor two lower than previously believed.

PACS numbers: 25.40.Ep, 26.20.+f, 26.30.+k

‡ e-mail: d.bemmerer@fzd.de

§ deceased

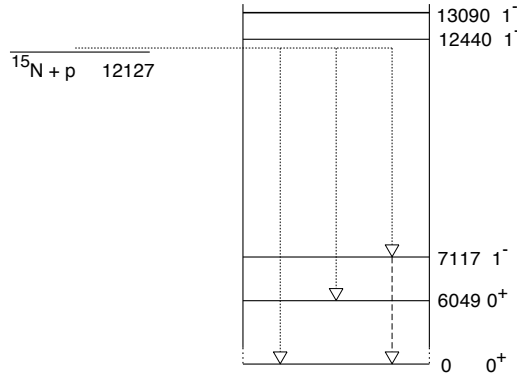


Figure 1. Energy levels of ^{16}O relevant to the $^{15}\text{N}(p,\gamma)^{16}\text{O}$ reaction at low energy, in keV [4]. Primary (dotted) and secondary γ -ray transitions are also shown.

1. Introduction

The $^{15}\text{N}(p,\gamma)^{16}\text{O}$ reaction (Q -value $Q = 12.127$ MeV) links the CN cycle [1, 2] to the CNO bi-cycle and all further CNO cycles [3]. The $^{15}\text{N}(p,\gamma)^{16}\text{O}$ cross section $\sigma(E)$ (E denotes the center of mass energy in keV, E_p the proton beam energy in the laboratory system) can be parameterized [3] by the astrophysical S-factor $S(E)$ defined as

$$S(E) = \sigma(E)E \exp(212.85/\sqrt{E}). \quad (1)$$

At astrophysically relevant energies $E < 1$ MeV, the $^{15}\text{N}(p,\gamma)^{16}\text{O}$ excitation function is influenced by two resonances at $E_p = 335$ and 1028 keV ($E_x = 12440$ and 13090 keV, figure 1), with respective widths of $\Gamma_p = 91$ and 130 keV, both decaying predominantly into the ground state of ^{16}O [4]. For the $E_x = 12440$ (13090) keV level, 1.2% (0.58%) decay branching to the 0^+ first excited state of ^{16}O at 6.049 MeV has been reported [4]. In addition, for the 13090 keV level, there is 3.1% decay branching to the 1^- third excited state at 7.117 MeV [4]. No other decays to ^{16}O excited states are known for $E_p \leq 1028$ keV [4].

The non-resonant cross section has been studied in previous experiments using NaI [5] and Ge(Li) [6] detectors, reporting cross section data for $E_p = 150 - 2500$ keV [6]. Citing discordant normalizations between those two studies [5, 6], only the data from one of these studies [6] have been used in reaction rate compilations [7, 8].

Recently, the asymptotic normalization coefficients (ANC's) for direct capture to the ground and several excited states in ^{16}O have been measured [9]. It was found that the low-energy non-resonant yield is dominated by ground state capture [9], but the new ANC leads to a much lower direct capture cross section (sum of direct capture to all states in ^{16}O) than previously [6]. The new ANC values have then been used in an R-matrix fit [9] including also the cross section data from refs. [5, 6], suggesting a factor two lower astrophysical S-factor than previously believed [6, 7, 8]. Another recent R-matrix analysis concentrating on ground state capture was based again on the direct data from refs. [5, 6], and it also indicates a much lower S-factor [10]. In view of the

conflicting data [5, 6] and the recent extrapolations [9, 10], new experimental data is clearly called for.

The aim of the present work is to experimentally determine the $^{15}\text{N}(\text{p},\gamma)^{16}\text{O}$ cross section directly at energies corresponding to hydrogen burning in novae. The relevant temperatures in novae [11, 12] are $T_6 = 200 - 400$ (T_6 denoting the central temperature of a star in units of 10^6 K), corresponding to Gamow energies [3] of $E_{\text{Gamow}} = 150\text{-}240$ keV. In order to obtain the new cross section data, spectra from a radiative proton capture experiment at LUNA that has been performed using nitrogen gas of natural isotopic composition (99.6% ^{14}N , 0.4% ^{15}N) have now been analyzed regarding the $^{15}\text{N}(\text{p},\gamma)^{16}\text{O}$ reaction.

2. Experiment

The experiment has been performed at the Laboratory for Underground Nuclear Astrophysics (LUNA) in Italy's Gran Sasso underground laboratory (LNGS). The LUNA facility has been designed for measuring low nuclear cross sections for astrophysical purposes [13, 14, 15, 16, 17, 18, 19], benefiting from its ultra-low laboratory γ -ray background [20, 21].

2.1. Target

A windowless, differentially pumped gas target cell filled with 1 mbar nitrogen gas of natural isotopic composition (0.366% ^{15}N [22]) has been irradiated with $E_p = 100 - 250$ keV H^+ beam from the 400 kV LUNA2 accelerator [23]. The emitted γ -rays have been detected in a 4π BGO summing crystal [24]. The calorimetric beam intensity values are known with 1.0% precision [24].

The natural isotopic composition of the target gas enabled parallel experiments on $^{14}\text{N}(\text{p},\gamma)^{15}\text{O}$ [16, 25] and $^{15}\text{N}(\text{p},\gamma)^{16}\text{O}$ (present work). The $^{14}\text{N}(\text{p},\gamma)^{15}\text{O}$ analysis is already published including full experimental details [16, 25]; the present work concentrates on aspects pertinent to obtaining the $^{15}\text{N}(\text{p},\gamma)^{16}\text{O}$ cross section.

During the experiment, nitrogen gas of natural isotopic composition and 99.9995% chemical purity was flowing through the windowless target cell with a flux of 2 liters/second. No recirculation was used, so the gas was discarded after one passage through the target. The effective ^{15}N target density for the present work has been obtained scaling the known target density (3.2% uncertainty including the beam heating correction [25]) with the standard isotopic composition [22]. A recent survey has found that >99% of nitrogen-bearing materials have isotopic abundances within 2.0% of the standard value [22], which is defined to be that of atmospheric air. The ^{15}N content of atmospheric air on different continents has been found to be constant to 2.6% [26], and commercial tank gas even falls within 1.0% of the standard [27]. In order to verify whether these findings also apply to the presently used tank gas, gas samples of the type of nitrogen used here and from the same supplier have been sent to three different

laboratories for isotopic analysis. The isotopic ratio was found to be within 3% of the standard. As relative uncertainty for the isotopic ratio, 3% is therefore adopted.

2.2. γ -ray detection

The γ -ray detection efficiency of the BGO detector [24] has been obtained by a dedicated simulation with GEANT4 [28]. The simulation has been validated at low γ -ray energy by measurements with calibrated γ -ray sources and at $E_\gamma \approx 7$ MeV by a detailed comparison with the results from the previous [25] GEANT3 simulation. An uncertainty of 3.0% is quoted here for the probability of detecting isotropically emitted 12 MeV γ -rays.

The GEANT4 summing detector efficiency depends, however, also on inputs from experiment, such as the decay scheme and the angular distribution of the emitted γ -radiation. If the capture does not proceed directly to the ground state, but to some excited state, several γ -rays may be emitted, leading to lower detection efficiency when compared to ground state capture.

In order to understand the decay scheme, germanium spectra taken at $E_p = 400$ keV (slightly above the $E_p = 335$ keV resonance) bombarding solid $\text{Ti}^{\text{nat}}\text{N}$ targets with proton beam [18] have been reanalyzed here. Experimental upper limits of 1.9% (1.8%) for the primary γ -rays for capture to the excited states at 7.117 (6.049) MeV in ^{16}O have been derived. In addition, from a reanalysis of germanium spectra [20] taken with the present gas target setup at $E_p = 200$ keV, an upper limit of 6% for the γ -ray from the decay of the 7.117 MeV state is deduced. These findings are consistent with the previous conclusion that for $E_p < 400$ keV, the reaction proceeds to $\geq 95\%$ by capture to the ground state in ^{16}O [6].

The GEANT4 simulation shows that the summing peak detection efficiency for γ -rays decaying through the 1^- level at 7.117 MeV is 27% lower than for ground state capture. The 0^+ level at 6.049 MeV does not decay by γ -emission, so capture to this level cannot be detected in the 12 MeV summing peak at all. Scaling these effects with the above mentioned experimental upper limits for the capture probability to the corresponding level, 1.9% systematic uncertainty for the total cross section is obtained due to possible capture to excited states.

The angular distribution has previously been found to be isotropic at the $E_p = 1028$ keV resonance [6], and for the present analysis, isotropy has been assumed. The simulation shows that due to the large solid angle covered by the BGO, the detection efficiency is enhanced by only 4% when assuming a complete $\sin^2\vartheta$ shape instead. In order to account for this effect, 4% is adopted as systematic uncertainty.

2.3. Analysis of the γ -ray spectra

During the experiment, γ -ray spectra were taken at twelve different incident energies between $E_p = 100$ -250 keV. For each beam energy, two in-beam spectra were recorded: one with 1 mbar nitrogen gas (natural isotopic composition) in the target, and one with 1 mbar helium gas (chemical purity 99.9999%) to monitor ion beam induced background.

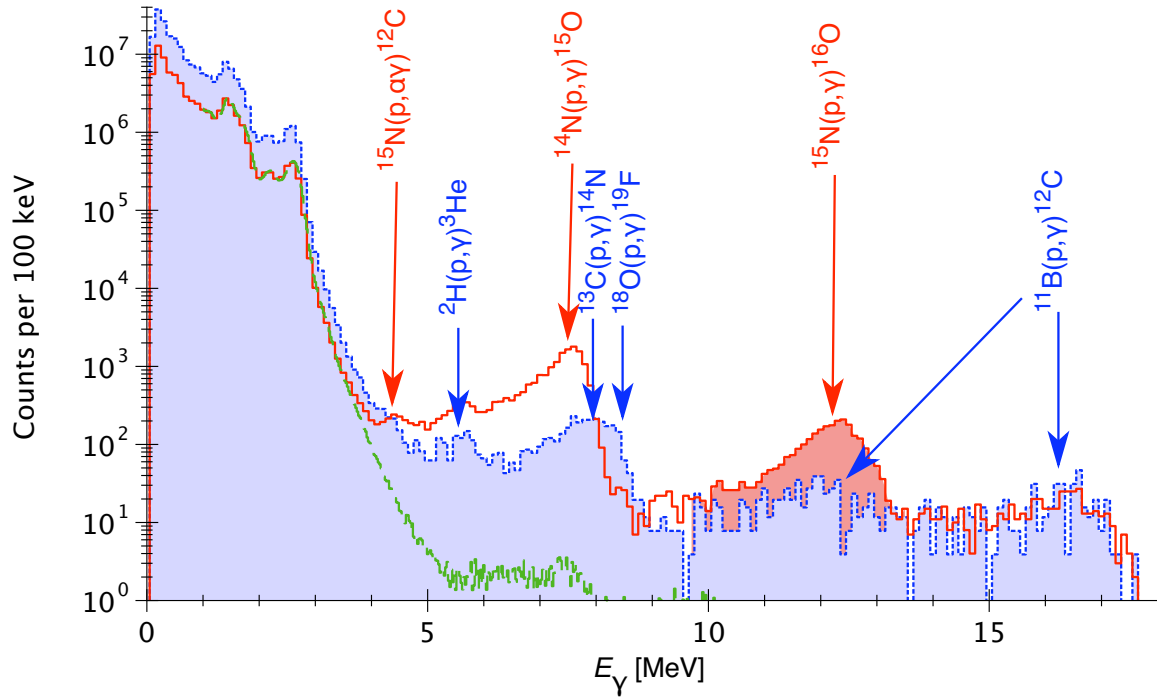


Figure 2. γ -ray spectrum recorded at $E_p = 150$ keV. Solid red (dotted blue) line: Nitrogen gas in the target (helium gas, rescaled to match the nitrogen spectrum in the 14.4 – 18.0 MeV region). Dashed green line, laboratory background, rescaled for equal livetime. See text for details.

In addition, a spectrum with 1 mbar argon gas in the target has been recorded at $E_p = 216$ keV. Laboratory background spectra were taken during accelerator downtimes.

The in-beam spectra can be classified in two groups, low beam energies $E_p = 100$ -150 keV (example, figure 2), and high beam energies $E_p = 190$ -250 keV (example, figure 3). Salient features of the spectra are discussed in the following.

At low γ -ray energies ($E_\gamma \leq 4$ MeV), the in-beam γ -ray spectra are dominated by the laboratory background and resultant pile-up. For 4 MeV $< E_\gamma \leq 8.5$ MeV, the following in-beam γ -lines are evident [20]:

- the 4.4 MeV γ -ray from the decay of the first excited state of ^{12}C populated both in the $^{11}\text{B}(p,\gamma)^{12}\text{C}$ and in the $^{15}\text{N}(p,\alpha\gamma)^{12}\text{C}$ reactions (well visible in all the nitrogen spectra, visible in some of the helium spectra),
- the ~ 5.5 MeV peak from the $^2\text{H}(p,\gamma)^3\text{He}$ reaction (visible only for $E_p \leq 150$ keV in both the nitrogen and helium spectra),
- the 6.1 MeV γ -ray from the decay of the second excited state of ^{16}O populated in the $^{19}\text{F}(p,\alpha\gamma)^{16}\text{O}$ reaction (visible only for $E_p \geq 180$ keV in the helium spectra),
- the 6.2 MeV and 6.8 MeV secondary γ -rays and the ~ 7.5 MeV summing peak from the $^{14}\text{N}(p,\gamma)^{15}\text{O}$ reaction (well visible in all the nitrogen spectra, not visible in the helium spectra),

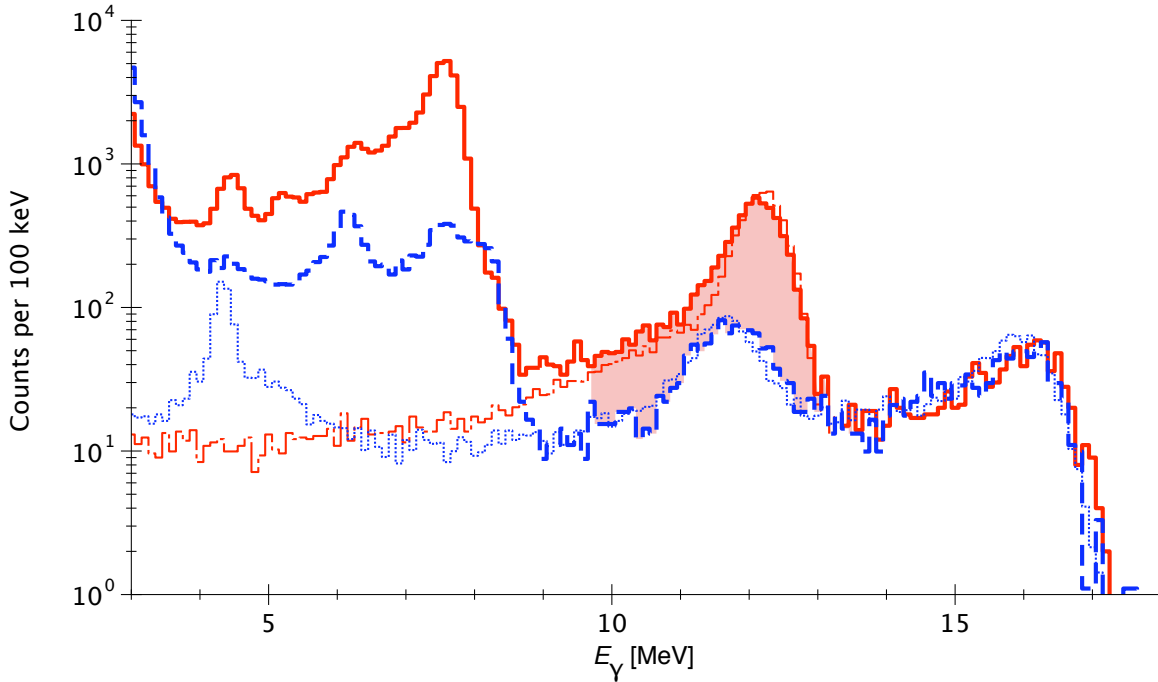


Figure 3. γ -ray spectrum, $E_p = 220$ keV. Red solid (dot-dashed) line: Experimental, nitrogen gas (simulated, assuming only the $^{15}\text{N}(p,\gamma)^{16}\text{O}$ reaction). Blue dashed (dotted) line: Experimental, helium gas, rescaled as in figure 2 (simulated with Sim. B, assuming only the $^{11}\text{B}(p,\gamma)^{12}\text{C}$ reaction).

- the ~ 7.7 MeV peak from the $^{13}\text{C}(p,\gamma)^{14}\text{N}$ reaction (well visible in the helium spectra, covered by the $^{14}\text{N}(p,\gamma)^{15}\text{O}$ lines in the nitrogen spectra), and
- the 8.1 MeV summing peak from the $^{18}\text{O}(p,\gamma)^{19}\text{F}$ reaction (visible only in a few helium spectra).

At $E_\gamma > 8.5$ MeV, the laboratory background [20] is negligible for the purposes of the present study (figure 2). At these high γ -ray energies, the spectrum is determined by only two reactions:

- First, the full energy peak of the $^{15}\text{N}(p,\gamma)^{16}\text{O}$ reaction to be studied, visible in the nitrogen spectra at $E_\gamma = Q + E \approx 12.3$ MeV. Because of the rather smeared out response function of the BGO detector to high-energy monoenergetic γ -rays, a region of interest (ROI) from 9.7-13.5 MeV (shaded in figs. 2, 3) has been adopted. The probability that a 12 MeV γ -ray emitted isotropically at the center of the detector leads to a count in this ROI is found to be 77% in the simulation.
- Second, two peaks from the $^{11}\text{B}(p,\gamma)^{12}\text{C}$ beam-induced background reaction ($Q = 15.957$ MeV), visible in both the nitrogen and helium spectra: a summing peak at $E_\gamma = Q + E \approx 16$ MeV and the primary ($E_\gamma \approx 12$ MeV) γ -ray from capture to the 4.439 MeV first excited state in ^{12}C . (The decay of that state has been discussed above.)

2.4. Subtraction of the $^{11}\text{B}(\text{p},\gamma)^{12}\text{C}$ background

In order to obtain the $^{15}\text{N}(\text{p},\gamma)^{16}\text{O}$ cross section, the background in the 9.7-13.5 MeV ROI induced by the $^{11}\text{B}(\text{p},\gamma)^{12}\text{C}$ reaction must be reliably determined and subtracted.

The ^{11}B counting rate can be monitored by the yield in the 14.4-18.0 MeV region, where no other beam-induced lines are present. This rate varied strongly from run to run, also at the same beam energy, so it was necessary to derive a background subtraction procedure based on data in the same experimental spectrum used also for the cross section determination. Assuming that the place of origin of the ^{11}B γ -rays is the collimator at the entrance of the target cell [20], which is hit by the beam halo (0.5-5% of the beam current on target), the mentioned variation of the ^{11}B counting rate can be explained with differences in the details of the proton beam focusing from run to run.

However, even for different absolute ^{11}B counting rates, the ratio between the ≈ 12 MeV and ≈ 16 MeV ^{11}B -induced counting rates depends only on the beam energy (due to energy-dependent branching ratios and angular distributions) and not on the focusing. This leads to the definition of the ratio $R_{12/16}^{\text{Boron}}$:

$$R_{12/16}^{\text{Boron}} \stackrel{!}{=} \frac{\text{Counts (9.7 - 13.5 MeV)}}{\text{Counts (14.4 - 18.0 MeV)}} \quad (2)$$

At each beam energy, the quantity $R_{12/16}^{\text{Boron}}$ has been determined experimentally from a monitor run with helium gas in the target (table 1). As a check on the reliability of using helium as monitor gas, at $E_p = 216$ keV, $R_{12/16}^{\text{Boron}}$ has been determined with argon gas instead of helium, with consistent results (table 1).

The experimental $R_{12/16}^{\text{Boron}}$ values are then compared with the results of two GEANT4 simulations called Sim. A and Sim. B. In both Sim. A and Sim. B, the known branching ratios and angular distribution of the $^{11}\text{B}(\text{p},\gamma)^{12}\text{C}$ reaction from ref. [29] are included.

Sim. A The point of origin of the ^{11}B γ -rays was assumed not to be the final collimator, but the beamstop (table 1).

Sim. B The point of origin of the ^{11}B γ -rays was assumed to be the final collimator as discussed above (table 1, figure 3).

For all data points, Sim. B is closer to the experimental data than Sim. A. However, at the lowest and highest proton beam energies the experimental $R_{12/16}^{\text{Boron}}$ values tend to be even higher than the simulated ones from Sim. B (table 1). In order to understand this phenomenon, it should be noted that the simulation results depend strongly on the assumed branching ratios, angular distributions, and angular correlations. The branching ratio is known experimentally also for off-resonant energies [29]. However, the angular distribution is only known at the $E_p = 163$ keV resonance [29]. It seems plausible that given this limited input data, the simulation does a better job close to $E_p = 163$ keV than far away, at the lowest and highest proton beam energies.

For the actual data analysis, the experimental $R_{12/16}^{\text{Boron}}$ values have been used. In order to err on the side of caution and quote a conservative uncertainty on the adopted

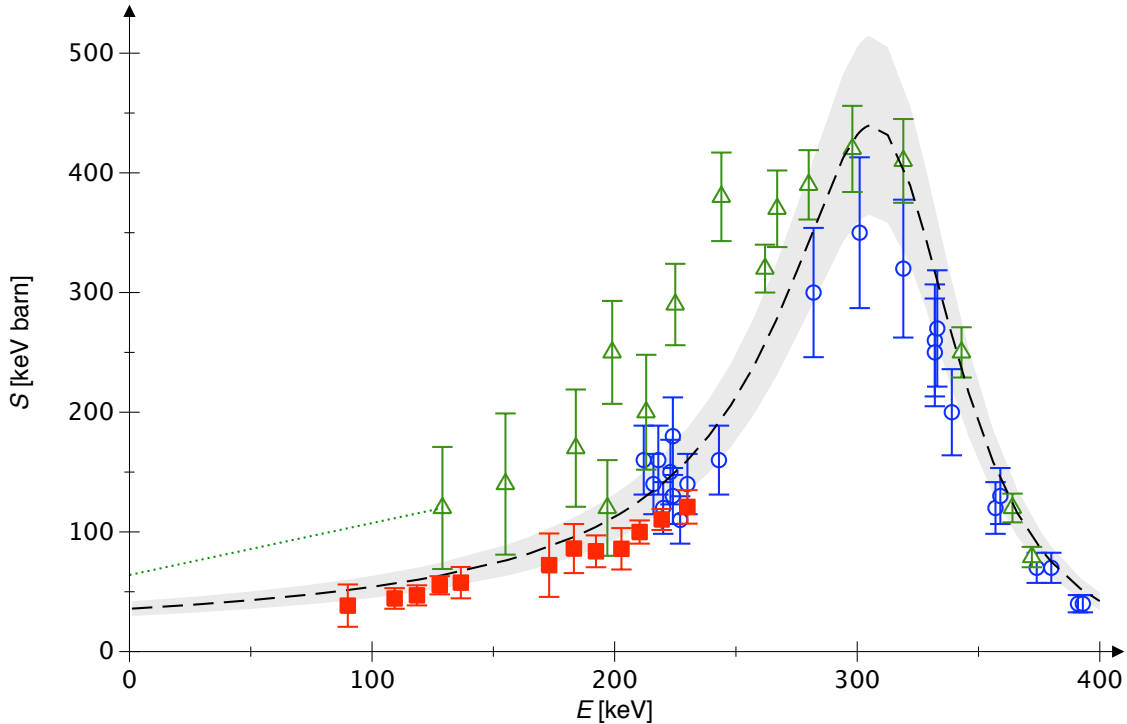


Figure 4. $^{15}\text{N}(p,\gamma)^{16}\text{O}$ astrophysical S-factor. Experimental data from ref. [5] (blue circles, limited to $E \geq 210\text{keV}$), ref. [6] (green triangles) and the present work (red filled squares). Error bars reflect statistical and systematic uncertainties summed in quadrature. Dotted line, previous low-energy extrapolation by the NACRE compilation [8]. Dashed line, previous R-matrix fit, and shaded area, its quoted 17% uncertainty [9].

$R_{12/16}^{\text{Boron}}$ value, for $\Delta R_{12/16}^{\text{Boron}}$ either the statistical uncertainty or ± 1.0 (an upper limit on the full difference between Sim. A and Sim. B) was used, whichever is greater (table 1).

Finally, the ^{11}B background to be subtracted in the 9.7-13.5 MeV ROI of the nitrogen spectrum is then obtained by multiplying the counts in the 14.4-18.0 MeV monitoring region in the same nitrogen spectrum with the experimental $R_{12/16}^{\text{Boron}}$ value from the corresponding helium run (table 1). The uncertainty due to the boron background subtraction has 1.8-43% effect on the S-factor data, and it dominates the uncertainty for most data points. Two types of runs have been excluded from the present analysis: Runs that show more ^{11}B background than ^{15}N yield in the ROI, and runs for which no helium monitor run has been performed.

2.5. Further experimental details

The effective interaction energy has been calculated assuming a constant astrophysical S-factor [3] over the typically 10 keV thick target, leading to 0.7-3.2% systematic uncertainty including also the accelerator energy calibration [23] uncertainty. All systematic uncertainties are summarized in table 2.

3. Results

Based on the spectrum integration discussed in the previous section, the $^{15}\text{N}(\text{p},\gamma)^{16}\text{O}$ cross section has been determined at twelve effective center-of-mass interaction energies E^{eff} between 90 and 230 keV (table 3). The statistical uncertainty is typically well below 10%.

The present S-factor data (figure 4) are about a factor two lower than the previous data by ref. [6], but still consistent at 2σ level given the previous high uncertainties. In the limited overlapping energy region, the present data seem to agree with ref. [5], if ref. [5]’s low-energy data points (affected by beam-induced background) are excluded. The data from the present work extend to energies lower than ever measured before and are significantly lower than the low-energy extrapolation adopted in the NACRE [8] compilation.

The present data are on average 20% lower than, but given the previous uncertainty still consistent with, the recent R-matrix fit based on an ANC measurement [9]. They are also lower than the fits shown in ref. [10]. These R-matrix fits [9, 10] had relied on direct experimental data from Refs. [5, 6] for the dominating resonant contribution, and it seems prudent to call for a new R-matrix fit, which is beyond the scope of the present work.

Previous one-zone nucleosynthesis calculations of novae [30] have shown that a factor two lower $^{15}\text{N}(\text{p},\gamma)^{16}\text{O}$ rate results in up to 22% reduction in the final ^{16}O yield, depending on the nova temperature. Further implications of the changed $^{15}\text{N}(\text{p},\gamma)^{16}\text{O}$ rate are yet to be studied.

4. Summary

The $^{15}\text{N}(\text{p},\gamma)^{16}\text{O}$ cross section has been measured at energies corresponding to hydrogen burning in novae. The present data are more precise than previous direct experiments [5, 6]. They are about a factor two lower than the values adopted in reaction rate compilations [7, 8].

Acknowledgments

We thank W. Brand (Max-Planck-Institute for Biogeochemistry Jena, Germany) for assistance with the isotopic abundance analysis. Financial support by INFN and in part by the European Union (TARI RII3-CT-2004-506222) and the Hungarian Scientific Research Fund (T49245 and K68801) is gratefully acknowledged.

References

- [1] Bethe H 1939 *Phys. Rev.* **55** 103
- [2] von Weizsäcker C F 1938 *Phys. Z.* **39** 633–646
- [3] Iliadis C 2007 *Nuclear Physics of Stars* (Wiley-VCH)

- [4] Tilley D, Weller H and Cheves C 1993 *Nucl. Phys. A* **564** 1–183
- [5] Hebbard D F 1960 *Nucl. Phys.* **15** 289–315
- [6] Rolfs C and Rodney W 1974 *Nucl. Phys. A* **235** 450–459
- [7] Caughlan G and Fowler W 1988 *At. Data Nucl. Data Tables* **40** 283–334
- [8] Angulo C *et al.* 1999 *Nucl. Phys. A* **656** 3–187
- [9] Mukhamedzhanov A M *et al.* 2008 *Phys. Rev. C* **78** 015804
- [10] Barker F C 2008 *Phys. Rev. C* **78** 044612
- [11] José J and Hernanz M 1998 *Astrophys. J.* **494** 680
- [12] José J, García-Berro E, Hernanz M and Gil-Pons P 2007 *Astrophys. J. Lett.* **662** L103–L106
- [13] Bonetti R *et al.* 1999 *Phys. Rev. Lett.* **82** 5205–5208
- [14] Casella C *et al.* 2002 *Nucl. Phys. A* **706** 203–216
- [15] Formicola A *et al.* 2004 *Phys. Lett. B* **591** 61–68
- [16] Lemut A *et al.* 2006 *Phys. Lett. B* **634** 483
- [17] Bemmerer D *et al.* 2006 *Phys. Rev. Lett.* **97** 122502
- [18] Marta M *et al.* 2008 *Phys. Rev. C* **78** 022802(R)
- [19] Formicola A *et al.* 2008 *J. Phys. G* **35** 014013
- [20] Bemmerer D *et al.* 2005 *Eur. Phys. J. A* **24** 313–319
- [21] Caciolli A *et al.* 2008 *Eur. Phys. J. A* **in press** (*Preprint arXiv:0812.3223*)
- [22] Coplen T B *et al.* 2002 *Pure Appl. Chem.* **74** 1987–2017
- [23] Formicola A *et al.* 2003 *Nucl. Inst. Meth. A* **507** 609–616
- [24] Casella C *et al.* 2002 *Nucl. Inst. Meth. A* **489** 160–169
- [25] Bemmerer D *et al.* 2006 *Nucl. Phys. A* **779** 297–317
- [26] Mariotti A 1983 *Nature* **303** 685–687
- [27] Junk G and Svec H 1958 *Geochim. Cosmochim. Acta* **14** 234–243
- [28] Agostinelli S *et al.* 2003 *Nucl. Inst. Meth. A* **506** 250–303
- [29] Cecil F *et al.* 1992 *Nucl. Phys. A* **539** 75 – 96
- [30] Iliadis C, Champagne A, José J, Starrfield S and Tupper P 2002 *Astrophys. J. Suppl. Ser.* **142** 105–137

Table 1. Spectrum integration and background subtraction. The raw counts in the ROI (9.7-13.5 MeV) and in the background monitoring region (14.4-18.0 MeV) are given. For the ratio $R_{12/16}^{\text{Boron}}$, the experimental data are from runs with helium gas in the target. The simulations A and B and the adopted uncertainty are explained in the text. The boron background in the ROI (column 8) is obtained by multiplying columns 3 and 7. The net counts in the peak (column 9) are obtained by subtracting column 8 from column 2.

E_p [keV]	Raw counts		$R_{12/16}^{\text{Boron}}$		Sim. B adopted		Boron background		Net counts	
	9.7-13.5	14.4-18.0	Experiment	Sim. A	Sim. B	adopted	9.7-13.5	9.7-13.5	Δ_{stat}	Δ_{Boron}
101	293	69	1.9±0.6	0.70	1.13	1.9±1.0	130±70	164	10%	43%
122	355	31	3.3±1.0	0.75	1.37	3.3±1.0	100±40	252	7%	14%
131	662	79	1.8±0.5	0.77	1.33	1.8±1.0	140±80	522	5%	15%
141	1703	172	1.1±0.2	0.80	1.44	1.1±1.0	190±170	1510	3%	11%
151	2739	433	1.6±0.2	0.80	1.46	1.6±1.0	700±400	2047	3%	21%
188	12126	2895	1.4±0.3	0.81	1.46	1.4±1.0	4100±2900	8064	1%	36%
201	1300	222	1.40±0.05	0.84	1.52	1.4±1.0	310±220	990	4%	22%
210	32569	3836	1.42±0.03	0.80	1.49	1.4±1.0	5400±3800	27120	1%	14%
216			1.45±0.09	0.80	1.45					
221	6360	902	1.72±0.07	0.78	1.46	1.7±1.0	1600±900	4805	2%	19%
229	1930	98	2.9±0.2	0.80	1.43	2.9±1.0	280±100	1649	3%	6%
238	1517	33	2.2±0.8	0.77	1.51	2.2±1.0	70±40	1443	3%	2%
250	958	18	6±4	0.81	1.38	6±4	110±70	847	4%	8%

At $E_p = 216$ keV, argon gas has been used instead of helium.

Table 2. Systematic uncertainties and their effect on the S-factor data.

Source of the uncertainty	Details found in	Effect on S-factor
Target density	Ref. [25]	3.2%
^{15}N isotopic ratio	Refs. [26, 22]	3.0%
Beam intensity	Refs. [24, 25]	1.0%
Effective energy	Ref. [23]	0.7% – 3.2%
γ -ray detection efficiency	Sec. 2.2	3.0%
γ -ray capture to excited states	Sec. 2.2	1.9%
γ -ray angular distribution	Sec. 2.2	4.0%
$^{11}\text{B}(p,\gamma)^{12}\text{C}$ background	Sec. 2.4	1.8% – 43%
Total systematic uncertainty:		8% – 44%

Table 3. Effective center-of-mass interaction energy E^{eff} , S-factor data, and relative uncertainties. The systematic uncertainty due to the boron background subtraction has been derived in table 1 and is repeated here (column 5). The boron uncertainty is already included in the total systematic uncertainty given below (column 4).

E^{eff} [keV]	$S(E^{\text{eff}})$ [keV barn]	$\Delta S/S$		
		statistical	total systematic	systematic (boron)
90.0	38.4	14%	44%	43%
109.3	44.4	11%	16%	14%
118.5	47.0	6%	17%	15%
127.9	55.4	3%	13%	11%
136.6	57.6	4%	22%	21%
173.0	72.2	2%	37%	36%
183.2	86.1	4%	24%	22%
192.3	83.8	1%	16%	14%
202.8	85.9	2%	20%	19%
210.3	99.9	3%	9%	6%
219.4	110.4	3%	7%	2%
230.0	120.9	5%	11%	8%

Revision of the $^{15}\text{N}(p,\gamma)^{16}\text{O}$ reaction rate and oxygen abundance in H–burning zones

A. Caciolli^{1,2}, C. Mazzocchi^{*3}, V. Capogrosso³, D. Bemmerer⁴, C. Brogini¹, P. Corvisiero⁵, H. Costantini⁵, Z. Elekes⁶, A. Formicola⁷, Zs. Fülöp⁶, G. Gervino⁸, A. Guglielmetti³, C. Gustavino⁷, Gy. Gyürky⁶, G. Imbriani⁹, M. Junker⁷, A. Lemut^{**5}, M. Marta^{***4}, R. Menegazzo¹, S. Palmerini¹⁰, P. Prati⁵, V. Roca⁹, C. Rolfs¹¹, C. Rossi Alvarez¹, E. Somorjai⁶, O. Straniero¹², F. Strieder¹¹, F. Terrasi¹³, H. P. Trautvetter¹¹, and A. Vomiero¹⁴

¹ Istituto Nazionale di Fisica Nucleare (INFN), Sezione di Padova, via Marzolo 8, I–35131 Padova, Italy

² Dipartimento di Scienze della Terra, Università di Siena, I–53100 Siena, and Centro di GeoTecnologie CGT, I–52027 San Giovanni Valdarno, Italy

³ Università degli Studi di Milano and INFN, Sezione di Milano, I–20133 Milano, Italy

⁴ Helmholtz–Zentrum Dresden–Rossendorf, Bautzner Landstr. 400, 01328 Dresden, Germany

⁵ Università di Genova and INFN Sezione di Genova, Genova, I–16146 Genova, Italy

⁶ Institute of Nuclear Research (ATOMKI), H–4026 Debrecen, Hungary

⁷ INFN, Laboratori Nazionali del Gran Sasso (LNGS), I–67010 Assergi (AQ), Italy

⁸ Dipartimento di Fisica Sperimentale, Università di Torino and INFN Sezione di Torino, I–10125 Torino, Italy

⁹ Dipartimento di Scienze Fisiche, Università di Napoli Federico II, and INFN Sezione di Napoli, I–80126 Napoli, Italy

¹⁰ Dipartimento di Fisica, Università degli studi di Perugia and INFN, Sezione di Perugia, I–06123, Perugia Italy

¹¹ Institut für Experimentalphysik, Ruhr–Universität Bochum, D–44780 Bochum, Germany

¹² INAF–Osservatorio Astronomico di Collurania, I–64100 Teramo, Italy

¹³ Seconda Università di Napoli, I–81100 Caserta, and INFN Sezione di Napoli, I–80126 Napoli, Italy

¹⁴ CNR IDASC SENSOR Lab and Dipartimento di Chimica e Fisica per l’Ingegneria e per i Materiali, Università di Brescia, Brescia, Italy

Preprint online version: July 25, 2011

ABSTRACT

Context. The NO cycle takes place in the deepest layer of a H–burning core or shell, when the temperature exceeds $T \simeq 30 \cdot 10^6$ K. The O depletion observed in some globular cluster giant stars, always associated with a Na enhancement, may be due to either a deep mixing during the RGB (red giant branch) phase of the star or to the pollution of the primordial gas by an early population of massive AGB (asymptotic giant branch) stars, whose chemical composition was modified by the hot bottom burning. In both cases, the NO cycle is responsible for the O depletion.

Aims. The activation of this cycle depends on the rate of the $^{15}\text{N}(p,\gamma)^{16}\text{O}$ reaction. A precise evaluation of this reaction rate at temperatures as low as experienced in H–burning zones in stellar interiors is mandatory to understand the observed O abundances.

Methods. We present a new measurement of the $^{15}\text{N}(p,\gamma)^{16}\text{O}$ reaction performed at LUNA covering for the first time the center of mass energy range 70–370 keV, which corresponds to stellar temperatures between $65 \cdot 10^6$ K and $780 \cdot 10^6$ K. This range includes the $^{15}\text{N}(p,\gamma)^{16}\text{O}$ Gamow–peak energy of explosive H–burning taking place in the external layer of a nova and the one of the hot bottom burning (HBB) nucleosynthesis occurring in massive AGB stars.

Results. With the present data, we are also able to confirm the result of the previous R–matrix extrapolation. In particular, in the temperature range of astrophysical interest, the new rate is about a factor of 2 smaller than reported in the widely adopted compilation of reaction rates (NACRE or CF88) and the uncertainty is now reduced down to the 10% level.

Key words. physical data and processes: nuclear reactions, abundances

1. Introduction

Hydrogen burning in stars proceeds through two different sets of nuclear reactions: the proton proton (pp) chain and the carbon nitrogen oxygen (CNO) cycle. While in low mass main sequence

stars the energy supply is provided by the pp–chain¹, the CNO cycle is the principal nuclear process in the core of high mass main sequence stars ($M \gtrsim 1.2 M_{\odot}$) as well as in the H–burning shell of giant stars Iben(1967). Furthermore, a hot CNO cycle may occur at the surface of H–accreting compact objects, like white dwarfs or neutron stars Jose & Hernanz(1998).

The set of nuclear reactions involved in the CNO cycle is illustrated in Fig. 1. Actually, it is a combination of two distinct cycles, called CN and NO, respectively. The proton capture on ^{15}N results in two possible channels, the $^{15}\text{N}(p,\alpha)^{12}\text{C}$

* present address: Inst. of Experimental Physics University of Warsaw ul. Hoza 69 00–682 Warszawa, Poland

** present address: Nuclear Science Division, Lawrence Berkeley National Laboratory, 1 Cyclotron Rd MS 88–R0192, Berkeley, CA 94720–8101, USA

*** present address: GSI Helmholtzzentrum für Schwerionenforschung, 64291 Darmstadt, Germany

¹ The pp–chain also dominates the H burning in extremely–metal–poor stars of any mass, due to the lack of C, N and O nuclei

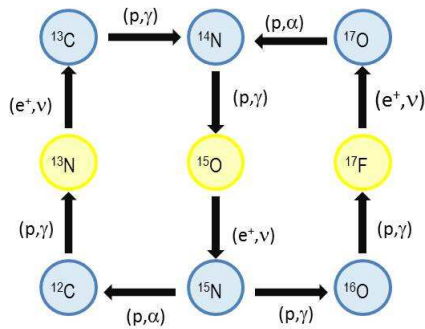


Fig. 1. The CNO bi–cycle.

and the $^{15}\text{N}(p,\gamma)^{16}\text{O}$, respectively: the ratio of the rates provides the linkage between the CN and the NO cycles. The CN cycle becomes fully active when the temperature attains $T_9 \gtrsim 0.016\text{--}0.020^2$, while the NO cycle requires higher temperatures ($T_9 \gtrsim 0.030\text{--}0.035^3$). In case of an active NO cycle, this process determines the abundances of all the stable oxygen isotopes (^{16}O , ^{17}O , ^{18}O). For this reason, a precise evaluation of the $^{15}\text{N}(p,\gamma)^{16}\text{O}$ reaction rate is needed to address several astrophysical problems, like deep mixing scenarios in red giant stars?, see e.g. [sweigart1979, langer1986, charb98, kraft93, boo95, wass95, denis2003, pal10, hot bottom burning nucleosynthesis in massive AGB stars Renzini & Voli(1981) or the H–burning nucleosynthesis in nova–like events Iliadis et al.(2002), Jose et al.(2007).

At low energies the cross section $\sigma(E)$ of the $^{15}\text{N}(p,\gamma)^{16}\text{O}$ reaction (Q –value = 12.127 MeV) is typically expressed in terms of the astrophysical S –factor $S(E)$ defined for this reaction as:

$$S(E) = \sigma(E)E \exp(212.85/\sqrt{E}) \quad (1)$$

where E is the center of mass energy in keV.

In hydrostatic H–burning, the Gamow peak energy of this reaction ranges between 30 and 100 keV. Larger values, up to 300 keV, may be attained during explosive burning. In this energy range, the astrophysical S –factor is influenced by two resonances at $E = 312$ and 964 keV⁴ related to excited states in ^{16}O at $E_x = 12440$ and 13090 keV, respectively. The reaction rates reported in the NACRE Angulo et al.(1999) and the CF88 Caughlan & Fowler(1988) compilations are based on the direct measurement presented by Rolfs and Rodney (1974). However, more recent R–matrix studies Mukhamedzhanov et al.(2008), Barker(2008), which also take into account a previous ANC measurement Mukhamedzhanov et al.(2008), suggested a substantial reduction of the $S(0)$ (i.e. the astrophysical factor at $E = 0$). This result is in agreement with older direct measurements Hebbard(1960), Brochard et al.(1973).

This discrepancy prompted an in–depth study of the reaction at LUNA (Laboratory for Underground Nuclear Astrophysics). The LUNA facility has been designed to study nuclear reactions of astrophysical interest at the same energies of the stellar interiors, by taking advantage of the ultra–low background Bemmerer et al.(2005), Caciolli et al.(2009) of the

INFN–Gran Sasso underground laboratory (a detailed description of LUNA and its experimental study of the pp chain and CNO cycle may be found in the following reviews: Costantini et al.(2009), Brogini et al.(2010)). First of all, a re–analysis of data taken with nitrogen gas target of natural isotopic composition (0.4% ^{15}N) at $E = 90\text{--}230$ keV has been performed Bemmerer et al.(2009). Then, a new measurement has been carried out at LUNA and Notre Dame LeBlanc et al.(2010). HPGe detectors and enriched TiN solid targets have been used to cover a wide energy range, namely: $E = 120\text{--}1800$ keV. Although the minimum energy is still too high to study most of the stellar H–burning environments, thanks to the excellent accuracy (7%) and the wide energy range, this new experiment provided a dataset suitable for an R–matrix extrapolation toward lower energies.

In this paper, we present a third experiment performed at LUNA, designed to explore lower energies. The use a BGO detector, having a higher γ –detection efficiency compared to the HPGe detectors, allowed us to easily cover the 312 keV resonance region and to extend the direct measurements down to 70 keV. The aim of this further effort is twofold. First of all, the new data set covers the Gamow peak corresponding to the explosive burning in Novae as well as hot bottom burning in massive AGB stars. Furthermore, it provides an independent test of the low energy R–matrix extrapolation.

In the next section we illustrate the experiment, the data analysis and the results. In particular, a comparison of the present, independent measurement with the low energy predictions of the R–matrix analysis LeBlanc et al.(2010), leads to the conclusion that the $^{15}\text{N}(p,\gamma)^{16}\text{O}$ reaction rate is now known within a 10% confidence interval. A summary of the astrophysical studies requiring an accurate evaluation of the $^{15}\text{N}(p,\gamma)^{16}\text{O}$ reaction rate follows.

2. The new underground experiment

The target and the γ –ray detection set–up are those used in previous measurements and have been already extensively described elsewhere (for instance see Limata et al.(2010)). The proton beam (30–150 μA) reaches the water cooled target after passing a 5 mm diameter collimator and a 1 m long copper tube, which is cooled to liquid nitrogen temperatures and works as a cold trap in order to prevent impurities scattered by the beam from depositing on the target surface. The pressure in the target chamber is $5 \cdot 10^{-7}$ mbar and no carbon deposition on the target is observed after the irradiation. This is checked by performing scans of the profile of the $^{14}\text{N}(p,\gamma)^{15}\text{O}$ resonance at $E_p = 278$ keV. The target chamber works as a Faraday cup and provides the integral of the charge deposited, hence the average beam intensity, with an overall uncertainty of 2% (a ~ 300 V high voltage is applied to the cold trap to suppress the secondary electron emission).

The target is surrounded by a 4π –BGO summing crystal (28 cm long, 20 cm diameter, and 6 cm coaxial hole, Casella et al.(2002)). The 4π –BGO is essential in order to increase the γ –detection efficiency, which is calculated with a simulation based on GEANT4 Agostinelli et al.(2003) and carefully checked with radioactive sources and with the γ –ray produced by the proton induced reaction $^{11}\text{B}(p,\gamma)^{12}\text{C}$ at the $E = 149$ keV resonance. The simulation needs experimental inputs, such as the decay scheme and the angular distribution of the emitted γ –radiation. The decay branching ratios for transitions to the excited state of ^{16}O have been measured by Rolfs and Rodney (1974), Bemmerer et al. (2009) and LeBlanc et al. (2010). The angular distribution has been found to be isotropic in a previous

² $T_9 = T(K)/10^9$.

³ The activation temperatures of both the CN and the NO cycles depend on the actual amount of C, N and O nuclei and, therefore, on the stellar metallicity.

⁴ In the center of mass reference. Beam energies are given in the center of mass reference unless otherwise stated

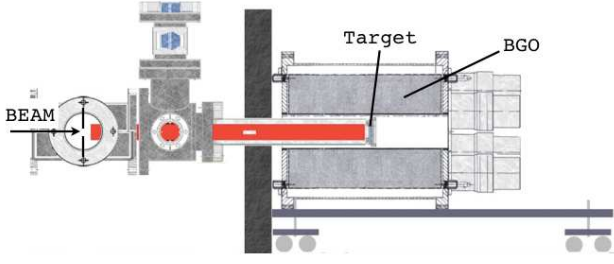


Fig. 2. Schematic representation of the last portion of the beam–line with the detection set–up.

LUNA work LeBlanc et al.(2010). By considering all the contributions described above in the simulation code, the total uncertainty on the efficiency is 3%.

The TiN forming the target material, enriched in ^{15}N , is deposited on a tantalum backing with the reactive sputtering technique Rigato et al.(2001). The target thickness is 100 nm, as verified through secondary neutral mass spectroscopy Vad et al.(2009) (the uncertainty on this measurement is included in the contribution to the target analysis in Table 2), corresponding to 15 keV energy loss at $E = 259$ keV. The stoichiometry Ti/N, which ranges from 0.97 to 1.18 according to the target, is measured for each target with the high Z elastic recoil detection (ERD) technique Bergmaier et al.(1998). Isotopic abundances between 96% and 99%, according to the target, are deduced from the observed height of the plateau in the yield of the $^{14}\text{N}(p,\gamma)^{15}\text{O}$ resonance at $E = 259$ keV, and from the ERD data. The results from these two methods agree within 2%. Finally, the target deterioration, caused by the impinging high–intensity proton beam has been studied by using the 430 keV resonance of $^{15}\text{N}(p,\alpha\gamma)^{12}\text{C}$ Marta et al.(2010). The targets have been analyzed by looking at the shape of the plateau in the yield distribution for the 430 keV resonance. The surface irradiated by the LUNA beam and the area outside the LUNA beam–spot are investigated, so that appropriate corrections for the target deterioration during measurements are derived.

The laboratory background in the $^{15}\text{N}(p,\gamma)^{16}\text{O}$ region of interest is about 6 counts/day. The beam induced background in the same region, produced by the $^{11}\text{B}(p,\gamma)^{12}\text{C}$ reaction, is monitored by means of the peak produced by this reaction at 16.1 MeV (see Fig. 3 as an example of the acquired spectra). The counts in this peak are usually more than in the 11 MeV peak produced by the same reaction, which lies within the $^{15}\text{N}(p,\gamma)^{16}\text{O}$ region of interest of the spectrum Bemmerer et al.(2009). We have rejected all measurements where the 16 MeV peak contained more than 3% of the counts in our region of interest.

The target profiles can be integrated with the cross section in order to calculate the expected yield as:

$$Y_{sim} = \int_{x_0}^{x_{max}} S(E_p) \cdot E_p \exp\left(\frac{212.85}{\sqrt{E_p}}\right) \eta_{BGO} \cdot n_{target}(x) \frac{^{15}\text{N}}{\text{N}} dx \quad (2)$$

where E_p is the energy in the laboratory system expressed in keV and it depends on the beam position x along the target thickness, η_{BGO} is the efficiency, and $n_{target}(x) \frac{^{15}\text{N}}{\text{N}}$ is the number of ^{15}N nuclides in the x position in the target. By comparing the experimental yield Y_{exp} with the calculated one, it is possible to determine the S–factor as follows:

$$S(E_{eff})_{exp} = \frac{Y_{exp}}{Y_{sim}} \cdot S(E_{eff})_{th} \quad (3)$$

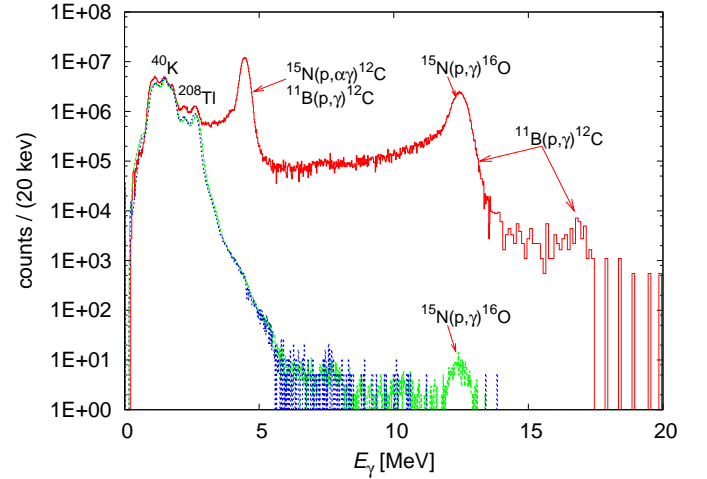


Fig. 3. Spectra taken at $E_p = 330$ keV (red), $E_p = 80$ keV (green), and laboratory background spectrum (blue), normalized to the same time.

Table 1. The absolute S–factor data and their statistical uncertainties from the present work. The systematic error is 11%.

E [keV]	S [keV barn]	ΔS^{stat} [keV barn]	E [keV]	S [keV barn]	ΔS^{stat} [keV barn]
72.8	52	4	236.9	153.0	1.1
81.3	49	2	246.3	172.0	1.7
89.3	53	6	256.4	201	3
105.1	59	4	266.3	227	3
114.8	53	3	274.5	254.7	1.4
123.5	56.4	1.8	283.5	283	3
132.7	64	2	293.7	315.4	1.6
143.7	68.3	1.0	302.6	320	2
151.3	55.9	1.1	311.7	309.1	1.2
162.3	79.2	0.5	321.1	277.6	1.0
170.7	79.8	0.9	330.4	227.4	0.7
180.1	87.2	1.0	340.2	183.0	0.9
189.1	93.5	1.1	349.1	134.0	0.9
198.4	102.6	0.8	354.1	124.0	1.2
207.9	114.0	1.6	358.8	101.0	1.0
217.3	123.0	1.0	363.6	95.1	0.9
227.4	136.0	1.1	368.3	81.0	0.8

where the effective energy is calculated according to the following definition Lemut(2008):

$$E_{eff} = \frac{\int_{x_0}^{x_{max}} S(E) \cdot E \exp\left(\frac{212.85}{\sqrt{E}}\right) \cdot n_{target}(x) \cdot \frac{^{15}\text{N}}{\text{N}} \cdot E \cdot dx}{\int_{x_0}^{x_{max}} S(E) \cdot E \exp\left(\frac{212.85}{\sqrt{E}}\right) \cdot n_{target}(x) \cdot \frac{^{15}\text{N}}{\text{N}} dx} \quad (4)$$

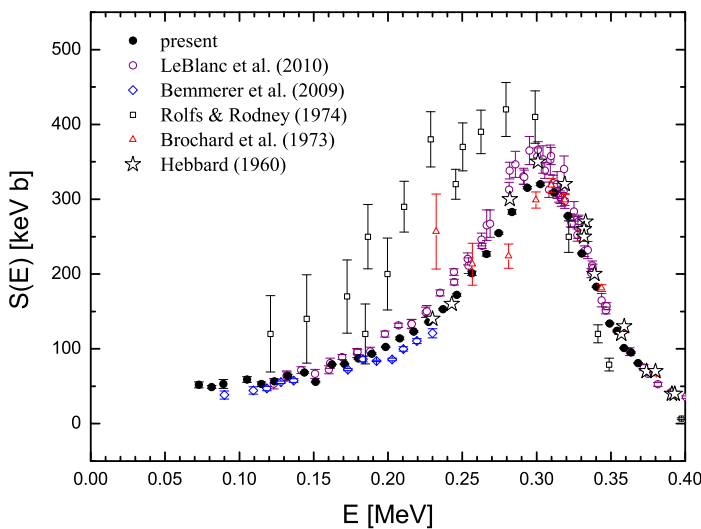
In Eq. (4) the theoretical S–factor is used. Four different theoretical S–factors are considered in Eq. (2) and Eq. (4): the one reported in LeBlanc et al.(2010) and the one reported in Mukhamedzhanov et al.(2011), a constant S–factor and a value obtained from a recursive analysis process. In all cases, the same results are obtained within 1% discrepancies which is included in the error on the effective energy.

As reported in Table 1, the $^{15}\text{N}(p,\gamma)^{16}\text{O}$ astrophysical S–factor is obtained for the center of mass energy range 70–370 KeV. The statistical uncertainty is always limited within a few percent, reaching a maximum value of 10% at $E = 72.8$ keV. All sources of systematic uncertainties are given in Table 2 and sum to a total systematic uncertainty of 10%.

Table 2. S–factor systematic uncertainties.

Source description	Estimated uncertainty
Target analysis	7.5%
stopping power	4.0%
^{15}N isotopic ratio	2.0%
Ti/N stoichiometry	2.0%
Beam intensity	2.0%
Effective energy	3.0%
γ –ray detection efficiency	3.0 %
$^{11}\text{B}(p,\gamma)^{12}\text{C}$ background	3.0%
Total systematic uncertainty	10.0%

A comparison of the derived astrophysical S–factor to the results of previous experiments is shown in Fig. 4. We confirm the

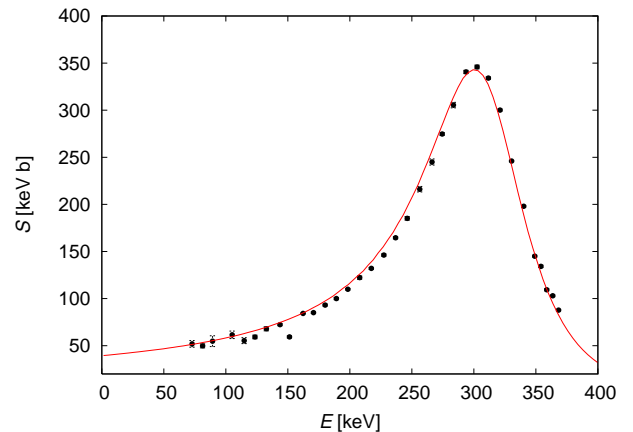
**Fig. 4.** The S–factor as a function of energy. Present data (black dots) are compared to the results of previous experiments.

previous finding concerning the need of a substantial reduction of the $S(0)$ value. The present result is significantly lower than the resonant cross section from Rolfs and Rodney (1974), i.e. the data set adopted in NACRE and CF88, and, by considering the systematic uncertainty, in good agreement with our previous HPGe measurement LeBlanc et al.(2010). In particular, according to the present absolute analysis, the cross section on top of the $E = 312$ keV resonance is $\sigma(312 \text{ keV}) = 6.0 \pm 0.6 \mu\text{b}$, where the quoted error includes the 10 % systematic uncertainty. In Table 3, we compare this result to the values of previous measurements. The weighted average of 3 measurements⁵ leads to a recommended value of $\bar{\sigma}(312 \text{ keV}) = 6.5 \pm 0.3 \mu\text{b}$. The shape of the R–Matrix fit has been also compared to the present data as shown in Fig. 5. Only for this comparison the present data have been corrected for the electron screening in the adiabatic approximation Assenbaum et al.(1987) (at most 10% at 70 keV) and they have been rescaled to the calculated average value. This rescaling is still within the systematic uncertainties of the present absolute data. They show an excellent agreement with the energy dependence of the LUNA R–Matrix fit LeBlanc et al.(2010).

⁵ The result obtained by Brochard et al.(1973) has been excluded, because no uncertainty was reported.

Table 3. Summary of 312 keV resonance cross sections in comparison to previous results (see text for details and references). The uncertainty reported by Hebbard (1960) has been obtained by assuming it to be 10% as reported by Barker(2008).

Present study	LeBlanc <i>et al.</i>	Rolfs and Rodney	Brochard <i>et al.</i>	Hebbard
[μb]	[μb]	[μb]	[μb]	[μb]
6.0 ± 0.6	6.5 ± 0.3	9.6 ± 1.3	6.3	6.5 ± 0.7

**Fig. 5.** The present data rescaled to the new recommended value of $\sigma(312 \text{ keV})$ (see text to details) and compared to the R–matrix predictions LeBlanc et al.(2010).

Finally, a new R–matrix analysis has been recently published by Mukhamedzhanov, La Cognata and Kroha (2011). By varying the fitting method, these authors obtain $S(0)$ values ranging between 33.1 and 40.1 keVb, which is in excellent agreement with the value reported by LeBlanc et al. ($S(0) = 39.6 \pm 2.6$ keVb).

For practical purposes, the nuclear reaction rate can be approximated by the following fitting formula LeBlanc et al.(2011):

$$N_A \langle \sigma v \rangle = a_1 10^9 T^{-\frac{2}{3}} \exp[a_2 T^{-\frac{1}{3}} - (T/a_3)^2] [1 + a_4 T + a_5 T^2] + a_6 10^3 T^{-\frac{3}{2}} \exp(a_7/T) + a_8 10^6 T^{-\frac{3}{2}} \exp(a_9/T), \quad (5)$$

where the best fit parameters are reported in Table 4.

Table 4. Best fit parameters for the $^{15}\text{N}(p,\gamma)^{16}\text{O}$ reaction rate given in LeBlanc et al.(2010).

$a_1 = 0.523$	$a_4 = 6.339$	$a_7 = -2.913$
$a_2 = -15.240$	$a_5 = -2.164$	$a_8 = 3.048$
$a_3 = 0.866$	$a_6 = 0.738$	$a_9 = -9.884$

3. Summary and Conclusions

In this paper we have discussed the experimental efforts done to improve our knowledge of the $^{15}\text{N}(p,\gamma)^{16}\text{O}$ reaction rate in the temperature range experienced by any H–burning zone in stellar

interiors. Such an important reaction is located at the branching point between the CN and NO cycles. The branching ratio, as a function of the temperature, is shown in Fig. 6, where the solid line has been obtained by means of the widely adopted reaction rate given by NACRE, while the dashed line represents the revised scenario as derived from the latest R-matrix study (see section 2). In both cases, the rate suggested by NACRE has

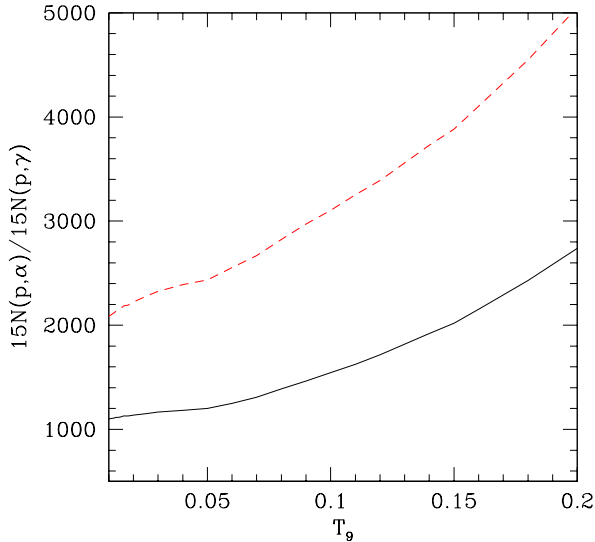


Fig. 6. The CN–NO branching ratio, as a function of the temperature, under different assumptions for the $^{15}\text{N}(p,\gamma)^{16}\text{O}$ reaction rate: NACRE (solid line) and the revised rate (dashed line).

been used for the competitive $^{15}\text{N}(p,\alpha)^{12}\text{C}$ reaction⁶. A look at the solid line shows that in the whole range of temperatures experienced by the core and the shell–H burning, the α -channel is between 1000 to 2000 times more efficient than the γ channel: just 1 to 2 protons out of every 2000 are consumed by the NO cycle. When the updated rate for the $^{15}\text{N}(p,\gamma)^{16}\text{O}$ is adopted, such a ratio becomes about a factor of 2 larger. Although such a variation has negligible consequences on the overall nuclear energy production, a change in the rate of the $^{15}\text{N}(p,\gamma)^{16}\text{O}$ affects the equilibrium abundances of the stable oxygen isotopes within the H burning zone. As an example, the equilibrium abundance of ^{16}O is reported as a function of the temperature in Fig. 7. Also in this case, the solid and the dashed lines represent the values obtained by adopting the NACRE and the revised rate of the $^{15}\text{N}(p,\gamma)^{16}\text{O}$ reaction, respectively.

Let us point out that the most important improvement resulting from the present analysis of the CN–NO branching concerns the significant reduction of the nuclear physics uncertainties, other than the change of the reaction rate with respect to the values reported by CF88 or NACRE. For stellar models and nucleosynthesis calculations implying H-burning whose Gamow peak energy is larger than the minimum value attained by the LUNA BGO experiment, namely $E_0 > 70$ KeV, which corresponds to a temperature $T > 65 \cdot 10^6$ K, a true experimental error (smaller than 10%) is now available for this important reaction rate. Note that only in a very few cases the reaction rate

⁶ This reaction has been recently studied with the THM method Cognata et al.(2009). The authors do not report a reaction rate but only the $S(0)$ value. Scaling the previous NACRE results on that value the following considerations do not change so we still adopt the NACRE results in the present work

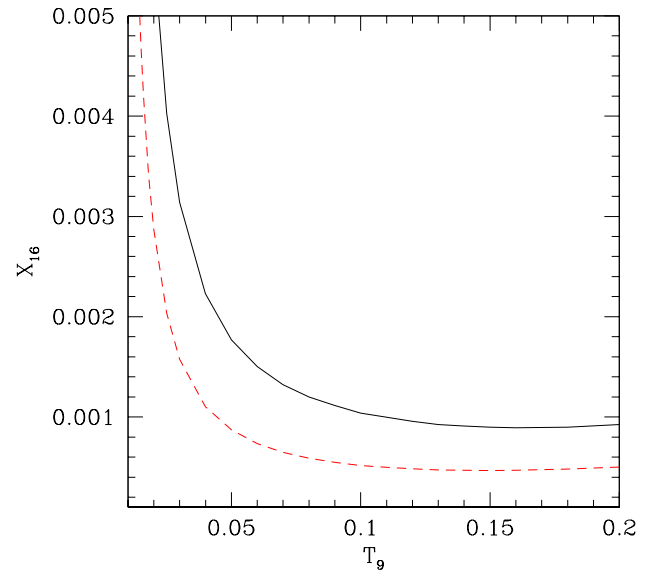


Fig. 7. The ^{16}O equilibrium abundance (mass fraction) as given by: $X_{16} = X_{15} \frac{16}{15} \frac{\langle \sigma v \rangle_{15\text{N}+p}}{\langle \sigma v \rangle_{16\text{O}+p}}$. The solid and the dashed lines represents the old (NACRE) and the new (revised) prescriptions for the $^{15}\text{N}(p,\gamma)^{16}\text{O}$ reaction rate. A solar ^{15}N mass fraction (X_{15}), as derived by Asplund et al. 2010, has been used. In both cases, NACRE prescriptions for the $\langle \sigma v \rangle_{16\text{O}+p}$ have been adopted.

has been measured down to the stellar Gamow peak energy (see, e.g., Bonetti et al.(1999)). In addition, basing on the good agreement found between the new LUNA measurements and the revised R-matrix fit (see previous section), we are confident that the quoted small uncertainty may be assumed also in the extrapolated region.

Among the many astrophysical applications of the present analysis, we recall the explosive H-burning in Novae, which occurs at temperature larger than 10^8 K and, therefore, well above the achieved experimental limit. A recent study by Iliadis et al. (2002), investigates the dependence of the nova nucleosynthesis calculations on the various nuclear physics inputs. They found that a reduction of a factor of two of the $^{15}\text{N}(p,\gamma)^{16}\text{O}$ reaction rate would imply a 30% reduction of the final oxygen abundance. Also the inner region of the convective envelope of massive AGB stars attains quite high temperature, up to $T_9 = 0.08$ – 0.09 (Renzini & Voli(1981), M. Forestini & C. Charbonnel(1997), D’antona & Mazzitelli(1996), Straniero et al.(2000), Lattanzio et al.(2000)). The resulting H burning, the so called hot bottom burning, coupled to the convective mixing, gives rise to a very promising nucleosynthesis scenario, where all the C, N and O isotopes are substantially affected. If the temperature is large enough (80×10^6 K), the Ne–Na and the Mg–Al cycles are also activated. In this context, it has been recently claimed that massive AGB stars played a fundamental role during the early evolution of globular clusters (Ventura et al.(2001)). According to this self-enrichment scenario, in between 50 to 100 Myr after the cluster formation, the first generation of intermediate mass stars (5 – $7 M_{\odot}$) reached the AGB. Then, during this evolutionary phase, they underwent a substantial modification of the envelope composition, as a consequence of the HBB and several dredge up episodes. Due to the huge AGB mass loss, fresh gas enriched in He, C, N and Na, but O depleted, refilled the space occupied by the young Globular Cluster. If the star formation process was still active at that epoch, some

of the stars we observed today should show the imprint of such a delayed chemical pollution by massive AGB. In particular, the O–Na anti–correlation, as observed in Giant, sub–Giant and turn–off stars of several globular clusters ?, e.g. and reference therein]kraft1997, Carretta2009, may be the consequence of this nucleosynthesis process. Such a conclusion follows from the evidence that the temperature required for the activation of the NO cycle is similar to that required for the activation of the Ne–Na cycle. Thus, when O is depleted at the bottom of the convective envelope, Na should be enhanced. For this reason, a precise determination of the $^{15}\text{N}(p,\gamma)^{16}\text{O}$ is one of the prerequisites to obtain a robust prediction of the O abundance and, in turn, to check the proposed self–pollution scenario for the observed O–Na anti–correlation.

The R–matrix studies also allow to extrapolate the precise experimental measurements of the $^{15}\text{N}(p,\gamma)^{16}\text{O}$ reaction rate down to the temperature range experienced by the H–burning taking place in main sequence, RGB and less–massive AGB stars. Also in these cases the uncertainty has been significantly reduced. Such an occurrence may be immediately translated in more robust astrophysical predictions.

Acknowledgments

We thank A. Bergmaier (Universität der Bundeswehr München) and Javier García Lopez (CNA, Centro Nacional de Aceleradores) of Seville for assistance with the isotopic abundance analysis. Financial support by INFN and in part by the European Union (TARI RII3–CT–2004– 506222, AIM 025646 and SPIRIT 227012), the Hungarian Scientific Research Fund (K68801), and DFG (BE 4100/2–1) is gratefully acknowledged.

References

- Agostinelli, S., Allison, J., Amako, K., et al. 2003, Nuclear Instruments and Methods in Physics Research Section A: Accelerators, Spectrometers, Detectors and Associated Equipment, 506, 250
- Angulo, C., Arnould, M., Rayet, M., et al. 1999, Nuclear Physics A, 656, 3
- Assenbaum, H. J., Langanke, K., & Rolfs, C. 1987, Zeitschrift für Physik A Hadrons and Nuclei, 327, 461, 10.1007/BF01289572
- Barker, F. C. 2008, Physical Review C (Nuclear Physics), 78, 044612
- Bemmerer, D., Cacioli, A., Bonetti, R., et al. 2009, Journal of Physics G: Nuclear and Particle Physics, 36, 045202 (10pp)
- Bemmerer, D., Confortola, F., Lemut, A., et al. 2005, Eur. Phys. J. A, 24, 313
- Bergmaier, A., Dollinger, G., & Frey, C. M. 1998, Nuclear Instruments and Methods in Physics Research Section B: Beam Interactions with Materials and Atoms, 136–138, 638, ion Beam Analysis
- Bonetti, R., Brogini, C., Campajola, L., et al. 1999, Phys. Rev. Lett., 82, 5205
- Bordeanu, C., Rolfs, C., Margineanu, R., Negoita, F., & Simion, C. 2008, Journal of Physics G: Nuclear and Particle Physics, 35, 014011 (6pp)
- Brochard, F., Chevallier, P., Disdier, D., & Scheibling, F. 1973, Le Journal de Physique, 34, 363
- Brogini, C., Bemmerer, D., Guglielmetti, A., & Menegazzo, R. 2010, Annual Review of Nuclear and Particle Science, 60, 53
- Cacioli, A., Agostino, L., Bemmerer, D., et al. 2009, Eur. Phys. J. A, 39, 179
- Carretta, E., Bragaglia, A., Gratton, R. G., et al. 2009, A&A, 505, 117
- Casella, C., Costantini, H., Lemut, A., et al. 2002, Nuclear Instruments and Methods in Physics Research Section A: Accelerators, Spectrometers, Detectors and Associated Equipment, 489, 160
- Caughlan, G. R. & Fowler, W. A. 1988, Atomic Data and Nuclear Data Tables, 40, 283
- Charbonnel, C. & do Nascimento, J. D., J. 1998, A&A, 336, 915
- Cognata, M. L., Goldberg, V. Z., Mukhamedzhanov, A. M., Spitaleri, C., & Tribble, R. E. 2009, Phys. Rev. C, 80, 012801
- Costantini, H., Formicola, A., Imbriani, G., et al. 2009, Reports on Progress in Physics, 72, 086301
- D’antona, F. & Mazzitelli, I. 1996, The Astrophysical Journal, 470, 1093
- Denissenkov, P. A. & Vandenberg, D. A. 2003, The Astrophysical Journal, 593, 509
- Hebbard, D. 1960, Nuclear Physics, 15, 289
- Iben, I., J. 1967, The Astrophysical Journal, 147, 624
- Iliadis, C., Champagne, A., Jose, J., Starrfield, S., & Tupper, P. 2002, The Astrophysical Journal Supplement Series, 142, 105
- Jose, J., Garcia-Berro, E., Hernanz, M., & Gil-Pons, P. 2007, The Astrophysical Journal Letters, 662, L103
- Jose, J. & Hernanz, M. 1998, The Astrophysical Journal, 494, 680
- Kraft, R. P., Sneden, C., Langer, G. E., & Shetrone, M. D. 1993, The Astronomical Journal, 106, 1490
- Kraft, R. P., Sneden, C., Smith, G. H., et al. 1997, The Astronomical Journal, 113, 279
- Langer, G. E., Kraft, R. P., Carbon, D. F., Friel, E., & Oke, J. B. 1986, Publications of the Astronomical Society of the Pacific, 98, 473
- Lattanzio, J., Forestini, M., & Charbonnel, C. 2000, Mem. Soc. Astron. Italiana, 71, 737
- LeBlanc, P. J., Imbriani, G., Görres, J., et al. 2010, Phys. Rev. C, 82, 055804
- LeBlanc, P. J., Imbriani, G., Görres, J., et al. 2011, Phys. Rev. C, 84, 019902
- Lemut, 2008, Eur. Phys. J. A, 36, 233
- Limata, B., Strieder, F., Formicola, A., et al. 2010, Phys. Rev. C, 82, 015801
- M. Forestini & C. Charbonnel. 1997, Astron. Astrophys. Suppl. Ser., 123, 241
- Marta, M., Trompler, E., Bemmerer, D., et al. 2010, Phys. Rev. C, 81, 055807
- Mukhamedzhanov, A. M., Bém, P., Burjan, V., et al. 2008, Physical Review C (Nuclear Physics), 78, 015804
- Mukhamedzhanov, A. M., La Cognata, M., & Kroha, V. 2011, Phys. Rev. C, 83, 044604
- Palmerini, S., Cognata, M. L., Cristallo, S., & Busso, M. 2011, The Astrophysical Journal, 729, 3
- Renzini, A. & Voli, M. 1981, A&A, 94, 175
- Rigato, V., Maggioni, G., Patelli, A., et al. 2001, Surface and Coating Technology, 142–144, 943
- Straniero, O., Limongi, M., Chieffi, A., et al. 2000, Mem. Soc. Astron. Italiana, 71, 719
- Sweigart, A. V. & Mengel, J. G. 1979, The Astrophysical Journal, 229, 624
- Vad, K., Csik, A., & Langer, G. A. 2009, Spectroscopy Europe, 21, 13
- Ventura, P., D’Antona, F., Mazzitelli, I., & Gratton, R. 2001, The Astrophysical Journal Letters, 550, L65
- Wasserburg, G. J., Boothroyd, A. I., & Sackmann, I.-J. 1995, The Astrophysical Journal Letters, 447, L37

Ultra-sensitive in-beam γ -ray spectroscopy for nuclear astrophysics at LUNA

A. Caciolli^{1,2}, L. Agostino³, D. Bemmerer^{4 a}, R. Bonetti^{5 b}, C. Broggin¹, F. Confortola³, P. Corvisiero³, H. Costantini³, Z. Elekes⁶, A. Formicola⁷, Zs. Fülöp⁶, G. Gervino⁸, A. Guglielmetti⁵, C. Gustavino⁷, Gy. Gyürky⁶, G. Imbriani⁹, M. Junker⁷, M. Laubenstein⁷, A. Lemut³, B. Limata⁹, M. Marta⁴, C. Mazzocchi⁵, R. Menegazzo¹, P. Prati³, V. Roca⁹, C. Rolfs¹⁰, C. Rossi Alvarez¹, E. Somorjai⁶, O. Straniero¹¹, F. Strieder¹⁰, F. Terrasi¹², and H.P. Trautvetter¹⁰
 (LUNA collaboration)

- ¹ INFN Sezione di Padova, Padova, Italy
² Dipartimento di Fisica, Università di Padova, Padova, Italy
³ Dipartimento di Fisica, Università di Genova, and INFN Sezione di Genova, Genova, Italy
⁴ Forschungszentrum Dresden-Rossendorf, Dresden, Germany
⁵ Istituto di Fisica Generale Applicata, Università di Milano, and INFN Sezione di Milano, Milano, Italy
⁶ ATOMKI, Debrecen, Hungary
⁷ INFN, Laboratori Nazionali del Gran Sasso, Assergi, Italy
⁸ Dipartimento di Fisica Sperimentale, Università di Torino, and INFN Sezione di Torino, Torino, Italy
⁹ Dipartimento di Scienze Fisiche, Università di Napoli "Federico II", and INFN Sezione di Napoli, Napoli, Italy
¹⁰ Institut für Experimentalphysik III, Ruhr-Universität Bochum, Bochum, Germany
¹¹ Osservatorio Astronomico di Collurania, Teramo, and INFN Sezione di Napoli, Napoli, Italy
¹² Seconda Università di Napoli, Caserta, and INFN Sezione di Napoli, Napoli, Italy

As accepted by Eur. Phys. J. A, 15 December 2008

Abstract. Ultra-sensitive in-beam γ -ray spectroscopy studies for nuclear astrophysics are performed at the LUNA (Laboratory for Underground Nuclear Astrophysics) 400 kV accelerator, deep underground in Italy's Gran Sasso laboratory. By virtue of a specially constructed passive shield, the laboratory γ -ray background for $E_\gamma < 3$ MeV at LUNA has been reduced to levels comparable to those experienced in dedicated offline underground γ -counting setups. The γ -ray background induced by an incident α -beam has been studied. The data are used to evaluate the feasibility of sensitive in-beam experiments at LUNA and, by extension, at similar proposed facilities.

PACS. 25.40.Lw Radiative capture – 25.55.-e ^3H -, ^3He -, and ^4He -induced reactions – 29.20.Ba Electrostatic accelerators – 29.30.Kv X- and gamma-ray spectroscopy

1 Introduction

The Laboratory for Underground Nuclear Astrophysics (LUNA) [1] in Italy's Gran Sasso national laboratory (LNGS, Laboratori Nazionali del Gran Sasso) is the first and, to date, only accelerator facility running deep underground. It is dedicated to the study of astrophysically relevant nuclear reactions directly at or near the energies of astrophysical relevance. The LNGS rock overburden of 3800 meters water equivalent attenuates the flux of cosmic-ray induced muons by six orders of magnitude with respect to the Earth's surface [2]. The neutron flux at LNGS is three orders of magnitude lower than at the Earth's surface [3].

Motivated by the successful study of several astrophysically relevant nuclear reactions at LUNA, new un-

derground accelerators are proposed e.g. at LNGS [4], at the planned DUSEL facility in the United States [5,6], at Boulby mine in the United Kingdom [7], and at several possible sites in Romania [8]. Like the existing LUNA facility, these new proposals are driven by the need for precise data for astrophysical applications.

However, more general analysis techniques have already benefited from a great increase in sensitivity owing to the introduction of offline underground γ -counting with well-shielded high-purity germanium (HPGe) detectors [9, 10]. Therefore it is conceivable that also in-beam analysis techniques involving γ -ray detection [11] may benefit from the laboratory background suppression achieved by going underground.

In a previous work [12], the feasibility of radiative capture experiments at LUNA has been investigated for γ -ray energies above 3 MeV, and the γ -ray background induced by a proton beam has been localized using the Doppler

^a e-mail: d.bemmerer@fzd.de

^b Deceased.

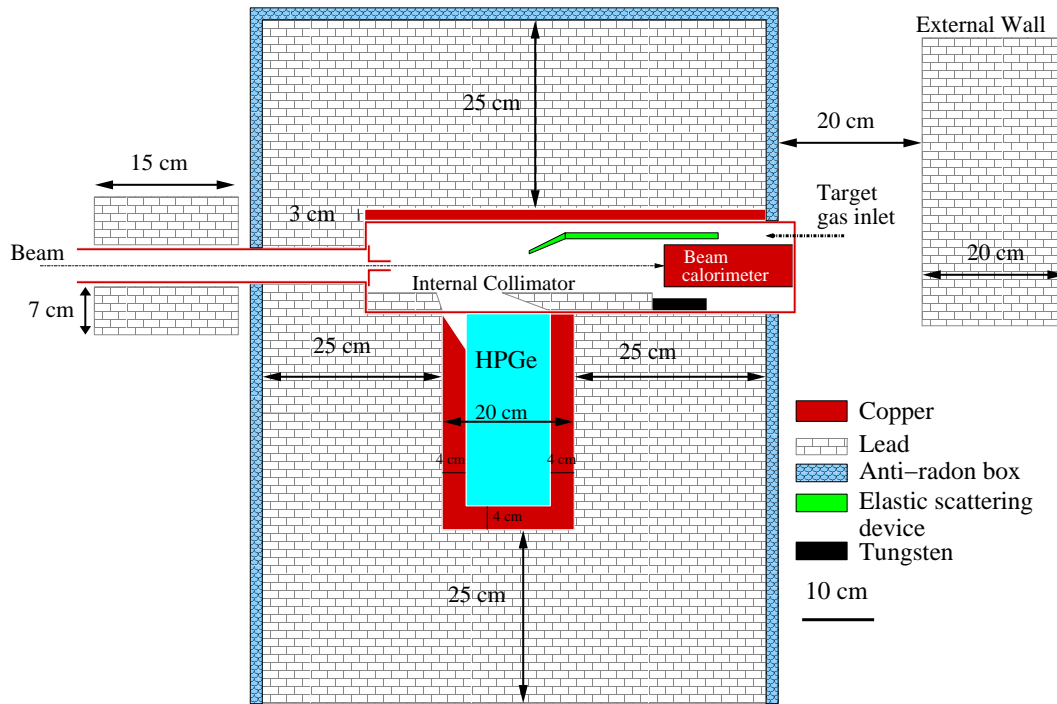


Fig. 1. Schematic view of experimental setup C (complete shielding).

shift. LUNA experiments where the analysis concentrates on γ -rays with $E_\gamma > 3$ MeV are special in that it is not necessary to strongly shield the detector against laboratory γ -ray background, simply because this background is negligible at LUNA [12], due to the reduced cosmic ray flux. When γ -rays with $E_\gamma < 3$ MeV are to be detected, however, the picture changes. For these low γ -ray energies, natural radioisotopes present at the LUNA site dominate the background, and a sophisticated shielding of setup and detector is required.

The γ -rays with $E_\gamma > 3$ MeV discussed in the previous study [12] are characteristic of radiative capture reactions with Q -values also above 3 MeV. In recent years, several such reactions have been studied at LUNA or are presently under study:

- the ${}^2\text{H}(p,\gamma){}^3\text{He}$ reaction [13], Q -value 5.493 MeV, important for hydrogen burning by the proton-proton chain in the Sun [14],
- the ${}^{14}\text{N}(p,\gamma){}^{15}\text{O}$ reaction [15, 16, 17, 18, 19], Q -value 7.297 MeV, bottleneck of the CNO cycle, important for solar neutrinos [20], globular cluster ages [21], and hydrogen shell burning in asymptotic giant branch stars [22, 23],
- the ${}^{25}\text{Mg}(p,\gamma){}^{26}\text{Al}$ reaction [24], Q -value 6.306 MeV, controlling the nucleosynthesis of radioactive ${}^{26}\text{Al}$, a tracer of live nucleosynthesis [25], and
- the ${}^{15}\text{N}(p,\gamma){}^{16}\text{O}$ reaction, Q -value 12.127 MeV, important in nova nucleosynthesis [26].

Recently, the technique of underground in-beam γ -spectrometry has been extended to radiative capture reactions with Q -values below 3 MeV:

- The ${}^3\text{He}(\alpha,\gamma){}^7\text{Be}$ reaction has been studied at LUNA, both by activation [27, 28, 29] and by in-beam γ -spectro-

metry [29, 30]. This reaction has a Q -value of 1.586 MeV. It controls the flux of ${}^7\text{Be}$ and ${}^8\text{B}$ neutrinos from the Sun [14, 20] and the production of ${}^7\text{Li}$ in big-bang nucleosynthesis [31].

- A study of the ${}^2\text{H}(\alpha,\gamma){}^6\text{Li}$ reaction is planned at LUNA. This reaction has a Q -value of 1.474 MeV and is important for big-bang nucleosynthesis [31].

Further astrophysically important reactions with low Q -value that merit study are, for example,

- the ${}^{12}\text{C}(p,\gamma){}^{13}\text{N}$ reaction [32], Q -value 1.943 MeV, important for pre-equilibrium CNO burning [20],
- the ${}^{12}\text{C}({}^{12}\text{C},\alpha){}^{20}\text{Ne}$ (Q -value 4.617 MeV, main γ -ray energy 1634 keV) and ${}^{12}\text{C}({}^{12}\text{C},p){}^{23}\text{Na}$ (Q -value 2.241 MeV, main γ -ray energy 440 keV) reactions [33], important for carbon burning in massive stars [34], and
- the ${}^{24}\text{Mg}(p,\gamma){}^{25}\text{Al}$ reaction [35], Q -value 2.272 MeV, important for hydrogen burning in massive stars [34].

The aim of the present work is to facilitate the underground study of radiative capture reactions for nuclear astrophysics. It concentrates on reactions with low Q -value or low energy of the emitted γ -rays, extending the previous study [12] to γ -ray energies below 3 MeV. The present considerations apply not only at LUNA, but can be extended to other potential underground accelerator sites [5, 6, 7, 8].

In addition, the previous study of proton-beam-induced γ -ray background [12] is taken one step further here, studying the γ -ray background induced by an intensive α -beam.

The present work is organized as follows. In section 2, the experimental setup is described. Section 3 shows the laboratory γ -ray background observed in several stages of

completion of the setup. Section 4 reports on in-beam γ -ray background studies with an intensive α -beam. In section 5, the background data are used to evaluate the feasibility of in-beam γ -spectroscopic experiments deep underground.

2 Experimental setup

The setup is sited at the LUNA2 400 kV accelerator [36] facility. It consists of a windowless, differentially pumped gas target and a shielded HPGe detector described below. The construction of this ultra-sensitive setup was necessary for the LUNA experiment on the ${}^3\text{He}(\alpha,\gamma){}^7\text{Be}$ reaction at unprecedented low energies [27, 28, 29, 30].

The HPGe detector is a Canberra ultra-low background p-type coaxial detector with 137% relative efficiency. The endcap of the detector is made of low-background copper, and the cryostat is connected to the crystal by a 25 cm long cold finger. The crystal is oriented at 90° with respect to the cold finger, so that the direct line of sight from the cryostat to the crystal can be shielded by a 25 cm thick layer of lead.

The ion beam from the LUNA2 accelerator first passes a disk-shaped watercooled collimator with 7 mm inner diameter, and then it enters the gas target chamber. The target chamber (fig. 1), made of oxygen free high conductivity (OFHC) copper, is 60 cm long and has 12 cm by 11 cm area. The ion beam is stopped, inside the target chamber, on a copper disk that serves as the hot side of a beam calorimeter with constant temperature gradient [37].

The shielding consists of several layers and surrounds detector and target chamber, excepting two holes for letting in the ion beam and for the beam calorimeter. It is designed in such a way that the germanium crystal of the detector is typically shielded by 4 cm copper and 25 cm lead. The innermost shielding layer surrounding the detector is made of OFHC copper bricks machined so that the detector fits inside with only 1-2 mm of space left free. A 3 cm thick OFHC copper plate above the target chamber carries the weight of the upper half of the lead shield (fig. 2). The remainder of the shield is made of lead bricks with low ${}^{210}\text{Pb}$ content (25 Bq/kg ${}^{210}\text{Pb}$, supplied by JLGoslar, Germany) and is 25 cm thick. The lead bricks have been cleaned with citric acid prior to mounting, in order to remove accumulated dust and surface oxidation. In order to avoid γ -rays from the decay of radon daughters, the setup is enclosed in a plexiglass anti-radon box that is flushed with the nitrogen gas evaporating from the HPGe detector's dewar. The gas volume inside the anti-radon box is approximately 4 liters.

Outside the anti-radon box, a 15 cm thick wall of the aforementioned low-background lead is placed upstream of the target chamber. In addition, a 20 cm thick wall of the same lead is placed behind the end of the calorimeter (fig. 1). Inside the target chamber, the γ -rays emitted within the gas target are collimated by 3 cm thick trapezoidal-shaped lead bricks that also serve as additional shield. An elastic scattering device for studies of

effective target gas density and gas contaminations is included inside the chamber [38]. In order to limit possible γ -emissions, the elastic scattering device has been made of Delrin.

For the purpose of the present study, three experimental configurations called setups A, B, and C are considered. Setups A, B, and C are all sited in the LUNA2 accelerator room deep underground.

- A. HPGe detector without any shield.
- B. HPGe detector with complete shield except for
 - inner trapezoidal lead collimator,
 - 20 cm lead wall behind the calorimeter, and
 - anti-radon box.
- C. HPGe detector with complete shield (fig. 1).

For comparison, also a fourth experimental configuration is considered, here called setup LLL: A HPGe detector of similar size (125% relative efficiency) and equal geometry to the present one. It is shielded with 25 cm low-background lead including an inner lining of quasi ${}^{210}\text{Pb}$ -free lead from a sunken Roman ship, and it has a highly efficient anti-radon box [9]. This detector is placed outside the LUNA2 accelerator room, in the LNGS low-background laboratory (LLL) [10]. Setup LLL is dedicated to measurements of extremely low γ -activities, as opposed to the in-beam setups A-C. As a consequence, no entrance pipe for the ion beam has been provided in setup LLL, improving the shielding.

Setup C has been used for the in-beam γ -spectroscopic part of the LUNA ${}^3\text{He}(\alpha,\gamma){}^7\text{Be}$ study [29, 30]. Setup LLL has been used for part of the ${}^7\text{Be}$ -activity counting in that same study [27, 28, 29, 30].

3 Laboratory γ -ray background studies for $E_\gamma < 3 \text{ MeV}$

The laboratory γ -ray background has been studied for setups A, B, and C, with running times of several days without ion beam for each setup. For comparison, also the spectrum taken with an inert sample (${}^4\text{He}+{}^4\text{He}$ irradiated OFHC copper [27]) on detector LLL is shown.

Comparing the unshielded setup A with the shielded setup B (fig. 3), a reduction of three orders of magnitude in the γ -ray continuum below 2615 keV is observed, and the summing lines above the 2615 keV ${}^{208}\text{Tl}$ line are no longer evident. In addition, the counting rate for the most important single γ -lines is reduced by three orders of magnitude or more (table 1).

Improving the shielding from setup B to the final setup C yields up to another order of magnitude suppression in the γ -continuum below 2615 keV. The ${}^{40}\text{K}$ (1461 keV) and ${}^{208}\text{Tl}$ (2615 keV) lines are reduced by a factor 2 and 3, respectively. The counting rates of these two lines are dominated by γ -emitters outside the setup: in construction materials for ${}^{40}\text{K}$, in the walls of the LNGS tunnel for the Thorium daughter ${}^{208}\text{Tl}$. These sources are already well shielded by setup B. The 15 cm thick lead wall behind the calorimeter and the internal lead collimator improve

E_γ [keV]	511	609	1120	1461	1730	1764	2615
Setup A, offline	762 \pm 4	3729 \pm 4	1278 \pm 3	4870 \pm 4	246 \pm 2	1350 \pm 2	1325 \pm 2
Setup B, offline	0.60 \pm 0.13	3.9 \pm 0.2	1.33 \pm 0.12	0.93 \pm 0.11	0.26 \pm 0.06	1.18 \pm 0.10	0.42 \pm 0.06
Setup B, α -beam	1.74 \pm 0.32	4.6 \pm 0.4	1.9 \pm 0.3	0.51 \pm 0.17	0.32 \pm 0.11	1.06 \pm 0.19	0.55 \pm 0.11
Setup C, offline	0.09 \pm 0.04	0.30 \pm 0.04	0.15 \pm 0.02	0.42 \pm 0.03	0.038 \pm 0.010	0.098 \pm 0.014	0.12 \pm 0.02
Setup C, α -beam	0.32 \pm 0.13	0.31 \pm 0.10	<0.08	0.37 \pm 0.08	<0.04	0.08 \pm 0.05	0.06 \pm 0.03
Setup LLL, offline	<0.04	0.055 \pm 0.018	0.013 \pm 0.008	0.098 \pm 0.018	<0.011	0.012 \pm 0.007	0.016 \pm 0.005

Table 1. Counting rate in counts/hour for selected γ -lines. The laboratory background (offline) runs in setups A, B, and C are discussed in section 3. The in-beam runs in setups B and C are discussed in section 4. For comparison, the corresponding numbers are also given for an inert sample counted in setup LLL at the LNGS low level laboratory. Upper limits, where applicable, are given for 2σ confidence level.

Reaction γ -ray ROI [keV]	$^{12}\text{C}(^{12}\text{C},\text{p})^{23}\text{Na}$ 425-455	$^2\text{H}(\alpha,\gamma)^6\text{Li}$ 1555-1585	$^{12}\text{C}(^{12}\text{C},\alpha)^{20}\text{Ne}$ 1619-1649	$^3\text{He}(\alpha,\gamma)^7\text{Be}$ 1731-1761	$^{12}\text{C}(\text{p},\gamma)^{13}\text{N}$ 2004-2034
Setup A, offline	$(2.016\pm 0.002)\cdot 10^2$	$(1.585\pm 0.004)\cdot 10^1$	$(1.481\pm 0.004)\cdot 10^1$	$(1.332\pm 0.004)\cdot 10^1$	$(5.73\pm 0.02)\cdot 10^0$
Setup B, offline	$(1.70\pm 0.07)\cdot 10^{-1}$	$(1.3\pm 0.2)\cdot 10^{-2}$	$(1.1\pm 0.2)\cdot 10^{-2}$	$(1.1\pm 0.2)\cdot 10^{-2}$	$(6.7\pm 1.4)\cdot 10^{-3}$
Setup B, α -beam	$(1.87\pm 0.12)\cdot 10^{-1}$	$(2.1\pm 0.4)\cdot 10^{-2}$	$(1.1\pm 0.3)\cdot 10^{-2}$	$(6\pm 2)\cdot 10^{-3}$	$(4\pm 2)\cdot 10^{-3}$
Setup C, offline	$(7.2\pm 0.2)\cdot 10^{-2}$	$(1.5\pm 0.3)\cdot 10^{-3}$	$(1.4\pm 0.3)\cdot 10^{-3}$	$(1.1\pm 0.3)\cdot 10^{-3}$	$(9\pm 3)\cdot 10^{-4}$
Setup C, α -beam	$(7.8\pm 0.6)\cdot 10^{-2}$	$(2.7\pm 1.2)\cdot 10^{-3}$	$(1.1\pm 0.8)\cdot 10^{-3}$	$(2.2\pm 1.1)\cdot 10^{-3}$	$(1.1\pm 0.8)\cdot 10^{-3}$

Table 2. Same as table 1, but instead of γ -line counting rates, the continuum background rate in counts/(keV hour) is given. The reactions mentioned in the first line of the table are discussed in section 5.

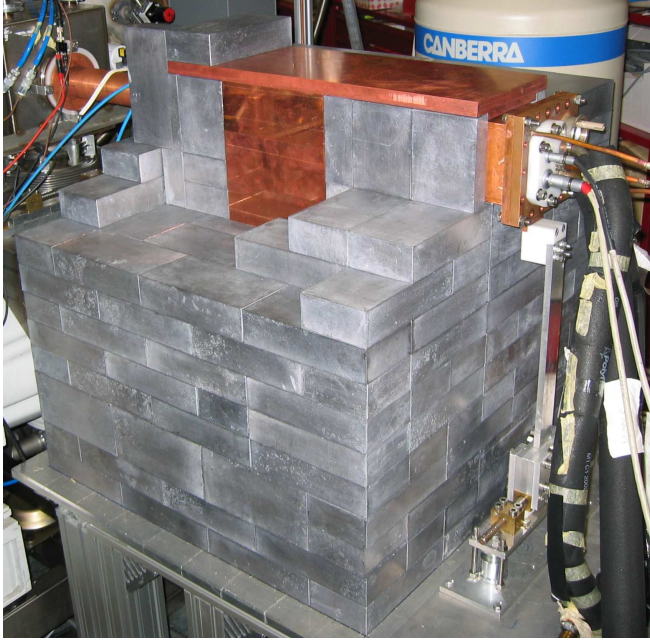


Fig. 2. Photo taken during the construction of the shield. The lower half of the lead shield is already complete, as well as the copper shield for the detector and the copper plate above the target chamber. The back plate and connectors of the beam calorimeter are visible in the upper right corner. The copper tube for the beam inlet is seen in the upper left corner. The upper half of the lead shield was not yet installed when the photo was taken.

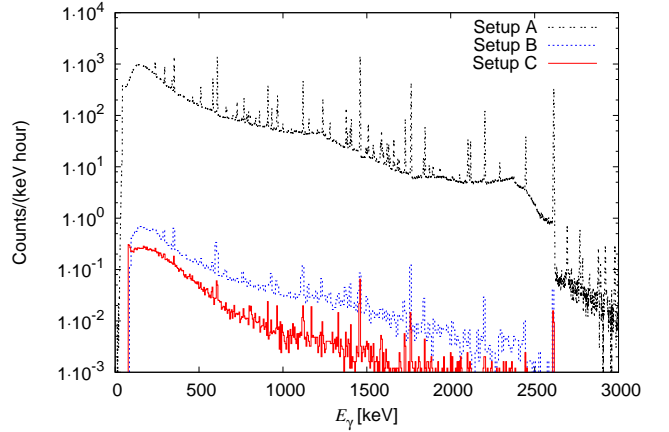


Fig. 3. Laboratory γ -ray background spectra for setups A (black dashed line), B (blue dotted line), and C (red full line). See table 1 for the counting rate of selected lines and table 3 for the assignment of the lines evident in spectrum C.

The counting rates in the 609, 1120, 1730, and 1764 keV lines (all assigned to ^{214}Bi in the present case) are improved by about a factor 10 from setup B to setup C. This is due to the operation of the anti-radon box that reduces the amount of ^{222}Rn ($t_{1/2} = 3.8$ d, progenitor of ^{214}Bi) present in the remaining air pockets near the detector.

A similar reduction is evident for the 511 keV annihilation line in setup C; it is just barely significant at 2σ level. Because of the deep-underground location, muon-induced pair production and decay of stopped μ^+ [39] only contribute negligibly to the counting rate in that line. Different from γ -ray spectroscopy systems at the surface of the Earth, in the present case this line can therefore be effec-

the effective shielding thickness for a limited solid angle; hence the limited improvement of only a factor 2-3.

E_γ [keV]	Nuclide	Source
352	^{214}Pb	Radon gas
511	$e^+ e^-$	β^+ emitters
583	^{208}Tl	Thorium chain, tunnel walls
609	^{214}Bi	Radon gas
768	^{214}Bi	Radon gas
911	^{228}Ac	Thorium chain, tunnel walls
965	^{228}Ac	Thorium chain, tunnel walls
969	^{228}Ac	Thorium chain, tunnel walls
1120	^{214}Bi	Radon gas
1173	^{60}Co	Detector contamination
1238	^{214}Bi	Radon gas
1333	^{60}Co	Detector contamination
1408	^{214}Bi	Radon gas
1461	^{40}K	Potassium in construction materials
1588	^{228}Ac	Thorium chain, tunnel walls
1730	^{214}Bi	Radon gas
1764	^{214}Bi	Radon gas
1847	^{214}Bi	Radon gas
2615	^{208}Tl	Thorium chain, tunnel walls

Table 3. List of γ -lines evident at 2σ level in the laboratory background of setup C (fig. 3).

tively attenuated by passive shielding against β^+ emitters, and by eliminating β^+ -emitting contaminations.

The remaining γ -lines evident in spectrum C (fig. 3) can all be traced back to natural radionuclides present in the laboratory, detector, or radon gas (table 3). No neutron-induced (n,γ), ($n,n'\gamma$), or activation lines [39] can be identified in spectrum C after 21 days counting time.

In order to judge the quality of the background suppression in spectrum C, this spectrum is compared with an inert sample [27] counted in setup LLL (fig. 4). The spectra have not been corrected for the slightly different size of the crystals: 137% in setups A-C and 125% in setup LLL. The γ -continuum below 1162 keV (Q -value of the β^- -decay of ^{210}Bi , daughter of ^{210}Pb) is up to one order of magnitude higher in setup C when compared to setup LLL. Some of this continuum stems from bremsstrahlung emitted by electrons created in ^{210}Bi β^- decay. The modern low-background lead used in setup C still has more ^{210}Pb than the Roman ship lead used for the inner shield lining in setup LLL.

The higher counting rates in the ^{40}K (1461 keV), ^{208}Tl (2615 keV), and radon (609, 1120, 1730, and 1764 keV) lines in setup C with respect to setup LLL, with a concomitant increase in the Compton continuum, are ascribed to the inevitable opening for the beam pipe, which leads to a small window of not optimally shielded solid angle.

4 γ -ray background induced by the α -beam

As a next step, two experiments with α -beam have been performed.

In the first in-beam experiment, the beamstop in setup B has been bombarded for 47 hours with a $^4\text{He}^+$ -beam of $E_\alpha = 350$ keV and $110 \mu\text{A}$ intensity from the LUNA2 accelerator. During this experiment, the gas target setup

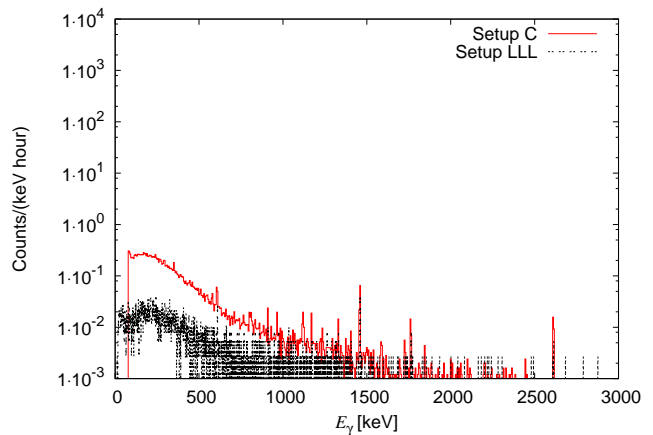


Fig. 4. Laboratory γ -ray background spectra, setup C (red full line, same as in fig. 3), and inert sample counted in setup LLL (black dashed line). See table 1 for the counting rate of selected lines and table 3 for the assignment of the lines evident in spectrum C.

was evacuated to better than 10^{-3} mbar. The in-beam spectrum shows no additional γ -lines with respect to the laboratory background (fig. 5).

The only difference between the in-beam and offline spectra in setup B that is significant at 2σ level is a higher counting rate in the 511 keV e^+e^- annihilation line. The continuum counting rates of relevance for in-beam γ -spectroscopic studies are consistent (table 2). In order to explain the 511 keV counting rate increase, one has to assume some creation of β^+ emitters by the α -beam. Due to the absence of other new γ -lines in the spectrum, it is impossible to assign a particular nuclide (and, by extension, a particular reaction producing that nuclide) as the supposed β^+ emitter. However, it should be noted that the in-beam 511 keV counting rate is still 400 times lower than in the unshielded case of setup A.

The second in-beam experiment, was performed with the fully shielded setup C and a $^4\text{He}^+$ -beam of $E_\alpha = 400$ keV and $240 \mu\text{A}$ intensity for a 62 hour long irradiation [29,30]. The gas target was filled with 0.7 mbar ^4He gas (chemical purity 99.9999%) during this experiment. Just as in the previous case, the in-beam spectrum shows no additional γ -lines with respect to the corresponding laboratory background (fig. 5).

The line counting rates (table 1), as well as the continuum counting rates of relevance for in-beam γ -spectroscopic studies (table 2) are consistent between in-beam and offline runs in setup C. Only at the lowest γ -ray energies, the in-beam continuum counting rate is slightly higher, but this difference is only significant at the 1σ level. For the 511 keV line, a slightly higher counting rate is observed in the in-beam spectrum, but the increase is not significant at the 2σ level.

Summarizing, in two exemplary configurations without gas ($p < 0.001$ mbar) and with 0.7 mbar ^4He gas in the target, the α -beam induced background was shown to be negligible when compared with the already low labo-

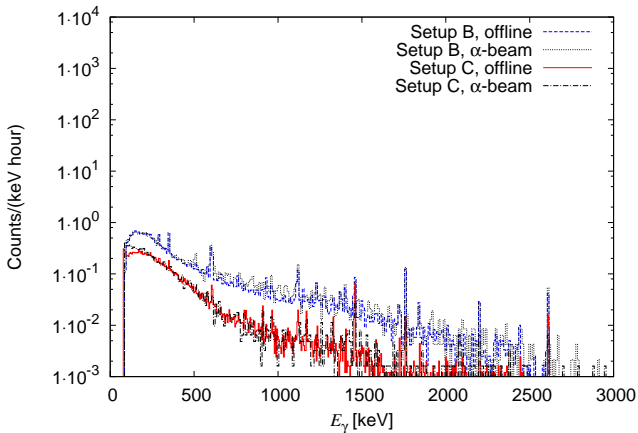


Fig. 5. Comparison of offline and in-beam γ -spectra: Setup B, offline (blue dashed line) and with α -beam (black dotted line). Setup C, offline (red full line) and with α -beam (black dot-dashed line).

ratory background. This conclusion has been verified for a number of specific nuclear reactions (table 2).

5 Feasibility of cross-section measurements at LUNA

In order to evaluate the feasibility of in-beam cross-section measurements, the present background data are used to calculate the hypothetical cross-section $\sigma_{S=N}(E_\gamma)$ for which the expected 'signal' S would be equal to the 'noise' N, here taken as the laboratory γ -ray background in a 30 keV wide γ -ray region of interest [$E_\gamma - 15$ keV; $E_\gamma + 15$ keV]

$$\sigma_{S=N}(E_\gamma) = \frac{\text{LabBG}(E_\gamma) \cdot 30 \text{ keV}}{\varepsilon_\gamma(E_\gamma) \cdot 6 \cdot 10^{17} \frac{\text{atoms}}{\text{cm}^2} \cdot 250 \mu\text{A} \cdot 3600 \text{ s}} \quad (1)$$

Here, $\text{LabBG}(E_\gamma)$ is the laboratory background counting rate per keV and hour plotted in fig. 3, for setup B or C, respectively. The γ -ray detection efficiency in the present geometry is $\varepsilon_\gamma(E_\gamma)$ (0.4% at $E_\gamma = 1.33$ MeV). An effective target thickness of $6 \cdot 10^{17}$ atoms/cm² is assumed, corresponding e.g. in the ${}^3\text{He}(\alpha, \gamma){}^7\text{Be}$ case to 9 keV energy loss in the target [27, 28]. Due to the steep decline of the Coulomb barrier penetrability with lower energy, as a rule of thumb in LUNA-type experiments an increase of the target thickness beyond 10^{18} atoms/cm² does not increase the yield any further [34]. As ion beam intensity, a typical LUNA value of 250 particle- μA is assumed, and a branching ratio of 1 for the γ -ray of interest has been supposed.

The laboratory background level is evaluated for a 30 keV wide region of interest in E_γ (fig. 6). This approach is valid for primary γ -rays from capture into a particular level in the compound nucleus, with a target thickness equivalent to 30 keV energy loss by the primary beam. For light target nuclei like ${}^3\text{He}$ and ${}^2\text{H}$, the Doppler shift for γ -rays emitted before or behind the detector makes it

necessary to maintain a 30 keV wide region of interest even if the energy loss in the target is lower. For secondary γ -rays, the resolution of the γ -ray from the decay of the relevant excited state in the Compound nucleus (again taking Doppler corrections into account) should be adopted instead of 30 keV in eq. (1). This leads to a somewhat improved sensitivity, so for secondary γ -rays the present $\sigma_{S=N}(E_\gamma)$ values (fig. 6) should be taken as a conservative upper limit.

To put the sensitivity data in the proper astrophysical context, some representative examples for nuclear reactions are worthy to be studied afresh are mentioned here. Concerning the reactions responsible for the production of ${}^6,7\text{Li}$ in big-bang nucleosynthesis ($T_9 \approx 0.3$ -0.9; T_9 stands for the temperature in 10^9 K), ${}^2\text{H}(\alpha, \gamma){}^6\text{Li}$ and ${}^3\text{He}(\alpha, \gamma){}^7\text{Be}$, the present sensitivity is sufficient for an experimental study directly at the Gamow energy (table 4). Such a study has indeed been performed in the ${}^3\text{He}(\alpha, \gamma){}^7\text{Be}$ case [29, 30]. The CNO-cycle reaction ${}^{12}\text{C}(p, \gamma){}^{13}\text{N}$ at temperatures typical for hydrogen shell burning is an analogous case; also here a direct study is feasible.

For the temperature at the center of the Sun, $T_9 \approx 0.016$, however, a study directly at the Gamow energy would be hampered by the prohibitively low cross-section for the two example reactions ${}^3\text{He}(\alpha, \gamma){}^7\text{Be}$ and ${}^{12}\text{C}(p, \gamma){}^{13}\text{N}$ (table 4).

Similar considerations apply for stable carbon burning, where temperatures of $T_9 = 0.5$ -1.0 are experienced. Two of the most important carbon burning reactions, ${}^{12}\text{C}({}^{12}\text{C}, \alpha){}^{20}\text{Ne}$ and ${}^{12}\text{C}({}^{12}\text{C}, p){}^{23}\text{Na}$, have recently been studied at the surface of the earth [33]. The off-resonance data were limited by the laboratory background [33]. One can estimate the non-resonant contribution, to which any hypothetical resonance should be added, to be constant with energy and equal to the value found in Ref. [33]. Based on this assumption, for these two reactions a non-resonant cross-section about four orders below the present $\sigma_{S=N}$ is found (table 4).

For the present estimates (fig. 6, table 4), the ion beam induced γ -background is assumed to be negligible at the γ -ray energies of interest. Whether or not this assumption is valid depends on the precise experimental setup, target, beam, and beam energy to be used. Therefore it is difficult to make generalized statements regarding the beam-induced background.

The present assumption of negligible beam induced γ -background was shown to be fulfilled in two selected cases with α -beam at LUNA energies (section 4), and previously in one selected case for proton beam [12]. All of these cases involved gas targets. It is much more difficult to reliably predict the beam-induced background from ${}^{12}\text{C}$ -beam at energies close to E_{Gamow} , because unlike the proton- and α -beam induced background this has not yet been investigated. In case a solid carbon target is selected, this presents an additional challenge. A dedicated study of ${}^{12}\text{C}$ -beam induced γ -background at energies of 1-2 MeV (much higher than the dynamic range of the current LUNA accelerator) is clearly called for as a first step

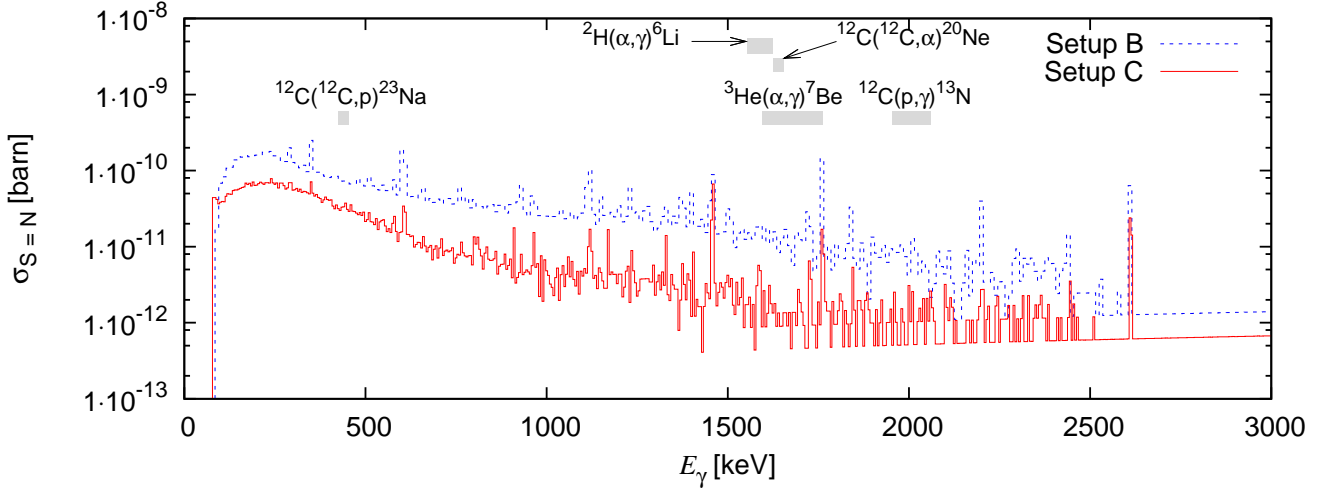


Fig. 6. Cross-section $\sigma_{S=N}(E_\gamma)$ defined by eq. (1), for setups B (blue dashed line) and C (red full line). The γ -ray energies of interest for the nuclear reactions listed in tables 2 and 4 are indicated by gray bars.

Reaction	Scenario	T_9 [10^9 K]	E_{Gamow} [keV]	$\sigma(E_{\text{Gamow}})$ [barn]	E_γ [keV]	$\sigma_{S=N}$ [barn]
${}^2\text{H}(\alpha,\gamma){}^6\text{Li}$	Big-bang nucleosynthesis	0.3	96	$2 \cdot 10^{-11}$	1570	$1.7 \cdot 10^{-12}$
${}^3\text{He}(\alpha,\gamma){}^7\text{Be}$	Big-bang nucleosynthesis	0.3	160	$1 \cdot 10^{-8}$	1746	$1.3 \cdot 10^{-12}$
	Proton-proton chain in the Sun	0.016	23	$4 \cdot 10^{-17}$	1609	$1.8 \cdot 10^{-12}$
${}^{12}\text{C}(p,\gamma){}^{13}\text{N}$	CNO cycle burning in the Sun	0.016	25	$2 \cdot 10^{-17}$	1968	$1.1 \cdot 10^{-12}$
	Hydrogen shell burning	0.085	76	$3 \cdot 10^{-11}$	2019	$1.2 \cdot 10^{-12}$
${}^{12}\text{C}({}^{12}\text{C},p){}^{23}\text{Na}$ (non-res.)	Core carbon burning	0.5	1500	$2 \cdot 10^{-16}$	440	$3 \cdot 10^{-11}$
${}^{12}\text{C}({}^{12}\text{C},\alpha){}^{20}\text{Ne}$ (non-res.)	Core carbon burning	0.5	1500	$2 \cdot 10^{-16}$	1634	$1.6 \cdot 10^{-12}$

Table 4. Reactions of astrophysical interest discussed in the text. The relevant astrophysical scenario, typical temperature T_9 and corresponding Gamow energy [34] E_{Gamow} are also given. The expected cross-section at E_{Gamow} has been estimated. The relevant γ -ray energy is also shown. For the case of setup C, the cross-section $\sigma_{S=N}(E_\gamma)$ has been calculated following eq. (1).

to underground experiments with heavy ion beams such as ${}^{12}\text{C}$.

In summary, for the present LUNA accelerator and present ultra-sensitive setup including a single large HPGe detector, it has been shown that cross sections of typically 1-10 pbarn can well be measured. The precise value depends on the γ -ray energy, and on the above discussed assumption that the beam induced background is under control. The extent to which the present feasibility data can be extended to proposed underground accelerator laboratories outside the LNGS facility [5,6,7,8] has to be evaluated based on the precise background conditions at those sites.

6 Summary and outlook

The feasibility of ultra-sensitive in-beam γ -ray spectroscopic studies for reactions with γ -rays of $E_\gamma < 3$ MeV in the exit channel has been investigated at the LUNA deep underground accelerator facility.

To this end, the laboratory and ion-beam-induced γ -ray background for γ -energies $E_\gamma < 3$ MeV has been studied. Using a sophisticated passive shielding, the laboratory

γ -ray background for in-beam γ -spectroscopic studies has been reduced to levels not far from those achieved in state-of-the-art offline underground γ -counting. For two selected cases, the γ -ray background induced by an intensive α -beam has been shown to be negligible when compared with the laboratory background.

The data were then used to compute a γ -ray energy dependent cross section for which the expected signal is equal to the expected background.

Based on several concrete cases, it has been shown that ultra-sensitive underground in-beam γ -ray spectroscopy has great potential for future contributions to experimental nuclear astrophysics.

Acknowledgments

The present work has been supported by INFN and in part by the EU (ILIAS-TA RII3-CT-2004-506222), OTKA (T49245 and K68801), and DFG (Ro 429/41).

References

1. U. Greife *et al.*, Nucl. Inst. Meth. A **350**, 327 (1994).

2. S. P. Ahlen *et al.*, Phys. Lett. B **249**, 149 (1990).
3. P. Belli *et al.*, Nuovo Cimento **101A**, 959 (1989).
4. Nuclear Physics European Collaboration Committee (NuPECC), Roadmap 2005, available at http://www.nupecc.org/pub/NuPECC_Roadmap.pdf.
5. W. Haxton, K. Philpott, R. Holtz, P. Long, and J. Wilkerson, Nucl. Inst. Meth. A **570**, 414 (2007).
6. DOE/NSF Nuclear Science Advisory Committee, arXiv:0809.3137.
7. F. Strieder, J. Phys. G **35**, 014009 (2008).
8. C. Bordeanu, C. Rolfs, R. Margineanu, F. Negoita, and C. Simion, J. Phys. G **35**, 014011 (2008).
9. C. Arpesella, Appl. Radiat. Isot. **47**, 991 (1996).
10. M. Laubenstein *et al.*, Appl. Radiat. Isot. **61**, 167 (2004).
11. S. Johansson, J. Campbell, and K. Malmqvist, editors, *Particle-Induced X-Ray Emission Spectrometry* (Wiley, 1995).
12. D. Bemmerer *et al.*, Eur. Phys. J. A **24**, 313 (2005).
13. C. Casella *et al.*, Nucl. Phys. A **706**, 203 (2002).
14. J. N. Bahcall, A. M. Serenelli, and S. Basu, Astrophys. J. **621**, L85 (2005).
15. A. Formicola *et al.*, Phys. Lett. B **591**, 61 (2004).
16. G. Imbriani *et al.*, Eur. Phys. J. A **25**, 455 (2005).
17. A. Lemut *et al.*, Phys. Lett. B **634**, 483 (2006).
18. D. Bemmerer *et al.*, Nucl. Phys. A **779**, 297 (2006).
19. M. Marta *et al.*, Phys. Rev. C **78**, 022802(R) (2008).
20. W. C. Haxton and A. M. Serenelli, Astrophys. J. **687**, 678 (2008).
21. G. Imbriani *et al.*, Astron. Astrophys. **420**, 625 (2004).
22. F. Herwig and S. M. Austin, Astrophys. J. **613**, L73 (2004).
23. F. Herwig, S. M. Austin, and J. C. Lattanzio, Phys. Rev. C **73**, 025802 (2006).
24. A. Formicola *et al.*, J. Phys. G **35**, 014013 (2008).
25. R. Diehl *et al.*, Nature **439**, 45 (2006).
26. C. Iliadis, A. Champagne, J. José, S. Starrfield, and P. Tupper, Astrophys. J. Suppl. Ser. **142**, 105 (2002).
27. D. Bemmerer *et al.*, Phys. Rev. Lett. **97**, 122502 (2006).
28. G. Gyürky *et al.*, Phys. Rev. C **75**, 035805 (2007).
29. F. Confortola *et al.*, Phys. Rev. C **75**, 065803 (2007).
30. H. Costantini *et al.*, Nucl. Phys. A **814**, 144 (2008).
31. P. D. Serpico *et al.*, Journal of Cosmology and Astroparticle Physics **2004**, 010 (2004).
32. C. Rolfs and R. Azuma, Nucl. Phys. A **227**, 291 (1974).
33. T. Spillane *et al.*, Phys. Rev. Lett. **98**, 122501 (2007).
34. C. Iliadis, *Nuclear Physics of Stars* (Wiley-VCH, 2007).
35. D. C. Powell *et al.*, Nucl. Phys. A **660**, 349 (1999).
36. A. Formicola *et al.*, Nucl. Inst. Meth. A **507**, 609 (2003).
37. C. Casella *et al.*, Nucl. Inst. Meth. A **489**, 160 (2002).
38. M. Marta *et al.*, Nucl. Inst. Meth. A **569** (2006).
39. G. Heusser, Nucl. Inst. Meth. B **83**, 223 (1993).

An actively vetoed Clover γ -detector for nuclear astrophysics at LUNA

T. Szücs^{1,2}, D. Bemmerer^{3a}, C. Brogini⁴, A. Cacioli^{4,5}, F. Confortola⁶, P. Corvisiero⁶, Z. Elekes¹, A. Formicola⁷, Zs. Fülöp¹, G. Gervino⁸, A. Guglielmetti⁹, C. Gustavino⁷, Gy. Gyürky¹, G. Imbriani^{10,11}, M. Junker⁷, A. Lemut^{6b}, M. Marta³, C. Mazzocchi⁹, R. Menegazzo⁴, P. Prati⁶, V. Roca^{10,11}, C. Rolfs¹², C. Rossi Alvarez⁴, E. Somorjai¹, O. Straniero^{11,13}, F. Strieder¹², F. Terrasi^{11,14}, and H.P. Trautvetter¹²
(LUNA collaboration)

¹ Institute of Nuclear Research (ATOMKI), Debrecen, Hungary

² University of Debrecen, Debrecen, Hungary

³ Forschungszentrum Dresden-Rossendorf (FZD), Dresden, Germany

⁴ INFN Sezione di Padova, Padova, Italy

⁵ Dipartimento di Fisica, Università di Padova, Padova, Italy

⁶ Dipartimento di Fisica, Università di Genova, and INFN Sezione di Genova, Genova, Italy

⁷ INFN, Laboratori Nazionali del Gran Sasso, Assergi, Italy

⁸ Dipartimento di Fisica Sperimentale, Università di Torino, and INFN Sezione di Torino, Torino, Italy

⁹ Università degli Studi di Milano, and INFN Sezione di Milano, Milano, Italy

¹⁰ Dipartimento di Scienze Fisiche, Università di Napoli "Federico II", and INFN Sezione di Napoli, Napoli, Italy

¹¹ INFN Sezione di Napoli, Napoli, Italy

¹² Institut für Experimentalphysik III, Ruhr-Universität Bochum, Bochum, Germany

¹³ Osservatorio Astronomico di Collurania, Teramo, Italy

¹⁴ Seconda Università di Napoli, Caserta, Italy

Version accepted by Eur.Phys.J. A, April 1, 2010

Abstract. An escape-suppressed, composite high-purity germanium detector of the Clover type has been installed at the Laboratory for Underground Nuclear Astrophysics (LUNA) facility, deep underground in the Gran Sasso Laboratory, Italy. The laboratory γ -ray background of the Clover detector has been studied underground at LUNA and, for comparison, also in an overground laboratory. Spectra have been recorded both for the single segments and for the virtual detector formed by online addition of all four segments. The effect of the escape-suppression shield has been studied as well. Despite their generally higher intrinsic background, escape-suppressed detectors are found to be well suited for underground nuclear astrophysics studies. As an example for the advantage of using a composite detector deep underground, the weak ground state branching of the $E_p = 223$ keV resonance in the $^{24}\text{Mg}(p,\gamma)^{25}\text{Al}$ reaction is determined with improved precision.

PACS. 25.40.Lw Radiative capture – 29.30.Kv X- and gamma-ray spectroscopy – 29.40.Wk Solid-state detectors – 26.20.Cd Stellar hydrogen burning

1 Introduction

Recent advances in observations [1, e.g.] and in modeling [2,3] of the Sun and of stars have heightened the need for precise nuclear data on reactions of astrophysical interest. One approach to provide such data is to place a high-intensity particle accelerator deep underground, where the laboratory background in γ -ray detectors is reduced so that radiative capture reactions can be studied with improved sensitivity.

The Laboratory for Underground Nuclear Astrophysics (LUNA) has implemented this strategy, first with a 50 kV accelerator [4] and now with a 400 kV accelerator [5] placed in the underground facility of Laboratori Nazionali del Gran Sasso (LNGS)¹ in Assergi, Italy. LNGS is shielded from cosmic rays by a rock overburden equivalent to 3800 m water.

Benefiting from the resulting low γ -ray background, several nuclear reactions of astrophysical importance have been studied in recent years at LUNA [6,7,8,9,10,11,12,13]. In many cases, cross sections lower than ever reached before have been measured. Motivated by these advances,

^a e-mail: d.bemmerer@fzd.de

^b Present address: Lawrence Berkeley National Laboratory, Berkeley, USA

¹ Web site of the laboratory: <http://www.lngs.infn.it>

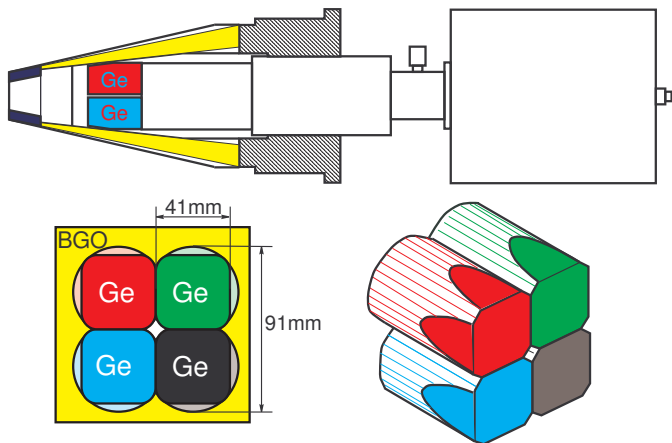


Fig. 1. Schematic cross section of the Clover-BGO system. The four germanium crystals are called red, green, black, and blue. The BGO escape-suppression shield (yellow) and the heavy-metal collimator on the front face (dark-blue) are also shown.

new underground accelerators have been proposed at a number of locations, namely: LNGS [14], the Canfranc laboratory in Spain [15], the planned DUSEL facility in the United States [16], Boulby mine in the United Kingdom [17], and Romania [18].

The present work is the third in a series [19,20] that aims to facilitate these efforts, by providing detailed background data on deep underground in-beam setups as a reference case. In the first article of the series, the laboratory background with no or only minor shielding was studied for high-purity germanium (HPGe) and bismuth germanate (BGO) γ -detectors, and it was shown that for $E_\gamma > 3$ MeV the laboratory γ -background at LUNA is typically three orders of magnitude lower than at the surface of the Earth [19]. The second article presented an ultra-low background (ULB) HPGe detector with a sophisticated passive shield at LUNA. For $E_\gamma \leq 3$ MeV, this in-beam setup [20] displayed a laboratory background close to that of dedicated, deep underground activity-counting setups [21].

Here, the effects of segmentation and of active shielding on the laboratory γ -background of a HPGe detector are studied. To this end, the background of a HPGe detector that has been used for a recent LUNA experiment [12] has been studied in detail. For some of the experiments, also a 5 cm thick lead shield has been added, allowing to investigate the combination of active and passive shielding. Finally, as an example of the potential applications of a composite HPGe detector deep underground, the weak branching ratio for the decay of the $E_p = 223$ keV resonance in the $^{24}\text{Mg}(p,\gamma)^{25}\text{Al}$ reaction to the ground state in ^{25}Al is redetermined.

2 Setup

For the experiment, a EURISYS Clover detector [22] has been used. This type of composite detector was selected

because it easily fits in the restricted space of an underground laboratory. It consists of four coaxial n-type HPGe detectors arranged like a four-leaf clover (fig. 1). The spacing between the crystals is only 0.2 mm, leading to a closely packed geometry. At the 1333 keV ^{60}Co line, a single crystal has a typical resolution of 2.2 keV and 20% relative efficiency.

The signals from the four crystals are split after the preamplifiers. One part is fed into four main amplifiers, and the signals are then digitized and recorded in self-triggered, histogramming mode. These four individual histograms were gainmatched and added channel by channel, to form just one histogram hereafter called "singles mode spectrum".

The second part is fed into an analog summing unit implementing the gain-matching and summing of the four signals. The analog sum signal is then passed to a fifth main amplifier and digitized. The signal can then be recorded either in free-running, self-triggered, mode (called hereafter "adback mode, free-running") or in anticoincidence with the signal from the BGO escape-suppression shield (called hereafter "adback mode, escape suppressed"). The virtual large detector formed by the adback mode has 122% relative efficiency, comparable to the HPGe detectors used for the previous background studies at LUNA [19,20].

The accidental suppression rate of the BGO escape-suppression shield was found to be 1%. The average number of hits per event was determined to be 1.1 for the laboratory background and 1.2 for the highest counting rate in-beam run, on the 278 keV resonance of the $^{14}\text{N}(p,\gamma)^{15}\text{O}$ reaction. The timing information from the individual crystals was not used. Due to the continuous character of the intensive ion beam at LUNA, no time correlation between ion beam and emitted γ -ray was possible.

In the present study, the Clover detector is always used in conjunction with a surrounding BGO scintillator. For the adback mode data, the BGO can act as a Compton suppression veto. For the singles mode data, the BGO was in effect only a passive shield. The detector was used in horizontal geometry, so that in adback mode, the BGO shield can act as a veto against penetrating muons passing the germanium detector volume.

3 Off-line experiments and results

For the underground experiments presented here, the Clover detector was placed deep underground in the LUNA facility [23] of LNGS. For a first set of measurements, it was mounted in horizontal geometry at the 45-2 beamline of the 400 kV LUNA2 accelerator, and no lead shielding was used. During the background measurement presented in the present section, the LUNA beam was off. This setup was used both for the off-line experiments without lead shield and for the in-beam experiment described below in sec. 4.

In a second part of the underground experiments, the detector was placed on the floor of the LUNA hall and

completely surrounded with a 5 cm thick shield of standard lead.

For comparison, measurements at the surface of the Earth were performed at FZD. The experimental hall has a ceiling equivalent to about 0.3 m water. No lead shielding was applied.

3.1 Laboratory background γ -lines

The main γ -lines present in the laboratory background (fig. 2) are identified as:

- 511 keV e^+e^- annihilation peak
- 570 and 1064 keV lines from ^{207}Bi . This isotope is a commonly observed contamination in BGO material, produced through the $^{206}\text{Pb}(p,\gamma)^{207}\text{Bi}$ reaction by cosmic rays. All BGO material shows some ^{207}Bi impurity, except in cases where the bismuth starting material has been obtained from lead-free ore.
- 609, 1120, and 2204 keV lines from the radon daughter ^{214}Bi . No anti-radon shielding was applied for the present study.
- 1173 and 1333 keV from some ^{60}Co contamination present in the BGO crystal.
- 1461 keV from ^{40}K present in the laboratory.
- 2615 keV from ^{208}Tl , in the Thorium chain. The background continuum caused by pileup of the laboratory background reaches up to 5200 keV, twice the energy of this highest γ -line (fig. 3).

Some further lines from radon daughters (^{228}Ac and ^{214}Bi) have also been observed but are neglected in the further discussion because they behave in an analogous manner to the three ^{214}Bi lines mentioned above.

The counting rates of the above mentioned γ -lines are summarized in table 1, for the two experiments at LUNA without and with lead shield, and for the reference case at the surface of the Earth. For comparison, the data from the previous study at the 45-1 beamline at LUNA using a single, large HPGe detector with 137% relative efficiency are also shown [20]. Those previous data [20] have been taken in several configurations. Here the previous data taken without shield and those taken with a sophisticated passive shield (25 cm selected lead with low ^{210}Pb content, 4 cm oxygen free high purity copper, anti-radon box) are shown for comparison.

As expected, the counting rates of the γ -lines from radioactive decays are hardly affected by going underground to LUNA because they are dominated by radioisotopes present in the walls of the laboratory or in the detector. When comparing the overground with the unshielded LUNA spectra, it is seen that the radon background (^{214}Bi) is a factor two lower at LUNA, due to the better ventilation of the LUNA site. The thorium background (^{208}Tl) is lower by a factor four, due to the different characteristics of the rock surrounding the LUNA site, as compared to the FZD hall. A similar effect is observed for the ^{40}K line and the e^+e^- annihilation peak. Only the γ -lines due to impurities contained in the BGO

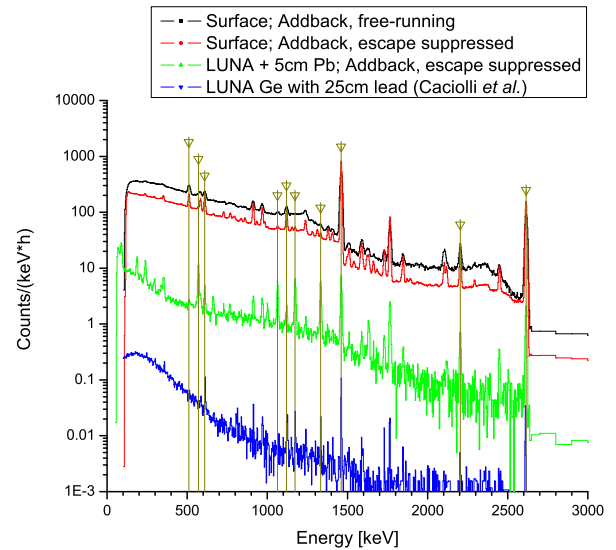


Fig. 2. Low energy part of the recorded laboratory γ -background spectra, compared with the previously described, strongly shielded setup at the 45-1 beamline at LUNA [20]. The lines marked with arrows are discussed in the text.

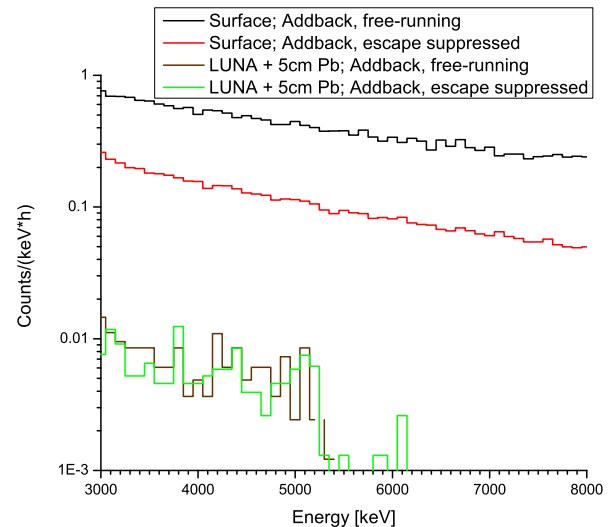


Fig. 3. High-energy part of the offline γ -spectra. At LUNA, the escape suppressed and the free-running spectra are indistinguishable in this energy range because the muon flux is so low that the remaining background is not dominated by muons any more, but by neutrons.

shield itself (^{207}Bi and ^{60}Co) do not change significantly between the different setups studied, as expected.

When comparing the unshielded and the shielded LUNA spectra, it is evident that already the present 5 cm lead shield leads to sizable reductions in the γ -line counting rates for all radioisotopes discussed above, except of course for the contaminations inherent to the BGO shield.

Table 1. Measured counting rates for radioactive decay lines, in counts per hour. Present data recorded with the Clover detector, are compared with the previous LUNA values [20] with a ULB detector and a passive shield consisting of 25 cm selected lead with low ^{210}Pb content, 4 cm oxygen free high purity copper, and an anti-radon box.

Source isotope E_γ [keV]		609	^{214}Bi 1120	2204	^{40}K 1461	^{208}Tl 2615	e^+e^- 511	^{207}Bi 570	1064	^{60}Co 1173 1333	
Clover, Earth's surface	singles	1013 \pm 52	509 \pm 26	182 \pm 10	6320 \pm 316	1163 \pm 58	1387 \pm 70	239 \pm 15	148 \pm 10	69 \pm 7	61 \pm 5
	adddback, free runn.	1405 \pm 81	750 \pm 47	318 \pm 19	10227 \pm 513	2046 \pm 104	1813 \pm 101	387 \pm 44	224 \pm 30	122 \pm 28	78 \pm 20
	adddback, esc. suppr.	1415 \pm 72	759 \pm 39	311 \pm 16	10065 \pm 503	1997 \pm 100	800 \pm 42	225 \pm 17	118 \pm 11	84 \pm 9	89 \pm 8
Clover at LUNA no shield	singles	532 \pm 27	258 \pm 13	90 \pm 5	861 \pm 43	284 \pm 14	306 \pm 16	244 \pm 13	149 \pm 8	54 \pm 3	52 \pm 3
	adddback, free runn.	750 \pm 38	398 \pm 20	150 \pm 8	1342 \pm 67	481 \pm 24	382 \pm 21	350 \pm 19	225 \pm 12	77 \pm 6	75 \pm 5
	adddback, esc. suppr.	717 \pm 36	380 \pm 19	147 \pm 8	1310 \pm 66	459 \pm 23	126 \pm 8	135 \pm 9	59 \pm 4	56 \pm 4	57 \pm 4
Clover at LUNA 5 cm Pb shield	singles	33 \pm 3	13 \pm 2	5.4 \pm 0.7	42 \pm 3	16.9 \pm 1.3	21 \pm 3	235 \pm 13	153 \pm 8	53 \pm 3	50 \pm 3
	adddback, free runn.	51 \pm 7	20 \pm 4	7.9 \pm 1.5	64 \pm 5	28.3 \pm 2.4	34 \pm 6	310 \pm 18	237 \pm 14	86 \pm 6	64 \pm 5
	adddback, esc. suppr.	30 \pm 3	15 \pm 2	7.6 \pm 0.9	71 \pm 4	21.0 \pm 1.6	5 \pm 3	98 \pm 6	47 \pm 3	59 \pm 4	58 \pm 4
ULB at LUNA [20]	no shield	3729 \pm 4	1278 \pm 3		4870 \pm 4	1325 \pm 2	762 \pm 4				
	25 cm Pb shield	0.30 \pm 0.04	0.15 \pm 0.02		0.42 \pm 0.03	0.12 \pm 0.02	0.09 \pm 0.04				

In order to estimate the possible effects of a full, state-of-the-art passive shielding on the present setup, it is useful to compare the present data with the data from the previous LUNA study [20] (table 1, last two lines). The unshielded starting point of the previous LUNA data is somewhat worse than for the present work, because in the present detector the BGO also acts as passive shield due to its high γ -attenuation coefficient. However, the factors of improvement seen when comparing the last two lines of table 1 show which low levels of background can in principle be reached using a full passive shield like in Ref. [20].

3.2 Laboratory background continuum

For in-beam experiments, the γ -ray continuum observed in regions outside of the laboratory background lines is of paramount importance. For reaction Q -values above 3 MeV, in principle also γ -rays of energies above 3 MeV can be emitted, in a region where there are no γ -lines from radioisotopes. Furthermore, for primary in-beam γ -rays the resolution is in many cases not limited by the detector, but by the effective target thickness, making the γ -lines rather wide, adding further importance to obtaining a low continuum in γ -detectors.

At the surface of the Earth, the two main sources of the γ -continuum are the Compton continuum of γ -rays and the energy loss or stopping of cosmic-ray induced particles like muons. An escape-suppression veto detector like the present BGO shield can strongly reduce both effects. In addition, placing the setup deep underground, thus reducing the muon flux, should lead to a further reduction of the γ -continuum, both for $E_\gamma < 3$ MeV [20] and $E_\gamma \geq 3$ MeV [19]. For example, a previous Monte Carlo simulation [24] predicts an overall factor of three reduction for $E_\gamma < 3$ MeV, when comparing overground spectra with a shallow underground facility at a depth of 30 m water equivalent.

In order to verify these expectations, the continuum counting rate has been determined for some regions of interest (ROI's) that are important for nuclear reactions that might conceivably be studied in underground accelerator experiments (table 2). These reactions and the as-

trophysical motivation driving their study have been discussed previously [20].

For $E_\gamma < 3$ MeV, it is clear from table 2 that the present detector, which has some internal contamination and is at maximum shielded with 5 cm lead, cannot reach the background suppression factors of the previous LUNA study [20] with its much better shield (table 2, last line).

For $E_\gamma \geq 3$ MeV overground, it is found from the present data that the escape suppression reduces the continuum counting rate by a factor 11. This reduction is comparable to the factor 10–50 reported for $E_\gamma = 7$ –11 MeV from a previous overground experiment using a HPGe detector shielded by a NaI escape-suppression shield [25].

By placing the detector deep underground at LUNA, in the same energy region the continuum counting rate is improved by an additional factor of 30 when compared with the overground, escape suppressed run (fig. 3). For $2.6 \text{ MeV} < E_\gamma < 5.2 \text{ MeV}$ (two times the energy of the ^{208}Tl γ -ray), the LUNA spectra are dominated by pileup from natural radionuclides. This background is not affected by the BGO veto detector, but it can instead be rejected using suitable electronic pileup rejection logic. However, for LUNA-type experiments such circuits may lead to increased uncertainty, because at low counting rate it is not easy to properly adjust them. Therefore, no pileup rejection circuit is used here.

At LUNA, the escape suppression does not produce any further effect for $E_\gamma > 5.2$ MeV, as expected when muons make a negligible contribution to the background (table 2). Similarly, the 5 cm lead shield does not lead to a further reduction in counting rate at LUNA, which can be explained by the fact that radioisotopes don't contribute significantly to the background for $E_\gamma \geq 5.2$ MeV. The remaining background values shown for the present detector are consistent with the previous data for a similar germanium detector with 5 cm lead shield at LUNA [19]. This background level is explained with neutron capture from the remaining flux of thermal and high-energetic neutrons present in LNGS [26].

Table 2. Continuum counting rate in counts/(keV hour) for several regions of interest relevant to radiative capture reactions.

Reaction γ -ray ROI [keV]		$^{12}\text{C}(^{12}\text{C},\text{p})^{23}\text{Na}$ 425-455	$^2\text{H}(\alpha,\gamma)^6\text{Li}$ 1545-1575	$^3\text{He}(\alpha,\gamma)^7\text{Be}$ 1738-1753	$^{12}\text{C}(\text{p},\gamma)^{13}\text{N}$ 2004-2034	$^{24}\text{Mg}(\text{p},\gamma)^{25}\text{Al}$ 2470-2500	$^{14}\text{N}(\text{p},\gamma)^{15}\text{O}$ 6000-8000
Clover, Earth's surface	singles	259.4 ± 0.2	16.02 ± 0.06	10.79 ± 0.07	8.48 ± 0.04	3.81 ± 0.03	$(128.9 \pm 0.8) \times 10^{-3}$
	addback, free running	317.3 ± 0.8	22.64 ± 0.21	15.84 ± 0.25	12.67 ± 0.16	6.33 ± 0.05	$(205.6 \pm 1.1) \times 10^{-3}$
	addback, escape suppressed	162.2 ± 0.2	11.48 ± 0.05	8.36 ± 0.06	5.75 ± 0.04	4.07 ± 0.03	$(19.2 \pm 0.4) \times 10^{-3}$
Clover at LUNA no shield	singles	64.57 ± 0.14	5.29 ± 0.04	3.09 ± 0.04	2.17 ± 0.02	0.72 ± 0.01	$(0.17 \pm 0.03) \times 10^{-3}$
	addback, free running	77.64 ± 0.18	7.52 ± 0.06	4.98 ± 0.07	3.13 ± 0.04	1.27 ± 0.02	$(0.15 \pm 0.04) \times 10^{-3}$
	addback, escape suppressed	30.52 ± 0.14	3.12 ± 0.04	2.71 ± 0.06	1.17 ± 0.03	0.73 ± 0.02	$(0.18 \pm 0.05) \times 10^{-3}$
Clover at LUNA 5 cm Pb shield	singles	6.35 ± 0.11	0.40 ± 0.03	0.19 ± 0.03	0.130 ± 0.015	0.06 ± 0.01	$(0.28 \pm 0.12) \times 10^{-3}$
	addback, free running	6.95 ± 0.17	0.57 ± 0.05	0.34 ± 0.05	0.21 ± 0.03	0.11 ± 0.02	$< 0.11 \times 10^{-3}$
	addback, escape suppressed	2.47 ± 0.07	0.26 ± 0.02	0.16 ± 0.03	0.076 ± 0.013	0.05 ± 0.01	$(0.29 \pm 0.13) \times 10^{-3}$
HPGe at LUNA ULB at LUNA	5 cm Pb shield [19] 25 cm Pb shield [20]	0.072 ± 0.002	0.0015 ± 0.0003	0.0011 ± 0.0003	0.0009 ± 0.0003		$< 0.1 \times 10^{-3}$

3.3 Addback factor

For the present data on the laboratory background lines (table 1), the addback factor [22]

$$\text{ABF} \stackrel{!}{=} \frac{C_{\text{addback, free-running}}}{C_{\text{singles}}} \quad (1)$$

has been calculated. Here, $C_{\text{addback, free-running}}$ is the counting rate in addback mode, free-running, and C_{singles} is the singles mode counting rate. The same has been done also for some γ -lines emitted in the $^{14}\text{N}(\text{p},\gamma)^{15}\text{O}$ reaction studied with the present detector and setup.

The data points all follow the same general curve, despite the very different points of emission of the various γ -rays: outside contaminations, radioactivity in the BGO shield, or decays in the air close to the detector (fig. 4). The present high-energy data points lie close to the previous fitted curve [27], confirming that the slope is somewhat higher than initially expected [22].

4 Decay of the $E_p = 223$ keV resonance in the $^{24}\text{Mg}(\text{p},\gamma)^{25}\text{Al}$ reaction as an example

4.1 General considerations

When studying the γ -decay of an excited nuclear state (e.g. the $E_x = 2485$ keV state in ^{25}Al , fig. 5), usually not only direct decay to the ground state of the nucleus, but also cascade decays via intermediate states are observed. Therefore in the observed γ -ray spectrum the signal from the transition to the ground state can be obscured by an artefact that appears at exactly the same energy, due to the true coincidence summing effect. This effect is usually corrected for in an analytic manner. However, in cases where the summing-in effect is large when compared to the true signal, such a correction can lead to considerable systematic uncertainty.

The magnitude of the summing-in correction is directly proportional to the absolute γ -detection efficiency. Therefore, one possible approach to limit summing-in is to move the detector to a larger distance, sacrificing efficiency and angular coverage. However, in low-energy nuclear astrophysics experiments, usually the γ -ray emission rate is

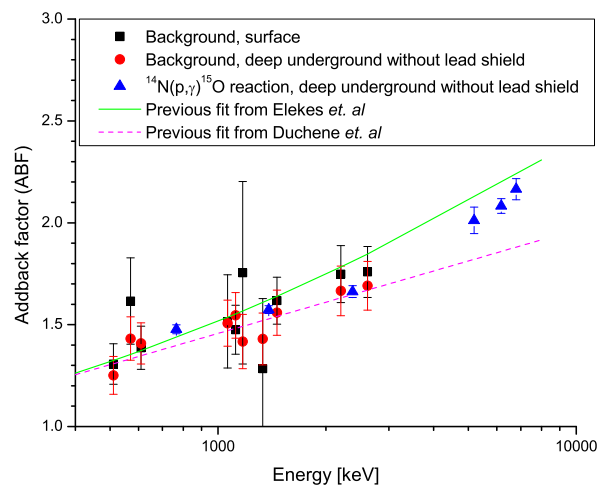


Fig. 4. Symbols, addback factor ABF calculated according to eq. 1 for γ -lines from the laboratory background (table 1): Squares, Earth's surface; circles, deep underground without lead shield. Triangles, ABF for γ -lines from the the $^{14}\text{N}(\text{p},\gamma)^{15}\text{O}$ reaction. Solid (dashed) line, previous fitted curves from Ref. [27] (from Ref. [22]).

low and their angular distribution not very well known. Solving the summing problem in this way therefore worsens two other problems, the low statistics and the dependence on the angular distribution. Therefore in the past at LUNA this approach could only be used for data on strong resonances [29].

An alternative approach is to use a composite detector. For the present case of four independent crystals, the summing-in effect is reduced by 4-ABF (i.e. four times the addback factor, ABF), while the γ -efficiency is only reduced by ABF. The angular coverage even remains unchanged. As an additional piece of information, the addback data can also be analyzed, and the comparison of singles and addback mode data can serve as a check on the analytical summing correction for the addback data.

A further advantage of using a composite detector, the much lower Doppler correction for each single crystal, has only limited importance for low-energy nuclear astro-

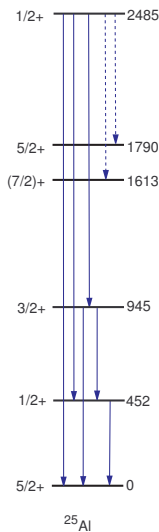


Fig. 5. Level scheme of ^{25}Al [28]. Full arrows, γ -transitions observed in the present experiment. Dashed arrows, γ -transitions where new upper limits have been derived.

physics studies. For Gamow peak energies of a few ten keV, the typical velocity of the recoil nuclei is lower than 1%, and the typical Doppler correction for LUNA-type experiments is of the same order as the energy resolution of the HPGe detector.

4.2 Branching ratio determination

In order to illustrate these considerations, the weak ($\approx 3\%$) ground state branching of the $E_p = 223$ keV resonance in the $^{24}\text{Mg}(p,\gamma)^{25}\text{Al}$ reaction (corresponding to the $E_x = 2485.3$ keV level in ^{25}Al , fig. 5) is redetermined here. This reaction plays a role in the hydrogen-burning MgAl chain [30].

For the experiment, a magnesium oxide target of natural isotopic composition (79% ^{24}Mg) was used. The Clover detector was placed at 55° with respect to the ion beam, with its front face at 9.5 cm distance from the target. The γ -detection efficiency is well-known from another experiment in exactly the same geometry [12], and the slope from 695 keV to 2485 keV is known to 1.0%. By scanning the target profile, an energy near the center of the target was selected. Then a spectrum was recorded on top of the resonance (fig. 6). With a strength of (12.7 ± 0.9) meV [31], the resonance is sufficiently intensive that off-resonance capture can be neglected for the present purposes. The laboratory background is comparable in intensity to the in-beam lines, as is apparent from the similar yield of the in-beam line at 2485 keV and the laboratory background line at 2615 keV (fig. 6). However, the background γ -lines lie at different energies, so the background does not limit the statistics of the 2485 keV ground state line (table 2).

The branching ratios for the decay of the resonance have then been determined (table 3). For the ground state capture line, the calculated summing-in correction was

Table 3. Branching ratios, in %, for the decay of the $E_p = 223$ keV resonance in the $^{24}\text{Mg}(p,\gamma)^{25}\text{Al}$ reaction. Where applicable, upper limits are given for 90% confidence level.

Decay	Literature [31]	Present work	
		addback	singles
$2485, \frac{1}{2}^+ \rightarrow 0, \frac{5}{2}^+$	2.7 ± 0.3	2.6 ± 0.2	2.69 ± 0.08
$\rightarrow 452, \frac{1}{2}^+$	81.7 ± 3.4	81.8 ± 1.2	81.6 ± 1.1
$\rightarrow 945, \frac{3}{2}^+$	15.6 ± 1.1	15.6 ± 0.5	15.7 ± 0.6
$\rightarrow 1613, \frac{7}{2}^+$	< 0.8	< 0.3	< 0.3
$\rightarrow 1790, \frac{5}{2}^+$	< 0.8	< 0.3	< 0.3

37% (7%) for the addback (singles) mode data, respectively. Assuming a conservative 20% relative uncertainty for all the summing-in and summing-out corrections, due to the summing correction there is 0.19% (0.04%) absolute uncertainty in the ground state branching for addback (singles) mode. For the addback case, this dominates the total uncertainty of 0.2%. The fact that the branching ratio as determined in the addback mode agrees with the singles mode data confirms that the summing-in correction is accurate.

For the primary γ -ray from the major transition, capture to the 452 keV first excited state, 3% (0.7%) summing-out correction was taken into account for addback (singles) mode. For the primary γ -ray from capture to the 945 keV state, 5% (1.0%) summing-out correction was taken into account, and again the addback and singles data are in agreement.

The newly determined branching ratios are in agreement with the literature data [31] but more precise. No significant branching is expected for the M3 transition to the $\frac{7}{2}^+$ level at 1613 keV and the E2 transition to the $\frac{5}{2}^+$ level at 1790 keV. The present data bear out this expectation, giving new experimental upper limits for these two transitions (table 3). The values obtained in singles mode are recommended for future compilations [28].

In the previous measurement [31], a large volume (140%) HPGe detector had been placed at 55° with respect to the beam direction, at 5.9 cm distance to the target. Based on these numbers, we estimate that in singles mode, the present summing-in correction is about a factor 9 lower than in Ref. [31], justifying the present lower uncertainty.

Another example studied recently is the $^{14}\text{N}(p,\gamma)^{15}\text{O}$ reaction, which controls the rate of the hydrogen-burning CNO cycle [30]. Due to the complicated interference pattern of several components in the R-matrix framework, the rather weak capture to the ground state in ^{15}O dominates the uncertainty of the total extrapolated $^{14}\text{N}(p,\gamma)^{15}\text{O}$ cross section at energies corresponding to solar hydrogen burning. The study of this transition is affected by summing-in corrections, and with the present detector and setup recently an experiment with greatly reduced summing corrections has been performed [12].

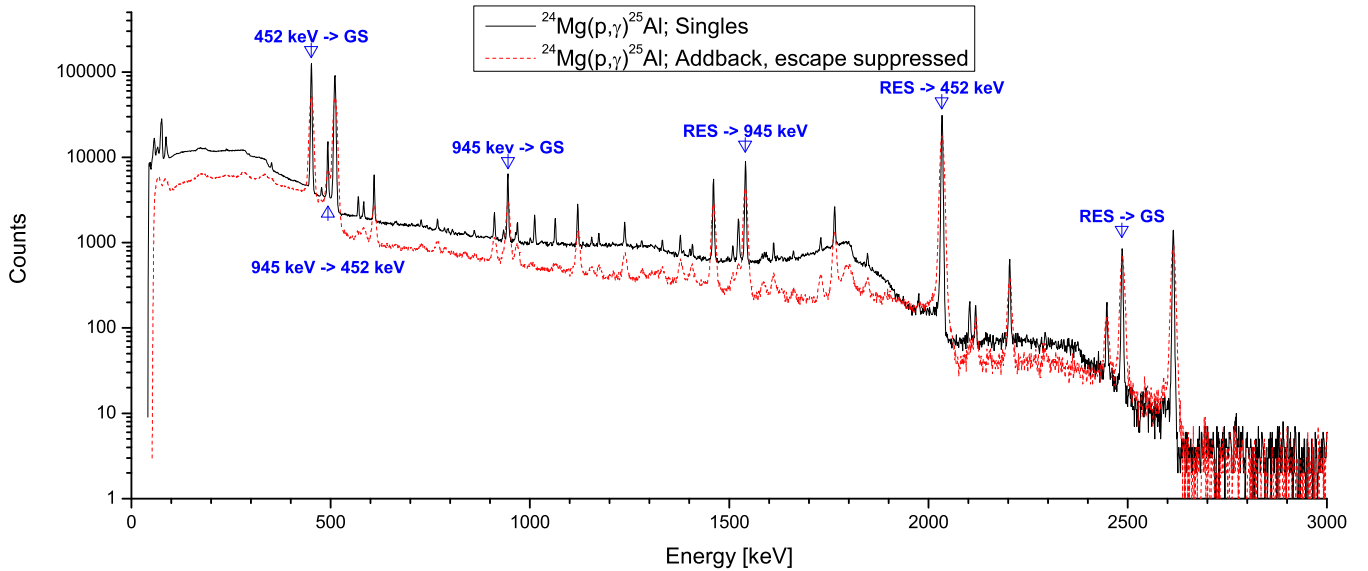


Fig. 6. In-beam γ -spectrum on the top of the $E_p = 223$ keV resonance in the $^{24}\text{Mg}(p,\gamma)^{25}\text{Al}$. Black full (red dashed) line, singles mode (addback mode, escape suppressed) data. The most important transitions are marked.

5 Discussion and outlook

A Clover-BGO detector system for nuclear astrophysics experiments has been used deep underground at LUNA. The laboratory background of one and the same detector has been studied in detail at LUNA and in an overground laboratory for reference. It is found that by going deep underground, the γ -continuum background counting rate can be reduced much more than by simply applying a cosmic-ray veto.

In free-running mode, the background characteristics of the present detector at LUNA are comparable to single detectors of similar size at LUNA, when a shielding similar to the present one is applied. The escape suppression was shown to further reduce the γ -continuum background counting rate.

In order to illustrate the applications of a composite, escape-suppressed detector in underground nuclear astrophysics, the weak ground state branching of the $E_p = 223$ keV resonance in the $^{24}\text{Mg}(p,\gamma)^{25}\text{Al}$ reaction has been determined with improved precision.

A further step in studying the potential of a composite, escape-suppressed detector in a deep underground accelerator laboratory such as LUNA would be to construct an ultra-low background composite detector with a long neck to accommodate a full lead and copper shield.

Acknowledgments

The present work has been supported by INFN and in part by the EU (ILIAS-TA RII3-CT-2004-506222), OTKA (T49245 and K68801), and DFG (Ro 429/41). T.S. acknowledges a Herbert Quandt fellowship at Technical University Dresden.

References

1. M. Asplund, N. Grevesse, and A. Jacques Sauval, *Nucl. Phys. A* **777**, 1 (2006).
2. C. Peña-Garay and A. Serenelli, ArXiv e-prints (2008), 0811.2424.
3. A. M. Serenelli, S. Basu, J. W. Ferguson, and M. Asplund, *Astrophys. J. Lett.* **705**, L123 (2009), 0909.2668.
4. U. Greife *et al.*, *Nucl. Inst. Meth. A* **350**, 327 (1994).
5. A. Formicola *et al.*, *Nucl. Inst. Meth. A* **507**, 609 (2003).
6. R. Bonetti *et al.*, *Phys. Rev. Lett.* **82**, 5205 (1999).
7. C. Casella *et al.*, *Nucl. Phys. A* **706**, 203 (2002).
8. A. Formicola *et al.*, *Phys. Lett. B* **591**, 61 (2004).
9. A. Lemut *et al.*, *Phys. Lett. B* **634**, 483 (2006).
10. D. Bemmerer *et al.*, *Phys. Rev. Lett.* **97**, 122502 (2006).
11. F. Confortola *et al.*, *Phys. Rev. C* **75**, 065803 (2007).
12. M. Marta *et al.*, *Phys. Rev. C* **78**, 022802(R) (2008).
13. D. Bemmerer *et al.*, *J. Phys. G* **36**, 045202 (2009).
14. Nuclear Physics European Collaboration Committee (NuPECC), Roadmap 2005, available at http://www.nupecc.org/pub/NuPECC_Roadmap.pdf.
15. Workshop on Nuclear Astrophysics Opportunities at the Underground Laboratory in Canfranc, Barcelona 19-20 February 2009, <http://www.fnuc.es/workshop/canfranc.html>.
16. DOE/NSF Nuclear Science Advisory Committee, arXiv:0809.3137.
17. F. Strieder, *J. Phys. G* **35**, 014009 (2008).
18. C. Bordeanu *et al.*, *J. Phys. G* **35**, 014011 (2008).
19. D. Bemmerer *et al.*, *Eur. Phys. J. A* **24**, 313 (2005).
20. A. Cacioli *et al.*, *Eur. Phys. J. A* **39**, 179 (2009).
21. M. Laubenstein *et al.*, *Appl. Radiat. Isot.* **61**, 167 (2004).
22. G. Duchêne *et al.*, *Nucl. Inst. Meth. A* **432**, 90 (1999).
23. H. Costantini *et al.*, *Rep. Prog. Phys.* **72**, 086301 (2009).
24. P. Vojtyla and P. P. Povinec, *Radioactivity in the Environment* **8**, 529 (2006).
25. G. Müller *et al.*, *Nucl. Inst. Meth. A* **295**, 133 (1990).

26. P. Belli *et al.*, *Nuovo Cimento A* **101**, 959 (1989).
27. Z. Elekes *et al.*, *Nucl. Inst. Meth. A* **503**, 580 (2003).
28. R. B. Firestone, *Nucl. Data Sheets* **110**, 1691 (2009).
29. G. Imbriani *et al.*, *Eur. Phys. J. A* **25**, 455 (2005).
30. C. Iliadis, *Nuclear Physics of Stars* (Wiley-VCH, 2007).
31. D. C. Powell *et al.*, *Nucl. Phys. A* **660**, 349 (1999).

Shallow-underground accelerator sites for nuclear astrophysics: Is the background low enough?

Tamás Szücs^{1,2}, Daniel Bemmerer^{1,a}, Thomas Cowan^{1,3}, Detlev Degering⁴, Zoltán Elekes^{2,1}, Zsolt Fülöp², György Gyürky², Arnd Junghans¹, Matthias Köhler⁴, Michele Marta^{1,b}, Ronald Schwengner¹, Andreas Wagner¹, and Kai Zuber³

¹ Helmholtz-Zentrum Dresden-Rossendorf (HZDR), Dresden, Germany

² Institute of Nuclear Research of the Hungarian Academy of Sciences (ATOMKI), Debrecen, Hungary

³ Technische Universität Dresden, Dresden, Germany

⁴ Verein für Kernverfahrenstechnik und Analytik Rossendorf (VKTA), Dresden, Germany

Received: 20 July 2011 / Revised: 23 December 2011

Published online: 30 January 2012

© The Author(s) 2012. This article is published with open access at Springerlink.com

Communicated by E. Bellotti

Abstract. In order to reliably estimate the rate of a charged particle induced nuclear reaction in a non-explosive astrophysical scenario, its cross-section must be measured far below the Coulomb barrier. However, at the corresponding energies the cross-section values are very low, so that the experimental counting rate is dominated by cosmic-ray induced background, even if a suitable anticoincidence shield is applied. This problem can be overcome by performing an accelerator-based experiment in a deep underground site, as has been done with great success at the LUNA 0.4 MV accelerator in Gran Sasso, Italy. Several underground accelerators with higher beam energy are in the planning phase worldwide. All of them are shielded by over 1000 m of rock, a depth at which cosmic-ray effects are negligible for the purposes of nuclear astrophysics experiments. It is shown here that a combined approach, using a shallow-underground laboratory below 47 m of rock and an active shield to veto surviving muons in simple detectors, results in a background level that is not far from that of deep underground sites. Data have been obtained using two “traveling” γ -detectors. They have been transported both shallow underground, to the Dresden Felsenkeller in Germany, and deep underground, to the Gran Sasso laboratory in Italy. As shallow-underground facilities are more easily accessible than deep-underground ones, the present finding holds the promise of greatly accelerated progress in the field of cross-section measurements for nuclear astrophysics.

1 Introduction

Many nuclear physics inputs are needed for the modeling of astrophysical scenarios [1–3], and progress must be made on two frontiers: Nuclei far from the valley of β -stability will become accessible at next generation radioactive ion beam facilities. For reactions of stable nuclei, the frontier is given by the lack of precise cross-section data at low energy.

These reactions are generally well studied at high energies, above the Coulomb barrier. However, the astrophysically relevant energy range lies far lower. Since extrapolations are fraught with uncertainty, it is desirable to measure the cross-section directly at the relevant energy, or at least close to it. There, the cross-section is very low,

so low that the laboratory background counting rate in a detector becomes a limiting factor.

This limitation can be overcome by placing the entire laboratory in a low-background setting underground. Rock overburdens of a few meters thickness suppress the nucleonic component of the cosmic-ray induced background to negligible levels [4]. However, the muonic component is only slowly attenuated when proceeding to greater depth [5]. Muons produce neutrons inside the shielding or the detector itself [6], giving rise to a background that is difficult to suppress. In order for the muon flux to become negligible, depths of 1000 m of rock or more are required [7]. This depth has been selected with great success by the Laboratory for Underground Nuclear Astrophysics (LUNA). LUNA is placed in the Gran Sasso laboratory in Italy, below 1400 m of rock, and with uniquely low background [8–10]. It hosted first a 50 kV accelerator and now a 0.4 MV single-ended accelerator for $^1\text{H}^+$ and $^4\text{He}^+$ ions [11].

^a e-mail: d.bemmerer@hzdr.de

^b Present address: GSI Helmholtzzentrum für Schwerionenforschung, Darmstadt, Germany

In recent years, underground nuclear astrophysics experiments have helped put the understanding of nuclear fusion in our Sun on firm experimental ground [12–17]. For further progress, new data at higher energies are needed. A recent expert forum on solar fusion cross-sections called for new data, *e.g.*, on the ${}^3\text{He}(\alpha,\gamma){}^7\text{Be}$ reaction. The same forum also highlighted the need for a higher-energy underground accelerator [18].

Several astrophysical scenarios other than the Sun require new and precise cross-section data for their modeling, as well. This is the case for the reactions of Big Bang nucleosynthesis [19]. In stars heavier than the Sun, hydrogen burning proceeds to higher masses, and there are a number of reactions requiring more precise study [20]. After hydrogen burning, helium and then carbon burning ensues. The relevant reactions of helium burning are still not understood on a sufficient level of precision [21]. This applies, *e.g.*, to the ${}^{12}\text{C}(\alpha,\gamma){}^{16}\text{O}$, ${}^{16}\text{O}(\alpha,\gamma){}^{20}\text{Ne}$, and ${}^{18}\text{O}(\alpha,\gamma){}^{22}\text{Ne}$ reactions. Similar considerations are valid for the reactions of carbon burning [22], *e.g.*, ${}^{12}\text{C}({}^{12}\text{C},\text{p}){}^{23}\text{Na}$, and for the neutron source reactions powering the astrophysical s-process.

All these cases involve light, stable nuclei as beams and targets, and the in-beam detection of γ -rays or neutrons. Therefore, they can be studied at ion accelerator facilities with a few MV accelerating potential and sufficient beam intensity, provided the laboratory background is low enough. Indeed, there is a call for new underground accelerators [23,24]. Relevant projects have been proposed in deep-underground settings, below a rock overburden of 1000 m or more [11,24,25].

It is shown here that already shallow-underground sites present satisfactory background conditions for a number of nuclear astrophysics experiments, if a suitable active shield, surrounding either just the detector or the whole laboratory, suppresses remaining muons. As a demonstration, a study of background in γ -ray detectors in the Felsenkeller shallow-underground laboratory (47 m rock overburden) in Dresden (Germany) has been carried out.

For underground accelerator-based experiments, the Q -value of a typical radiative capture reaction is usually much larger than the beam energy E in the center-of-mass system. Therefore, the γ -ray energy for capture to the ground state $E_\gamma = Q + E$ (neglecting the small Doppler and recoil corrections) is usually dominated by the Q -value, and in many cases $E_\gamma > 2.615$ MeV. The background and the feasibility of radiative capture experiments strongly depend on the γ -ray energy.

In sect. 2, the background for $E_\gamma \leq 2.615$ MeV is reviewed at different sites, based on literature data. The main characteristics of the Felsenkeller shallow-underground facility included in this background comparison are described in sect. 3. In sect. 4 and 5, a background comparison between the Earth's surface, shallow-, and deep-underground sites is performed by subsequently transporting one and the same detector to each of the three sites. The implications for the feasibility of experiments using simple single-detector setups underground are discussed in sect. 6, and a summary is given in sect. 7.

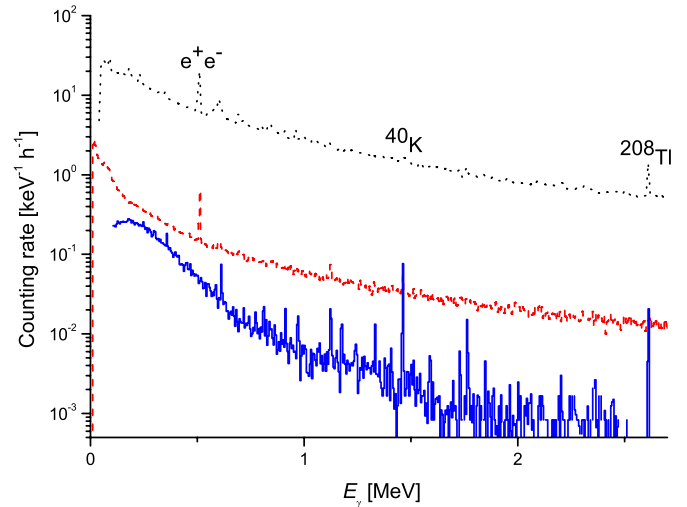


Fig. 1. (Color online) Review of previous background data using HPGe detectors without active shielding, but with full lead and copper shield. The data are rescaled to match 122% relative efficiency. Earth's surface (black dotted line [26]), shallow underground (red dashed line [27]), deep underground (blue full line [9]).

2 Review of previous data on the background in passively shielded germanium detectors at several depths

Before turning to the new experimental data obtained here, in the present section the background situation in detectors without active shielding underground is briefly reviewed based on the literature. The discussion concentrates on γ -energies below the 2.615 MeV line of ${}^{208}\text{Tl}$, where abundant data are available [4]. Data from nuclear astrophysics related setups are selected for this comparison, where possible.

At these γ -energies, a thick lead shield is essential to suppress the background from radionuclides. However, an additional rock overburden also helps reduce the continuum component of the background [4]. Published data from three well-shielded p-type HPGe detector setups, each of them with the optimal shielding configuration for its depth [4], are shown to illustrate this point:

- 1) The first HPGe detector is hosted in a 15 cm thick lead shield at the Earth's surface [26]. For surface-based experiments, 15 cm is the optimum shielding thickness, as the background does not decrease significantly when using even thicker shields [4].
- 2) The second HPGe detector is contained in a shield of 15 cm lead and 5 cm copper shallow underground at Felsenkeller [27] (see also sect. 3 of the present work).
- 3) The third one is hosted in a shield of 25 cm lead and 4 cm copper deep underground at Gran Sasso, in a setup dedicated to ultra-low background in-beam γ -spectrometry [9].

The relative efficiencies of the three detectors are of the same order of magnitude (100% [26], 90% [27], 137% [9]).

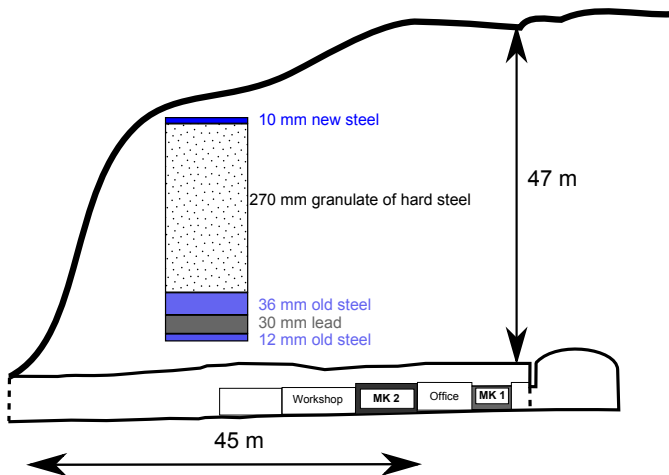


Fig. 2. Cross-section of tunnel IV of the Felsenkeller underground facility. The current underground counting facility with its two measuring chambers MK1 [28] and MK2 [29] is also shown. The inset shows the makeup of the shielding of measuring chamber MK2, from the outside (top) to the inside (bottom).

In order to facilitate a quantitative comparison between their background levels, the counting rates from the three detectors are rescaled to match 122% relative efficiency, the efficiency of the HPGe detector used in sect. 5.

From this limited review of published data, concentrating on nuclear astrophysics related setups, it can be seen that for $0.100 \text{ MeV} \leq E_\gamma \leq 2.615 \text{ MeV}$, the background shallow underground is a factor 40 lower than at the Earth's surface, and again a factor 3–20 lower deep underground (fig. 1). As a consequence, passively shielded shallow-underground facilities may provide some kind of intermediate solution between surface-based and deep-underground experiments, when it comes to in-beam γ -spectrometric experiments for nuclear astrophysics with detected γ -rays of $E_\gamma < 2.615 \text{ MeV}$.

3 The Felsenkeller site and laboratory

The Felsenkeller area is located in an ancient quarry in the Weißeritz valley, 5 km from Dresden city center. The underground facility consists of nine tunnels, called tunnel I–IX, that have been dug in the 1850's to host the ice cellar of the nearby Felsenkeller brewery.

A low-background radioactivity counting facility was installed in 1982 in tunnel IV [28], with a measuring chamber called MK1 that was shielded by a low-radioactivity serpentinite rock. In 1995, a new measuring chamber called MK2 has been added to the facility [29]. The walls of MK2 are 36 cm thick, in part consisting of old, ^{60}Co -free steel from an epoch predating the nuclear age (fig. 2). The average rock overburden above the VKTA facility is 47 m, equivalent to 110 m water (m.w.e.), leading to a reduction of the muon flux by a factor of 30–50 depending on the angle being studied.

The analytics facility of tunnel IV, operated by VKTA Dresden, is a founding member of the European CEL-LAR Collaboration of underground low-background laboratories. It hosts several HPGe γ -detectors and a tritium counting facility. Recently a new ultra-low background germanium detector made of specially selected components went into operation [27]. In recent years, also nuclear astrophysics [30] and rare nuclear decay [31] studies have been performed at Felsenkeller.

Tunnels I–III and V–IX are used as storage sites by local businesses. They have a typical diameter of 6 m and the same rock overburden as tunnel IV.

4 New data using a “traveling” LaBr_3 detector

In order to extend the background comparison performed in sect. 2 to higher γ -energies, $2.615 \text{ MeV} < E_\gamma$, two new experiments have been performed¹. In both cases, one and the same detector has been used subsequently at the three sites Earth's surface, shallow underground, and deep underground. By using exactly the same device, any observed background differences can be attributed to the characteristics of the laboratory, not the ones of the specific detector.

The shallow-underground data for the comparison have been recorded in the MK2 chamber of Felsenkeller (sect. 3). Deep-underground data have been taken in the Gran Sasso laboratory in Italy (1400 m rock overburden). The comparison data at the Earth's surface have been taken in the basement of a three-story building on the HZDR Rossendorf campus. In the present section, the measurements with a lanthanum bromide (LaBr_3) detector are presented. Data with a high-purity germanium (HPGe) detector are shown in the subsequent sect. 5.

The LaBr_3 detector had a cylindrical shape with 6.5 cm length, 8.3 cm diameter, and 350 cm^3 volume. For the measurements at the Earth's surface and at Felsenkeller, it was inserted in the center of a large BGO anticompton shield of 23 cm length that had been designed for the use with a EUROBALL Cluster detector.

Up to the 2.615 MeV line of ^{208}Tl , the LaBr_3 spectrum (fig. 3) is dominated by the intrinsic ^{138}La activity of LaBr_3 and by quenched α -particles from the decay of its intrinsic ^{227}Ac contamination [32]. Consequently, at these γ -energies the observed counting rate does not depend on the rock overburden at the laboratory. In the range from 2.615 MeV up to 5 MeV, the effect of pileup of α -emitters in the crystal is visible, which again leads to a sizable depth-independent contribution to the counting rate. Because of these effects, only the part of the LaBr_3 spectra above 5 MeV is used for the comparison, where ^{138}La , natural radionuclides, and α -emitters in the crystal do not play a role.

¹ In this work, the symbol E_γ is used throughout to denote the γ -ray equivalent energy at which the background is registered in the detector under study.

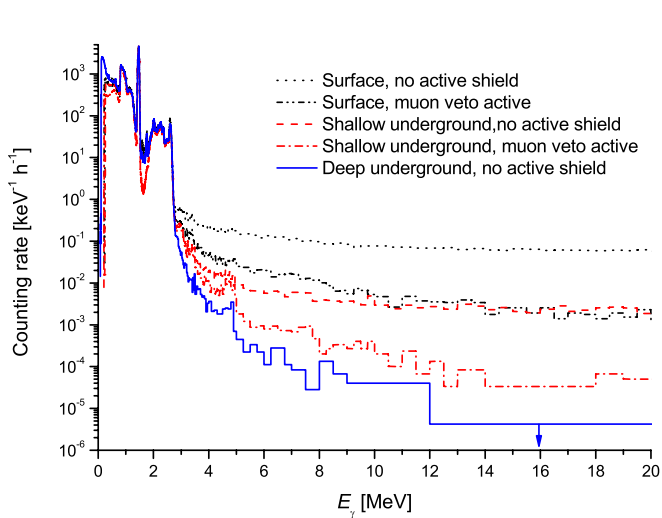


Fig. 3. (Color online) Background in one and the same actively shielded LaBr_3 detector: Earth's surface, without (black dotted line) and with (black dot-dot-dashed line) active muon veto. Shallow underground, without (red dashed line) and with (red dot-dashed line) active muon veto. Deep underground without active muon veto (blue solid line).

For $5 \text{ MeV} < E_\gamma < 12 \text{ MeV}$, the counting rate at the Earth's surface is dominated by the energy loss of passing or stopping muons, and by the capture of energetic neutrons created by muons in material surrounding the detector. Both these effects are attenuated in the shallow-underground laboratory Felsenkeller (red dashed line in fig. 3), where the muon flux is reduced by a factor of 30. The remaining muons, but not the neutrons produced by them, are suppressed further by applying the active shield (red dot-dashed line in fig. 3).

Deep underground, the muon flux is a factor 10^6 lower than at the surface, but the counting rate in the $5 \text{ MeV} < E_\gamma < 12 \text{ MeV}$ region is only a factor 10^3 lower. This suppression factor of 10^3 is consistent with previous work [8, 10]. It is due to the fact that a depth-independent flux of high-energy neutrons created by (α, n) reactions and spontaneous fission of ^{238}U in the rock [33] dominates the deep-underground background. A neutron shield would help here, but the counting rates deep underground are already sufficiently low without it [8]. For the deep-underground run with this detector, no active shield was used.

For $12 \text{ MeV} < E_\gamma$, neutrons play less of a role, and the effect of the muon flux reduction with depth and/or active shield is well visible. No counts were observed in 30 h counting time in the deep-underground spectrum in this energy range, so the given value for $12 \text{ MeV} < E_\gamma$ is a 1σ upper limit.

5 New data using a “traveling” HPGe detector

The second “traveling” detector was a Clover-type HPGe detector of 7.1 cm length, with a tapered front face of 8.2–9.1 cm sidelength and 470 cm^3 volume. It is configured in addback mode [34] (122% relative efficiency) and

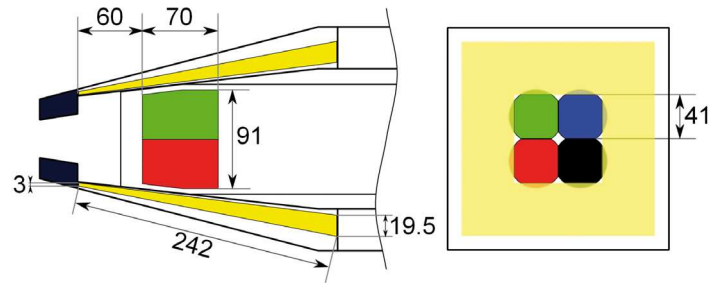


Fig. 4. (Color online) Schematic view of the HPGe detector (four sections: green, red, black, and blue) and its BGO escape-suppression shield (yellow) that were used for the present study. Dimensions are given in mm. The four individual crystals have a tapered cylindrical shape. Left panel: View from the side. Right panel: Front view.

used in anticoincidence with a surrounding BGO scintillator of 24 cm length (fig. 4). The BGO escape suppression thus forms also an efficient muon veto. Further details on this particular detector are included in a previous publication [10]. In that paper, the deep-underground spectra of this device have already been published [10].

For the purposes of the present work, additional runs were made with the same detector in the Felsenkeller shallow-underground laboratory, and at the Earth's surface in the basement of a three-story building on the HZDR Rossendorf campus. The surface-based data showed the so-called muon peak [35] at 50–60 MeV in this detector's spectrum, roughly the energy expected for its size. This peak is suppressed by a factor of 160 by the BGO anticoincidence, showing how efficiently this suppression works.

This detector was then transported to Felsenkeller (spectrum in fig. 5). Naturally occurring radionuclides dominate the background up to the 2.615 MeV line of ^{208}Tl . Note that in this energy region and in this detector, the shallow-underground background is even lower than the deep-underground one. This surprising fact is due to the thick iron and lead walls of the MK2 measuring chamber in Felsenkeller, whereas no similar shielded chamber was used at Gran Sasso. For the LaBr_3 detector discussed in sect. 4, the effect of the MK2 walls was less striking due to its higher intrinsic background. Still, for an inter-laboratory comparison the data with the traveling HPGe and LaBr_3 detectors should only be used above the 2.615 MeV line of ^{208}Tl .

As in the case of the LaBr_3 detector, in order to completely exclude depth-independent effects such as the MK2 walls and intrinsic α -emitters from a ^{210}Po contamination [36], the comparison should be limited to the high-energy region, $5.3 \text{ MeV} \leq E_\gamma$. Indeed, the effect of the BGO active shield is best seen in this region, where muon-induced effects dominate.

For $5.3 \text{ MeV} \leq E_\gamma \leq 8.0 \text{ MeV}$, the counting rate without active shield is dominated by the energy loss of passing muons, both in the surface-based and in the shallow-underground runs. The ratio of the surface to the shallow-underground data is a factor of 40, the same as the sup-

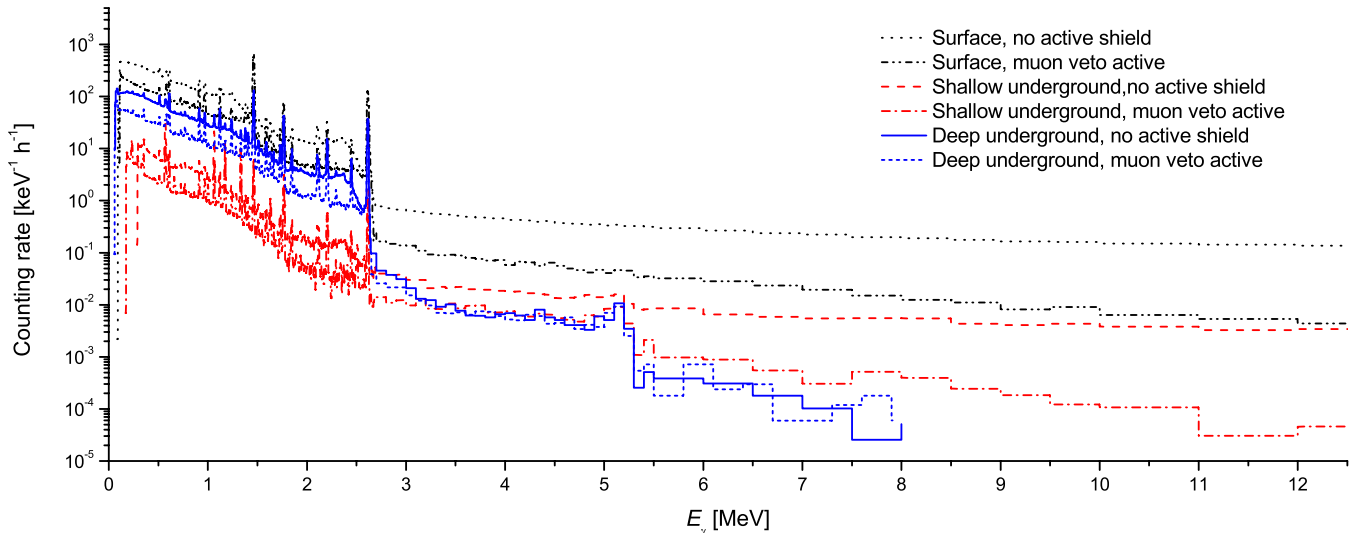


Fig. 5. (Color online) Background in one and the same Clover HPGe detector: Earth's surface, without (black dotted line) and with active muon veto (black dot-dot-dashed line). Shallow underground, without (red dashed line) and with active muon veto (red dot-dashed line). Deep underground [10] (limited to 0–8 MeV), without (blue solid line) and with active muon veto (blue short dashed line).

pression of the muon flux. Deep underground, an additional factor of 3×10^4 suppression is expected for the direct effects of muons, bringing this source of background to a negligible level. Instead, as discussed above, again depth-independent neutrons emitted from the walls of the laboratory due to (α, n) reactions dominate the counting rate. These neutrons are not affected by the escape-suppression shield, so the deep-underground counting rate with and without muon veto is the same in this energy region [10].

As a result, for $5.3 \text{ MeV} \leq E_\gamma \leq 8.0 \text{ MeV}$ the counting rate in one and the same detector deep underground is only a factor 2.4 ± 0.3 lower than shallow underground, if an active muon veto is used. Due to the dynamic range of the deep-underground data for this particular detector, no direct comparison is possible for $8.0 \text{ MeV} < E_\gamma$, but the trend can be estimated from the LaBr₃ data, which extend to higher energies.

6 Implications for the feasibility of accelerator-based experiments

In order to gauge the feasibility of accelerator-based experiments on radiative capture reactions, some real or hypothetical setup has to be assumed. Depending on whether the γ -rays to be detected lie outside the range of natural radionuclides ($E_\gamma > 2.615 \text{ MeV}$) or inside it ($E_\gamma \leq 2.615 \text{ MeV}$), different shielding scenarios are optimal, therefore for those two γ -energy ranges two different setups called setup A and B, respectively, are assumed.

Setup A: For reactions with emitted γ -rays of $E_\gamma > 2.615 \text{ MeV}$, as discussed above γ -lines from environmental radionuclides do not play a role, and a lead shield around the detector or around the whole counting room as in the MK2 case cannot be expected to further improve

the background. Therefore, for these reactions a setup used previously for in-beam γ -spectroscopy experiments at LUNA [16, 10, 17] is selected for the feasibility discussion. Setup A consists of the present Clover HPGe detector (sect. 5), with its endcap at 9.5 cm distance from the target and the present active BGO veto. For this setup, a typical random veto rate of 1% due to background hitting the BGO has been found [10]. For γ -rays emitted in cascade, a typical peak suppression of 5% has been observed due to the second γ -ray of a cascade hitting the BGO shield [16, 17]. The latter effect vanishes for a single emitted γ -ray, as in capture to the ground state of the compound nucleus.

Setup B: For reactions with emitted γ -rays of $E_\gamma < 2.615 \text{ MeV}$, a lead shield is necessary to suppress environmental γ -lines. For studying these cases, the present LaBr₃ and HPGe data (sect. 4 and 5) cannot be used due to the lack of proper lead shielding. It would have been prohibitively difficult to transport not only the detectors, but also one and the same full lead shield to the above discussed three sites. For the cases with $E_\gamma < 2.615 \text{ MeV}$, instead the previous background data from well-shielded setups (sect. 2) are used, rescaled for their relative efficiencies as stated above (fig. 1). The same detector-target distance as in setup A is assumed. This hypothetical setup is called setup B.

A typical target of $6 \cdot 10^{17}$ active target atoms/cm² is assumed, with the composition given in table 1. The S -factor or resonance strength and branching ratio are adopted from the given reference (table 1). A beam intensity of 250 particle- μA is assumed.

For the cases considered here, one or more γ -rays are emitted per reaction. However, in many cases including most of the examples given here, capture to the ground state dominates at the energies under study, or is even

Table 1. Signal counting rate in a single-detector setup for capture to the ground state of the final nucleus, at the center-of-mass energy E . For ^{12}C in Au, a ratio of 5:1 [37] is assumed. See the text for further details. The background counting rate at different depths is also given.

Reaction	E [keV]	Ref.	γ -ray ROI [keV]	Target	Setup	Full energy peak γ -efficiency	Signal [h $^{-1}$]	Laboratory background counting rate [h $^{-1}$]		
								Earth's surface	Shallow undergr.	Deep undergr.
$^{12}\text{C}(^{12}\text{C},\text{p})^{23}\text{Na}^{(a)}$	2200	[22]	438-441	^{12}C in Au	B	9.0×10^{-3}	0.80	20.3 ± 0.5	0.53 ± 0.02	0.179 ± 0.018
$^3\text{He}(\alpha,\gamma)^7\text{Be}$	200	[38]	1779-1789	^3He gas	B	3.9×10^{-3}	190	10.5 ± 0.4	0.250 ± 0.016	0.010 ± 0.004
$^{12}\text{C}(\text{p},\gamma)^{13}\text{N}$	80	[39]	2009-2027	^{12}C in Au	B	3.5×10^{-3}	0.52	14.6 ± 0.4	0.39 ± 0.02	0.017 ± 0.005
$^{16}\text{O}(\alpha,\gamma)^{20}\text{Ne}$	1300	[40]	5991-6035	Al_2O_3	A	1.2×10^{-3}	0.025	1.39 ± 0.05	$0.039 \pm 0.007^{(b)}$	0.021 ± 0.006
$^{12}\text{C}(\alpha,\gamma)^{16}\text{O}$	800	[21]	7929-7968	^{12}C in Au	A	8.9×10^{-4}	0.018	0.59 ± 0.05	$0.024 \pm 0.008^{(b)}$	0.006 ± 0.004
$^{18}\text{O}(\alpha,\gamma)^{22}\text{Ne}$	385	[41]	10045-10058	$\text{Al}_2^{18}\text{O}_3$	A	6.7×10^{-4}	0.045	0.082 ± 0.005	$0.0015 \pm 0.0006^{(b)}$	$0.0006 \pm 0.0004^{(c)}$
$^{15}\text{N}(\text{p},\gamma)^{16}\text{O}$	70	[42]	12163-12205	Ti^{15}N	A	5.3×10^{-4}	0.012	0.188 ± 0.013	$0.0019 \pm 0.0011^{(b)}$	$< 0.0002^{(c)}$

^(a) Decay of the first excited state of ^{23}Na .

^(b) Consistent background is found with the present Clover HPGe detector in an unshielded part of the Felsenkeller facility outside MK2.

^(c) Rescaled from the LaBr_3 background.

the only significant reaction mechanism. For these cases, the region of interest (ROI) width has been determined from the energetic target thickness, folded with the resolution. For the fixed-energy γ -rays from the $^{12}\text{C}(^{12}\text{C},\text{p})^{23}\text{Na}$ and $^{18}\text{O}(\alpha,\gamma)^{22}\text{Ne}$ reactions, the width of the γ -ray ROI is taken as two times the full width at half maximum (FWHM) γ -energy resolution.

It should be noted that the given background levels are a lower limit, neglecting ion beam induced background. However, this latter problem usually did not limit experiments at LUNA [11].

In principle, an experiment is also possible when the signal is much lower than the background. However, the time required to reach a given statistics scales with the ratio of background to signal. The running times for the type of experiment discussed here are of the order of weeks or even months per data point, so that an experiment cannot be concluded in a realistic time when the background is much higher than the signal. Therefore, the signal counting rate should be higher than or at least comparable to the background in order for experiments to be feasible.

When adopting this criterion, it is apparent that for five of the reactions listed, an experiment at the surface of the Earth is impossible. For the remaining two, namely $^3\text{He}(\alpha,\gamma)^7\text{Be}$ and $^{18}\text{O}(\alpha,\gamma)^{22}\text{Ne}$, recent experiments at the Earth's surface either did not reach low energies [43] or were still limited by background [41].

When comparing the background values at the three sites listed in the right three columns of table 1, two observations can be made. First, for all the cases studied here, the shallow-underground scenario offers already a background that is a factor of 25–100 lower than at the Earth's surface, sufficiently low for the experiments to be feasible. Second, the background in deep underground is even lower than that in shallow underground: In the vetoed setup A for $5.3 \text{ MeV} < E_\gamma < 8.0 \text{ MeV}$, by a factor of 2.4 ± 0.3 . In the non-vetoed setup B for $1.5 \text{ MeV} < E_\gamma < 2.7 \text{ MeV}$, by a factor of 19 ± 1 . A smaller difference is observed at lower energy, $E_\gamma \approx 0.4 \text{ MeV}$, where bremsstrahlung from ^{210}Bi dominates the particular deep-underground spectrum [9] used for the comparison.

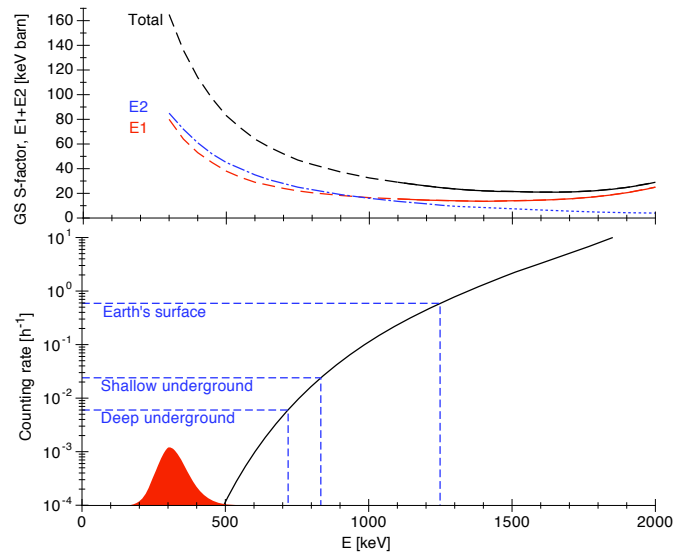


Fig. 6. (Color online) Top panel: Astrophysical S -factor for ground-state capture in $^{12}\text{C}(\alpha,\gamma)^{16}\text{O}$, from R -matrix fits for its $E1$ [21] and $E2$ [44] contributions. The energy range with (without) experimental cross-section data is indicated by a full (dashed) line. Bottom panel: Predicted $^{12}\text{C}(\alpha,\gamma)^{16}\text{O}$ counting rate in the present single-detector setup A, compared to the background in the various sites. The Gamow peak for $T_9 = 0.2$ is also given, in linear scale.

In order to illustrate the gain in sensitivity when moving from the Earth's surface to the different underground scenarios, the $^{12}\text{C}(\alpha,\gamma)^{16}\text{O}$ reaction is selected. At astrophysical energies, this reaction is believed to be dominated by capture to the ground state in ^{16}O [21], and for this transition both high-energy experimental data and R -matrix fits [44,21] exist. There is about 30% uncertainty in the extrapolated S -factor [21], whereas stellar modelers call for 10% precision [45]. Taking advantage of the lower background, it is possible to approach the Gamow peak significantly in a shallow underground setting (fig. 6), halving the distance between the energies where data exist and the astrophysical energy.

The data also show that deep underground, it is possible to go even further down in energy, closer to the Gamow peak. For the single-detector scenario considered here, the counting rates would then become very low, less than one count per week. As a consequence, probably much larger detector arrays should be considered to fully exploit the advantages of working deep underground.

For a large γ -detector array, the present escape-suppression scheme of a BGO veto detector immediately surrounding each germanium crystal is not practical any more. Instead, a muon veto can in principle be achieved in two different ways: By covering the outside of the large detector array with a veto detector that is many square meters large [46], or by using many closely packed germanium detectors that function as a veto detector for each other, using γ -ray tracking and pulse shape discrimination techniques [47].

A detailed study of how a large detector array with an appropriate muon veto, which is complicated and costly to build, would function in a deep- or shallow-underground setting is beyond the scope of the present work. Instead, here the feasibility discussion is limited to setups of much lower complexity and cost, including just one detector, and comparing one and the same detector in different sites.

7 Summary

A dedicated study of the background in a standard in-beam γ -spectroscopy setup has been performed at the Earth's surface and in shallow- and deep-underground facilities. Active shielding has been used to suppress the direct effects of cosmic-ray muons. Based on the data, the feasibility of accelerator-based nuclear astrophysics experiments has been evaluated for several key cases, in a single-detector setup.

It has been shown that experiments at the surface of the Earth are not a realistic option for any of the reactions considered here. Instead, an underground setting is needed. Owing to the fact that nuclear reaction experiments require low but not ultra-low background (*e.g.*, [48]), the present data show that already shallow-underground sites offer satisfactory background conditions for a number of in-beam γ -spectrometry experiments in a single-detector setup. It was also shown that even better background conditions are reached deep underground.

This finding opens the door for a complementary approach to place our understanding of stellar nucleosynthesis on a firm experimental foundation, much the same way as has been achieved with fusion in the Sun: The ease of access to shallow-underground facilities and standard detectors should be exploited to quickly gain low-energy data near the Gamow peak, while large detector arrays in deep-underground sites push the data limit even lower, in some cases to astrophysical energies.

This work was supported in part by the Herbert Quandt Foundation, DFG (BE 4100/2-1), OTKA (K101328, NN83261), TÁMOP-4.2.2/B-10/1-2010-0024, EuroGENESIS, and the EU (European Social Fund).

Open Access This article is distributed under the terms of the Creative Commons Attribution Noncommercial License which permits any noncommercial use, distribution, and reproduction in any medium, provided the original author(s) and source are credited.

References

1. C. Rolfs, W. Rodney, *Cauldrons in the Cosmos* (University of Chicago Press, Chicago, 1988).
2. C. Iliadis, *Nuclear Physics of Stars* (Wiley-VCH, Weinheim, 2007).
3. R.N. Boyd, *An introduction to Nuclear Astrophysics* (The University of Chicago Press, Chicago, 2008).
4. G. Heusser, *Annu. Rev. Nucl. Part. Sci.* **45**, 543 (1995).
5. J.A. Formaggio, C. Martoff, *Annu. Rev. Nucl. Part. Sci.* **54**, 361 (2004).
6. A. da Silva *et al.*, *Nucl. Instrum. Methods A* **354**, 553 (1995).
7. D. Mei, A. Hime, *Phys. Rev. D* **73**, 053004 (2006).
8. D. Bemmerer *et al.*, *Eur. Phys. J. A* **24**, 313 (2005).
9. A. Cacioli *et al.*, *Eur. Phys. J. A* **39**, 179 (2009).
10. T. Szücs *et al.*, *Eur. Phys. J. A* **44**, 513 (2010).
11. C. Brogini, D. Bemmerer, A. Guglielmetti, R. Menegazzo, *Annu. Rev. Nucl. Part. Sci.* **60**, 53 (2010).
12. R. Bonetti *et al.*, *Phys. Rev. Lett.* **82**, 5205 (1999) arXiv:nucl-ex/9902004.
13. A. Formicola *et al.*, *Phys. Lett. B* **591**, 61 (2004).
14. A. Lemut *et al.*, *Phys. Lett. B* **634**, 483 (2006).
15. D. Bemmerer *et al.*, *Phys. Rev. Lett.* **97**, 122502 (2006).
16. M. Marta *et al.*, *Phys. Rev. C* **78**, 022802(R) (2008).
17. M. Marta *et al.*, *Phys. Rev. C* **83**, 045804 (2011) arxiv:1103.5393.
18. E. Adelberger *et al.*, *Rev. Mod. Phys.* **83**, 195 (2011) arXiv:1004.2318.
19. F. Iocco, G. Mangano, G. Miele, O. Pisanti, P.D. Serpico, *Phys. Rep.* **472**, 1 (2009) arxiv:0809.0631.
20. M. Wiescher, J. Görres, E. Uberseder, G. Imbriani, M. Pignatari, *Annu. Rev. Nucl. Part. Sci.* **60**, 381 (2010).
21. L. Buchmann, C. Barnes, *Nucl. Phys. A* **777**, 254 (2006).
22. T. Spillane *et al.*, *Phys. Rev. Lett.* **98**, 122501 (2007).
23. The DOE/NSF Nuclear Science Advisory Committee, *The Frontiers of Nuclear Science, A Long Range Plan* (DOE/NSF Nuclear Science Advisory Committee, 2008), arXiv:0809.3137.
24. Nuclear Physics European Collaboration Committee, *Long Range Plan: Perspectives of Nuclear Physics in Europe* (NuPECC, 2010).
25. A. Lemut *et al.*, *Phys. Rev. ST Accel. Beams* **14**, 100101 (2011).
26. M. Erhard, *Photoaktivierung des p-Kerns ^{92}Mo am Bremsstrahlungsmessplatz von ELBE*, PhD thesis, TU Dresden (2009).
27. M. Köhler *et al.*, *Appl. Radiat. Isot.* **67**, 736 (2009).
28. W. Helbig, S. Niese, D. Birnstein, *Isotopenpraxis* **20**, 60 (1984).
29. S. Niese, M. Köhler, B. Gleisberg, J. Radioanal. Nucl. Chem. **233**, 167 (1998).
30. C. Nair *et al.*, *Phys. Rev. C* **81**, 055806 (2010) arxiv:1005.2158.
31. J. Dawson *et al.*, *Phys. Rev. C* **78**, 035503 (2008) arxiv:0804.1198.

32. F. Crespi *et al.*, Nucl. Instrum. Methods A **602**, 520 (2009).
33. H. Wulandari, J. Jochum, W. Rau, F. von Feilitzsch, Astropart. Phys. **22**, 313 (2004).
34. G. Duchêne *et al.*, Nucl. Instrum. Methods A **432**, 90 (1999).
35. R. Wordel *et al.*, Nucl. Instrum. Methods A **369**, 557 (1996).
36. R.L. Brodzinski, J.H. Reeves, F.T. Avignone, H.S. Miley, Nucl. Instrum. Methods A **254**, 472 (1987).
37. S. Seuthe *et al.*, Nucl. Instrum. Methods A **260**, 33 (1987).
38. F. Confortola *et al.*, Phys. Rev. C **75**, 065803 (2007).
39. C. Angulo *et al.*, Nucl. Phys. A **656**, 3 (1999).
40. H. Costantini *et al.*, Phys. Rev. C **82**, 035802 (2010).
41. S. Dababneh *et al.*, Phys. Rev. C **68**, 025801 (2003).
42. D. Bemmerer *et al.*, J. Phys. G **36**, 045202 (2009).
43. T.A.D. Brown *et al.*, Phys. Rev. C **76**, 055801 (2007) arxiv:0710.1279.
44. R. Kunz *et al.*, Phys. Rev. Lett. **86**, 3244 (2001).
45. S.E. Woosley, A. Heger, Phys. Rep. **442**, 269 (2007) arXiv:astro-ph/0702176.
46. B. Bodmann *et al.*, Nucl. Instrum. Methods A **286**, 214 (1990).
47. E. Farnea *et al.*, Nucl. Instrum. Methods A **621**, 331 (2010).
48. B. Aharmim *et al.*, Phys. Rev. Lett. **101**, 111301 (2008) arxiv:0806.0989.

LUNA: Nuclear Astrophysics Deep Underground

CARLO BROGGINI*

Istituto Nazionale di Fisica Nucleare (INFN), Sezione di Padova, Padova, Italy
broggini@pd.infn.it

DANIEL BEMMERER

Forschungszentrum Dresden-Rossendorf, Dresden, Germany
d.bemmerer@fzd.de

ALESSANDRA GUGLIELMETTI

Università degli studi di Milano and
Istituto Nazionale di Fisica Nucleare (INFN), Sezione di Milano, Milano, Italy
alessandra.guglielmetti@mi.infn.it

ROBERTO MENEGAZZO

Istituto Nazionale di Fisica Nucleare (INFN), Sezione di Padova, Padova, Italy
roberto.menegazzo@pd.infn.it

Key Words Nuclear astrophysics, underground measurements, solar hydrogen burning, big-bang nucleosynthesis

Abstract Nuclear astrophysics strives for a comprehensive picture of the nuclear reactions responsible for synthesizing the chemical elements and for powering the stellar evolution engine. Deep underground in the Gran Sasso laboratory the cross sections of the key reactions of the proton-proton chain and of the Carbon-Nitrogen-Oxygen (CNO) cycle have been measured right down to the energies of astrophysical interest. The salient features of underground nuclear astrophysics are summarized here. The main results obtained by LUNA in the last twenty years are reviewed, and their influence on the comprehension of the properties of the neutrino, of the Sun and of the Universe itself are discussed. Future directions of underground nuclear astrophysics towards the study of helium and carbon burning and of stellar neutron sources in stars are pointed out.

CONTENTS

Introduction 2

Thermonuclear reactions	3
Underground nuclear astrophysics	4
<i>Laboratory background</i>	4
<i>Beam induced background</i>	5
<i>LUNA at Gran Sasso</i>	6
Experimental apparatus at LUNA	6
<i>Accelerators</i>	6
<i>Targets and ancillary measurements</i>	7
<i>Detectors</i>	8
Hydrogen burning in the Sun	8
<i>proton-proton chain</i>	9
<i>Carbon-Nitrogen-Oxygen cycle</i>	10
<i>Neutrinos</i>	10
Hydrogen burning studied at LUNA	11
${}^2\text{H}(p,\gamma){}^3\text{He}$: <i>the energy source of the proto-star</i>	11
${}^3\text{He}({}^3\text{He},2p){}^4\text{He}$: <i>in search of the resonance</i>	12
${}^3\text{He}({}^4\text{He},\gamma){}^7\text{Be}$: <i>solar neutrino oscillations</i>	12
${}^{14}\text{N}(p,\gamma){}^{15}\text{O}$: <i>the composition of the Sun and the age of the Universe</i>	13
<i>Ongoing measurements</i>	14
Outlook	15
Conclusions	16

1 Introduction

The stars which like diamonds fill the sky at night fascinating our mind are not perfect and everlasting bodies as believed by the ancient philosophers. On the contrary, gravity triggers the birth of a star which then works as a more or less turbulent chemical factory (1) to finally die out in a quiet or violent way, depending on its initial mass (2). As a matter of fact, only hydrogen, helium and lithium are synthesized in the first minutes after the big-bang. All the other elements of the periodic table are produced in the thermonuclear reactions taking place inside the stars, where the nuclear roots of life itself are embedded in (3,4). The aim of nuclear astrophysics is to reach a comprehensive picture of all these reactions which realize the transmutation of the chemical elements and which provide the energy to run the engine of stellar evolution (5).

The knowledge of the reaction cross-section at the stellar energies lies at the heart of nuclear astrophysics. At these energies the cross sections are extremely small. Such smallness makes the star life-time of the length we observe, but it also makes impossible the direct measurement in the laboratory. The rate of the reactions, characterized by a typical energy release of a few MeV, is too low, down to a few events per year, in order to stand out from the background. LUNA, Laboratory for Underground Nuclear Astrophysics, started twenty years ago to

*Corresponding author

run nuclear physics experiments in an extremely low-background environment: the Gran Sasso Laboratory. Since you cannot distinguish the timbre of a piano note in a crowded circus, but you can do so if you are in a music hall, then the LUNA physicists are tuning their accelerators and detectors in the 'music hall' deeply inside the mountain 'to listen' to the tiny signal from nucleo-synthesis reactions, reproducing this way in the laboratory what Nature makes inside the stars.

In this review the main features of thermonuclear reactions at very low energy, the characteristics of the background attainable in Gran Sasso and the experimental apparatus employed by LUNA will first be described. Then, an overview of hydrogen burning in stars will be given and the LUNA main results will be discussed, with emphasis on their impact on the picture of the Sun and of the neutrino. Finally, the next steps of underground nuclear astrophysics, mainly devoted to the study of the helium and carbon burning and of the neutron sources in stars, will be outlined.

2 Thermonuclear reactions

Thermonuclear reactions between nuclei occur inside the star in a relatively narrow energy window, placed at an energy much lower than the height of the barrier arising from the Coulomb repulsion between nuclei. As a consequence, the reaction can only take place owing to the quantum mechanical tunnel effect which leads to a very small, but not vanishing, probability for the incoming nucleus to penetrate the Coulomb barrier and to reach its reaction partner.

Because of the tunnel effect, at these energies the reaction cross-section $\sigma(E)$ drops almost exponentially with decreasing energy E :

$$\sigma(E) = \frac{S(E)}{E} \exp(-2\pi\eta) \quad (1)$$

where $S(E)$ is the so-called astrophysical S -factor and $2\pi\eta = 31.29 Z_1 Z_2 (\mu/E)^{1/2}$. Z_1 and Z_2 are the electric charges of the nuclei, μ is the reduced mass (in a.m.u.), and E is the energy (in keV) in the center of mass system (2,3). For most of the reactions, the astrophysical S -factor varies only slowly with energy and contains all the nuclear physics information.

The reaction rate in the hot plasma of a star, with temperatures in the range of tens to hundreds of millions Kelvin, is obtained by weighting the reaction cross section $\sigma(E)$ with the energy distribution of the colliding nuclei: a Maxwell-Boltzmann $\phi(E)$ peaked at energies of 1-10 keV. The product between $\sigma(E)$ and $\phi(E)$ identifies the energy window where the reactions occur in the star: the Gamow peak. At lower energies the cross section is too small whereas at higher energies the nuclei in the tail of the Maxwell-Boltzmann are too few. Finally, the energy balance of the nuclear reaction is determined by the Q -value, which corresponds to the mass difference between the entrance and exit channels.

In order to obtain the precise nuclear physics data required by modern astrophysics one should measure the relevant reaction cross section directly at the energy of the astrophysical scenario to be studied. For the solar reactions the

cross-section values at the Gamow peak range from picobarn to femtobarn and even below ($1 \text{ barn} = 10^{-24} \text{ cm}^2$). These extremely low cross sections, while trying the patience of the physicists with ultra-low count rates, are a blessing to mankind in general, because they allow hydrogen burning to proceed in the Sun at a placid pace for several billions of years to come.

However, the low count rates pose another experimental problem: in direct laboratory measurements at the Earth's surface the signal to background ratio is too small. So, instead of a direct measurement, the observed energy dependence of the cross-section at high energies is extrapolated to the low energy region. However, any extrapolation is fraught with uncertainty. For example, there might be narrow resonances at low energy or even resonances below the reaction threshold that influence the cross section at the Gamow peak. Those effects cannot always be accounted for by an extrapolation.

In addition, another effect can be studied at low energies: electron screening (6, 7, 8, 9). In the laboratory, the electron cloud surrounding the target nucleus partially screens its positive electric charge. This reduces the height of the Coulomb barrier, thus increasing the tunneling probability and eventually the reaction cross-section. The screening effect has to be taken into account in order to derive the cross-section for bare nuclei, which is the input data to nucleosynthesis network codes. These codes, in turn, have to take into account the screening by electrons in the stellar plasma (6).

All these effects mean that, despite the impressive-sounding temperatures of many millions Kelvin in stellar interiors, actually the study of the star requires nuclear physics experiments at very low energy, measuring exceedingly small cross sections.

3 Underground nuclear astrophysics

For stable stellar hydrogen burning, the relevant temperatures range from 20 to $100 \cdot 10^6 \text{ K}$, corresponding to Gamow peak energies of 10–50 keV, depending on the precise reaction of interest. The challenge of the measurement at the Gamow peak is to suppress the laboratory and beam induced background and then to enhance the signal by boosting the beam intensity, target density, and detection efficiency.

3.1 Laboratory background

The laboratory γ -background has two main sources: natural and cosmic-ray induced radioactivity. The decay of radioisotopes from the natural decay chains are evident with many characteristic γ -lines in the region below 2.6 MeV, where the highest energy γ due to natural radioactivity is found. Figure 1 illustrates the different steps in background reduction that are necessary for nuclear astrophysics experiments.

From a naked detector to a commercially available graded shield (10), including 10 cm lead, there is already a sizable reduction. This is due to the suppression of the soft component of cosmic-rays and of the γ -rays from nearby radioiso-

topes. By going to a shallow underground laboratory at 100 m.w.e. (meters water equivalent) and applying a more sophisticated shield, another reduction is possible (11). At this point the remaining background is dominated by muon induced events.

These muon induced events stem from the decay of the radioactive nuclei due to muon spallation and to the capture of stopping negative muons, from the inelastic scattering and capture of the muon induced neutrons, from the energy loss of muons passing through the detector. The prompt effects of the muons can be reduced by surrounding the detector with a veto counter. On the contrary, the muon induced radioactivity may have a relatively long life-time (1-10 s), so a veto counter will not help against it. Instead, this remaining background can be overcome by moving to a deep underground laboratory (12,13), where the muon flux is strongly reduced (e.g. by six orders of magnitude (14) at the 3800 m.w.e. deep Gran Sasso laboratory).

At higher γ -ray energies, i.e. $E_\gamma > 2.6$ MeV, these considerations become more transparent. In this γ -energy region no significant improvement in background can be reached by applying an additional lead shield. Instead, going to a shallow-underground laboratory helps somewhat, and a muon veto reduces the background. When going deep underground, the muon flux becomes negligible, and the veto does not further reduce the background counting rate. A further reduction below this very low γ -background observed at LUNA (15,16) can in principle be achieved by shielding the set-up against neutrons. The neutron flux in Gran Sasso is already reduced by three orders of magnitude as compared to the outside and it is due to the (α ,n) reactions in the rock (17).

For the sake of completeness, we remind that nuclear astrophysics is just one of the fields explored deep underground. The salient features of underground physics have been reviewed in the past (18). Major underground activities are the detection of neutrinos generated by the hydrogen burning in the Sun (19,20), by the radioactivity in the Earth (21) and by cosmic-rays in the Earth's atmosphere (22), the search for rare processes such as neutrinoless double- β decay (23), proton decay (24) and dark matter interactions(25). Recently a compendium of major facilities has been presented (26).

3.2 Beam induced background

In any experiment with an ion beam, the beam interacts also with nuclei other than the target to be studied. Such nuclei could be found in the beam transport system (mainly beam limiting apertures, but also drift tubes, magnets and residual gas) but also as parts of the target itself. Such interactions can give rise to γ -ray background.

This ion beam induced background is clearly independent of the underground depth and must be dealt with by reducing the inventory of materials hit by the ion beam and by appropriate precautions to eliminate particularly worrisome components. For low-energy nuclear astrophysics experiments this task is greatly facilitated by two aspects. Firstly, contaminants with atomic number greater than the target to be studied will generally have lower interaction probability

than the target itself because of their higher Coulomb barrier. Many experiments study light nuclei of $Z \leq 8$, so common materials such as aluminum or steel will generally not give background. Secondly, the otherwise commonly found activation of beamline components is not an issue with low-energy proton or α -beam. In cases where the background still plays a role, it must be carefully identified, localized (15, e.g.) and eliminated.

3.3 LUNA at Gran Sasso

There are several possible techniques to measure cross sections at the Gamow peak. All of them have so far been pursued just in one laboratory: LUNA.

For nuclear reactions where charged particles are emitted, generally an in-beam measurement at the surface of the Earth is possible. This is true except for cases where coincident background due to cosmic rays is a problem. If so, only an underground measurement is feasible, as it has been demonstrated for the ${}^3\text{He}({}^3\text{He},2\text{p}){}^4\text{He}$ reaction (27, 28).

For nuclear reactions where only γ -rays are emitted, there are in principle two approaches. In-beam γ -spectrometry deep underground has been applied to the studies of the ${}^2\text{H}(\text{p},\gamma){}^3\text{He}$ (29), ${}^{14}\text{N}(\text{p},\gamma){}^{15}\text{O}$ (30, 31, 32, 33, 34), ${}^3\text{He}({}^4\text{He},\gamma){}^7\text{Be}$ (35, 36) and ${}^{15}\text{N}(\text{p},\gamma){}^{16}\text{O}$ (37) reactions.

The in-beam approach has to take some uncertainty into account due to the usually not well known angular distribution of the emitted γ -rays. This weakness can be overcome in selected cases where the created nucleus is radioactive, thus allowing an independent cross-check. An activation study with deep underground activity-counting has been performed in the study of ${}^3\text{He}({}^4\text{He},\gamma){}^7\text{Be}$ (38, 39). All these approaches benefit from the reduced background deep underground.

4 Experimental apparatus at LUNA

The measurement of the cross section and the determination of the astrophysical S-factor for thermonuclear reactions require an experimental apparatus basically composed of an accelerator, a target and a detection system.

4.1 Accelerators

Two different accelerators have been used at LUNA: a compact 50 kV "home-made" machine (40) and a commercial 400 kV one (41). Common features of the two accelerators are the high beam current, the long term stability and the precise beam energy determination. The first feature is required to maximize the reaction rate, the second is due to the long time typically needed for a cross section measurement, while the third is important because of the exponential-like energy dependence of the cross section.

The 50 kV machine was designed and built at the Ruhr Universität in Bochum and then moved to Gran Sasso. It consisted of a duoplasmatron ion source, an ion beam extraction and acceleration system and a double-focusing 90° analysing magnet. Its compact shape optimized the beam transmission. All in all the

machine (40) was able to deliver beams of protons, ${}^3\text{He}^+$ and ${}^4\text{He}^+$ of 300-500 μA at energies between 10 and 50 keV with an energy spread of less than 20 eV and a long term stability. This allowed the study of two fundamental reactions of the p-p chain: ${}^3\text{He}({}^3\text{He},2\text{p}){}^4\text{He}$ and ${}^2\text{H}(\text{p},\gamma){}^3\text{He}$ at solar Gamow peak energies and of the screening effect in the ${}^2\text{H}({}^3\text{He},\text{p}){}^4\text{He}$ reaction.

Even though it produced outstanding results (28,29,42), this machine should be considered as a pilot project towards a higher energy facility, namely the 400 kV accelerator (41) shown in Fig. 2. This electrostatic accelerator is embedded in a tank filled with a mixture of N_2/CO_2 gas at 20 bar, working as insulator. The high voltage is generated by an Inline-Cockroft-Walton power supply located inside the tank. The radio-frequency ion source, directly mounted on the accelerator tube can provide beams of 1 mA hydrogen and 500 μA He^+ over a continuous operating time of 40 days. The ions can be sent into one of two different and parallel beam lines, this way allowing the installations of two different target set-ups. In the energy range 150-400 keV, the accelerator can provide up to 500 μA of protons and 250 μA of alphas at the target stations, with 0.3 keV accuracy on the beam energy, 100 eV energy spread and 5 eV/h long-term stability. Finally, the accelerator is controlled by PLC-based computers which allow for a safe operation over long periods without an operator present in situ.

4.2 Targets and ancillary measurements

LUNA measurements have been performed either with solid or gas targets. Solid targets may contain a larger number of atoms per cm^2 with respect to gas targets: typical areal densities are in the range $2\cdot 10^{17}$ - $2\cdot 10^{18}$. They also allow for the measurement of the cross-section angular dependence since the beam-hit position on the target can be rather precisely determined. Gas targets, instead, are more stable to beam bombardment and may reach an extreme purity, essential to minimize the beam induced background. In this case areal densities used in LUNA are between $5\cdot 10^{16}$ and $1\cdot 10^{18}$. While for solid targets LUNA has taken advantage of well known production techniques such as implantation, evaporation or sputtering (31), for gas targets a specific set-up, consisting of a windowless gas target (i.e a differentially pumped target) with recirculation system (43,39), has been designed and installed at Gran Sasso and is partially shown in Fig.3.

A typical disadvantage of a gas target is the so called "beam heating" effect, due to the power deposition which gives rise to the heating and the thinning of the gas along the beam path. Different techniques are necessary to obtain the real number of atoms per cm^2 in the beam region. A specific set-up based on the Rutherford scattering was designed (44) and it allowed for a systematic uncertainty on the gas density determination due to the beam heating effect below 2% (38). Alternatively, the target thickness along the beam can be obtained by the energy shift of a proper well known resonance (45,33).

Solid targets, in turn, may rapidly deteriorate with the intense beam impinging onto, thus changing the density profile which is an essential ingredient of the reaction rate. In order to monitor the target thickness and its stability under beam, the resonance scan technique may be used. This consists in selecting a

resonance of the reaction to be studied or of a parasitic reaction and measuring the yield profile as a function of the beam energy. The selected resonance should be characterized by an energy width smaller or equal to the target thickness. The target thickness as well as the maximum yield can be repeatedly monitored during the whole measurement time.

For the cross section measurement it is essential to know the beam current on target. While for a solid target the current is measured through a conventional Faraday cup, for a gas target this is not possible due to the ion charge state changes (46). Therefore, LUNA has developed a beam calorimeter (43) with a constant temperature gradient between a hot and a cold side. The power to the hot side is provided by the beam and by resistors embedded in the end-cap of the calorimeter. The number of projectiles is then obtained by the difference in heating powers dissipated by the resistors with and without beam divided by the kinetic energy of the projectiles themselves at the calorimeter surface. If properly calibrated, the calorimeter can give a systematic uncertainty of the order of 1% on the beam current (43). Calorimeter calibration is an example of the measurements done in laboratories at the Earth surface and important to complete and integrate the results obtained underground.

4.3 Detectors

Apart from the ${}^3\text{He}({}^3\text{He},2\text{p}){}^4\text{He}$ reaction where protons had to be detected and this was accomplished by commercial silicon detectors as single stage or ΔE -E telescopes, all the other LUNA measurements required the detection of γ -rays. Here the choice of the most suitable detector depends on the desired physical information. The 4π BGO summing crystal used at LUNA (43), a cylinder 28 cm long with a 20 cm diameter and a 6 cm bore-hole, can reach an efficiency as high as 70% for 7 MeV γ -ray thus allowing the measurement of extremely low reaction yields. As a counterpart, the BGO energy resolution is very poor and does not allow measurements of cascades and branching ratios to different levels since most of the γ ray transitions are summed in a single peak. With a germanium detector the efficiency dramatically decreases to the level of a few permille but the energy resolution is much better thus allowing to disentangle complex gamma cascades. Moreover, angular distribution measurements are possible by moving the detector to different angles with respect to the ion beam. Nevertheless, summing effects can disturb the data evaluation for close geometry configurations. This can be addressed by using a composite detector like a Clover (47), i.e. 4 small germanium detectors closed inside the same cryostat, this way reducing summing-in corrections.

5 Hydrogen burning in the Sun

As the solar mass contracted from an initially large gas cloud, half of the gravitational energy released has been radiated into the space and half converted into kinetic energy of the hydrogen and helium nuclei, thus increasing the temperature of the system (2). This way the solar mass was losing energy, contracting

and heating up. If gravitational energy were the only energy source then the Sun would have ended its life when only 30 million years old, as estimated by Lord Kelvin in the 19th century. On the contrary, at the central temperature of about 10 million degrees the kinetic energy of the hydrogen nuclei was high enough to penetrate with significant probability the Coulomb barrier and to switch on the hydrogen burning: $4^1\text{H} \Rightarrow ^4\text{He} + 2e^+ + 2\nu_e$, i.e. the fusion of hydrogen into helium with the production of positrons and neutrinos. The mass of the helium nucleus is lower than 4 times the proton mass, as a consequence about 0.7% of the hydrogen rest mass is converted into energy in each of the transmutations.

Hydrogen fusion supplies the energy necessary to halt the contraction and it provides all the energy required for the long and quiet life of the star. The Sun is a middle-aged main sequence star which shines by burning hydrogen fuel. It started burning hydrogen about 4.5 billion years ago and, in about 5 billion years, it will burn helium to finally end-up as a celestial body mainly consisting of carbon and oxygen. In the central region of the Sun, at the temperature of 15 million degrees and with a density of about 150 gr cm^{-3} , the hydrogen burning does not take place in one step only but it proceeds through series of two body reactions: the proton-proton (pp) chain and the CNO cycle. The relative importance of the different reactions is determined by the abundance of the nuclear species which are fusing together and by their fusion cross section at the Gamow peak energy.

5.1 proton-proton chain

The first step and bottleneck of the chain is the production of deuterium (48). It takes place through two different weak processes (Fig. 4): $^1\text{H}(p, e^+ \nu)^2\text{H}$ (giving rise to the so called pp neutrinos) and $^1\text{H}(p e^-, \nu)^2\text{H}$ (pep neutrinos). The latter, being a three body process, is strongly suppressed (about a factor 400) as compared to the former. Once produced, the deuterium quickly burns with hydrogen to synthesize ^3He . At this point a complex and rich scenario opens with several possible branches. $^3\text{He}(p, e^+ \nu)^4\text{He}$ (hep neutrinos) has a negligible rate since it is a weak process further suppressed, as compared to $^1\text{H}(p, e^+ \nu)^2\text{H}$, because of the atomic number of helium. The most probable fate of ^3He is to fuse with another ^3He nucleus to finally produce ^4He in the strong reaction $^3\text{He}(^3\text{He}, 2p)^4\text{He}$. In about 14% of the cases the fusion takes place with the much more abundant ^4He through the electromagnetic process $^3\text{He}(^4\text{He}, \gamma)^7\text{Be}$. At this level the chain branches again due to the competition between the electron capture decay of ^7Be : $^7\text{Be}(e^-, \nu)^7\text{Li}$ (^7Be neutrinos) and the fusion of ^7Be with hydrogen: $^7\text{Be}(p, \gamma)^8\text{B}$. The former is a weak process which is about a factor thousand more probable than the latter since it has no Coulomb barrier suppression. Once produced, ^7Li quickly fuses with hydrogen to produce ^8Be which is extremely unstable and splits into two helium nuclei. $^7\text{Be}(p, \gamma)^8\text{B}$ seldom occurs but it is of crucial importance since it leads to the 'high' energy neutrinos emitted in the ^8B decay to ^8Be .

5.2 Carbon-Nitrogen-Oxygen cycle

In the Carbon-Nitrogen-Oxygen cycle (CNO cycle) the conversion of hydrogen into helium is achieved with the aid of the carbon previously synthesized in older stars (3). Carbon works as a catalyst, it is not destroyed by the cycle and it strongly affects the rate of the CNO cycle with its abundance. Since $^{15}\text{N}(p,\gamma)^{16}\text{O}$ has a cross section which is about a factor two thousand lower than $^{15}\text{N}(p,\alpha)^{12}\text{C}$, the second CNO cycle is strongly suppressed as compared to the first one. In the Sun the CNO cycle accounts for just a small fraction of the nuclear energy production (less than 1%) and it is ruled by $^{14}\text{N}(p,\gamma)^{15}\text{O}$, the bottleneck reaction. Only at the temperature of 20 millions degree it would give the same contribution as the pp chain, whereas it would dominate at higher temperatures, where the effects of the Coulomb barriers do not strongly affect anymore the energy production rate.

5.3 Neutrinos

Neutrinos are particle which interact weakly with matter, they travel at a speed which is essentially the speed of light and they reach the Earth 8 minutes after their birth in the central region of the Sun. The calculation of their flux is straightforward when we know that hydrogen fusion $4^1\text{H} \Rightarrow ^4\text{He} + 2e^+ + 2\nu_e$ is producing 26.7 MeV energy and if we make the much reasonable assumption that the present luminosity of the Sun corresponds to the present nuclear energy production rate (49) (it takes more than 10^4 years to the electromagnetic energy to reach the surface of the Sun). We only have to divide the solar luminosity, $3.85 \cdot 10^{26}$ Watt, by the energy required to have one neutrino, $13.35 \text{ MeV} \equiv 2.14 \cdot 10^{-12}$ Joule, to obtain a rate of $1.80 \cdot 10^{38}$ neutrinos per second. This corresponds to a flux of about 60 billions neutrinos per squared centimeter per second on the Earth. Instead, nuclear physics, in particular the cross section of the different reactions of the pp chain and of the CNO cycle, is the key ingredient to calculate the energy spectrum of the solar neutrinos: the different branches give rise to neutrinos of different energy.

In particular, pp neutrinos have a flux of $6.04 \cdot 10^{10} \text{ cm}^{-2}\text{s}^{-1}$ (50), corresponding to 92% of the total neutrino flux. Their continuous spectrum has the end-point energy of 0.42 MeV, which makes their detection extremely difficult. ^7Be neutrinos are produced with two different energies: 0.86 MeV (89.7% branching ratio) and 0.38 MeV. The 0.86 MeV ^7Be neutrinos are the second biggest component of the spectrum, amounting to 7% of the total with a flux of $4.55 \cdot 10^9 \text{ cm}^{-2}\text{s}^{-1}$. ^8B neutrinos have a much lower flux, $4.72 \cdot 10^6 \text{ cm}^{-2}\text{s}^{-1}$: fewer than one neutrino over ten thousand is coming from the ^8B decay. However, their relatively high end-point energy, about 15 MeV, makes their detection the least difficult one. As a matter of fact, ^8B neutrinos are the best studied neutrinos from the Sun so far. The CNO cycle is producing neutrinos with end-point energy of 1.20 MeV (^{13}N) and 1.73 MeV (^{15}O). The latest results of the standard solar model (50) predicts a 0.5% contribution of the CNO neutrinos to the total flux.

In 1964 J.N. Bahcall and R. Davis Jr. proposed to detect solar neutrinos in

order to see into the interior of the Sun and thus directly verify the hypothesis of nuclear energy generation in stars (51, 52). About 40 years of much refined experimental and theoretical work have been required to show that the source of the energy radiated by the Sun is the hydrogen fusion in the solar interior. In addition, solar neutrinos told us something extremely important about the nature of neutrino itself: it oscillates. Produced as electron neutrino inside the Sun, it may be a muon or tau neutrino when reaching the Earth.

6 Hydrogen burning studied at LUNA

LUNA started as a pilot project in the year 1991. In the following paragraphs we will discuss the brush-strokes given by LUNA during the last 20 years to the current picture of the Sun and of the neutrino.

6.1 ${}^2\text{H}(\text{p},\gamma){}^3\text{He}$: the energy source of the proto-star

Inside the Sun, the ${}^2\text{H}(\text{p},\gamma){}^3\text{He}$ reaction controls the equilibrium abundance of deuterium. In a different scenario, ${}^2\text{H}(\text{p},\gamma){}^3\text{He}$ is the reaction which rules the life of proto-stars before they enter the main sequence phase. Proto-star models predict that a star forms by accretion of interstellar material onto a small contracting core. Until the temperature remains below 10^6 K, the main source of energy is the gravitational contraction. When the temperature approaches 10^6 K the first "nuclear fire" is switched on inside the star: the primordial deuterium is converted into ${}^3\text{He}$ via ${}^2\text{H}(\text{p},\gamma){}^3\text{He}$, thus providing 5.5 MeV for each reaction. The total amount of nuclear energy generated by this d-burning is comparable with the whole gravitational binding energy of the star. The on-set of d-burning slows down the contraction, increases the lifetime of the star and freezes its observational properties until the original deuterium is fully consumed. A reliable knowledge of the rate of ${}^2\text{H}(\text{p},\gamma){}^3\text{He}$ down to a few keV (the Gamow peak in a proto-star) is a fundamental prerequisite for the proto-stellar models.

${}^2\text{H}(\text{p},\gamma){}^3\text{He}$ is also a cornerstone in the big-bang nucleosynthesis (BBN). Because of the deuterium "bottleneck" (53), i.e. the photo-disintegration of deuterium, the formation of ${}^3\text{He}$ is delayed until the temperature drops to about $8 \cdot 10^8$ K. Once again, the knowledge of the cross section at low energies is required.

The ${}^2\text{H}(\text{p},\gamma){}^3\text{He}$ cross section measurement was performed at LUNA with the 50 kV accelerator connected to a differentially pumped gas-target system designed to fit the large BGO γ -ray detector (43). The BGO, placed around the deuterium target, was detecting the 5.5 MeV γ -ray with 70% efficiency. The LUNA results (29) are given in Fig. 5 together with two previous measurements (54, 55) of the astrophysical factor $S(E)$ at low energy. The agreement with the theoretical calculations is excellent (56).

6.2 ${}^3\text{He}({}^3\text{He},2\text{p}){}^4\text{He}$: in search of the resonance

The initial activity of LUNA has been focused on the ${}^3\text{He}({}^3\text{He},2\text{p}){}^4\text{He}$ cross section measurement within the solar Gamow peak (15-27 keV). Such a reaction is a key one of the pp chain. A resonance at the thermal energy of the Sun was suggested long time ago (57,58) to explain the observed ${}^8\text{B}$ solar neutrino flux. Such a resonance would decrease the relative contribution of the alternative reaction ${}^3\text{He}({}^4\text{He},\gamma){}^7\text{Be}$, which generates the branch responsible for ${}^7\text{Be}$ and ${}^8\text{B}$ neutrino production in the Sun.

The final set-up was made of eight 1 mm thick silicon detectors of $5\times 5\text{ cm}^2$ area placed around the beam inside the windowless target chamber filled with ${}^3\text{He}$ at the pressure of 0.5 mbar. The simultaneous detection of two protons has been the signature which unambiguously identified a ${}^3\text{He}({}^3\text{He},2\text{p}){}^4\text{He}$ fusion reaction (Q -value: 12.86 MeV). Fig. 6 shows the results from LUNA (27,28) together with higher energy measurements (59,60,61) of the astrophysical factor $S(E)$.

For the first time a nuclear reaction has been measured in the laboratory at the energy occurring in a star. Its cross section varies by more than two orders of magnitude in the measured energy range. At the lowest energy of 16.5 keV it has the value of 0.02 pb, which corresponds to a rate of about 2 events/month, rather low even for the "silent" experiments of underground physics. No narrow resonance has been found within the solar Gamow peak and, as a consequence, the astrophysical solution of the ${}^8\text{B}$ and ${}^7\text{Be}$ solar neutrino problem based on its existence has been ruled out.

6.3 ${}^3\text{He}({}^4\text{He},\gamma){}^7\text{Be}$: solar neutrino oscillations

${}^3\text{He}({}^4\text{He},\gamma){}^7\text{Be}$ (Q -value: 1.586 MeV) is the key reaction for the production of ${}^7\text{Be}$ and ${}^8\text{B}$ neutrinos in the Sun since their flux depends almost linearly on its cross section. Unless a recoil separator is used (62), the cross section can be determined either from the detection of the prompt γ rays (63,64,65,66,67,68,69) or from the counting of the produced ${}^7\text{Be}$ nuclei (67,70,71,72,62). The latter requires the detection of the 478 keV γ due to the excited ${}^7\text{Li}$ populated in the decay of ${}^7\text{Be}$ (half-life: 53.22 days).

Both methods have been used in the past to determine the cross section in the energy range $E_{c.m.} \geq 107\text{ keV}$ but the $S_{3,4}$ extracted from the measurements of the induced ${}^7\text{Be}$ activity was 13% higher than that obtained from the detection of the prompt γ -rays (73).

The underground experiment has been performed with the ${}^4\text{He}^+$ beam from the 400 kV accelerator in conjunction with a windowless gas target filled with ${}^3\text{He}$ at 0.7 mbar. The beam enters the target chamber and is stopped on the calorimeter (Fig. 3). The ${}^7\text{Be}$ nuclei produced by the reaction inside the ${}^3\text{He}$ gas target are implanted into the calorimeter cap which, after the irradiation, is removed and placed in front of a germanium detector for the measurement of the ${}^7\text{Be}$ activity.

In the first phase of the experiment, the ${}^3\text{He}({}^4\text{He},\gamma){}^7\text{Be}$ cross section has been obtained from the activation data (38,39) alone with a total uncertainty of about

4%. In the second phase, a new high accuracy measurement using simultaneously prompt and activation methods was performed down to the center of mass energy of 93 keV. The prompt capture γ -ray was detected by a 135% germanium heavily shielded and placed in close geometry with the target. The spectrum taken at 250 keV beam energy is given in Fig. 7. The astrophysical factor obtained with the two methods (35) is the same within the quoted experimental error (Fig.8). Similar conclusions have then been reached in a new simultaneous activation and prompt experiment (74) which covers the $E_{c.m.}$ energy range from 330 keV to 1230 keV.

The energy dependence of the cross section seems to be theoretically well determined at low energy. If we leave the normalization as the only free parameter, we can rescale the fit of (75) to our data and we obtain $S_{3,4}(0)=0.560\pm 0.017$ keV barn. Thanks to our small error, the total uncertainty on the ${}^8\text{B}$ solar neutrino flux goes from 12 to 10%, whereas the one on the ${}^7\text{Be}$ flux goes from 9.4 to 5.5% (35). The ${}^7\text{Be}$ flux is now theoretically predicted with an error as small as the experimental one which should soon be achieved by Borexino (76). Thanks to such small errors, it will be possible to have a precise study of the signature typical of neutrino oscillations in matter, i.e. the energy dependence of the oscillation probability.

The energy window covered by LUNA is above the solar Gamow peak but well within the Gamow peak of big-bang nucleosynthesis. Our precise results clearly rule out the ${}^3\text{He}({}^4\text{He},\gamma){}^7\text{Be}$ cross section as possible source of the discrepancy between the predicted primordial ${}^7\text{Li}$ abundance (77) and the much lower observed value (78,79).

6.4 ${}^{14}\text{N}(p,\gamma){}^{15}\text{O}$: the composition of the Sun and the age of the Universe

${}^{14}\text{N}(p,\gamma){}^{15}\text{O}$ (Q -value: 7.297 MeV) is the slowest reaction of the CNO cycle and it rules its energy production rate. In particular, it is the key reaction to know the ${}^{13}\text{N}$ and ${}^{15}\text{O}$ solar neutrino flux, which depends almost linearly on its cross section, as well as to determine the age of the globular clusters, which, consisting of 10^4 - 10^6 gravitationally bound stars, are the oldest population of the galaxies. The luminosity of the turn-off point in the Hertzsprung-Russel diagram of a globular cluster, i.e. the point where the main sequence turns toward cooler and brighter stars, is used to determine the age of the cluster and to derive a lower limit on the age of the Universe (80). A star at the turn-off point is burning hydrogen in the shell through the CNO cycle, this is the reason why the ${}^{14}\text{N}(p,\gamma){}^{15}\text{O}$ cross section plays an important role in the age determination.

In the first phase of the LUNA study, data have been obtained down to 119 keV energy with solid targets of TiN and a 126% germanium detector. This way, the five different radiative capture transitions which contribute to the ${}^{14}\text{N}(p,\gamma){}^{15}\text{O}$ cross section at low energy were measured. The total cross section was then studied down to very low energy in the second phase of the experiment by using the 4π BGO summing detector placed around a windowless gas target filled with

nitrogen at 1 mbar pressure (the BGO spectrum at 100 keV beam energy is shown in Fig. 9). At the lowest center of mass energy of 70 keV a cross section of 0.24 pbarn was measured, with an event rate of 11 counts/day from the reaction.

The results obtained first with the germanium detector (30,31) and then with the BGO set-up (32) were about a factor two lower than the existing extrapolation (81, 73, 82) from previous data (83, 84) at very low energy (Fig.10), while in agreement with results from indirect methods (85, 86, 87, 88, 89, 90).

As a consequence, the CNO neutrino yield in the Sun is decreased by about a factor two, and the age of the globular clusters is increased by 0.7-1 billion years (91) up to 14 billion years. The lower cross section is affecting also stars which are much more evolved than our Sun: in particular, the dredge-up of carbon to the surface of asymptotic giant branch stars (92) is more efficient (93).

The main conclusion from the LUNA data has been confirmed by an independent study at higher energy (94). However, there is a 15% difference between the total S-factor extrapolated by the two experiments at the Gamow peak of the Sun. In particular, this difference arises from the extrapolation of the capture to the ground state in ^{15}O , a transition strongly affected by interference effects between several resonances and the direct capture mechanism.

In order to provide precise data for the ground state capture, a third phase of the $^{14}\text{N}(p,\gamma)^{15}\text{O}$ study has been performed with a composite germanium detector in the beam energy region immediately above the 259 keV resonance, where precise data effectively constrain a fit for the ground state transition in the R-matrix (95) framework. This way the total error on the S-factor was reduced to 8%: $S_{1,14}(0)=1.57\pm 0.13$ keV barn (34). This is significant because, finally solved the solar neutrino problem, we are now facing the solar composition problem: the conflict between helioseismology and the new metal abundances that emerged from improved modeling of the photosphere (50, 96). Thanks to the relatively small error, it will soon be possible to measure the metallicity of the core of the Sun (i.e. the contents of elements different from hydrogen and helium) by comparing the detected CNO neutrino flux with the predicted one. As a matter of fact, the CNO neutrino flux is decreased by about 35% in going from the high to the low metallicity scenario. This way it will be possible to test whether the early Sun was chemically homogeneous (97), a key assumption of the standard Solar Model.

6.5 Ongoing measurements

The solar phase of LUNA has almost reached the end. A new and rich program of nuclear astrophysics mainly devoted to the Mg-Al and Ne-Na cycles has already started at the 400 kV facility about 2 years ago with the measurement of $^{25}\text{Mg}(p,\gamma)^{26}\text{Al}$ (98). These cycles become important for second generation stars with central temperatures and masses higher than those of our Sun (3,5). Due to the higher Coulomb barriers, these cycles are relatively unimportant for energy generation while being essential for the nucleosynthesis of elements with mass number higher than 20. Low energy resonances (or the low energy part of the direct capture) inaccessible in a laboratory at the Earth surface, could become

measurable underground. Some of the selected reactions have already been measured over ground but an underground re-investigation can substantially improve the knowledge of the related reaction rate in the different astrophysical scenarios responsible, in particular, of the texture of the isotopes which are filling the Universe.

LUNA is now measuring $^{15}\text{N}(p,\gamma)^{16}\text{O}$ with enriched ^{15}N targets. $^{15}\text{N}(p,\gamma)^{16}\text{O}$ is the leak reaction from the first to the second CNO cycle. The results already obtained with nitrogen of natural isotopic composition (0.366% ^{15}N) (37) extend to energies lower than ever measured before and provide a cross section which is about a factor two lower than previously believed at novae energies.

The measurement under preparation is not connected to the hydrogen burning cycles but it is a key reaction of big-bang nucleosynthesis: $^2\text{H}(^4\text{He}, \gamma)^6\text{Li}$. As a matter of fact, such reaction determines the amount of primordial ^6Li in the Universe. Recently, the ^6Li isotope has been detected in a number of metal poor stars (99, 100) and its quantity has been found to be 2-3 orders of magnitude higher than what expected from BBN (77).

7 Outlook

As we have seen, the approach to measure cross sections directly at the energy of astrophysical interest has been used with great success for the reactions governing stellar hydrogen-burning. In order to keep pace with the rapid progress of observational astronomy and astrophysical modeling, the same should now be done for the nuclear reactions governing helium and carbon burning and producing inside stars the neutrons which give rise to the so-called astrophysical s-process. Owing to the different nature of these reactions, new techniques and new equipment are necessary for this task.

The $^{12}\text{C}(\alpha,\gamma)^{16}\text{O}$ reaction is often referred to as the "Holy Grail" of nuclear astrophysics (101, 102, 103, 104, 105, 106). It plays a fundamental role in the evolution of stars during the helium-burning phase and determines the abundance ratio between carbon and oxygen, the two elements of fundamental importance to the development of life. This abundance ratio, in turn, influences the nucleosynthesis of elements up to the iron peak for massive stars, the cooling timescale of white dwarfs and the properties of thermonuclear as well as core collapse supernovae.

The $^{12}\text{C}+^{12}\text{C}$ fusion reactions form the onset of carbon burning. Their rate determines the evolution of massive stars up to a modest end as a white dwarf or a fiery death as core-collapse supernovae (115, 116). It also affects the ignition conditions and time scales of thermonuclear supernovae. Recent studies, while uncovering interesting facts (117, 111), stopped short of the astrophysical energy range due to the high laboratory background.

The $^{13}\text{C}(\alpha,n)^{16}\text{O}$ and $^{22}\text{Ne}(\alpha,n)^{25}\text{Mg}$ reactions provide the neutrons for the build-up of the s-process isotopes (118, 119, 102, 120, 113). Most of the elements heavier than iron are produced through this process, which involves a series of subsequent neutron captures and β -decays.

In order to address these exciting cases, it has been called for the installation

of a new accelerator with a larger voltage up to a few MV in a deep underground laboratory (121). In addition to protons and α -particles, it should also be able to accelerate ions up to carbon or even oxygen, so that also carbon burning can be studied. As to the beam current, for all these ions an intensity of typically 1 mA will be required for the necessary sensitivity.

Such a project is presently under discussion at several different sites in Europe and North America. It would be natural to install a new underground accelerator at the site of the present LUNA machine, the LNGS laboratory, with its excellent infrastructure and proven low background. However, due to limited underground laboratory space there, also possible other sites must be actively studied.

One recent example is the Canfranc laboratory in Spain (122), which is less well-shielded (2400 m.w.e.) than Gran Sasso and therefore has a higher remaining muon flux. However, at the present LUNA site the background is dominated by neutrons, not muons, (15), and the neutron flux at the two sites is actually comparable. The access to this site is by horizontal road tunnel, facilitating the installation of complex, maintenance-intensive equipment like an accelerator.

In the United States, two accelerators with connected beamlines are included in the DUSEL underground science facility planned at the site of the previous Homestake experiment (123). One machine should have similar tasks as the present LUNA 400 kV accelerator, but with greatly increased beam intensity, whereas the second accelerator should be in the MV range and address the science cases described above.

A different approach is followed in two projects in Boulby (United Kingdom, 2800 m.w.e.) and Praid (Romania, 900 m.w.e.) (124, 125): Here the laboratory should be placed in a salt matrix deep underground, with its generally much lower levels of uranium and thorium and, therefore, also lower neutron flux.

Regardless of the outcome of the ongoing siting discussion, both astrophysics and nuclear physics will greatly benefit from the new precision that will be enabled by a future, higher-voltage accelerator underground. A better understanding of nuclear burning in stars by direct new data will allow to model stellar scenarios that are now understood only in general terms. In addition, improved experimental data for nuclear fusion reactions near or below the Coulomb barrier will open a fresh challenge for theoretical modeling of these reactions.

8 Conclusions

LUNA started underground nuclear astrophysics twenty years ago in the core of Gran Sasso, below 1400 meters of dolomite rock. The extremely low background has allowed for nuclear physics experiments with very small count rate, down to a few events per year. The important reactions responsible for the hydrogen burning in the Sun have been studied for the first time down to the relevant stellar energies. As a consequence, fifty years after the first pioneering cross section measurements, nuclear physics is not anymore an important error source of the solar model and solar neutrinos can now be exploited to probe the deep interior of the Sun. When applied to astrophysical scenarios different from the

Sun, LUNA results increase the limit on the age of the Universe up to 14 billion years.

LUNA has already experienced the important progress achievable in the comprehension of the hydrogen burning thanks to the underground environment. In the next two decades underground nuclear astrophysics will try to reach similar results in the study of the helium and carbon burning and of the neutron sources in the stars.

Acknowledgments

It is a pleasure to thank our colleagues of LUNA without whom the results reviewed in this paper would have not been obtained.

LITERATURE CITED

1. Eddington A, *Nature* 16:14 (1920).
2. Clayton DD, *Principles of Stellar Evolution and Nucleosynthesis* (University of Chicago Press, 1984).
3. Rolfs C, Rodney W, *Cauldrons in the Cosmos* (University of Chicago Press, Chicago, 1988).
4. Clayton DD, *Handbook of Isotopes in the Cosmos: Hydrogen to Gallium* (Cambridge University Press, Cambridge, 2003).
5. Iliadis C, *Nuclear Physics of Stars* (Wiley-VCH, Weinheim, 2007).
6. Salpeter EE, *Australian Journal of Physics* 7:373 (1954).
7. Assenbaum H, Langanke K, Rolfs C, *Z. Phys. A* 327:461 (1987).
8. Raiola *et al.* *F, Eur. Phys. J. A* 19:283 (2004).
9. Huke A, *et al.*, *Phys. Rev. C* 78:015803 (2008).
10. Gilmore G, *Practical γ -ray spectrometry, 2nd edition* (John Wiley and Sons, New York, 2008).
11. Köhler M, *et al.*, *Appl. Radiat. Isot.* 67:736 (2009).
12. Caciolli A, *et al.*, *Eur. Phys. J. A* 39:179 (2009).
13. Laubenstein M, *et al.*, *Appl. Radiat. Isot.* 61:167 (2004).
14. Ahlen SP, *et al.*, *Phys. Lett. B* 249:149 (1990).
15. Bemmerer D, *et al.*, *Eur. Phys. J. A* 24:313 (2005).
16. Szücs T, *et al.*, *Eur. Phys. J. A* 44:513 (2010).
17. Wulandari H, Jochum J, Rau W, von Feilitzsch F, *Astropart. Phys.* 22:313 (2004).
18. Formaggio JA, Martoff C, *Annu. Rev. Nucl. Part. Sci.* 54:361 (2004).
19. Bethe H, *Phys. Rev.* 55:103 (1939).
20. von Weizsäcker CF, *Phys. Z.* 39:633 (1938).
21. Araki T, *et al.*, *Nature* 436:499 (2005).
22. Gaisser TK, Honda M, *Annu. Rev. Nucl. Part. Sci.* 52:153 (2002), arXiv:hep-ph/0203272.
23. Elliott SR, Vogel P, *Annu. Rev. Nucl. Part. Sci.* 52:115 (2002), arXiv:hep-ph/0202264.

24. Perkins DH, *Annu. Rev. Nucl. Part. Sci.* 34:1 (1984).
25. Gaitskell RJ, *Annu. Rev. Nucl. Part. Sci.* 54:315 (2004).
26. Bettini A, *J. Phys. Conf. Ser.* 120:082001 (2008), arXiv:0712.1051.
27. Junker M, et al., *Phys. Rev. C* 57:2700 (1998).
28. Bonetti R, et al., *Phys. Rev. Lett.* 82:5205 (1999).
29. Casella C, et al., *Nucl. Phys. A* 706:203 (2002).
30. Formicola A, et al., *Phys. Lett. B* 591:61 (2004).
31. Imbriani G, et al., *Eur. Phys. J. A* 25:455 (2005).
32. Lemut A, Bemmerer D, et al., *Phys. Lett. B* 634:483 (2006).
33. Bemmerer D, et al., *Nucl. Phys. A* 779:297 (2006).
34. Marta M, et al., *Phys. Rev. C* 78:022802(R) (2008).
35. Confortola F, et al., *Phys. Rev. C* 75:065803 (2007).
36. Costantini H, et al., *Nucl. Phys. A* 814:144 (2008).
37. Bemmerer D, et al., *J. Phys. G* 36:045202 (2009).
38. Bemmerer D, et al., *Phys. Rev. Lett.* 97:122502 (2006).
39. Gyürky G, et al., *Phys. Rev. C* 75:035805 (2007).
40. Greife U, et al., *Nucl. Inst. Meth. A* 350:327 (1994).
41. Formicola A, et al., *Nucl. Inst. Meth. A* 507:609 (2003).
42. Costantini H, et al., *Phys. Lett. B* 482:43 (2000).
43. Casella C, et al., *Nucl. Inst. Meth. A* 489:160 (2002).
44. Marta M, et al., *Nucl. Inst. Meth. A* 569:727 (2006).
45. Görres J, et al., *Nucl. Inst. Meth.* 177:295 (1980).
46. Allison SK, *Rev. Mod. Phys.* 30:1138 (1958).
47. Elekes Z, et al., *Nucl. Inst. Meth. A* 503:580 (2003).
48. Bahcall JN, *Neutrino astrophysics* (Cambridge and New York, Cambridge University Press, 1989).
49. Castellani V, et al., *Phys. Rep.* 281:309 (1997), arXiv:astro-ph/9606180.
50. Peña-Garay C, Serenelli A, ArXiv e-prints (2008), 0811.2424.
51. Bahcall JN, *Phys. Rev. Lett.* 12:300 (1964).
52. Davis R, *Phys. Rev. Lett.* 12:303 (1964).
53. Weinberg S, *Gravitation and Cosmology* (John Wiley and Sons, 1972).
54. Griffiths GM, Lal M, Scarfe CD, *Can. J. Phys.* 41:724 (1963).
55. Schmid GJ, et al., *Phys. Rev. Lett.* 76:3088 (1996).
56. Marcucci L, Nollett K, Schiavilla R, Wiringa R, *Nucl. Phys. A* 777:111 (2006).
57. Fowler WA, *Nature* 238:24 (1972).
58. Fetisov VN, Kopysov YS, *Phys. Lett. B* 40:602 (1972).
59. Dwarakanath MR, Winkler H, *Phys. Rev. C* 4:1532 (1971).
60. Krauss A, Becker HW, Trautvetter HP, Rolfs C, *Nucl. Phys. A* 467:273 (1987).
61. Kudomi N, et al., *Phys. Rev. C* 69:015802 (2004), arXiv:astro-ph/0306454.
62. di Leva A, et al., *Phys. Rev. Lett.* 102:232502 (2009).
63. Holmgren HD, Johnston RL, *Phys. Rev.* 113:1556 (1959).
64. Parker P, Kavanagh R, *Phys. Rev.* 131:2578 (1963).
65. Nagatani K, Dwarakanath M, Ashery D, *Nucl. Phys. A* 128:325 (1969).

66. Kräwinkel H, et al., *Z. Phys. A* 304:307 (1982).
67. Osborne J, et al., *Phys. Rev. Lett.* 48:1664 (1982).
68. Alexander T, Ball G, Lennard W, Geissel H, *Nucl. Phys. A* 427:526 (1984).
69. Hilgemeier M, et al., *Z. Phys. A* 329:243 (1988).
70. Robertson R, et al., *Phys. Rev. C* 27:11 (1983).
71. Volk H, Kräwinkel H, Santo R, Wallek L, *Z. Phys. A* 310:91 (1983).
72. Nara Singh B, Hass M, Nir-El Y, Haquin G, *Phys. Rev. Lett.* 93:262503 (2004).
73. Adelberger E, et al., *Rev. Mod. Phys.* 70:1265 (1998).
74. Brown TAD, et al., *Phys. Rev. C* 76:055801 (2007), 0710.1279.
75. Descouvemont P, et al., *At. Data Nucl. Data Tables* 88:203 (2004).
76. Arpesella C, et al., *Phys. Rev. Lett.* 101:091302 (2008).
77. Coc A, et al., *Astrophys. J.* 600:544 (2004).
78. Ryan S, et al., *Astrophys. J.* 530:L57 (2000).
79. Bonifacio P, et al., *Astron. Astrophys.* 390:91 (2002).
80. Krauss L, Chaboyer B, *Science* 299:65 (2003).
81. Caughlan G, Fowler W, *At. Data Nucl. Data Tables* 40:283 (1988).
82. Angulo C, et al., *Nucl. Phys. A* 656:3 (1999).
83. Lamb W, Hester R, *Phys. Rev.* 108:1304 (1957).
84. Schröder U, et al., *Nucl. Phys. A* 467:240 (1987).
85. Bertone P, et al., *Phys. Rev. Lett.* 87:152501 (2001).
86. Bertone PF, et al., *Phys. Rev. C* 66:055804 (2002).
87. Mukhamedzhanov A, et al., *Phys. Rev. C* 67:065804 (2003).
88. Nelson SO, et al., *Phys. Rev. C* 68:065804 (2003).
89. Yamada K, et al., *Phys. Lett. B* 579:265 (2004).
90. Schürmann D, et al., *Phys. Rev. C* 77:055803 (2008).
91. Imbriani G, et al., *Astron. Astrophys.* 420:625 (2004).
92. Herwig F, *Ann. Rev. Astron. Astrophys.* 43:435 (2005).
93. Herwig F, Austin SM, *Astrophys. J.* 613:L73 (2004).
94. Runkle RC, et al., *Phys. Rev. Lett.* 94:082503 (2005).
95. Lane AM, Thomas RG, *Rev. Mod. Phys.* 30:257 (1958).
96. Haxton WC, Serenelli AM, *Astrophys. J.* 687:678 (2008).
97. Haxton W, *Journal of Physics Conference Series* 173:012014 (2009), 0809.3342.
98. Costantini H, et al., *Rep. Prog. Phys.* 72:086301 (2009).
99. Smith V, Lambert D, Nissen P, *Astrophys. J.* 408:262 (1993).
100. Asplund M, et al., *Astrophys. J.* 644:229 (2006).
101. Weaver TA, Woosley SE, *Phys. Rep.* 227:65 (1993).
102. Wallerstein G, et al., *Rev. Mod. Phys.* 69:995 (1997).
103. Buchmann L, Barnes C, *Nucl. Phys. A* 777:254 (2006).
104. Woosley SE, Heger A, *Phys. Rep.* 442:269 (2007), arXiv:astro-ph/0702176.
105. Tur C, Heger A, Austin SM, *Astrophys. J.* 671:821 (2007), 0705.4404.
106. Tang XD, et al., *Phys. Rev. Lett.* 99:052502 (2007).
107. Schürmann D, et al., *European Physical Journal A* 26:301 (2005).
108. Matei C, et al., *Phys. Rev. Lett.* 97:242503 (2006).

109. Görres J, et al., Phys. Rev. C 62:055801 (2000).
110. Wilmes S, et al., Phys. Rev. C 66:065802 (2002).
111. Spillane T, et al., Phys. Rev. Lett. 98:122501 (2007).
112. Harissopulos S, et al., Phys. Rev. C 72:062801 (2005), arXiv:nucl-ex/0509014.
113. Heil M, et al., Phys. Rev. C 78:025803 (2008).
114. Jaeger M, Kunz R, Mayer A, Hammer JW, Staudt G, et al., Phys. Rev. Lett. 87:202501 (2001).
115. Woosley SE, Heger A, Weaver TA, Rev. Mod. Phys. 74:1015 (2002).
116. Hillebrandt W, Niemeyer JC, Ann. Rev. Astron. Astroph. 38:191 (2000), arXiv:astro-ph/0006305.
117. Barrón-Palos L, et al., Nucl. Phys. A 779:318 (2006).
118. Cameron AGW, Publ. Astron. Soc. Pacific 69:201 (1957).
119. Burbidge EM, Burbidge GR, Fowler WA, Hoyle F, Rev. Mod. Phys. 29:547 (1957).
120. Straniero O, Gallino R, Cristallo S, Nucl. Phys. A 777:311 (2006), arXiv:astro-ph/0501405.
121. Nuclear Physics European Collaboration Committee (NuPECC), Roadmap 2005, available at http://www.nupecc.org/pub/NuPECC_Roadmap.pdf.
122. Workshop on Nuclear Astrophysics Opportunities at the Underground Laboratory in Canfranc, Barcelona/Spain, 2009.
123. DOE/NSF Nuclear Science Advisory Committee, (2008), arXiv:0809.3137.
124. Strieder F, J. Phys. G 35:014009 (2008).
125. Bordeanu C, et al., J. Phys. G 35:014011 (2008).

Table 1: Nuclear reactions of astrophysical interest recommended for study at future underground accelerator facilities.

Type	Reaction	Q -value [MeV]	E_{Gamow} [keV]	Reference
(α, γ)	${}^2\text{H}(\alpha, \gamma){}^6\text{Li}$	1.5	100-500	(12)
	${}^{12}\text{C}(\alpha, \gamma){}^{16}\text{O}$	7.2	300	(107, 108, 106)
	${}^{14}\text{N}(\alpha, \gamma){}^{18}\text{F}$	4.4	200-700	(109)
	${}^{15}\text{N}(\alpha, \gamma){}^{19}\text{F}$	4.0	500	(110)
${}^{12}\text{C}$ -induced	${}^{12}\text{C}({}^{12}\text{C}, \alpha){}^{20}\text{Ne}$	4.6	1500	(111, 12)
	${}^{12}\text{C}({}^{12}\text{C}, \text{p}){}^{23}\text{Na}$	2.2	1500	(111, 12)
(α, n)	${}^{13}\text{C}(\alpha, \text{n}){}^{16}\text{O}$	2.2	200	(112, 113)
	${}^{22}\text{Ne}(\alpha, \text{n}){}^{25}\text{Mg}$	-0.5	500	(114)

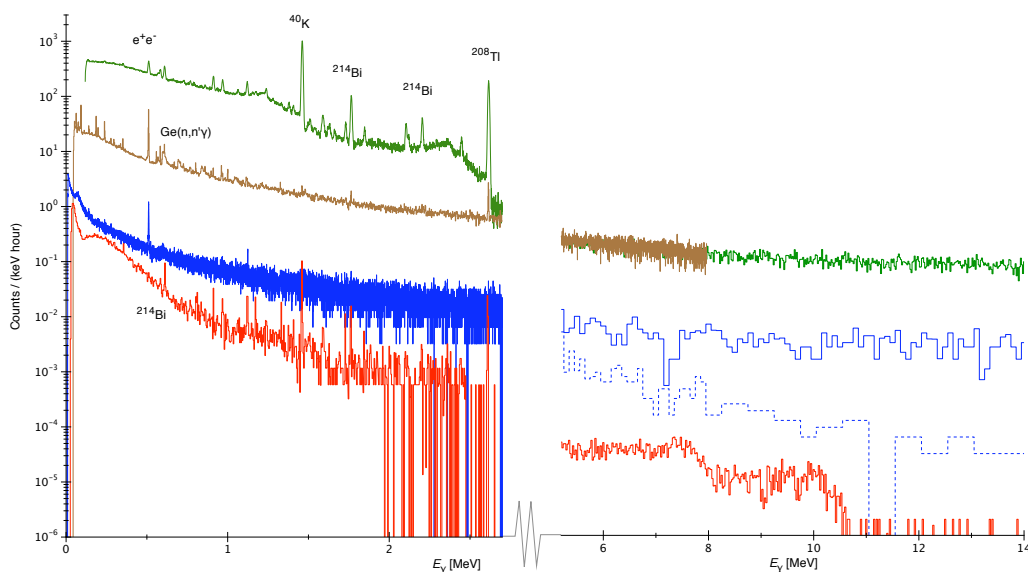


Figure 1: Laboratory γ -ray background measured with a 100% relative efficiency germanium detector at $E_\gamma < 2.7$ MeV and with a BGO detector (scaled for equal volume with the germanium) for 5.2 MeV $< E_\gamma < 14$ MeV. Green: Earth's surface, no shield. Brown: Earth's surface, lead shield. Blue: 110 m.w.e. underground Felsenkeller laboratory (Dresden), lead shield (11). Blue dashed line: actively vetoed spectrum in the 110 m.w.e. underground Felsenkeller lab. Red: 3800 m.w.e. LUNA lab, lead shield for the germanium (12), no lead shield for the BGO (15).

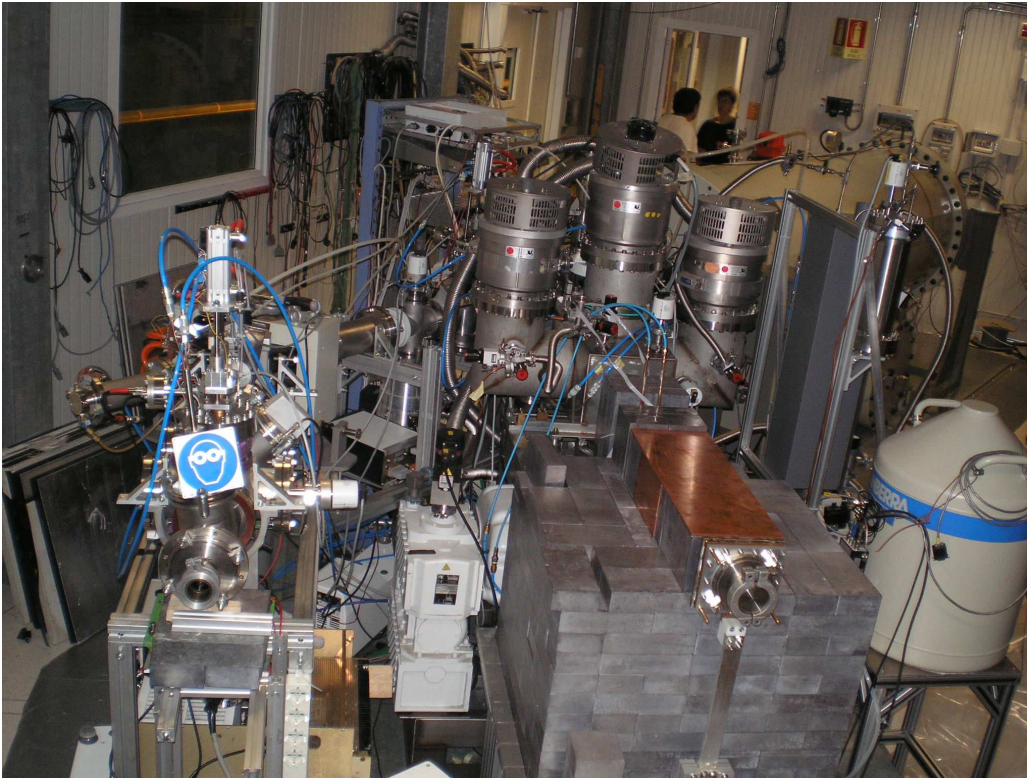


Figure 2: The LUNA set-up with the two different beam lines in the foreground and the accelerator in the back. The beam line to the left is dedicated to the measurements with solid target whereas the one on the right hosts the windowless gas target. The set-up for the study of ${}^3\text{He}({}^4\text{He},\gamma){}^7\text{Be}$ is shown during installation with the shield only partially mounted.

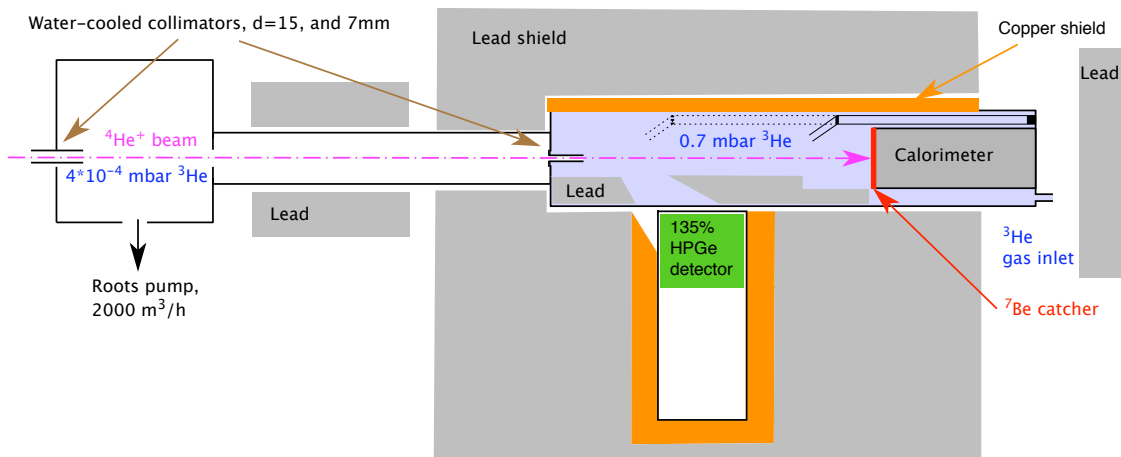


Figure 3: The set-up for the study of ${}^3\text{He}({}^4\text{He},\gamma){}^7\text{Be}$. The device to detect Rutherford scattering, the calorimeter and the germanium detector are indicated.

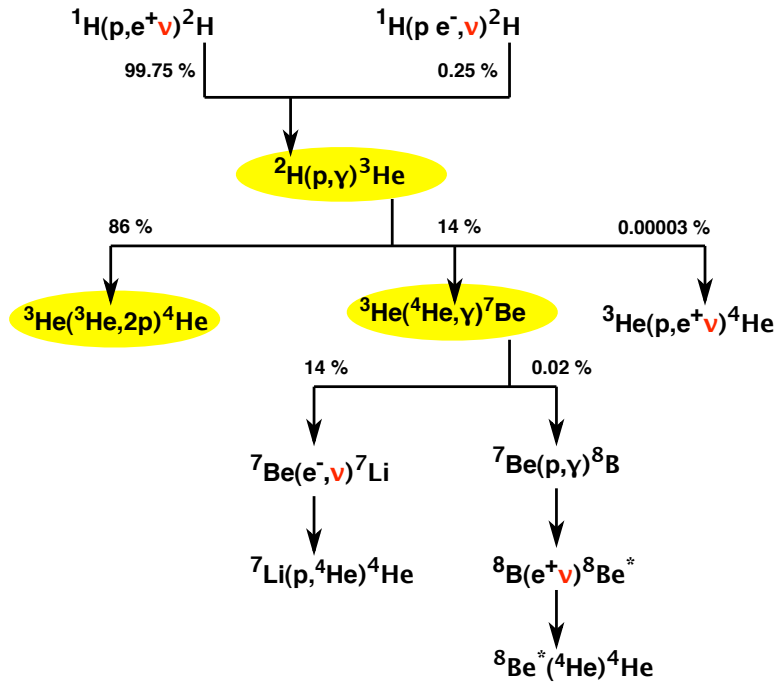


Figure 4: The proton-proton chain. The reactions studied by LUNA are highlighted in yellow.

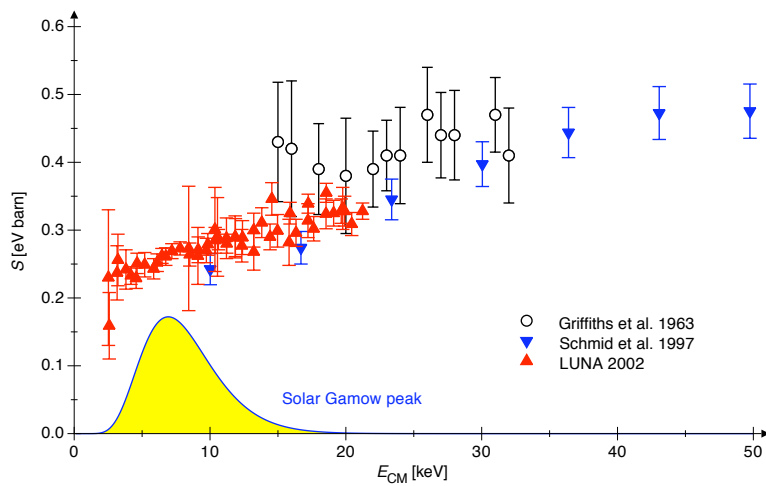


Figure 5: The $^2\text{H}(p, \gamma)^3\text{He}$ astrophysical factor $S(E)$ with the total error.

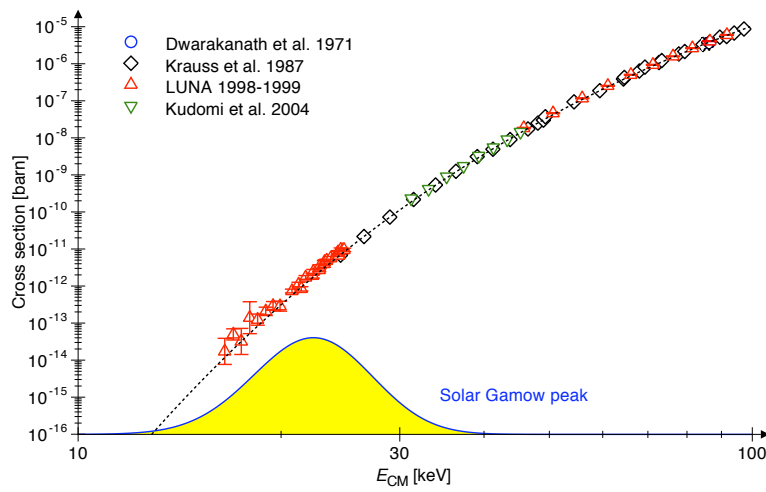


Figure 6: Cross section of the ${}^3\text{He}({}^3\text{He},2\text{p}){}^4\text{He}$ reaction. Data from LUNA (27,28) and from other groups (59,60,61). The line is the extrapolation based on the measured $S(E)$ -factor (28).

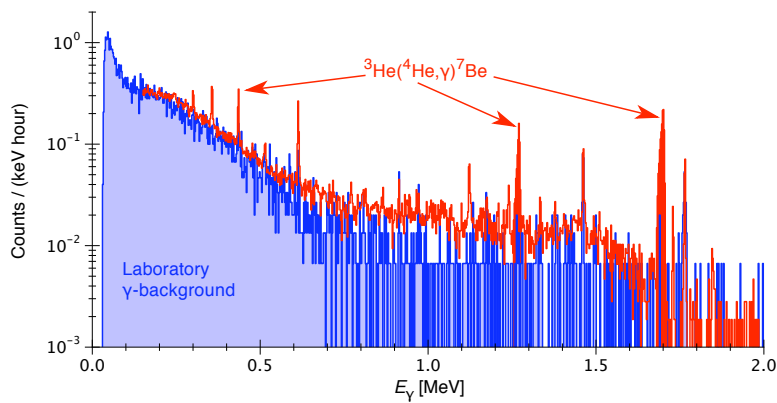


Figure 7: ${}^3\text{He}({}^4\text{He},\gamma){}^7\text{Be}$ spectrum at 250 keV beam energy (red) and the laboratory background (blue).

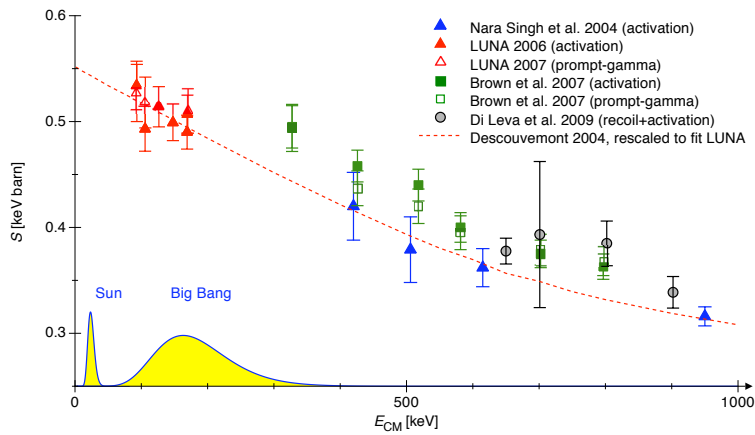


Figure 8: Astrophysical $S(E)$ -factor for ${}^3\text{He}({}^4\text{He}, \gamma){}^7\text{Be}$. The results from the modern, high precision experiments are shown with their total error.

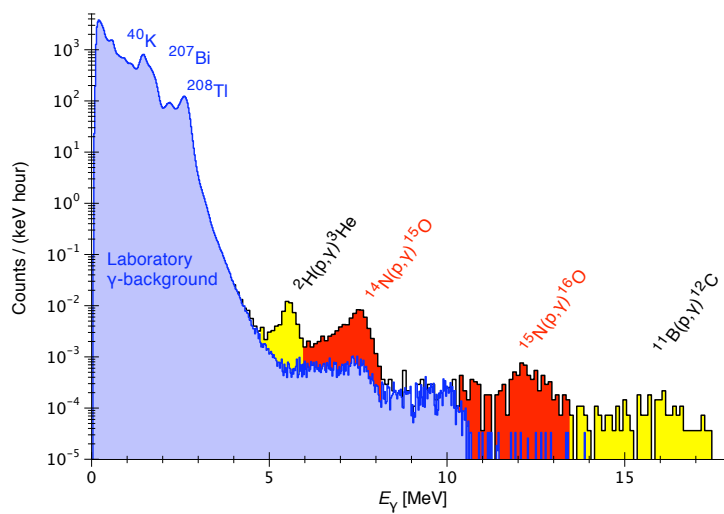


Figure 9: BGO spectrum taken with 100 keV proton beam on Nitrogen of natural isotopic abundance. Red: peaks from ${}^{14}\text{N}(p, \gamma){}^{15}\text{O}$ and ${}^{15}\text{N}(p, \gamma){}^{16}\text{O}$. Yellow: beam induced background. Blu: laboratory background. In spite of the small isotopic abundance of ${}^{15}\text{N}$ (0.366% only) the peak due to ${}^{15}\text{N}(p, \gamma){}^{16}\text{O}$ can be easily seen thanks to the much reduced background.

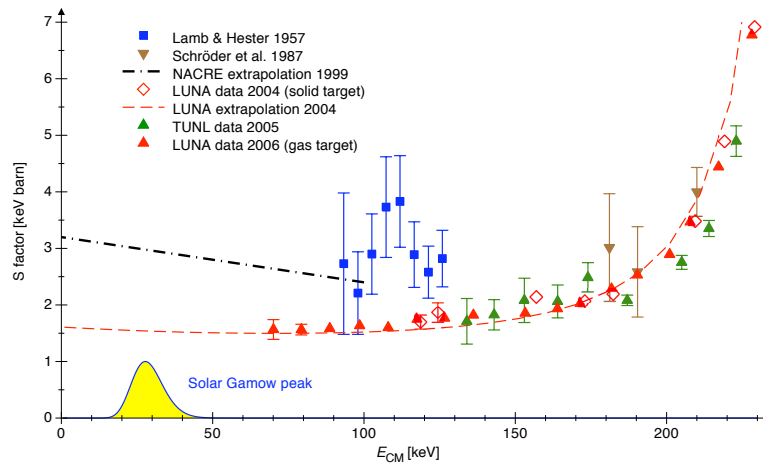


Figure 10: Astrophysical $S(E)$ -factor of the $^{14}\text{N}(p,\gamma)^{15}\text{O}$ reaction. The errors are statistical only (the systematic ones are similar).

Solar fusion cross sections II: the pp chain and CNO cycles

E. G. Adelberger, A. García, R. G. Hamish Robertson, and K. A. Snover

*Department of Physics and Center for Experimental Nuclear Physics and Astrophysics,
University of Washington, Seattle, WA 98195 USA*

A. B. Balantekin, K. Heeger, and M. J. Ramsey-Musolf

Department of Physics, University of Wisconsin, Madison, WI 53706 USA

D. Bemmerer and A. Junghans

Forschungszentrum Dresden-Rossendorf, D-01314 Dresden, Germany

C. A. Bertulani

Department of Physics and Astronomy, Texas A&M University, Commerce, TX 75429 USA

J.-W. Chen

Department of Physics and Center for Theoretical Sciences, National Taiwan University, Taipei 10617, Taiwan

H. Costantini and P. Prati

Università di Genova and INFN Sezione di Genova, Genova, Italy

M. Couder, E. Uberseder, and M. Wiescher

Department of Physics and JINA, University of Notre Dame, Notre Dame, IN 46556 USA

R. Cyburt

JINA and National Superconducting Cyclotron Laboratory, Michigan State University, East Lansing, MI 48824 USA

B. Davids

TRIUMF, 4004 Wesbrook Mall, Vancouver, BC, Canada V6T 2A3

S. J. Freedman

*Department of Physics, University of California, Berkeley, and
Lawrence Berkeley National Laboratory, Berkeley, CA 94720 USA*

M. Gai

*Laboratory for Nuclear Sciences at Avery Point, University of Connecticut, CT 06340-6097 and
Department of Physics, Yale University, New Haven, CT 06520-8124 USA*

D. Gazit

*Institute for Nuclear Theory, University of Washington, Seattle, WA 98195 USA and
Racah Institute of Physics, The Hebrew University, Jerusalem, 91904, Israel*

L. Gialanella and G. Imbriani

Dipartimento di Scienze Fisiche, Università di Napoli, and INFN Sezione di Napoli, Napoli, Italy

U. Greife

Department of Physics, Colorado School of Mines, Golden, CO 80401 USA

M. Hass

Department of Particle Physics and Astrophysics, The Weizmann Institute, Rehovot, Israel

W. C. Haxton

*Department of Physics, University of California, Berkeley, and Lawrence Berkeley National Laboratory,
Berkeley, CA 94720 and Institute for Nuclear Theory, University of Washington, Seattle, WA 98195 USA*

T. Itahashi

Research Center for Nuclear Physics, Osaka University, Ibaraki, Osaka 567-0047 Japan

K. Kubodera

Department of Physics and Astronomy, University of South Carolina, Columbia, SC 29208 USA

K. Langanke

GSI Helmholtzzentrum für Schwerionenforschung, D-64291 Darmstadt, Germany, Institut für Kernphysik, Universität Darmstadt, Germany and Frankfurt Institute for Advanced Studies, Frankfurt, Germany

D. Leitner, M. Leitner, P. Vetter, and L. Winslow

Lawrence Berkeley National Laboratory, Berkeley, CA 94720 USA

L. E. Marcucci

Department of Physics "E. Fermi", University of Pisa, and INFN Sezione di Pisa, Largo B. Pontecorvo 3, I-56127, Pisa, Italy

T. Motobayashi

The Institute of Physical and Chemical Research (RIKEN), 2-1 Hirosawa, Wako, Saitama 351-0198, Japan

A. Mukhamedzhanov and R. E. Tribble

Cyclotron Institute, Texas A&M University, College Station, TX 77843 USA

Kenneth M. Nollett

Physics Division, Argonne National Laboratory, 9700 S. Cass Ave., Argonne, IL 60439 USA

F. M. Nunes

National Superconducting Cyclotron Laboratory and Department of Physics and Astronomy, Michigan State University, East Lansing, MI 48824 USA

T.-S. Park

Department of Physics and BAERI, Sungkyunkwan University, Suwon 440-746 Korea

P. D. Parker

Wright Nuclear Structure Laboratory, Yale University, New Haven, CT 06520 USA

R. Schiavilla

Department of Physics, Old Dominion University, Norfolk, VA 23529 and Jefferson Laboratory, Newport News, VA 23606 USA

E. C. Simpson

Department of Physics, University of Surrey, Guildford, Surrey GU2 7XH, United Kingdom

C. Spitaleri

INFN Laboratori Nazionali del Sud & DMFCI, Università di Catania, Catania, Italy

F. Strieder and H.-P. Trautvetter

Institut für Experimentalphysik III, Ruhr-Universität Bochum, Bochum, Germany

K. Suemmerer

GSI Helmholtzzentrum für Schwerionenforschung GmbH, Planckstraße 1, D-64291 Darmstadt, Germany

S. Typel

Excellence Cluster Universe, Technische Universität München, Boltzmannstraße 2, D-85748 Garching and GSI Helmholtzzentrum für Schwerionenforschung GmbH, Planckstraße 1, D-64291 Darmstadt, Germany

We summarize and critically evaluate the available data on nuclear fusion cross sections important to energy generation in the Sun and other hydrogen-burning stars and to solar neutrino production. Recommended values and uncertainties are provided for key cross sections, and a recommended spectrum is given for ^8B solar neutrinos. We also discuss opportunities for further increasing the precision of key rates, including new facilities, new experimental techniques, and improvements in theory. This review, which summarizes the conclusions of a workshop held at the Institute

for Nuclear Theory, Seattle, in January 2009, is intended as a 10-year update and supplement to Reviews of Modern Physics **70** (1998) 1265.

Contents

I. INTRODUCTION	3	3. Transition to the ground state and 6.79 MeV in ^{15}O	36
A. Solar Fusion II: the 2009/10 effort	4	4. Transition to the 6.17 MeV state	38
B. Contents of this review	5	5. Total $S_{14}(0)$ and conclusions	39
II. NUCLEAR REACTIONS IN HYDROGEN-BURNING STARS	6	B. Other CNO-cycle reactions	40
A. Rates and S-factors	7	1. $^{12}\text{C}(p,\gamma)^{13}\text{N}$	40
B. Screening of stellar and laboratory reactions	9	2. $^{15}\text{N}(p,\alpha)^{12}\text{C}$	40
C. Fitting and extrapolating S-factors	10	3. $^{15}\text{N}(p,\gamma)^{16}\text{O}$	41
1. Theory constraints: model-based methods	11	4. $^{16}\text{O}(p,\gamma)^{17}\text{F}$	42
2. Theory constraints: <i>ab initio</i> methods	12	5. $^{17}\text{O}(p,\alpha)^{14}\text{N}$	42
3. Adopted procedures	13	6. $^{17}\text{O}(p,\gamma)^{18}\text{F}$	42
D. Treatment of uncertainties	14	7. $^{18}\text{O}(p,\alpha)^{15}\text{N}$	42
III. THE pp REACTION	14	XII. INDIRECT METHODS AND THEIR VALIDATION	42
A. Progress in potential models	15	A. The asymptotic normalization coefficient method	43
B. Progress in effective field theory (EFT)	15	B. The Coulomb dissociation method	44
1. Hybrid EFT (EFT*)	15	C. The Trojan Horse method	45
2. Pionless EFT	16	D. Summary	45
3. Comment on Mosconi <i>et al.</i>	16	XIII. FUTURE FACILITIES AND CURRENT CAPABILITIES	46
C. Summary	16	A. Inverse kinematics measurements using recoil separators	46
IV. THE $d(p,\gamma)^3\text{He}$ RADIATIVE CAPTURE REACTION	17	B. Underground facilities	47
A. Data sets	17	Acknowledgments and Dedication	50
B. Theoretical studies	18	Appendix: Treating Uncertainties	50
C. Summary	18	A. Introduction	50
V. THE $^3\text{He}(^3\text{He},2p)^4\text{He}$ REACTION	18	B. The inflation factor method	51
A. Data sets and fitting	19	C. Application of the inflation factor method	52
VI. THE $^3\text{He}(\alpha,\gamma)^7\text{Be}$ REACTION	20	D. Other methods	52
A. Experimental measurements	20	References	52
B. Theory	21	I. INTRODUCTION	
1. Model selection for $S_{34}(0)$ determination	22	In 1998 the Reviews of Modern Physics published a summary and critical analysis of the nuclear reaction cross sections important to solar burning. That effort, Adelberger <i>et al.</i> (1998) and denoted here as Solar Fusion I, began with a meeting hosted by the Institute for Nuclear Theory, University of Washington, 17-20 February 1997. A group of international experts in the nuclear physics and astrophysics of hydrogen-burning stars met to begin critical discussions of the existing data on relevant nuclear reactions, with the aim of determining “best values” and uncertainties for the contributing low-energy S-factors. The group also considered opportunities for further improvements in both measurements and theory.	
2. Region of $S_{34}(E)$ fitting	22	Such data and related nuclear theory have been crucial to the standard solar model (SSM) and the neutrino fluxes it predicts. Indeed, measurements of nuclear reactions gave the field its start. In 1958 Holmgren and Johnston (1958, 1959) showed that the rate for $^3\text{He}+^4\text{He} \rightarrow ^7\text{Be} + \gamma$ was ~ 1000 times larger than expected, and thus that the pp chain for ^4He synthesis would have additional terminations beyond $^3\text{He}+^3\text{He} \rightarrow ^4\text{He} + 2p$. This result led Davis to recognize that his chlorine detector	
3. Theoretical uncertainty in the $S_{34}(0)$ determination	22		
4. S-factor derivatives	22		
5. Comment on phase shifts	22		
C. $S_{34}(0)$ determination	23		
VII. THE $^3\text{He}(p,e^+\nu_e)^4\text{He}$ REACTION	24		
A. hep calculations	24		
B. Summary	25		
VIII. ELECTRON CAPTURE BY ^7Be, pp, and CNO NUCLEI	26		
IX. THE $^7\text{Be}(p,\gamma)^8\text{B}$ REACTION	28		
A. The direct $^7\text{Be}(p,\gamma)^8\text{B}$ reaction	28		
1. Beam-target overlap	28		
2. ^8B backscattering	29		
3. Proton energy loss corrections	29		
B. Theory	29		
C. ^8B Coulomb dissociation measurements	31		
D. Direct $^7\text{Be}(p,\gamma)^8\text{B}$ analysis and $S_{17}(0)$ determination	32		
X. THE SPECTRUM OF ^8B NEUTRINOS	34		
XI. THE CNO CYCLES	35		
A. The reaction $^{14}\text{N}(p,\gamma)^{15}\text{O}$	35		
1. Current status and results	35		
2. R-matrix analysis and normalization	36		

might be able to see the higher energy neutrinos from these other terminations, and spurred Bahcall and others to develop a quantitative model of the Sun capable of predicting those fluxes (Bahcall and Davis Jr., 1982).

At the time of the 1997 meeting, three decades of effort in solar neutrino physics had produced four measurements that were at variance with the SSM and the standard model of electroweak interactions. The measurements came from the pioneering work of Ray Davis, Jr. (Davis Jr., 1994; Davis Jr. *et al.*, 1968); the observation of ^8B neutrinos in the Kamiokande water Cherenkov detector (Fukuda *et al.*, 1996); and the GALLEX (Kirsten *et al.*, 2003) and SAGE (Gavrin *et al.*, 2003) radiochemical detectors sensitive primarily to pp and ^7Be neutrinos. The resulting pattern of fluxes that emerged from these experiments was difficult to reconcile with any plausible variation in the SSM, requiring a much sharper reduction in the ^7Be neutrino flux than in the ^8B flux, despite the greater sensitivity of the latter to changes in the solar core temperature.

For this reason it was argued in Solar Fusion I that the measurements provided evidence for new physics beyond the standard model. New solar neutrino experiments that promised much more precise data – the 50-kiloton successor to Kamiokande, Super-Kamiokande, and the heavy-water-based Sudbury Neutrino Observatory (SNO), with sensitivity to both electron and heavy-flavor neutrinos – were then underway. The authors of Solar Fusion I, recognizing that the impact of these new experiments would depend in part on the quality of the nuclear microphysics input to the SSM, thus undertook an extended study of the key reaction rates for the pp chain and CNO bi-cycle. The effort appears to have been of some value to the community, as Solar Fusion I has become one of the most heavily cited papers in nuclear astrophysics.

A. Solar Fusion II: the 2009/10 effort

Ten years after publication of Solar Fusion I a proposal was made to the INT to revisit this process, in order to produce a new evaluation that would reflect the considerable progress made in the past decade, as well as new motivations for further constraining the SSM. Examples of advances in the nuclear physics include the LUNA II program at Gran Sasso (Costantini *et al.*, 2009), which has provided remarkable low-energy measurements of key reactions such as $^3\text{He}(\alpha,\gamma)^7\text{Be}$ and $^{14}\text{N}(\text{p},\gamma)^{15}\text{O}$; several high-precision measurements addressing the key pp-chain uncertainty identified in Solar Fusion I, $^7\text{Be}(\text{p},\gamma)^8\text{B}$; the application of new theoretical techniques to the p+p and hep neutrino reactions; and the resolution of several unresolved questions about screening corrections in plasmas.

The context for these measurements has also changed. In 1997 the field’s central concern was, in some sense, a qualitative one, the origin of the solar neutrino problem. This question was answered in spectacular fashion by

the dual discoveries of Super-Kamiokande (Fukuda *et al.*, 2001) and SNO (Ahmad *et al.*, 2001) – two distinct neutrino oscillations responsible for the missing atmospheric and solar neutrinos, largely determining the pattern of the light neutrino masses. But issues remain, and most of these require precision. There is intense interest in extending direct measurements to the low-energy portion of the solar neutrino spectrum ($\lesssim 2$ MeV), where experiments with good energy resolution can determine the separate contributions of pep, CNO, ^7Be , and pp neutrinos. There is the potential to further constrain the solar neutrino mixing angle θ_{12} : the solar luminosity determines the pp flux to high accuracy, and the low-energy spectrum lies in the vacuum region of the MSW triangle, in contrast to the high-energy ^8B neutrinos, where matter effects are significant. Thus precise low-energy measurements have considerable “leverage” to test θ_{12} and the consistency of the conclusions we have drawn from SNO, Super-Kamiokande, and the KamLAND reactor neutrino experiment. Borexino, now entering its calibration phase, is the first effort in this program of high-precision spectroscopy of low-energy solar neutrinos.

But the resolution of the solar neutrino problem has also returned the field to its roots: Davis built the chlorine detector to probe the interior of the Sun and thereby test directly the theory of stellar evolution and nuclear energy generation (Bahcall and Davis Jr., 1982). Davis was diverted from that goal by the missing solar neutrinos. But as the weak interaction effects responsible for that anomaly are now reasonably well understood, solar neutrinos again have become a quantitative tool for astronomy. Indeed, the program carried out by SNO and Super-Kamiokande has already yielded one remarkable constraint on the Sun, a direct determination of the core temperature to high precision, through measurement of the ^8B neutrino flux ($\phi(^8\text{B}) \propto T_c^{22}$). The 8.6% precision of the SNO NCD-phase results (Aharimim *et al.*, 2008), $\phi(^8\text{B}) = (5.54_{-0.31}^{+0.33+0.36}) \times 10^6/\text{cm}^2/\text{s}$, implies a sensitivity to core temperature of $\sim 0.5\%$.

New questions have arisen about the Sun that neutrinos could potentially address, provided the associated laboratory astrophysics has been done. One important success of the SSM in the 1990s was in predicting the local sound speed $c(r)$. Comparisons between $c(r)$ deduced from helioseismology and the predictions of the SSM yielded agreement at $\sim 0.2\%$ throughout much of the Sun. Bahcall and others argued (Bahcall *et al.*, 2001) that helioseismology is a more severe and detailed test of the SSM than neutrino production, so that SSM success in reproducing $c(r)$ made a particle-physics resolution of the solar neutrino problem more likely.

The sound speed is a function of the Sun’s interior pressure and density profiles, which in turn reflect thermal transport properties that depend on the Sun’s metal content, through the opacity. Thus the comparison between helioseismology and the SSM tests a key assumption of the SSM, that the metals are distributed uniformly throughout the Sun, apart from small corrections

due to diffusion. This assumption allows one to equate SSM interior metal abundances to convective-zone abundances deduced from analyses of photospheric absorption lines. Such analyses had been based on 1D models of the photosphere. Recently *ab initio* 3D analyses have been developed, yielding significant improvements in predicted line shapes and in the consistency of metal abundance determinations from various atomic and molecular lines. However, this work also reduced metallicity estimates from $Z \sim 0.0169$ to ~ 0.0122 (Asplund *et al.*, 2005), destroying the once excellent agreement between helioseismology and the SSM.

It has been suggested that this difficulty may reflect, contrary to the SSM, differences in solar core and convective-zone metallicities that could have arisen from the late-stage evolution of the solar disk: as a great deal of metal was scoured out of the disk by the formation of the giant planets, the last few percent of gas deposited onto the Sun could have been depleted of metals (Haxton and Serenelli, 2008). Indeed, recent studies of “solar twins” show abundance trends that correlate with the existence of planets (Israelian *et al.*, 2009; Ramírez *et al.*, 2009). Haxton and Serenelli (2008) argued that a direct measurement of solar core metallicity could be made by observing CNO solar neutrinos.

In both of the above examples – using neutrinos to determine the solar core temperature and metallicity – nuclear physics uncertainties remain one of the limiting factors in the analyses.

The proposal to revisit in 2009 the deliberations of 1997 thus had several motivations:

- providing a set of standard S-factors and uncertainties that reflect the progress made in laboratory and theoretical nuclear astrophysics over the last decade;
- enabling more precise analyses of solar neutrino experiments designed to constrain neutrino oscillations and other new physics, e.g., future pp and pep neutrino experiments that exploit these well understood fluxes; and
- enabling analyses in which solar neutrinos are used as a probe of the solar core.

The 2009 INT workshop¹ was modeled after that of 1997, with invitations extended to and accepted by representa-

tives from most of the experimental groups active in the nuclear physics of hydrogen burning stars. There was also active involvement of theorists, reflecting the progress that has been made in *ab initio* calculations. The workshop participants are the authors of this manuscript. As in 1997, early organizing included the selection of working group leaders who identified key papers, which were then entered in a database for review, prior to the start of the workshop. These materials were then summarized and discussed during the workshop, as the various working groups considered the state of the data and outlined any additional work that would be needed for this review. The process of critically analyzing both new and older data and working toward a consensus on best-value cross sections and uncertainties continued throughout 2009. A few new topics not considered in 1997 but now recognized to be quite important, such as the shape of the ^8B neutrino spectrum, were addressed. (The ^8B neutrino spectrum is one of the inputs to SNO and Super-Kamiokande analyses.) The workshop included working groups on indirect techniques for constraining cross sections, to summarize the progress that has been made in validating such approaches, and on new facilities and instrumentation, in view of the facility investments that are being considered in laboratory nuclear astrophysics (above and below ground).

B. Contents of this review

The review begins in Section II with a description of hydrogen burning by the pp chain and CNO bi-cycle, and the neutrino byproducts of these reaction chains. The role of S-factors and the associated questions of screening and of extrapolating data to the solar Gamow peak are discussed. We provide a fairly complete overview of progress in theory, which in some cases provides our only estimate of S-factors, and in other cases determines the forms of the functions that are needed for data extrapolations.

Discussions of individual reactions are organized by chapter: Secs. III-IX discuss the pp chain reactions $p+p \rightarrow d+e^++\nu_e$; $d+p \rightarrow ^3\text{He}+\gamma$; $^3\text{He}+^3\text{He} \rightarrow ^4\text{He}+p+p$; $^3\text{He}+^4\text{He} \rightarrow ^7\text{Be}+\gamma$; $^3\text{He}+p \rightarrow ^4\text{He}+e^++\nu_e$; ^7Be , pp, and CNO nuclei electron capture; and $^7\text{Be}+p \rightarrow ^8\text{B}+\gamma$. Sec. X discusses the spectrum of ^8B neutrinos produced in the β decay to a broad resonance in ^8Be . Sec. XI discusses $^{14}\text{N}+p \rightarrow ^{15}\text{O}+\gamma$ and other reactions contribut-

¹ The workshop was proposed in a letter to the Institute for Nuclear Theory’s National Advisory Committee (NAC) and approved by the NAC and INT Director at the time of the NAC’s August 2008 annual meeting. Wick Haxton (lead), Eric Adelberger, Heide Costantini, Peter Parker, R. G. Hamish Robertson, Kurt Snover, Frank Strieder, and Michael Wiescher formed the organizing committee and served as co-editors of this paper. Additional community members joined this group to act as working group heads: Jiunn-Wei Chen, Barry Davids, Stuart Freedman, Alejandro Garcia, Uwe Greife, Michael Hass, Gianluca Imbriani, Kuniharu Kubodera, Daniela Leitner, Laura Marcucci,

Filomena Nunes, Tae-Sun Park, Paolo Prati, Hanns-Peter Trautvetter, and Stefan Typel. The working group heads were responsible for organizing discussions, creating section drafts, and responding to subsequent criticisms of the drafts. Organizing committee members, in their capacity as co-editors, were responsible for creating from the drafts a coherent document, and for addressing any issues unresolved by the working groups. Workshop presentations are archived on the INT’s web site, http://www.int.washington.edu/PROGRAMS/solar_fusion.html.

ing to the CNO cycles. Sec. XII describes the progress that has been made in developing and validating indirect methods, while Sec. XIII describes future facilities and instrumentation that could further advance the field.

The conclusions of this review, in some cases, required the working groups to make some judgments. There are discrepant data sets, and there are cases where data extrapolations have some dependence on models. We have tried to treat such questions as consistently as possible, aware that excessively optimistic treatments of uncertainties could be misleading, while excessively conservative treatments would degrade the value of the best experiments done in the field. In most cases our working groups were able to reach consensus. In cases where significant differences remained among the experts, we have tried to identify the source of the disagreement, so that “consumers” will be aware that full consensus may have to await future measurements.

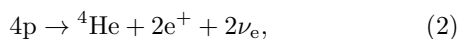
Table I summarizes the conclusions of this review.

II. NUCLEAR REACTIONS IN HYDROGEN-BURNING STARS

Observations of stars reveal a wide variety of stellar conditions, with luminosities relative to solar spanning a range $L \sim 10^{-4}$ to $10^6 L_\odot$ and surface temperatures $T_s \sim 2000$ – 50000 K. The simplest relation one could propose between luminosity L and T_s is

$$L = 4\pi R^2 \sigma_{\text{SB}} T_s^4 \Rightarrow L/L_\odot = (R/R_\odot)^2 (T_s/T_\odot)^4, \quad (1)$$

where σ_{SB} is the Stefan-Boltzmann constant, and L_\odot , T_\odot , and R_\odot are the solar values. This relation suggests that stars of a similar structure might lie along a one-parameter path (in this simplified example, defined by a function of the blackbody radii, $(R/R_\odot)^2$) in the luminosity (or magnitude) vs. temperature (or color) plane. In fact, there is a dominant path in the Hertzsprung–Russell color–magnitude diagram along which roughly 80% of the stars reside. This is the main sequence, those stars supporting themselves by hydrogen burning through the pp chain,



or CNO cycles. The laboratory nuclear astrophysics of hydrostatic hydrogen burning is the focus of this review.

As one such star, the Sun is an important test of our theory of main sequence stellar evolution: its properties – age, mass, surface composition, luminosity, and helioseismology – are by far the most accurately known among the stars. The SSM traces the evolution of the Sun over the past 4.6 Gyr of main sequence burning, thereby predicting the present-day temperature and composition profiles, the relative strengths of competing nuclear reaction chains, and the neutrino fluxes resulting from those chains. The SSM makes four basic assumptions:

- The Sun evolves in hydrostatic equilibrium, maintaining a local balance between the gravitational force and the pressure gradient. Knowledge of the equation of state as a function of temperature, density, and composition allows one to implement this condition in the SSM.
- Energy is transported by radiation and convection. The solar envelope, about 2.6% of the Sun by mass, is convective. Radiative transport dominates in the interior, $r \lesssim 0.72R_\odot$, and thus in the core region where thermonuclear reactions take place. The opacity is sensitive to composition.
- The Sun generates energy through hydrogen burning, Eq. (2). Figure 1 shows the competition between the pp chain and CNO cycles as a function of temperature: the relatively cool temperatures of the solar core favor the pp chain, which in the SSM produces $\sim 99\%$ of the Sun’s energy. The reactions contributing to the pp chain and CNO bi-cycle are shown in Fig. 2. The SSM requires as input rates for each of the contributing reactions, which are customarily provided as S-factors, defined below. Typically cross sections are measured at somewhat higher energies, where rates are larger, then extrapolated to the solar energies of interest. Corrections also must be made for the differences in the screening environments of terrestrial targets and the solar plasma.
- The model is constrained to produce today’s solar radius, mass, and luminosity. The primordial Sun’s metal abundances are generally determined from a combination of photospheric and meteoritic abundances, while the initial ${}^4\text{He}/\text{H}$ ratio is adjusted to reproduce, after 4.6 Gyr of evolution, the modern Sun’s luminosity.

The SSM predicts that, as the Sun evolves, the core He abundance increases, the opacity and core temperature rise, and the luminosity increases (by a total of $\sim 44\%$ over 4.6 Gyr). The details of this evolution depend on a variety of model input parameters and their uncertainties: the photon luminosity L_\odot , the mean radiative opacity, the solar age, the diffusion coefficients describing the gravitational settling of He and metals, the abundances of the key metals, and the rates of the nuclear reactions.

If the various nuclear rates are precisely known, the competition between burning paths can be used as a sensitive diagnostic of the central temperature of the Sun. Neutrinos probe this competition, as the relative rates of the ppI, ppII, and ppIII cycles comprising the pp chain can be determined from the fluxes of the pp/pep, ${}^7\text{Be}$, and ${}^8\text{B}$ neutrinos. This is one of the reasons that laboratory astrophysics efforts to provide precise nuclear cross section data have been so closely connected with solar neutrino detection.

Helioseismology provides a second way to probe the solar interior, and thus the physics of the radiative zone

TABLE I The Solar Fusion II recommended values for $S(0)$, its derivatives, and related quantities, and for the resulting uncertainties on $S(E)$ in the region of the solar Gamow peak – the most probable reaction energy – defined for a temperature of 1.55×10^7 K characteristic of the Sun’s center. See the text for detailed discussions of the range of validity for each $S(E)$. Also see Sec. VIII for recommended values of CNO electron capture rates, Sec. XI.B for other CNO S-factors, and Sec. X for the ${}^8\text{B}$ neutrino spectral shape. Quoted uncertainties are 1σ .

Reaction	Section	$S(0)$ (keV-b)	$S'(0)$ (b)	$S''(0)$ (b/keV)	Gamow peak uncertainty (%)
$p(p, e^+ \nu_e) d$	III	$(4.01 \pm 0.04) \times 10^{-22}$	$(4.49 \pm 0.05) \times 10^{-24}$	–	± 0.7
$d(p, \gamma) {}^3\text{He}$	IV	$(2.14^{+0.17}_{-0.16}) \times 10^{-4}$	$(5.56^{+0.18}_{-0.20}) \times 10^{-6}$	$(9.3^{+3.9}_{-3.4}) \times 10^{-9}$	$\pm 7.1^a$
${}^3\text{He}({}^3\text{He}, 2p) {}^4\text{He}$	V	$(5.21 \pm 0.27) \times 10^3$	-4.9 ± 3.2	$(2.2 \pm 1.7) \times 10^{-2}$	$\pm 4.3^a$
${}^3\text{He}({}^4\text{He}, \gamma) {}^7\text{Be}$	VI	0.56 ± 0.03	$(-3.6 \pm 0.2) \times 10^{-4}{}^b$	$(0.151 \pm 0.008) \times 10^{-6}{}^c$	± 5.1
${}^3\text{He}(p, e^+ \nu_e) {}^4\text{He}$	VII	$(8.6 \pm 2.6) \times 10^{-20}$	–	–	± 30
${}^7\text{Be}(e^-, \nu_e) {}^7\text{Li}$	VIII	See Eq. (40)	–	–	± 2.0
$p(pe^-, \nu_e) d$	VIII	See Eq. (46)	–	–	$\pm 1.0^d$
${}^7\text{Be}(p, \gamma) {}^8\text{B}$	IX	$(2.08 \pm 0.16) \times 10^{-2}{}^e$	$(-3.1 \pm 0.3) \times 10^{-5}$	$(2.3 \pm 0.8) \times 10^{-7}$	± 7.5
${}^{14}\text{N}(p, \gamma) {}^{15}\text{O}$	XI.A	1.66 ± 0.12	$(-3.3 \pm 0.2) \times 10^{-3}{}^b$	$(4.4 \pm 0.3) \times 10^{-5}{}^c$	± 7.2

^aError from phenomenological quadratic fit. See text.

^b $S'(0)/S(0)$ taken from theory; error is that due to $S(0)$. See text.

^c $S''(0)/S(0)$ taken from theory; error is that due to $S(0)$. See text.

^dEstimated error in the pep/pp rate ratio. See Eq. (46)

^eError dominated by theory.

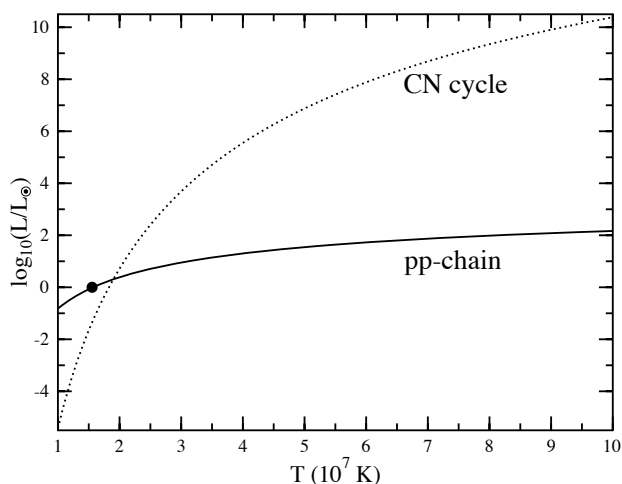


FIG. 1 The stellar energy production as a function of temperature for the pp chain and CN cycle, showing the dominance of the former at solar temperatures. Solar metallicity has been assumed. The dot denotes conditions in the solar core: the Sun is powered dominantly by the pp chain.

that the SSM was designed to describe. The sound speed profile $c(r)$ has been determined rather precisely over the outer 90% of the Sun and, as previously discussed, is now in conflict with the SSM, when recent abundance determinations from 3D photospheric absorption line analyses are used.

A. Rates and S-factors

The SSM requires a quantitative description of relevant nuclear reactions. Both careful laboratory measurements constraining rates at near-solar energies and a supporting theory of sub-barrier fusion reactions are needed.

At the temperatures and densities in the solar interior (e.g., $T_c \sim 15.5 \times 10^6$ K and $\rho_c \sim 153$ g/cm³ at the Sun’s center), interacting nuclei reach a Maxwellian equilibrium distribution in a time that is infinitesimal compared to nuclear reaction time scales. Therefore, the reaction rate between two nuclei can be written (Burbidge *et al.*, 1957; Clayton, 1968)

$$r_{12} = \frac{n_1 n_2}{1 + \delta_{12}} \langle \sigma v \rangle_{12}. \quad (3)$$

Here the Kronecker delta prevents double counting in the case of identical particles, n_1 and n_2 are the number densities of nuclei of type 1 and type 2 (with atomic numbers Z_1 and Z_2 , and mass numbers A_1 and A_2), and $\langle \sigma v \rangle_{12}$ denotes the product of the reaction cross section σ and the relative velocity v of the interacting nuclei, averaged over the collisions in the stellar gas,

$$\langle \sigma v \rangle_{12} = \int_0^\infty \sigma(v) v \Phi(v) dv. \quad (4)$$

Under solar conditions nuclear velocities are very well approximated by a Maxwell–Boltzmann distribution. It follows that the relative velocity distribution is also a Maxwell–Boltzmann, governed by the reduced mass μ of the colliding nuclei,

$$\Phi(v) dv = \left(\frac{\mu}{2\pi kT} \right)^{3/2} \exp\left(-\frac{\mu v^2}{2kT} \right) 4\pi v^2 dv. \quad (5)$$

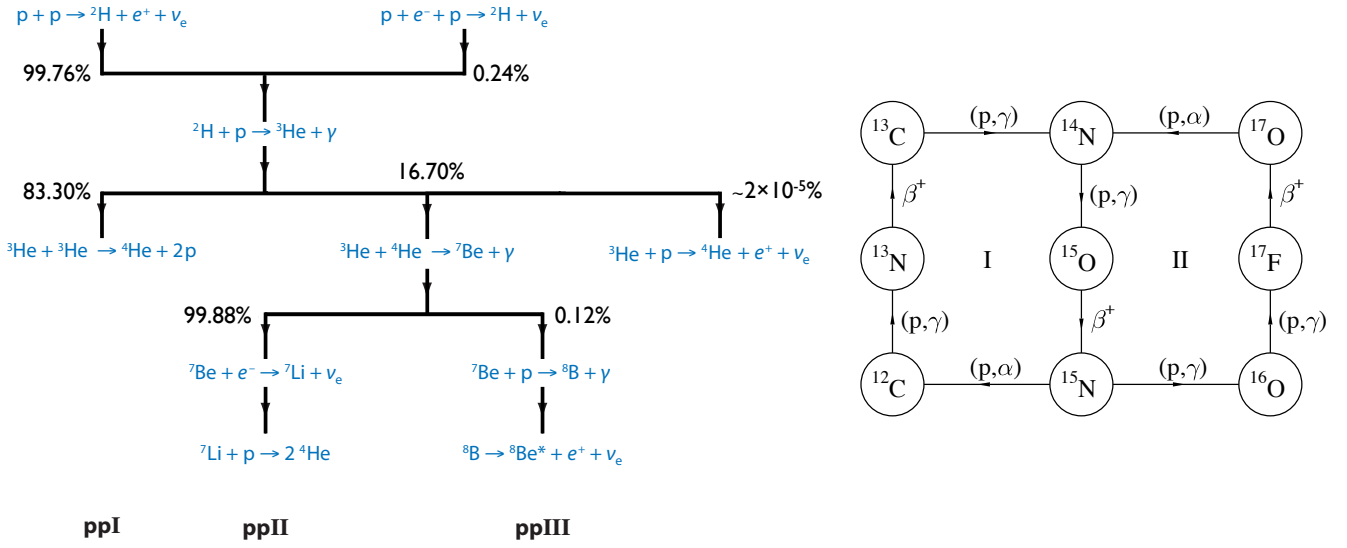


FIG. 2 The left frame shows the three principal cycles comprising the pp chain (ppI, ppII, and ppIII), with branching percentages indicated, each of which is “tagged” by a distinctive neutrino. Also shown is the minor branch ${}^3\text{He} + p \rightarrow {}^4\text{He} + e^+ + \nu_e$, which burns only $\sim 10^{-7}$ of ${}^3\text{He}$, but produces the most energetic neutrinos. The right frame shows the CNO bi-cycle. The CN cycle, marked I, produces about 1% of solar energy and significant fluxes of solar neutrinos.

Therefore,

$$\langle \sigma v \rangle_{12} = \sqrt{\frac{8}{\pi \mu (kT)^3}} \int_0^\infty E \sigma(E) \exp\left(-\frac{E}{kT}\right) dE, \quad (6)$$

where E is the relative kinetic energy and k is the Boltzmann constant. In order to evaluate $\langle \sigma v \rangle_{12}$ the energy dependence of the reaction cross section must be determined.

Almost all of the nuclear reactions relevant to solar energy generation are nonresonant and charged-particle induced. For such reactions it is helpful to remove much of the rapid energy dependence associated with the Coulomb barrier, by evaluating the probability of s-wave scattering off a point charge. The nuclear physics (including effects of finite nuclear size, higher partial waves, antisymmetrization, and any atomic screening effects not otherwise explicitly treated) is then isolated in the S-factor, defined by

$$\sigma(E) = \frac{S(E)}{E} \exp[-2\pi\eta(E)], \quad (7)$$

with the Sommerfeld parameter $\eta(E) = Z_1 Z_2 \alpha / v$, where $v = \sqrt{2E/\mu}$ is the relative velocity and α the fine structure constant ($\hbar = c = 1$). Because the S-factor is slowly varying, one can extrapolate $S(E)$ more reliably from the range of energies spanned by data to the lower energies characterizing the Gamow peak.

A substitution of Eq. (7) into Eq. (6) followed by a Taylor expansion of the argument of the exponentials then

yields (Bahcall, 1989)

$$\begin{aligned} \langle \sigma v \rangle_{12} &= \sqrt{\frac{2}{\mu kT}} \frac{\Delta E_0}{kT} f_0 S_{\text{eff}} \exp[-3E_0/(kT)] \\ &= 1.301 \times 10^{-14} \text{ cm}^3/\text{s} \left(\frac{Z_1 Z_2}{A}\right)^{1/3} \\ &\times f_0 \frac{S_{\text{eff}}}{\text{MeV b}} T_9^{-2/3} \exp[-3E_0/(kT)], \quad (8) \end{aligned}$$

where

$$\frac{E_0}{kT} = (\pi Z_1 Z_2 \alpha / \sqrt{2})^{2/3} [\mu / (kT)]^{1/3},$$

$$\frac{\Delta E_0}{kT} = 4 \sqrt{\frac{E_0}{3kT}}, \quad A = \frac{A_1 A_2}{A_1 + A_2},$$

and

$$\begin{aligned} S_{\text{eff}} &= S(0) \left(1 + \frac{5kT}{36E_0}\right) + S'(0)E_0 \left(1 + \frac{35kT}{36E_0}\right) \\ &+ \frac{1}{2}S''(0)E_0^2 \left(1 + \frac{89kT}{36E_0}\right). \end{aligned}$$

E_0 , the Gamow peak energy where the integrand of Eq. (6) takes on its maximum value, is the most probable energy of reacting nuclei. ΔE_0 corresponds to the full width of the integrand at $1/e$ of its maximum value, when approximated as a Gaussian. Equation (8) includes a factor f_0 , discussed below, to correct for the effects of electronic screening on nuclear reactions occurring in the solar plasma.

Rates in an astrophysical plasma can be calculated given $S(E)$ which by virtue of its slow energy dependence, in the case of non-resonant reactions, can be approximated by its zero-energy value $S(0)$ and possible corrections determined by its first and second derivatives, $S'(0)$ and $S''(0)$. It is these quantities that we need to determine by fitting laboratory data, or in cases where such data cannot be obtained, through theory. For most of the reactions contributing to the pp chain and CNO bi-cycle, data have been obtained only for energies in regions above the Gamow peak, e.g., typically $E \gtrsim 100$ keV, so that extrapolations to lower energies depend on the quality of the fit to higher energy data. Ideally one desires a fitting function that is well motivated theoretically and tightly constrained by the existing, higher-energy data. The purpose of this review is to provide current best values and uncertainties for $S(0)$ and, if feasible, its derivatives.

S-factor uncertainties, when folded into SSM calculations, then limit the extent to which that model can predict observables, such as the depth of the convective zone, the sound speed profile, and the neutrino fluxes. It has become customary in the SSM to parameterize the consequences of input uncertainties on observables through logarithmic partial derivatives, determined by calculating the SSM response to variations in individual input parameters. SSM compilations of the logarithmic partial derivatives provide, for example, a way to assess the importance of each S-factor uncertainty on neutrino flux predictions.

The partial derivatives $\alpha(i, j)$ for each neutrino flux ϕ_i and SSM input parameter β_j are defined by

$$\alpha(i, j) \equiv \frac{\partial \ln [\phi_i / \phi_i(0)]}{\partial \ln [\beta_j / \beta_j(0)]} \quad (9)$$

where $\phi_i(0)$ and $\beta_j(0)$ denote the SSM best values. The $\alpha(i, j)$ for 19 SSM input parameters β_j are given by Peña-Garay and Serenelli (2008) in their 2008 SSM update. The β_j include parameters such as the Sun's age and luminosity, the abundances of important metals, and S-factors.

The partial derivatives define the power-law dependencies of neutrino fluxes with respect to the SSM best-value prediction $\phi_i(0)$,

$$\phi_i = \phi_i(0) \prod_{j=1}^N \left[\frac{\beta_j}{\beta_j(0)} \right]^{\alpha(i, j)} = \phi_i(0) \prod_{j=1}^N [1 + \delta\beta_j]^{\alpha(i, j)}, \quad (10)$$

where the product extends over N SSM input parameters, and where $\delta\beta_j \equiv \Delta\beta_j / \beta_j(0)$ is the fractional uncertainty of input parameter β_j with respect to its SSM best value. This expression separates the impact of SSM parameter variations on ϕ_i into a solar piece – the infinitesimal SSM response described by $\alpha(i, j)$ – and a laboratory or theory piece – the estimated uncertainty $\delta\beta_j$ of an input parameter (in our case, that of an S-factor). From SSM tabulations of the $\alpha(i, j)$, one can

estimate the change in a SSM flux prediction ϕ_i , when a given SSM parameter β_j is perturbed away from its SSM best value by an amount $\delta\beta_j$, without redoing the SSM calculation. For example, to assess the impact of an improved nuclear cross section measurement on ϕ_i , one sets $\delta\beta_j$ to the estimated uncertainty of the corresponding S-factor, to obtain the corresponding variation in ϕ_i . In this way one can identify nuclear physics improvements that will have the most impact on reducing flux uncertainties. Alternatively, the process can be inverted: a flux measurement could in principle be used to constrain an uncertain input parameter.

For example, Peña-Garay and Serenelli (2008) define the dependence of $\phi(^8\text{B})$ on the S-factors under discussion here,

$$\phi(^8\text{B}) \propto (1 + \delta S_{11})^{-2.73} (1 + \delta S_{33})^{-0.43} (1 + \delta S_{34})^{0.85} \\ \times (1 + \delta S_{17})^{1.0} (1 + \delta S_{e7})^{-1.0} (1 + \delta S_{14})^{-0.02}, \quad (11)$$

where S_{11} denotes the S-factor for p+p reaction, etc., and $\delta S_{11} \equiv \Delta S_{11} / S_{11}(0)$ denotes its fractional uncertainty. This review gives the best current values for the needed δS s.

B. Screening of stellar and laboratory reactions

One must take into account differences in the atomic environments to correctly relate screened laboratory and solar cross sections, $\sigma_s^{\text{lab}}(E)$ and $\sigma_s^{\text{solar}}(E)$, to each other or to the underlying bare cross section $\sigma_b(E)$. Screening enhances solar cross sections by reducing the Coulomb barrier that reacting ions must overcome. As light nuclei in the solar core are almost completely ionized, the solar electron screening correction f_0 ,

$$f_0(E) \equiv \frac{\sigma_s^{\text{solar}}(E)}{\sigma_b(E)}, \quad (12)$$

can be treated in a weak-screening approximation (Salpeter, 1954). The impact of the modified potential,

$$V(r) = \frac{\alpha Z_1 Z_2}{r} \exp\left(-\frac{r}{R_D}\right), \quad (13)$$

on reactions depends on the ratio of the Coulomb potential at the Debye radius R_D to the temperature,

$$f_0 \sim \exp\left(\frac{Z_1 Z_2 \alpha}{R_D k T}\right) = \exp\left(0.188 Z_1 Z_2 \zeta \rho_0^{1/2} T_6^{-3/2}\right), \quad (14)$$

where $\zeta R_D = [kT / (4\pi\alpha\rho)]^{1/2}$, ρ is the number density of nucleons, ρ_0 is a dimensionless density measured in g/cm^3 , $\zeta = \left[\sum_i X_i (Z_i^2 / A_i) + (f_0' / f_0) \sum_i X_i (Z_i / A_i) \right]^{1/2}$, X_i is the mass fraction of nuclei of type i , and T_6 is the dimensionless temperature in units of 10^6 K. The

factor $f'_0/f_0 \sim 0.92$ corrects for the effects of electron degeneracy in the solar core (Salpeter, 1954).

The weak-screening approximation requires the average interaction energy between particles to be smaller than the average particle kinetic energy (Baimbetov *et al.*, 1995; Kobzev *et al.*, 1995). This places a constraint on the argument of Eq. (14), $Z_1 Z_2 \alpha / (R_D kT) \ll 1$, that is satisfied in the solar core if $Z_1 Z_2 \lesssim 10$ (Gruzinov, 1998), a condition met by the low-Z reactions of the pp chain and CNO bi-cycle. However corrections to the Salpeter formula are expected at some level. Nonadiabatic effects have been suggested as one source, e.g., when a high Gamow energy guarantees reacting nuclei having velocities significantly higher than the typical ion velocity, so that the response of slower plasma ions might be suppressed. At the time of Solar Fusion I such dynamic corrections were a source of controversy. Dynamic corrections were first discussed by Mitler (1977) and later studied by Carraro *et al.* (1988). Subsequent work showed that Salpeter's formula would be valid independent of the Gamow energy due to the nearly precise thermodynamic equilibrium of the solar plasma (Brown and Sawyer, 1997; Gruzinov, 1998; Gruzinov and Bahcall, 1998). The arguments, summarized in Solar Fusion I, were significantly extended in 2002 by Bahcall *et al.* (2002), who pointed out a number of contradictions in investigations claiming larger corrections, and showed that a field theoretic approach led to the expectation of only small ($\sim 4\%$) corrections to the standard formula, for solar conditions. However controversies have not entirely died out (Mao *et al.*, 2009).

The Salpeter correction relates the solar and bare cross sections, $\sigma_s^{\text{solar}}(E)$ and $\sigma_b(E)$. As the reactions studied in the laboratory generally involve target nuclei bound in neutral atoms and molecules, not bare ions, a second step is needed to extract $\sigma_b(E)$ from laboratory data. As in the Sun, electrons in the laboratory target tend to reduce the barrier, so that the screened cross section $\sigma_s^{\text{lab}}(E)$ will exceed that for bare ions $\sigma_b(E)$. The enhancement is given by (Assenbaum *et al.*, 1987)

$$f_{\text{lab}}(E) \equiv \frac{\sigma_s^{\text{lab}}(E)}{\sigma_b(E)} \sim \exp \left[\frac{\pi \eta(E) U_e}{E} \right] \geq 1 \quad \text{for } U_e \ll E, \quad (15)$$

where U_e is an electron-screening potential energy. This energy can be estimated from the difference in atomic binding energies between the compound atom and the projectile plus target atoms of the entrance channel. Because the correction depends on the ratio U_e/E , one expects screening corrections to be most important for very low projectile energy.

In contrast with the case of solar screening, a great deal can be done experimentally (Angulo *et al.*, 1993; Assenbaum *et al.*, 1987; Engstler *et al.*, 1988, 1992; Greife *et al.*, 1995; Prati *et al.*, 1994; Rolfs, 2001; Rolfs and Somorjai, 1995) to test our understanding of electron screening in terrestrial targets. Studies of reactions involving light nuclei (Engstler *et al.*, 1988; Strieder *et al.*, 2001) revealed

an upturn in cross section at low energies, as predicted by Eq. (15). For example, results for ${}^3\text{He}(d,p){}^4\text{He}$ (Aliotta *et al.*, 2001) could be represented by Eq. (15) for a screening potential $U_e = 219 \pm 15$ eV. While this potential is significantly larger than the one obtained from the adiabatic approximation, $U_{ad} = 119$ eV, the analysis requires one to assume an energy dependence of the bare cross section $\sigma_b(E)$. This adds a difficult-to-quantify theoretical uncertainty to the extracted potential. It may be possible to remove much of this uncertainty through an indirect measurement of $\sigma_b(E)$ by the Trojan Horse Method (Lattuada *et al.*, 2001; Spitaleri *et al.*, 2001; Strieder *et al.*, 2001; Tumino *et al.*, 2003).

There exist various surrogate environments that have been exploited by experimentalists to test our understanding of plasma screening effects. Screening in $d(d,p)t$ has been studied for gaseous targets and for deuterated metals, insulators, and semiconductors (Raiola *et al.*, 2004). For a summary of the results see Haxton *et al.* (2006): it is believed that the quasi-free valence electrons in metals create a screening environment quite similar to that found in stellar plasmas. Experiments in metals have confirmed important predictions of the Debye model, such as the temperature dependence $U_e(T) \propto T^{-1/2}$.

The tendency of experimentally determined values of U_e to exceed theoretical estimates by a factor ~ 2 has been noted by Assenbaum *et al.* (1987); Rolfs (2001); Rolfs and Somorjai (1995). Various possible explanations have been considered (Balantekin *et al.*, 1997; Fiorentini *et al.*, 2003; Flambaum and Zelevinsky, 1999; Hagino and Balantekin, 2002; Shoppa *et al.*, 1993). A possible solution of the laboratory screening problem was proposed in Langanke *et al.* (1996) and in Bang *et al.* (1996), that the stopping of ions in matter differs at low energy from that obtained by extrapolating from stopping power tables at higher energies (Andersen and Ziegler, 1977). Smaller stopping powers were indeed verified experimentally (Golser and Semrad, 1991; Rolfs, 2001) and explained theoretically (Bertulani, 2004; Bertulani and de Paula, 2000).

Screening corrections for laboratory reactions are important in extracting S-factors in cases where data extend to very low energies. In this review two cases of interest are ${}^3\text{He}+{}^3\text{He} \rightarrow p+p+{}^4\text{He}$, where the lowest data point is at $E = 16$ keV, and ${}^{14}\text{N}(p,\gamma){}^{15}\text{O}$, where measurements extend down to 70 keV.

C. Fitting and extrapolating S-factors

$S(0)$ (and its derivatives $S'(0)$ and $S''(0)$) needed in Eq. (8) could be taken from a polynomial fit to data. A quadratic form often provides an excellent representation of the data up to a few hundred keV. However, as the procedure is purely empirical, it provides no theoretical justification for extrapolating beyond the last known data point. For example, a quadratic fit to the labora-

tory data for ${}^7\text{Be}(p,\gamma){}^8\text{B}$ would miss the upturn in the S-factor at low energy expected from theory, as this increase occurs beyond the range of existing data. For this reason, we restrict our use of empirical fitting functions to cases where the data sets encompass the full range of energies relevant to astrophysics.

1. Theory constraints: model-based methods

One class of important theoretical constraints makes use of the peripheral nature of non-resonant radiative capture reactions close to the threshold. If the reaction occurs at separations much larger than the sum of the nuclear radii, one can derive the coefficients for the Taylor series for $S(E)$ independent of models, as only the asymptotic forms of the bound and scattering initial- and final-state wave functions are relevant. This idea has been exploited in several ways.

Williams and Koonin (1981) used Bessel function expansions of Coulomb wave functions and a hard-sphere approximation to derive an expansion of the low-energy logarithmic derivative,

$$\frac{1}{S(E)} \frac{dS(E)}{dE} = a + bE. \quad (16)$$

This approach was further developed by Mukhamedzhanov and Nunes (2002), who considered variables such as the remnant Coulomb barrier, the initial and final centrifugal barriers, and the binding energy (but not the interactions of the colliding nuclei in the entrance channel). They found that the near-threshold behavior of $S(E)$ could be sensitive to such parameters. Baye and collaborators, employing zero-energy solutions of the Schrödinger equation and their energy derivatives, showed that model-independent values for the coefficients in the Taylor expansion for $S(E)$ around $E = 0$ could be extracted from the asymptotic normalization coefficient (ANC) of the bound state wave function and the scattering lengths of the scattering states, thus including effects from interactions in the continuum (Baye, 2000, 2004, 2005; Baye and Brainis, 2000).

Despite the successful application of the Taylor series expansion for $S(E)$, it was noticed that the series has a restricted domain of convergence, determined by the binding energy E_B of the final state. This is a consequence of a pole in the relevant radial integral at $E = -E_B$ (Baye, 2000; Jennings *et al.*, 1998a,b). This limitation becomes particularly severe for weakly bound nuclei: for ${}^7\text{Be}(p,\gamma){}^8\text{B}$, $|E_B| \sim 138$ keV barely reaches the domain of experimental data. Thus the alternatives of a Laurent expansion of the S-factor in the photon energy $E_\gamma = E + E_B$, an expansion of $(E + E_B)S(E)$, and the explicit treatment of the pole have been explored as alternatives in the analysis of experimental data (Cyburt and Davids, 2008; Cyburt *et al.*, 2004). See also Typel

and Baur (2005) for explicit expressions of the cross sections without the convergence limitation.

Model-based calculations of fusion cross sections also provide a template for fitting and extrapolating experimental data. Models can be constrained by the known properties of the system under study and can be applied over a wide range of energies. While they often predict the energy dependence of $S(E)$ accurately, in many cases an overall renormalization is needed to give the correct magnitude of the S-factor. The need for this scaling is qualitatively understood, as model calculations of interior wave functions are generally done in restricted spaces, and thus lack high-momentum (and certain low-momentum) components of the true wave function, with consequences for the normalization. (The goal of predicting both the shape and normalization of S-factors is motivating the development of quasi-exact *ab initio* methods, as discussed below.)

Modeling approaches involve various levels of complexity. The simplest microscopic reaction theories are the potential models, in which the internal structure of the colliding nuclei is ignored. The dynamics of the process is reduced to a single coordinate, the distance vector between the two nuclei. The potential-model Hamiltonian is typically a phenomenological one, e.g., a Woods-Saxon potential, with parameters that can be determined by fitting data, such as the elastic cross section.

More realism is provided by cluster models like the resonating group method (RGM) or the generator-coordinate method (GCM), which take into account the many-body substructure of the reacting nuclei. These models employ fully antisymmetrized many-body wave functions of the compound system, though constructed in a restricted model space. The full wave function is described as a superposition of many-body cluster wave functions of fixed internal structure moving against each other. The interaction is described by phenomenological nucleon-nucleon potentials with parameters that are adjusted for each reaction under consideration.

Another description of fusion reaction cross sections comes from the R-matrix. Space is divided into two regions, the interior where nuclear forces are important, and the exterior where the interaction between the nuclei is assumed to be only Coulombic. The full scattering wave function connecting different channels i is expanded in partial waves with total angular momentum J . The Schrödinger equation for the interior Hamiltonian is solved, with boundary conditions at the channel radii a_i encoding the correct asymptotic behavior. The solutions of the Schrödinger equation determine the level energies E_λ and reduced widths $\gamma_{\lambda i}$ that appear in the expression for the R-matrix

$$R_{ij}(E) = \sum_{\lambda=1}^N \frac{\gamma_{\lambda i} \gamma_{\lambda j}}{E - E_\lambda}, \quad (17)$$

for each J , in the standard approach of Lane and Thomas (1958). Simple expressions relate the reaction cross sections at energy E to the R-matrix. The cross section

should be insensitive to the choice of the channel radii. In most applications the R-matrix is viewed as a parameterization of measured reaction cross sections in terms of fitted level energies and reduced widths. A connection to an underlying reaction model is not required. The R-matrix allows one to properly account for penetrability effects, and to adjust the complexity of the fitting in response to various practical considerations, such as the energy range of interest.

R-matrix resonance parameters (level energies and reduced widths) are not directly comparable to the experimental quantities due to level shifts associated with the chosen boundary conditions. Generalizing earlier ideas of Barker (1971) and Angulo and Descouvemont (2000), an alternative parametrization of R-matrix theory has been developed by Brune (2002) where all level shifts vanish and the partial widths and level energies are identical to the observed parameters. This approach simplifies the incorporation of known nuclear properties in the fitting procedure and the comparison with experimental resonance properties.

2. Theory constraints: *ab initio* methods

Ab initio methods – defined here as methods that provide a quasi-exact solution to the many-body Schrödinger equation, such as the hyperspherical harmonic expansion (HH) and Green’s function Monte Carlo (GFMC) methods, or that express observables in terms of a controlled expansion, such as effective field theory – play two critical roles. Two reactions discussed in this review, $p+p \rightarrow d+e^++\nu_e$ and ${}^3\text{He}+p \rightarrow {}^4\text{He}+e^++\nu_e$, are presently beyond the reach of experiment. Thus we are entirely dependent on theory for the corresponding S-factors. The convincing demonstration that the rate for $p+p \rightarrow d+e^++\nu_e$ can be calculated to a precision of $\lesssim 1\%$ is one of the important achievements of *ab initio* nuclear theory, as described in Sec. III.

Furthermore, *ab initio* methods potentially could be applied to all other reactions in the pp chain (and, farther in the future, to the CNO bi-cycle) to provide a more reliable basis for extrapolating data. One of the impressive examples of progress to date, the agreement between data for $d(p,\gamma){}^3\text{He}$ and theory (calculations employing variational HH wave functions in combination with an electromagnetic current operator with both one- and two-body components), is discussed in Sec. IV and illustrated in Fig. 3.

Ab initio methods break into two broad categories, potential-based calculations and effective field theory expansions. The former are distinguished from model-based methods discussed in Sec. II.C.1 in two regards. First, they use a realistic interaction that fits two-body scattering data in detail, as well as certain bound-state properties of the lightest nuclei. Thus the interaction has both a rich operator structure and an explicit treatment of the short-distance repulsive core. Second, they

combine this potential,

$$H_A = \sum_{i=1}^A t_i + \sum_{i<j}^A v_{ij}^{\text{phen}} + \sum_{i<j<k}^A v_{ijk}^{\text{phen}}, \quad (18)$$

with numerical techniques that can accurately treat an interaction of such complexity and with such disparate spatial scales, producing a quasi-exact solution of the many-body Schrödinger equation. The form of the three-body potential in Eq. (18), which contributes for $A \geq 3$ but plays a less important role than the dominant two-body potential, is typically taken from theory. Once the wave functions are obtained, they can be combined with electroweak transition operators to produce estimates of observables. The transition operators include both one-body terms determined from the coupling of the single nucleon to the electroweak current, and two-body corrections, typically derived from one-boson-exchange diagrams. Examples of the potential approach, including discussions of the associated issue of transition operators, are found in Secs. III, IV, and VII.

The second approach is based on effective field theory (EFT). EFTs exploit the gap between the long-wavelength properties of nuclei that govern nuclear reactions near threshold, and the short-range interactions in the NN potential that make an exact solution of the Schrödinger equation technically difficult. The calculations are restricted to a limited basis describing the long-wavelength behavior, and the omitted degrees of freedom are absorbed into effective operators that can be organized in powers of Q/Λ_{cut} , where Q is the momentum characterizing the physics of interest and Λ_{cut} is the momentum characterizing the omitted physics. If carried out completely, no simplification is achieved, because the low-momentum EFT Lagrangian has an infinite number of such operators. EFT becomes useful when there is a significant gap between Q and Λ_{cut} , so that only a small number of the effective operators corresponding to the leading powers in Q/Λ_{cut} must be retained, to reproduce long-wavelength observables to a specified accuracy. The coefficients of the leading operators can then be determined by fitting data: if enough constraints exist to fix all of the needed low-energy constants, then accurate predictions can be made about new processes. The application of this method to $p+p \rightarrow d+e^++\nu_e$ and ${}^3\text{He} + p \rightarrow {}^4\text{He} + e^+ + \nu_e$ is described in some detail in Secs. III and VII, respectively. This approach can also be applied to $d(p,\gamma){}^3\text{He}$.

One of the potential-based methods now being developed for reactions should be highlighted because of its established success in predicting bound-state properties throughout most of the $1p$ shell. The quantum Monte Carlo (QMC) approach combines the variational Monte Carlo (VMC) and GFMC methods (Pieper, 2008). The VMC calculation produces an approximate wave function by minimizing the energy of a variational wave function including elaborate two- and three-body correlations. The GFMC method is then employed to make the

needed small improvements to the VMC result required for a true solution to the Schrödinger equation.

The GFMC method requires a local potential, so its use has been restricted to the Argonne v_{18} NN potential (Wiringa *et al.*, 1995), denoted AV18. There is also an important three-nucleon interaction, determined by fitting 17 bound- and narrow-state energies for $A \leq 8$ (Pieper *et al.*, 2001). The high quality of the QMC predictions for energies of bound states and sharp resonances in nuclei with $A \leq 12$, and for charge radii, electromagnetic moments, and other observables, has been thoroughly established (Pieper *et al.*, 2001, 2002, 2004).

Recent VMC-based calculations of capture cross sections using realistic potentials (Marcucci *et al.*, 2006; Nollett, 2001; Nollett *et al.*, 2001) represent a first step in extending the QMC program to reactions. These calculations used VMC wave functions for bound states in ${}^3\text{H}$, ${}^3\text{He}$, ${}^4\text{He}$, ${}^6\text{Li}$, ${}^7\text{Li}$, and ${}^7\text{Be}$, as well as an exact deuteron. Initial states in the reactions $d(\alpha, \gamma){}^6\text{Li}$, ${}^3\text{H}(\alpha, \gamma){}^7\text{Li}$, and ${}^3\text{He}(\alpha, \gamma){}^7\text{Be}$ were computed as products of the reactant VMC wave functions and a correlation, matched to experimental phase shifts, to describe the relative motion of the interacting nuclei. Work has focused, in particular, on building in the proper long-range clustering of the final states, as this is important in reproducing the proper energy dependence of S-factors. Results for ${}^3\text{H}(\alpha, \gamma){}^7\text{Li}$ closely match the measured absolute S-factor. However, the prediction for ${}^3\text{He}(\alpha, \gamma){}^7\text{Be}$ lies below the data by about a factor of 1.3 to 1.45.

Better QMC calculations of those and other cross sections are possible. VMC wave functions were used partly because of the technical difficulty of computing quantities off-diagonal in the energy eigenstates using GFMC; this problem has now been solved, and electroweak matrix elements between discrete levels have been computed (Marcucci *et al.*, 2008; Pervin *et al.*, 2007). Scattering wave functions are also now being computed directly from the NN+NNN potential, with successful calculations of low-energy neutron- ${}^4\text{He}$ scattering wave functions reported by Nollett *et al.* (2007) using particle-in-a-box formulations of the QMC methods.

While we have used the QMC approach to illustrate the progress in quasi-exact approaches, there are other important efforts underway to compute cross sections beyond $A=4$ from realistic NN potentials. Examples include the *ab initio* no-core shell model both alone (Navrátil *et al.*, 2006a,b) and in combination with the resonating group method (Quaglioni and Navrátil, 2009); the Lorentz integral transform method (Efros *et al.*, 2007); and the unitary correlation operator method (Neff and Feldmeier, 2008). The hyperspherical harmonics method, which will be discussed in connection with the $d(p, \gamma){}^3\text{He}$ and hep reactions, is also being extended to heavier systems.

We anticipate that quasi-exact methods will soon be practical for many scattering and capture processes in light nuclei. Calculations based on exact solutions of accurate interactions will predict not only the energy de-

pendences of solar fusion reactions but also absolute cross sections. Theory may thus provide a firm basis for validating and extrapolating data and for resolving systematic differences between measured data sets.

3. Adopted procedures

These are the procedures we adopt for fitting and extrapolating data:

- In two cases, $p+p \rightarrow d+e^+\nu_e$ and ${}^3\text{He}+p \rightarrow {}^4\text{He}+e^+\nu_e$, S-factor estimates depend entirely on theory. The goal in such cases should be the application of both potential and EFT or EFT-inspired methods, yielding consistent results with quantified uncertainties. As detailed in Sec. III, one is close to achieving this for S_{11} , with two methods providing consistent answers and uncertainties of $\lesssim 1\%$, and with a third method (EFT) potentially reaching similar precision, if ancillary measurements can better determine the needed low-energy constant. In the case of S_{hep} , a less critical cross section, the further developments of methods like Green's function Monte Carlo will provide an important check on the current state-of-the-art, a variational calculation in which a correlated hyperspherical harmonics expansion was used.
- In cases where data exist through the energy range of astrophysical interest, much can be done independent of theory. A polynomial representation of $S(E)$, e.g., values for $S(0)$, $S'(0)$, and $S''(0)$, could be obtained by directly fitting the data. However, as $S(E)$ represents the bare cross section, theory may still be needed to remove the effects of screening in the terrestrial target. As detailed above, there is some confidence that theory determines the functional form of the screening (Eq. (15)), so that such effects can be subtracted given sufficient low-energy data to fix the numerical value of the screening potential (which theory appears to predict less reliably). This issue arises in S_{33} .
- In cases where data exist but are not adequate to fully characterize the cross section in the region of astrophysical interest, we advocate the use of fitting functions motivated by theory to extrapolate data, with data determining the normalization. To the extent that well-justified models differ in their predictions, additional uncertainties must be assigned to $S(0)$ and its derivatives. Judgment is required in assessing the models and determining how they should be applied, e.g., the range in E over which a given model is likely to be valid. Each working group was asked to consider such issues, and to present and justify the procedures it followed to assess associated fitting uncertainties.

D. Treatment of uncertainties

The treatment of uncertainties – the statistical and systematic errors in data and the impact of imperfect theory in fitting and extrapolating data – is discussed in some detail in the Appendix. There are cases where several high-quality data sets exist, each with errors that presumably reflect both the statistical and evaluated systematic uncertainties of the experiment, that disagree by more than the error bars would indicate. In treating such cases, an error-bar “inflation factor” is commonly introduced, to account for the apparent underestimation of systematic errors. We have done so following Particle Data Group (PDG) conventions (Amsler *et al.*, 2008), with one minor modification described in the Appendix. Uncertainties quoted in this review correspond to one standard deviation (68% confidence level).

As discussed in the Appendix, there are alternative prescriptions for apportioning the unidentified systematics – and thus the inflations – among the experiments that disagree. However our group concluded that the PDG procedure was the best choice both for technical reasons and because the procedure is widely used in the physics community.

III. THE pp REACTION

The rate for the initial reaction in the pp chain, $p+p \rightarrow d + e^+ + \nu_e$, is too small to be measured in the laboratory. Instead, this cross section must be calculated from standard weak interaction theory.

As in Solar Fusion I, the adopted value and range for the logarithmic derivative is taken from Bahcall and May (1969),

$$S'_{11}(0) = S_{11}(0) (11.2 \pm 0.1) \text{ MeV}^{-1}. \quad (19)$$

This result is in excellent agreement with those obtained from linear fits to the modern potential-model calculations of Schiavilla *et al.* (1998), which yield values of 11.14 MeV^{-1} and 11.16 MeV^{-1} for the full and impulse-approximation calculations. As the Gamow peak energy is $\sim 6 \text{ keV}$ for temperatures characteristic of the Sun’s center, the linear term generates a $\lesssim 8\%$ correction to the $E = 0$ value. The 1% uncertainty in Eq. (19) corresponds to a $\lesssim 0.1\%$ uncertainty in the total reaction rate. This is negligible compared to other uncertainties described below. Therefore, in the following, we focus on $S_{11}(0)$.

At zero relative energy $S_{11}(0)$ can be written (Bahcall and May, 1968, 1969),

$$S_{11}(0) = 6\pi^2 m_p \alpha \ln 2 \frac{\bar{\Lambda}^2}{\gamma^3} \left(\frac{G_A}{G_V} \right)^2 \frac{f_{pp}^R}{(ft)_{0^+ \rightarrow 0^+}}, \quad (20)$$

where α is the fine-structure constant; m_p is the proton mass; G_V and G_A are the usual Fermi and axial-vector weak coupling constants; $\gamma = (2\mu B_d)^{1/2} = 0.23161 \text{ fm}^{-1}$

is the deuteron binding wave number; μ is the proton-neutron reduced mass; B_d is the deuteron binding energy; f_{pp}^R is the phase-space factor for the pp reaction with radiative corrections; $(ft)_{0^+ \rightarrow 0^+}$ is the ft value for superallowed $0^+ \rightarrow 0^+$ transitions; and $\bar{\Lambda}$ is proportional to the transition matrix element connecting the pp and deuteron states.

Inserting the current best values, we find

$$S_{11}(0) = 4.01 \times 10^{-25} \text{ MeV b} \left(\frac{(ft)_{0^+ \rightarrow 0^+}}{3071 \text{ s}} \right)^{-1} \times \left(\frac{G_A/G_V}{1.2695} \right)^2 \left(\frac{f_{pp}^R}{0.144} \right) \left(\frac{\bar{\Lambda}^2}{7.035} \right). \quad (21)$$

We now discuss the best estimates and the uncertainties for each of the factors appearing in Eq. (21).

We take $(ft)_{0^+ \rightarrow 0^+} = (3071.4 \pm 0.8) \text{ s}$, the value for superallowed $0^+ \rightarrow 0^+$ transitions that has been determined from a comprehensive analysis of experimental rates corrected for radiative and Coulomb effects (Hardy and Towner, 2009). This value determines the weak mixing matrix element $|V_{ud}| = 0.97418(27)$, the value adopted by the PDG (Amsler *et al.*, 2008). This ft value is also consistent with $(3073.1 \pm 3.1) \text{ s}$ used in Solar Fusion I.

For G_A/G_V , we use the PDG value $G_A/G_V = 1.2695 \pm 0.0029$ which is consistent with 1.2654 ± 0.0042 used in Solar Fusion I.

For the phase-space factor f_{pp}^R , we have taken the value without radiative corrections, $f_{pp}^R = 0.142$ (Bahcall and May, 1969) and increased it by 1.62% to take into account radiative corrections to the cross section (Kurylov *et al.*, 2003). The main source of error is from neglected diagrams in which the lepton exchanges a weak boson and a photon with different nucleons. These diagrams are estimated to modify f_{pp}^R by $\sim 0.1\%$, based on scaling the similar nucleus-dependent correction in superallowed β decay (Kurylov *et al.*, 2003). It would be useful to check this estimate through direct computations. We adopt $f_{pp}^R = 0.144(1 \pm 0.001)$, which is consistent with $0.144(1 \pm 0.005)$ used in Solar Fusion I.

The dominant uncertainty in $S_{11}(0)$ comes from the normalized Gamow-Teller (GT) matrix element $\bar{\Lambda}$. A great deal of theoretical work since Solar Fusion I has focused on reducing this uncertainty. In Solar Fusion I $\bar{\Lambda}$ was decomposed into $\bar{\Lambda} = \Lambda(1 + \delta)$, where Λ represents the contribution of the one-body transition operator and $\Lambda\delta$ that from two-body corrections. Λ thus involves an evaluation of the Gamow-Teller operator between the initial-state pp wave function and the final-state deuteron wave function. $\Lambda^2 = 6.92(1 \pm 0.002^{+0.014}_{-0.009})$ was adopted, where the first and second uncertainties reflect, respectively, variations in empirical values of the deuteron and low-energy pp scattering parameters, and the model dependence of the nuclear potential (Kamionkowski and Bahcall, 1994). The value and uncertainty of the exchange current contribution, $\delta = 0.01^{+0.02}_{-0.01}$, was determined from the range of values of published calculations,

following the conservative recommendation of Bahcall and Pinsonneault (1992).

Two major steps have contributed to reducing the uncertainty on $\bar{\Lambda}$ since Solar Fusion I. The first is a much deeper understanding of the correlation between the uncertainties in Λ and $\delta\Lambda$: the overall uncertainty in $\bar{\Lambda}$ can be described by a universal parameter that can be fixed by a single measurement. The study of Schiavilla *et al.* (1998) demonstrated this phenomenologically in the context of potential-model approaches, while later analysis via EFT provided a more formal justification (Butler *et al.*, 2001; Park *et al.*, 2003). The second step is the use of the precisely known tritium β decay rate Γ_β^T , as first proposed by Carlson *et al.* (1991), to fix this universal parameter. This has been done in both potential models (Schiavilla *et al.*, 1998) and in the hybrid EFT approach (Park *et al.*, 2003). We briefly describe these developments.

A. Progress in potential models

The most elaborate calculation for the pp fusion process in the potential-model approach (see Sec. II.C.2) was carried out by Schiavilla *et al.* (1998). A comparison of the results for five representative modern potentials – potentials designed to accurately reproduce nucleon-nucleon scattering data – yielded $\Lambda^2 = 6.975 \pm 0.010$. This study demonstrated the importance of using the tritium β decay rate to constrain the two-body GT transition operator. (Both the Fermi and GT operators contribute to tritium β decay, but the former can be reliably calculated because of the conserved vector current and the smallness of isospin breaking effects, $\sim 0.06\%$.) If one adjusts the uncertain strength of the exchange current so that the tritium β decay rate is reproduced, the variation in $S_{11}(0)$ that otherwise would come from the choice of the phenomenological potential is largely removed. Predictions for five representative high-precision phenomenological potentials fall in a narrow interval $7.03 \lesssim \bar{\Lambda}^2 \lesssim 7.04$ (Schiavilla *et al.*, 1998).

We note two other sources of model dependence that contribute to the overall uncertainty in $\bar{\Lambda}$. First, as three-body potentials and currents contribute to the tritium β decay rate, uncertainties in modeling such effects will influence the extracted constraint on the two-body currents needed for $S_{11}(0)$. The best estimate of the consequences of this uncertainty for $S_{11}(0)$, $\sim 0.8\%$, comes from the chiral (or pionful) EFT* approach described below. Second, the experimental uncertainties in the effective range parameters for nucleon-nucleon scattering will propagate to $\bar{\Lambda}$. We have assigned a 0.5% uncertainty in $\bar{\Lambda}^2$ to this source, pending future work in EFT to better quantify this uncertainty. By adding in quadrature these uncertainties of 0.8% and 0.5% and the smaller uncertainty associated with the above potential range, $\bar{\Lambda}^2 = 7.035 \pm 0.005$, we obtain the potential model esti-

mate

$$\bar{\Lambda}^2 = 7.035(1 \pm 0.009). \quad (22)$$

B. Progress in effective field theory (EFT)

The application of EFT, described in Sec. II.C.2, to the calculation of the pp fusion rate (and several other electroweak processes in light nuclei) is one of the notable developments since Solar Fusion I. There have been two lines of EFT calculations of pp fusion, described below.

1. Hybrid EFT (EFT*)

Electroweak nuclear transitions in EFT

$$\mathcal{M}^{\text{EFT}} = \langle \Psi_f^{\text{EFT}} | \sum_i \mathcal{O}_i^{\text{EFT}} + \sum_{i<j} \mathcal{O}_{ij}^{\text{EFT}} | \Psi_i^{\text{EFT}} \rangle, \quad (23)$$

require initial and final nuclear wave functions and the transition operators to be derived from EFT. However, this has not yet been achieved in EFT with dynamical pions for pp fusion. Instead, a hybrid approach (Park *et al.*, 2003) called EFT* (or MEEFT) has been developed in which transition operators are taken from chiral perturbation theory (χ PT), but sandwiched between phenomenological wave functions, Ψ_i^{phen} and Ψ_f^{phen} , generated by a potential model. As discussed below, this approach is a substantial improvement over the earlier calculation of Park *et al.* (1998).

For the low-energy GT transition that governs pp fusion, the one-body transition operators $\mathcal{O}_i^{\text{EFT}}$ are well known, while the two-body operators $\mathcal{O}_{ij}^{\text{EFT}}$ contain only one unknown low-energy constant (LEC). This LEC, denoted by \hat{d}^R , parameterizes the strength of contact-type four-nucleon coupling to the axial current. Park *et al.* (2003) chose to determine \hat{d}^R from the tritium β -decay rate Γ_β^T . The fact that Ψ^{phen} is not exactly an eigenstate of the EFT Hamiltonian can in principle be a source of concern, but it is plausible that the mismatch affects primarily the short-distance behavior of the wave function, so that the procedure of fixing the relevant LEC(s) to data can remove most of the inconsistency: While $\mathcal{L}_{\chi\text{PT}}$ by construction is valid only well below Λ_{QCD} , the use of the phenomenological Hamiltonian, Eq. (18), introduces high momentum components above Λ_{QCD} . To test this procedure, one can introduce a cutoff Λ_{NN} to eliminate high-momentum components in the two-nucleon relative wave function, fitting the LEC as a function of this parameter. One expects, if the fitting of the LEC reasonably accounts for missing or inconsistent short-distance physics, little Λ_{NN} dependence would be found in the calculated pp fusion rate. The residual dependence on Λ_{NN} , when this cutoff is varied over a physically reasonable range, provides a measure of the model independence of an EFT* calculation.

The Park *et al.* (2003) calculation included up to next-to-next-to-next-to-leading order (N³LO) terms in chiral expansion, and after fitting \hat{d}^R to Γ_β^T , yielded $\bar{\Lambda}^2 = 7.03(1 \pm 0.008)$. The uncertainty was estimated from the changes in $\bar{\Lambda}^2$ when Λ_{NN} is varied over an energy range typical of vector meson masses, 500 to 800 MeV. A rough estimate based on higher order chiral contributions was also made. Specifically, the contributions of the first four chiral orders to $\bar{\Lambda}$ follow the pattern (1+0.0%+0.1%+0.9%), while the fifth-order term is estimated to be $\sim 0.4\%$. We assume that the second- and third-order terms are accidentally small, while the fourth- and fifth-order terms reflect the convergence of the expansion in $m_\pi/\Lambda_{QCD} \sim 1/7$. Three-body currents contribute in sixth order. We therefore use the size of the fifth-order term, 0.4%, as a measure of the uncertainty due to neglected higher order contributions (including three-body currents).

Full EFT calculations that use Ψ^{EFT} instead of Ψ^{phen} , thus eliminating operator-wave function inconsistencies, are an important goal. Progress toward this goal includes recent constructions of EFT-based nuclear interactions; see, *e.g.*, Epelbaum (2006) and Gazit *et al.* (2009).

2. Pionless EFT

This approach can be applied to processes where the characteristic momentum p is much smaller than the pion mass m_π (Bedaque *et al.*, 1999; Chen *et al.*, 1999; Kaplan *et al.*, 1996), which is the case for solar pp fusion. Pions can then be integrated out, so that all nucleon-nucleon interactions and two-body currents are described by point-like contact interactions with a systematic expansion in powers of p/m_π . The one- and two-body contributions individually depend on the momentum cut-off but the sum does not. Thus, Λ and $\Lambda\delta$ in pp fusion are correlated. In pionless EFT only one two-body current (with coupling $L_{1,A}$) is needed in the description of deuteron weak breakup processes, through next-to-next-to-leading order (NNLO) in the p/m_π expansion (Butler *et al.*, 2001). This two-body current is a GT operator. Other two-body currents are either missing due to conservation of the vector current, or involve matrix elements suppressed due to the pseudo-orthogonality of the initial- and final-state wave functions. This means the universal number $L_{1,A}$ encodes the two-body contributions for all low-energy weak deuteron breakup processes, so that a single measurement will fix the rates of all such processes. The other approaches discussed above share this feature.

The computation of $\bar{\Lambda}$ in pionless EFT was carried out to the second order by Kong and Ravnal (2001) and Ando *et al.* (2008) and then to the fifth order by Butler and Chen (2001). Constraints on $L_{1,A}$ from two nucleon systems (Butler *et al.*, 2002; Chen *et al.*, 2003) yield $\bar{\Lambda}^2 = 6.99 \pm 0.21$. The MuSun experiment (Andreev *et al.*, 2008) is taking data on μ capture on deuterium.

The experimental goal is to constrain $\bar{\Lambda}^2$ to $\lesssim 1.5\%$ for pionless EFT (Chen *et al.*, 2005) and chiral EFT* (Ando *et al.*, 2002).

3. Comment on Mosconi *et al.*

Mosconi *et al.* (2007) have compared ν -d reaction cross sections for various models that differ in their treatments of two-body transition operators, concluding from this comparison that the results obtained in potential models, EFT*, and pionless EFT have uncertainties as large as 2-3%. Although they address only ν -d cross sections, a comment is in order here because this process is closely related to that for pp fusion. Mosconi *et al.* (2007) reach their conclusions by examining the scatter of unconstrained calculations of the ν -d cross section. However, all state-of-the-art calculations use Γ_β^T to reduce two-body current and other uncertainties, as we have detailed here. Once this requirement is imposed, the scatter in the calculated value of ν -d cross sections is significantly reduced.

C. Summary

We have seen that the various approaches discussed above yield accurate and very consistent values for $\bar{\Lambda}^2$. The remaining factors in Eq (18) also have uncertainties, but these are common to all the calculations. Adding all the uncertainties in quadrature, we find that the current best estimates for $S_{11}(0)$ are

$$\begin{aligned} 4.01(1 \pm 0.009) \times 10^{-25} \text{ MeV b} & \quad \text{potential models} \\ 4.01(1 \pm 0.009) \times 10^{-25} \text{ MeV b} & \quad \text{EFT*} \\ 3.99(1 \pm 0.030) \times 10^{-25} \text{ MeV b} & \quad \text{pionless EFT.} \end{aligned} \quad (24)$$

The larger uncertainty in the pionless EFT result is due to the relatively weak constraints on $L_{1,A}$ that can be imposed within two-nucleon systems but, as mentioned, this situation will soon be improved. The agreement of the central values obtained in the potential model and EFT* indicates the robustness of the results as long as the two-body current is constrained by tritium β decay. Meanwhile, the agreement of the error estimates in the two approaches is primarily due to the fact that, as explained above, the dominant part of the uncertainty has been estimated using the same argument. Based on the result obtained in the potential model and EFT*, we adopt as the recommended value

$$S_{11}(0) = 4.01(1 \pm 0.009) \times 10^{-25} \text{ MeV b.} \quad (25)$$

We adopt the Bahcall and May (1969) value for $S'_{11}(0)$

$$S'_{11}(0) = S_{11}(0)(11.2 \pm 0.1) \text{ MeV}^{-1}, \quad (26)$$

Bahcall and May (1969) also estimated dimensionally that $S''_{11}(0)$ would enter at the level of $\sim 1\%$, for temperatures characteristic of the solar center. As this is now

comparable to the overall error in S_{11} , we recommend that a modern calculation of $S''_{11}(0)$ be undertaken.

IV. THE $d(p,\gamma)^3\text{He}$ RADIATIVE CAPTURE REACTION

The radiative capture of protons on deuterium is the second reaction occurring in the pp chain. Because this reaction is so much faster than the pp weak rate discussed in the previous section, it effectively instantaneously converts deuterium to ^3He , with no observable signature. Thus uncertainties in its rate have no consequences for solar energy generation. By comparing the pp and $d(p,\gamma)^3\text{He}$ rates, one finds that the lifetime of a deuterium nucleus in the solar core is ~ 1 s, and that the equilibrium abundance of deuterium relative to H is maintained at $\sim 3 \times 10^{-18}$.

However, the $d(p,\gamma)^3\text{He}$ reaction plays a more prominent role in the evolution of protostars. As a cloud of interstellar gas collapses on itself, the gas temperature rises to the point of $d(p,\gamma)^3\text{He}$ ignition, $\sim 10^6$ K. The main effect of the onset of deuterium burning is to slow down the contraction and, in turn, the heating. As a consequence, the lifetime of the proto-star increases and its observational properties (surface luminosity and temperature) are frozen until the original deuterium is fully consumed (Stahler, 1988). Due to the slow evolutionary timescale, a large fraction of observed proto-stars are in the d-burning phase, while only a few are found in the earlier, cooler, rapidly evolving phase. A reliable knowledge of the rate of $d(p,\gamma)^3\text{He}$ down to a few keV (the Gamow peak in a proto-star) is of fundamental importance for modeling proto-stellar evolution.

The pd reaction also plays an important role in Big Bang nucleosynthesis, which begins when the early universe has cooled to a temperature of ~ 100 keV. The uncertainty in the pd reaction in the relevant energy window (25-120 keV) propagates into uncertainties in the deuterium, ^3He and ^7Li abundances, scaling roughly as

$$\frac{d}{H} \propto R_{pd}^{-0.32} \quad \frac{^3\text{He}}{H} \propto R_{pd}^{0.38} \quad \frac{^7\text{Li}}{H} \propto R_{pd}^{0.59}, \quad (27)$$

where R_{pd} is the value of S_{12} relative to the fiducial value in Cyburt (2004). Thus a 10% error in the pd capture rate propagates into roughly 3.2%, 3.8% and 5.9% uncertainties in the light element primordial abundances, d, ^3He and ^7Li , respectively.

A. Data sets

The extensive experimental data sets for pd radiative capture include total cross sections and spin polarization observables at center-of-mass energies E ranging from several tens of MeV to a few keV, covering all the relevant astrophysical energies. In the regime $E \lesssim 2$ MeV (below the deuteron breakup threshold), the relevant experimental data include Bailey *et al.* (1970); Casella *et al.*

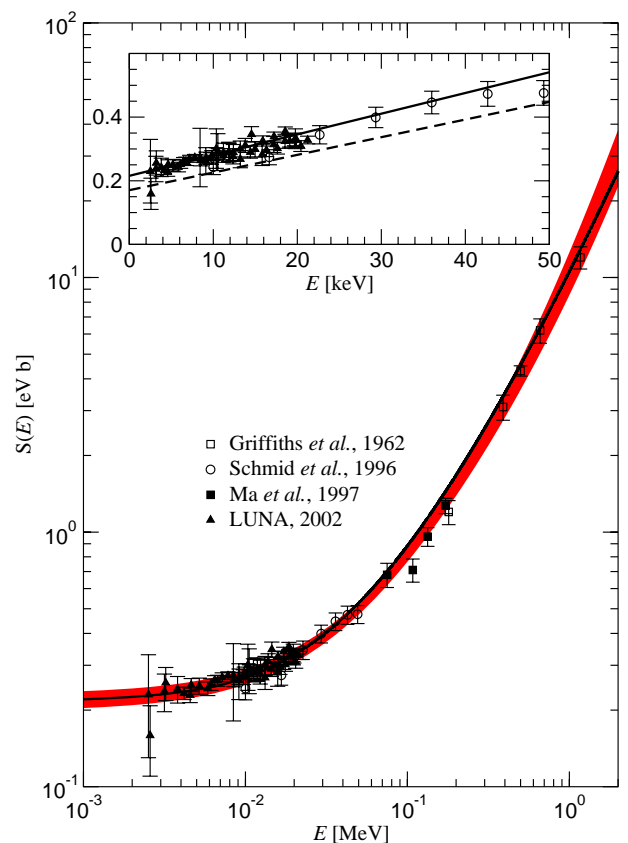


FIG. 3 (Color online) The astrophysical S_{12} -factor datasets (Casella *et al.*, 2002; Griffiths *et al.*, 1962; Ma *et al.*, 1997; Schmid *et al.*, 1996) are plotted together with theoretical predictions of Marcucci *et al.* (2005). The solid line represents the “full” theoretical calculation, while the red band represents the 68% lower and upper bounds of the adopted quadratic best fit to the four experimental datasets (see text and Eq. (29) for more explanation). In the insert, the S_{12} -factor of the $^2\text{H}(p,\gamma)^3\text{He}$ reaction in the energy range 0-50 keV, obtained with the Argonne v_{18} two-nucleon and Urbana IX three-nucleon Hamiltonian model in the impulse approximation (dashed line) and with inclusion of interaction currents (solid line), is compared with the experimental results.

(2002); Griffiths *et al.* (1963, 1962); Ma *et al.* (1997); Schmid *et al.* (1995, 1996). The Griffiths *et al.* (1963) and Bailey *et al.* (1970) low energy data may be $\sim 15\%$ too high because of the use of incorrect stopping powers (Ma *et al.*, 1997; Schmid *et al.*, 1995, 1996). Also, the Schmid *et al.* (1995, 1996) data sets may have not propagated their energy-dependent systematic uncertainties. In Fig. 3, the data for S_{12} used for the best fit in Sec. IV.C are plotted together with theoretical predictions of Marcucci *et al.* (2005). The observed linear dependence of S_{12} on E at low energies, as well as the angular distributions of the cross section and polarization observables, indicate that the $d(p,\gamma)^3\text{He}$ reaction proceeds predominantly through s- and p-wave capture, induced, respectively, by magnetic

($M1$) and electric ($E1$) dipole transitions. The $M1$ transitions (proceeding through ${}^2S_{1/2}$ and ${}^4S_{3/2}$ pd channels) are especially interesting, as the one-body $M1$ operator cannot connect the main s-state components of the pd and ${}^3\text{He}$ wave functions at low energies. Because of this “pseudo-orthogonality” only the small components of the wave functions contribute in the impulse approximation (IA). In contrast, as exchange-current operators are not similarly hindered, their matrix elements are exceptionally large relative to those obtained with the one-body $M1$ operator. The suppression of matrix elements calculated in the IA and their consequent enhancement by exchange-current contributions are a feature common to other $M1$ -induced processes in $A=3$ and 4 systems, such as the nd and $n^3\text{He}$ radiative captures at thermal neutron energies.

B. Theoretical studies

The most extensive and recent theoretical studies of the $d(p,\gamma){}^3\text{He}$ reaction at low energies have been carried out by Marcucci *et al.* (2005). The calculated S_{12} , shown in Fig. 3, is in excellent agreement with data. To describe the pd continuum and ${}^3\text{He}$ bound states, these authors used variational wave functions built in a correlated-hyperspherical-harmonics (CHH) basis for a Hamiltonian consisting of the Argonne v_{18} two-nucleon (Wiringa *et al.*, 1995) and the Urbana IX (Pudliner *et al.*, 1995) three-nucleon potentials. This Hamiltonian is known to reproduce a variety of three-nucleon bound- and scattering-state properties, including binding energies, charge radii, elastic and inelastic cross sections, and low-energy polarization observables, while the accuracy of the CHH variational method is comparable to that of other quasi-exact methods (Nogga *et al.*, 2003).

The nuclear electromagnetic current consists of one-body terms (the IA currents), originating from the convection and spin-magnetization currents of individual protons and neutrons, and two- and three-body exchange currents, constructed from the corresponding potentials by a procedure that preserves current conservation (CC). The method by which this is achieved has been improved over the years (Riska, 1984; Schiavilla *et al.*, 1998), and its latest implementation is discussed at length by Marcucci *et al.* (2005). The currents are still model dependent, of course, as CC places no constraints on their transverse components.

The calculated value for $S_{12}(0)$ including exchange-current contributions is 0.219 eV b, in excellent agreement with the value extrapolated from the LUNA measurements (0.216 ± 0.010 eV b), and evaluations by Cyburt (2004) (0.227 ± 0.014 eV b), Descouvemont *et al.* (2004) (0.223 ± 0.007 eV b) and Serpico *et al.* (2004) (0.214 ± 0.007 eV b). In Descouvemont *et al.* (2004) systematic and statistical errors are combined before following a standard fitting procedure. However, as this artificially reduces the impact of systematic errors, their cited

uncertainties have been underestimated. Serpico *et al.* (2004) properly separates systematic and statistical errors in their treatment, but do not cite 68% confidence limits, also yielding an error that is too small. The evaluation by Cyburt (2004) separates systematic and statistical uncertainties and cites errors consistent with 68% confidence limits, yielding realistic uncertainties.

C. Summary

In this report, we evaluate the Casella *et al.* (2002), Griffiths *et al.* (1962), Schmid *et al.* (1996) and Ma *et al.* (1997) data, determining $S_{12}(E)$ as a function of the center-of-mass energy by fitting the four data sets by a quadratic polynomial in E . We adopt this fitting procedure, despite our earlier arguments favoring fitting formulas that are motivated by theory, because the energy window of interest is fully covered by the experiments. This yields

$$S_{12}(0) = 0.214^{+0.017}_{-0.016} \text{ eV b}, \quad (28)$$

in agreement with previous evaluations. The error is larger here, because of the exclusion of the Bailey *et al.* (1970) data.

We also determined the 68% upper and lower bounds for the quadratic parameterizations, valid for $E \lesssim 1$ MeV, the range spanned by the data we considered. The results are (see also Fig. 3)

$$\begin{aligned} S_{12}^{\text{lower}}(E) &= 0.1983 + 5.3636 \left(\frac{E}{\text{MeV}} \right) \\ &\quad + 2.9647 \left(\frac{E}{\text{MeV}} \right)^2 \text{ eV b} \\ S_{12}^{\text{best}}(E) &= 0.2145 + 5.5612 \left(\frac{E}{\text{MeV}} \right) \\ &\quad + 4.6581 \left(\frac{E}{\text{MeV}} \right)^2 \text{ eV b} \\ S_{12}^{\text{upper}}(E) &= 0.2316 + 5.7381 \left(\frac{E}{\text{MeV}} \right) \\ &\quad + 6.5846 \left(\frac{E}{\text{MeV}} \right)^2 \text{ eV b}. \end{aligned} \quad (29)$$

The results determine the S-factor and its uncertainty in the vicinity of the solar Gamow peak. In particular, for a temperature characteristic of the Sun’s center, 1.55×10^7 K,

$$S_{12}(E_0 = 6.64 \text{ keV}) = 0.252 \pm 0.018 \text{ eV b}, \quad (30)$$

so that the estimate uncertainty is $\sim 7.1\%$.

V. THE ${}^3\text{He}({}^3\text{He},2p){}^4\text{He}$ REACTION

The ${}^3\text{He}({}^3\text{He},2p){}^4\text{He}$ reaction is the termination of the ppI cycle and thus, as Solar Fusion I describes in more

detail, uncertainties in this cross section played a prominent role in early speculations about a nuclear astrophysics solution to the solar neutrino problem. As an increase in $S_{33}(E)$ would reduce the branchings to the ppII and ppIII cycles – thus also reducing the neutrino fluxes measured by Davis – the possibility of an undiscovered narrow resonance at energies beyond the reach of early experiments was raised by Fetisov and Kopysov (1972) and Fowler (1972). This motivated efforts to measure $S_{33}(E)$ at lower energies, and particularly stimulated the efforts of the LUNA collaboration in the 1990s to map the cross section in the solar Gamow peak (Arpesella *et al.*, 1996; Bonetti *et al.*, 1999; Greife *et al.*, 1994; Junker *et al.*, 1998). The principal result since Solar Fusion I is the completion of this program by Bonetti *et al.* (1999), extending measurements to the lower edge of the Gamow peak at 16 keV, making $S_{33}(E)$ the most directly constrained S-factor within the pp chain.

$S_{33}(E)$ remains of significant importance, as it controls the ppI/ppII+ppIII branching ratio and thus the ratio of the pp/pep to ${}^7\text{Be}/{}^8\text{B}$ neutrino fluxes. This ratio is important to future strategies to better constrain neutrino oscillation parameters and matter effects, through comparison of high-energy (matter influenced) and low-energy (vacuum) fluxes. The ratio of S_{33} to S_{34} enters in computing the neutrino energy losses of the Sun, and thus influences the connection between the Sun’s photon luminosity and its total energy production.

A. Data sets and fitting

We consider data available at the time of Solar Fusion I (Arpesella *et al.*, 1996; Bacher and Tombrello, 1965; Dwarkanath and Winkler, 1971; Greife *et al.*, 1994; Junker *et al.*, 1998; Krauss *et al.*, 1987) as well two new data sets: the extreme low energy data of LUNA (Bonetti *et al.*, 1999) and results from the OCEAN experiment (Kudomi *et al.*, 2004) at energies slightly above the solar Gamow region. In order to follow the recommended fitting prescription discussed in the Appendix, one needs a detailed discussion of systematic uncertainties, particularly common mode systematics. This requirement reduces the datasets considered to just four experiments. The earliest of these originates from the Muenster group (Krauss *et al.*, 1987), followed by the two LUNA publications Junker *et al.* (1998) (which supersedes Arpesella *et al.* (1996)) and Bonetti *et al.* (1999); and the OCEAN effort Kudomi *et al.* (2004). Krauss *et al.* (1987) and Kudomi *et al.* (2004) identified a common systematic error for their respective data sets while the LUNA group provided statistical and systematic errors at each experimental energy measured. In order to use a uniform treatment we calculated an average systematic error for the latter data sets. Larger systematic errors were noted only at the lowest energies (due to uncertainties in stopping power) where the total error is dominated by statistics.

Past efforts have fit data to an S-factor including screening corrections, with the bare S-factor a polynomial up to quadratic order,

$$S_{33}(E) = S_{33}^{\text{bare}}(E) \exp\left(\frac{\pi\eta(E)U_e}{E}\right) \quad (31)$$

$$S_{33}^{\text{bare}}(E) = S_{33}(0) + S'_{33}(0)E + \frac{1}{2}S''_{33}(0)E^2.$$

Although model calculations of $S_{33}^{\text{bare}}(E)$ are available (see, e.g., Typel *et al.* (1991)), a phenomenological representation for the bare S-factor is appropriate because the data extend to the Gamow peak. There is no need for a theoretical model to guide an extrapolation, apart from the functional form of the screening potential.

The selected data for this review cover the range from the solar Gamow peak to 350 keV, providing a limited range with which to perform a four parameter fit to the S-factor including electron screening ($S_{33}(0)$, $S'_{33}(0)$, $S''_{33}(0)$, U_e). We test the robustness of the fit parameters, by varying the order of the polynomial for the bare S-factor. Our results are in Table II.

TABLE II Table of fit parameters and their total errors for constant, linear, and quadratic representations of the bare S-factor.

parameter	constant	linear	quadratic
$S_{33}(0)$ (MeV b)	4.84 ± 0.13	4.95 ± 0.15	5.32 ± 0.23
$S'_{33}(0)$ (b)	N.A.	-1.06 ± 0.51	-6.44 ± 1.29
$S''_{33}(0)$ (MeV^{-1} b)	N.A.	N.A.	30.7 ± 12.2
U_e (eV)	395 ± 50	360 ± 55	280 ± 70
χ^2_{tot}	35.4	34.1	31.8
$\chi^2_{\text{tot}}/\text{dof}$	0.40	0.39	0.37

Our quadratic fit agrees quite well with the fit derived by Krauss *et al.* (1987), adopted in the reaction rate compilation of Caughlan and Fowler (1988). However, there is a significant spread in fit parameter values for the different order polynomial fits, with slight decreases in the total χ^2 . One can also see this spread in fit results from other groups (Bonetti *et al.*, 1999; Junker *et al.*, 1998; Kudomi *et al.*, 2004). This suggests that the data do not have the resolving power to accurately determine all fit parameters: there are strong correlations for the choices of data and fitting functions made here. Adopting any *single* fit will underestimate the uncertainties due to the degeneracy between parameter values. From Bayes’s theorem, assuming that the S-factor in this region ($E < 350$ keV) can be described without cubic terms, we can derive constraints on the parameters by weighting each fit in Table II by its total χ^2 value. This method takes into account the spread from fit-to-fit. We find

$$S_{33}(0) = 5.21 \pm 0.27 \text{ MeV b} \quad (32)$$

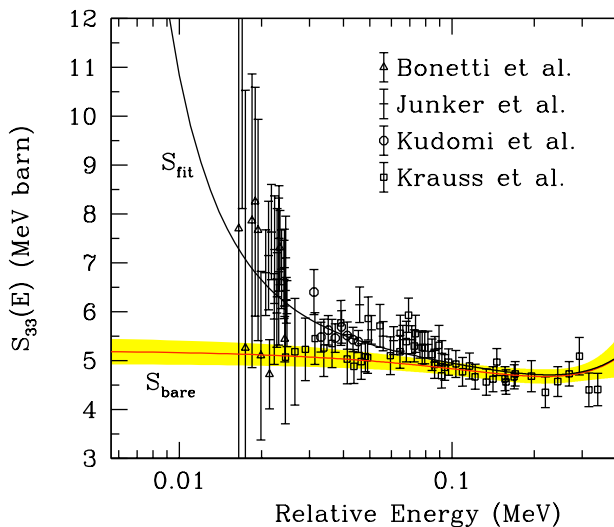


FIG. 4 (Color online) The data, the best quadratic+screening result for $S_{33}(E)$, and the deduced best quadratic fit (red line) and allowed range (yellow band) for S_{33}^{bare} . See text for references.

$$\begin{aligned} S'_{33}(0) &= -4.90 \pm 3.18 \text{ b} \\ S''_{33}(0) &= 22.4 \pm 17.1 \text{ MeV}^{-1} \text{ b} \\ U_e &= 305 \pm 90 \text{ eV}. \end{aligned}$$

The results reveal that existing data cannot strongly constrain all of the fitting parameters separately, and in particular do not sharply constrain U_e . To improve constraints on the screening potential one will need more precise data from near the Gamow peak, as well as new measurements up to the MeV range (with well documented systematics) to better determine the higher-order terms in the quadratic fit. New theory efforts in determining the shape of this S-factor would also be beneficial, as new low energy ${}^3\text{He}$ - ${}^3\text{He}$ elastic scattering data could be used as an additional constraint.

However, our principal concern is the precision with which $S_{33}^{\text{bare}}(E)$ can be determined in the vicinity of the Gamow peak, not the separate parameters. From the fit's correlation matrix we find

$$\begin{aligned} S_{33}^{\text{best}}(E) &= 5.21 - 4.90 \left(\frac{E}{\text{MeV}} \right) + 11.21 \left(\frac{E}{\text{MeV}} \right)^2 \text{ MeV b} \\ \delta S_{33}(E) &= \left[0.075 - 1.516 \left(\frac{E}{\text{MeV}} \right) + 14.037 \left(\frac{E}{\text{MeV}} \right)^2 \right. \\ &\quad \left. - 15.504 \left(\frac{E}{\text{MeV}} \right)^3 + 71.640 \left(\frac{E}{\text{MeV}} \right)^4 \right]^{1/2} \text{ MeV b} \end{aligned}$$

where

$$S_{33}^{\text{bare}}(E) \equiv S_{33}^{\text{best}}(E) \pm \delta S_{33}(E). \quad (33)$$

Because these results were obtained with a phenomenological fitting function, their reliability has been establish

only for the energy range covered by the data employed in the fit. Thus Eq. (33) should be used for energies $E \lesssim 350$ keV. For a temperature 1.55×10^7 K corresponding to the Sun's center, we find at the Gamow peak

$$S_{33}^{\text{bare}}(E_0 = 21.94 \text{ keV}) = 5.11 \pm 0.22 \text{ MeV b}, \quad (34)$$

so that the estimated uncertainty is 4.3%.

VI. THE ${}^3\text{He}(\alpha, \gamma){}^7\text{Be}$ REACTION

When Solar Fusion I appeared, the most recent ${}^3\text{He}({}^4\text{He}, \gamma){}^7\text{Be}$ measurement was 10 years old. The four new measurements that have been published since that time, in response to a challenge by John Bahcall, are the focus of this section.

For energies of interest, $E \lesssim 1$ MeV, ${}^3\text{He}({}^4\text{He}, \gamma){}^7\text{Be}$ is a nonresonant reaction, predominantly external direct capture (Christy and Duck, 1961) by electric dipole emission from s- and d-wave initial states to the two bound states of ${}^7\text{Be}$. Reaction measurements have been made by detecting the prompt γ -rays, the ${}^7\text{Be}$ activity, and the ${}^7\text{Be}$ recoils. Below we discuss the measurements, the theory needed to extrapolate the measurements to astrophysical energies, and our determination of $S_{34}(0)$.

A. Experimental measurements

Groups at the Weizmann Institute (Singh *et al.*, 2004) and at the University of Washington-Seattle (Brown *et al.*, 2007) carried out cross section measurements in the center-of-mass energy range $E = 0.42$ to 0.95 MeV and 0.33 to 1.23 MeV, respectively, using gas cells with Ni entrance windows. The LUNA collaboration (Bemmerer *et al.*, 2006a; Confortola *et al.*, 2007; Gyürky *et al.*, 2007) (see also Costantini *et al.* (2008)) carried out low-background measurements from $E = 0.093$ to 0.170 MeV at the LUNA facility in the Gran Sasso underground laboratory, and a European collaboration (Di Leva *et al.*, 2009) (here called ERNA) made measurements from $E = 0.65$ to 2.51 MeV, both with windowless gas cells.

An important concern in Solar Fusion I was whether ${}^3\text{He}({}^4\text{He}, \gamma){}^7\text{Be}$ measurements made by detecting the ${}^7\text{Be}$ activity might be affected by background ${}^7\text{Be}$ produced by contaminant reactions. Possibilities include ${}^6\text{Li}(d, n){}^7\text{Be}$ or ${}^{10}\text{B}(p, \alpha){}^7\text{Be}$, which could occur given proton or deuteron contamination in the ${}^4\text{He}$ beam in combination with ${}^6\text{Li}$ or ${}^{10}\text{B}$ contamination in the gas cell, for example, in the foil or beam stop. Only one of the older experiments - that of Osborne - involved measurements of both prompt γ s and ${}^7\text{Be}$ activity (see Solar Fusion I for older references). While the Osborne experiment found agreement between the ${}^3\text{He}({}^4\text{He}, \gamma){}^7\text{Be}$ cross sections determined by the two methods, in general the cross section determined from activity-based experiments was somewhat larger than that determined from prompt- γ experiments.

In the new experiments, all but the Weizmann group measured both prompt γ s and ${}^7\text{Be}$ activity, while ERNA also measured ${}^7\text{Be}$ recoils. In each of these experiments, the cross sections deduced by the different methods were consistent, leading to upper limits on nonradiative capture of 2-5% from $E = 0.09$ to 2.5 MeV. This is consistent with theoretical calculations that indicate much smaller rates expected for $E0$ capture and other electromagnetic processes that could produce ${}^7\text{Be}$ without accompanying energetic prompt γ s (Snover and Hurd, 2003). All new experiments except that of the Weizmann group employed ${}^4\text{He}$ beams and ${}^3\text{He}$ targets, thus minimizing potential problems with background ${}^7\text{Be}$ production. In the new experiments sensitive checks ruled out contaminant ${}^7\text{Be}$ production at lower levels. Thus we see no reason to doubt the new activity measurements.

${}^7\text{Be}$ activity measurements provide a direct determination of the total cross section. In contrast, as prompt γ -ray yields are anisotropic, one must take into account detector geometry and the anisotropy to determine a total cross section. [The $\sim 30\%$ capture branch to the 429-keV first excited state of ${}^7\text{Be}$ has usually been determined from the isotropic 429 keV \rightarrow ground state yield.] Unfortunately, no angular distribution measurements exist at the needed level of precision. The theoretical angular distributions of Tombrello and Parker (1963a) (see also Kim *et al.* (1981)) were used to correct the prompt LUNA data, while the UW-Seattle data agree better with an assumed isotropic γ_0 angular distribution than with theory. As the prompt anisotropy corrections can be comparable to the overall quoted cross section uncertainty, we decided to exclude the prompt data from our analysis. We do this in part because little additional precision would be gained by combining the highly correlated prompt and activation data. Hence we base our analysis on activation data, plus the ERNA recoil data.

The ERNA data and the older data of Parker and Kavanagh (1963) extend well above 1 MeV, where measurements may provide information useful for constraining theoretical models of $S_{34}(E)$. Of these two data sets, only ERNA shows evidence for a significant rise in $S_{34}(E)$ above 1.5 MeV (see Fig. 1 of Di Leva *et al.* (2009)).

B. Theory

Relative (but not absolute) S-factors at energies below 1 MeV vary by only a few percent among credible models, with small differences arising from non-external contributions and initial-state phase shifts. The two bound states of ${}^7\text{Be}$ populated by ${}^3\text{He}(\alpha, \gamma){}^7\text{Be}$ direct capture have large overlaps with ${}^3\text{He} + {}^4\text{He}$ cluster configurations. The Pauli principle requires radial nodes in these overlaps, guaranteeing a small (but nonzero) short-range contribution because of cancellation in the matrix-element integral.

Considerable accuracy below 1 MeV can be achieved by a pure external-capture model, with hard-sphere scat-

tering at a radius chosen to reproduce measured phase shifts. In such a model ${}^3\text{He}$ and ${}^4\text{He}$ are treated as point particles, and final states are modeled only by their long-range asymptotic parts. This is the approach of the Tombrello and Parker (1963a) model, used to fit S_{34} in Solar Fusion I. A more realistic treatment of contributions from 2.8 to 7.0 fm is provided by potential models (Buck *et al.*, 1985; Buck and Merchant, 1988; Dubovichenko and Dzhazairov-Kakhramanov, 1995; Kim *et al.*, 1981; Mohr, 2009; Mohr *et al.*, 1993), which generate wave functions from a Woods-Saxon or similar potential, constrained by measured phase shifts.

Microscopic models take explicit account of nucleon short-range correlations. In the resonating-group method (RGM) a simplified nucleon-nucleon interaction is tuned to observables in the system being investigated (e.g., energies of the ${}^7\text{Be}$ bound states), and the phase shifts are computed, not fitted. The RGM wave functions are sums of states consisting of simple cluster substructure; in most ${}^7\text{Be}$ calculations, they are antisymmetrized products of Gaussians for ${}^4\text{He}$ and ${}^3\text{He}$, multiplied by a function of the coordinate describing cluster separation.

The RGM calculations of Kajino (1986) and the potential-model of Langanke (1986) (which employed antisymmetrized many-body wave functions) predicted the energy dependence of the ${}^3\text{He}(\alpha, \gamma){}^7\text{Li}$ reaction quite accurately, prior to the precise measurement of Brune *et al.* (1994). On the other hand, there is some variation of the computed ${}^3\text{He}(\alpha, \gamma){}^7\text{Be}$ S-factors among RGM models using different interaction types and different Gaussian widths within the clusters. This variation has been shown to correlate with measures of the diffuseness of the ${}^7\text{Be}$ ground state (Csóto and Langanke, 2000; Kajino, 1986). Substantial changes in the S-factor and phase shifts also occur when ${}^6\text{Li} + p$ configurations are added to the RGM wave functions (Csóto and Langanke, 2000; Mertelmeier and Hofmann, 1986).

Calculations using highly accurate nucleon-nucleon potentials are now possible. In Nollett (2001), both bound states were computed using the variational Monte Carlo method, while the relative motion of the initial-state nuclei was modeled by one-body wave functions from the earlier potential-model studies. This approach should provide additional realism to the nuclear wave function at short range, and it features initial states that fit the measured phase shifts. It produced very nearly the same $S_{34}(E)$ energy dependence as Kajino (1986), and an absolute $S_{34}(0)$ that is lower by about 25%.

Through a numerical coincidence, the branching ratio for captures to the two final states is very nearly constant at low energy (Kajino, 1986). This circumstance and the external-capture nature of the reaction suggest that laboratory data can be extrapolated to low energy by fitting a single rescaling parameter that multiplies a model $S_{34}(E)$ to match the data. Such a rescaling does not have a strong physical justification for microscopic models, as they do not have undetermined spectroscopic factors. However, rescaled microscopic models should be

at least as accurate as potential models and more accurate than the hard-sphere model.

A different approach was followed in Cyburt and Davids (2008), where a parameterized function fit was made to three of the four modern data sets over a wider energy interval than we used to determine our recommended $S_{34}(0)$ (see below), with the result $S_{34}(0) = 0.580 \pm 0.043$ keV b. Their fitting function is motivated by recent work emphasizing external capture and subthreshold poles in low-energy S-factors (Jennings *et al.*, 1998a,b; Mukhamedzhanov and Nunes, 2002), and it matches expressions for zero phase shift derived in Mukhamedzhanov and Nunes (2002). For S_{34} , the d-waves have small phase shifts, and the function describes d-wave capture quite well. In the more-important s-wave capture, the function does not match detailed models of $S_{34}(E)$, irrespective of fitted parameters; its closeness to the expressions of Mukhamedzhanov and Nunes (2002) suggests that some other functional form is needed to account for nonzero phase shifts.

1. Model selection for $S_{34}(0)$ determination

To determine $S_{34}(0)$ from experimental capture data, we use the microscopic models of Kajino (1986) and Nollett (2001) (Kim A potential), rescaled to fit the data below $E = 1$ MeV (see below). We selected these two models based on several factors.

- i) They both accurately reproduce the s-wave phase shifts (as given by the phase-shift analysis of Tombrello and Parker (1963b)) and the long-range asymptotics of the ${}^7\text{Be}$ bound states. The Kajino model reproduces the phase shifts without having been fitted to them.
- ii) They contain more short-range physics than hard-sphere or potential models, which may extend the energy range over which they describe the reaction correctly.
- iii) They agree well with each other even though they were generated by very different computational approaches.
- iv) They reproduce the measured energy dependence of $S_{34}(E)$ well, up to at least $E = 1.5$ MeV (see Fig. 5, also Fig. 3 of Di Leva *et al.* (2009)).
- v) They calculate other electromagnetic observables in ${}^7\text{Li}$ and ${}^7\text{Be}$, that are in reasonable agreement with experiment.

2. Region of $S_{34}(E)$ fitting

We restricted the energy range for fitting to $E \leq 1$ MeV. The scatter among models (which differ mainly at short range) becomes much larger at energies above 1

MeV, suggesting that the calculations are most reliable at lower energies, where poorly-constrained short-range contributions to $S_{34}(E)$ are minimized. In Nollett (2001), the contribution of ${}^3\text{He}$ - ${}^4\text{He}$ separations less than 4 fm was about 4% of $S_{34}(0)$ and about 8% of $S_{34}(1 \text{ MeV})$. Since a uniform 4% at all energies could be absorbed into the rescaling, the difference between short-range contributions at 0 and 1 MeV suggests 4% as a conservative estimate of the rescaling error.

3. Theoretical uncertainty in the $S_{34}(0)$ determination

We estimate a theoretical uncertainty in the $S_{34}(0)$ determination by rescaling several models to the capture data in the same manner used to determine the recommended value of $S_{34}(0)$, and examining the resulting spread in $S_{34}(0)$ values. We restrict our consideration to microscopic models that reproduce the s-wave phase shifts, choosing those of Walliser *et al.* (1984), Csóto and Langanke (2000) (only those with ${}^3\text{He} + {}^4\text{He}$ clusterization), Nollett (2001), and new variants of the Nollett (2001) calculation possessing phase shifts perturbed from the empirical values.

The full spread among the chosen set of models is ± 0.030 keV b, relative to the Kajino (1986) and Nollett (2001) (Kim A potential) fits. We somewhat arbitrarily recommend two-thirds of this value; i.e., ± 0.02 keV b, as an approximate $1\text{-}\sigma$ theoretical error. The scatter among these models is not independent of the rescaling uncertainty estimated above; hence, we have not included an explicit rescaling contribution in this estimate.

4. S-factor derivatives

The data do not provide a useful constraint on low-energy derivatives of $S_{34}(E)$. Microscopic models that reproduce the phase shifts and simpler models that focus on wave-function asymptotics produce values of $S'_{34}(0)/S_{34}(0)$ in the range -0.55 to -0.79 MeV^{-1} . These values depend on both the model and the method of estimation. Only Williams and Koonin (1981), Walliser *et al.* (1983), and Walliser *et al.* (1984) published enough information to allow one to extract an estimate for S''_{34} , yielding $S''_{34}(0)/S_{34}(0) = 0.26$ to 0.43 MeV^{-2} . We base our recommendations on the Nollett (2001) (Kim A) model, which yields effectively $S'_{34}(0)/S_{34}(0) = -0.64 \text{ MeV}^{-1}$ and $S''_{34}(0)/S_{34}(0) = 0.27 \text{ MeV}^{-2}$ from a quadratic fit below 0.5 MeV.

5. Comment on phase shifts

As the bound-state ${}^7\text{Be}$ wave functions have known asymptotic forms, differences of the low-energy $S(E)$ among models arise from differing s-wave phase shifts and from short-range contributions. The short-range contributions, which are difficult to compute convincingly, are

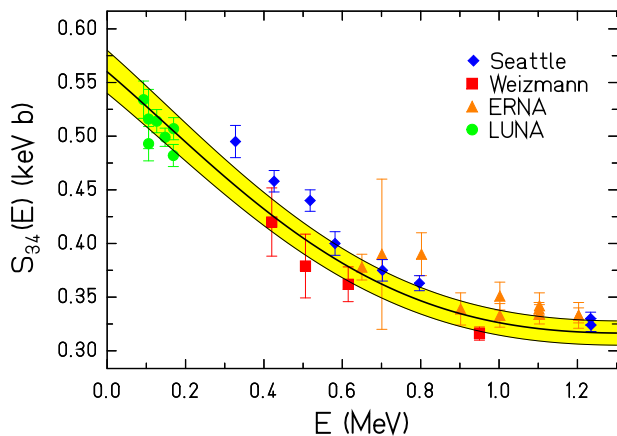


FIG. 5 (Color online) $S_{34}(E)$ vs. E . Data points: LUNA - green circles; Weizmann - red squares; UW-Seattle - blue diamonds; ERNA - brown triangles. Solid curve - best fit scaled Nollert theory to the data with $E \leq 1.002$ MeV. The yellow band indicates the $\pm 1\text{-}\sigma$ error band. Data are shown with statistical-plus-varying-systematic errors only; overall systematic errors are not included.

probed by capture experiments above 1 MeV. With the exception of Mohr *et al.* (1993) and Mohr (2009), phase-shift fitting for studies of the ${}^3\text{He}(\alpha, \gamma){}^7\text{Be}$ reaction has been based almost entirely on the phase-shift analysis of Tombrello and Parker (1963b). While this phase-shift analysis provides a useful constraint, it depends mainly on a single experiment from the early 1960s, and it does not include an error estimation. The modern Mohr *et al.* (1993) experiment extended to lower energies, but it has no published error estimate or phase-shift analysis.

C. $S_{34}(0)$ determination

Figure 5 shows the low energy data with $E \leq 1.23$ MeV, and the fit obtained by scaling the Nollert (Kim A potential) theory to best match the data with $E \leq 1.002$ MeV. We used the analytic function

$$S_{34}(E) = S_{34}(0) e^{-0.580E} \times (1 - 0.4054E^2 + 0.577E^3 - 0.1353E^4), \quad (35)$$

where E is in units of MeV. Below one MeV this expression is valid to better than 0.3%, on average.

The best-fit curve in Fig. 5 was obtained by fitting each data set separately with the scaled theory, and then fitting the set of four $S_{34}(0)$ values to determine the mean $S_{34}(0)$ value and its error.

As can be seen from Table III, the fits to the individual data sets are good, indicating consistency with the theoretical energy dependence, within the limited energy ranges of each set. The fit to the combined set of four $S(0)$ values is of marginal quality, indicating a lack of good agreement in the absolute normalizations of the different experiments. The combined fit has $\chi^2/dof = 2.3$

TABLE III Experimental $S_{34}(0)$ values and $1\text{-}\sigma$ uncertainties determined from fits of the scaled Nollert (Kim A potential) theory to published data with $E \leq 1.002$ MeV. Total errors are quoted, including inflation factors, and systematic errors of LUNA: $\pm 2.9\%$; Weizmann: $\pm 2.2\%$; UW-Seattle: $\pm 3.0\%$; ERNA: $\pm 5.0\%$.

Experiment	$S_{34}(0)$ (keV b)	Error (keV b)	Inflation Factor
LUNA	0.550	0.017	1.06
Weizmann	0.538	0.015	1.00
UW-Seattle	0.598	0.019	1.15
ERNA	0.582	0.029	1.03
Combined result	0.560	0.016	1.72

($dof = 3$), corresponding to $P(\chi^2, dof) = 0.07$. All of the errors given in Table III include the inflation factors determined from the goodness of fit (see the Appendix, Sec. XIII.B). Fits to these data using the scaled theory of Kajino yield slightly smaller χ^2 values, and reproduce the low-energy UW-Seattle data somewhat better; however, the mean $S_{34}(0)$, 0.561 keV b, is essentially identical to the result obtained with Nollert’s theory.

We have focused here on measurements published since Solar Fusion I. We do so because in general they are better documented than the older ones, and address issues such as contaminant ${}^7\text{Be}$ production in a quantitative manner that lends greater confidence to the results. One may judge from the Kajino-fit analysis presented in Brown *et al.* (2007), that including older measurements would lower the mean $S(0)$ by at most 0.01 keV b or so. Thus including the older measurements would not change our result significantly.

Given the marginal quality of the mean experimental $S_{34}(0)$ fit, we round off the values given above, and quote a “best” result,

$$S_{34}(0) = 0.56 \pm 0.02(\text{expt}) \pm 0.02(\text{theor}) \text{ keV b}, \quad (36)$$

based on activation data and the ERNA recoil data, and taking the theoretical error from Sec. VI.B.3.

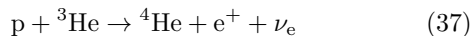
Our best $S_{34}(0)$ estimate may be compared to the value $S_{34}(0) = 0.53 \pm 0.05$ keV b given in Solar Fusion I.

New capture experiments below 1 MeV would be most valuable for reducing the experimental uncertainty in $S_{34}(E)$, particularly ones that maximize overlap with the existing modern data sets. New scattering and capture experiments above 1 MeV, as well as precise angular distribution measurements, could be useful for constraining future theoretical calculations.¹

¹ Note added in proof: Recent fermionic molecular dynamics (FDM) calculations (Neff *et al.*, 2010) of $S_{34}(E)$ are in excellent agreement, in both absolute magnitude and energy dependence, with the experimental data shown in Fig. 5 and with the high-

VII. THE ${}^3\text{He}(p, e^+ \nu_e){}^4\text{He}$ REACTION

The hep reaction



is the source of the pp chain's most energetic neutrinos, with an endpoint energy of 18.8 MeV. The Super-Kamiokande and SNO collaborations have placed interesting limits on the hep neutrino flux by searching for these neutrinos in the energy window above the ${}^8\text{B}$ neutrino endpoint, even though the expected flux is very low (see Fig. 7). The hep rate is beyond the reach of current experiments: this process is induced by the weak interaction and further suppressed by a Coulomb barrier and by other aspects of the nuclear physics, as explained below. Thus theory provides our only estimate of S_{hep} .

The calculation of S_{hep} is a difficult challenge. The leading one-body (1B) Gamow-Teller (GT) transition operator cannot connect the main s-state components of the $p+{}^3\text{He}$ and ${}^4\text{He}$ initial- and final-state wave functions.² Hence, at the 1B level the reaction proceeds through the small components of the ${}^3\text{He}$ and ${}^4\text{He}$ wave functions, such as d-state components. Consequently, the relative importance of other transition operators, such as axial meson-exchange currents (MEC), is enhanced, as is the contribution from p-wave $p+{}^3\text{He}$ capture, normally kinematically suppressed at solar temperatures. The situation is further complicated by the fact that the axial 1B and MEC “corrections” have opposite signs, making s-wave hep capture even more suppressed.

A. hep calculations

Some of the features mentioned above are shared by the hen process ($n+{}^3\text{He} \rightarrow {}^4\text{He}+\gamma$), in particular the strong suppression of 1B contributions. The possibility of deducing S_{hep} from the known hen cross section was explored in early studies: while these reactions are not isospin mirrors, there is a close relationship between the isovector spin contribution to hen and the GT contribution to hep. However the hep S-factors determined in these studies differed, in some cases, by orders of magnitude.

In an attempt to understand the origin of this large uncertainty, fully microscopic calculations of both the hep

and hen reactions were performed by Carlson *et al.* (1991) and Schiavilla *et al.* (1992), using a realistic Hamiltonian with two- and three-nucleon interactions. Among the approximations made in the Schiavilla *et al.* (1992) calculation were the description of the $p+{}^3\text{He}$ initial state as s-wave and the omission of the dependence of the weak operators on the lepton pair momentum. Corrections to the 1B GT operator were evaluated, with the largest two-body (2B) contributions coming from the excitation of intermediate Δ -isobars. The Δ -isobar degrees of freedom were explicitly included in the nuclear wave functions, using a scaled-down approach to the full $N + \Delta$ coupled-channel problem known as the transition-correlation operator method. Carlson *et al.* (1991) and Schiavilla *et al.* (1992) found that effects such as the different initial-state interactions for $n+{}^3\text{He}$ and $p+{}^3\text{He}$ were so substantial that the known hen cross section was not a useful constraint on hep. Two estimates were given for the hep S-factor at zero energy (Schiavilla *et al.*, 1992),

$$S_{\text{hep}}(0) = \left\{ \begin{array}{c} 1.4 \\ 3.1 \end{array} \right\} \times 10^{-20} \text{ keV b}, \quad (38)$$

depending on the method used to fix the weak $N - \Delta$ coupling constant, $g_{\beta N \Delta}$: the larger of the results corresponds to the naïve quark model prediction for $g_{\beta N \Delta}$, while in the smaller, $g_{\beta N \Delta}$ was determined empirically from tritium β decay. The Solar Fusion I best value for S_{hep} is the average of the values in Eq. (38).

This problem was revisited nearly a decade later, following improvements in the description of bound and continuum four-body wave functions. The wave functions of Marcucci *et al.* (2000) were obtained with the correlated-hyperspherical-harmonics (CHH) variational method (Viviani *et al.*, 1995, 1998), using the Argonne v_{18} (AV18) two-nucleon (Wiringa *et al.*, 1995) and Urbana IX (UIX) three-nucleon interactions (Pudliner *et al.*, 1995). The method produced binding energies of ${}^3\text{He}$ and ${}^4\text{He}$ and the singlet and triplet $p+{}^3\text{He}$ scattering lengths in excellent agreement with experiment.

The Marcucci *et al.* (2000) calculation included all s- and p-wave capture channels in the $p+{}^3\text{He}$ initial state and all multipole contributions in the expansion of the weak vector and axial-vector transition operators. The weak operators corresponding to the space component of the 1B weak vector current and the time component of the 1B axial current, both of order v/c , have significant exchange-current corrections of the same order from pion-exchange. These two-body operators were constructed to satisfy (approximately) the constraints of current conservation and PCAC (partial conservation of the axial-vector current). Corrections to the allowed GT operator include both $(v/c)^2$ 1B and exchange-current contributions. The treatment of the latter followed Carlson *et al.* (1991) and Schiavilla *et al.* (1992) in using the transition-correlation operator scheme and in fixing $g_{\beta N \Delta}$ to the experimental GT strength in tritium β decay.

energy ERNA data up to 2.5 MeV. The FDM is a nearly *ab initio* microscopic method employing realistic effective interactions.

² While the radial wave functions of the four nucleons in ${}^4\text{He}$ can all be 1s, with the various single-particle states distinguished by spin and isospin, this is not the case for the three protons in $p+{}^3\text{He}$: the Pauli principle requires that one must be radially excited. The GT transition operator does not alter radial quantum numbers, only spin and isospin. Thus the GT matrix element between $p+{}^3\text{He}$ and ${}^4\text{He}$ is suppressed due to the s-wave orthogonality.

TABLE IV S_{hep} in units of 10^{-20} keV b, calculated with CHH wave functions generated from the AV18/UIX Hamiltonian (Marcucci *et al.*, 2000) for three $p+{}^3\text{He}$ center-of-mass energies E . The “One-body” and “Full” labels denote calculations with the one-body and full (one- and two-body) nuclear weak transition operators. Contributions from the ${}^3\text{S}_1$ channel and from all s- and p-wave channels are listed separately.

	$E = 0$ keV		$E = 5$ keV		$E = 10$ keV	
	${}^3\text{S}_1$	s+p	${}^3\text{S}_1$	s+p	${}^3\text{S}_1$	s+p
One-body	26.4	29.0	25.9	28.7	26.2	29.2
Full	6.38	9.64	6.20	9.70	6.36	10.1

Table IV gives the resulting S_{hep} at three center-of-mass energies. The energy dependence is rather weak. The p waves have a significant effect, accounting for about one-third of the total cross section at $E=0$. Despite the delicacy of the calculation, Marcucci *et al.* (2000) concluded that the degree of model dependence was moderate: the calculations were repeated for the older Argonne v_{14} (Wiringa *et al.*, 1984) two-nucleon and Urbana VIII (Wiringa, 1991) three-nucleon interactions, but the predictions for S_{hep} differed only by 6%. The best estimate of Marcucci *et al.* (2000), $S_{\text{hep}} = (10.1 \pm 0.6) \times 10^{-20}$ keV b, is about four times the value given in Solar Fusion I.

A further development came with the use of heavy-baryon chiral perturbation theory (HBChPT) to derive the needed electroweak current operators systematically, with Park *et al.* (2003) carrying out the expansion to next-to-next-to-next-to leading order (N^3LO), thereby generating all possible operators to this order. These operators represent the short-range physics that resides above the scale of the EFT, which Park *et al.* (2003) defined via a Gaussian regulator with a cutoff Λ , a parameter that was varied in the calculations between 500 and 800 MeV (see Sec. III). S_{hep} was obtained by calculating the matrix elements of these EFT current operators with phenomenological wave functions, obtained using the AV18/UIX Hamiltonian and the CHH method. (See Sec. III for a more extended discussion of such hybrid EFT* approaches.)

To this order, the resulting currents are 1B and 2B: three-body operators arise at order N^4LO . The expansion reproduces the one-pion exchange-current corrections to the space component of the vector current and charge component of the axial current, as dictated by chiral symmetry, while the time component of the vector current has no MEC corrections. The MEC contributions to the axial GT operator include both a one-pion-exchange term and a (non-derivative) two-nucleon contact-term. The low-energy constant determining the strength of the contact term must be determined from an observable. Following the treatment of $g_{\beta N \Delta}$ by Marcucci *et al.* (2000), this was done by fitting the GT transition strength extracted from tritium β decay.

Table V gives the values determined by Park *et al.*

TABLE V The hep GT matrix element $\bar{L}_1(q; A)$ (in $\text{fm}^{3/2}$) for the transition from the initial ${}^3\text{S}_1$ $p+{}^3\text{He}$ state to the final ${}^4\text{He}$ state, as a function of the cutoff Λ (Park *et al.*, 2003), at $E=0$. $\bar{L}_1(q; A)$ is evaluated at $q = 19.2$ MeV, the momentum carried out by the lepton pair. S_{hep} (in 10^{-20} keV b) is also given.

Λ (MeV)	500	600	800
$\bar{L}_1(q; A)$: 1B	-0.081	-0.081	-0.081
$\bar{L}_1(q; A)$: 2B (no contact term)	0.093	0.122	0.166
$\bar{L}_1(q; A)$: 2B (with contact term)	-0.044	-0.070	-0.107
$\bar{L}_1(q; A)$: 2B-total	0.049	0.052	0.059
S_{hep}	9.95	9.37	7.32

(2003) for $S_{\text{hep}}(0)$ and for the GT matrix element between the ${}^3\text{S}_1$ $p+{}^3\text{He}$ initial and the ${}^4\text{He}$ final states, as a function of Λ . By fixing the strength of the contact term to an observable, one hopes in such hybrid EFT* approaches to remove most of the calculation’s cutoff dependence. Heuristically, the contact term compensates for high-momentum components in the phenomenological wave functions that would not be there had both operators and wave functions been derived rigorously from EFT, with a common cutoff. However, the table shows that significant cutoff-dependence remains in the total amplitude because of cancellation between the 1B and 2B contributions: the variation in S_{hep} is $\sim 15\%$. This is taken as the uncertainty in the Park *et al.* (2003) estimate for S_{hep} , $S_{\text{hep}}(0) = (8.6 \pm 1.3) \times 10^{-20}$ keV b. The result is consistent with that of Marcucci *et al.* (2000).

The prediction of Park *et al.* (2003) was used by Bahcall *et al.* (2006) and by Peña-Garay and Serenelli (2008) in their latest determinations of the hep neutrino flux, $\phi_\nu(\text{hep}) = (8.22 \pm 1.23) \times 10^3 \text{ cm}^{-2} \text{ s}^{-1}$, where the error reflects again the 15% uncertainty quoted above. The value for $\phi_\nu(\text{hep})$ is in agreement with the Super-Kamiokande (Fukuda *et al.*, 2001) and SNO (Aharmin *et al.*, 2006) upper limits at 90% confidence level, 40×10^3 and $23 \times 10^3 \text{ cm}^{-2} \text{ s}^{-1}$, respectively.

B. Summary

Given the two consistent calculations presented above, with the internal checks on the sensitivities to input wave functions and to cutoffs, and given the compatibility with the limits established by Super-Kamiokande and SNO, we recommend

$$S_{\text{hep}}(0) = (8.6 \pm 2.6) \times 10^{-20} \text{ keV b}, \quad (39)$$

where the uncertainty is obtained by doubling the cutoff-dependence found in the Park *et al.* (2003) calculation. One anticipates that the cutoff dependence would be reduced if the operator expansion were carried out beyond N^3LO . Thus such a program could increase confidence in Eq. (39) and narrow the uncertainty, even without a

fully consistent treatment of both operators and wave functions.

Other ancillary calculations that could strengthen confidence in this S-factor estimate include

- new studies of the hep reaction in which a broad spectrum of Hamiltonian models are explored, as was done by Schiavilla *et al.* (1998) for the pp reaction;
- study of related electroweak reactions where rates are known, such as muon capture, as was done by Marcucci *et al.* (2002) and Gazit (2008) for $\mu^- + {}^3\text{He} \rightarrow {}^3\text{H} + \nu_\mu$; and
- further work to understand the relationship between the suppressed processes hep and hen.

VIII. ELECTRON CAPTURE BY ${}^7\text{Be}$, pp, AND CNO NUCLEI

Electron capture is the source of line features in the solar neutrino spectrum, and represents an important pathway for energy production in the pp chain. Solar electron-capture lifetimes differ substantially from laboratory values because light nuclei are highly ionized and because the continuum electron density is large.

The relative rates of ${}^7\text{Be}$ electron capture and ${}^7\text{Be}(p,\gamma){}^8\text{B}$ determine the ppII/ppIII branching ratio and thus the ratio of the ${}^7\text{Be}$ and ${}^8\text{B}$ neutrino fluxes. The electron capture proceeds by the mirror transition to the ground state of ${}^7\text{Li}$ ($3/2^-$) and by an allowed transition to the first excited state ($1/2^-$, 478 keV). By normalizing the solar rate to the known terrestrial decay rate, the nuclear physics dependence of the solar rate can be eliminated. The ratio of rates depends on the relative electron probability densities averaged over the nucleus. This requires a calculation of the atomic probability densities governing the K and L terrestrial electron capture rates, the continuum electron probability densities at the nucleus for the solar rate, and corrections to the solar rate resulting from incomplete ionization. The solar continuum calculation was done by Bahcall (1962), and estimates of the bound-electron contributions have been made by Iben, Jr. *et al.* (1967), Bahcall and Moeller (1969), and Bahcall (1994). The solar continuum calculations have typically been done by employing the Debye-Hückel approximation for plasma screening. Electrons within the local Debye sphere screen the nuclear potential, thus lowering the electron density at the nucleus and the electron capture rate, while protons penetrating that radius would enhance the rate.

Our recommended rate is based on the calculation of Bahcall and Moeller (1969), with updates including the currently adopted ${}^7\text{Be}$ half-life of 53.22 ± 0.06 days, a total-to-continuum capture ratio of 1.217 ± 0.002 (Bahcall, 1994), and a terrestrial L/K capture ratio of 0.040 ± 0.006 (Voytas *et al.*, 2001). We use the original estimate

of Bahcall (1962) for the terrestrial K-electron probability at the nucleus. The result,

$$R({}^7\text{Be} + e^-) = 5.60(1 \pm 0.02) \times 10^{-9}(\rho/\mu_e) \times T_6^{-1/2}[1 + 0.004(T_6 - 16)] \text{ s}^{-1}, \quad (40)$$

valid for $10 < T_6 < 16$, is identical to Eq. (26) of Solar Fusion I. Here ρ is the density in units of g/cm^3 , T_6 is the temperature in units of 10^6K , and μ_e is the mean molecular weight per electron. The assigned uncertainty of 2% is dominated by possible corrections to the Debye-Hückel approximation for charge fluctuations (reflecting the small number of electrons within the Debye sphere), and by breakdowns in the adiabatic approximation, as evaluated by Johnson *et al.* (1992) in self-consistent thermal Hartree calculations. The small rate enhancement they found, 1.3%, is incorporated into and dominates the error in Eq. (40).

Despite the lack of changes since Solar Fusion I, there have been developments in two areas, each concerned with screening corrections. First, a series of precise measurements of the terrestrial electron capture rate have been carried out to assess the dependence of screening on target chemistry, which could alter the L/K ratio (because of L-capture sensitivity to changes in the valence electrons). Over the past decade such changes, first suggested by Segrè (1947), have been explored in a series of half-life measurements in which ${}^7\text{Be}$ was implanted in metals and insulators, or encapsulated in fullerene (Das and Ray, 2005; Limata *et al.*, 2006; Nir-El *et al.*, 2007; Norman *et al.*, 2001; Ohtsuki *et al.*, 2004; Ray *et al.*, 1999, 2002, 2006; Wang *et al.*, 2006). The pattern of results is somewhat confused, with claims of variations up to 1.1%, but with other studies limiting effects to levels $\lesssim (0.2\text{-}0.4)\%$ (Limata *et al.*, 2006; Nir-El *et al.*, 2007), despite use of host materials with substantially different electron affinities. Our tentative conclusion is that the uncertainty assigned in Eq. (40) is sufficient to allow for likely variations in terrestrial screening corrections.

Second, questions about the adequacy of solar plasma screening corrections, detailed in Solar Fusion I, have not died out. Quarati and Scarfone (2007, 2009) reconsidered the plasma fluctuation contributions to the electron-capture rate of ${}^7\text{Be}$, concluding that corrections of 7 - 10% are required. The *ansatz* of Quarati and Scarfone (2007) was previously considered and rejected by Bahcall *et al.* (2002), however. The influence of protons on the rate of ${}^7\text{Be}$ electron capture in the Sun was claimed to be more significant by Belyaev *et al.* (2007) than was previously thought. Davids *et al.* (2008), however, reject their argument, pointing out that only the previously investigated electromagnetic contributions of protons play a role, and that the approximations under which a putative three-body electromagnetic contribution was calculated are invalid.

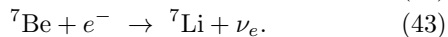
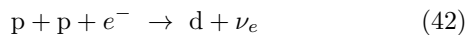
The electron captures on p+p and on CNO nuclei compete with the corresponding β decays, and thus these rates have been conventionally normalized to solar β decay rates. As electron capture and β decay depend on

the same allowed nuclear matrix element, the ratio is independent of the nuclear physics. The result from Solar Fusion I, from Bahcall and May (1969), is

$$R^{\text{Tree}}(\text{pep}) = 1.102(1 \pm 0.01) \times 10^{-4}(\rho/\mu_e) \\ \times T_6^{-1/2}[1 + 0.02(T_6 - 16)]R^{\text{Tree}}(\text{pp}), \quad (41)$$

where the superscript ‘‘Tree’’ indicates that the relationship omits radiative corrections, which are discussed below. The range of validity is $10 < T_6 < 16$.

Radiative corrections were evaluated by Kurylov *et al.* (2003) for the two pp-chain reactions under discussion,



The radiative corrections were given as

$$\frac{\Gamma_{\text{Capt}}}{\Gamma_{\text{Tree}}^{\text{Capt}}} = \left[1 + \frac{\alpha}{\pi} g_{\text{Capt}}(E_e, Q) \right] \equiv C^{\text{rad}}(E_e, Q), \quad (44)$$

where Γ_{Capt} is the total decay width, $\Gamma_{\text{Capt}}^{\text{Tree}}$ is the tree-level width without radiative corrections, and $g_{\text{Capt}}(E_e, Q)$ is a calculated factor that depends on both the total energy E_e of the captured electron and the Q -value of the transition. Figure 6 shows the resulting correction factors.

Because Eq. (40) corresponds to a ratio of stellar and terrestrial electron capture rates, the radiative corrections should almost exactly cancel: although the initial atomic state in the solar plasma differs somewhat from that in a terrestrial experiment, the short-range effects that dominate the radiative corrections should be similar for the two cases. [Indeed, this is the reason the pp and ${}^7\text{Be}$ electron corrections shown in Fig. 6 are nearly identical.] However the same argument cannot be made for the ratio of pep electron capture to pp β decay, as the electron kinematics for these processes differ. With corrections Eq. (41) becomes

$$R(\text{pep}) = \frac{\langle C^{\text{rad}}(\text{pep}) \rangle}{\langle C^{\text{rad}}(\text{pp}) \rangle} 1.102(1 \pm 0.01) \times 10^{-4}(\rho/\mu_e) \\ \times T_6^{-1/2}[1 + 0.02(T_6 - 16)]R(\text{pp}), \quad (45)$$

where the radiative corrections have been averaged over reaction kinematics. Kurylov *et al.* (2003) found a 1.62% radiative correction for the β decay rate, $\langle C^{\text{rad}}(\text{pp}) \rangle \sim 1.016$ (see discussion in Sec. III), while $\langle C^{\text{rad}}(\text{pep}) \rangle \sim 1.042$. Thus $\langle C^{\text{rad}}(\text{pep}) \rangle / \langle C^{\text{rad}}(\text{pp}) \rangle \sim 1.026$, so that our final result becomes

$$R(\text{pep}) = 1.130(1 \pm 0.01) \times 10^{-4}(\rho/\mu_e) \\ \times T_6^{-1/2}[1 + 0.02(T_6 - 16)]R(\text{pp}). \quad (46)$$

While certain improvements could be envisioned in the Kurylov *et al.* (2003) calculation – for example, in the matching onto nuclear degrees of freedom at some characteristic scale $\sim \text{GeV}$ – rather large changes would be

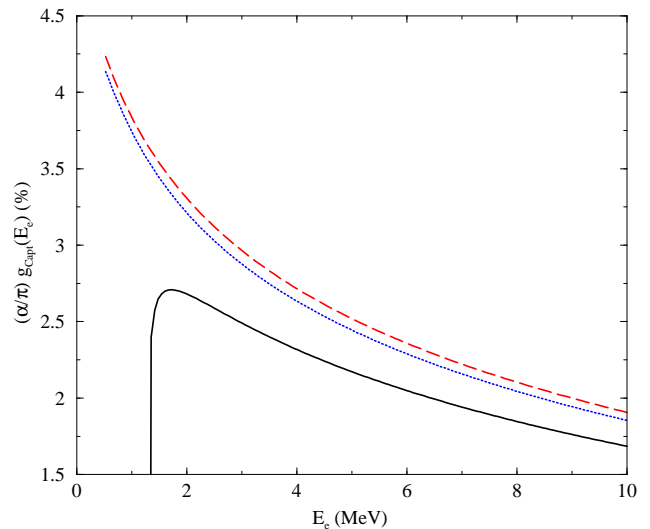


FIG. 6 (Color online) Calculated radiative corrections for $p+p+e^- \rightarrow d+\nu_e$ (dashed line) and ${}^7\text{Be}+e^- \rightarrow {}^7\text{Li}+\nu_e$ (dotted line). The solid line is for $p+e^- \rightarrow n+\nu_e$. Figure from Kurylov *et al.* (2003).

needed to impact the overall rate at the relevant 1% level. For this reason, and because we have no obvious basis for estimating the theory uncertainty, we have not included an additional theory uncertainty in Eq. (46). However, scrutiny of the presently unknown hadronic and nuclear effects in $g_{\text{Capt}}(E_e, Q)$ would be worthwhile. As one of the possible strategies for more tightly constraining the neutrino mixing angle θ_{12} is a measurement of the pep flux, one would like to reduce theory uncertainties as much as possible.

The electron capture decay branches for the CNO isotopes ${}^{13}\text{N}$, ${}^{15}\text{O}$, and ${}^{17}\text{F}$ were first estimated by Bahcall (1990). In his calculation, only capture from the continuum was considered. More recently, Stonehill *et al.* (2004) have re-evaluated these line spectra by including capture from bound states. Between 66% and 82% of the electron density at the nucleus is from bound states. Nevertheless, the electron-capture component is more than three orders of magnitude smaller than the β^+ component for these CNO isotopes, and it has no effect on energy production. However, the capture lines are in a region of the neutrino spectrum otherwise unoccupied except for ${}^8\text{B}$ neutrinos, and they have an intensity that is comparable to the ${}^8\text{B}$ neutrino intensity per MeV (Fig. 7), which may provide a spectroscopically cleaner approach to measuring the CNO fluxes than the continuum neutrinos do.

The recommended values for the ratio of line neutrino flux to total neutrino flux are listed in Table VI.

The ratio depends weakly on temperature and density, and thus on radius in the Sun. The values given are for the SSM and do not depend significantly on the details of the model. The branching ratio for ${}^7\text{Be}$ decay to the

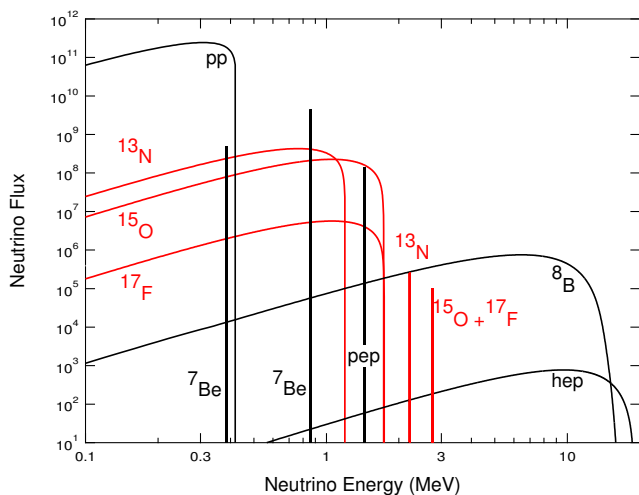


FIG. 7 (Color online) Solar neutrino fluxes based on the “OP” calculations of Bahcall *et al.* (2005), with the addition of the new line features from CNO reactions. Line fluxes are in $\text{cm}^{-2} \text{s}^{-1}$ and spectral fluxes are in $\text{cm}^{-2} \text{s}^{-1} \text{MeV}^{-1}$. Figure adapted from Stonehill *et al.* (2004).

TABLE VI The ratios of neutrino line intensity to the total intensity, after integration over the solar model.

Source	$R_{\text{line}}/R_{\text{total}}$	Ref.
p+p	2.35×10^{-3} ^a	Bahcall (1990)
$^3\text{He}+\text{p}$	4×10^{-8} ^b	Bahcall (1990)
	$\leq 7 \times 10^{-7}$ ^c	Bahcall (1990)
^7Be	0.8951 ^d	see text
	0.1049 ^e	
^8B	2×10^{-7}	Bahcall (1990)
^{13}N	7.9×10^{-4}	Stonehill <i>et al.</i> (2004)
^{15}O	4.0×10^{-4}	Stonehill <i>et al.</i> (2004)
^{17}F	5.9×10^{-4}	Stonehill <i>et al.</i> (2004)

^aincludes a 2.6% radiative correction from Kurylov *et al.* (2003)

^bto ^4He ground state

^cto ^4He excited state

^dto ^7Li ground state

^eto ^7Li excited state

first excited state in the laboratory is a weighted average of the results from Balamuth *et al.* (1983), Donoghue *et al.* (1983), Mathews *et al.* (1983), Davids *et al.* (1983), Norman *et al.* (1983a,b), and an average of earlier results, $10.37 \pm 0.12\%$ (see Balamuth *et al.* (1983)). The adopted average, $10.45 \pm 0.09\%$ decay to the first excited state, is corrected by a factor 1.003 for the average electron energy in the solar plasma, 1.2 keV (Bahcall, 1994), to yield a recommended branching ratio of $10.49 \pm 0.09\%$.

IX. THE $^7\text{Be}(p,\gamma)^8\text{B}$ REACTION

The $^7\text{Be}(p,\gamma)^8\text{B}$ reaction at low energies is predominantly nonresonant $E1$, s - and d -wave capture into the weakly-bound ground state of ^8B (Robertson, 1973). At solar energies the reaction proceeds by external direct capture, with matrix-element contributions dominated by ^7Be - p separations on the order of tens of fermis. The energy dependence near the Gamow peak cannot be determined from simple extrapolations of higher energy data, but must be taken from models. The narrow 1^+ resonance at $E_p = 720$ keV as well as resonances at higher energies are usually treated separately, and have little influence on solar rates.

In Solar Fusion I only one direct $^7\text{Be}(p,\gamma)^8\text{B}$ measurement was found to be sufficiently well documented to allow an independent assessment of the systematic errors. Consequently the recommended $S_{17}(0)$ was based on a single experiment, that of Filippone *et al.* (1983). Since Solar Fusion I new direct $^7\text{Be}(p,\gamma)^8\text{B}$ measurements have been carried out at Bordeaux/Orsay (Hamache *et al.*, 1998, 2001), the Weizmann Institute (Baby *et al.*, 2003a,b) (see also Hass *et al.* (1999)), Bochum (Strieder *et al.*, 2001) and the University of Washington-Seattle/TRIUMF (Junghans *et al.*, 2010, 2002, 2003). These modern measurements form the basis for our Solar Fusion II $S_{17}(0)$ recommendation.

Other new measurements include two performed with ^7Be beams (Bardayan *et al.*, 2009; Gialanella *et al.*, 2000). Although inverse measurements of this sort are much more difficult, they offer the attraction of different systematic errors. However, these experiments did not reach a precision useful for our purposes and thus play no role in our current assessment.

In addition to direct measurements, $S_{17}(0)$ has been determined indirectly from Coulomb dissociation, as summarized below in Sec. IX.C, and from peripheral heavy-ion transfer and breakup reactions. General aspects of such techniques are discussed in Sec. XII.

A. The direct $^7\text{Be}(p,\gamma)^8\text{B}$ reaction

All modern $^7\text{Be}(p,\gamma)^8\text{B}$ experiments have employed the same basic method of counting β -delayed α s from the decay of ^8B to determine the reaction yield. However, different experimental techniques were used, and different levels of precision were achieved in the procedures for converting measured yields into cross sections and S -factors. Below we discuss the most important issues.

1. Beam-target overlap

In a conventional experiment with a beam area smaller than the target area, it can be difficult to determine accurately the overlap of the beam with the target, due to non-uniformities in the areal density of typical tar-

gets. This is frequently the case for radioactive target experiments, as target designs are often quite compact, with cross sections comparable to the beam area, in order to minimize unused target material. This potential problem has been avoided in the most recent ${}^7\text{Be}(p,\gamma){}^8\text{B}$ experiments by using small-area targets irradiated by uniform beam fluxes. The reaction yield is then proportional to the product of the beam flux and the total number of ${}^7\text{Be}$ atoms. The latter quantity can be determined accurately from the ${}^7\text{Be}$ decay radioactivity. As the target density may have tails extending to large radii, and as the beam density may not be perfectly uniform, it is necessary to carry out ancillary measurements to demonstrate the accuracy of this technique. Measurements can include separate determinations of the radial dependence of the beam density and the target density, and/or the radial dependence of the product of the beam and target densities. While the Bochum, Weizmann, and UW-Seattle/TRIUMF experiments all used the small-area target/uniform-beam-flux method, only the latter two experiments provided sufficient information to permit an independent assessment of procedures.

2. ${}^8\text{B}$ backscattering

A systematic error in ${}^7\text{Be}(p,\gamma){}^8\text{B}$ measurements that was identified after Solar Fusion I is the loss of ${}^8\text{B}$ reaction products due to backscattering out of the target (Strieder *et al.*, 1998; Weissman *et al.*, 1998). This loss is particularly significant for high-Z target backings and low proton energy. The Filippone *et al.* (1983) and Bordeaux/Orsay experiments used Pt backings, for which the backscattering corrections are significant. In the Bordeaux/Orsay experiment, calculated backscattering corrections were applied to the data, while the Filippone *et al.* (1983) experiment was performed prior to the identification of ${}^8\text{B}$ backscattering as a serious concern. Junghans *et al.* (2003) estimated that the backscattering correction for the Filippone *et al.* (1983) data would be between -2% and -4% (a factor of two smaller than the estimate given in Weissman *et al.* (1998)). Here we ignore this correction because it is well within the overall precision claimed in the Filippone *et al.* (1983) experiment and because it is incomplete, as effects due to target thickness nonuniformity (unknown) and surface composition have not been included.

For the other modern experiments, ${}^8\text{B}$ backscattering losses are not an issue: the Bochum experiment used a low-Z backing, while the UW-Seattle/TRIUMF experiments used an intermediate-Z backing and demonstrated by direct measurement that backscattering losses were very small. The Weizmann experiment used implanted targets with an intermediate-Z substrate.

3. Proton energy loss corrections

Low-energy data must be corrected by energy-averaging to account for proton energy loss in the target. This requires knowledge of the energy loss profile of the target and the target composition, as well as the monitoring of possible carbon buildup during bombardment. The most detailed determination of these quantities was made in the UW-Seattle/TRIUMF experiments, where the target profile was determined from the narrow ($\Gamma \ll 1$ keV) ${}^7\text{Be}(\alpha,\gamma){}^{11}\text{C}$ resonance at $E_\alpha = 1377$ keV. In Junghans *et al.* (2010) a more detailed resonance profile analysis of the previously published data was presented, allowing for possible depth-dependent target composition. The varying systematic errors on the low energy “BE3” thick-target data were increased over the original results in Junghans *et al.* (2003) due primarily to larger assumed dE/dx uncertainties.

In the Filippone *et al.* (1983) experiment, the energy loss profile of the target was deduced from the measured shape of the 12-keV wide ${}^7\text{Li}(p,\gamma)$ resonance at $E_p = 441$ keV, assuming the ${}^7\text{Li}$ and ${}^7\text{Be}$ distributions in the target were the same. In the Bordeaux/Orsay experiment, Rutherford backscattering and (d,p) measurements were used to determine the target composition and proton energy loss. In the Bochum and Weizmann experiments, the $\Gamma = 36$ keV ${}^7\text{Be}(p,\gamma)$ resonance at $E_p = 720$ keV was used to determine the proton energy loss. The Weizmann experiment used implanted targets with known composition, verified by direct secondary ion mass spectrometry measurements. In the Filippone *et al.* (1983) and Bochum measurements, limits on the composition were inferred from the fabrication process.

Other important factors include determination and monitoring of the ${}^7\text{Be}$ target activity, corrections for sputtering losses, and determination of the efficiency for α detection. For the implanted target of the Weizmann experiment, target sputtering losses were shown to be negligible. The UW-Seattle/TRIUMF experiments have the most extensive error analysis of the modern experiments. Measurements were made with two targets of different thicknesses (labeled BE1 and BE3) and with two different methods for determining the detection efficiency for α s. The resulting statistical and systematic errors are the smallest yet achieved.

B. Theory

Among the many theoretical models that have been published, the simplest are those in which the interaction between the ${}^7\text{Be}$ nucleus and proton are described by a Woods-Saxon or similar potential (Aurdal, 1970; Barker, 1980; Bertulani, 1996; Davids and Typel, 2003; Esbensen, 2004; Kim *et al.*, 1987; Krauss *et al.*, 1993; Nunes *et al.*, 1997a,b, 1998; Riisager and Jensen, 1993; Robertson, 1973; Tombrello, 1965; Typel *et al.*, 1997). The main constraints on such models are the ground-

state energy, the energies of low-lying resonances, and s-wave scattering lengths (Angulo *et al.*, 2003). Charge symmetry has been used to obtain potentials from ${}^7\text{Li}+n$ scattering lengths and the ${}^7\text{Li}(n, \gamma){}^8\text{Li}$ cross section, but persistent difficulties in simultaneously reproducing the absolute cross sections for ${}^7\text{Be}(p, \gamma){}^8\text{B}$ and ${}^7\text{Li}(n, \gamma){}^8\text{Li}$ may reflect the greater sensitivity of neutron capture to the inner part of the wave function (Barker, 1980; Esbensen, 2004). Among potential models, only those of Nunes *et al.* (1997a,b, 1998) include coupling to inelastic channels, open above the 430 keV threshold for excitation of ${}^7\text{Be}$. No significant effect was found, consistent with results of microscopic models.

Potential models yield a reasonably accurate description of the external part of the direct capture. The wave function at $r < 5$ fm is not tightly constrained in potential models but contributes to the capture at all energies, particularly above 500 keV (Csoto, 1997; Jennings *et al.*, 1998b). However, one requirement is the existence of a node in s-wave scattering states, as the scattered wave function must be orthogonal to those of the closed He core assumed in the description of ${}^7\text{Be}$ (Aurdal, 1970). Model spectroscopic factors have been taken from shell-model studies, fixed to match transfer-reaction results (including the asymptotic normalization coefficients discussed in Sec. XII), or determined by rescaling computed S-factors to match capture data.

R-matrix models of direct capture (Barker, 1995; Barker and Mukhamedzhanov, 2000) resemble potential models in their lack of explicit ${}^7\text{Be}$ substructure, their need for fitting constraints, their apparent fidelity at large ${}^7\text{Be}$ -p separation, and their relative lack of short-range details. Similar data are fitted and similar results produced. The R-matrix as applied to direct capture differs from the discussion in Sec. II only in its need for radiative widths and attention to the long-range tails of bound states (Barker, 1995).

“Microscopic” models explicitly containing eight nucleons can include substructure within ${}^7\text{Be}$ and configurations not reducible to ${}^7\text{Be}+p$, calculated from the (effective) nucleon-nucleon interaction. The antisymmetry between the last or scattering proton and those within ${}^7\text{Be}$ is maintained. Fully microscopic calculations to date generally apply versions of the resonating group method (RGM) to significantly simplify the many-body problem (Csoto, 1997; Csoto *et al.*, 1995; Descouvemont, 2004; Descouvemont and Baye, 1988, 1994; Johnson *et al.*, 1992). For S_{17} the interaction is usually tuned to reproduce the proton separation energy of ${}^8\text{B}$, but may also be adjusted to reproduce the scattering length of ${}^7\text{Be}+p$ in the $S = 2$, $L = 0$ channel that dominates capture at zero energy (Descouvemont, 2004). RGM models do roughly as well as potential models in the external (> 5 fm) region while providing a more realistic description of structure in the internal region. Nonetheless, RGM results depend on the choice of nucleon-nucleon interaction and on the data used to fix parameters. RGM predictions of absolute cross sections tend to be high relative to measured val-

ues. Thus RGM results are frequently rescaled, so that theory is used only to predict the energy dependence of S-factors, in extrapolating higher energy data to the region of the Gamow peak.

Other microscopic approaches have used effective interactions in combination with the shell model, adapted to treat weakly-bound and unbound states of p -shell nuclei (Bennaceur *et al.*, 1999; Halderson, 2006). These studies focused on spectroscopic properties of $A = 8$ nuclei rather than the radiative capture. While this approach is not as well developed as the RGM method, it has produced low-energy S-factors similar to those of the RGM and other models. The absolute S-factor of Bennaceur *et al.* (1999) is in good agreement with the data, while that of Halderson (2006) is $\sim 40\%$ larger than experiment.

Ideally microscopic calculations would be carried out with realistic nucleon-nucleon interactions, but this is challenging due to the complexity of the interaction and the need for very large spaces. The only published example is that of Navratil *et al.* (2006a,b), in which the overlap integrals between ${}^8\text{B}$ and ${}^7\text{Be}+p$ were computed from seven- and eight-body wave functions obtained with the *ab initio* no-core shell model (NCSM). Due to the finite range of the harmonic oscillator basis, the long tails of the ${}^7\text{Be}+p$ overlaps were corrected by matching their logarithmic derivatives to Whittaker functions at intermediate distances. These overlaps were then used as final states, with initial scattering states drawn from previous potential-model studies. The resulting $S_{17}(0)$, 22.1 eV b, is close to the experimental value. The calculated $S_{17}(E)$ is relatively insensitive to the choice of initial state for $E < 100$ keV, but more so at higher energies (e.g., with variations of 20% at 1.6 MeV).

The envelope of predicted energy dependences of theoretical models has about a 30% spread over the energy range fitted below. While efforts have been made to fit $S_{17}(E)$ with as little theoretical input as possible, some degree of model input appears necessary (Cyburt *et al.*, 2004).

We adopt the RGM calculation of Descouvemont (2004) as the standard to extrapolate the experimental data to energies of astrophysical interest. Among available RGM calculations, this one is the most complete numerically. Of the two NN interactions used in Descouvemont (2004), the Minnesota interaction was judged to describe light nuclei more accurately. The predicted $S_{17}(0) = 24.69$ eV b is 19% larger than our recommended value, while the calculated shape of $S_{17}(E)$ provides a marginally better fit to the data, compared to other models we considered. Other ${}^8\text{B}$ and ${}^8\text{Li}$ properties computed in this model also match experiment reasonably well. Nevertheless, the substantial theoretical error bar assigned to our end result of Sec. IX.D – to remove much of the dependence on choice of model – dominates the overall uncertainty in our value for $S_{17}(0)$.

Low-order polynomial representations of $S_{17}(E)$ that span both the solar Gamow peak and energies where data are available have poor convergence due to a pole in the

S-factor at -138 keV (Jennings *et al.*, 1998a,b; Williams and Koonin, 1981). Thus instead we fit the models over a more limited energy range important to stellar fusion, 0 to 50 keV. A quadratic expansion then provides a good representation. This procedure yields $S'_{17}(0)/S_{17}(0)$ between $-1.4/\text{MeV}$ and $-1.83/\text{MeV}$ for the models used in our fitting. We recommend as a best value and probable range

$$\frac{S'_{17}(0)}{S_{17}(0)} = (-1.5 \pm 0.1)/\text{MeV}. \quad (47)$$

The corresponding values for $S''_{17}(0)/S_{17}(0)$ vary from $7.2/\text{MeV}^2$ to $20.4/\text{MeV}^2$; we recommend

$$\frac{S''_{17}(0)}{S_{17}(0)} = (11 \pm 4)/\text{MeV}^2. \quad (48)$$

The ranges are consistent with other published values where derivatives were defined by similar procedures (Barker, 1983; Bennaceur *et al.*, 1999; Descouvemont and Baye, 1988; Kolbe *et al.*, 1988). Published values outside our recommended ranges (Adelberger *et al.*, 1998; Baye, 2000; Baye and Brainis, 2000; Baye and Descouvemont, 1985; Baye *et al.*, 1998; Jennings *et al.*, 1998b; Johnson *et al.*, 1992; Williams and Koonin, 1981) are either mathematical derivatives at $E = 0$ or fits over a wider energy interval. For the adopted Descouvemont (2004) model with MN potential, the corresponding numbers are $S'_{17}(0)/S_{17}(0) = -1.51/\text{MeV}$ and $S''_{17}(0)/S_{17}(0) = 13.5/\text{MeV}^2$.

C. ${}^8\text{B}$ Coulomb dissociation measurements

Estimates of direct (p, γ) capture cross sections can be derived from Coulomb Dissociation (CD) measurements (see Sec. XII). Because of the complexity of the associated analysis and the absence of convincing benchmarks for the CD method, the Solar Fusion I authors concluded that it would be premature to use information from the CD of ${}^8\text{B}$ in deriving a recommended value for $S_{17}(0)$. However, the CD of ${}^8\text{B}$ was identified as a prime test case for this method, because this reaction can be studied both directly and indirectly, is characterized by a low proton binding energy, and is dominated by $E1$ transitions. Three groups have performed CD experiments with radioactive ${}^8\text{B}$ beams of incident energies between 44 and 254 A MeV. A comparison of their results to those from radiative proton capture allows one to assess the precision that might be possible with the CD method.

Exclusive CD measurements were performed at 47 A MeV (Iwasa *et al.*, 1996; Motobayashi *et al.*, 1994) and 52 A MeV (Kikuchi *et al.*, 1997, 1998) at RIKEN, at 83 A MeV at MSU (Davids *et al.*, 2001a,b), and at 254 A MeV at GSI (Iwasa *et al.*, 1999; Schümann *et al.*, 2003, 2006). For the RIKEN and GSI experiments, the most recent publications supersede the previously published ones. The RIKEN experiment measured the CD of ${}^8\text{B}$

in complete kinematics including γ -rays, but had to cope with a large background induced by reactions in the He bag between the target and the fragment detectors. The MSU experiment suffered from a low detection efficiency, particularly at high p- ${}^7\text{Be}$ relative energies. The GSI experiment eliminated background by reconstruction of the break-up vertex and utilized a focusing spectrometer with large momentum acceptance that provided high geometric detection efficiency. These considerations suggest that the GSI measurement of Schümann *et al.* (2006) represents the most complete experimental study of ${}^8\text{B}$ CD to date.

The extraction of $S_{17}(E)$ from the differential CD cross section $d\sigma/dE$, which varies rapidly with energy, is not trivial. The poor energy resolution in CD experiments, together with the influence of experimental cuts, require careful simulations of this distribution using a theoretical model. In addition to the dominant single $E1$ photon exchange, other potentially important factors are $E2$ transitions, nuclear break-up, and higher-order corrections. All of these effects are expected to be smaller at the higher energy of the GSI experiment than at the lower energies of the RIKEN and MSU experiments. However, a proper analysis of the GSI experiment requires relativistic modeling, a step so far taken only in perturbation theory (Bertulani, 2005; Ogata and Bertulani, 2009).

For the RIKEN case, Kikuchi *et al.* (1997) presented differential cross sections $d\sigma/d\theta_8$, where θ_8 is the scattering angle of the excited ${}^8\text{B}^*$ system reconstructed from the ${}^7\text{Be}$ and p momentum vectors, relative to that of the incoming ${}^8\text{B}$. The measured distribution was compared to first-order perturbative calculations that included $E1$ and both nuclear and Coulomb $\ell = 2$ transition amplitudes. At low relative energies, the authors found good agreement of their measured distributions with those from a model that assumes only a dipole contribution. Later investigations of the same data employed more sophisticated reaction models, stressing the importance of all the effects mentioned above (Alt *et al.*, 2003, 2005; Esbensen *et al.*, 2005; Goldstein *et al.*, 2007; Ogata *et al.*, 2006; Summers and Nunes, 2005). For example, the value of $S_{17}(0)$ obtained from the continuum-discretized coupled-channels (CDCC) analysis of Ogata *et al.* (2006) is 13% larger than that determined in the first-order calculation of Kikuchi *et al.* (1998).

At MSU, inclusive measurements were performed to test the prediction that interference between $E1$ and $E2$ transitions in the CD of ${}^8\text{B}$ would produce asymmetries in the longitudinal momentum distributions of the emitted fragments (Esbensen and Bertsch, 1996). Longitudinal momentum distributions of the ${}^7\text{Be}$ fragments from the break-up of ${}^8\text{B}$ on Pb and Ag targets at beam energies of 44 and 81 A MeV were measured (Davids *et al.*, 1998, 2001b). Asymmetries in these distributions were incontrovertibly observed and were interpreted with both first-order perturbative and CDCC calculations. The $E2$ strengths deduced from first order perturbation theory were found to be somewhat smaller than or consistent

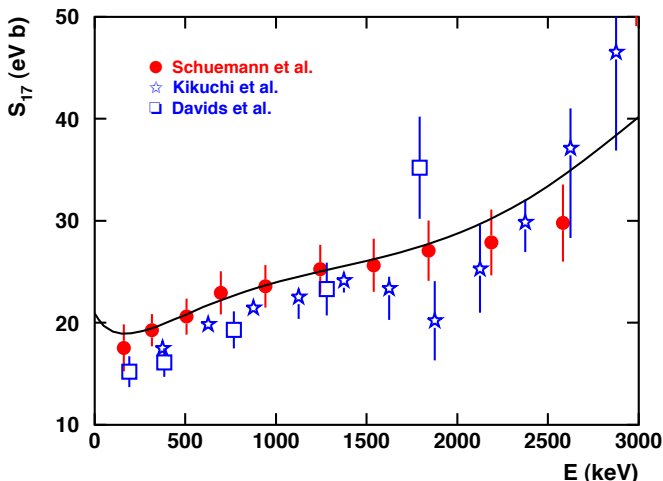


FIG. 8 (Color online) S_{17} values from CD experiments. Full red circles: latest analysis of the GSI CD experiment (Schüemann *et al.*, 2006); open blue stars: Kikuchi *et al.* (1998) analyzed in first-order perturbation theory; open blue squares: Davids and Typel (2003). The error bars include statistical and estimated systematic errors. The curve is taken from the cluster-model theory of Descouvemont *et al.* (2004), normalized to $S_{17}(0) = 20.8$ eV b.

with all published models of ${}^8\text{B}$ structure. Later, the longitudinal momentum distributions of the emitted protons were studied in the exclusive MSU measurement at 83 A MeV (Davids *et al.*, 2001a,b) and found to be consistent with the ${}^7\text{Be}$ distributions observed in the inclusive measurement. The $S_{17}(E)$ distribution was extracted from $d\sigma/dE$ (Davids and Typel, 2003) with a requirement that $\theta_8 < 1.8^\circ$, corresponding classically to an impact parameter of 30 fm; a small $E2$ contribution derived from the inclusive measurements was taken into account.

Schüemann *et al.* (2006) published the most extensive set of differential cross sections for the GSI experiment. All distributions were gated by $\theta_8 < 1^\circ$, corresponding to an impact parameter of 18.5 fm. The measured distributions were compared to theoretical ones filtered by the experimental efficiency and resolution using a GEANT-3 simulation. The event generator employed a simple first-order perturbation-theory description of Coulomb breakup with only $E1$ transitions included. The authors chose this simple model for its ease in numerical calculations and for its fidelity in reproducing, e.g., the inclusive θ_8 distribution (Fig.11 of Schüemann *et al.* (2006)) and the surprisingly symmetric θ_{cm}^p distributions of the protons in the ${}^8\text{B}^*$ reference system (Fig. 13 in Schüemann *et al.* (2006)). Consequently, $S_{17}(E)$ was deduced from this model under the assumption that, contrary to theoretical expectations, $E2$ transitions could be ignored. The data points resulting from all three CD experiments are shown in Fig. 8. (Note that the RIKEN data points were taken from the first-order perturbation-theory analysis by Kikuchi *et al.* (1998).)

The different assumptions made in analyzing the ex-

periments as well as the number and precision of the CD $S_{17}(E)$ data points prevent a precise determination of the shape, which therefore has to be taken from the radiative-capture measurements. In Fig. 8 we display the best-fit curve for the direct (p, γ) data, including the dominant $E1$ multipole but not the $M1$ contribution (see Sec. IX.D).

It is difficult to quantitatively assess the impact of the different theories and energy ranges used in analyzing the three CD experiments on the derived $S_{17}(0)$ values. The resulting values are 21.4 ± 2.0 eV b for the RIKEN experiment, as reanalyzed by Ogata *et al.* (2006); 20.6 ± 1.4 eV b for the GSI experiment; and $17.8_{-1.2}^{+1.4}$ eV b for the MSU experiment. Empirically these values are consistent with the range Solar Fusion I defined for direct measurements, $S_{17}(0) = 19_{-2}^{+4}$ eV b. Moreover, the good agreement between the shapes of the GSI CD and the radiative capture data eliminates the concern about systematically different slopes of $S_{17}(E)$ derived from the respective methods. However, we believe it would be premature to include the CD results in our determination of a recommended value for $S_{17}(0)$, as a better understanding of the role of $E2$ transitions and higher order effects in ${}^8\text{B}$ breakup at various energies is needed. Further discussions can be found in Sec. XII.

D. Direct ${}^7\text{Be}(p, \gamma){}^8\text{B}$ analysis and $S_{17}(0)$ determination

Figure 9 shows the modern ${}^7\text{Be}(p, \gamma){}^8\text{B}$ data with center-of-mass energy $E \leq 1250$ keV. We analyzed the Filippone *et al.* (1983) data using the ${}^7\text{Li}(d, p)$ cross section given in Solar Fusion I. Total errors, including systematic errors, are shown on each data point, to facilitate a meaningful comparison of different data sets. All data sets exhibit a similar $S_{17}(E)$ energy dependence, indicating that they differ mainly in absolute normalization.

Following the discussion in Sec. IX.B, we determine our best estimate of $S_{17}(0)$ by extrapolating the data using the scaled theory of Descouvemont (2004) (MN calculation). We performed two sets of fits, one to data below the resonance, with $E \leq 475$ keV, where we felt the resonance contribution could be neglected. In this region, all the individual $S_{17}(0)$ error bars overlap, except for the Bochum result, which lies low.

We also made a fit to data with $E \leq 1250$ keV, where the 1^+ resonance tail contributions had to be subtracted. We did this using the resonance parameters of Junghans *et al.* (2003) ($E_p=720$ keV, $\Gamma_p=35.7$ keV and $\Gamma_\gamma=25.3$ meV), adding in quadrature to data errors an error of 20% of the resonance subtraction. In order to minimize the error induced by variations in energy-averaging between experiments, we excluded data close to the resonance, from 490 to 805 keV, where the S-factor is strongly varying and the induced error is larger than 1.0 eV b. Above the resonance, the data have smaller errors. Only the Filippone *et al.* (1983) and Weizmann group error bars overlap the UW-Seattle/TRIUMF error bars.

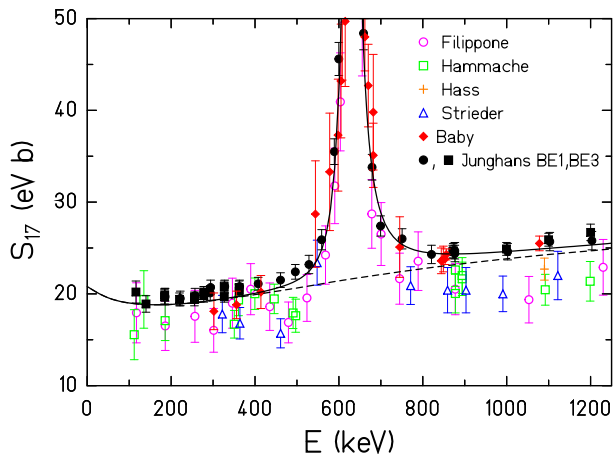


FIG. 9 (Color online) $S_{17}(E)$ vs. center-of-mass energy E , for $E \leq 1250$ keV. Data points are shown with total errors, including systematic errors. Dashed line: scaled Descouvemont (2004) curve with $S_{17}(0) = 20.8$ eV b; solid line: including a fitted 1^+ resonance shape.

Figure 9 shows the best-fit Descouvemont (2004) (MN interaction) curve from the $E \leq 475$ keV fit (together with the 1^+ resonance shape determined in Junghans *et al.* (2003), shown here for display purposes). Our fit results are shown in Table VII. The errors quoted include the inflation factors, calculated as described in the Errors Appendix. The main effect of including the inflation factors is to increase the error on the combined result by the factor 1.7 for $E \leq 475$ keV, and by 2.0 for $E \leq 1250$ keV. Both the $S_{17}(0)$ central values and uncertainties from the combined fits for these two energy ranges agree well, the latter because the added statistical precision in the $E \leq 1250$ keV fit is mostly offset by the larger inflation factor.

We also did fits in which the low energy cutoff was varied from 375 to 475 keV and the high energy exclusion region was varied from 425-530 to 805-850 keV. The central value of $S_{17}(0)$ changed by at most 0.1 eV b. On this basis we assigned an additional systematic error of ± 0.1 eV b to the results for each fit region.

To estimate the theoretical uncertainty arising from our choice of the nuclear model, we also performed fits using the shapes from other plausible models: Descouvemont (2004) plus and minus the theoretical uncertainty shown in Fig. 8 of that paper; Descouvemont and Baye (1994); the CD-Bonn 2000 calculation shown in Fig. 15 of Navrátil *et al.* (2006b); and four potential model calculations fixed alternately to reproduce the ${}^7\text{Li} + n$ scattering lengths, the best-fit ${}^7\text{Be} + p$ scattering lengths, and their upper and lower limits (Davids and Typel, 2003). The combined-fit results for all these curves, including Descouvemont (2004), are shown in Table VIII.

We estimate the theoretical uncertainty on $S_{17}(0)$ from the spread of results in Table VIII: ± 1.4 eV b for the $E \leq 475$ keV fits, and ${}^{+1.5}_{-0.6}$ eV b from the $E \leq 1250$ keV fits (the smaller error estimate in the latter case reflects

TABLE VII Experimental $S_{17}(0)$ values and (inflated) uncertainties in eV b, and χ^2/dof determined by fitting the Descouvemont (2004) MN calculation to data with $E \leq 475$ keV and with $E \leq 1250$ keV, omitting data near the resonance in the latter case.

Fit Range	$E \leq 475$ keV			$E \leq 1250$ keV		
	$S_{17}(0)$	σ	χ^2/dof	$S_{17}(0)$	σ	χ^2/dof
Baby	20.2	1.4 ^a	0.5/2	20.6	0.5 ^a	5.2/7
Filippone	19.4	2.4	4.7/6	18.0	2.2	15.8/10
Hammache	19.3	1.1	4.8/6	18.2	1.0	12.5/12
Hass				18.9	1.0	0/0
Junghans BE3	21.6	0.5	7.4/12	21.5	0.5	12.3/17
Strieder	17.2	1.7	3.5/2	17.1	1.5	5.1/6
Mean	20.8	0.7	9.1/4	20.3	0.7	18.1/5

^aWe include an additional 5% target damage error on the lowest 3 points, consistent with the total error given in the text of Baby *et al.* (2003a) (M. Hass, private communication, 2009).

TABLE VIII Experimental $S_{17}(0)$ values and (inflated) uncertainties in eV b, and χ^2 determined by fitting nine calculations to the data sets of Table VII. The $E \leq 475$ keV fits have $dof = 4$ and the $E \leq 1250$ keV fits have $dof=5$. D04 is Descouvemont (2004), DB94 is Descouvemont and Baye (1994), and NBC06 is Navrátil *et al.* (2006b).

Fit Range	$E \leq 475$ keV			$E \leq 1250$ keV		
	$S_{17}(0)$	σ	χ^2	$S_{17}(0)$	σ	χ^2
D04 (central)	20.8	0.7	9.1	20.3	0.7	18.1
D04 (upper)	20.1	0.7	10.0	19.7	0.7	18.5
D04 (lower)	21.5	0.7	8.1	21.0	0.7	17.3
DB94	21.4	0.7	8.4	21.5	0.7	16.7
NBC06	22.1	0.7	7.4	21.8	0.8	18.5
${}^7\text{Be} + p$ (central)	21.2	0.7	8.7	20.2	0.7	19.7
${}^7\text{Be} + p$ (upper)	19.4	0.8	11.7	17.3	0.7	21.6
${}^7\text{Be} + p$ (lower)	21.7	0.7	8.2	21.0	0.7	19.4
${}^7\text{Li} + n$	20.5	0.7	9.7	19.1	0.7	20.9

the exclusion of the poorer potential-model fits). We note that the estimated uncertainties are substantially larger than those given in Junghans *et al.* (2003) and in Descouvemont (2004).

We expect the model dependence³ of the fit to be greater above the resonance because of the demonstrated dependence of the S-factor in this range on

³ Recently Yamaguchi *et al.* (2009) discussed a contribution of a possible higher energy (3.2 MeV) 2^- resonance to ${}^7\text{Be}(p,\gamma)$. They estimate its contribution by taking the transition strength to be a Weisskopf unit. As low-lying E1 transitions are typically strongly inhibited, this estimate is unlikely to be realistic. Our S-factor estimate is based on a fit to low-energy data that would be free from any significant influence of this distant resonance, regardless of such assumptions.

the less-constrained short-range part of the wave functions (Csóttó, 1997; Descouvemont, 2004; Jennings *et al.*, 1998b). We base our $S_{17}(0)$ recommendation on the $E \leq 475$ keV fit,

$$S_{17}(0) = 20.8 \pm 0.7(\text{expt}) \pm 1.4(\text{theor}) \text{ eV b.} \quad (49)$$

This value is in agreement with, but substantially more precise than, the Solar Fusion I recommendation, $S_{17}(0) = 19_{-2}^{+4}$ eV b.

X. THE SPECTRUM OF ${}^8\text{B}$ NEUTRINOS

The ${}^8\text{B}$ neutrino spectrum differs from an allowed shape primarily because the principal state populated in the decay is a broad resonance. A precise determination of the neutrino spectrum is important to the analyses of the ${}^8\text{B}$ neutrino data obtained by the Super-Kamiokande and SNO collaborations. Uncertainties in the spectrum are a source of systematic error in these experiments, potentially affecting conclusions about the hep flux, MSW spectral distortions, etc. The neutrino spectrum can be determined from laboratory measurements of ${}^8\text{B}$ β^+ decay in which the decays of final-state ${}^8\text{Be}$ resonances are observed.

The ${}^8\text{B}$ β^+ decay from the $J^\pi = 2^+$ ground state is followed by the emission of two α particles from excited 2^+ states of ${}^8\text{Be}$ (see Fig. 10). Although the region of interest is dominated by a single state in ${}^8\text{Be}$ with $E_x \sim 3$ MeV, the width of this resonance is quite large, $\Gamma \sim 1.5$ MeV. Consequently the α spectrum yields a continuum, so that other 2^+ states need to be considered. The α spectrum was first measured by Farmer and Class (1960), and later by Wilkinson and Alburger (1971). R-matrix analyses were presented by Barker (1989) and Warburton (1986) (but see the caveat of Bhattacharya and Adelberger (2002)). Bahcall *et al.* (1996) used the existing data to produce a recommended neutrino spectrum that was widely used in subsequent analyses of neutrino experiments.

Ortiz *et al.* (2000) claimed a discrepancy with previous determinations of the α spectrum. Subsequently Winter *et al.* (2003) and Bhattacharya *et al.* (2006) studied the spectrum via experiments with very different systematic uncertainties, finding excellent agreement with each other but disagreement with the claim of Ortiz *et al.* (2000). It was reported (A. García, private communication, 2009) that Ortiz *et al.* (2000) now recognize that they underestimated uncertainties related to the energy loss generated by carbon buildup in their targets, so that a claim of a disagreement with earlier measurements no longer should be made. We recommend using the α spectrum of Winter *et al.* (2006) and the consistent and higher precision spectrum of Bhattacharya *et al.* (2006). These experiments do not suffer from the energy calibration problems that affected earlier experiments, as discussed by Bahcall *et al.* (1996). Finally we recommend the neu-

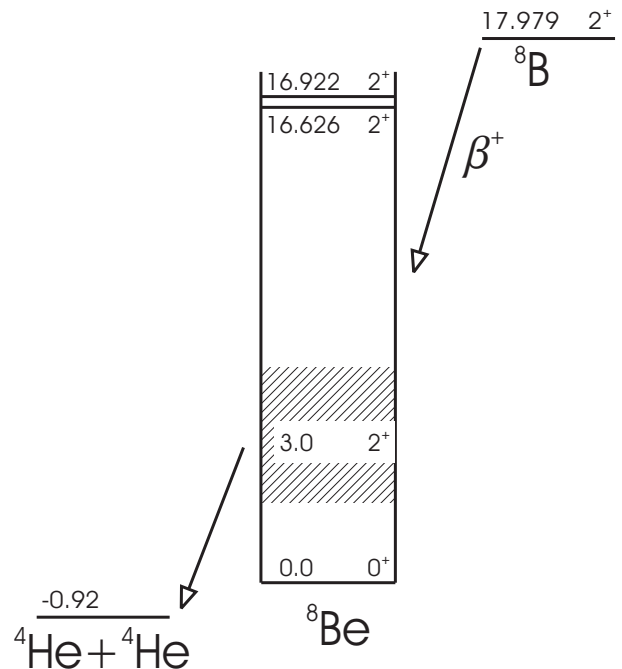


FIG. 10 Energy levels from the ${}^8\text{B}(\beta^+){}^8\text{Be}(2\alpha)$ decay chain.

trino spectrum tabulated in Winter *et al.* (2006)⁴. [The neutrino spectrum was not calculated by Bhattacharya *et al.* (2006).]

The positron spectrum can be deduced from the α spectrum in a similar fashion, and is useful as a test of data consistency. The measurements of Napolitano *et al.* (1987) have been shown by Winter *et al.* (2006) to be in good agreement with the results from the α spectrum.

Forbidden corrections are at the level of a few percent. Many measurements have been performed to determine needed matrix elements (Bowles and Garvey, 1978; De Braekeleer *et al.*, 1995; McKeown *et al.*, 1980; Nathan *et al.*, 1975; Paul *et al.*, 1977; Tribble and Garvey, 1974, 1975). Radiative corrections are smaller at a fraction of one percent and have been calculated by Sirlin (1967) and by Batkin and Sundaresan (1995). Both sets of corrections are described by Winter *et al.* (2006), and incorporated into the spectrum given there. Bahcall (1991) showed that red-shift distortions associated with the Sun's gravitational potential are insignificant, affecting the spectrum at the fractional level of $\sim 10^{-5}$. Bacrania *et al.* (2007) have placed a 90% confidence-level bound on the branching ratio for ${}^8\text{B}$ β decay to the 0^+ ground state of ${}^8\text{Be}$ (a second-forbidden transition) of 7.3×10^{-5} (see Fig. 10), limiting uncertainties in the high energy portion of the ${}^8\text{B}$ neutrino spectrum.

⁴ The strength function and the neutrino and positron spectra are in electronic repositories available online through Phys. Rev. C.

XI. THE CNO CYCLES

The need for two mechanisms to account for the stellar burning of hydrogen to helium was recognized in the pioneering work of Bethe and collaborators. The pp chain, which dominates energy production in low-mass main-sequence stars, can operate in metal-free stars, synthesizing ${}^4\text{He}$ from H, while creating equilibrium abundances of deuterium, ${}^3\text{He}$, and ${}^7\text{Be}/{}^7\text{Li}$, the elements participating in intermediate steps of Fig. 2.

Heavier main-sequence stars produce their energy dominantly through the CNO cycles, where reactions are characterized by larger Coulomb barriers. Hence, the energy production rises more steeply with increasing temperature ($\epsilon_{\text{CNO}} \propto T^{18}$ compared to $\epsilon_{\text{pp}} \propto T^4$ at solar core temperature, as illustrated in Fig. 1). The CNO cycle was proposed by Bethe and Weizsäcker to account for the evolutionary tracks of massive stars. Unlike the pp-chain, the CNO bi-cycle of Fig. 2 requires pre-existing metals to process H into ${}^4\text{He}$. Thus the contribution to energy generation is directly proportional to the solar-core number abundance of the primordial metals. The CN-cycle, denoted by I in Fig. 2, is an important SSM neutrino source. It also accounts for about 1% of solar energy generation. The cycle conserves the number abundance, but alters the distribution of solar metals as it burns into equilibrium, eventually achieving equilibrium abundances proportional to the inverse of the respective rates. In the Sun this leads to the conversion of almost all of the core's primordial ${}^{12}\text{C}$ into ${}^{14}\text{N}$. This change in the chemical composition alters the core's opacity and, at the 3% level, the heavy element mass fraction Z , SSM effects first explored by Bahcall and Ulrich (1988).

The ${}^{14}\text{N}(p,\gamma)$ reaction – the slowest reaction in the CN cycle at low temperatures and thus the rate-controlling step – determines whether equilibrium has been achieved. The ${}^{14}\text{N}$ lifetime is shorter than the age of the Sun for temperatures $\gtrsim 1.33 \times 10^7$ K. Therefore equilibrium for the CN cycle has been reached only for $R \lesssim 0.1R_{\odot}$, corresponding to the central 7% of the Sun by mass. Consequently, over a significant portion of the outer core, ${}^{12}\text{C}$ has been converted to ${}^{14}\text{N}$, but further reactions are inhibited by the ${}^{14}\text{N}(p,\gamma)$ bottleneck.

A. The reaction ${}^{14}\text{N}(p,\gamma){}^{15}\text{O}$

1. Current status and results

Figure 11 shows the level structure of ${}^{15}\text{O}$, relative to the threshold energy for ${}^{14}\text{N}(p,\gamma)$.

Solar Fusion I gave $3.5_{-1.6}^{+0.4}$ keV b as the recommended total S-factor for the ${}^{14}\text{N}(p,\gamma){}^{15}\text{O}$ reaction. This was based on the energy dependence determined by Schröder *et al.* (1987). In the Schröder *et al.* (1987) analysis the ground state transition accounted for half of the total S-factor at zero energy, primarily because of the contribution of a subthreshold resonance at $E = -504$ keV

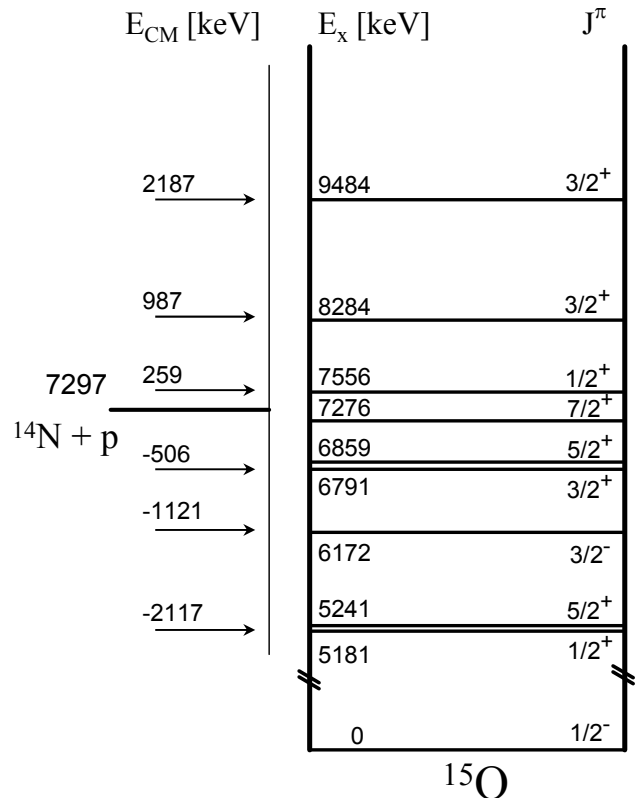


FIG. 11 The energy levels of ${}^{15}\text{O}$ and their relationship to the threshold energy for ${}^{14}\text{N}(p,\gamma)$.

(corresponding to the 6.79 MeV state in ${}^{15}\text{O}$). However, a reanalysis based on an R-matrix calculation by Angulo and Descouvemont (2001) indicated that the strength of the ground state transition in Schröder *et al.* (1987), $S_{14}^{\text{gs}}(0) = 1.55$ keV b, had been significantly overestimated, and should be reduced to 0.08 keV b.

This finding prompted a series of new experiments using direct (Bemmerer *et al.*, 2006b; Formicola *et al.*, 2004; Imbriani *et al.*, 2005; Lemut *et al.*, 2006; Marta *et al.*, 2008; Runkle *et al.*, 2005) and indirect approaches (Bertone *et al.*, 2001, 2002; Mukhamedzhanov *et al.*, 2003; Nelson *et al.*, 2003; Schürmann *et al.*, 2008; Yamada *et al.*, 2004). The prompt-capture γ -radiation was measured in experiments by the TUNL group (Runkle *et al.*, 2005) in a surface laboratory and by the LUNA group (Formicola *et al.*, 2004; Imbriani *et al.*, 2005; Marta *et al.*, 2008) in Gran Sasso. From these experiments – carried out with Ge detectors – the contributions of each transition could be extracted. In an additional measurement by the LUNA Collaboration (Bemmerer *et al.*, 2006b; Lemut *et al.*, 2006) the total cross section was determined. These recent experiments cover an energy range from 70 to 480 keV, still far from the solar Gamow window at $E_0 = 27$ keV. Additional information is provided by experiments that probe the width of the subthreshold state at $E = -506$ keV by the Doppler shift attenuation method

(Bertone *et al.*, 2001; Schürmann *et al.*, 2008) and by Coulomb excitation (Yamada *et al.*, 2004). Asymptotic normalization coefficients (ANC) for the ground state and selected excited states were determined from transfer reaction measurements for $^{14}\text{N}(^3\text{He,d})^{15}\text{O}$ by Bertone *et al.* (2002) and Mukhamedzhanov *et al.* (2003). All experiments and subsequent analyses confirmed that the value for the ground-state contribution determined in the extrapolations of Schröder *et al.* (1987) had been too high. Current estimates of $S_{14}^{\text{gs}}(0)$ range from 0.08 keV b (Angulo and Descouvemont, 2001) to 0.45 keV b (Runkle *et al.*, 2005). Hence, the S-factor for $^{14}\text{N}(p,\gamma)^{15}\text{O}$ is now determined largely by the transition to the 6.79 MeV state. Minor contributions arise from transitions to the 5.18, 5.24, 6.17, 6.86 and 7.28 MeV states in ^{15}O .

2. R-matrix analysis and normalization

We have performed an R-matrix fit to the three strongest transitions using the data of Imbriani *et al.* (2005), Marta *et al.* (2008), Runkle *et al.* (2005), and Schröder *et al.* (1987) and the code of Descouvemont (Descouvemont and Baye, 2010). In this way we obtain the most robust weighted mean. The recent direct experiments (Bemmerer *et al.*, 2006b; Formicola *et al.*, 2004; Imbriani *et al.*, 2005; Lemut *et al.*, 2006; Marta *et al.*, 2008; Runkle *et al.*, 2005) cover only a relatively narrow energy window. Thus, as no new information is available for the higher lying resonances, a reliable extrapolation to zero energy requires the high-energy data of Schröder *et al.* (1987). However, systematic differences are apparent in the data sets of Imbriani *et al.* (2005), Runkle *et al.* (2005), and Schröder *et al.* (1987). In order to minimize systematic uncertainties, all data sets were renormalized to the weighted mean of the strength of the 259 keV resonance in $^{14}\text{N}(p,\gamma)^{15}\text{O}$. Table IX summarizes the available absolute determinations of the resonance strength with a weighted mean of $\omega\gamma_{259} = 13.1 \pm 0.6$ meV. The uncertainty was obtained by calculating the error on the weighted mean, excluding the common systematic uncertainty on the stopping power of protons in nitrogen (Ziegler *et al.*, 2008). The latter was summed in quadrature with the weighted mean error to obtain the final uncertainty.

In Schröder *et al.* (1987) the data were normalized to an absolute cross section determination at $E = 760$ keV, $\sigma(E = 760 \text{ keV}) = 620 \pm 80$ nb. This value is an adopted mean based on several experimental methods, while the measurement relative to $\omega\gamma_{259}$ gives $\sigma(E = 760 \text{ keV}) = 609$ nb (Schröder *et al.*, 1987). Thus, based on the difference between the value for $\omega\gamma_{259}$ used by Schröder *et al.* (1987), 14 meV (Becker *et al.*, 1982), and the new determination, 13.1 ± 0.6 meV, a precise renormalization of $\sigma(E = 760 \text{ keV})$ can be made, relative to this resonance. One finds $\sigma(E = 760 \text{ keV}) = 570$ nb. Moreover, we note that the energy dependence of Schröder *et al.* (1987) was corrected for summing contributions, as dis-

TABLE IX Summary of the published values for $\omega\gamma_{259}$, along with their estimated statistical, systematic, and total uncertainties. All quantities are in units of meV. The last row gives the recommended value.

	$\omega\gamma_{259}$	stat.	syst.	total
Becker <i>et al.</i> (1982) ^a	14			1.0
Runkle <i>et al.</i> (2005)	13.5		1.2	1.2
Imbriani <i>et al.</i> (2005)	12.9	0.4	0.8	0.9
Bemmerer <i>et al.</i> (2006b)	12.8	0.3	0.5	0.6
recommended value	13.1			0.6

^aused in Schröder *et al.* (1987)

cussed by Imbriani *et al.* (2005). The renormalizations for Runkle *et al.* (2005) and Imbriani *et al.* (2005) are 3% and 2%, respectively.

The ANCs for the ground, 6.79 MeV, and 6.17 MeV states as well as Γ_γ of the 6.79 MeV state are important parameters in the R-matrix analysis determining $S(0)$. Parameter values determined in the analysis will reflect the quality of the input data. Thus the R-matrix results can be validated by comparing these values with those determined independently by transfer reactions and other indirect measurements (see Table X).

3. Transition to the ground state and 6.79 MeV in ^{15}O

The transitions to the ground and 6.79 MeV states in ^{15}O are connected through the reduced proton width of the -0.506 MeV subthreshold state. This width can also be expressed in terms of the subthreshold state ANC via the Whittaker function at the R-matrix radius a that appears in Eq. (3.60) of Descouvemont and Baye (2010) (see references therein). Both transitions are discussed together here.

Transition to the 6.79 MeV state: The reaction mechanism for the transition to the 6.79 MeV state appears rather simple, primarily an external capture process whose magnitude is determined by the value of the ANC. Hence $S_{14}^{6.79}(0)$ is dominated by the external capture process. In the present analysis the data of Runkle *et al.* (2005), Imbriani *et al.* (2005), and Schröder *et al.* (1987) are included after renormalization, as described above. As the recent low-energy data do not strongly constrain the R-matrix radius, high-energy data are needed. The resulting $S_{14}^{6.79}(E)$ fails to reproduce the high-energy data for radii $5.5 \text{ fm} < a < 6.5 \text{ fm}$, as in Fig. 4 of Angulo and Descouvemont (2001). A better fit can be obtained by choosing smaller radii. However, this choice also impacts fits for the ground state transition, which favor larger radii. Consequently, we have not used the transition to the 6.79 MeV state to determine the R-matrix radius in this way. Instead, R-matrix fits were done

- i) taking all renormalized data (Imbriani *et al.*, 2005; Runkle *et al.*, 2005; Schröder *et al.*, 1987) into ac-

TABLE X Published ANC values and Γ_γ for the 6.79 MeV transition. All ANC values are given in the coupling scheme of Angulo and Descouvemont (2001). The recommended values in the last row were obtained as a weighted mean considering as weights the experimental errors only. Finally, the recommended uncertainty was obtained by summing in quadrature the weighted mean error and an average theoretical uncertainty. The latter is according to information provided by the authors. As existing measurements of $\Gamma_\gamma(6.79 \text{ MeV})$ are discrepant, no recommended value is given.

	$C_{gs^{3/2}} \text{ (fm}^{-1/2}\text{)}^a$	$C_{6.79} \text{ (fm}^{-1/2}\text{)}$	$C_{6.17^{1/2}} \text{ (fm}^{-1/2}\text{)}^b$	$C_{6.17^{3/2}} \text{ (fm}^{-1/2}\text{)}^a$	$\Gamma_\gamma(6.79) \text{ (eV)}$
Mukhamedzhanov <i>et al.</i> (2003)	7.4 ± 0.4	4.9 ± 0.5	0.47 ± 0.03	0.53 ± 0.03	
Bertone <i>et al.</i> (2002)	7.9 ± 0.9	4.6 ± 0.5	0.45 ± 0.05	0.51 ± 0.06	
Bertone <i>et al.</i> (2001)					$0.41^{+0.34}_-0.13^c$
Yamada <i>et al.</i> (2004)					$0.95^{+0.6}_-0.95$
Schürmann <i>et al.</i> (2008)					> 0.85
recommended value	7.4 ± 0.5	4.8 ± 0.5	0.47 ± 0.03	0.53 ± 0.04	

^achannel spin $I = 3/2$

^bchannel spin $I = 1/2$

^cthe quoted uncertainty represents a 90% confidence limit

count;

ii) limiting the data sets to $E < 1.2 \text{ MeV}$; and

iii) same as i), but introducing an unidentified $J^\pi = 5/2^-$ pole at $E = 6 \text{ MeV}$.

In each case the ANC values and the radii were determined. The results for the three cases are

- i) $C_{6.79} = 4.61 \pm 0.02 \text{ fm}^{-1/2}$ for $a = 4.14 \text{ fm}$ and $S_{114}^{6.79}(0) = 1.11 \text{ keV b}$. This solution has the lowest χ^2 but was rejected for the reasons given above.
- ii) $C_{6.79} = 4.65 \pm 0.02 \text{ fm}^{1/2}$ for $a = 4.6 \text{ fm}$ and $S_{114}^{6.79}(0) = 1.15 \text{ keV b}$.
- iii) $C_{6.79} = 4.69 \pm 0.02 \text{ fm}^{1/2}$ for $a = 5.4 \text{ fm}$ and $S_{114}^{6.79}(0) = 1.18 \text{ keV b}$.

The latter two fits are in very good agreement with Runkle *et al.* (2005) and about 5% lower than Imbriani *et al.* (2005). All three fits are shown in Fig. 12.

In summary, the dominant systematic uncertainty for $S_{114}^{6.79}(0)$ arises from the interpretation of the high-energy data. This uncertainty is estimated from cases i) to iii) to be about 4%. One could speculate that the deviation of the higher energy data from the R-matrix fit is due to broad unidentified structures in this transition (Fig. 12). We recommend $S_{114}^{6.79}(0) = 1.18 \pm 0.05 \text{ keV b}$. The error includes both systematic and statistical uncertainties, though the former are much larger.

The weighted mean of the ANC for the 6.79 MeV state from indirect measurements, $C_{6.79} = 4.8 \pm 0.5 \text{ fm}^{-1/2}$ (Table X), is in excellent agreement with the results of the R-matrix analysis.

Ground state transition: Three data sets (Imbriani *et al.*, 2005; Runkle *et al.*, 2005; Schröder *et al.*, 1987), normalized to $\omega\gamma_{259}$ as discussed above, were used in the ground-state analysis. The results from Marta *et al.* (2008) – three data points with high precision above the 259 keV resonance and essentially free from summing effects – are relative to the yield of the transition to the 6.79

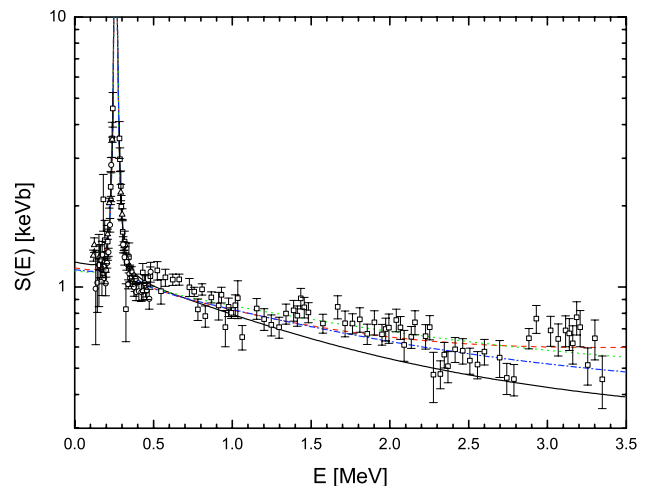


FIG. 12 (Color online) R-matrix fits to the $^{14}\text{N}(p,\gamma)^{15}\text{O}$ 6.79 MeV transition together with the data of Schröder *et al.* (1987) (open squares), Imbriani *et al.* (2005) (open triangles), and Runkle *et al.* (2005) (open circles). The cases i, ii, and iii (see text) are represented by the dotted green, dash-dotted blue, and dashed red lines, respectively. The black line is a calculation similar to iii), but without the unidentified $J^\pi = 5/2^-$ pole at $E=6 \text{ MeV}$, comparable to fits in past work.

MeV state. These data were normalized to the weighted mean of the renormalized S-factor (see Sec. XI.A.2) from Schröder *et al.* (1987), Runkle *et al.* (2005), and Imbriani *et al.* (2005) in the energy region $311 \text{ keV} < E < 360 \text{ keV}$.

The R-matrix fit was based on the same poles as in Angulo and Descouvemont (2001) with starting parameters as given in Ajzenberg-Selove (1991). The sensitivity to radius was tested for a broad range of ANC values, $6 \text{ fm}^{-1/2} < C_{gs^{3/2}} < 9 \text{ fm}^{-1/2}$. The minimum χ^2 was obtained for $a = 5.6 \pm 0.1 \text{ fm}$. Thus, we selected $a = 5.5 \text{ fm}$ as an appropriate average for the ground and 6.79

MeV states, employing this value for all subsequent R-matrix fits. This value was used previously in Runkle *et al.* (2005), Imbriani *et al.* (2005), Marta *et al.* (2008), and Mukhamedzhanov *et al.* (2003). The reduced width for the subthreshold state was fixed through $C_{6.79}$ (see above) to $\gamma^2=0.37$ MeV. The narrow resonances at 0.987 MeV ($\Gamma_p = 3.6$ keV, see Fig. 13) and 2.191 MeV ($J^\pi = 5/2^-$, $\Gamma_p = 10$ keV) are not relevant for $S_{114}^{\text{gs}}(0)$ and thus were excluded from the fit. In order to optimize the fit off-resonance, contributions to χ^2 from points near the 2.191 MeV and 0.259 MeV ($\Gamma_p \sim 1$ keV) resonances were omitted. As slopes are steep and counting rates peak near the resonances, the inclusion of near-resonance data forces the fit in arbitrary ways. The region excluded depends on resonance width and on target thickness, which can spread the effects of a resonance over a larger energy interval. We omitted data in the interval between $E_R - 20\Gamma$ and $E_R + 1.5\Delta$, where Δ is the target thickness. Target thickness effects are especially prominent in the data of Schröder *et al.* (1987), representing the integral over the target thickness of ~ 30 keV.

In the fit the χ^2 decreases with increasing ANC, reaching a minimum at $C_{\text{gs}^{3/2}} \sim 11 \text{ fm}^{-1/2}$, a value outside the ranges determined by Mukhamedzhanov *et al.* (2003) and Bertone *et al.* (2002). At the $9 \text{ fm}^{-1/2}$ upper bound for $C_{\text{gs}^{3/2}}$, we obtain $S_{114}^{\text{gs}}(0) = 0.29$ keV b, while at the $6 \text{ fm}^{-1/2}$ lower bound, $S_{114}^{\text{gs}}(0) = 0.24$ keV b. These fits do not include the possibility of a small contribution from $C_{\text{gs}^{1/2}}$, interfering with the 259 keV resonance. We expand the uncertainty to account for such a possibility, recommending $S_{114}^{\text{gs}}(0) = 0.27 \pm 0.05$ keV b with $\Gamma_\gamma(\text{int}) = 1.1$ eV. The latter value is the internal part of the -0.504 MeV subthreshold state radiative width (at $E = 0$), a fit parameter in the R-matrix calculation. The total radiative width, which can be compared to experimental values obtained from, e.g., lifetime measurements, is derived following the approach of Holt *et al.* (1978) and Barker and Kajino (1991), giving $\Gamma_\gamma(6.79) = |\Gamma_\gamma(\text{int})^{1/2} \pm \Gamma_\gamma(\text{ch})^{1/2}|^2$, where the relative sign of the two amplitudes is unknown. The channel (external) radiative width $\Gamma_\gamma(\text{ch}) = 0.57$ eV can be directly calculated from the adopted value of $C_{\text{gs}^{3/2}}$. If the minus sign is chosen in the relationship for $\Gamma_\gamma(6.79)$, one obtains a lifetime in excess of 4 fs, in disagreement with Bertone *et al.* (2001) and Schürmann *et al.* (2008). If the plus sign is chosen, a lifetime shorter than 0.2 fs is obtained. Such a lifetime is presently beyond the reach of Doppler shift lifetime measurements, but still in agreement with Schürmann *et al.* (2008). However, the Coulomb excitation work of Yamada *et al.* (2004) gives a lower limit of 0.4 fs, apparently ruling out such a short lifetime. We conclude that the current experimental situation is unsatisfactory and calls for further work. Lifetimes larger than 0.4 fs require $C_{\text{gs}^{3/2}} < 6 \text{ fm}^{-1/2}$, again in disagreement with Bertone *et al.* (2002) and Mukhamedzhanov *et al.* (2003). The somewhat larger range in $C_{\text{gs}^{3/2}}$ used in the present analysis, compared to the uncertainty recommended in Table X, takes account of this dilemma.

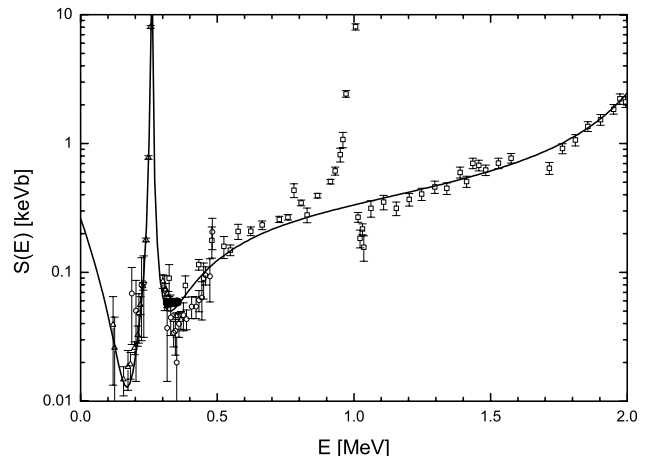


FIG. 13 R-matrix fit to the $^{14}\text{N}(p,\gamma)^{15}\text{O}$ ground state transition. The filled circles are from Marta *et al.* (2008). All other data are labeled as in Fig. 12.

Most recent treatments of $^{14}\text{N}(p,\gamma)^{15}\text{O}$ direct measurements have failed to address issues connected with the total radiative width.

4. Transition to the 6.17 MeV state

This transition was analyzed with the poles given by Angulo and Descouvemont (2001) except that we also allowed for an external capture contribution (channel spin $I = 3/2$), improving the fit substantially. The primary uncertainty in predicting $S_{114}^{6.17}(0)$ arises from the choice of the poles, i.e., more poles at higher energies and their interference pattern, respectively, could be included in the fit. However, a full study of all possible minor contributions is far beyond the scope of the present work and would be hampered by the lack of precise data. The best fit yields $S_{114}^{6.17}(0) = 0.13$ keV b with $C_{6.17^{1/2}} = 0.43 \pm 0.02 \text{ fm}^{-1/2}$ and $C_{6.17^{3/2}} = 0.49 \pm 0.02 \text{ fm}^{-1/2}$. These ANCs are in good agreement with those deduced by Mukhamedzhanov *et al.* (2003) and Bertone *et al.* (2002) (see Table X). Previous results without the contribution from channel spin 3/2 external capture led to $S_{114}^{6.17}(0) = 0.08$ keV b (Imbriani *et al.*, 2005) and 0.04 keV b (Runkle *et al.*, 2005). Thus, we have adopted $S_{114}^{6.17}(0) = 0.13 \pm 0.06$ keV b where the error reflects the uncertainty in the R-matrix input as well as the spread of this value in the literature (Angulo and Descouvemont, 2001; Imbriani *et al.*, 2005; Nelson *et al.*, 2003; Runkle *et al.*, 2005). In Nelson *et al.* (2003) a $M1$ contribution was inferred from an analyzing power experiment. The fit only extends to $E \sim 327$ keV and trends above the data for higher energies. Runkle *et al.* (2005) showed that there is no significant difference in $S_{114}^{6.17}(0)$ results from including the $M1$ contribution specified by Nelson *et al.* (2003).

TABLE XI $S_{114}(0)$ and the fractional uncertainty $\Delta S_{114}(0)$ for the different transitions. Note that $\text{tr}(5.24) \rightarrow 0$ includes contributions from the transition $\text{tr} \rightarrow 6.86 \rightarrow 5.24$ and $\text{tr} \rightarrow 7.28 \rightarrow 5.24$ with $S_{114}(0) = 0.037 \pm 0.011$ and 0.019 ± 0.006 keV b, respectively (from Schröder *et al.* (1987) with a 30% uncertainty). The contribution of $\text{tr}(7.28) \rightarrow 0$ observed by Schröder *et al.* (1987) is negligible.

transition	$S_{114}(0)$ (keV b)	$\Delta S_{114}(0)$	reference
$\text{tr} \rightarrow 0$	0.27 ± 0.05	19%	present
$\text{tr} \rightarrow 6.79$	1.18 ± 0.05	4%	present
$\text{tr} \rightarrow 6.17$	0.13 ± 0.06	38%	present
$\text{tr} \rightarrow 5.18$	0.010 ± 0.003	30%	Imbriani <i>et al.</i> (2005)
$\text{tr}(5.24) \rightarrow 0^a$	0.070 ± 0.021	30%	Imbriani <i>et al.</i> (2005)
R-Matrix sum	1.66 ± 0.08^b	5%	
additional systematic uncertainty ^c		5%	
total	1.66 ± 0.12	7%	

^avalue from the analysis of the secondary transition

^buncertainty from the R-matrix analysis only

^cfrom normalization to $\omega\gamma_{259}$

5. Total $S_{114}(0)$ and conclusions

We have obtained $S_{114}^{\text{tot}}(0)$ from the data sets of Imbriani *et al.* (2005), Marta *et al.* (2008), and Schröder *et al.* (1987), normalized to the 259 keV resonance, and supported by an R-matrix analysis that defines the extrapolation to astrophysical energies. The R-matrix analysis focused on the systematic uncertainties associated with fitting and extrapolating the data, and made use of indirect measurements (Bertone *et al.*, 2001, 2002; Mukhamedzhanov *et al.*, 2003; Schürmann *et al.*, 2008; Yamada *et al.*, 2004) to constrain parameters in the fitting. Systematic uncertainties in this analysis dominate the errors: statistical uncertainties have minor consequences for the resulting $S_{114}^{\text{tot}}(0)$. The R-matrix radius a is a key parameter, fixed in the present analysis to the best-choice value of 5.5 fm (Sec. XI.A.3). The extrapolation for the strongest transition to the 6.79 MeV state is robust within 4%, while the extrapolations for transitions to the ground and 6.17 MeV states are less constrained. The transitions to the 5.18, 5.24, 6.86, and 7.28 MeV states combine to contribute 0.08 keV b to $S_{114}^{\text{tot}}(0)$, $\sim 5\%$ of the total. These contributions were obtained from literature (Imbriani *et al.*, 2005; Schröder *et al.*, 1987), scaled to the weighted mean of $\omega\gamma_{259}$. The errors on the individual transitions were enlarged to a more realistic uncertainty of 30%. Note that some of the weak transitions often have been neglected in past work. Finally, an additional systematic error of 5% due to the normalization of $\omega\gamma_{259}$ (see Table IX) is included. Table XI summarizes the various contributions.

We find, after summing all contributions, $S_{114}^{\text{tot}}(0) = 1.66 \pm 0.12$ keV b. The S-factor fits derived in the present study are shown in Figs. 12, 13, and 14 together with the renormalized data of Imbriani *et al.* (2005), Marta *et al.* (2008), Runkle *et al.* (2005), and Schröder *et al.* (1987). Figure 15 compares our results for the total $S_{114}^{\text{tot}}(E)$ with the data from Lemut *et al.* (2006) and Bemmerer *et al.*

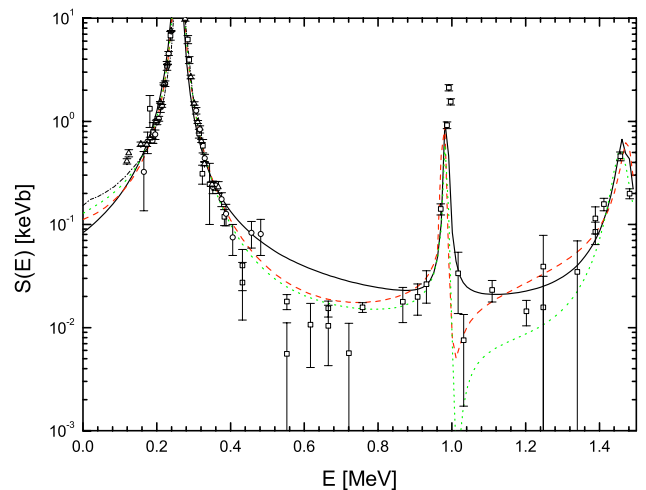


FIG. 14 (Color online) R-matrix fit to the $^{14}\text{N}(p,\gamma)^{15}\text{O}$ 6.17 MeV transition. The symbols are the same as in Fig. 12. The dotted green line corresponds to the present analysis. The solid black, dashed red, and dash-dotted black lines are the R-matrix fits of Imbriani *et al.* (2005), Runkle *et al.* (2005), and Nelson *et al.* (2003), respectively.

(2006b). Below $E = 108$ keV the gas-target results and the R-matrix fit are not inconsistent, given uncertainties; at higher energies, $E \sim 200$ keV, the average deviation is $\sim 8\%$. These data are an absolute determination of the S-factor and thus do not depend on the normalization of $\omega\gamma_{259}$.

$S_{114}^{\text{tot}}(E)$ below $E \sim 130$ keV can be approximated to better than 1% by a second order polynomial

$$\begin{aligned}
 S_{114}^{\text{tot}}(0) &= 1.66 \text{ keV b} \\
 S_{114}^{\text{tot}'}(0) &= -0.0033 \text{ b} \\
 S_{114}^{\text{tot}''}(0) &= 4.4 \times 10^{-5} \text{ b/keV}.
 \end{aligned} \tag{50}$$

The absolute scale of this energy dependence has an un-

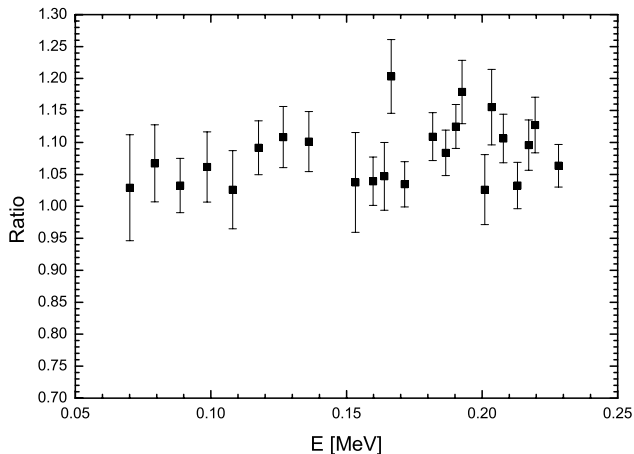


FIG. 15 Comparison of the S_{14}^{tot} obtained from the present R-matrix fit and gas target data. Note that the gas target data are corrected for electron screening (see Table 2 in Bemmerer *et al.* (2006b)) according to calculations of Assenbaum *et al.* (1987).

certainty of $\pm 7\%$. Recently, a coupled channel analysis of the data for $^{14}\text{N}(p,\gamma)^{15}\text{O}$ has been reported (Grineviciute *et al.*, 2008) which gives $S_{14}^{\text{tot}}(0) = 1.68$ keV b, in excellent agreement with the results presented here.

Further work on $^{14}\text{N}(p,\gamma)^{15}\text{O}$ is needed. A better understanding of the reaction mechanism governing the transition to the 6.79 MeV state at high energies would help reduce systematic uncertainties. Moreover, additional experimental and theoretical work on the transition to the 6.17 MeV state is needed, as the existing database is lacking. A new determination of Γ_γ for the 6.79 MeV state with an alternative method would be desirable to constrain the R-matrix fit and to resolve slight discrepancies in existing data. Elastic scattering experiments could give an additional constraint. Finally, a high-precision measurement of $\omega\gamma_{259}$ with significant improvements in the accuracy of stopping power data would reduce the systematic uncertainty in the normalization.⁵

⁵ Note added in proof: A new R-matrix analysis of $^{14}\text{N}(p,\gamma)^{15}\text{O}$ reaction appeared (Azuma *et al.*, 2010) after submission of the present work. This analysis, which served as a validity test for the AZURE code, yielded $S_{14}^{\text{tot}}(0) = 1.81$ keV b, 9% larger than the central value recommended here. No uncertainty was provided. The differences between Azuma *et al.* (2010) and Solar Fusion II are connected with the 6.79 MeV transition. In the present work (i) a normalization procedure is employed to address needed corrections in the high-energy data and (ii) a background pole is introduced to achieve a better representation of that data. Without such adjustments, the procedure of Azuma *et al.* (2010) produces a fit that underestimates the high-energy data and consequently yields a larger $S_{14}^{6.79}(0)$. Nevertheless, the present and Azuma *et al.* (2010) results are consistent if one assigns a reasonable uncertainty to the latter.

B. Other CNO-cycle reactions

While the $^{14}\text{N}(p,\gamma)^{15}\text{O}$ reaction controls the cycling rate and the energy production by CN reactions at solar temperatures, other reactions in the cycle determine the extent to which the reaction flow moves out of the CN cycle toward heavier metals, oxygen in particular. These trends in turn affect the opacity evolution and temperature profiles as a function of solar age. There has been significant recent progress in determining the rates of many of these other reactions. The reader is referred to Solar Fusion I for summaries of other reactions for which there has not been new work reported since 1998. More recent reviews have been given by Angulo *et al.* (1999) (the “NACRE” compilation) and by Wiescher *et al.* (2010).

1. $^{12}\text{C}(p,\gamma)^{13}\text{N}$

In the starting phase of the CN cycle, before it has reached its equilibrium, this reaction controls the buildup of ^{14}N (Haxton and Serenelli, 2008). A recent study using the ANC method by Burtebaev *et al.* (2008) yields a reaction rate consistent with that of Angulo *et al.* (1999), the rate recommended here.

2. $^{15}\text{N}(p,\alpha)^{12}\text{C}$

As the $^{15}\text{N}(p,\alpha)^{12}\text{C}$ reaction competes with $^{15}\text{N}(p,\gamma)^{16}\text{O}$, a parallel study of the two is highly desirable. In Solar Fusion I, a weighted average of $S_{15}^\alpha(0) = 67.5 \pm 4.0$ MeV b was recommended using the results of Redder *et al.* (1982) and Zyskind and Parker (1979). Recently the $^{15}\text{N}(p,\alpha)^{12}\text{C}$ reaction has been measured by La Cognata *et al.* (2007), using the indirect Trojan Horse Method (TH method) (see Sec. XII). The new data have been analyzed along with $^{15}\text{N}(p,\gamma)^{16}\text{O}$, using a common R-matrix approach. The TH method allows one to extend the explored energy range down to about 20 keV, without the complication of electron screening enhancements that enter for direct measurements. Thus the TH measurements provide complementary information that can be helpful in checking the overall consistency of S-factor fits. La Cognata *et al.* (2007) determined $S_{15}^\alpha(0) = 68 \pm 11$ MeV b from TH measurements. New R-matrix fits to direct data of Redder *et al.* (1982) by La Cognata *et al.* (2009) yielded $S_{15}^\alpha(0) = 73 \pm 5$ and 74 ± 9 MeV b, depending on the respective energy ranges fit (see La Cognata *et al.* (2009) for details), and $S_{15}^\alpha(0) = 70 \pm 13$ MeV b for the indirect TH method data of La Cognata *et al.* (2007). An R-matrix fit by Barker (2008a), which did not include the TH method results, gave $S_{15}^\alpha(0) = 80$ MeV b. We recommend the value $S_{15}^\alpha(0) = 73 \pm 5$ MeV b obtained by La Cognata *et al.* (2009) by fitting direct data as the new best value for the $^{15}\text{N}(p,\alpha)^{12}\text{C}$

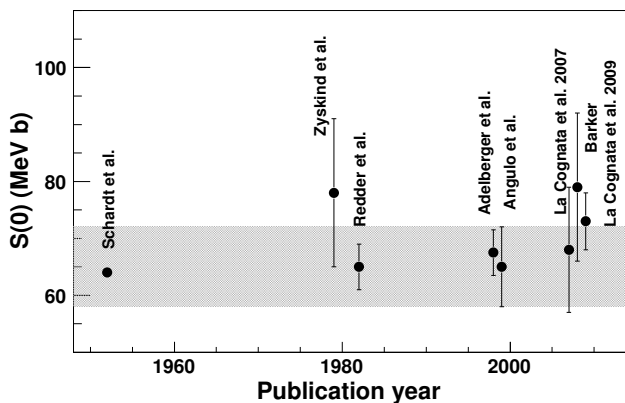


FIG. 16 Summary of the available measurements of $S_{15}^{\alpha}(0)$, showing values as originally reported on the dates indicated. The shaded band corresponds to the NACRE compilation (Angulo *et al.*, 1999). From La Cognata *et al.* (2009), by permission.

reaction (see Table XII). It is consistent with the two direct measurements, the indirect TH method data, and the R-matrix fit by Barker. A summary given by La Cognata *et al.* (2009) of $S_{15}^{\alpha}(0)$ determinations is shown in Fig. 16. In Table XII the derivatives shown are those reported by Zyskind and Parker (1979), and may therefore not be completely consistent with the R-matrix energy dependence calculated by La Cognata *et al.* (2009).

3. $^{15}\text{N}(p,\gamma)^{16}\text{O}$

The $^{15}\text{N}(p,\gamma)^{16}\text{O}$ reaction provides the path to form ^{16}O in stellar hydrogen burning⁶, thus transforming the CN cycle into the CNO bi-cycle and CNO tri-cycle. In stellar environments, the reaction proceeds at very low energies, where it is dominated by resonant capture to the ground state through the first two interfering $J^{\pi} = 1^{-}$ s-wave resonances at $E_R = 312$ and 964 keV. In addition there is some direct capture to the ground state. Direct measurements have been reported by Hebbard (1960) for proton energies down to 220 keV and by Rolfs and Rodney (1974) down to proton energies of 155 keV. These measurements disagree significantly below 300 keV. In order to fit their low-energy data, Rolfs and Rodney (1974) included the interference of the two 1^{-} resonant capture amplitudes with the nonresonant (direct) component to the ground state of ^{16}O calculated in the hard-sphere approximation. The absolute normalization of the direct term is entirely determined by the ANC of the

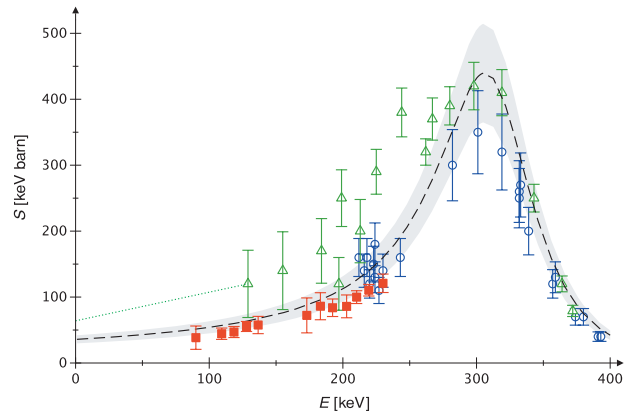


FIG. 17 (Color online) $S(0)$ for the $^{15}\text{N}(p,\gamma)^{16}\text{O}$ reaction. Data from Hebbard (1960) (blue circles, limited to $E \geq 210$ keV), Rolfs and Rodney (1974) (green triangles), and Bemmerer *et al.* (2009) (red squares). Error bars reflect statistical and systematic uncertainties summed in quadrature. Dashed line, previous R-matrix fit and shaded area, its quoted 17% uncertainty, from Mukhamedzhanov *et al.* (2008). Dotted line: previous extrapolation by Angulo *et al.* (1999). Figure from Bemmerer *et al.* (2009), by permission.

bound state for $^{15}\text{N} + p \rightarrow ^{16}\text{O}$. The spectroscopic factor adopted by Rolfs and Rodney (1974) corresponds to an ANC almost an order of magnitude larger than the one determined from $^{15}\text{N}(^3\text{He},d)^{16}\text{O}$ by Mukhamedzhanov *et al.* (2008).

A new analysis of the direct data using the two-level, two-channel R-matrix was presented by Mukhamedzhanov *et al.* (2008). The contribution from the $\alpha - ^{12}\text{C}$ channel was also taken into account. The determined astrophysical factor $S_{15}^{\gamma}(0) = 36 \pm 6$ keV b is about a factor of two lower than the previously accepted value $S_{15}^{\gamma}(0) = 64 \pm 6$ keV b from Rolfs and Rodney (1974). Hebbard (1960) reported $S_{15}^{\gamma} = 32 \pm 6$ keV b at 23.44 keV, which was converted by Mukhamedzhanov *et al.* (2008) to $S_{15}^{\gamma}(0) = 29.8 \pm 5.4$ keV b using the polynomial extrapolation given by Hebbard. Mukhamedzhanov *et al.* (2008) conclude that for every 2200 ± 300 cycles of the main CN cycle, one CN catalyst is lost due to this reaction, rather than 880 cycles recommended by Rolfs and Rodney (1974) and 1000 cycles recommended by the NACRE compilations (Angulo *et al.*, 1999). Their result coincides with the R-matrix analysis by Barker (2008b), which yielded a leak rate of 1/2300. Barker's analysis was completed before the ANC data were available and shows a larger spread of S values.

New measurements of this reaction at LUNA by Bemmerer *et al.* (2009) yielded cross sections with improved precision for energies between 90 to 230 keV (Fig. 17). The extent of the agreement between the new LUNA data and the Hebbard data point to a possible unidentified systematic error affecting the low-energy data of Rolfs and Rodney (1974). The value $S_{15}^{\gamma}(0) = 36 \pm 6$ keV b obtained by Mukhamedzhanov *et al.* (2008) may be

⁶ Most of the ^{16}O found in the Sun originates not from hydrogen burning in the Sun itself, but instead from the ashes of helium burning in earlier stars.

regarded as an interim recommendation pending an updated analysis taking full account of new data (e.g., completion of the analyses for recent LUNA and Notre Dame experiments). Further measurements at higher energies are also desirable in order to constrain the R-matrix fits.

4. $^{16}\text{O}(\text{p},\gamma)^{17}\text{F}$

The cross section is dominated by direct capture to the ground and first excited states of ^{17}F . Because the latter is weakly bound, its S-factor rises rapidly at low energies and the ground-state transition plays a minor role. Calculations of the direct capture process by Rolfs (1973), Morlock *et al.* (1997), Baye *et al.* (1998), and Baye and Brainin (2000) give a quantitative account of the energy dependence of both transitions. Baye *et al.* (1998) calculate $S_{16}^{\gamma}(0)$ with two choices for the nuclear force, obtaining $S_{16}^{\gamma}(0) = 10.2$ and 11.0 keV b when normalized to the data of Rolfs (1973) and Morlock *et al.* (1997). The value adopted here is $S_{16}^{\gamma}(0) = 10.6 \pm 0.8$ keV b and the derivative is $S_{16}^{\gamma\prime}(0) = -0.054$ b. A recent reevaluation by Iliadis *et al.* (2008) using both R-matrix theory and a potential model yielded reaction rates at temperatures $\geq 10^7\text{K}$ that are consistent with these values (Angulo *et al.*, 1999), but with a lower assigned uncertainty.

5. $^{17}\text{O}(\text{p},\alpha)^{14}\text{N}$

The $^{17}\text{O}(\text{p},\alpha)^{14}\text{N}$ reaction closes branch II of the CNO bi-cycle. The reaction rate at solar energies is dominated by a subthreshold resonance at $E_R = -3.1$ keV and a resonance at $E_R = 65.1$ keV. Several recent experiments have clarified the strength and location of a 2^- resonance at 183.3 keV that plays a significant role at the higher temperatures characteristic of novae and asymptotic giant branch stars (Chafa *et al.*, 2005, 2007; Moazen *et al.*, 2007). Chafa *et al.* (2007) find a low-energy cross section about a factor of three smaller than that given by Angulo *et al.* (1999), reflecting a re-evaluation of the proton width of the subthreshold resonance. No calculated value for $S_{17}^{\alpha}(0)$ has been published.

6. $^{17}\text{O}(\text{p},\gamma)^{18}\text{F}$

The cross section shows a number of resonances in the range relevant to the hot CNO cycle in novae. Effort has been recently devoted by Chafa *et al.* (2005, 2007) and Fox *et al.* (2004) to measuring the resonance parameters in both $^{17}\text{O}(\text{p},\gamma)^{18}\text{F}$ and $^{17}\text{O}(\text{p},\alpha)^{14}\text{N}$. While the higher-lying resonances are not directly relevant to solar CNO processing, they do have a significant influence in modern interpretations of the work of Rolfs (1973), who measured the direct capture cross section that dominates at solar energies. Fox *et al.* (2005) and Chafa *et al.* (2007) both concluded that significant corrections are required. The recommended $S_{17}^{\gamma}(0)$ in Table XII is taken from Chafa

et al. (2007). The large uncertainty ($\sim 50\%$) makes a new round of measurements of the direct capture cross section desirable.⁷

7. $^{18}\text{O}(\text{p},\alpha)^{15}\text{N}$

The $^{18}\text{O}+\text{p}$ interaction represents a branching point in the CNO cycle: the $^{18}\text{O}(\text{p},\alpha)^{15}\text{N}$ reaction leads to a recycling of CN catalytic material, while $^{18}\text{O}(\text{p},\gamma)^{19}\text{F}$ may lead to a loss of this material, depending on the fate of the produced ^{19}F . Nine resonances below 1 MeV influence the astrophysical rate for $^{18}\text{O}(\text{p},\alpha)^{15}\text{N}$, with those at 20, 144, and 656 keV dominating (Angulo *et al.*, 1999). The presence of strong resonances in the astrophysical regime makes extraction of a value for $S_{18}^{\alpha}(0)$ inappropriate.

The strength of the 20-keV resonance had been known only from spectroscopic measurements performed by Champagne and Pitt (1986) through the transfer reaction $^{18}\text{O}(^3\text{He},\text{d})^{19}\text{F}$ and through the direct capture reaction $^{18}\text{O}(\text{p},\gamma)^{19}\text{F}$ measured by Wiescher *et al.* (1980). The cross section at 20 keV is a factor $\sim 10^{11}$ smaller than the one at 70 keV owing to the Coulomb barrier penetration factor. This makes a direct measurement of the cross section impossible with present-day nuclear physics facilities. Furthermore the spin and parity of the 8.084 MeV level in ^{19}F (corresponding to a 90 keV resonance in the $^{18}\text{O}(\text{p},\alpha)^{15}\text{N}$ cross section) was not known. In order to reduce the nuclear uncertainties affecting the reaction rate, which La Cognata *et al.* (2008) estimated at about an order of magnitude, a new round of measurements has been made with the TH method by La Cognata *et al.* (2008, 2009, 2010). The deduced strength of the 20 keV resonance $\omega\gamma = 8.3_{-2.6}^{+3.8} \times 10^{-19}$ eV eliminates much of the broad range given by NACRE (Angulo *et al.*, 1999), $\omega\gamma = 6_{-5}^{+17} \times 10^{-19}$ eV, and decreases the uncertainty of the reaction rate by about a factor 8.5 (La Cognata *et al.*, 2008, 2009, 2010). In addition, the spin ($3/2^-$) and strength of the 90-keV resonance, which was seen in the work of Lorentz-Wirzba *et al.* (1979), were determined. The La Cognata *et al.* (2008, 2009, 2010) and Lorentz-Wirzba *et al.* (1979) strengths agree.

XII. INDIRECT METHODS AND THEIR VALIDATION

Three classes of experiments contribute to our understanding of solar fusion reactions, direct cross section measurements, indirect methods, and ancillary nuclear structure techniques for determining the properties of resonances (energies, γ and particle widths, and spins and parities). Indirect methods involve the use of nuclear reactions related to, but not identical to, the solar

⁷ Note in proof: The direct capture cross section was recently extracted from new measurements between lab energies of 193 and 519 keV (Newton *et al.*, 2010).

TABLE XII Summary of updates to S-values and derivatives for CNO reactions.

Reaction	Cycle	S(0) keV b	S'(0) b	S''(0) keV ⁻¹ b	References
$^{12}\text{C}(p, \gamma)^{13}\text{N}$	I	1.34 ± 0.21	2.6×10^{-3}	8.3×10^{-5}	Recommended: Solar Fusion I
$^{13}\text{C}(p, \gamma)^{14}\text{N}$	I	7.6 ± 1.0 7.0 ± 1.5	-7.83×10^{-3}	7.29×10^{-4}	Recommended: Solar Fusion I NACRE: Angulo <i>et al.</i> (1999)
$^{14}\text{N}(p, \gamma)^{15}\text{O}$	I	1.66 ± 0.12	-3.3×10^{-3}	4.4×10^{-5}	Recommended: this paper
$^{15}\text{N}(p, \alpha)^{12}\text{C}$	I	$(7.3 \pm 0.5) \times 10^4$	351	11	Recommended: this paper
$^{15}\text{N}(p, \gamma)^{16}\text{O}$	II	36 ± 6 64 ± 6 29.8 ± 5.4			Mukhamedzhanov <i>et al.</i> (2008) Rolfs and Rodney (1974) Hebbard (1960)
$^{16}\text{O}(p, \gamma)^{17}\text{F}$	II	10.6 ± 0.8	-0.054		Recommended: this paper
$^{17}\text{O}(p, \alpha)^{14}\text{N}$	II		Resonances		Chafa <i>et al.</i> (2007)
$^{17}\text{O}(p, \gamma)^{18}\text{F}$	III	6.2 ± 3.1	1.6×10^{-3}	-3.4×10^{-7}	Chafa <i>et al.</i> (2007)
$^{18}\text{O}(p, \alpha)^{15}\text{N}$	III		Resonances		See text
$^{18}\text{O}(p, \gamma)^{19}\text{F}$	IV	15.7 ± 2.1	3.4×10^{-4}	-2.4×10^{-6}	Recommended: Solar Fusion I

reactions under study, as tools to probe properties of the solar reactions. References have been made in this review to three indirect methods, asymptotic normalization coefficients, Coulomb dissociation, and the Trojan horse method. As the connection between the indirect observable and the solar reaction of interest must be established through reaction theory, such methods entail a greater degree of model dependence, impacting systematic uncertainties. But indirect methods also have many virtues: they can be applied when direct measurements are difficult or impossible, have systematic uncertainties that are different from those of direct measurements, and provide supplementary information that can constrain R-matrix and other models used in the extrapolation of data from direct measurements. The role of indirect measurements in validating and constraining models is apparent from the discussions, for example, of Sec. XI.A.

A. The asymptotic normalization coefficient method

The asymptotic normalization coefficient method constrains $S(0)$ by exploiting the peripheral nature of many radiative capture reactions in nuclear astrophysics. Because of Coulomb and/or centrifugal barriers, most (p, γ) and (α, γ) reactions are peripheral at solar energies. The cross section for a nonresonant radiative capture reaction $A(p, \gamma)B$ at zero relative energy depends only on the long-distance behavior of the $p+A$ wave function (and on the overlap of that extended wave function with B). The detailed short-range behavior of the scattering state $p+A$ or bound state B , governed by the strong interaction and nuclear length scales, are not relevant to the reaction mechanism. The bound-state wave function at long distances will contain a component corresponding to two separated clusters, p and A , with the cluster relative radial motion given by a Whittaker function. The

asymptotic normalization coefficient (ANC) is defined as the amplitude of this component (apart from an overall phase) (Mukhamedzhanov and Timofeyuk, 1990; Xu *et al.*, 1994). A distinct ANC will govern the nonresonant capture into each final state, i.e., the ground or bound excited states of B . Therefore, if one can identify another nuclear reaction that includes the vertex $A + p \leftrightarrow B$ and is sensitive only to the tail of the radial overlap function, the needed ANC can be determined from that reaction. This measurement in a different system then determines the radiative capture cross section at zero relative energy (Mukhamedzhanov *et al.*, 2001), up to small corrections determined by the scattering wave function and the potential in the continuum (Capel and Nunes, 2006; Typel and Baur, 2005). While the method is limited to $S(0)$, providing a data point below the Gamow peak, this often complements the data from direct measurements, which are frequently limited to energies above the Gamow peak.

In most applications, the ANC is deduced from transfer reactions. The extraction relies on the distorted wave Born approximation (DWBA) and the direct proportionality between the transfer cross section and the square of the ANC. Provided that the transfer reaction is completely peripheral and the measured angular distributions are well described within the single-step DWBA, the ANC can be extracted. The main source of uncertainty comes from the optical model description, typically $\gtrsim 10\%$ for reactions above the Coulomb barrier. For this reason, it is often important to also measure the elastic channel of the corresponding transfer reaction over a wide angular range, to help constrain optical model parameters. Investigations of effects beyond the single-step DWBA arising from target excitation suggest that deformed targets with strong couplings to low-lying excited states are not good candidates for the ANC method (Azhari *et al.*, 2001). Some of the applications of the

method involve loosely bound nuclei, opening up the possibility of multi-step processes through continuum states as viable alternatives to the direct reaction mechanism. So far there has only been one reaction for which the magnitude of this effect has been evaluated; in this case it was found to be negligible (Moro *et al.*, 2003), but a more systematic study should be done.

In Solar Fusion I the $^{16}\text{O}(p,\gamma)^{17}\text{F}$ reaction was identified as a good test for the method. As a consequence, the $^{16}\text{O}(^3\text{He},d)^{17}\text{F}$ reaction was measured at 30 MeV. The angular distributions of the ground state and the first excited state were well described within the DWBA and the inferred S factors agreed with the radiative capture data to better than 9% (Gagliardi *et al.*, 1999).

There have been many subsequent applications of this method, mostly involving peripheral transfer reactions on intermediate mass targets. Here we focus on those relevant to validating the method for solar fusion reactions. Two transfer reactions, $^{10}\text{B}(^7\text{Be},^8\text{B})^9\text{Be}$ and $^{14}\text{N}(^7\text{Be},^8\text{B})^{13}\text{C}$, were used to extract the ANC for $S_{17}(0)$ (Azhari *et al.*, 1999a,b). For both targets, the peripheral nature of the transfer reactions were checked carefully by evaluating the sensitivity of the extracted ANC to the single particle parameters of the binding potential in the DWBA analysis. Similar analyses have been done by invoking a radial cutoff in the distorted wave calculation (Fernandez *et al.*, 2000; Mukhamedzhanov *et al.*, 1997). In Tabacaru *et al.* (2006) a joint analysis was performed, yielding $S_{17}(0)=18.0 \pm 1.9$ eV b, which can be compared to the best value from direct measurements, $20.8 \pm 0.7 \pm 1.4$ eV b. In addition, the low-energy reaction $^7\text{Be}(d,n)^8\text{B}$ at $E_{\text{lab}}=7.5$ MeV (Liu *et al.*, 1996; Ogata *et al.*, 2003) was studied, but difficulties were encountered in the analysis. The (d,n) reaction model depends on the poorly constrained exit-channel neutron optical potential. In addition, the use of low energies, necessary to satisfy the peripherality condition given the low Z of the deuteron, leads to significant compound nuclear contributions, introducing additional uncertainties.

This review includes several illustrations of the use of ANC determinations to validate R-matrix descriptions of direct reaction data. In Sec. XI.A the example of the subthreshold-state (6.79 MeV) contribution to $^{14}\text{N}(p,\gamma)^{15}\text{O}$ is described in some detail: the ANC determined from the R-matrix fit is in good agreement with that extracted by Bertone *et al.* (2002) and Mukhamedzhanov *et al.* (2003) from $^{14}\text{N}(^3\text{He},d)^{15}\text{O}$. Analogous work using $^{15}\text{N}(^3\text{He},d)^{16}\text{O}$ to study $^{15}\text{N}(p,\gamma)^{16}\text{O}$ is discussed in Sec. XI.B.

As ANCs can be related to spectroscopic factors, the latter can also be used to parameterize cross sections. However, spectroscopic factors have an additional dependence on the single-particle bound state orbitals assumed in their extraction. Consequently radiative capture reactions parameterized through ANCs and spectroscopic factors have somewhat different uncertainties. Further discussion can be found in Mukhamedzhanov *et al.* (2001) and Bertone *et al.* (2002).

Finally, it should be mentioned that breakup reactions $B + T \rightarrow A + p + T$ can also be used to extract ANCs when they meet the peripherality condition (Trache *et al.*, 2004). However a detailed study of the uncertainties involved in the reaction theory has not yet been completed.

B. The Coulomb dissociation method

Coulomb dissociation (CD), originally proposed as a method for extracting information on astrophysical fusion cross sections by Rebel, was developed theoretically shortly thereafter (Baur *et al.*, 1986). The process occurs when a beam of fast projectiles interacts with a heavy target such as Pb. An energetic virtual photon from the target can then dissociate the projectile, liberating a nucleon or α particle. To the extent that the experimentalist can exploit the kinematics of this process to enhance the contributions from the long-distance exchange of single photons, this process can then be related by detailed balance to the corresponding radiative capture reaction. But several effects complicate this simple picture. Whereas nonresonant radiative captures generally proceed almost exclusively by $E1$ transitions, the strong $E2$ field in CD can be important. Moreover, the simple radiative capture/CD correspondence is complicated by multiple photon exchange and by the strong interaction, which can lead to nuclear diffraction dissociation and Coulomb-nuclear interference. Strong interaction effects can be reduced by restricting measurements to small angles, where long-range electromagnetic transitions dominate nuclear interactions. Multiple photon exchange (also known as post-acceleration) can be reduced by increasing the beam energy, shortening the time the projectile spends in the target's field.

In Solar Fusion I a proposal was made to test the validity of the CD method quantitatively through comparison with a corresponding radiative capture measurement. The radiative capture reaction was to have suitable properties, including a low Q value, a nonresonant $E1$ reaction mechanism, reactants with similar mass/charge ratios, and a final nuclear state with relatively simple structure. Although no perfect reaction was identified, $^7\text{Be}(p,\gamma)^8\text{B}$ appears to be a good choice. Several new measurements were made, and a great deal of theoretical effort was invested in their interpretation and in extracting the S factor. This work is summarized in Sec. IX.C and will not be discussed further here, except to repeat the conclusion that, while in several cases agreement between the CD method and direct measurements has been demonstrated at the 10-20% level, remaining uncertainties in the magnitude of $S(0)$, in independently determining the shape of $S(E)$, and in the theory argue that the inclusion of CD data in the current S_{17} evaluation would be premature.

Efforts also have been made to validate the CD method for the $^{14}\text{C}(n,\gamma)^{15}\text{C}$ reaction. Although this reaction is

not directly relevant to solar fusion, the radiative capture rate is now known to a precision of $\sim 10\%$ (Reifarth *et al.*, 2008). The corresponding CD of ^{15}C on ^{208}Pb has recently been remeasured at RIKEN (Nakamura *et al.*, 2009). Reaction models predict that the ^{15}C breakup has an insignificant nuclear contribution and is dominated by $E1$ transitions, provided the analysis is limited to events in which the ^{15}C center-of-mass scattering angle and the relative energy of the breakup fragments are small. Independent analyses of these data (Esbensen, 2009; Summers and Nunes, 2008) find that the neutron capture cross section extracted from CD agrees very well with the direct measurement and has comparable precision. This appears to be a favorable case for the theoretical treatment due to the dominant nonresonant $E1$ reaction mechanism, small $E2$ and nuclear contributions, and relative simplicity of ^{15}C , which can be described reasonably in a single-particle $^{14}\text{C}+n$ potential model. While the agreement in this case is promising, some caution is warranted because the radiative capture measurement has not been confirmed by an independent measurement.

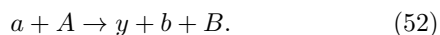
The ANC and CD methods are both well suited to measurements with low intensity radioactive beams because the transfer reaction and CD cross sections are much larger than the corresponding radiative capture reactions. Moreover, they are both applicable to radiative capture reactions.

C. The Trojan Horse method

The Trojan Horse (TH) method (Baur, 1986; Spitaleri *et al.*, 2004) is an indirect technique to determine the astrophysical S factor for rearrangement reactions. It allows inference of the cross section of the binary process



at astrophysical energies through measurement of the TH reaction



The measurement is done with quasi-free kinematics, in which a TH a having a strong $x + y$ cluster structure is accelerated to energies above the Coulomb barrier. After penetrating the Coulomb barrier, the nucleus a breaks up, leaving x to interact with the target A while the projectile fragment y flies away. From the measured cross section of reaction (52), the energy dependence of the binary subprocess (51) is determined. While the reaction (52) can occur in a variety of ways, the TH reaction mechanism should dominate in a restricted region of three-body phase space in which the momentum transfer to the spectator nucleus y is small, i.e., quasi-elastic scattering conditions apply. Since the transferred particle x in the TH reaction (52) is virtual, its energy and momentum are not related by the on-shell equation $E_x = p_x^2/(2m_x)$.

The main advantage of the TH method is that the low-energy cross sections can be deduced from a reaction

that is not strongly suppressed by Coulomb barriers or strongly altered by electron screening (Assenbaum *et al.*, 1987; Spitaleri *et al.*, 2001). The TH cross section can be used to determine the energy dependence of the bare nuclear S factor for the binary process (51) down to zero relative kinetic energy of x and A . The absolute value of $S(E)$, however, must be determined by normalizing to direct measurements at higher energies. To ensure quasi-free kinematics one should measure the momentum distribution of the spectator fragment y and the angular distributions of the fragments of the binary sub-reaction to check for contributions from non-TH mechanisms. As a check on distortions due to final state interactions, the momentum distribution of the spectator can be measured and compared with that of the spectator in the free TH nucleus (Pizzone *et al.*, 2009). Final state distortions can be treated in DWBA calculations (La Cognata *et al.*, 2010).

The uncertainty of the $S(E)$ extracted from the TH method includes contributions from statistics, uncertainties due to the need to normalize the TH data, finite experimental energy resolution, and backgrounds due to other reaction mechanisms. The first successful test of the TH method was conducted for the $^7\text{Li}(p, \alpha)^4\text{He}$ reaction (Lattuada *et al.*, 2001). The extracted $S(0) = 55 \pm 6$ keV b includes an uncertainty of 10% from the normalization of the TH data to the direct data (Engstler *et al.*, 1992) and 5.5% from other sources, mainly statistics. In addition, in Sec. XLB.2 we compare results for TH and direct determinations of the cross section for $^{15}\text{N}(p, \alpha)^{12}\text{C}$. Although promising, the TH method requires further validation by experiment, and its significant dependence on reaction theory calls for more investigation of the approximations by which TH reactions are related to their astrophysical analogs.

The TH method also provides an important test of electron screening potentials, which can be obtained from comparisons of direct and TH cross sections.

D. Summary

The three indirect techniques discussed here provide alternatives to direct measurements of astrophysically important reaction rates. In some cases they provide the only practical means for determining stellar reaction rates. While their connection to solar reactions requires an additional level of reaction theory, experimental tests of their validity have often yielded agreement with direct measurements within 10-20%. Significant progress has been made since Solar Fusion I in benchmarking indirect techniques. Indirect methods are best applied to cases where there is a supporting body of experimental data that can be used to constrain the needed nuclear model input, such as optical potentials and effective interactions.

In actual practice, the distinction between direct and indirect methods is not sharp, but rather a matter of de-

gree. While a measurement may probe a stellar reaction directly, it often does so at a different energy or in a different screening environment. Thus direct methods also depend on reaction theory, to extrapolate data to stellar energies or, in cases like S_{33} where data in the Gamow peak have been obtained, to correct for the effects of screening in terrestrial targets. Still, the connection to stellar physics is typically much closer. Models play a less important role, and increasingly the needed modeling can be done microscopically, as direct measurements involve light nuclei.

For this reason we maintain a distinction between direct and indirect methods in this review, basing our recommendations on results from the former. However, indirect methods have had a significant impact on our analysis: they have been used in this review to constrain R-matrix fits to direct data and to check the consistency of conclusions based on analyses and modeling of direct data.

We recommend extending the benchmarking of indirect methods against direct methods over a wider range of reactions, as more data would be useful in quantifying the uncertainties in such techniques.

XIII. FUTURE FACILITIES AND CURRENT CAPABILITIES

We noted in the introduction to this review the crucial role nuclear astrophysics experiments have played in the development of a quantitative SSM and in motivating solar neutrino experiments. We outlined the important goals that remain in this field – tests of weak interactions and of solar properties that make use of high precision solar neutrino measurements, helioseismology mappings of $c(r)$, and detailed solar modeling. There are also a host of related problems – Big Bang nucleosynthesis, red-giant evolution, the evolution of supernova progenitors, and a variety of transient explosive phenomena in astrophysics – where a quantitative understanding of the nuclear physics is essential. This chapter deals with the experimental facilities that have allowed progress in this field, and discusses the instrumental developments that will be important if we are to continue a similar rate of progress over the next decade.

The measurements that support the development of a quantitative theory of main-sequence stellar evolution primarily involve low energy proton- and α -capture reactions that traditionally have been studied with small accelerators. The machines must be able to provide proton or α beams of sufficient intensity to allow cross section measurements near the very low energies of the Gamow peak.

Because low energy charged-particle reaction cross sections are small, experiments must be designed for signal rates much smaller than background rates associated with cosmic rays, the natural radioactivity of the laboratory environment, and the induced activity arising

from beam interactions with target impurities. The ambient background can be roughly divided into muons and neutrons associated with cosmic rays, and γ rays and neutrons from natural radioactivity (uranium, thorium, potassium, and radon from surrounding geology). Today most charged-particle reaction measurements for nuclear astrophysics are being performed at above ground facilities, with various techniques then employed to mitigate backgrounds. The common technique is passive shielding around the detection region. Typically a layered combination of lead, copper, and polyethylene is used to reduce γ and neutron backgrounds within detectors with relatively small volumes. But additional strategies are available to further reduce backgrounds and thus allow measurements at energies nearer those relevant for astrophysics, including

1. use of more sophisticated detector setups with both passive and active shielding and with triggers to aid in event identification;
2. measurements in inverse kinematics using recoil separators in facilities above ground; and
3. measurements with direct kinematics using accelerators that are sufficiently deep underground to suppress penetrating cosmic-ray muons and the neutrons and other secondary activities they induce.

Passive shielding, active shielding, and coincidence gating techniques can enhance event identification and significantly reduce backgrounds in above-ground laboratory environments. As most resonance levels of astrophysical interest decay via γ -cascades (Rowland *et al.*, 2002) $\gamma\gamma$ -coincidence techniques can be used to significantly reduce the single- γ background. Q-value gating techniques, where only events in coincidence with the summing peak of the radiative capture reaction are accepted (Couture *et al.*, 2008), can allow one to extend measurements to lower energies, but at the cost of a decreased overall counting efficiency due to the coincidence requirement.

Alternative techniques have been developed to reduce backgrounds without such losses in detection efficiency. Two ideas that have demonstrated their promise are measurements in inverse kinematics – one detects the reaction recoil particles rather than the light particles or γ s of the reaction – and measurements in underground environments. Below we describe past and current experience with these two techniques as well as the future facilities, in progress or planned, that would allow these techniques to be further advanced.

A. Inverse kinematics measurements using recoil separators

In an inverse-kinematics experiment a heavy ion induces (p,γ) or (α,γ) reactions when it interacts in a hydrogen or helium gas target. The projectiles and reaction products move within a narrow cone in the forward

direction. A recoil separator is used to reject the primary beam while focusing the reaction products for detection. The charged recoils can be detected with higher efficiency than the γ s produced in conventional proton- or α -beam experiments. By detecting the γ s in coincidence with the reaction products, dramatic reductions in backgrounds can be achieved. Existing recoil separator facilities for nuclear astrophysics experiments include DRAGON at ISAC in TRIUMF (Hutcheon *et al.*, 2003), the Daresbury separator at HRIBF in Oak Ridge (Fitzgerald *et al.*, 2005), ERNA at the DTL in Bochum (Rogalla *et al.*, 2003), and the RMS at KUTL in Kyushu, Japan (Sagara *et al.*, 2005).

Recoil separators are not useful for (α, n) reactions because separator acceptance angles are too small, given the momentum transfer in this process.

Recoil separators present several experimental challenges (Rogalla *et al.*, 2003), particularly for the low energies important in solar fusion cross section measurements. At such energies, the energy spread and the angular aperture are, for most solar fusion reactions, larger than the acceptance of any of the recoil separators cited above.

The following conditions must be fulfilled in experiments on absolute cross sections:

- the transmission of the recoils must be exactly known and should ideally be 100%;
- the charge-state distribution of the recoil products must be known or the reaction must be studied for all charge states produced (Di Leva *et al.*, 2008); and
- the interaction region must be well defined.

Therefore, experiments coming on-line in the near future are all planning to use compact high-density gas-jet targets instead of extended windowless gas targets.

Recoils of solar fusion reactions typically have relatively large emission angles and large energy spreads, both of which increase with decreasing reaction energies E , when $E < Q$. The angular distribution of recoils following emission of capture γ -rays of energy E_γ is characterized by an emission cone half-angle of

$$\theta = \arctan \frac{E_\gamma}{p} \quad (53)$$

where p is the momentum of the beam ($c \equiv 1$). The total energy spread ΔE of the recoil accompanying γ emission is

$$\frac{\Delta E}{E} = \frac{4E_\gamma}{p}. \quad (54)$$

Furthermore a large spatial separation between the reaction products and the beam is required, as the primary beam intensity is typically many orders of magnitude larger than that of the recoiling reaction products.

A clean separation is difficult for recoils with large energy spreads, making low-energy solar fusion reactions particularly challenging. Recoil separators are therefore more typically used for higher energies characteristic of helium- or explosive hydrogen-burning reactions. For example, the recoil-separator measurements of S_{34} at the ERNA facility in Bochum were limited to data above a center-of-mass energy of 700 keV (Di Leva *et al.*, 2009). Below this energy the angular divergence of the recoils exceeds the angular acceptance of the separator, ± 25 mrad (Di Leva *et al.*, 2008).

Two dedicated next-generation separators for low-energy nuclear astrophysics studies with stable ion beams will soon come on line, the St. George facility at Notre Dame's Nuclear Science Laboratory (Couder *et al.*, 2008) and the ERNA separator at the CIRCE facility in Caserta, Italy. The latter is based on a redesign of the Bochum ERNA separator (Rogalla *et al.*, 2003). Both separators feature large acceptances in angle and energy and will be equipped with high density gas-jet targets to ensure well defined interaction regions. Figure 18 shows the layout of the St. George recoil separator. The design is optimized for low-energy radiative α -capture reactions important to stellar helium burning. It has a large angular acceptance of ± 40 mrad, an energy acceptance of $\pm 7.5\%$, and a mass resolving power $M/\Delta M \sim 100$ (Couder *et al.*, 2008).

B. Underground facilities

In all direct-kinematics capture-reaction measurements using γ or neutron spectroscopy, whether performed above ground or underground, sources of environmental radioactivity must be controlled. Background sources include radioactivity from intrusions and impurities in the rock and from construction materials, as well as sources intrinsic to targets and detectors. External sources can be reduced by careful shielding of the target and the detector environment. In addition, beam-induced backgrounds (e.g., backgrounds from activation of impurities in the target) must be controlled through careful ion beam optics and choice of vacuum component materials. Active shielding techniques and complex event identification can also help.

In surface facilities, however, the most difficult backgrounds are frequently those associated with cosmic rays. This background can be removed by exploiting the natural shielding provided by the rock overburden in underground sites. The improvements possible with this strategy have been demonstrated by the 50 keV LUNA I and 400 keV LUNA II programs at Gran Sasso. The laboratory's depth, ~ 3.0 km.w.e. (kilometers of water equivalent, flat-site equivalent (Mei and Hime, 2006)), reduces the fluxes of muons and secondary neutrons, relative to surface values, by factors of 10^6 and 10^3 , respectively. Consequently, the LUNA I collaboration (Bonetti *et al.*, 1999) was able to map S_{33} throughout the Gamow peak:

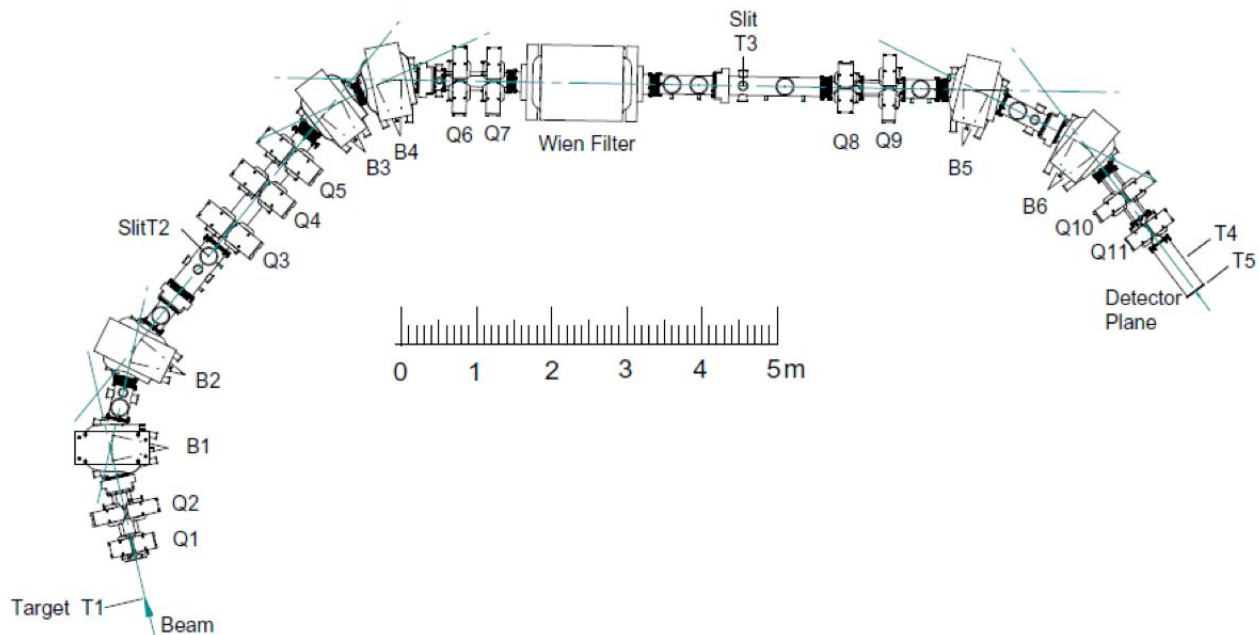


FIG. 18 Layout of the St. George recoil separator.

a counting rate of one event per month was achieved at the lowest energy, $E = 16$ keV, with an uncertainty of 20 fb or 2×10^{-38} cm². Other critical pp chain and CNO cycle cross sections were made at energies far lower than previously possible (Formicola *et al.*, 2003; Greife *et al.*, 1994; Imbriani *et al.*, 2005; Junker *et al.*, 1998).

The successes of LUNA have inspired plans for the new underground facilities we discuss in this section. Figure 19 shows a schematic of the present LUNA II set-up in Gran Sasso, which consists of a commercial 400 kV accelerator, a windowless gas target, and a solid target line.

Nuclear astrophysics has rather modest depth requirements. The hadronic cosmic-ray component is quickly attenuated, leaving penetrating high-energy muons as the dominant source of background at depth. These muons interact in the rock to produce neutrons and a continuous spectrum of high energy γ s. Thus the main requirement is an overburden sufficient to reduce muon-associated activities to a level well below natural background levels associated with activities in the laboratory's rock and concrete walls. The neutron fluxes in Gran Sasso, $\sim 4 \times 10^{-6}$ /cm²/s (Bemmerer *et al.*, 2005; Laubenstein *et al.*, 2004), and in Spain's underground laboratory Canfranc, $(3.80 \pm 0.44) \times 10^{-6}$ /cm²/s (Carmona *et al.*, 2004), are almost entirely due to local radioactivity. Taking these deep-laboratory values as typical of the environmental background component, one can determine the depth necessary to reduce the cosmic-ray-associated neutron contribution to 1% of the total. The simulations of Mei and Hime (2006) yield ~ 1.5 km.w.e. (flat site equivalent).

lent).

Similar results are found for the γ -ray flux. The LUNA $^{14}\text{N}(p,\gamma)$ counting goal was 10^{-4} counts/keV/hr. The cosmic-ray muon-induced rate at 1.5 km.w.e. would be approximately an order of magnitude lower (Haxton *et al.*, 2007). As almost all deep physics laboratories now operating are at depths in excess of 1.5 km.w.e, one concludes that many locations are suitable for nuclear astrophysics – at least until order-of-magnitude reductions in the laboratory environmental neutron and γ -ray background are made.

Based on the success of the LUNA collaboration, several underground accelerator facilities are now being proposed. Table XIII shows the parameters of these facilities. The plans reflect design improvements from fifteen years of experience with LUNA.

The present LUNA facility is small and limited to the measurement of proton- and α -capture reactions below 400 keV, with typical beam currents between 100 and 200 μA . The available beam current has limited the statistical accuracy of data taken at the lowest energies. In addition, many reactions have complex resonance structures that must be adequately mapped, to provide the information needed to extrapolate cross sections to Gamow energies. This requires measurements over a broader energy range than is currently available at LUNA. Therefore, the LUNA collaboration has submitted a letter of intent for the installation of a higher energy accelerator that would allow the LUNA program to grow beyond solar fusion physics. This upgrade proposal is currently

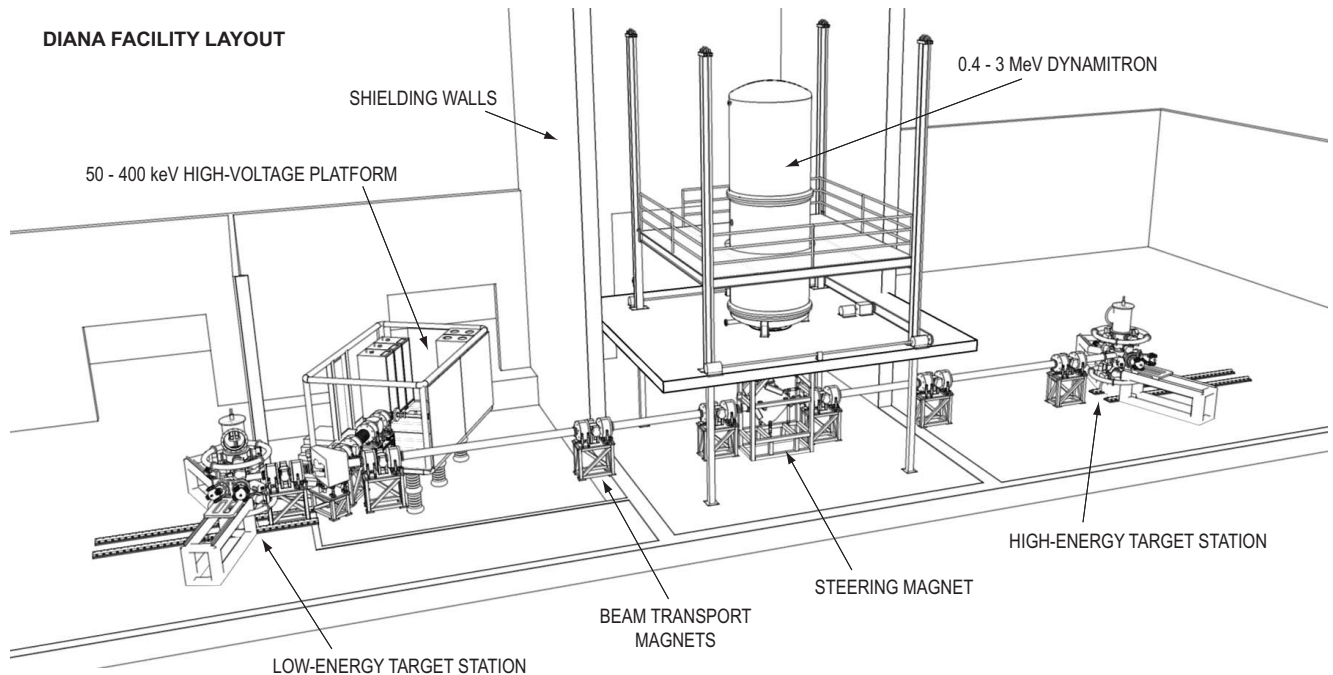


FIG. 20 Proposed layout of the DIANA facility.

arise when cross sections are measured at different facilities, with different targets and detector configurations. The accelerators will have a substantial overlap in their energy ranges due to the design of the ion source on the high-voltage platform of the low energy accelerator. This will reduce uncertainties in combining data sets. The pro-

posed beam current of several mA is at least one order of magnitude higher than any presently available. This enhances counting rates, but also requires increased attention to beam-induced backgrounds as well as targets capable of handling the power. Figure 20 shows DIANA’s conceptual design.

Acknowledgments and Dedication

We would like to thank the Institute for Nuclear Theory for hosting and supporting the Solar Fusion II workshop and for providing technical assistance during the writing of this review. We thank A. Champagne, P. Descouvemont, A. Di Leva, and J. Toebbe for their generous help, including many discussions and advice or assistance with fitting. The research described in this review was supported by various agencies including the U.S. Department of Energy, the U.S. National Science Foundation, the Deutschen Forschungsgemeinschaft (cluster of excellence “Origin and Structure of the Universe” and grant SFB 634) and the Alliance Program EMMI of the Helmholtz Association.

We dedicate Solar Fusion II to John Bahcall, who proposed and led the effort on Solar Fusion I. John’s advocacy for laboratory astrophysics and his appreciation of its importance to solar neutrinos paved the way for many advances in our field.

Appendix: Treating Uncertainties

A. Introduction

This section describes our method for dealing with discrepant data sets that may occur, for example, when deriving recommended $S(0)$ values from experimental measurements of nuclear reaction cross sections.

While the conventional χ^2 minimization method is adequate for analysing data sets that are in good agreement, there is no rigorous method for dealing with discrepant data sets and their underlying unidentified systematics. But reasonable procedures exist. In Solar Fusion II we adopt the Scale Factor method, here called the inflation factor method (IFM), that is used by the PDG (Amsler *et al.*, 2008). In this method, the fit errors from a conventional χ^2 minimization are inflated by a factor that depends on $\sqrt{\chi^2/\nu}$, where ν is the number of degrees of freedom. This method is well known, widely used, and straightforward to apply.

TABLE XIII Attributes of proposed second-generation underground facilities for nuclear astrophysics.

FACILITY	LUNA Laboratory Underground for Nuclear Astrophysics	DIANA Dakota Ion Accelerators for Nuclear Astrophysics	ELENA Experimental Low-Energy Nuclear Astrophysics	CUNA Canfranc Nuclear Astrophysics Facility
Location	Gran Sasso, Italy	Homestake Mine, USA	Boulby Mine, UK	Canfranc, Spain
Rock type	hard limestone	metamorphic rock	salt	hard limestone
Depth (km.w.e, flat site)	3.1	4.3	2.8	~ 2.0
Low energy accelerator	50-400 keV 0.5-1.0 mA RF ion source (p,He ⁺)	50-400 kV HV platform ≥ 10mA ~ ECR ion sources, single, multiply charged	none	none
High energy accelerator	0.4-3.5 MeV electrostatic up to 0.3 mA ECR ion source	0.35-3.0 MeV electrostatic up to 10 mA ECR ion sources single, multiply charged	3.0 MeV accelerator electrostatic 0.5 mA ECR ion source	up to 5.0 MeV electrostatic

While the IFM is the only one discussed in the PDG Introduction, alternatives exist. We discuss some examples at the end of this Appendix.

B. The inflation factor method

The IFM addresses systematic uncertainties when combining results from different and possibly discrepant data sets. The method inflates errors in proportion to the quoted errors originally given by the experimenters.

Discrepant data may be defined by the P -value of the fit, where $P \equiv P(\chi^2, \nu)$ is the probability of obtaining a χ^2 value at least as large as the observed value. The inflation factor is conventionally chosen to be $\sqrt{\chi^2/\nu}$ and is commonly applied in cases where $\chi^2/\nu > 1$. We use an alternative inflation factor $\sqrt{\chi^2/\chi^2(P=0.5)}$ to account for the fact that, for small ν and non-discrepant data, the expected value of χ^2 is smaller than unity. For large ν , the two scaling factors are equivalent.

The IFM scales all experimental errors by the same fractional amount, resulting in equal internal and external errors on the mean. Because one generally cannot identify a specific mechanism accounting for discrepant data, this procedure (like all other procedures) has no rigorous mathematical justification. However qualitative arguments support its reasonableness. As the method maintains the relative precision of discrepant data sets, it apportions a larger absolute fraction of the identified systematic error to the less precise data sets. This is consistent with naive expectations that a large, unidentified systematic error is more likely to “hide” within a low-precision data set than within a high-precision one, given the advantages a high-precision data set offers an

experimentalist who does “due-diligence” cross checks to identify systematic errors. The IFM is generally considered the most appropriate procedure in the absence of information that would support alternatives, such as omitting certain data, or increasing errors on some data but not others.

We employ error inflation whenever $\chi^2 > \chi^2(P=0.5)$, and no error scaling otherwise. With this general rule, errors are inflated a bit even when χ^2 is only slightly in excess of $\chi^2(P=0.5)$, despite the lack of compelling evidence of discrepancy in such a case. This procedure yields a continuous formula and avoids the introduction of an arbitrary threshold for inflation.

In extreme cases one may obtain errors that are deemed too small. For example, when analyzing data containing a few results with small errors and a larger number of results with large errors, the large-error data will reduce the error on the mean by increasing ν , even though they may have little effect on the central value. In such a case, we agree with the PDG’s recommendation that, to mitigate this problem, data be excluded which have an error larger than some (arbitrary) limit, specifically $3\delta\sqrt{N}$, where N is the number of measurements and δ is the unscaled error on the mean. However, applying this exclusion criterion may not be adequate to resolve this difficulty in all cases.

While the IFM makes no assumptions about the reasons for discrepant data, in actual applications it may be apparent that not all data sets are equally reliable. In such cases judgment is necessary, and data selection is appropriate. Data should be discarded if the error analysis is poorly documented or inadequate. Data may be discarded if the procedure used to generate them involves questionable assumptions, or if corrections were not made

for effects now known to be important. Data errors may be modified (e.g. increased) if such new information is available.

C. Application of the inflation factor method

The following is based on the discussion in the Introduction of the PDG compilation of Amsler *et al.* (2008):

1. In general, statistical and systematic data errors should be identified and specified separately. Systematic errors should be subdivided into varying (random) and common-mode (normalization) errors. For a single data set, normally the statistical and *varying* systematic errors should be combined in quadrature and used as data errors in a χ^2 minimization to determine unknown parameters. The resulting fit error(s) should be multiplied by the inflation factor (see below). The common-mode error is then folded in quadrature with the inflated fit error to determine the overall normalization error.

For multiple data sets, the systematic errors should be examined to determine if they are independent among the different data sets. Parameters determined from multiple, independent data sets may be combined in a separate χ^2 minimization in which each parameter value is characterized by its total error determined by combining statistical and systematic (normalization) errors in quadrature. Again, this fit error should be multiplied by the inflation factor. If the systematic errors in different data sets are correlated, then this correlation must be taken into account in the fitting. A convenient method for handling correlations is described in the 2008 PDG compilation.

2. Whenever $\chi^2 > \chi^2(P = 0.5)$ the fit errors should be increased by the multiplicative inflation factor $\sqrt{\chi^2/\chi^2(P = 0.5)}$, where $\chi^2(P = 0.5)$ is the χ^2 corresponding to a P value of 0.5 for ν degrees of freedom. The χ^2 and ν should be stated, along with the inflation factor when it is larger than unity. Large reported inflation factors serve to alert the reader to potential problems.
3. Data with uncertainties larger than $3\sqrt{N}\delta$, where N is the number of measurements and δ is the (unscaled) error on the mean should be excluded. One should be aware of possible error underestimation in certain cases as mentioned above. The resolution of such situations may require additional judgment.

D. Other methods

Other error analysis methods follow somewhat different strategies. The cost function methods used in CO-DATA analyses (Cohen and Taylor, 1987) are designed

to reduce the χ^2 by selective re-weighting of data; i.e. by increasing the errors nonuniformly on the data, in such a manner as to minimize the “cost”, i.e. the error on the mean. Alternatively, D’Agostini (1994) has advocated a procedure for fitting multiple data sets in which one minimizes the sum of a data χ^2 and a normalization χ^2 .

One method that has been applied to the analysis of solar fusion cross section is that of Cyburt (2004) (see also Cyburt and Davids (2008)). This approach introduces a “discrepancy error”, σ_{disc} , that is added in quadrature with the normalization errors of individual experiments when fitting mixed data sets. Effectively this procedure distributes the unexplained discrepancy equally over the data sets, regardless of their stated accuracy, in contrast to the PDG procedure, which assigns the discrepancy in way that preserves the relative stated accuracy of data sets. The Cyburt (2004) method leads, in cases where there is excess dispersion, to increased de-weighting of the more precise data points, compared to the IFM. In addition, the contribution of σ_{disc} to the error of the mean does not decrease as the number of measurements N increases.

The Cyburt (2004) and IFM methods reflect two limits in how one apportions an unexplained discrepancy among data sets: one could construct other models that interpolate between these two limits (equal vs. proportionate allocation of the discrepancy error). The argument for the IFM procedure has been stated previously: it is easier to miss a large systematic error within a low-quality data set than within a high-quality one. In addition, it avoids a situation where archival data of poor quality, containing an unidentified systematic error, unduly impact the weight that would otherwise be accorded a new experiment of exceptional quality – thereby inappropriately diluting the impact of the best results. Alternatives to the IFM tend to produce roughly equivalent results unless the discrepancies among data sets are large. We are fortunate in this paper to be dealing with discrepancies that are modest.

References

- Adelberger, E. G., *et al.*, 1998, Rev. Mod. Phys. **70**, 1265.
 Aharmin, B., *et al.*, 2008, Phys. Rev. Lett. **101**, 111301.
 Aharmin, B., *et al.*, 2006, Ap. J. **653**, 1545.
 Ahmad, Q. R., *et al.*, 2001, Phys. Rev. Lett. **87**, 071301.
 Ajzenberg-Selove, F., 1991, Nucl. Phys. A **523**, 1.
 Aliotta, M., 2009, <http://www.fnuc.es/workshop/Presentaciones/Aliotta.pdf>.
 Aliotta, M., *et al.*, 2001, Nucl. Phys. A **690**, 790.
 Alt, E. O., B. F. Irgaziev, and A. M. Mukhamedzhanov, 2003, Phys. Rev. Lett. **90**, 122701.
 Alt, E. O., B. F. Irgaziev, and A. M. Mukhamedzhanov, 2005, Phys. Rev. C **71**, 024605.
 Amsler, C., *et al.* (Particle Data Group), 2008, Phys. Lett. B **667**, 1.
 Andersen, H., and J. F. Ziegler, 1977, *The Stopping and Ranges of Ions in Matter* (Pergamon (N.Y.)).

- Ando, S., T. S. Park, K. Kubodera, and F. Myhrer, 2002, Phys. Lett. B **533**, 25.
- Ando, S., *et al.*, 2008, Phys. Lett. B **668**, 187.
- Andreev, V. A., *et al.* (MuSun Collaboration), 2008, <http://www.npl.uiuc.edu/exp/musun>.
- Angulo, C., and P. Descouvemont, 2000, Phys. Rev. C **61**, 064611.
- Angulo, C., and P. Descouvemont, 2001, Nucl. Phys. A **690**, 755.
- Angulo, C., *et al.*, 1993, Z. Phys. A **345**, 231.
- Angulo, C., *et al.*, 1999, Nucl. Phys. A **656**, 3.
- Angulo, C., *et al.*, 2003, Nucl. Phys. A **716**, 211.
- Arpesella, C., *et al.*, 1996, Phys. Lett. B **389**, 452.
- Asplund, M., N. Grevesse, and A. J. Sauval, 2005, in *Conference Proceedings Vol. 336, Cosmic Abundances as Records of Stellar Evolution and Nucleosynthesis*, edited by T. G. Barnes, III and F. N. Bash (Astronomical Society of the Pacific), p. 25.
- Assenbaum, H. J. K., K. Langanke, and C. Rolfs, 1987, Z. Phys. A **327**, 461.
- Aurdal, A., 1970, Nucl. Phys. A **146**, 385.
- Azhari, A., *et al.*, 1999a, Phys. Rev. Lett. **82**, 3960.
- Azhari, A., *et al.*, 1999b, Phys. Rev. C **60**, 055803.
- Azhari, A., *et al.*, 2001, Phys. Rev. C **63**, 055803.
- Azuma, R. E., *et al.*, 2010, Phys. Rev. C **81**, 045805.
- Baby, L. T., *et al.*, 2003a, Phys. Rev. Lett. **90**, 022501.
- Baby, L. T., *et al.*, 2003b, Phys. Rev. C **67**, 065805.
- Bacher, A. D., and T. A. Tombrello, 1965, Rev. Mod. Phys. **37**, 433.
- Bacrania, M. K., N. M. Boyd, R. G. H. Robertson, and D. W. Storm, 2007, Phys. Rev. C **76**, 055806.
- Bahcall, J. N., 1962, Phys. Rev. **128**, 1297.
- Bahcall, J. N., 1989, *Neutrino Astrophysics* (Cambridge University Press).
- Bahcall, J. N., 1990, Phys. Rev. D **41**, 2964.
- Bahcall, J. N., 1991, Phys. Rev. D **44**, 1644.
- Bahcall, J. N., 1994, Phys. Rev. D **49**, 3923.
- Bahcall, J. N., S. Basu, M. Pinsonneault, and A. M. Serenelli, 2005, Ap. J. **618**, 1049.
- Bahcall, J. N., L. S. Brown, A. V. Gruzinov, and R. F. Sawyer, 2002, A.&A. **388**, 660.
- Bahcall, J. N., and R. Davis Jr., 1982, in *Essays in Nuclear Astrophysics*, edited by C. A. Barnes, D. D. Clayton, and D. Schramm (Cambridge University Press), p. 243.
- Bahcall, J. N., and R. M. May, 1968, Ap. J. **152**, L17.
- Bahcall, J. N., and R. M. May, 1969, Ap. J. **155**, 501.
- Bahcall, J. N., and C. P. Moeller, 1969, Ap. J. **155**, 511.
- Bahcall, J. N., and M. H. Pinsonneault, 1992, Rev. Mod. Phys. **64**, 885.
- Bahcall, J. N., M. H. Pinsonneault, and S. Basu, 2001, Ap. J. **555**, 990.
- Bahcall, J. N., A. M. Serenelli, and S. Basu, 2006, Ap. J. Suppl. **165**, 400.
- Bahcall, J. N., and R. K. Ulrich, 1988, Rev. Mod. Phys. **60**, 297.
- Bahcall, J. N., *et al.*, 1996, Phys. Rev. C **54**, 411.
- Bailey, G. M., *et al.*, 1970, Can. J. Phys. **48**, 3059.
- Baimbetov, B. F., K. T. Nurenkov, and T. S. Ramazanov, 1995, Phys. Lett. A **202**, 211.
- Balamuth, D. P., *et al.*, 1983, Phys. Rev. C **27**, 1724.
- Balantekin, A. B., C. A. Bertulani, and M. S. Hussein, 1997, Nucl. Phys. A **627**, 324.
- Bang, J. M., L. S. Ferreira, E. Maglione, and J. M. Hansteen, 1996, Phys. Rev. C **53**, R18.
- Bardayan, D. W., *et al.*, 2009, Eur. Phys. J. A **42**, 457.
- Barker, F. C., 1971, Aust. J. Phys. **24**, 777.
- Barker, F. C., 1980, Aust. J. Phys. **33**, 177.
- Barker, F. C., 1983, Phys. Rev. C **28**, 1407.
- Barker, F. C., 1989, Aust. J. Phys. **42**, 25.
- Barker, F. C., 1995, Nucl. Phys. A **588**, 693.
- Barker, F. C., 2008a, Phys. Rev. C **78**, 044611.
- Barker, F. C., 2008b, Phys. Rev. C **78**, 044612.
- Barker, F. C., and T. Kajino, 1991, Aust. J. Phys. **44**, 369.
- Barker, F. C., and A. M. Mukhamedzhanov, 2000, Nucl. Phys. A **673**, 526.
- Batkin, I. S., and M. K. Sundaresan, 1995, Phys. Rev. D **52**, 5362.
- Baur, G., 1986, Phys. Lett. B **178**, 135.
- Baur, G., C. A. Bertulani, and H. Rebel, 1986, Nucl. Phys. A **458**, 188.
- Baye, D., 2000, Phys. Rev. C **62**, 065803.
- Baye, D., 2004, Phys. Rev. C **70**, 015801.
- Baye, D., 2005, Nucl. Phys. A **758**, 114.
- Baye, D., and E. Brainis, 2000, Phys. Rev. C **61**, 025801.
- Baye, D., and P. Descouvemont, 1985, Ann. Phys. **165**, 115.
- Baye, D., P. Descouvemont, and M. Hesse, 1998, Phys. Rev. C **58**, 545.
- Becker, H. W., *et al.*, 1982, Z. Phys. A **305**, 319.
- Bedaque, P. F., H. W. Hammer, and U. van Kolck, 1999, Phys. Rev. Lett. **82**, 463.
- Belyaev, V. B., M. Tater, and E. Truhlik, 2007, Phys. Rev. C **75**, 034608.
- Bemmerer, D., *et al.*, 2005, Eur. Phys. J. A **24**, 313.
- Bemmerer, D., *et al.*, 2006a, Phys. Rev. Lett. **97**, 122502.
- Bemmerer, D., *et al.*, 2006b, Nucl. Phys. A **779**, 297.
- Bemmerer, D., *et al.*, 2009, J. Phys. G **36**, 045202.
- Bennaceur, K., F. Nowacki, J. Okolowicz, and M. Pi Oszajczak, 1999, Nucl. Phys. A **651**, 289.
- Bertone, P. F., *et al.*, 2001, Phys. Rev. Lett. **87**, 152501.
- Bertone, P. F., *et al.*, 2002, Phys. Rev. C **66**, 055804.
- Bertulani, C. A., 1996, Z. Phys. A **356**, 293.
- Bertulani, C. A., 2004, Phys. Lett. B **585**, 35.
- Bertulani, C. A., 2005, Phys. Rev. Lett. **94**, 072701.
- Bertulani, C. A., and D. T. de Paula, 2000, Phys. Rev. C **62**, 045802.
- Bettini, S., 2009, <http://www.fnuc.es/workshop/Presentaciones/Bettini.pdf>.
- Bhattacharya, M., and E. G. Adelberger, 2002, Phys. Rev. C **65**, 055502.
- Bhattacharya, M., E. G. Adelberger, and H. E. Swanson, 2006, Phys. Rev. C **73**, 055802.
- Bonetti, R., *et al.*, 1999, Phys. Rev. Lett. **82**, 5205.
- Bowles, T. J., and G. T. Garvey, 1978, Phys. Rev. C **18**, 1447.
- Brown, L. S., and R. F. Sawyer, 1997, Ap. J. **489**, 968.
- Brown, T. A. D., *et al.*, 2007, Phys. Rev. C **76**, 055801.
- Brune, C. R., 2002, Phys. Rev. C **66**, 044611.
- Brune, C. R., R. W. Kavanagh, and C. E. Rolfs, 1994, Phys. Rev. C **50**, 2205.
- Buck, B., R. A. Baldock, and J. A. Rubio, 1985, J. Phys. G **11**, L11.
- Buck, B., and A. C. Merchant, 1988, J. Phys. G **14**, L211.
- Burbidge, E. M., G. R. Burbidge, W. A. Fowler, and F. Hoyle, 1957, Rev. Mod. Phys. **29**, 547.
- Burtebaev, N., S. B. Igamov, R. J. Peterson, R. Yarmukhamedov, and D. M. Zazulin, 2008, Phys. Rev. C **78**, 035802.
- Butler, M., and J.-W. Chen, 2001, Phys. Lett. B **520**, 87.
- Butler, M., J.-W. Chen, and X. Kong, 2001, Phys. Rev. C **63**, 035501.

- Butler, M., J.-W. Chen, and P. Vogel, 2002, Phys. Lett. B **549**, 26.
- Capel, P., and F. M. Nunes, 2006, Phys. Rev. C **73**, 014615.
- Carlson, J., D. O. Riska, R. Schiavilla, and R. B. Wiringa, 1991, Phys. Rev. C **44**, 619.
- Carmona, J. M., *et al.*, 2004, Astropart. Phys. **21**, 523.
- Carraro, C., A. Schaeffer, and S. E. Koonin, 1988, Ap. J. **331**, 565.
- Casella, C., *et al.*, 2002, Nucl. Phys. A **706**, 203.
- Caughlan, G. R., and W. A. Fowler, 1988, At. Data and Nucl. Data Tables **40**, 283.
- Chafa, A., *et al.*, 2005, Phys. Rev. Lett. **95**, 031101.
- Chafa, A., *et al.*, 2007, Phys. Rev. C **75**, 035810.
- Champagne, A. E., and M. L. Pitt, 1986, Nucl. Phys. A **457**, 367.
- Chen, J.-W., K. M. Heeger, and R. G. H. Robertson, 2003, Phys. Rev. C **67**, 025801.
- Chen, J.-W., T. Inoue, X. Ji, and Y. Li, 2005, Phys. Rev. C **72**, 061001(R).
- Chen, J.-W., G. Rupak, and M. J. Savage, 1999, Nucl. Phys. A **653**, 386.
- Christy, R., and I. Duck, 1961, Nucl. Phys. **24**, 89.
- Clayton, D. D., 1968, *Principles of Stellar Evolution and Nuclear Synthesis* (McGraw-Hill).
- Cohen, E. R., and B. N. Taylor, 1987, Rev. Mod. Phys. **59**, 1121.
- Confortola, F., *et al.*, 2007, Phys. Rev. C **75**, 065803.
- Costantini, H., *et al.*, 2008, Nucl. Phys. A **814**, 144.
- Costantini, H., *et al.*, 2009, Rep. Prog. Phys. **72**, 086301.
- Couder, M., *et al.*, 2008, Nucl. Inst. Meth. A **587**, 35.
- Couture, A., *et al.*, 2008, Phys. Rev. C **77**, 015802.
- Csoto, A., 1997, Phys. Lett. B **394**, 247.
- Csoto, A., and K. Langanke, 2000, Few-Body Syst. **29**, 121.
- Csoto, A., K. Langanke, S. E. Koonin, and T. D. Shoppa, 1995, Phys. Rev. C **52**, 1130.
- Cyburt, R. H., 2004, Phys. Rev. D **70**, 023505.
- Cyburt, R. H., and B. Davids, 2008, Phys. Rev. C **78**, 064614.
- Cyburt, R. H., B. Davids, and B. K. Jennings, 2004, Phys. Rev. C **70**, 045801.
- D'Agostini, G., 1994, Nucl. Inst. Meth. A **346**, 306.
- Das, P., and A. Ray, 2005, Phys. Rev. C **71**, 025801.
- Davids, B., A. V. Gruzinov, and B. K. Jennings, 2008, Phys. Rev. C **77**, 019801.
- Davids, B., and S. Typel, 2003, Phys. Rev. C **68**, 045802.
- Davids, B., *et al.*, 1998, Phys. Rev. Lett. **81**, 2209.
- Davids, B., *et al.*, 2001a, Phys. Rev. Lett. **86**, 2750.
- Davids, B., *et al.*, 2001b, Phys. Rev. C **63**, 065806.
- Davids, C. N., *et al.*, 1983, Phys. Rev. C **28**, 885.
- Davis Jr., R., 1994, Prog. Part. Nucl. Phys. **32**, 13.
- Davis Jr., R., D. S. Harmer, and K. C. Hoffman, 1968, Phys. Rev. Lett. **20**, 1205.
- De Braekeleer, L., *et al.*, 1995, Phys. Rev. C **51**, 2778.
- Descouvemont, P., 2004, Phys. Rev. C **70**, 065802.
- Descouvemont, P., and D. Baye, 1988, Nucl. Phys. A **487**, 420.
- Descouvemont, P., and D. Baye, 1994, Nucl. Phys. A **567**, 341.
- Descouvemont, P., and D. Baye, 2010, Rep. Prog. Phys. **73**, 036301.
- Descouvemont, P., *et al.*, 2004, At. Data and Nucl. Data Tables **88**, 203.
- Di Leva, A., *et al.*, 2008, Nucl. Inst. Meth. A **595**, 381.
- Di Leva, A., *et al.*, 2009, Phys. Rev. Lett. **102**, 232502.
- DIANA Collaboration, 2009, http://ecrgroup.lbl.gov/Astro_DUSEL.htm.
- Donoghue, T. R., *et al.*, 1983, Phys. Rev. C **28**, 875.
- Dubovichenko, S. B., and A. V. Dzhezairov-Kakhramanov, 1995, Phys. Atom. Nucl. **58**, 579.
- Dwarakanath, M. R., and H. Winkler, 1971, Phys. Rev. C **4**, 1532.
- Efros, V. D., W. Leidemann, G. Orlandini, and N. Barnea, 2007, J. Phys. G **34**, R459.
- Engstler, S. A., *et al.*, 1988, Phys. Lett. B **202**, 179.
- Engstler, S. A., *et al.*, 1992, Z. Phys. A **342**, 471.
- Epelbaum, E., 2006, Prog. Part. Nucl. Phys. **57**, 654.
- Esbensen, H., 2004, Phys. Rev. C **70**, 047603.
- Esbensen, H., 2009, Phys. Rev. C **80**, 024608.
- Esbensen, H., and G. F. Bertsch, 1996, Nucl. Phys. A **600**, 37.
- Esbensen, H., G. F. Bertsch, and K. A. Snover, 2005, Phys. Rev. Lett. **94**, 042502.
- Farmer, B. J., and C. M. Class, 1960, Nucl. Phys. **15**, 626.
- Fernandez, J. C., R. Crespo, and F. M. Nunes, 2000, Phys. Rev. C **61**, 064616.
- Fetisov, V. N., and Y. S. Kopysov, 1972, Phys. Lett. B **40**, 602.
- Filippone, B. W., A. J. Elwyn, C. N. Davids, and D. D. Koetke, 1983, Phys. Rev. C **28**, 2222.
- Fiorentini, G., C. Rolfs, F. L. Villante, and B. Ricci, 2003, Phys. Rev. C **67**, 014603.
- Fitzgerald, R., *et al.*, 2005, Nucl. Phys. A **748**, 351.
- Flambaum, V. V., and V. G. Zelevinsky, 1999, Phys. Rev. Lett. **83**, 3108.
- Formicola, A., *et al.*, 2003, Nucl. Inst. Meth. A **507**, 609.
- Formicola, A., *et al.*, 2004, Phys. Lett. B **591**, 61.
- Fowler, W. A., 1972, Nature **238**, 24.
- Fox, C., *et al.*, 2004, Phys. Rev. Lett. **93**, 081102.
- Fox, C., *et al.*, 2005, Phys. Rev. C **71**, 055801.
- Fukuda, S., *et al.*, 2001, Phys. Rev. Lett. **86**, 5651.
- Fukuda, Y., *et al.*, 1996, Phys. Rev. Lett. **77**, 1683.
- Gagliardi, C. A., *et al.*, 1999, Phys. Rev. C **59**, 1149.
- Gavrin, V. N., *et al.*, 2003, Nucl. Phys. B **118**, 39.
- Gazit, D., 2008, Phys. Lett. B **666**, 472.
- Gazit, D., S. Quaglioni, and P. Navrátil, 2009, Phys. Rev. Lett. **103**, 102502.
- Gialanella, L., *et al.*, 2000, Eur. Phys. J. A **7**, 303.
- Goldstein, G., P. Capel, and D. Baye, 2007, Phys. Rev. C **76**, 024608.
- Golser, R., and D. Semrad, 1991, Phys. Rev. Lett. **66**, 1831.
- Greife, U., *et al.*, 1994, Nucl. Inst. Meth. A **350**, 327.
- Greife, U., *et al.*, 1995, Z. Phys. A **351**, 107.
- Griffiths, G. M., M. Lal, and C. D. Scarfe, 1963, Can. J. Phys. **41**, 724.
- Griffiths, G. M., E. A. Larson, and L. P. Robertson, 1962, Can. J. Phys. **40**, 402.
- Grineviciute, J., *et al.*, 2008, J. Phys. G **35**, 055201.
- Gruzinov, A. V., 1998, Ap. J. **469**, 503.
- Gruzinov, A. V., and J. N. Bahcall, 1998, Ap. J. **504**, 996.
- Gyurky, G., *et al.*, 2007, Phys. Rev. C **75**, 035805.
- Hagino, K., and A. B. Balantekin, 2002, Phys. Rev. C **66**, 055801.
- Halderson, D., 2006, Phys. Rev. C **73**, 024612.
- Hammache, F., *et al.*, 1998, Phys. Rev. Lett. **80**, 928.
- Hammache, F., *et al.*, 2001, Phys. Rev. Lett. **86**, 3985.
- Hardy, J. C., and I. S. Towner, 2009, Phys. Rev. C **79**, 055502.
- Hass, M., *et al.*, 1999, Phys. Lett. B **462**, 237.
- Haxton, W. C., P. D. Parker, and C. E. Rolfs, 2006, Nucl. Phys. A **777**, 226.

- Haxton, W. C., and A. M. Serenelli, 2008, *Ap. J.* **687**, 678.
- Haxton, W. C., *et al.*, 2007, *Nucl. Inst. Meth. A* **570**, 414.
- Hebbard, D. F., 1960, *Nucl. Phys.* **15**, 289.
- Holmgren, H. P., and R. Johnston, 1958, *Bull. Am. Phys. Soc.* II **3**, 26.
- Holmgren, H. P., and R. Johnston, 1959, *Phys. Rev.* **113**, 1556.
- Holt, R. J., H. E. Jackson, R. M. Laszewski, J. E. Monahan, and J. R. Specht, 1978, *Phys. Rev. C* **18**, 1962.
- Hutcheon, D. A., *et al.*, 2003, *Nucl. Inst. Meth. A* **498**, 190.
- Iben, Jr., I., K. Kalata, and J. Schwartz, 1967, *Ap. J.* **150**, 1001.
- Iliadis, C., C. Angulo, P. Descouvemont, M. Lugaro, and P. Mohr, 2008, *Phys. Rev. C* **77**, 045802.
- Imbriani, G., *et al.*, 2005, *Eur. Phys. J. A* **25**, 455.
- Israelian, G., *et al.*, 2009, *Nature* **462**, 189.
- Iwasa, N., *et al.*, 1996, *J. Phys. Soc. Japan* **65**, 1256.
- Iwasa, N., *et al.*, 1999, *Phys. Rev. Lett.* **83**, 2910.
- Jennings, B. K., S. Karataglidis, and T. D. Shoppa, 1998a, *Phys. Rev. C* **58**, 579.
- Jennings, B. K., S. Karataglidis, and T. D. Shoppa, 1998b, *Phys. Rev. C* **58**, 3711.
- Johnson, C. W., E. Kolbe, S. E. Koonin, and K. Langanke, 1992, *Ap. J.* **392**, 320.
- Junghans, A. R., K. A. Snover, E. C. Mohrmann, E. G. Adelberger, and L. Buchmann, 2010, *Phys. Rev. C* **81**, 012801(R).
- Junghans, A. R., *et al.*, 2002, *Phys. Rev. Lett.* **88**, 041101.
- Junghans, A. R., *et al.*, 2003, *Phys. Rev. C* **68**, 065803.
- Junker, M., *et al.*, 1998, *Phys. Rev. C* **57**, 2700.
- Kajino, T., 1986, *Nucl. Phys. A* **460**, 559.
- Kamionkowski, M., and J. N. Bahcall, 1994, *Ap. J.* **420**, 884.
- Kaplan, D. B., M. J. Savage, and M. B. Wise., 1996, *Nucl. Phys. B* **478**, 629.
- Kikuchi, T., *et al.*, 1997, *Phys. Lett. B* **391**, 261.
- Kikuchi, T., *et al.*, 1998, *Eur. Phys. J. A* **3**, 213.
- Kim, B. T., T. Izumoto, and K. Nagatani, 1981, *Phys. Rev. C* **23**, 33.
- Kim, K. H., M. H. Park, and B. T. Kim, 1987, *Phys. Rev. C* **35**, 363.
- Kirsten, T., *et al.*, 2003, *Nucl. Phys. B* **118**, 33.
- Kobzev, G. A., I. T. Iakubov, and M. M. Popovich, 1995, *Transport and Optical Properties of a Nonideal Plasma* (Plenum).
- Kolbe, E., K. Langanke, and H. J. Assenbaum, 1988, *Phys. Lett. B* **214**, 169.
- Kong, X., and F. Ravndal, 2001, *Phys. Rev. C* **64**, 044002.
- Krauss, A., *et al.*, 1987, *Nucl. Phys. A* **467**, 273.
- Krauss, H., K. Grün, T. Rauscher, and H. Oberhummer, 1993, *Annalen der Physik* **2**, 256.
- Kudomi, N., *et al.*, 2004, *Phys. Rev. C* **69**, 015802.
- Kurylov, A., M. J. Ramsey-Musolf, and P. Vogel, 2003, *Phys. Rev. C* **67**, 035502.
- La Cognata, M., V. Z. Goldberg, A. M. Mukhamedzhanov, C. Spitaleri, and R. E. Tribble, 2009, *Phys. Rev. C* **80**, 012801(R).
- La Cognata, M., *et al.*, 2007, *Phys. Rev. C* **76**, 065804.
- La Cognata, M., *et al.*, 2008, *Phys. Rev. Lett.* **101**, 152501.
- La Cognata, M., *et al.*, 2009, *Publ. Astron. Soc. Austral.* **26**, 237.
- La Cognata, M., *et al.*, 2010, *Ap. J.* **708**, 796.
- Lane, A. M., and R. G. Thomas, 1958, *Rev. Mod. Phys.* **30**, 257.
- Langanke, K., 1986, *Nucl. Phys. A* **457**, 351.
- Langanke, K., T. D. Shoppa, C. A. Barnes, and C. Rolfs, 1996, *Phys. Lett. B* **369**, 211.
- Lattuada, M., *et al.*, 2001, *Ap. J.* **562**, 1076.
- Laubenstein, M., *et al.*, 2004, *Appl. Rad. Iso.* **61**, 167.
- Lemut, A., *et al.*, 2006, *Phys. Lett. B* **634**, 483.
- Limata, B. N., *et al.*, 2006, *Eur. Phys. J. A* **27**, 193.
- Liu, W., *et al.*, 1996, *Phys. Rev. Lett.* **77**, 611.
- Lorentz-Wirzba, H., *et al.*, 1979, *Nucl. Phys. A* **313**, 346.
- Ma, L., *et al.*, 1997, *Phys. Rev. C* **55**, 588.
- Mao, D., K. Mussack, and W. Däppen, 2009, *Ap. J.* **701**, 1204.
- Marcucci, L. E., K. M. Nollett, R. Schiavilla, and R. B. Wiringa, 2006, *Nucl. Phys. A* **777**, 111.
- Marcucci, L. E., M. Pervin, S. C. Pieper, R. Schiavilla, and R. B. Wiringa, 2008, *Phys. Rev. C* **78**, 065501.
- Marcucci, L. E., R. Schiavilla, S. Rosati, A. Kievsky, and M. Viviani, 2002, *Phys. Rev. C* **66**, 054003.
- Marcucci, L. E., M. Viviani, R. Schiavilla, A. Kievsky, and S. Rosati, 2005, *Phys. Rev. C* **72**, 014001.
- Marcucci, L. E., *et al.*, 2000, *Phys. Rev. C* **63**, 015801.
- Marta, M., *et al.*, 2008, *Phys. Rev. C* **78**, 022802(R).
- Mathews, G. J., R. C. Haight, R. G. Lanier, and R. M. White, 1983, *Phys. Rev. C* **28**, 879.
- McKeown, R. D., G. T. Garvey, and C. A. Gagliardi, 1980, *Phys. Rev. C* **22**, 738.
- Mei, D.-M., and A. Hime, 2006, *Phys. Rev. D* **73**, 053004.
- Mertelmeier, T., and H. M. Hofmann, 1986, *Nucl. Phys. A* **459**, 387.
- Mitler, H. E., 1977, *Ap. J.* **212**, 513.
- Moazen, B. H., *et al.*, 2007, *Phys. Rev. C* **75**, 065801.
- Mohr, P., 2009, *Phys. Rev. C* **79**, 065804.
- Mohr, P., *et al.*, 1993, *Phys. Rev. C* **48**, 1420.
- Morlock, R., *et al.*, 1997, *Phys. Rev. Lett.* **79**, 3837.
- Moro, A. M., R. Crespo, F. M. Nunes, and I. J. Thompson, 2003, *Phys. Rev. C* **67**, 047602.
- Mosconi, B., P. Ricci, E. Truhlik, and P. Vogel, 2007, *Phys. Rev. C* **75**, 044610.
- Motobayashi, T., *et al.*, 1994, *Phys. Rev. Lett.* **73**, 2680.
- Mukhamedzhanov, A., *et al.*, 2003, *Phys. Rev. C* **67**, 065804.
- Mukhamedzhanov, A. M., C. A. Gagliardi, and R. E. Tribble, 2001, *Phys. Rev. C* **63**, 024612.
- Mukhamedzhanov, A. M., and F. M. Nunes, 2002, *Nucl. Phys. A* **708**, 437.
- Mukhamedzhanov, A. M., and N. K. Timofeyuk, 1990, *Yad. Fiz.* **51**, 679.
- Mukhamedzhanov, A. M., *et al.*, 1997, *Phys. Rev. C* **56**, 1302.
- Mukhamedzhanov, A. M., *et al.*, 2008, *Phys. Rev. C* **78**, 015804.
- Nakamura, T., *et al.*, 2009, *Phys. Rev. C* **79**, 035805.
- Napolitano, J., S. J. Freedman, and J. Camp, 1987, *Phys. Rev. C* **36**, 298.
- Nathan, A. M., G. T. Garvey, P. Paul, and A. K. Warburton, 1975, *Phys. Rev. Lett.* **35**, 1137.
- Navrátil, P., C. A. Bertulani, and E. Caurier, 2006a, *Phys. Lett. B* **634**, 191.
- Navrátil, P., C. A. Bertulani, and E. Caurier, 2006b, *Phys. Rev. C* **73**, 065801.
- Neff, T., and H. Feldmeier, 2008, *J. Phys. Conf. Ser.* **111**, 012007.
- Neff, T., H. Feldmeier, and K. Langanke, 2010, *Proceedings of Science: 11th Symposium on Nuclei in the Cosmos*.
- Nelson, S. O., *et al.*, 2003, *Phys. Rev. C* **68**, 065804.
- Newton, J. R., *et al.*, 2010, *Phys. Rev. C* **81**, 045801.
- Nir-El, Y., *et al.*, 2007, *Phys. Rev. C* **75**, 012801(R).

- Nogga, A., *et al.*, 2003, Phys. Rev. C **67**, 034004.
- Nollett, K. M., 2001, Phys. Rev. C **63**, 054002.
- Nollett, K. M., S. C. Pieper, R. B. Wiringa, J. Carlson, and G. M. Hale, 2007, Phys. Rev. Lett. **99**, 022502.
- Nollett, K. M., R. B. Wiringa, and R. Schiavilla, 2001, Phys. Rev. C **63**, 024003.
- Norman, E. B., *et al.*, 1983a, Phys. Rev. C **27**, 1728.
- Norman, E. B., *et al.*, 1983b, Phys. Rev. C **28**, 1409.
- Norman, E. B., *et al.*, 2001, Phys. Lett. B **519**, 15.
- Nunes, F. M., R. Crespo, and I. J. Thompson, 1997a, Nucl. Phys. A **615**, 69.
- Nunes, F. M., R. Crespo, and I. J. Thompson, 1997b, Nucl. Phys. A **627**, 747.
- Nunes, F. M., R. Crespo, and I. J. Thompson, 1998, Nucl. Phys. A **634**, 527.
- Ogata, K., and C. A. Bertulani, 2009, Prog. Theor. Phys. **121**, 1399.
- Ogata, K., S. Hashimoto, Y. Iseri, M. Kamimura, and M. Yahiro, 2006, Phys. Rev. C **73**, 024605.
- Ogata, K., M. Yahiro, Y. Iseri, and M. Kamimura, 2003, Phys. Rev. C **67**, 011602(R).
- Ohtsuki, T., H. Yuki, M. Muto, J. Kasagi, and K. Ohno, 2004, Phys. Rev. Lett. **93**, 112501.
- Ortiz, C. E., A. Garcia, R. A. Waltz, M. Bhattacharya, and A. K. Komives, 2000, Phys. Rev. Lett. **85**, 2909.
- Park, T.-S., K. Kubodera, D.-P. Min, and M. Rho, 1998, Ap. J. **507**, 443.
- Park, T. S., *et al.*, 2003, Phys. Rev. C **67**, 055206.
- Parker, P. D., and R. W. Kavanagh, 1963, Phys. Rev. **131**, 2578.
- Paul, P., M. Suffert, and P. Gorodetzky, 1977, Phys. Lett. B **71**, 71.
- Peña-Garay, C., and A. Serenelli, 2008, arXiv:0811.2424 .
- Pervin, M., S. C. Pieper, and R. B. Wiringa, 2007, Phys. Rev. C **76**, 064319.
- Pieper, S. C., 2008, in *Proceedings of the "Enrico Fermi" Summer School, Course CLXIX, Nuclear Structure far from Stability: New Physics and new Technology*, edited by A. Covello, F. Iachello, R. A. Ricci, and G. Maino (IOS Press, Amsterdam), p. 111.
- Pieper, S. C., V. R. Pandharipande, R. B. Wiringa, and J. Carlson, 2001, Phys. Rev. C **64**, 014001.
- Pieper, S. C., K. Varga, and R. B. Wiringa, 2002, Phys. Rev. C **66**, 044310.
- Pieper, S. C., R. B. Wiringa, and J. Carlson, 2004, Phys. Rev. C **70**, 054325.
- Pizzone, R. G., *et al.*, 2009, Phys. Rev. C **80**, 025807.
- Prati, P., *et al.*, 1994, Z. Phys. A **350**, 171.
- Prati, P., *et al.*, 2008, in *Frontiers in Nuclear Structure, Astrophysics, and Reactions*, edited by P. Demetriou, R. Julin, and S. V. Harissopulos (AIP, Vol. 1012), p. 305.
- Pudliner, B. S., V. R. Pandharipande, J. Carlson, and R. B. Wiringa, 1995, Phys. Rev. Lett. **74**, 4396.
- Quaglioni, S., and P. Navrátil, 2009, Phys. Rev. C **79**, 044606.
- Quarati, P., and A. M. Scarfone, 2007, Ap. J. **666**, 1303.
- Quarati, P., and A. M. Scarfone, 2009, J. Phys. G **36**, 025203.
- Raiola, F., *et al.*, 2004, Eur. Phys. J. A **19**, 283.
- Ramírez, R., J. Meléndez, and M. Asplund, 2009, A.&A. **508**, L17.
- Ray, A., *et al.*, 1999, Phys. Lett. B **455**, 69.
- Ray, A., *et al.*, 2002, Phys. Lett. B **531**, 187.
- Ray, A., *et al.*, 2006, Phys. Rev. C **73**, 034323.
- Redder, A., *et al.*, 1982, Z. Phys. A **305**, 325.
- Reifarth, R., *et al.*, 2008, Phys. Rev. C **77**, 015804.
- Riisager, K., and A. S. Jensen, 1993, Phys. Lett. B **301**, 6.
- Riska, D. O., 1984, Phys. Scr. **31**, 471.
- Robertson, R. G. H., 1973, Phys. Rev. C **7**, 543.
- Rogalla, R., *et al.*, 2003, Nucl. Inst. Meth. A **513**, 573.
- Rolfs, C., 1973, Nucl. Phys. A **217**, 29.
- Rolfs, C., 2001, Prog. Part. Nucl. Phys. **46**, 23.
- Rolfs, C., and W. S. Rodney, 1974, Nucl. Phys. A **235**, 450.
- Rolfs, C., and E. Somorjai, 1995, Nucl. Inst. Meth. B **99**, 297.
- Rowland, C., C. Iliadis, and A. E. Champagne, 2002, Nucl. Inst. Meth. A **480**, 610.
- Runkle, R. C., *et al.*, 2005, Phys. Rev. Lett. **94**, 082503.
- Sagara, K., *et al.*, 2005, Nucl. Phys. A **758**, 427.
- Salpeter, E. E., 1954, Aust. J. Phys. **7**, 373.
- Schiavilla, R., R. B. Wiringa, V. R. Pandharipande, and J. Carlson, 1992, Phys. Rev. C **45**, 2628.
- Schiavilla, R., *et al.*, 1998, Phys. Rev. C **58**, 1263.
- Schmid, G. J., *et al.*, 1995, Phys. Rev. C **52**, R1732.
- Schmid, G. J., *et al.*, 1996, Phys. Rev. Lett. **76**, 3088.
- Schröder, U., *et al.*, 1987, Nucl. Phys. A **467**, 240.
- Schümann, F., *et al.*, 2003, Phys. Rev. Lett. **90**, 232501.
- Schümann, F., *et al.*, 2006, Phys. Rev. C **73**, 015806.
- Schürmann, D., *et al.*, 2008, Phys. Rev. C **77**, 055803.
- Segrè, E., 1947, Phys. Rev. **71**, 274.
- Serpico, P. D., *et al.*, 2004, J. Cosmology and Astro-Part. Phys. **12**, 10.
- Shoppa, T. D., S. E. Koonin, K. Langanke, and R. Seki, 1993, Phys. Rev. C **48**, 837.
- Singh, B. S. N., M. Hass, Y. Nir-El, and G. Haquin, 2004, Phys. Rev. Lett. **93**, 262503.
- Sirlin, A., 1967, Phys. Rev. **164**, 1767.
- Snover, K. A., and A. E. Hurd, 2003, Phys. Rev. C **67**, 055801.
- Spitaleri, C., *et al.*, 2001, Phys. Rev. C **63**, 055801.
- Spitaleri, C., *et al.*, 2004, Phys. Rev. C **69**, 055806.
- Stahler, S. W., 1988, Ap. J. **322**, 804.
- Stonehill, L. C., J. A. Formaggio, and R. G. H. Robertson, 2004, Phys. Rev. C **69**, 015801.
- Strieder, F., C. Rolfs, C. Spitaleri, and P. Corvisiero, 2001, Naturwissenschaften **88**, 461.
- Strieder, F., *et al.*, 1998, Eur. Phys. J. A **3**, 1.
- Strieder, F., *et al.*, 2001, Nucl. Phys. A **696**, 219.
- Summers, N. C., and F. M. Nunes, 2005, J. Phys. G **31**, 1437.
- Summers, N. C., and F. M. Nunes, 2008, Phys. Rev. C **78**, 011601(R).
- Tabacaru, G., *et al.*, 2006, Phys. Rev. C **73**, 025808.
- Tombrello, T., 1965, Nucl. Phys. **71**, 459.
- Tombrello, T. A., and P. D. Parker, 1963a, Phys. Rev. **131**, 2582.
- Tombrello, T. A., and P. D. Parker, 1963b, Phys. Rev. **130**, 1112.
- Trache, L., F. Carstoiu, C. A. Gagliardi, and R. E. Tribble, 2004, Phys. Rev. C **69**, 032802(R).
- Tribble, R. E., and G. T. Garvey, 1974, Phys. Rev. Lett. **32**, 314.
- Tribble, R. E., and G. T. Garvey, 1975, Phys. Rev. C **12**, 967.
- Tumino, A., *et al.*, 2003, Phys. Rev. C **67**, 065803.
- Typel, S., and G. Baur, 2005, Nucl. Phys. A **759**, 247.
- Typel, S., G. Blüge, K. Langanke, and W. A. Fowler, 1991, Z. Phys. A **339**, 249.
- Typel, S., H. H. Wolter, and G. Baur, 1997, Nucl. Phys. A **613**, 147.
- Viviani, M., A. Kievsky, and S. Rosati, 1995, Few-Body Syst. **18**, 25.
- Viviani, M., S. Rosati, and A. Kievsky, 1998, Phys. Rev. Lett. **81**, 1580.

- Voytas, P. A., *et al.*, 2001, Phys. Rev. Lett. **88**, 012501.
- Walliser, H., H. Kanada, and Y. C. Tang, 1984, Nucl. Phys. A **419**, 133.
- Walliser, H., Q. K. K. Liu, H. Kanada, and Y. C. Tang, 1983, Phys. Rev. C **28**, 57.
- Wang, B., *et al.*, 2006, Eur. Phys. J. A **28**, 375.
- Warburton, E. K., 1986, Phys. Rev. C **33**, 303.
- Weissman, L., *et al.*, 1998, Nucl. Phys. A **630**, 678.
- Wiescher, M., *et al.*, 1980, Nucl. Phys. A **349**, 165.
- Wiescher, M., *et al.*, 2010, Ann. Rev. Nucl. Part. Sci. **61**, in press.
- Wilkinson, D. H., and D. E. Alburger, 1971, Phys. Rev. Lett. **26**, 1127.
- Williams, R. D., and S. E. Koonin, 1981, Phys. Rev. C **23**, 2773.
- Winter, W. T., S. J. Freedman, K. E. Rehm, and J. P. Schiffer, 2006, Phys. Rev. C **73**, 025503.
- Winter, W. T., *et al.*, 2003, Phys. Rev. Lett. **91**, 252501.
- Wiringa, R. B., 1991, Phys. Rev. C **43**, 1585.
- Wiringa, R. B., R. A. Smith, and T. L. Ainsworth, 1984, Phys. Rev. C **29**, 1207.
- Wiringa, R. B., V. G. J. Stoks, and R. Schiavilla, 1995, Phys. Rev. C **51**, 38.
- Xu, H. M., C. A. Gagliardi, R. E. Tribble, A. M. Mukhamedzhanov, and N. K. Timofeyuk, 1994, Phys. Rev. Lett. **73**, 2027.
- Yamada, Y., *et al.*, 2004, Phys. Lett. B **579**, 265.
- Yamaguchi, H., *et al.*, 2009, Phys. Lett. B **672**, 230.
- Ziegler, J. F., *et al.*, 2008, SRIM program, version 2008, <http://www.srim.org>.
- Zyskind, J., and P. D. Parker, 1979, Nucl. Phys. A **320**, 404.